# THE NANOSTRUCTURE AND DEGRADATION OF C-S-H IN PORTLAND AND BLENDED CEMENTS

Ana Violeta Oliveira Morais de Sousa Girão

Submitted in accordance with the requirements for the degree of Doctor of Philosophy (PhD).

The University of Leeds

Faculty of Engineering - School of Civil Engineering

Submission date: April /2007.

The candidate confirms that the work submitted is her own and appropriate credit has been given where reference has been made to the work of others.

# ACKNOWLEDGEMENTS

I am thankful to the Engineering and Physical Sciences Research Council for the funding under Grant No. GR/S45874/01.

First, I would like to gratefully thank Dr. Ian G. Richardson for all the supervision, encouragement, support and help provided, as well as for all the useful discussions.

Second, I would like to thank all the people involved in the project and that provided me with useful feedback and invaluable insights: Dr. E. Gartner (Lafarge Central Research), Dr. C. Porteneuve (W. R. Grace & Co), Dr. J. Hill (U.K. Nirex Ltd) and Miss J. Sagar (Castle Cement). I am also very thankful to everyone in LEMAS, especially Prof. R. Brydson, Dr. A. Brown and Mr. J. Harrington for all the electron microscopy training, help and support. I also would like to thank Dr. H. Dyson for all the knowledge and information kindly passed to me, as well as for all the support, patience and friendship.

Third, I am very thankful to all my colleagues and staff members that somehow always encouraged me along the way, in particular my very good friends Saiful, Qiu, Rachel, Stuart and Helen. Thank you so much for all your patience, support and encouragement during the greatest time I had during all this time! Thank you so much!!!

Fourth, I am so very thankful to my dearest and breath-taking friends Filipa, Hugo, Luciano, Rob, Fiona and Lisa! I thank you deeply for your love, friendship, support, patience and for just being there when I really needed a friend! Thank you all so much from the bottom of my heart, where I will always carry you!!!! I also thank my good friends Eva, Dan and Fabrizio!

Fifth, I thank all my friends, family for putting up three years without me around! You were always on my heart and my mind!

Finally last, but always first in my heart, I deeply thank my mother and my sister that always encouraged me, gave me so much support and put up with my absence for three years! I am so lucky in having you always by my side! I love you both very very much!!!! *Ad eternum*!

# ABSTRACT

The microstructure and composition of water and KOH activated hardened pastes of commercial neat white Portland cement (WPC) and blends with 30% fly ash (PFA) have been characterised using a multi-technique approach, with particular emphasis on the nature of the C-S-H phase. The neat and fly ash blended pastes were activated with water or a 5M KOH solution and cured for one year at 25°C, one month at 55°C and one month at 85°C. The mean length of the aluminosilicate anion structure of C-S-H ($^{29}$Si MAS NMR) increased with age and it was higher in the fly ash blended systems. Formulae were presented for the average structural units in the C-S-H present in the systems analysed by TEM-EDX. SEM micrographs showed that as hydration occurred, the microstructure became denser because outer product C-S-H was formed in the water filled spaces and additional C-S-H resulted from the pozzolanic reaction. The chemical composition of C-S-H could not be determined by SEM-EDX because of intermixing with other phases; TEM-EDX was necessary. Inner product C-S-H morphology was fine and homogeneous and that of outer product C-S-H was fibrillar in the water activated systems and foil-like with alkali activation. Fly ash replacement did not change the morphology of Ip and Op C-S-H. Small fully hydrated cement and PFA particles were filled with a less dense Ip C-S-H with morphology very similar to the foil-like one. TEM-EDX showed that, in general, the mean Ca/(Al+Si) atomic ratio was lower in the water activated blends than that in the neat cement pastes due to the fly ash reaction. The composition-structure data were discussed in terms of models for the nanostructure of C-S-H

Higher curing temperature accelerated the rate of the cement hydration. The mean length of the aluminosilicate of the C-S-H anions was much higher than that of C-S-H formed at lower temperatures, and it was also higher in the blended pastes than with neat cement. Backscattered electron images showed that the grey level of C-S-H in the systems cured at 55°C and 85°C was in places quite similar to that of the calcium hydroxide: that is, it was brighter than in pastes cured at lower temperature. SEM also showed that the microstructure of the systems cured at higher temperature exhibited non uniform porosity. Inner product C-S-H with a fine scale, homogeneous morphology, was abundant in all systems cured at 55°C and 85°C. Op C-S-H was generally fibrillar with water, and foil-like with alkali. However, the higher temperature curing did result

in coarser fibrillar morphology (water activated systems) than that formed at lower temperatures.

The C-S-H gel formed in the commercial WPC-30% PFA blended paste hydrated for one year at 25°C and water leached for twelve weeks was also characterised in this work. A matrix effect was clearly observed by $^{29}$Si MAS NMR. Cross-linking of the aluminosilicate anion structure of C-S-H occurred after leaching the sample for four weeks. Formulae were also presented for the average structural units in the C-S-H present in the unleached and four weeks water leached systems analysed by TEM-EDX. Ip C-S-H morphology was fine and homogeneous and Op C-S-H had fibrillar morphology. There were many areas in the microstructure of the leached sample where Op C-S-H with foil-like morphology coexisted with fibrillar Op C-S-H.

# TABLE OF CONTENTS

# LIST OF TABLES

# LIST OF FIGURES

# LIST OF ABBREVIATIONS AND SYMBOLS

**A** – Aluminium oxide ($Al_2O_3$)

**AFm** - $Al_2O_3$-$Fe_2O_3$-mono phases

**AFt** - $Al_2O_3$-$Fe_2O_3$-tri phases

**$Al^{oct}$ or Al[VI]** - Octahedrally coordinated aluminium

**$Al^{tet}$ or Al[IV]** – Tetrahedrally coordinated aluminium

**ASR** – Alkali-silica reaction

**ASTM** - American Society for Testing and Materials

**BEI** – Backscattered Electron Imaging

**$\alpha$-$C_3S$** – $\alpha$ Polymorph phase of tricalcium silicate ($Ca_3SiO_5$)

**$\beta$-$C_2S$** – $\beta$ Polymorph phase of Dicalcium silicate ($Ca_2SiO_4$)

**C** – Calcium oxide (CaO)

$\bar{C}$ - Carbon dioxide ($CO_2$)

**cc/g** – Cubic centilitre per gram

**cm** - Centimetre

**C/S** – Calcium/silicate ratio (Ca/Si)

**$C_2S$** – Dicalcium silicate ($Ca_2SiO_4$)

**$C_3A$** - Tricalcium aluminate phases ($Ca_3Al_2O_6$)

**$C_3S$** – Tricalcium silicate ($Ca_3SiO_5$)

**$C_4AF$** - Calcium aluminate ferrite phases ($Ca_2Al_xFe_{2-x}O_5$)

**CH** – Calcium hydroxide ($Ca(OH)_2$)

**CP MAS NMR** – Cross-Polarization Magic Angle Spinning Solid-State Nuclear Magnetic Resonance

**C-S-H** – Calcium silicate hydrate

**DEF** – Delayed ettringite formation

**DSC** – Differential Scanning Calorimetry

**DTG** - Differential Thermogravimetric Analysis

**EELS** – Electron Energy Loss Spectroscopy

**EGA** – Evolved Gas Analysis

**ELNES** – Energy-Loss Near Edge Spectroscopy

**EMPA or EPMA** – Electron Microprobe Analysis

**F** – Iron oxide ($Fe_2O_3$)

**Ggbfs or ggbs** – Ground granulated blast furnace slag

**H** – Water ($H_2O$)

**HD** – High density

**Ip** - Calcium silicate hydrate inner product

**K** – Potassium oxide ($K_2O$)

**LD** – Low density

**LOI** – Loss on ignition

**M** – Magnesium oxide (MgO)

***M*** – Molarity ($mol/dm^3$)

**MAS NMR** – Magic Angle Spinning Solid-State Nuclear Magnetic Resonance

**MCL** – Mean silicate (aluminosilicate) chain length

**ml** - Millilitre

**mm** - Millimetre

**μm** – Micrometer

**N** – Sodium oxide (NaO)

**nm** - Nanometer

**NMR** – Nuclear Magnetic Resonance

**Op** – Calcium silicate hydrate outer product

**OPC** – Ordinary Portland cement

**P** – Phosphorus pentoxide ($P_2O_5$)

**PC** – Portland cement

**PFA** – Pulverised fly ash

**ppm** - Parts per million

**$Q^0$** – Isolated silicate unit

**$Q^1$** – Disilicate or chain end silicate units

**$Q^2$** – Chain middle silicate groups

**$Q^2$(1Al)** – Silicate tetrahedron connected to another silicate tetrahedron and one $AlO_4$ tetrahedron via bridging oxygene

**$Q^3$** – Chain branching or cross linking silicate groups

**$Q^4$** – Three dimensional framework silicate groups

**$Q^n$(mAl) or Si(nAl)** – Silicate tetrahedron Q connected via n (number of bridging oxygen) connected to mAl and (n-m) silicate atoms {(n=O-4) and (m=O+On)}

**QXDA** – Quantitative X-ray Diffraction Analysis

**S** – Silicate ($SiO_2$)

$\bar{S}$ - Sulfur trioxide ($SO_3$)

**S/S** – Solution/solid ratio

**SEM/EDX** – Scanning Electron Microscopy/ Energy Dispersive X-ray Analysis

δ - Chemical shift

**STA** – Simultaneous Thermal Analysis (Thermogravimetric Analysis and Differential Thermal Analysis (TG/DTA))

**T** – Titanium dioxide ($TiO_2$)

**T/CH** - Tobermorite/calcium hydroxide point of view (Richardson and Groves' structural model for the C-S-H gel)

**T/J** – Tobermorite/jennite point of view (Taylor's structural model for the C-S-H gel)

**TEM-EDX** – Transmission Electron Microscopy-Energy Dispersive X-ray Analysis

**TG** – Thermogravimetric Analysis

**TMS** - Trimethylsilylation

**TMS-GPC** – Trimethylsilylation-Gel Permeation Chromatography

**w/s** – Water/solid ratio

**WPC** – White Portland cement

**XRD** – X-ray Diffraction (powder)

**XRF** – X-ray Fluorescence

# I – INTRODUCTION

## 1.1 – GENERAL INTRODUCTION

Concrete is a building material prepared from several constituent materials, usually made from the combination of a cement binder, mineral aggregates and water. Cement is a powdered material (clinker) that reacts with water, developing strong adhesive qualities and forming a hardened mass. These cements are more appropriately known as hydraulic cements, and Portland cements are the most widely used.

Several products result from the exothermic hydration reaction, and the calcium silicate hydrate gels, the C-S-H gels, are the main binding phases in all Portland cement-based systems. Therefore, the study of C-S-H is fundamental to the understanding of cement chemistry and its performance. The morphology and the micro/nanostructure of C-S-H define the final properties of a hardened cement paste, such as strength and durability, capillary pore network, permeability to water or other liquids/solutions, and rate at which ions/gases diffuse in it. These properties are also influenced by many factors such as the chemical composition of the cement, the solid/solution ratio, the curing temperature, the degree of hydration and the presence of other additives[1].

The chemical composition of C-S-H varies according to the nature of the cement-based system. C-S-H is generally amorphous but, in a short-range scale, similarities are found with the natural crystalline minerals tobermorite and jennite. Tobermorite, $Ca_4(Si_6O_{18}H_2)\cdot Ca\cdot 4H_2O$ with a Ca/Si ratio of 0.83, presents a layered structure containing linear silicate chains of the 'dreierkette' form. Jennite, $Ca_9Si_6O_{18}(OH)_6\cdot 8H_2O$, also has dreierkette silicate chains but a higher Ca/Si ratio of 1.5. Consequently, several models for the C-S-H structure were proposed and most of them can be divided in two different categories: the tobermorite–'solid-solution' calcium hydroxide, denominated as the T/CH viewpoint; and the tobermorite-jennite, denominated as the T/J viewpoint. Richardson and Groves' structural model proposed for C-S-H in 1992[2], includes formulations for both structural viewpoints and enables

the structural characterisation of the amorphous C-S-H gel, as well as its application onto a diverse range of cementitious systems[3].

Blended cements containing recovered waste products from industry, like ground granulated blast furnace slag (ggbfs or ggbs), pulverised fly ash (PFA), or microsilica, are also widely used. Hence, it is a way of replacing part of the Portland cement and enhancing its properties, as well as a method of recycling some industry waste products. Fly ash is a pozzolanic replacement that reacts with calcium hydroxide previously formed in the cement hydration, to give additional C-S-H[1].

As stated before, many factors affect the nature of C-S-H, and an example is the curing temperature. Heat curing is often used to accelerate early age strength of precast concrete. Precast heat-cured concrete is frequently used in walls, steps, posts, pad stones, stairs, floors, etc... Curing at high temperature has many implications on the concrete properties, more particularly in the C-S-H chemical composition, micro/nanostructure and, consequently, in the physical properties, like durability, creep and shrinkage. Characterisation of C-S-H in cement-based systems cured at high temperature provides very significant information, especially regarding issues like delayed ettringite formation (DEF) and alkali-silica reaction (ASR) that induce concrete expansion and cracking.

Degradation of cement-based systems is considered to be an atypical hydration process. Leaching is a kind of degradation particularly important for the long-term storage of nuclear and other forms of wastes such as concrete dams. In water leaching degradation, it is expected that the calcium hydroxide will be the first hydrate phase to be leached, followed by C-S-H. After all of the calcium hydroxide is leached, C-S-H will respond by rearranging itself into a highly polymerized phase. As leaching proceeds, the C-S-H structure collapses giving a disintegrated cement paste.

## 1.2 – POINTS OF STUDY

The exact nature of the C-S-H phases is not yet completely understood and the aim of this work was to obtain more detailed information regarding the morphology and the micro/nanostructure of the C-S-H gels formed in neat and blended pastes. In order to study the micro/nanostructure of C-S-H, the proposed work had the following goals:

- Determination of the chemical composition and silicate anion structure of C-S-H in commercial neat and blended white Portland cement, with class F pulverised fly ash;

- Find the most appropriate structural model for the nanostructure of C-S-H in the different studied systems;

- Determination of the degradation characteristics of C-S-H when undergoing water leaching.

The proposed objectives can only be achieved with a multi-technique approach. Analytical Transmission Electron Microscopy (TEM-EDX) and $^{29}Si$ Solid-State Nuclear Magnetic Resonance (MAS NMR) were the main techniques used in order to characterise the chemical composition and micro/nanostructure of C-S-H. Scanning electron microscopy with analytical analysis (SEM-EDX), thermogravimetric techniques (STA), powder X-ray Diffraction (XRD), and isothermal calorimetry were also used. TEM-EDX and NMR provided important data to establish the silicate anion structure of C-S-H as well as the appropriate structural model in which the systems fit. In addition, TEM and SEM-EDX provided qualitative data on the morphology of the C-S-H gels, very useful for the evaluation of the heterogeneity of the particles and also for a general overview of the cement paste surface.

The cement-based system used was a white Portland cement (WPC), as a control sample. WPC was chosen in order to avoid a high iron content that would cause some problems in the MAS NMR acquisition and interpretation. Two WPC blends with a

30% and 60% of fly ash replacement were also prepared. The neat pastes were prepared to water/cement ratio of 0.5 and the blended pastes to a water/binder ratio of 0.5. The neat and blended pastes were activated with distilled water or an alkali solution, a KOH 5M solution. The degree of hydration of the neat and blended cement pastes was followed at 25°C and established for one day, one month and one year. The effect of curing temperature at 55°C and 85°C for one month was carried out. The latter effect was compared with the effect of curing the systems at 25°C. Degradation by water leaching of a water activated 30% PFA blended paste after one year of hydration, was also performed.

Understanding the micro/nanostructure of the C-S-H gels in several commercial cementitious systems will help out engineers to predict the properties and performance of concrete. This information will also provide fundamental assistance in modelling encapsulation of radioactive and hazardous wastes in commercial cement-based systems.

## 1.3 – THESIS OUTLINE

A literature review is presented in Chapter II. This review covers the general chemical composition of Portland cement and the separate hydration of each of the main components of cement clinker, particularly the hydration of alite and belite. Several of the proposed structural models for C-S-H are discussed and compared. The formation and characterisation of the C-S-H phase by various techniques used in this work are also considered. Separate sections were created for literature related to white Portland cement and fly ash. In the end, final sections consider some atypical hydration processes such as curing at high temperature and degradation of cement-based systems.

In Chapter III, the experimental procedures used in this work are described. Each section is started by a general explanation regarding the experimental technique, followed by a detailed description of the applied method.

The experimental results and discussion are exposed in Chapters IV to VII. Chapter IV deals with the degree of hydration at room temperature, and Chapters V and VI with the effect of curing temperature at 55°C and 85°C. Chapter VII covers the degradation study by water leaching.

Finally, Chapter VIII is a summary of the main conclusions considered in this work. This chapter also includes some suggestions for future works.

# II – LITERATURE REVIEW

## 2.1 – PORTLAND CEMENT: CHEMICAL COMPOSITION

In this first section, the mineral and chemical composition of Portland cement is discussed. The hydration of the individual clinker minerals is also considered as well as their significance and part in the total hydration of a Portland cement.

Hydraulic cements are powders that set and harden through chemical reactions with an appropriate amount of water, and continue to develop strength even after they have set. The more important properties of a cement paste are setting, microstructure, bond formation, density, pore structure, surface area and mechanical properties. These properties will have a major influence in the final properties of a concrete such as workability, setting, bleeding and segregation, and its mechanical properties[1].

The most important known hydraulic cement is Portland cement (PC). The hydration of a Portland cement is a complex process because it is a multi-component system and there are many factors that influence its kinetics, such as:

- The phase composition of the cement and presence of foreign ions within the individual clinker phases;
- The fineness of the cement, its particle size distribution and specific surface area;
- The water/solid (w/s) or solution/solid ratio (s/s) used;
- The presence of chemical admixtures;
- The presence of additives, such as ground granulated blast furnace slag (ggbfs or ggbs), pulverised fly ash (PFA), etc.

Bearing in mind the complexity of the whole process of Portland cement hydration, it is useful to discuss first the hydration of the individual clinker minerals present in it.

A different kind of notation is used when referring to the different oxides present in the cement clinker. In cement chemical nomenclature, the used abbreviations are[1]:

| | | | | | |
|---|---|---|---|---|---|
| $C = CaO$ | $S = SiO_2$ | $A = Al_2O_3$ | $F = Fe_2O_3$ | $M = MgO$ | $K = K_2O$ |
| $\bar{S} = SO_3$ | $N = Na_2O$ | $T = TiO_2$ | $P = P_2O_5$ | $H = H_2O$ | $\bar{C} = CO_2$ |

### 2.1.1 – Alite

The main and most important constituent in Portland cement is alite, a tricalcium silicate, $Ca_3SiO_5$, modified in composition by the presence of foreign ions, especially $Mg^{2+}$, $Al^{3+}$ and $Fe^{3+}$, in the form of oxides. Alite controls the setting and hardening by the amorphous calcium silicate gels, at ages up to twenty eight days. The hydration of alite is usually described by the main polymorph of the corresponding tricalcium silicate, $C_3S$, the monoclinic phase $\alpha$-$C_3S$. Tricalcium silicate reacts quickly with water to give an amorphous, or poorly crystalline, calcium silicate hydrate, the C-S-H phase (the hyphens emphasize the indefinite composition) and calcium hydroxide, CH. The calcium hydroxide natural mineral analogue is known as portlandite. The following chemical equation illustrates the hydration of $C_3S$[1]:

$$C_3S + (y + z)\,H \Rightarrow C_xSH_y + z\,CH \qquad (Eqn.2.1)$$

The determination of x, the Ca/Si ratio, is usually made by electron microscopy with a generally accepted mean of 1.7-1.8, for $C_3S$ pastes.

If the kinetics of $C_3S$ hydration is followed by isothermal conduction calorimetry, the corresponding curve would be similar to the one presented, in Figure 2.1, where there is an initial peak followed by an induction period and then an accelerated period with a major peak in heat evolution.

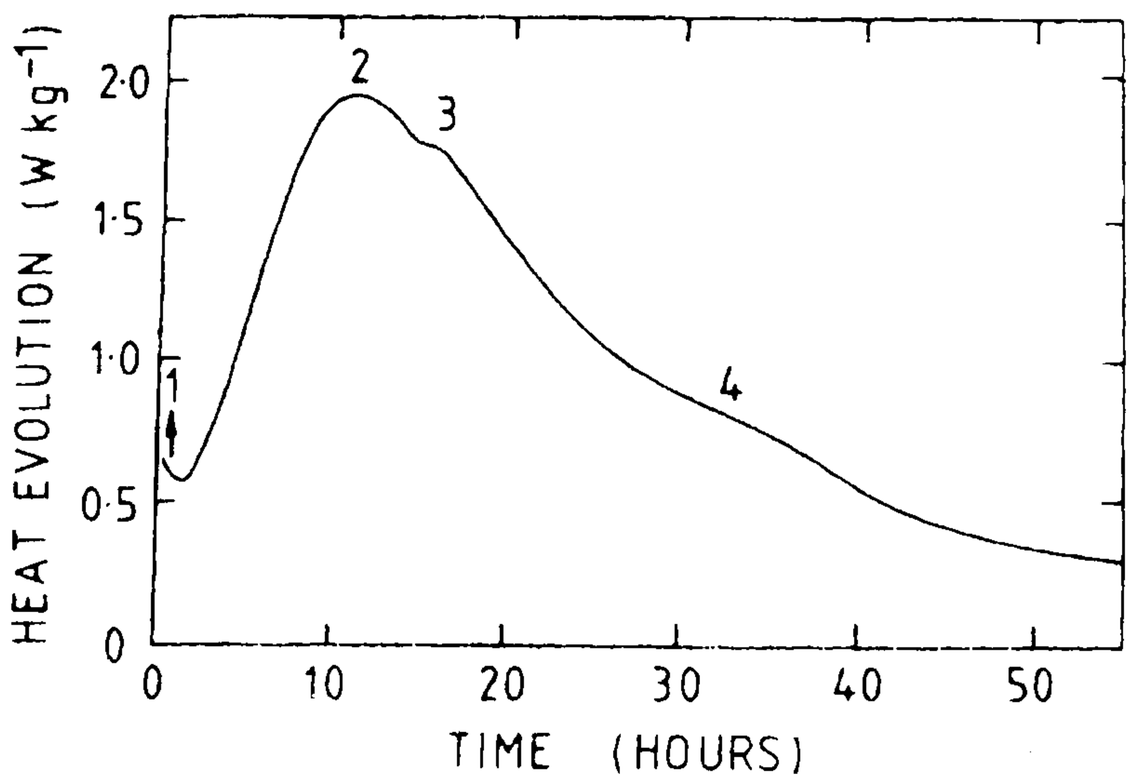


**Figure 2.1** – Rate of heat evolution at 20°C for a typical Portland cement[1].

Generally, five different stages can be distinguished in a calorimetric curve for $C_3S$ and Portland cements: a maximum peak for the initial reaction, followed by a minimum in the curve which corresponds to the induction period (phase 1); an acceleratory period where a second maximum is reached and where the main reactions take place (phase 2 and 3); a decelerated stage followed by a flat stable curve where the reactions keep on taking place in a continuous and slowly mode (phase 4). Several attempts were made to explain the induction period and its termination[4], and it is still not possible to make a clear distinction between the induction period and the early part of the acceleratory period.

### 2.1.2 – Belite

Belite is the second most abundant component of a Portland cement clinker. Just like alite, it is an orthosilicate ($Ca_2SiO_4$) also modified in composition by the presence of the same foreign ions. Once again, the hydration of belite can be described by the hydration of the correspondent pure dicalcium silicate, $C_2S$, in the form of $\beta$-$C_2S$, which is the polymorph usually present in cement clinker. When dicalcium silicate hydrates it also gives C-S-H and CH, but the kinetics are much slower compared with $C_3S$, and lead to less formation of CH. It usually reacts 30% in the first twenty eight days and 90% in one year[1,5]. The hydration reaction will depend on several factors, as mentioned before.

### 2.1.3 – Calcium Aluminates/Aluminoferrite and Sulfate Phases

The main aluminate phases present in anhydrous PC are tricalcium aluminate, $C_3A$ ($Ca_3Al_2O_6$), and calcium aluminate ferrite, $C_4AF$ ($Ca_2Al_xFe_{2-x}O_5$), and their hydration products will strongly depend on the PC composition. The calcium aluminate phase present in most of the ordinary Portland cement (OPC) clinkers is the tricalcium form $C_3A$ but substantially modified in composition and/or in structure by the presence of foreign ions such as $Si^{4+}$, $Fe^{3+}$, $Na^+$ and $K^+$. $C_3A$ can rapidly set when reacting with water, unless some gypsum ($CaSO_4 \cdot 2(H_2O)$) is added as a set-controlling agent. One of its possible hydration products are the AFt-type phases ($Al_2O_3$-$Fe_2O_3$-tri) becoming AFm-type phases, although it will depend on the type and composition of the OPC. AFm-type ($Al_2O_3$-$Fe_2O_3$-mono) phases are formed when the proper amounts of the ions they contain are brought together when cement hydration occurs. Some of those phases are hexagonal crystals but much of them are poorly crystalline and are intermixed with the C-S-H phase. Their general formula is $[Ca_2(Al,Fe)(OH)_6] \cdot X \cdot xH_2O$, where X is a singly changed anion or half or a doubly charged anion, and the term mono corresponds to the single formula unit of $CaX_2$. A crystal may contain more than one kind of X anion, and the most common are $OH^-$, $SO_4^{2-}$ and $CO_3^{2-}$. These are the several groups of AFm-type phases such as $C_4AH_x$, $C_4A\bar{C}_{0.5}H_x$ and $C_4A\bar{C}H_x$ phases, as well as $C_4A\bar{S}H_x$ phases. $C_4A\bar{S}H_{12}$ (or $C_3A \cdot C\bar{S} \cdot H_{12}$) is variously known as the monosulfate phase, and it forms solid solutions in which up to one half of the $SO_4^{2-}$ is replaced by $OH^-$. There are also other AFm-type phases containing aluminium or iron. The next table summarises the type of AFm-type phase's groups that have several layer structures, as well the most relevant compounds to cement chemistry[1,5]:

**Table 2.1** – Group of AFm-type phases[1].

| GROUP OF AFm PHASES | |
|---|---|
| **Aluminium containing** | $C_4AH_x$, $C_4A\overline{C}_{0.5}H_x$ and $C_4A\overline{C}H_x$<br>$C_4A\overline{S}H_x$: $C_4A\overline{S}H_{12}$ - **Monosulfate**<br>$C_3A{\cdot}CaCl_2{\cdot}10H_2O$ or $[Ca_2Al(OH)_6]Cl{\cdot}2H_2O$ – **-Friedel' salt** (in the presence of chloride ions)<br>$C_2ASH_8$ – Natural **Strätlingite** or gehlenite hydrate<br>Naturally occurring: hydrocalumite |
| **Iron containing** | $C_4FH_{13}$<br>$C_4F\overline{S}H_x$: $C_4F\overline{S}H_{12}$<br>$C_3F{\cdot}CaCl_2{\cdot}10H_2O$ |

Other hydration products resulting from $C_3A$ and the calcium aluminoferrite phase are the AFt-type phases. AFt-type phases, ($Al_2O_3$-$Fe_2O_3$-tri), have the general formula $[Ca_3(Al,Fe)(OH)_6{\cdot}12H_2O]_2{\cdot}X_3{\cdot}xH_2O$, where $x \leq 2$ and X represents one formula unit of a doubly charged, or, with reservations, two formula units of a single charged anion. Although these phases are formed under similar conditions as AFm-type phases, the range of anions which can occupy the X site is smaller, and the AFt-type phases are formed at higher ratios of CaX to $C_3(A,F)$. Within the AFt-type phases, the most important ones are ettringite and thaumasite, the latter with silicon replacing aluminium in the structure. The following scheme describes the most important calcium aluminate hydration products, depending on the composition of the PC clinker[4,6]:

## CHAPTER II – LITERATURE REVIEW

**i) In the presence of calcium sulfate (gypsum):**

$$C_3A \xrightarrow{C\bar{S}+H} C_6A\bar{S}_3H_{32}\ \text{(ettringite)} \xrightarrow{C_3A+H} C_4A\bar{S}H_{12}\ \text{(monosulfate)} + C_4AH_x$$

**ii) In the absence of gypsum:**

$$C_3A \xrightarrow{CH+H} C_4AH_{13}$$

**iii) In the presence of gypsum:**

$$C_4AF \rightarrow \text{AFt phases}$$

**iv) In the absence of gypsum:**

$$C_4AF \rightarrow \text{AFm phases } (C_2(A,F)H_8 \text{ and/or } C_4(A,F)H_x)$$

$$(C_2(A,F)H_8 \xrightarrow{\text{In presence of iron}} \text{Hydrogarnet phase } C_3(A,F)H_6$$

**v) In the presence of lime (CaO):**

$$C_4AF \rightarrow C_4(A,F)H_x$$

**vi) In the presence of ettringite or AFt phases:**

$$C_6A\bar{S}_3H_{32}\ \text{(ettringite)} + C_3A \rightarrow \text{Afm phases}$$

**Figure 2.2 -** Hydration schemes for the most important calcium aluminate/ferrite phases[4,6].

Ettringite, $C_6A\bar{S}_3H_{32}$, which also occurs as a natural mineral, is formed during the early hydration of most PC cements. As shown in equation i) from the above figure, in Portland cements, the hydration of $C_3A$ in the presence of gypsum initially produces ettringite which is then slowly converted into the thermodynamically stable monosulfate, an AFm-type phase. The phenomenon of ettringite formation, after hardening of a cementitious material, is called delayed ettringite formation (DEF). It has always been considered as a cause of damage in the materials, but some caution must be taken before "blaming" DEF for any expansion observed in those materials. Although temperature is a critical factor in relation to DEF, the formation of ettringite after heating a sample does not necessarily produce expansion and, not all expansion is due to DEF. Indeed, delayed ettringite formation will depend on many factors like the nature of the paste, and it cannot be generalised to the whole range of cement pastes because secondary or recrystallised deposits of ettringite are found in most mature cement pastes

and concrete[7]. Thaumasite, $[Ca_3Si(OH)_6 \cdot 12H_2O](SO_4)(CO_3)$ or $C_3S\bar{S}\,\bar{C}H_{15}$, is another AFt-type phase and strongly similar to ettringite, but with $Si^{4+}$ replacing $Al^{3+}$. It can be formed from the reaction when cement is exposed to both sulfate and carbonation attacks, and its presence can cause some cracking or severe strength loss to the cement paste, but as usual, it will also depend on the nature of cement paste. Hydrogarnet phases, $C_3(A,F)H_6$, have structures related to the one of garnet, $Ca_3Al_2Si_3O_{12}$. In the hydrogarnet phases, some or all of the silicon is substituted and all or some of the $Al^{3+}$ may be also replaced by $Fe^{3+}$ ions, forming solid solutions within a compositional region bounded by $C_3AH_6$, $C_3FH_6$, $C_3AS_3$ and $C_3FS_3$. The most stable hydrogarnet phase is $C_3AH_6$ and can result from both $C_3A$ and/or $C_4AF$ hydration. Brucite, hydrotalcite and related phases can also be produced as hydration products from Portland cements. Brucite, $Mg(OH)_2$, results from magnesium salt attack on PC concrete, and also from hydration of PC with a high MgO content, although its presence can also be observed in OPC. A range of phases structurally related to brucite are found, related as the AFm phases are to CH; that is, some of the $Mg^{2+}$ ions can be replaced by $Al^{3+}$ or $Fe^{3+}$, and the charge balanced by anions which, together with water, occupy interlayer sites. Hydrotalcite, $Mg_6Al_2(CO_3)(OH)_{16} \cdot 4(H_2O)$, results from the hydration of slag blended cements and as a minor hydration product of PC, with a similar composition to meixnerite, $Mg_6Al_2(OH)_{18} \cdot 4(H_2O)$. Meixnerite, like AFm-type phases where anion exchange reactions occur, can readily take up $CO_2$, giving a material similar to hydrotalcite[1]. It is also necessary to consider the sulfate phases present in a PC clinker. Gypsum present in cement is usually of natural origin but some other products also belong to the group of hydrated sulfate phases such as hemihydrates ($CaSO_4 \cdot 0.8H_2O$ or $CaSO_4 \cdot 0.5H_2O$) and syngenite ($KC\bar{S}_2H$)[1].

In summary, the most important information to bear in mind is that in OPC. $C_3A$ hydration leads to the initial formation of AFt-type phases which are, generally, converted later into AFm-type phases. The calcium aluminoferrite phases, $C_4AF$ and $C_2(A,F)$, when hydrated, also form AFt-type phases but, once again, lead later to the formation of AFm-type phases. Although the reaction is very much slower than the one of $C_3A$, both hydration rates are slightly retarded by the presence of CH.

## 2.2 – THE C-S-H PHASE

In this section, the C-S-H phase formation in $C_3S$ and $C_2S$ pastes is discussed, as well as the analytical techniques used to completely characterize the C-S-H phase: the structure of the C-S-H phase is also discussed, covering the structural models that have been proposed. An overview of its morphology and microstructure, as well its nanostructure in cement and blended pastes is also made.

### 2.2.1 - $C_3S$ and $C_2S$ Hydration

#### 2.2.1.1 – Thermal Analysis

Richardson[8] examined the hydration reactions of $C_3S$ and found that although there was a significant variation in the Ca/Si ratio at the micron- and nanometre-scale, the average Ca/Si was ~ 1.65, and also that CH often occurred as massive crystals but also intermixed with C-S-H at the micron-scale. The determination of CH present in a paste can be made by several methods, including thermoanalytical methods such as TG, DTG, DTA and DSC[1], as well as QXDA. There were found to be some significant differences between the thermoanalytical methods and QXDA, and although the former ones can be inaccurate if experimental conditions are not taken in consideration, STA (TG + DTA) is an acceptable method for an estimation of the CH and water content, and also shows some of the other phase contents in a cement paste, such as C-S-H, AFm, and CH. Regarding hydrogarnet formation, DTG studies[9] performed for aluminoferrite phases, have shown that after twenty four hours of hydration, and in the absence of gypsum, three steps in the curve are observed at 100, 170 and 280°C, corresponding to loss of water from a mixture of hexagonal hydrates and hydrogarnet, respectively. After twenty eight days, the intensity corresponding to loss of water from hydrogarnet increases indicating that a solid solution of $C_3AH_6$ and $C_3FH_6$ is present. Considering the C-S-H phase, the loss of water is continuous, with a sharp typical peak around the 100°C. The AFm-type phases lose water between 150-200°C, the AFt-type phases around 120°C and, finally, CH loses water between 410-540°C. Figure 2.3 shows several TG and DTA curves found for a fully reacted $C_3S$ paste in different

experimental conditions. Curve 1 in both TG and DTA plots corresponds to the typical TG and DTA curves found in mature $C_3S$ pastes.

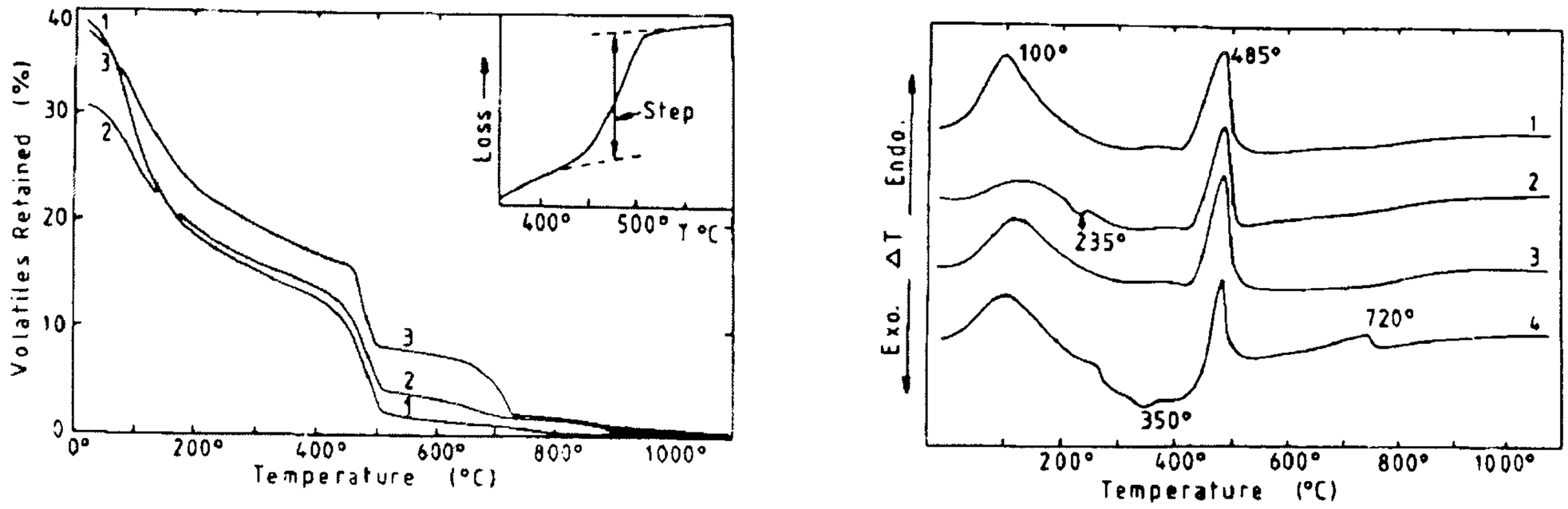


**Figure 2.3** – TG (left) and DTA curve (right) found for a mature $C_3S$ paste[10].

In the TG plots, curve 1 shows a first weight loss around 100°C which corresponds to the dehydration of the C-S-H phase and a second weight loss occurs around 485°C resulting from the dehydration of CH. Table 2.2 summarises the ordinary thermal analysis data known in cement chemistry:

**Table 2.2** – Summary of thermal analysis data[11].

| Component | Peak Position[1] (°C) |
|---|---|
| **Tobermorite**[2] | 130 |
| **Ettringite** | 120-130 |
| **Anhydrous Gypsum** | 140-170 (Endothermic) |
| **C-S-H Gel** | < 150 |
| **Amorphous Hydrates** | 200-300 |
| **Syngenite** | 290 |
| **Brucite** | 420 |
| **Portlandite (CH)** | 450-550 |
| **Carbonated Samples (Vaterite)** | 450-600 (Endothermic) |
| **Carbonated Samples (Calcite)** | 600-650 |
| **Quartz** | 578 (Endothermic) |
| **$CaCO_3$** | 750-850 |
| **Tharndite** | 880 (Endothermic) |

[1] At 10°C per minute by DTA specific instrumentation

[2] Peak appears at about 120 and 130°C, or as a shoulder on the leading edge of an ettringite peak.

QXDA has also been used to determine the water content of the C-S-H phase[1] and unreacted $C_3S$.

### 2.2.1.2 – TMS

The method of trimethylsilylation, TMS, provides a detailed study of the role of silicate polymerization in the process of $C_3S$ hydration, as well as in cement pastes. TMS methods follow the degree of polymerization of the silicate chains and their relative distribution. Besides microstructure, the change of the anionic structure during hydration will also define the complex chemical phenomena of hardening. The method itself involves a common procedure used in analytical chemistry, derivatisation. With this method, the samples are chemically modified in order to be more easily separated, distinguished from each other and, finally quantified. In this particular method of trimethylsilylation, the first step of derivatisation involves leaching the solid with an acid which leads to the formation of silicic acids that correspond to the original silicate ion structures[12]. The following equation illustrates that step:

$$Ca_2SiO_4 + 4HCl \Rightarrow Si(OH)_4 + 2CaCl_2 \qquad (Eqn.\ 2.2)$$

The formed silicic acids will tend to polymerised thus, in order to avoid it, the acids are end-blocked by the addition of trimethylsilyl (TMS) groups:

$$Si(OH)_4 + 4(CH_3)_3SiCl \Rightarrow (CH_3Si)_4SiO_4 + 4HCl \qquad (Eqn.\ 2.3)$$

The total reaction is:

$$Ca_2SiO_4 + 4(CH_3)_3SiCl \Rightarrow (CH_3Si)_4SiO_4 + 2CaCl_2 \qquad (Eqn.\ 2.4)$$

Finally, after the initial process of derivatisation of the silicate ion structures, the solution is analysed by gel permeation chromatography (GPC), also known as size-exclusion chromatography. The solution passes through a packed column that works as a molecular sieve where the pore network will define which molecules will reach first

the detector used in this technique. the process of elution. Therefore, larger molecules are excluded from the pore network and are the first ones reaching the detector and the smaller molecules will take longer to diffuse and reach the end of the column. The molecules are eluted in order of decreasing molecular weight[12]. The following figure shows the different polymers in white Portland cement paste, separated by gel permeation chromatography (GPC):

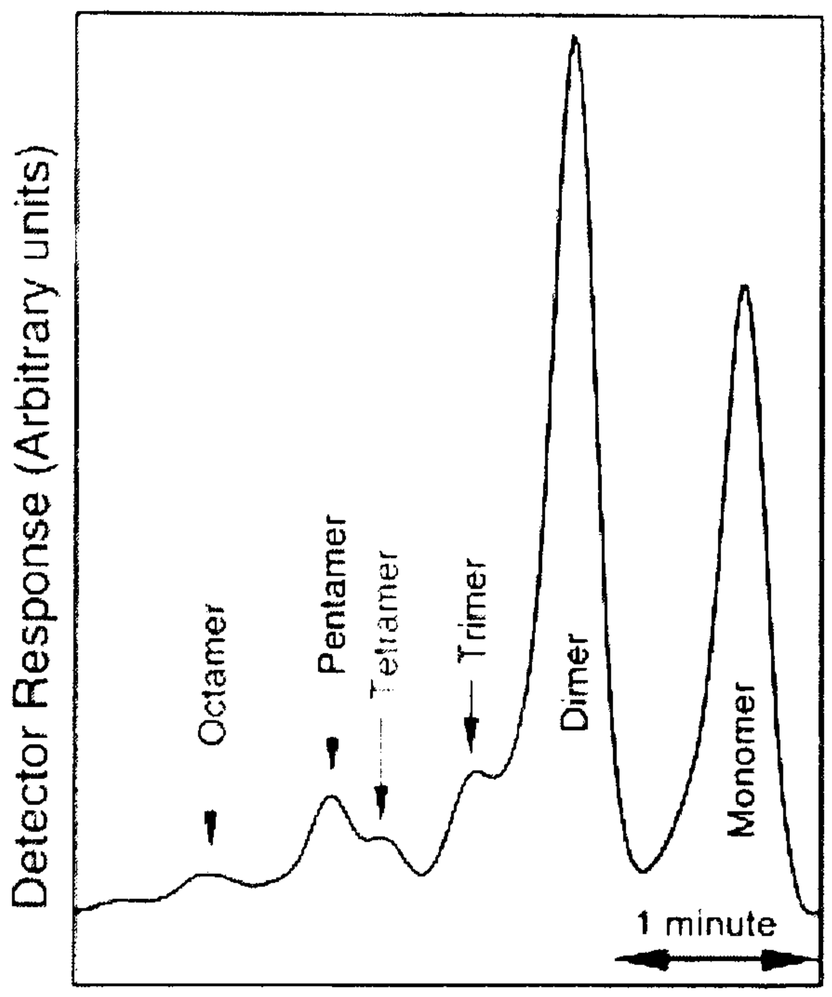


**Figure 2.4** – TMS-GPC chromatogram of a white Portland cement paste hydrated for 3 months[13].

In the $C_3S$ hydration, TMS studies showed that the degree of silicate polymerization increases as reaction proceeds, although it is not a continuous process like with an organic polymer. A few years later, after Tamas and Varady[14] presented a first consistent TMS study on $C_3S$ and dicalcium silicate ($C_2S$). Mohan and Taylor[15] ended some conflict in the results of other investigators, and demonstrated that only pastes of similar degrees of reaction should be compared and, more important, established the anion polymerization and the development of the silicate chains. In a first stage, and during the first few days, $C_3S$ reacts to give CH, and breaks down to produce monomers and a resulting form of C-S-H containing dimer, but no appreciable polymer. In a second stage, which lasts for about six months, $C_3S$ continues to produce monomers which, at the same time, form dimers and are consequently followed by further

polymerization. Since little or no $C_3S$ remains, the polymeric anions can only be formed by alteration of the C-S-H phase already formed, but it is an extremely slow process and only detectable after the $C_3S$ hydration is substantially complete. The dimer content reaches a maximum of around 50-60% after six months and then falls to around 40% after one year, while that of the polymeric forms steadily increases to 40-60%. Although the TMS methods indicate the proportion of the silicon in the different polymers present, it has two limitations: side reactions can occur and it is rarely possible to account for more than 80-90% of the total silicon.

#### 2.2.1.3 – Solid State MAS NMR

In order to complement the TMS methods, the use of $^{29}Si$ Magic Angle Spinning Solid State NMR (MAS NMR) is the best option. NMR techniques are purely physical and bulk techniques, avoiding the problem of side reactions or alterations in the structure, and also providing data related not directly to the fractions of the silicon present in different anionic species like in the TMS methods, but to the fractions present in different environments, giving mean chain length values. TMS gives an absolute distribution of the different kind of polymerized silicate chains. Since the $^{29}Si$ isotope has an intrinsic magnetic moment, as do some isotopes of other elements important in cement chemistry, namely $^{1}H$, $^{27}Al$ and $^{17}O$, it is possible to acquire very important information about the local environment and coordination of those elements[1,5,16]. This is especially useful with poorly crystalline materials such as C-S-H where XRD gives almost no significant information on its structure. If a solid sample is spun at the "magic angle" of 54°74' to the magnetic field, the orientation effect and consequent line broadening are eliminated and resolution of the fine structure in a spectrum is possible. Thus, peaks for the different Si site environments can be solved and different $SiO_4$, and also $SiO_6$ units (thaumasite), tetrahedral and octahedral coordination respectively, can be distinguished through their chemical shift ($\delta$) difference. $^{29}Si$ NMR chemical shifts in solid silicates, or aluminosilicates, depend mainly on the degree of condensation of the silicon-oxygen tetrahedra, and increasing anion condensation will lead to increasing $^{29}Si$ shielding. Bell *et al.*[17] following some previous work, conducted one investigation of solid state $^{29}Si$ MAS NMR, for inorganic materials. They defined well separated ranges

of the chemical shift which could be related to the extent of polymerization in a crystalline silicate. Applying those results and some previous ones[5] to the calcium silicate hydrate gels that are formed in the hydration of tricalcium silicate. it is known that the nearest neighbour environment of silicon in cement pastes is almost invariably tetrahedral coordination ($SiO_4$ group). Its chemical shift is determined by the number of SiOT bridges formed by the given $SiO_4$ tetrahedron T; the degree of $SiO_4$ polymerization; and the number of Si or Al atoms in the second coordination of the central silicon with a given number of SiOT bridges, the degree of tetrahedra Al substitution. Regarding the degree of $SiO_4$ polymerization, characteristic high-field shifts are observed with increasing number n of SiOT bridges at the central silicon atom of the $Q^n$ (i.e. $Si(OSi)_n(O^-)_{4-n}$) structural unit. Q is a silicate tetrahedron and n is the number of oxygen atoms which bridge to adjacent tetrahedron. Thus, $Q^0$ denotes isolated $SiO_4$ tetrahedron (orthosilicates), $Q^1$ disilicates $Si_2O_7$ and the end tetrahedra of a chain, $Q^2$ middle groups, $Q^3$ for branching sites in a chain and $Q^4$ for a three-dimensional network in which every oxygen in the $SiO_4$ tetrahedron is shared by two Si atoms. The following table shows the chemical shifts for each $Q^n$ structural unit in several silicates:

**Table 2.3** - Characteristic NMR shifts of silicate species in cement pastes[17].

| Type of silicates | Designation | Tetrahedral Structure | Range/ppm |
|---|---|---|---|
| **Ortho(mono)silicates** | $Q^0$ | O-<br>O-SiO-<br>O- | -66 to -74 |
| **Disilicates (endchain groups)** | $Q^1$ | O-<br>O-SiOSi<br>O- | -75 to -82 |
| **Chain middle groups** | $Q^2$ | O-<br>SiOSiOSi<br>O- | -85 to -89 |
| **Chain branching sites** | $Q^3$ | Si<br>O<br>SiOSiOSi<br>O- | -95 to -100 |
| **Three dimensional framework** | $Q^4$ | Si<br>O<br>SiOSiOSi<br>O<br>Si | -103 to -115 |

A $^{29}Si$ MAS NMR spectrum of $C_3S$ anhydrous reveals chemical shifts between -69 and -75 ppm, corresponding to nine resonances in seven resolved lines and two of those having double intensity, as the following figure shows:

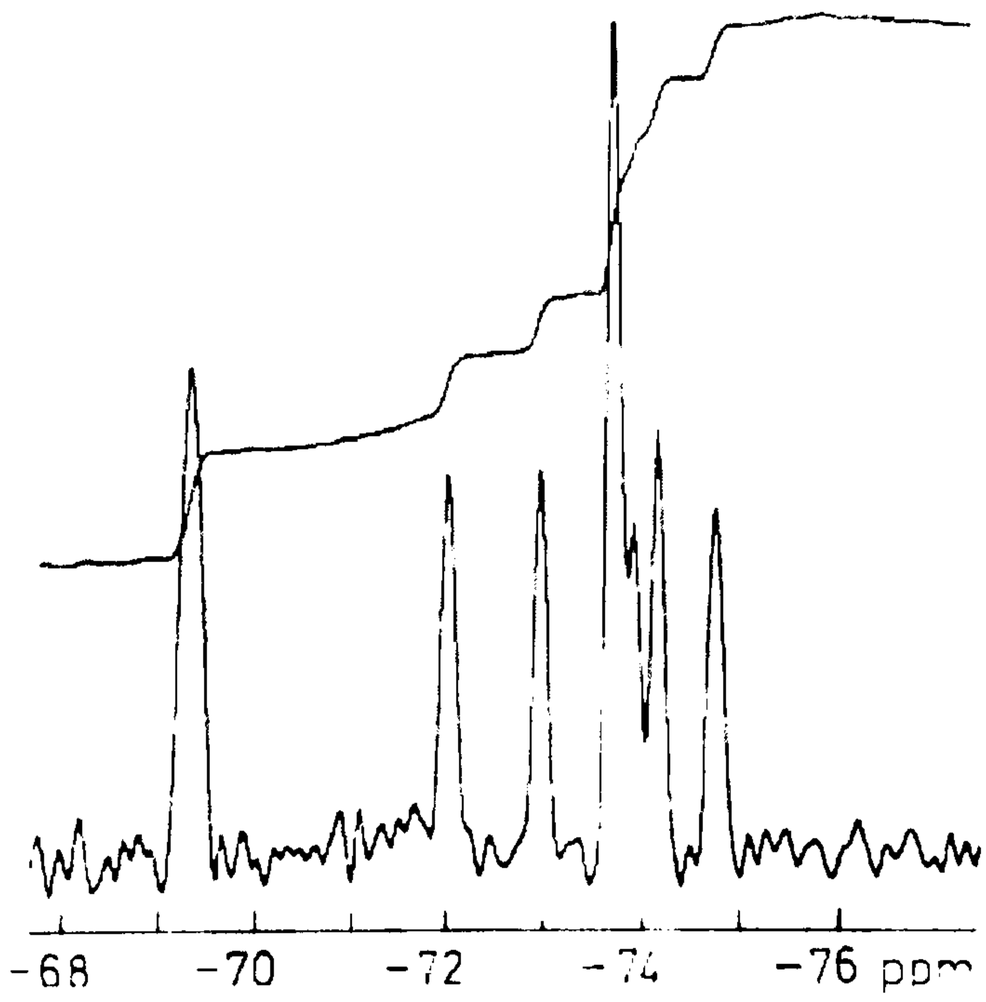


**Figure 2.5** - $^{29}Si$ MAS NMR spectrum of anhydrous $C_3S$[18].

When $C_3S$ pastes are formed, the content of $Q^0$ (monomer) begins to decrease after a few hours, with formation of $Q^1$ (dimer), later accompanied by $Q^2$ (middle groups); no $Q^3$ or $Q^4$ (chain branch sites and three-dimensional network) are detected. Rodger *et al.*[19] found a good correlation between the degree of hydration, indicated by the changing relative areas of $Q^0$ and $Q^1$ peaks, the increase of cumulative heat liberated and the increase in the amount of CH formed, confirming previous results from TMS studies. They found that the product formed in the first few hours only contained monomeric anions and that the dimer only begins to form later. The $Q^1/Q^2$ ratio reached a maximum in dimer content indicated by TMS, but the monomer did not disappear while further hydration resulted in a slow, small decrease in this ratio indicating a higher degree of polymerization. Brough *et al.*[20] concluded that the $C_3S$ hydration appears to take place in two distinct stages, as other previous investigations with TMS methods also found[21,22]. Initially, dimerization occurs as:

Monomer + Monomer ⇨ Dimer (*Eqn. 2.5*)

($2Q^0 \Rightarrow Q^1$)

Then, polymerization occurs as the chains grow by the linking of dimers (or longer chains) with monomers:

Dimer + Monomer + Dimer ⇨ Pentamer (*Eqn. 2.6*)

Dimer + Monomer + Pentamer ⇨ Octomer (*Eqn. 2.7*)

This also enabled calculations from the observed proportion of the $Q^n$ species, the proportions of monomeric silicate units which react to form dimers, or which form links between chain-end groups resulting in polymerization. $^{29}Si$ MAS NMR complements TMS studies and the results are consistent with the previously explained for TMS methods. Finally, it is also consistent with the 2, 5, 8... (3n-1) polymerization sequence, reported by Hirljac *et al.*[22]. This sequence leads to a number of proposed structural models for the C-S-H phase, which will be discussed in this chapter, section 2.2.2. A form of simplifying interpretation of spectra is to use the Cross-Polarization NMR

technique (CP MAS NMR) in which only Si atoms close to protons give signal so the resonances of the anhydrous phases are eliminated, i.e. it is possible to discriminate between silicon atoms in tetrahedral sites associated to one or more protons due to hydration, and ones that do not and are present in the anhydrous material[17,19,20,23,24,25]. Thus, this technique distinguishes between monomer present in the anhydrous phases and those present in a hydration product, which is almost certain to carry hydrogen. $^{29}Si$ MAS NMR studies of $C_3S$ pastes are often used as a model for ordinary Portland cement (OPC) if they have the same w/s ratio and have been cured under the same conditions[1,8,13,26,27,28]. $^{29}Si$ MAS NMR has also been used to study polymorphs of $C_2S$[18,29,30]. It was established that $\alpha$, $\beta$ and $\gamma$-$Ca_2SiO_4$ polymorphs presented chemical shifts around -70.3, -71.4 and -73.5 ppm, respectively. The following Figure shows the obtained spectra for $\gamma$-$Ca_2SiO_4$ that also contained some $\beta$-$Ca_2SiO_4$[29]:

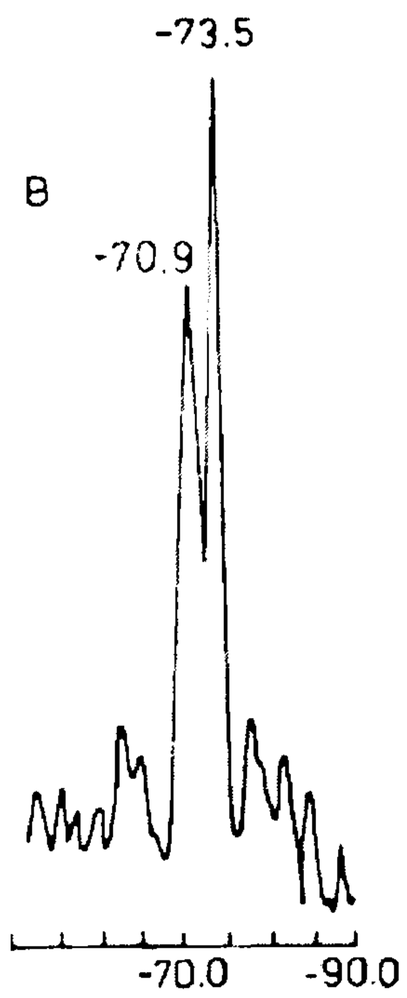


**Figure 2.6** – $^{29}Si$ MAS NMR spectrum for $\gamma$-$Ca_2SiO_4$ (-73.5 ppm), and $\beta$-$Ca_2SiO_4$ (-70.9 ppm)[29].

In $^{27}Al$ MAS NMR, it is possible to see two distinct peaks for the tetrahedral and octahedrally coordinated aluminium, in aluminosilicates. Since $Al^{3+}$ is a guest ion in the silicate phases of cement clinker, when the C-S-H phase is formed from alite (and belite), aluminium is incorporated in its structure. Figure 2.7 exemplifies the different coordination sites in a $^{27}Al$ MAS NMR spectrum.

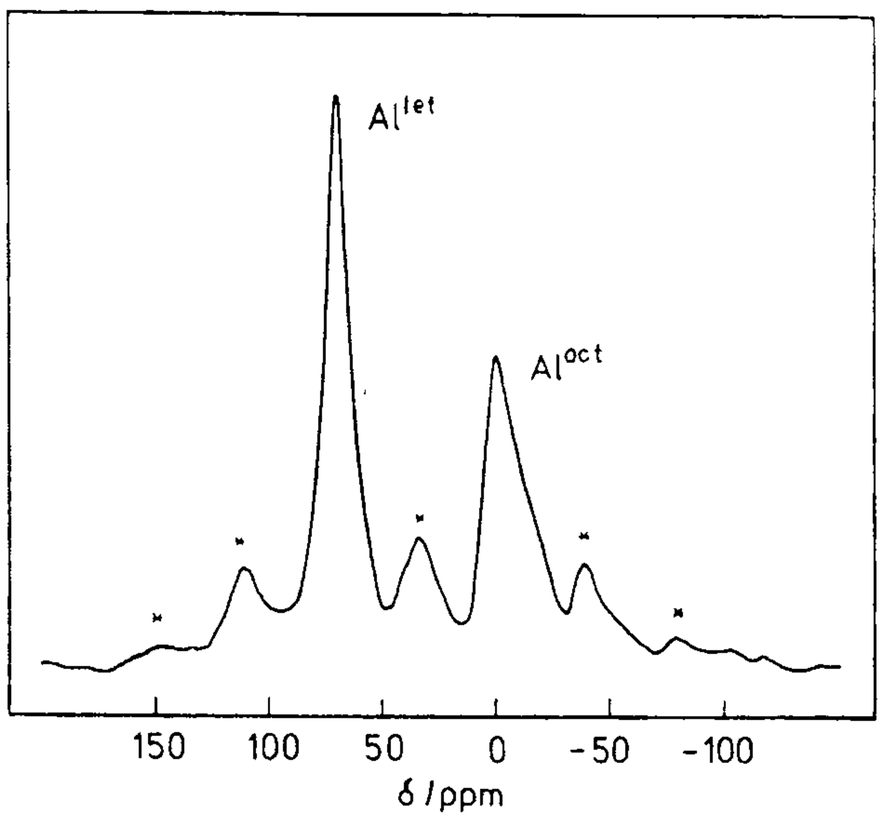


**Figure 2.7** – $^{27}$Al MAS NMR spectrum of the layer aluminosilicate margarite, where $Al^{tet}$ and $Al^{oct}$ denote tetrahedrally and octahedrally coordinated aluminium, respectively (* indicates spinning sidebands)[16].

Aluminosilicates result from an isomorphous replacement of the $SiO_4$ tetrahedra with $AlO_4^-$ tetrahedra. The extra charge introduced by the substitution must be balanced by additional cationic charge elsewhere in the structure of the final aluminosilicate[16]. In the three-dimensional framework, each $AlO_4$ tetrahedron connected to another $SiO_4$ tetrahedron shifts the $^{29}$Si signal by about 5-6 ppm to low field. Thus, in basic aluminosilicates, it is possible to distinguish the chemical shift ranges for the tetrahedra with aluminium substitution. Here, Si(mAl) designates a $SiO_4$ tetrahedron connected to $mAlO_4$ and (4-m) $SiO_4$ tetrahedron. Using the $Q^n$ structural unit, where Q is a silicate tetrahedron and n is the number of oxygen atoms which bridge to adjacent tetrahedron, the aluminium substitution leads to the notation of $Q^n$(mAl) where m corresponds to the number of Al substituting silicon in that site. The Al/Si ratio and distribution/ordering of Si and Al ions in the framework, will affect the final physical and chemical properties of cements[18]. Skibsted *et al.*[31] reported the first evidence for aluminium guest ion substitution in alite and belite. $^{27}$Al MAS NMR of alite showed a single peak correspondent to a four-coordinated aluminium, Al[IV], with a chemical shift of $80 < \delta < 91$ ppm. Their results demonstrated that Al preferentially substitutes for tetrahedral coordinated silicon in alite.

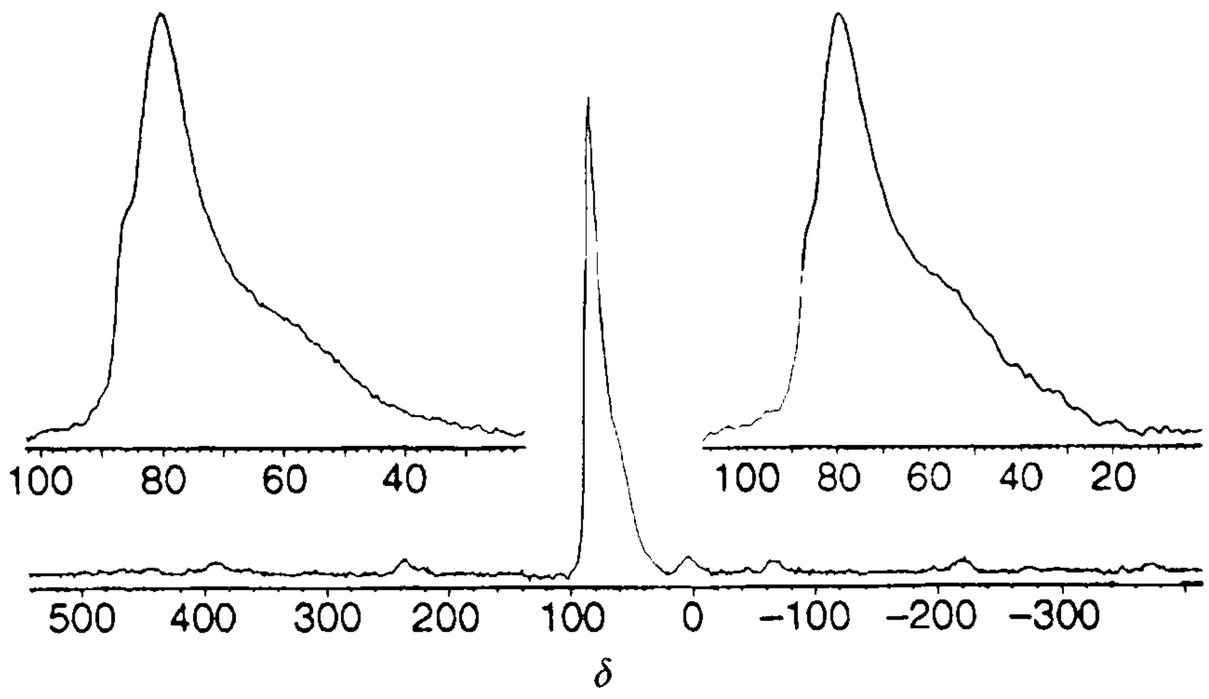


**Figure 2.8** - $^{27}$Al MAS NMR spectra of monoclinic alite[31].

Tong *et al.*[32,33] used $^{29}$Si MAS and CP MAS NMR to follow β-$C_2S$ hydration. They concluded that the mechanism is substantially similar to the one for $C_3S$ hydration, and also that the overall composition and morphology of C-S-H formed appears to be identical to the one formed from $C_3S$, and presents a Ca/Si ratio in the range 1.6-2.0. Another important conclusion arising from those studies, besides the similarities and differences between the two systems, is the fact that they also did not find any $Q^3$ or $Q^4$ peaks in the spectra corresponding to the hydration products of β-calcium disilicate, i.e., meaning that no higher polymerized C-S-H was found. Other $^{29}$Si MAS NMR studies revealed that for anhydrous $C_2S$, the spectrum shows a single peak around -71.3 ppm [18,34,35], as the next figure shows:

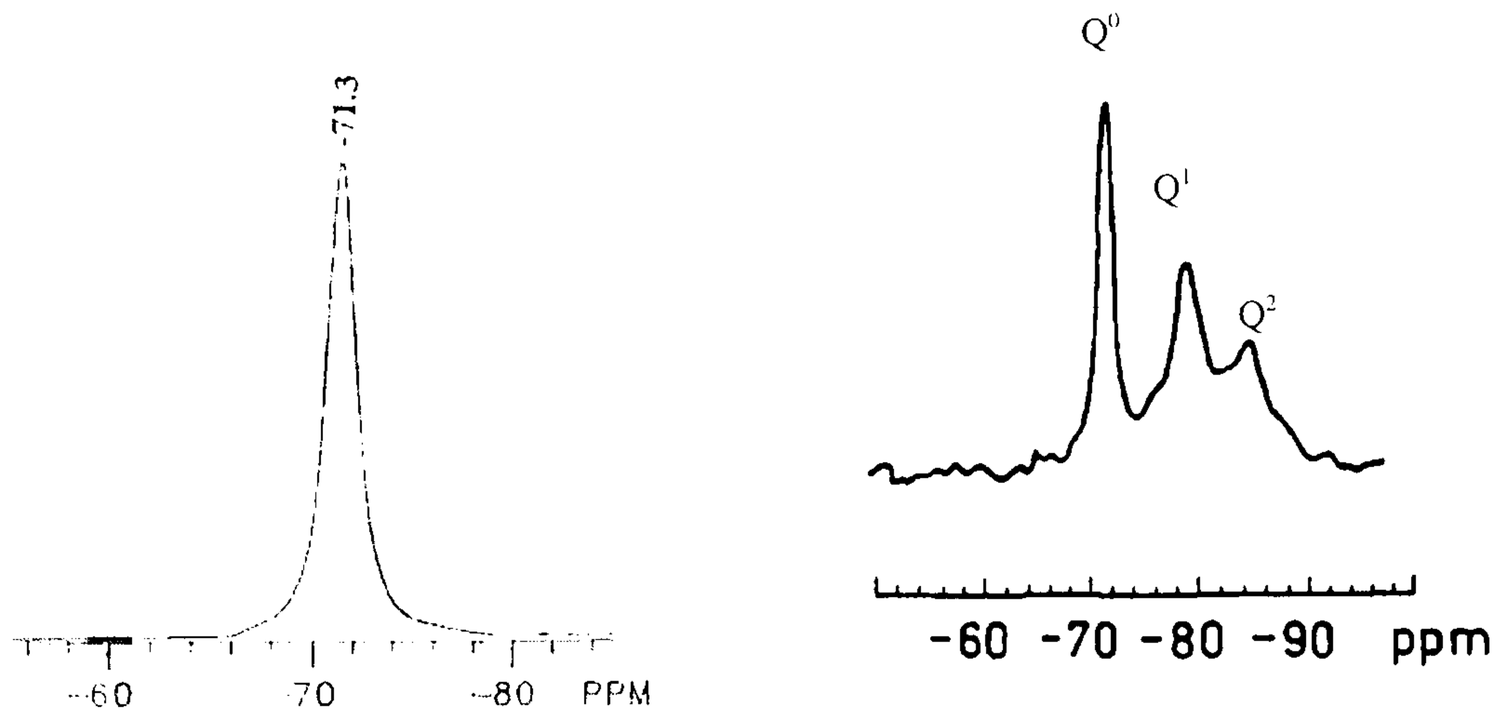


**Figure 2.9** – $^{29}$Si MAS NMR spectra of anhydrous $C_2S$[35] and a $C_2S$ paste[33].

As mentioned before, another structural factor that affects a $^{29}$Si chemical shift is the aluminium content in the framework. Skibsted *et al.*[31], besides reporting that Al

preferentially substitutes for tetrahedral coordinated Si in alite. also demonstrated the same for belite, using $^{27}$Al MAS NMR (Figure 2.10). The observation of a single Al[IV] resonance for belite, $\delta \sim 96.1$ ppm, demonstrated that Al substitutes for tetrahedral Si because the crystal structure for $\beta$-$C_2S$ shows that all the Si atoms are equivalent. They also found another resonance at $\delta \sim 10$ ppm, corresponding to the Al[VI] site. but the absence of octahedral places or vacancies in the crystal structure for $\beta$-$C_2S$ suggests that this observed resonance originates from a separate aluminate phase.

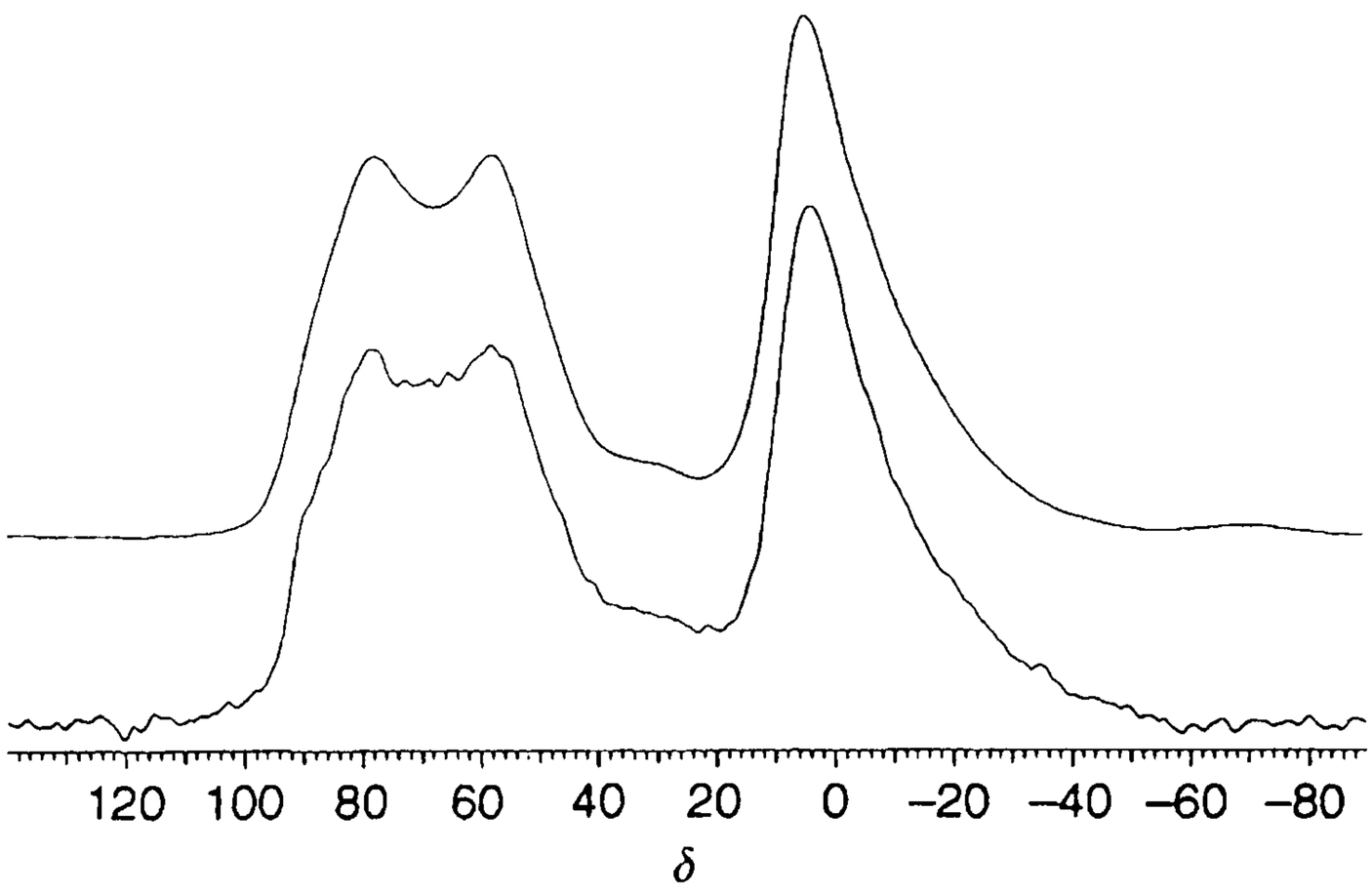


**Figure 2.10** - $^{27}$Al MAS NMR of Al guest ions in belite[31].

$\beta$-$C_2S$ hydration was also studied using $^{17}$O and $^{29}$Si MAS-NMR by Cong and Kirkpatrick[36]. They already knew that upon hydration, the isolated silicate tetrahedra $Q^0$ of $C_3S$ and $\beta$-$C_2S$ would polymerize to $Q^1$ and $Q^2$ sites in C-S-H. If isotopically unenriched calcium silicates are reacted with $^{17}$O-enriched water, all the $^{17}$O NMR signals present in the reaction products must be from the $^{17}$O originally in the water. For the C-S-H phase, $^{17}$O NMR allowed the direct observation of oxygen in Si-O-Si (bridging oxygen), Si-O-Ca (non-bridging oxygen), Ca-OH and possibly Si-OH O-sites in C-S-H formed by hydration of $\beta$-$C_2S$ and, as expected, Ca-OH sites were also present in $Ca(OH)_2$ which accompanied the C-S-H phase. The following figures correspond to belite $^{29}$Si and $^{17}$O spectra, as well to the belite hydration evolution:

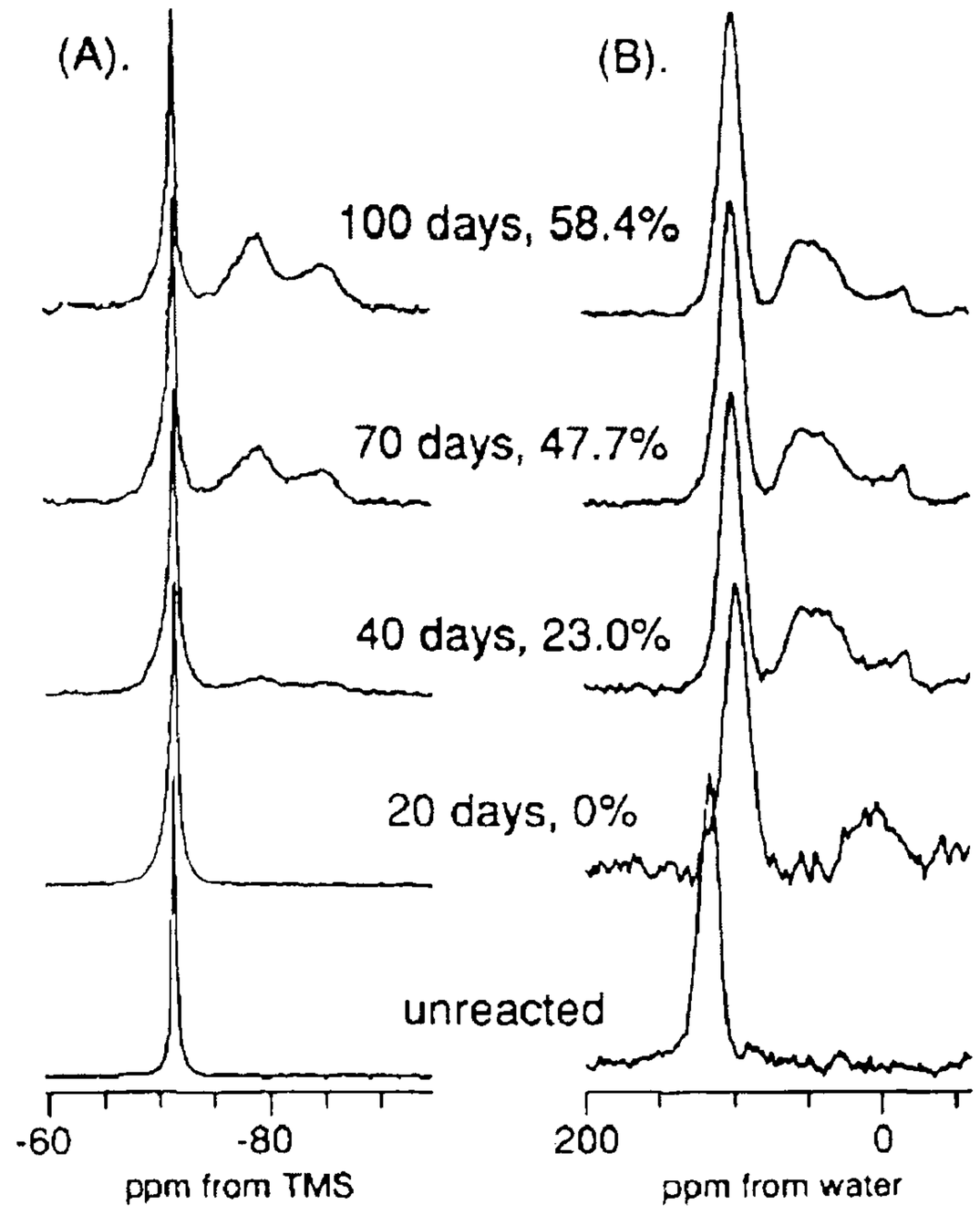


**Figure 2.11** – $^{29}Si$ (A) and $^{17}O$ (B) MAS NMR spectra of hydrated β-$C_2S$[36].

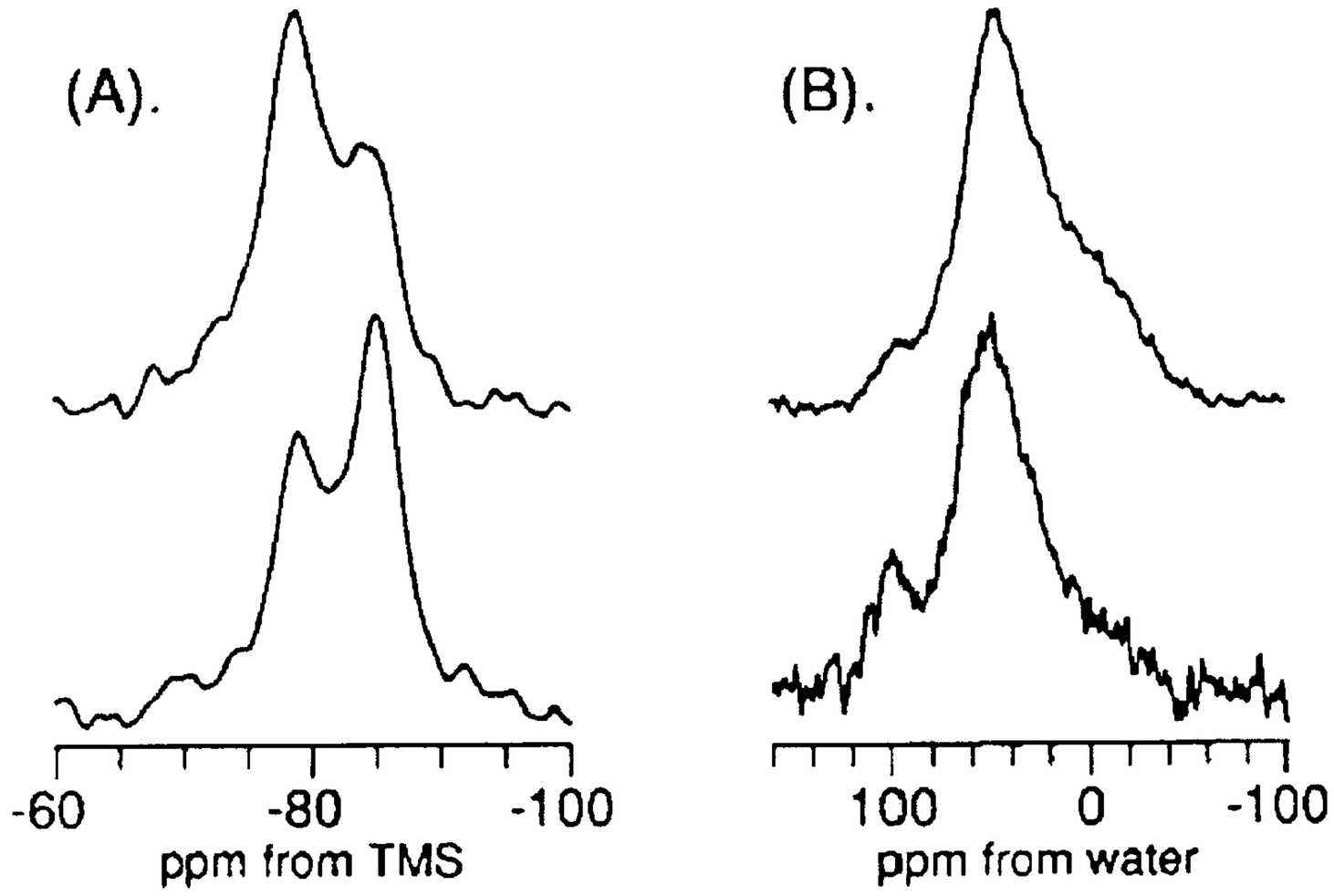


**Figure 2.12** – $^{29}Si$-$^{1}H$ (A) and $^{17}O$-$^{1}H$ (B) CP MAS NMR spectra of β-$C_2S$ hydrated for 100 days[36].

Considering the aluminosilicate/aluminoferrite phase hydration, many works have described the hydration kinetics for the formation of ettringite and its conversion into monosulfate. For instance, according to Chudek *et al.*[37], Skibsted *et al.*[38] and Andersen *et al.*[39], the signal observed in a $^{27}$Al MAS NMR spectrum of an hydrated OPC paste, for a chemical shift at 79 ppm (tetrahedrally coordinated Al) is due to aluminium guest-ions in the C-S-H phase, and a second peak around 10 ppm corresponded to a minor quantity of hydrated phases. After hydration, a Al[VI] signal is attributed to ettringite at 13 ppm, another peak around 9.8-8.6 ppm (depending on the magnetic field) belongs to monosulfate and, finally, a third signal with a chemical shift at 74.6 ppm corresponds to tetrahedral coordinated Al incorporated in the C-S-H phase, bearing in mind that, after hydration, the chemical shift for Al[IV] changes ca. 10 ppm towards lower frequency ($Al^{3+}$) to ~65 ppm. It was also concluded that $C_3A$ and $C_4AF$ are not observed due to their strong quadrupolar couplings. In $C_4AF$, this is due also to strong dipolar couplings between $^{27}$Al nuclear spins and the spins of the unpaired electrons of the $Fe^{3+}$ ions, resulting in severe line broadening of the resonances from this phase and others, as mentioned before. Skibsted *et al.*[40] also found that in synthetic ferrites before their hydration, the Al present in the ferrite phase contributes little or nothing to the observed $^{27}$Al MAS NMR spectrum (in their experimental conditions). Therefore, the $^{27}$Al MAS NMR spectrum can be considered as the sum of subspectra coming only from $C_3A$ and from Al guest-ions present in alite and belite. In a $^{29}$Si MAS NMR spectrum for thaumasite, the Si site shows a chemical shift around -180 ppm and it was also studied using $^{29}$Si CP MAS NMR spectroscopy[41]. In summary, $^{27}$Al MAS NMR studies revealed that the chemical shift for AFt-type phases, in general, is 12 ppm and for AFm phases or $C_4AH_{13}$, is around 8 ppm.

#### 2.2.1.4 – Electron Microscopy

As stated before, the study and knowledge of C-S-H phase microstructure and composition is vital to understand the properties of a cement paste, and to obtain all the important information. In order to achieve it, one of the most powerful techniques used is electron microscopy. Taplin presented the first microstructural distinction between two different types of products resulting from a cement hydration[42]. Outer product

(Op) C-S-H formed in the originally water-filled spaces, and inner product (Ip) C-S-H formed within the boundaries of the original clinker particles. This scheme is quite straightforward and has been adopted widely with the support of several reported works, although other authors have proposed alternative classifications[42] since Taplin. Following this structural distinction, Groves *et al.*[43] examined ion-beam-thinned sections of a synthetic $C_3S$ paste, by Transmission Electron Microscopy, TEM. This technique allowed them to easily examine morphology of the pastes analysed. Although carbonation of the samples was not avoided and carbonation will interfere with any analysis of a cement paste and may lead to incorrect conclusions, it was found that residual particles of $C_3S$ were embedded in a morphological homogeneous gel, Ip, formed from the original $C_3S$ particles. The Ip was linked to a morphological distinct fibrillar (needle-like and sometimes radial) gel, the Op. The most important conclusion that was achieved with this work was that there is no significant difference between the Ca/Si ratios of both products. Besides this, it was also found that the calcium carbonate (calcite) resulting from carbonation of the samples occurred as microcrystals within the Op, and CH as imperfect large crystals. The use of scanning electron microscopy (SEM) is also very important in the study of cement and concrete. Representative flat polished samples can be observed by SEM and analytical EDX analysis can also be performed. SEM provides information regarding the microstructure/bonding between the different components in a concrete sample, and also the morphology of the hydrate phases. From SEM imaging, it is also possible to obtain data/information about the porosity of a certain cement-based sample[44]. As hydration takes place in the cement paste, the microstructure starts to build up. The resulting hydrate phases fill in the spaces between the cement grains leading to the development of a solid mass. The latter is mainly constituted by C-S-H that deposits around the grains, and CH that forms in the water filled pores. Figure 2.13 shows a typical backscattered image of a Portland cement mortar:

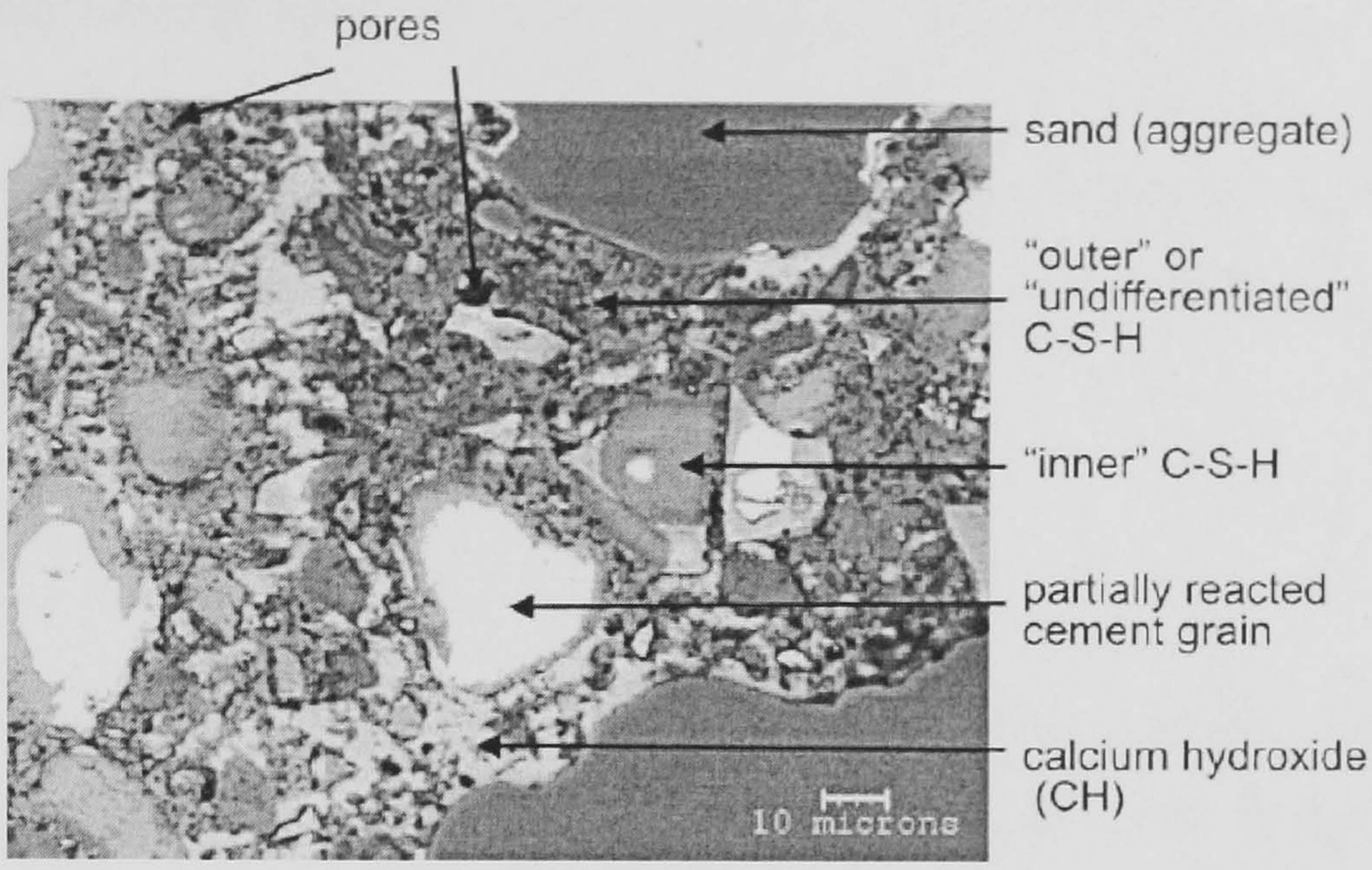


**Figure 2.13** – Typical backscattered image of a Portland cement mortar with the microstructural constituents distinguished[44].

STA, TMS studies, solid-state NMR and electron microscopy are a few of the most common techniques used in order to obtain partial characterization of the C-S-H phase. STA, TMS and NMR are bulk techniques that identify some of the phases usually present in a cement paste, and also provide qualification/quantification of the silicon structure in C-S-H. Analytical electron microscopy gives information regarding the morphology and phase composition.

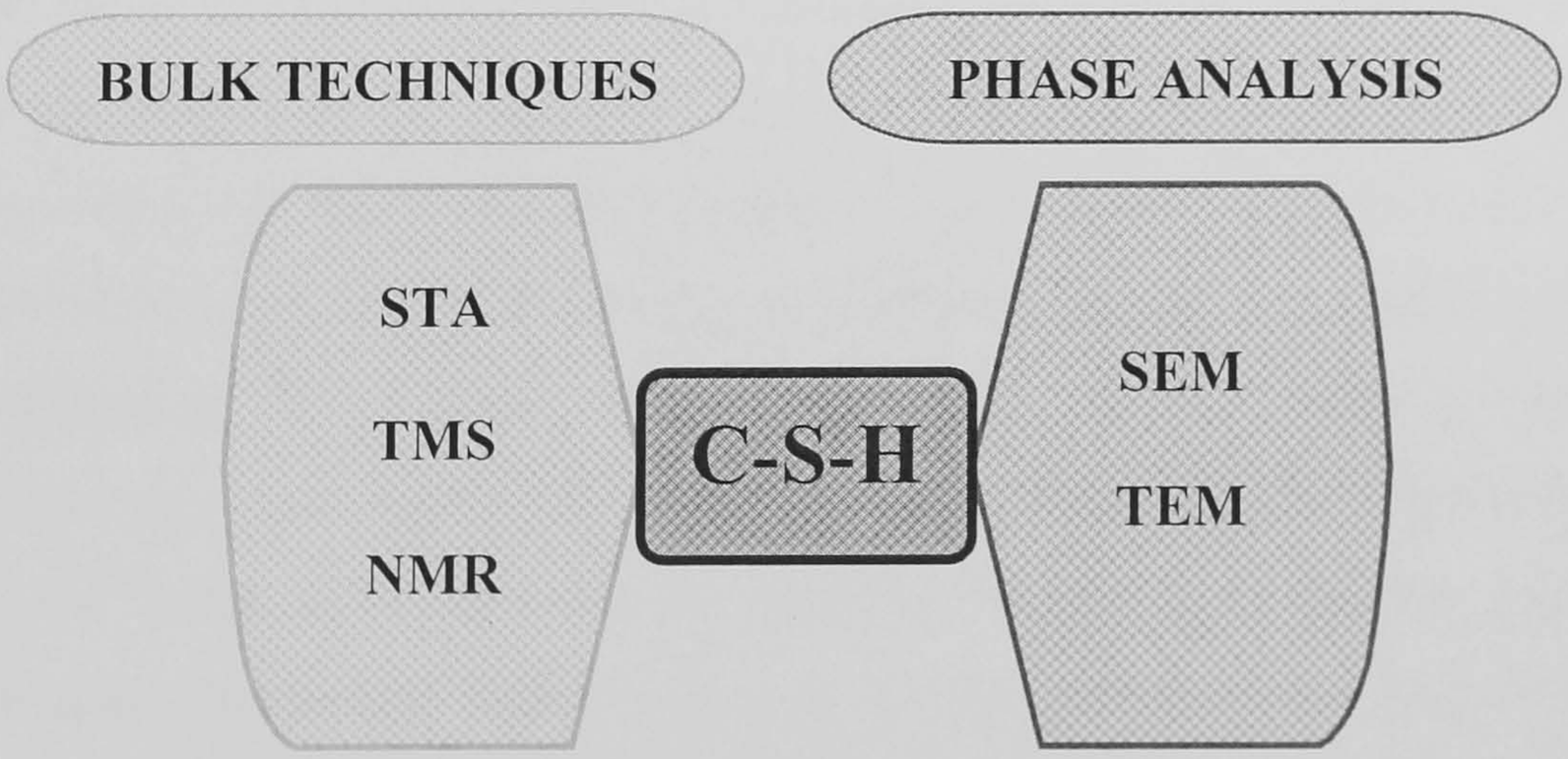


**Figure 2.14** – Schematic diagram showing the relationship between the different techniques used for the C-S-H phase characterization.

The latter section dealt with very simple and pure systems such as $C_3S$ and $C_2S$ pastes, because their hydration process will be fundamental when discussing the proposed structural models or when characterizing more complex systems as in 2.2.3, where many other aspects regarding the analytical application of techniques, particularly electron microscopy, will be discussed with more detail.

### 2.2.2 – Structural Models

The C-S-H phase is an amorphous, or nearly amorphous, disordered gel but from early evidence, it also presents some local short-range structural order. Based on several studies, Taylor[45,46] proposed a structural model for C-S-H formed in $C_3S$ pastes, at room temperature. The model consisted of a combination of highly disordered layer structure in which the layers are similar to the ones of two imperfect crystalline hydrated calcium silicates, 1.4-nm tobermorite ($Ca_5Si_6O_{26}H_{18}$)[47], where 1.4-nm denotes the lattice spacing *c*, and jennite ($Ca_9Si_6O_{32}H_{22}$)[48]. Both calcium silicate hydrates present a layered structure with linear silicate chains (Si-O), called dreierkette-type because the chains have an empirical composition $SiO_3^{2-}$ repeating at intervals of three tetrahedra. If the chain is fragmented into shorter chains, they would contain 2, 5, 8...or, in general, (3n-1) tetrahedra, which is in accord with the (3n-1) sequence of polymers reported in TMS studies, as mentioned before. In tobermorite, each layer consists of a central part with an empirical formula $CaO_2$ in which all the oxygen are shared with those of $SiO_4$ tetrahedra belonging to $SiO_4$ chains that envelop the $CaO_2$ sublayer from both sides. In each $SiO_4$ triplet, there are two types of tetrahedra: the paired ones which are the tetrahedra that share two of their oxygen with the oxygen of the CaO sublayer, and the bridging one, positioned between two paired tetrahedra to form a continuous $SiO_4$ chain; one oxygen atom of the bridging tetrahedra is coordinated to the main layer. The interlayer space between the individual layers is filled with $Ca^{2+}$ ions, to balance out the negative charge of the layers, and also with water molecules. The jennite layered structure is very similar to that of tobermorite but the main difference is that it is more ordered than in tobermorite and, in jennite, half of the chains are alternately replaced by rows of OH groups, resulting in a much larger *a* axis in the crystalline unit cell[24]. The following figures show representations of the

idealised chemical structure of 1.4-nm tobermorite and jennite[4] and the dreierkette-type chain present in both of the structures[1]:

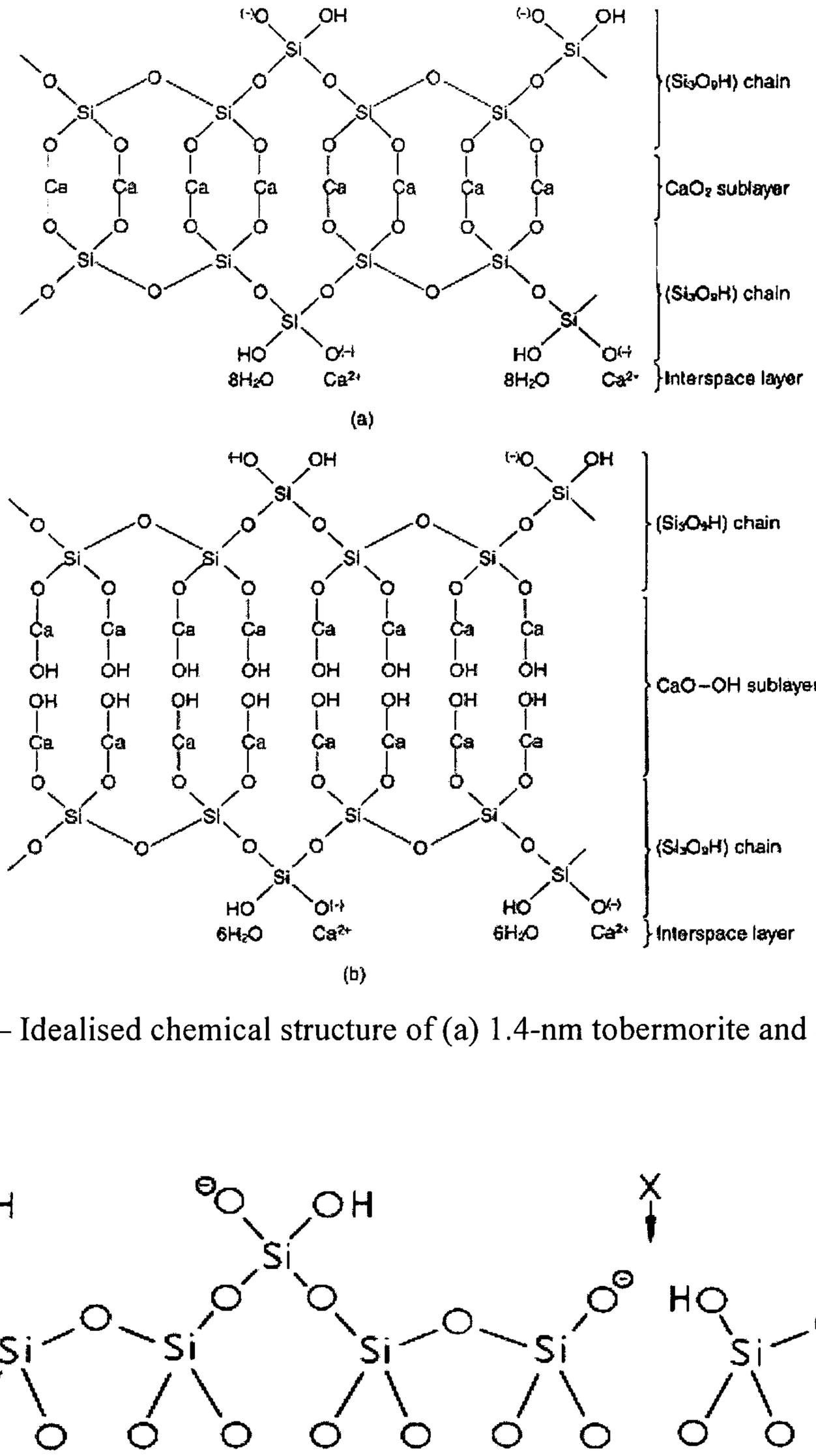


**Figure 2.15** – Idealised chemical structure of (a) 1.4-nm tobermorite and (b) jennite[4].

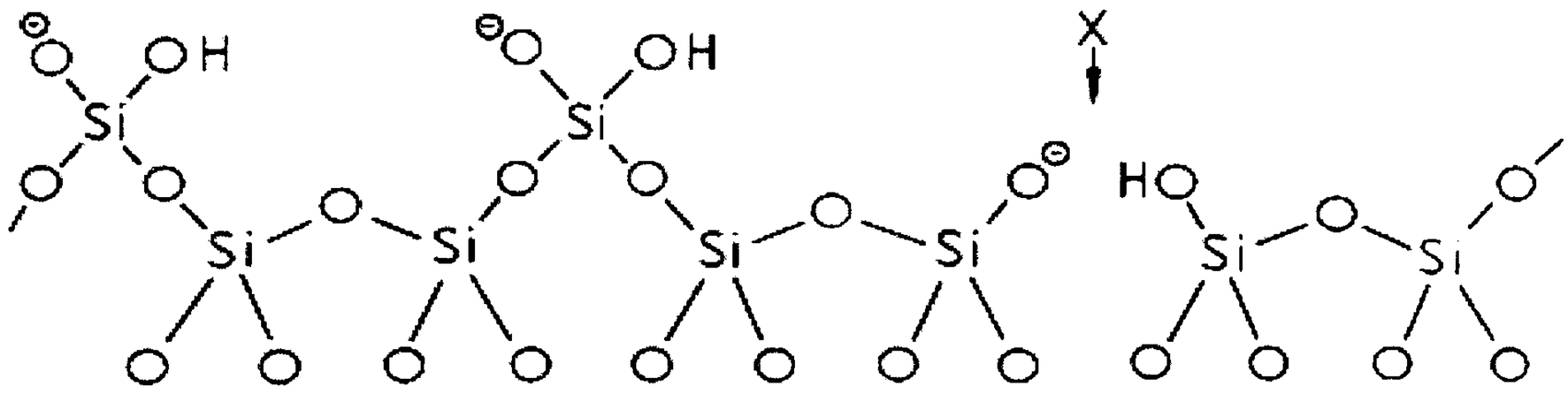


**Figure 2.16** – Silicate chain of the type present in 1.4-nm tobermorite and jennite: the dreierkette-type chain. The tetrahedra in the lower row correspond to the paired ones and those in the upper row, the bridging tetrahedra. At X, a bridging tetrahedron is missing[1].

Many tobermorites, either natural or synthetic, show some deviations from the ideal composition and those variations can be caused by the following effects: some of the bridging tetrahedra may be absent from the dreierkette chain, increasing the Ca/Si ratio; interlayer links may be formed, decreasing the Ca/Si ratio; and partial substitution of Si by Al is balanced by an increase in the interlayer calcium, by introduction of alkali cations, or by both charge compensations. Therefore, Taylor's model considers a combination of anomalous tobermorite and jennite structures and, at early ages, the two structures are present in comparable proportions, and all the bridging tetrahedra are absent. At later stages, the jennite-type layers become more dominant and the bridging tetrahedra are present to an increasing extent. Hence, the silicate anion structure polymerises from $Si_2O_7$ groups to chains of various lengths. This transition from 1.4-nm tobermorite to jennite explains the observed changes in anion distribution with time, changing from a more to a less imperfect structure. The low degree of order is attributed to the presence of both structures, together with variability in anion type and water content. Taylor also compared other type of C-S-H phases, such as C-S-H(I) and C-S-H(II), both considerably more crystalline than the C-S-H formed in cement pastes under normal conditions. C-S-H(I) is a quasi-crystalline phase with an imperfect tobermorite-like structure, and C-S-H (II) is similarly related to jennite, presenting a denser structure. Considering the Ca/Si ratios, the next table presents the extreme values for infinite chains and dimers in 1.4-nm tobermorite and jennite[45]:

**Table 2.4** - Limiting values for Ca/Si ratios in Taylor's model[45].

| | **Ca/Si ratio Dimer** | **Ca/Si ratio Infinite chains** |
|---|---|---|
| **1.4-nm Tobermorite** | 2.25 | 0.83 |
| **Jennite** | 2.25 | 1.5 |

Briefly, the structural model for the C-S-H phase proposed by Taylor, consists in the following:

- Most layers are structurally related to imperfect ones of jennite and a smaller proportion are similarly related to the 1.4nm- tobermorite;

- Many, or all, the silicate tetrahedra are missing from chains, especially in the tobermorite ones;
- Some of the AFm phases present are intimately mixed with the C-S-H gel:
- This model explains the Ca/Si ratio and the increase with time of the average silicate anion size.

Regarding this last consideration in Taylor's mixed tobermorite-jennite-type model, the following figure shows the calculated Ca/Si ratio plotted against a function of chain length for jennite and 1.4-nm tobermorite, modified by omission of bridging tetrahedra[1].

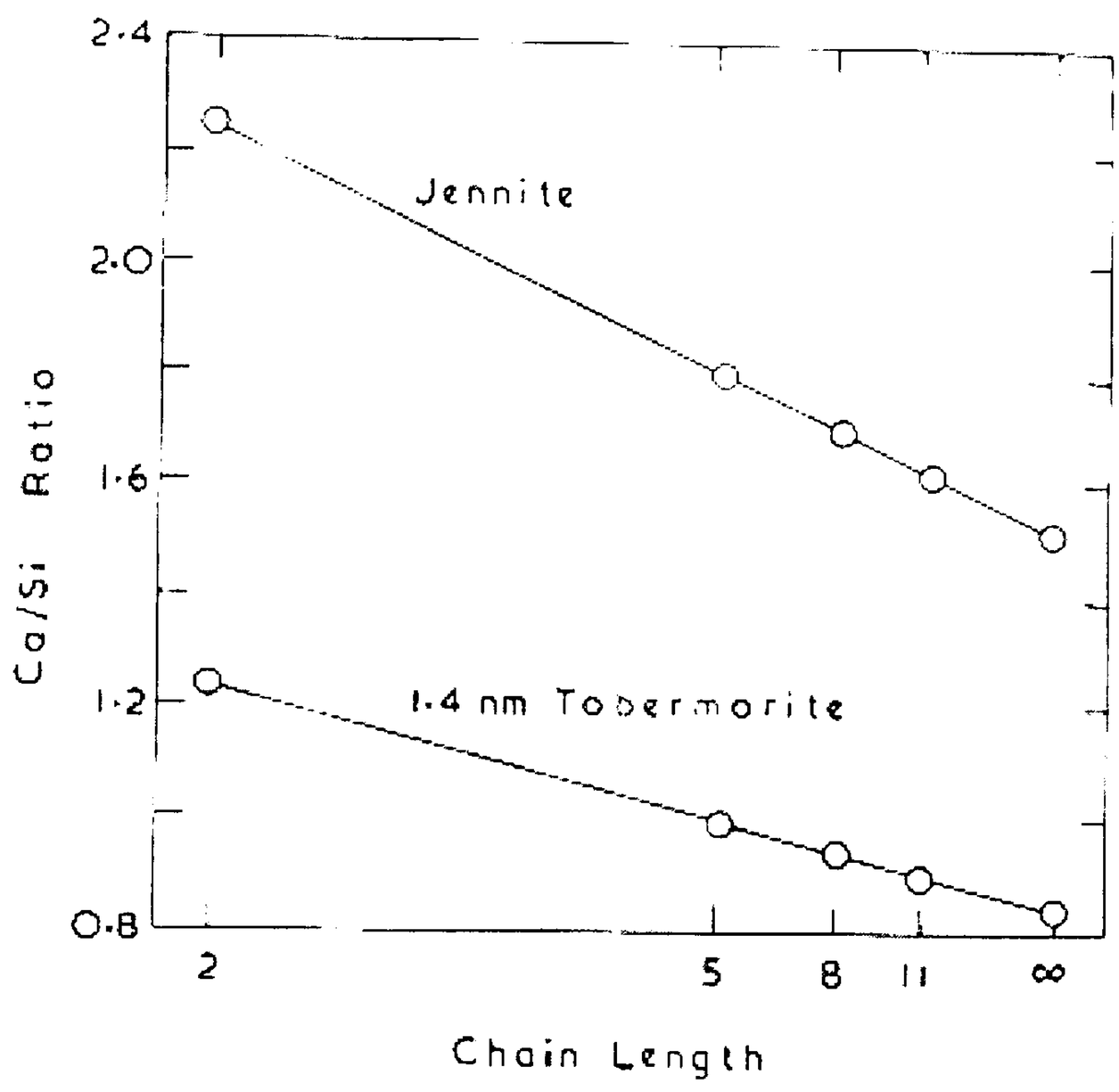


**Figure 2.17** – Calculated Ca/Si ratio plotted against a function of chain length for jennite and 1.4-nm tobermorite[1].

It was possible to observe that a Ca/Si ratio of about 1.8 could arise from a mixture of the two structures, both with dimeric chains, or from a jennite-type structure with, on average, pentameric chains.

Richardson and Groves[2] proposed a general model for the C-S-H phase, based on a more thermodynamic approach. This model was not intended to replace Taylor's model but another structural perspective could also be considered, depending on the conditions under which the C-S-H phase was formed. Besides considering the tobermorite/jennite (T/J) viewpoint, another formulation was introduced: layers of tobermorite-based structure interstratified with "solid solution" $Ca(OH)_2$, the tobermorite/calcium hydroxide (T/CH) point of view. The two-component solid solution systems of $Ca(OH)_2$ and a C-S-H phase (often an established crystalline C-S-H phase, tobermorite or jennite) of low Ca/Si ratio can be described by the following general formula:

$$xCaO \cdot SiO_2 \cdot yH_2O \qquad (Eqn.\ 2.8)$$

where x = 0.833 and y = 0.917 for 1.4-nm tobermorite. $Ca(OH)_2$ is considered as an integral component with no independent existence within the structure, designated by "bound" $Ca(OH)_2$. The "free" calcium hydroxide is the one reserved for any crystalline $Ca(OH)_2$ which may be present. This solid solution-type approach results from evidence observed from chemical extraction methods which showed that $Ca(OH)_2$ could be leached more easily from high Ca/Si ratio C-S-H gels than from low initial Ca/Si ratios, indicating that there is a limiting value of extractable calcium from C-S-H gels. The general formula proposed for C-S-H, considering that C-S-H has isolated silicate chains of varying length and with a variable number of –OH groups attached to Si atoms, and it is in a solid solution with a variable amount of $Ca(OH)_2$:

$$Ca_XH_{2(n+1-X)}Si_nO_{(3n+1)} \cdot zCa(OH)_2 \cdot mH_2O \qquad (Eqn.\ 2.9)$$

n defines the length of the silicate chain; 2(n+1-X) the number of hydroxyl units attached to the chain; z the number of $Ca(OH)_2$ units in the solid solution; m the number of water molecules bound but not present as hydroxyl groups; X the calcium ions necessary to charge-balance the silicate chain; and (X + z) is the total of calcium ions present. The model also considers that the chains are not cross-linked as shown by solid-state $^{29}Si$ MAS NMR studies of C-S-H gels where there are only signals for the

chain-end silicon ($Q^1$ units) and middle-chain silicon ($Q^2$ units). In order to account for the hydroxyl water, the model can be represented by the next formula:

$$\{Ca_{2n}H_wSi_{(3n-1)}O_{(9n-2)}\} \cdot (OH)_{w+n(y-2)} \cdot Ca_{n.y/2} \cdot mH_2O \qquad (Eqn.\ 2.10)$$

Within the brackets, the tobermorite-like core is present; n is the number of units (integer for individual and non-integer for mixtures of units), w is the amount of hydroxyl water, and (3n-1) the mean length of the silicate chains. In here, the silicate anion distribution of the tobermorite units is taken to mirror that of the jennite units, allowing a more flexible approach to the hydroxyl water content of the C-S-H. Therefore, when w increases, structurally, it corresponds to increasing the number of Si-O-Ca-OH and –Si-OH bonds, at the expense of –Si-O-Ca-O-Si-.

As a result, Taylor's model can be considered as a special case of Richardson and Groves' model, where C-S-H is composed of structural units derived from jennite and, to a lesser extent, 1.4-nm tobermorite by omission of bridging tetrahedra. Taylor's tobermorite-based structural units are derived from Equation 2.10 if y = 1 and the degree of protonation of the silicate chains, w/n = 1. For jennite-based structural units, y = 5 and w/n = 1. In order to distinguish between the calcium in the main layer and in the interlayer, the position of the remainder of the (n.y/2) $Ca^{2+}$ ions outside the brackets in Equation 2.10, depends on the structural viewpoint adopted. From Taylor's point of view, they occur in layers of $Ca(OH)_2$ sandwiched between silicate layers of tobermorite-like structure. If the new point of view is adopted, then the calcium ions form part of the main layer. Another difference between the two models is that Taylor's model consists on ½ of possible SiOH groups and ½ Ca coordinated; Richardson and Groves' model allows full range of OH from 0-100%. This gives rise to a greater range of Ca/Si ratio and the model perspective also enables the possible mean chain length (MCL) to be extended. The following table shows some differences between the two models, Taylor's model (T/J viewpoint) and Richardson and Groves' model (T/CH point of view):

**Table 2.5** - Ca/Si ratios assumed by the T/J and T/CH viewpoints[2,49].

| | T/J | T/CH |
|---|---|---|
| **Ca/Si$_{min.}$** (Tobermorite-based infinite units, $T_\infty$) | 0.83 | 0.67 |
| **Ca/Si$_{max.}$** (Jennite-based dimer, $J_2$) | 2.25 | 2.50 |

The next figures show the tobermorite and jennite-based dimers with the maximum degree of protonation, w/n = 2, where (a) shows a schematic diagram demonstrating chemical accounting; (b) and (c) show more realistic structural representations derived using crystal structure data.

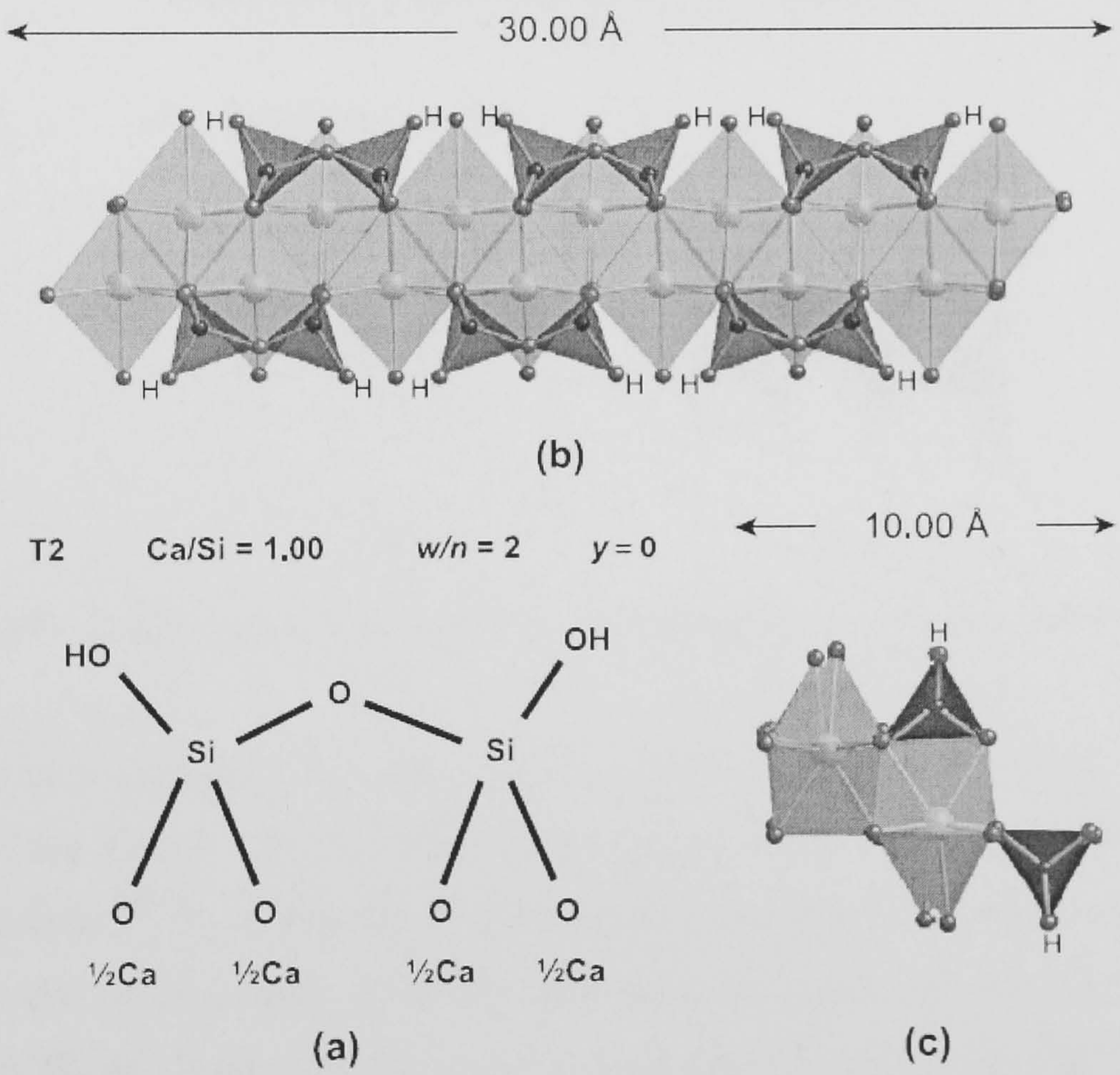


**Figure 2.18** – Tobermorite-based dimer with a maximum degree of protonation (w/n = 2)[3].

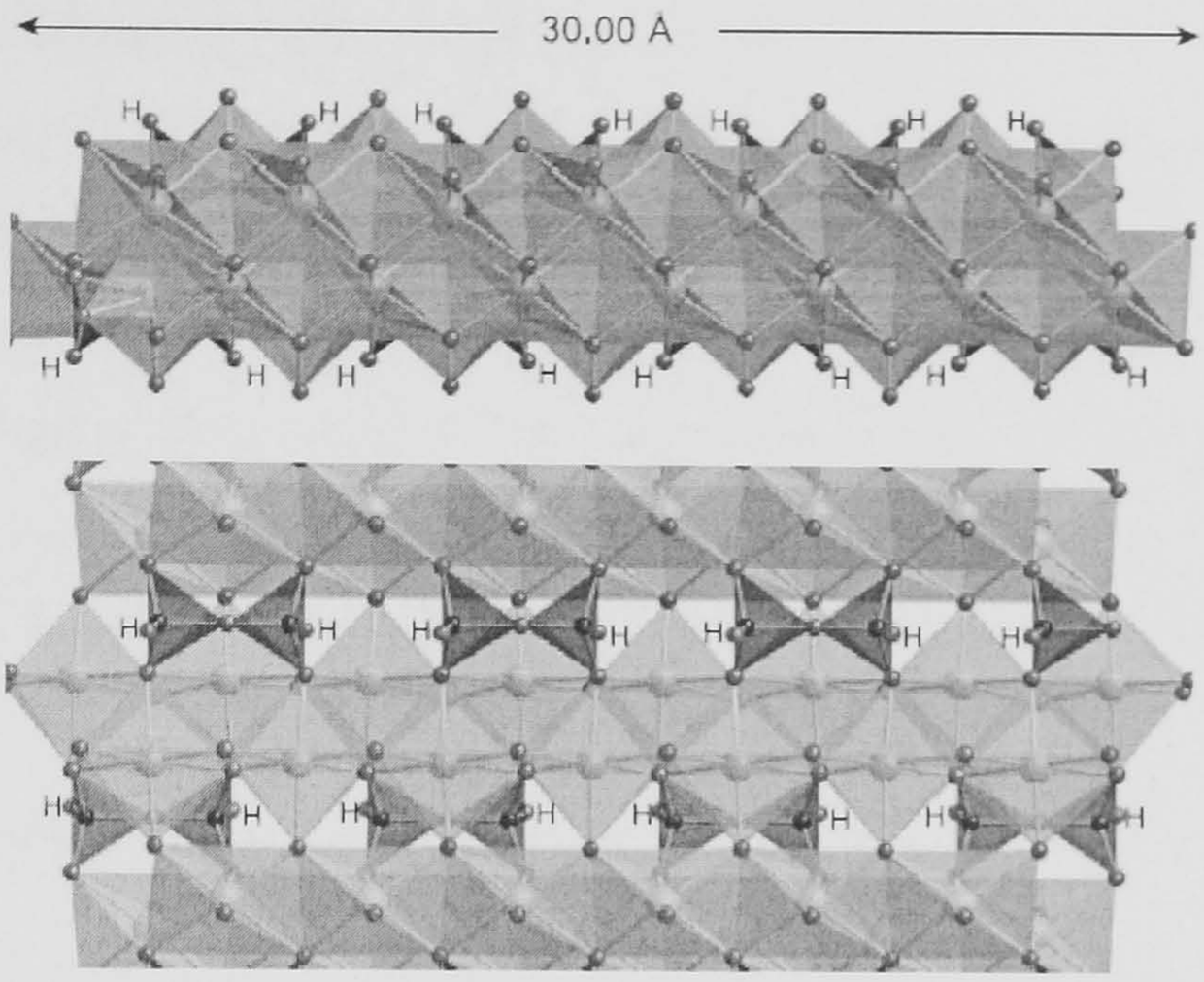


**Figure 2.19** – Jennite-based dimer with a maximum degree of protonation (w/n = 2)[3].

Most of the data present in the literature is consistent with the T/J point of view, but Richardson and Groves observed that these results could also be interpreted by the T/CH perspective[49-51]. A year later, Richardson and Groves[49] extended their model, considering the incorporation of minor and trace elements into the calcium silicate hydrate (C-S-H) gel. From OPC blends with ggbfs, they found that the Op was mainly a single- phase and Ip from alite, belite and slag is compositionally equivalent to Op but Ip had the addition of elements of brucite-based and AFm-type phases, and Mg,Al-hydroxide-type phases. Based on much evidence for Al (or minor amounts of Fe) substitution in the C-S-H gels, Equation 2.10 becomes:

$$\{Ca_{2n}H_w(Si_{1-a}R^{(4)}_a)_{(3n-1)}O_{(9n-2)}\} \cdot I^{c+}_{a(3n-1)/c} \cdot (OH)_{w+n(y-2)} \cdot Ca_{n.y/2} \cdot mH_2O \qquad (Eqn.\ 2.11)$$

where if $0 \leq y \leq 2$ then $n(2-y) \leq w \leq 2n$, if $2 \leq y \leq 4$ then $0 \leq w \leq 2n$. and if $4 \leq y \leq 6$ then $0 \leq w \leq n(6-y)$. $R^{(4)}$ is a trivalent cation (mainly Al in tetrahedral coordination), and $I^{c+}$ is an interlayer ion (either a monovalent alkali cation or $Ca^{2+}$) which charge-balances the $R^{3+}$ substitution for $Si^{4+}$. Aluminium is assumed to substitute only for Si in the bridging tetrahedra of the dreierkette structure[13], since there are n-1 bridging sites, $0 \leq a \leq (n-1)/(3n-1)$. Therefore, Equation 2.9 for the T/CH viewpoint is transformed from Equation 2.11 by $X = \frac{1}{2}(6n- w)$ and $z = \frac{1}{2}(w + n(y-2))$ into:

$$Ca_XH_{(6n-2X)}(Si_{1-a}R^{(4)}_a)_{(3n+1)}O_{(9n-2)} \cdot I^{c+}_{a(3n-1)/c} \cdot zCa(OH)_2 \cdot mH_2O \qquad (Eqn.\ 2.12)$$

Richardson and Groves also considered Al substitution in C-S-H gels. Aluminium substitution plays a significant role in the chemical behaviour of a cement paste. It also influences the cation/anion solubility and the suitability of the cement paste for hazardous waste applications. In a $^{29}Si$ MAS NMR spectrum the observed resonances at about -79.5 and -84.5 ppm, originating from $Q^1$ and $Q^2$ sites respectively were again observed but in addition another resonance was observed at around -82 ppm, which they assigned to a $Q^2(1Al)$ site. It corresponds to a $SiO_4$ chain unit connected to one $SiO_4$ and one $AlO_4$ tetrahedron. They also found that aluminium can only substitute for Si in the bridging site, $Q^2$. The tetrahedral coordination for aluminium in the C-S-H gel was also supported by observation of a broad resonance at about 70 ppm in the $^{27}Al$ MAS NMR. Although some authors considered that Al substitution could also occur in non-bridging tetrahedra[52,53], several other NMR studies and Electron Energy Loss Spectroscopy (EELS) studies confirmed the Al incorporation in C-S-H in the bridging tetrahedra resulting in a resonance at ~81 ppm from a $Q^2(1Al)$ site, as well the assignment of the resonance at about 74.6 ppm in a $^{27}Al$ NMR spectrum to tetrahedrally coordinated aluminium incorporated in the C-S-H phase[29,54-57]. The following figure illustrates the two possible aluminium substitutions but it was demonstrated that aluminium only substitutes in the bridging tetrahedra, as seen in the middle representation (b).

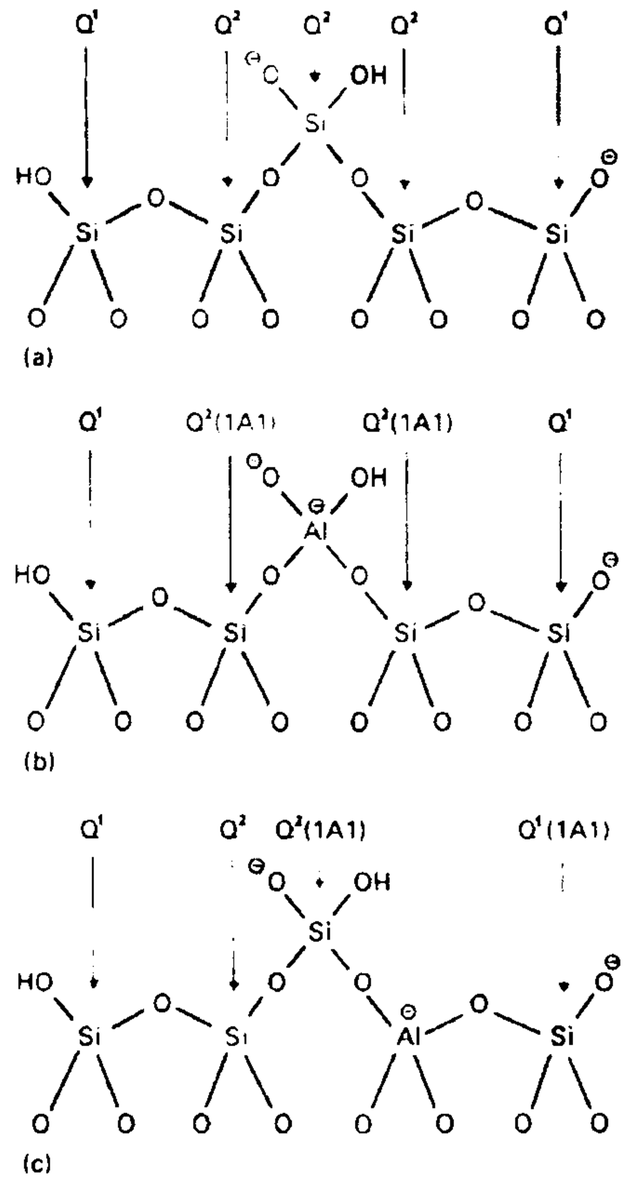


**Figure 2.20** – Schematic representation of a pentameric silicate chain of the type present in dreierkette-based models for the structure of C-S-H. (a) $Q^1$ and $Q^2$ units are identified and the middle $Q^2$ unit is the "bridging" tetrahedron. (b) The same as (a) but with $Al^{3+}$ substituted for $Si^{4+}$ in the bridging tetrahedron. (c) The same as (a) but with $Al^{3+}$ substituted for $Si^{4+}$ in the non-bridging tetrahedron[13].

Finally, Richardson and Groves also concluded that:

- Increasing Al substitution reduces the Si/Ca ratio;
- The degree of substitution of Si by Al is evaluated from the mean Ca/Si ratio of the single-phase C-S-H. Al incorporation is easier in low Ca/Si ratios systems because it is associated with the calcium available for substitution;
- For the limiting Ca/Si ratio of 2.25 where no Al can be incorporated, the mean aluminosilicate chain length is 2, since in dimers there are no bridging tetrahedra and no substitution is possible;
- From $^{27}Al$ MAS NMR data, when the gel is saturated with respect to calcium, the Al occurs in 6-fold coordination, therefore, it appears improbable that tetrahedral Al would occur in jennite-type units which are saturated;
- Pozzolanic reactions and KOH activated pastes lead to more highly polymerized C-S-H.

Richardson[3] also demonstrated that a proper structural model for C-S-H must take in consideration the observed compositional variations and distributions of composition, within any particular system. Therefore, it should account for the following observations:

- In commercial cements, the mean Ca/Si ratio of C-S-H varies considerably between ~2.3-0.7;
- In $C_3S$ and OPC pastes, the mean Ca/Si ratio of C-S-H does not vary with age;
- C-S-H shows a very fine-scale compositional heterogeneity;
- Generally, C-S-H becomes compositionally more homogeneous with age;
- In many cement-based systems, C-S-H contains significant amounts of substituent ions, the most important being $Al^{3+}$.

Richardson showed the application of the proposed model to hardened pastes of tricalcium silicate, β-dicalcium silicate, PC, and blends of PC with blast-furnace slag, metakaolin and silica fume. Many of the experimental results presented in Richardson's work[3] will be more detailed discussed in the next section.

Cong and Kirkpatrick[58-62] proposed a structural model similar to the Richardson and Groves' model. Cong and Kirkpatrick's model is also a defect-tobermorite structural model for C-S-H, in which the structure is based on that of 1.4-nm tobermorite but more disordered, containing a significant concentration of defects. As in Richardson and Groves' model, Cong and Kirkpatrick considered the presence of $Ca^{2+}$ ions and water molecules in the interlayers, as well as the missing tetrahedra and layers of $Ca(OH)_2$ occurring within the stacking sequences, the T/CH point of view. The diversity observed among different C-S-H samples was explained by disorder in the stacking among adjacent layers and structural disorder within each layer. Therefore, this model did not add anything new to the previous proposed model.

Another proposed model[3] based on tobermorite was the one from Nonat and Lecoq. Nonat and Lecoq considered three distinct C-S-H phases, corresponding to three different calcium hydroxide concentrations. The model was based in two different

hypotheses: a first one that corresponded to tobermorite-based structural units with absent Si-OH groups; a second hypothesis that involved the presence of calcium and hydroxyl cations in the interlayer space.

A few years after Cong and Kirkpatrick, Grutzeck[63] proposed another model in the attempt of creating an universal model and that could be used as a link to the majority of the experimental data in the literature. Grutzeck considered it in a way that it should be simple, easy to apply and rigorous in its formulation, and based his model on a sorosilicate-like structure. Sorosilicate minerals are a subclass of the silicates which present two silicate tetrahedra linked by one oxygen ion and, therefore, the basic chemical unit is the anion group $Si_2O_7^{6-}$. Although this class includes normal silicate tetrahedra as well the double tetrahedra, it only has a few common members in comparison with all the other silicate subclasses. In Grutzeck's model, it is suggested that the dimeric C-S-H that forms soon after setting and hardening, may be a metastable phase in its own right, a rigid gel precursor phase whose stability is related to its calcium content. The proposed model differs from the rest of the models because it proposes a relatively rapid equilibrium followed by a much slower diffusion-controlled phase change process. Usually, the dimeric C-S-H is formed later, at the end of the induction period, given by NMR evidence. Although both models predict the same final mature paste containing a mixture of dimer and dreierkette chain, Grutzeck's model explains the presence of consistently large amounts of dimer throughout the entire hydration process, depending on hydration time and temperature, but does not explain the dreierkette chain structure because it can not form dimers[64]. The most inconsistent conclusion taken from this model is probably the fact that a sorosilicate-like C-S-H with a rudimentary sorosilicate-like structure can easily accommodate aluminium in octahedral coordination[63], but not in tetrahedral coordination. Therefore, this goes against all the previous studies which confirmed the tetrahedral-coordination of aluminium in C-S-H and the only octahedral environment that was found belongs to other phases present in the cement pastes, as stated before. Grutzeck's model is not universal and rigorous in its formulation.

The most recently proposed model is the one by Jennings and Tennis[65] and presented by Chen *et al.*[66]. The original colloid model by Powers, suffered some extensions and refinements but, basically, it is based on several studies made considering the concept of two distinct densities of C-S-H and accounts for a number of physical characteristics of C-S-H gel in mature pastes including density, surface area, fractal character, pore structure and size of the individual particles. Considering that the C-S-H gel is an aggregation of precipitated, colloidal-sized particles, they concluded that aging is a process of increasing the number of bounds between globules of C-S-H, causing the C-S-H to become stronger and denser. C-S-H is divided in two different densities: low density (LD C-S-H) and high density (HD C-S-H), both of them with different and specific pore sizes[67-69]. As stated by Jennings and Tennis, only a colloid model can explain the observed physical properties and some changes in the microstructure of C-S-H, presented in their experiments. Nevertheless, the model does not consider most of the experimental observations that Richardson and Groves considered in their models, as well as Taylor's model. Mainly, in this model, the ways in which the Ca/Si ratio can vary in the dreierkette-based structural model are discussed, but the used arguments are not very different from the ones used by Richardson and Groves[2]. Jennings and Tennis' model might be suitable when considering the meso/macrostructure of C-S-H but not when considering the nano/microstructure of the C-S-H phase where the most appropriate structural model is the one from Richardson and Groves[2].

In summary, six of the proposed structural models for the C-S-H phase were discussed and it is possible to conclude that the most suitable model is the Richardson and Groves' model. Jennings and Tennis' model should also be considered as it might be valid when regarding the meso/macrostructure of the C-S-H phase.

### 2.2.3 – Morphology, Microstructure and Nanostructure

The C-S-H phase has been widely studied from the viewpoint of microstructure and nanostructure, but many questions are still to be answered. Several techniques have been used in order to characterize C-S-H as well other phases resulting from cement and

blended cement hydration. Taylor and Newbury[70] performed electron microprobe analysis (EMPA) on a mature cement paste twenty three years old, which provided the chemical compositions of the different phases present (Figure 2.21). They made an attempt to determine a possible significant compositional difference between the C-S-H phase in the inner and outer products, Ip and Op, respectively. It was found that they are quite similar and only the Mg/Ca ratios were variable in the Ip C-S-H, reflecting variations in the Mg contents both between and within the alite and belite originally present. The Fe content tends to concentrate in the hydrogarnet phases, intermixed with other phases, and they also found small amounts of AFm phases, including monosulfate. The next figure shows a general impression of the distribution of compositions from C-S-H, CH, hydrogarnet or mixtures of two or all of the phases, in terms of (Al + Fe/Ca) ratio versus Si/Ca ratio.

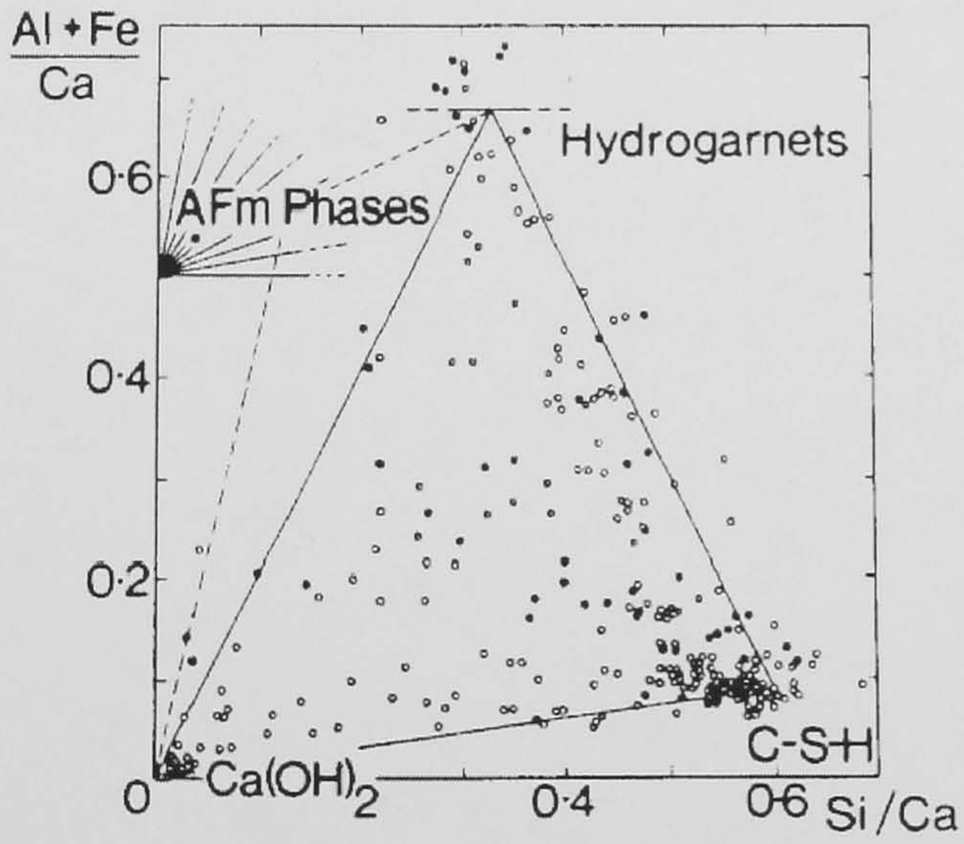


**Figure 2.21** – Electron microprobe spot analyses performed in a mature cement paste[70].

Richardson and Groves[71] performed microanalysis and studied the microstructure of hardened OPC blended pastes with ground granulated blast furnace slag (ggbfs or ggbs). Partial replacement of OPC with ggbs, pulverised fuel fly ash (PFA), or silica fume, produces a significantly less permeable paste with improved resistance to attack from sulfates, chloride, acids and alkali-silica reaction. The use of ggbs, PFA or silica fume is also a way of re-using waste products from manufacture. These additives undergo a so-called pozzolanic reaction where they react and consume CH, mainly generated from the cement hydration of alite, to give C-S-H. They also act like a hydraulic binder, as

any pozzolanic material. The nature of the pozzolanic reaction will be discussed later. Ground blast furnace slag is produced during the manufacture of pig-iron. when slag is cooled down rapidly by pelletization or granulation. forming a glassy material. After being ground to fineness similar to that of OPC, it reacts with water to produce hydrates. depending on its composition, glass content and particle size distribution. Regarding the microstructures present in blended pastes and OPC pastes, C-S-H can be morphologically distinguished as Ip C-S-H and Op C-S-H. Op C-S-H is formed in the originally water-filled spaces, and Ip C-S-H formed within the boundaries of the original anhydrous grains. In pure OPC, the Op C-S-H morphology is fibrillar as shown by transmission electron microscopy (TEM) micrographs, but Op C-S-H acquires a foil-like aspect with slag introduction (Ca/Si decreases), gradually replacing the previous morphology. AFt/AFm-type phases also occur in the blends and have identical morphologies as AFt and AFm-type phases present in neat OPC pastes. Regarding Ip C-S-H regions, they are morphologically identical to the ones found in pure OPC. with a coarse and globular morphology. Morphology is also affected by the paste activation, either using water or an alkaline solution, the latter leading to Op C-S-H morphology with a foil-like aspect. Larger grains of slag or alite often have a rim of fine textured C-S-H which can persist for many years and which are easily spotted within the Op C-S-H. At the Ip/Op C-S-H interface, plates of AFm-type phases and relicts of AFt-type phases needles are also observed. Almost round, poorly crystalline particles rich in iron and aluminium, which often also contain significant amounts of titanium can also be observed. The latter might be a poorly crystalline form of calcium-deficient hydrogarnet. Ca/Si ratios in both Ip and Op C-S-H are similar to the ones found in neat OPC pastes, with an average value of 1.7. Richardson and Groves also found that although there was no significant difference between the Ca/Si ratios in Ip C-S-H formed from alite and slag, the aluminium content is substantially greater in the Ip C-S-H formed from slag, as well as the magnesium content. Magnesium does not migrate from the volume originally occupied by the slag grain because it is fixed to form hydrotalcite with part of the migrating aluminium. Finally. Richardson and Groves also concluded that increasing the slag content reduced the Ca/Si ratio and increased the Al/Ca ratio in both Ip and Op C-S-H. The sulphur content of the AFm-type phases also

increased with the increasing slag substitution. Figures 2.22 and 2.23 illustrate the morphology of Ip and Op C-S-H in selected neat and blended cement pastes.

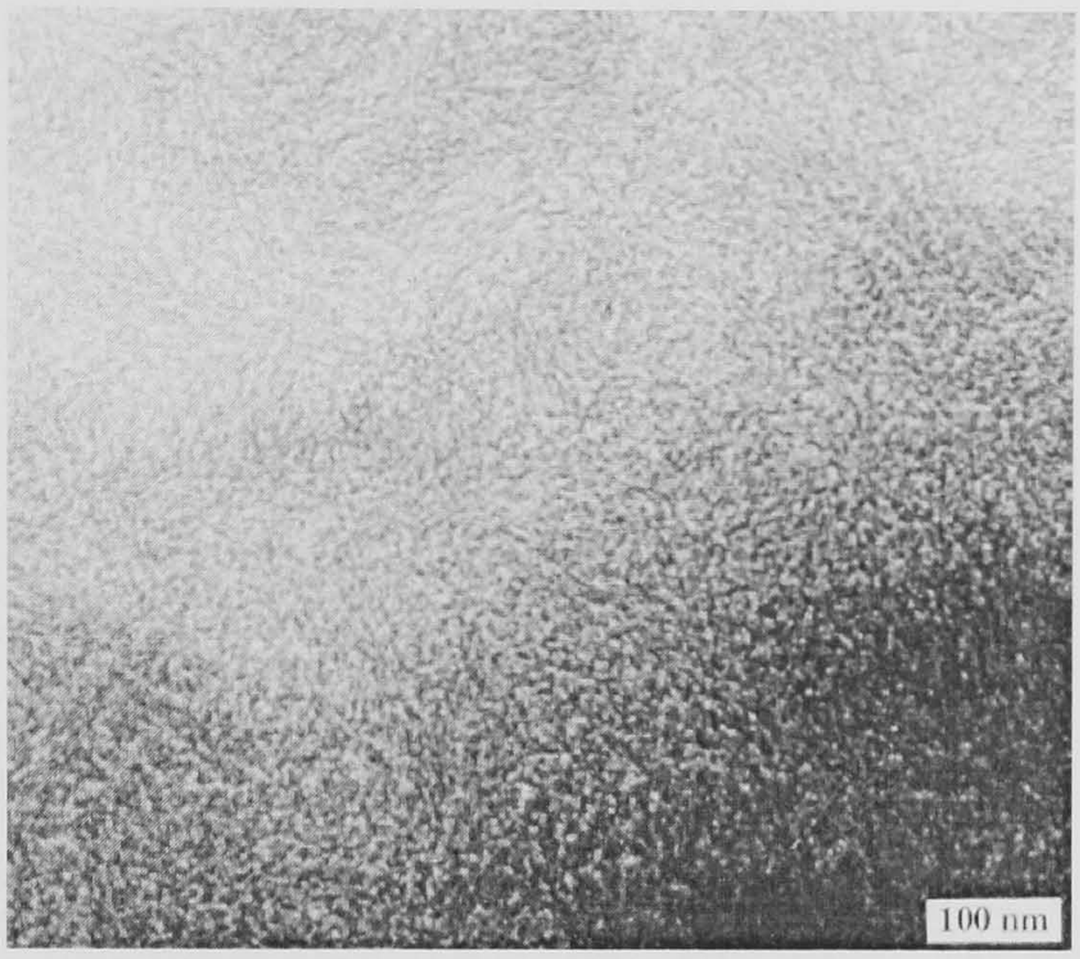


**Figure 2.22** – Transmission electron micrograph showing Ip C-S-H in OPC paste[13].

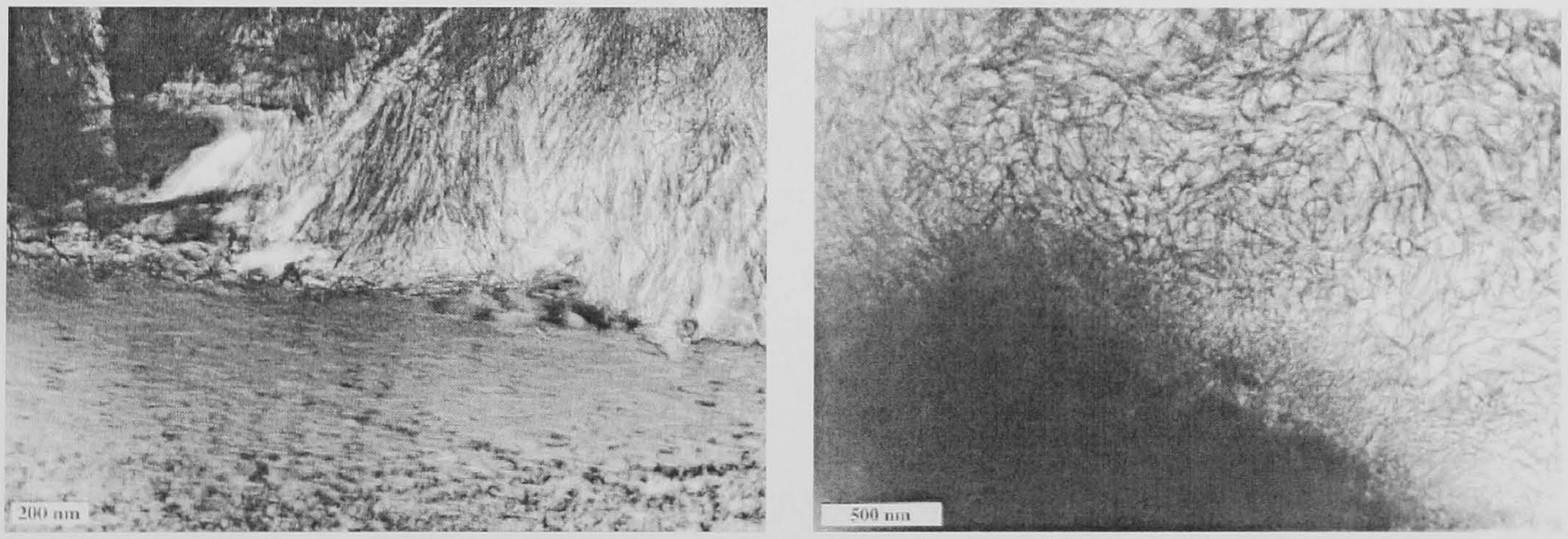


**Figure 2.23** – Morphology difference between Op C-S-H in neat OPC (left) and OPC/slag, both water activated pastes (right)[13].

A year later, the same authors demonstrated the major importance of TEM, comparing TEM studies with EMPA studies, performed on OPC and $C_3S$ pastes[72]. The difference between the morphology of Ip and Op C-S-H was confirmed, but not in terms of Ca/Si ratio; Ip C-S-H occasionally was intermixed with small amounts of AFt/AFm-type phases, a magnesium-rich phase and CH. It was also concluded that, in general, the composition of C-S-H does not change significantly with age but changes from one area

to another in the same sample. The microanalysis by EMPA is in agreement with the TEM-EDX results but it is impossible to obtain analytical data from a single-phase in EMPA, avoiding admixture with other phases. When not analysing finely divided materials, the main reason that confirms the requirement of TEM studies in cement chemistry is the ability of carrying out chemical analysis correctly and unambiguously on each phase in a cement paste. Following their studies, Richardson and co-workers[8,13,55,56,73-77], used $^{29}$Si MAS NMR and TEM-EDX to study the C-S-H gel present in both water and alkali-activated (KOH solution) pastes of β-$C_2S$, $C_3S$, neat OPC and white Portland cement (WPC), blends of OPC/slag, WPC/slag, WPC/PFA and WPC/metakaolin, 100% slag paste, and alkali activated silica. The following conclusions were found:

- C-S-H gels (Ip and Op) present in both water and alkali-activated pastes are different being nearly amorphous in the first case, and semi-crystalline in the case of alkali-activation;
- Aluminium, the main substituent in C-S-H, substituted for silicon in tetrahedral sites and only at the central tetrahedron (bridging tetrahedra of dreierkette chains) of the pentamer, or longer silicate chains;
- Due to compositional resemblance, the proposed Richardson and Grove' structural model principles could be applied to the OPC/slag and OPC/PFA hardened cement pastes;
- Ip C-S-H from larger cement grains had a fine-scale and homogeneous morphology but Ip C-S-H from slag grains were chemically distinct in composition by having a higher content of Mg and Al;
- Hydrated remains of small particles contained a less dense and more porous product, surrounded by dense C-S-H;
- The Ca/Si ratio for C-S-H in pure cement pastes varied from ~1.2 to ~2.3, with a mean value of ~1.75;
- The Ca/(Si+Al) ratio for C-S-H in water activated cement/slag pastes varied from ~0.7 to ~2.4;

- With increasing slag content, the Si/Ca and Al/Ca ratios for C-S-H also increased as well as the aluminosilicate chains length. The morphology of C-S-H changed from fibrillar to a foil-like morphology (Figure 2.24);
- The microstructure of $C_3S$ pastes was a very useful reference for more complex systems such as neat OPC, OPC/ slag or OPC/silica fume blends, and alkali-activated slag cements.


**Figure 2.24** – TEM micrographs of fibrillar Op C-S-H in a mature OPC paste. On the right side, a foil-like Op C-S-H in an alkali-activated 100% slag paste[8].

Besides all the fundamental information given by thermogravimetry and SEM/TEM-EDX data, the microstructure and the silicate anion structure of the C-S-H phase can be characterised by two complementary techniques, as explained before: TMS-GPC, which gives semi-quantitative data on the fractions of silicon present in different anionic species, and $^{29}Si$ MAS NMR, which allows a quantitative analysis, giving information on the fractions of Si present in silicate tetrahedra with different environments. It has been shown by both techniques that the dimeric silicate species predominate in the first twenty four hours of hydration followed by the formation of higher polymeric species, pentamer, octamer, etc in the (3n-1) sequence. From $^{29}Si$ single pulse MAS NMR, it is possible to calculate a mean silicate chain length by the following formula, considering $C_3S$ pastes with no aluminium substitution at the chain bridging sites:

$$MCL = \frac{2}{\frac{Q^1}{Q^1 + Q^2}} \qquad (Eqn.\ 2.13)$$

In the spectra of slag blended pastes, the peaks corresponding to unreacted components are simple to identify, but the hydrate peaks are not that easy to be fit due to overlapping. In order to deconvolute the spectra and if the blends are activated with KOH solution, then this alkali activation leads to very similar hydration products and microstructure to the ones resulting from water activation. The main difference is that in the alkaline pastes, the C-S-H phase is structurally better ordered and CH is microcrystalline, as Groves[78] determined in a previous TEM study of low water/cement ratio pastes. Therefore, this improves the resolution of the spectra leading to narrower NMR line widths, and allows the determination of the peaks that are present. After that, the spectra are ultimately fitted independently. There is a sharp peak $Q^0$ at – 71.3 ppm corresponding to belite phase superposed on a broader peak due to many peaks corresponding to alite. The hydrate peaks in the alkali-activated pastes are more defined and easier to fit, as next figure illustrates:

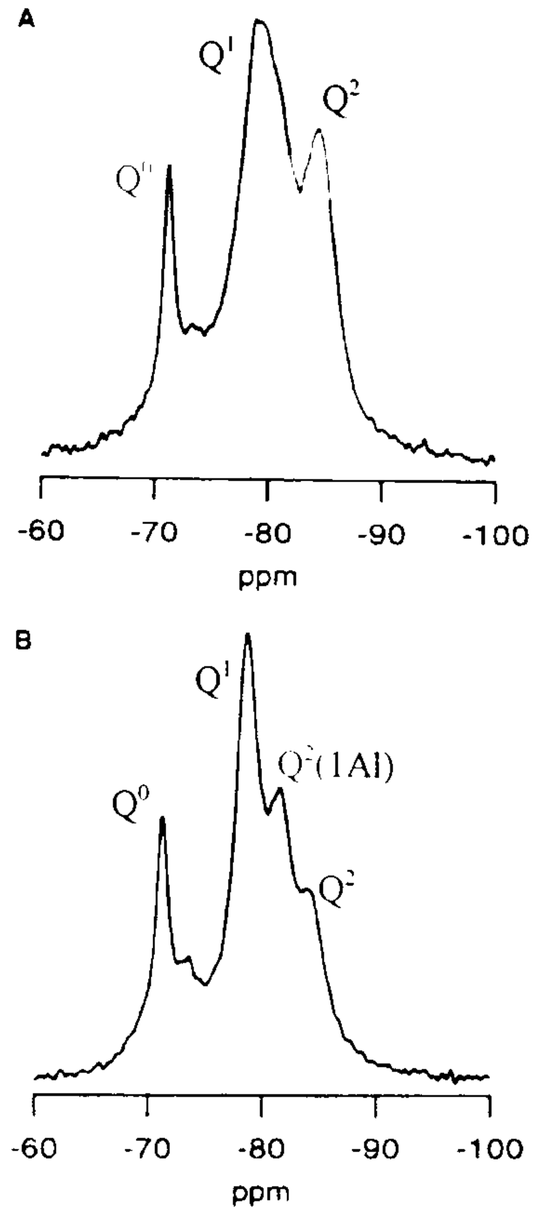


**Figure 2.25** – (A) Single-pulse $^{29}$Si NMR spectrum for water activated 50%WPC/50% slag blend hydrated for 5 months. (B) Single-pulse $^{29}$Si NMR spectrum for a 5*M* KOH-activated 50% WPC/50% slag blend hydrated for 5 months[13].

The fit of these spectra became a powerful aid in the deconvolution of the spectra corresponding to the water activated corresponding spectra, leading to the following general conclusions resumed in the next table:

**Table 2.6** - $^{29}$Si MAS NMR peak assignment in spectra corresponding to slag blended pastes[13].

| Assignment | δ/ppm |
|---|---|
| **Unreacted belite ($Q^0$)** | -71.3 |
| **Unreacted slag** | -73.0 |
| **$Q^1$** | -79.0 |
| **$Q^2$(1Al)** | -82.0 |
| **$Q^2$** | -85.0 |

It should be noted that the presented values are only approximated values and often vary due to their dependence on the nature of the cement-based system. The average Al/Si ratios for the C-S-H phase can be calculated from the deconvoluted peak areas using

Equation 2.14. The values calculated, using Equation 2.14, are in good agreement with values found by microanalysis in the TEM:

$$Al/Si = \frac{1/2\,Q^2(1Al)}{Q^1 + Q^2 + Q^2(1Al)} \qquad (Eqn.\ 2.14)$$

The same can be applied in the calculation of the mean aluminosilicate chain length, with Al substituting at the bridging sites:

$$MCL = \frac{2}{\left(\frac{Q^1}{Q^1 + Q^2 + 3/2\,Q^2(1Al)}\right)} \qquad (Eqn.\ 2.15)$$

In this section, different analytical techniques and resulting data for complete characterization of the C-S-H phase were discussed, as well as the relationships between nano/microstructure, Ip and Op C-S-H, their different morphologies and Ca/Si ratios, behaviour of different types of blended cement pastes analysed and aluminium substitution in the C-S-H phase.

## 2.3 – WHITE PORTLAND CEMENT

A particular kind of Portland cement is considered in this section because the studied cement systems were prepared with white Portland cement (WPC) and its chemistry is slightly different from the chemistry of ordinary Portland cement (OPC), the latter more widely used.

White Portland cement, WPC, is manufactured from purer raw materials than the ones usually used in OPC manufacture. The purer raw materials can be china clay (kaolinite) and a selected white chalk or limestone. If these raw materials do not contain enough free silica in order to produce the required level of silicates, then ground white sand can be added to them. WPC contains an iron oxide ($Fe_2O_3$) content of less than about 0.3%,

and the manganese and chromium oxides must be one order and two orders of magnitude lower than 0.3%, respectively. Therefore, it is expected that typically lower $C_3A$ content also means much lower $C_4AF$ content. Although it is more expensive than OPC, the use of WPC in this work is justified by its low iron content, a paramagnetic element, which causes NMR line broadening. The hydration products of WPC are quite similar to the hydrate phases present in OPC, although that will always depend on the initial chemical composition of any cement. Regarding TMS-GPC studies (Figure 2.4), the (3n-1) sequence is followed with increasing hydration time and consequent polymerization. $^{29}Si$ MAS NMR and $^{1}H$-$^{29}Si$ CP MAS NMR has also been used in the characterisation of WPC[13,79], and some of the obtained results for a five month neat WPC paste[13] are shown in Figure 2.26:

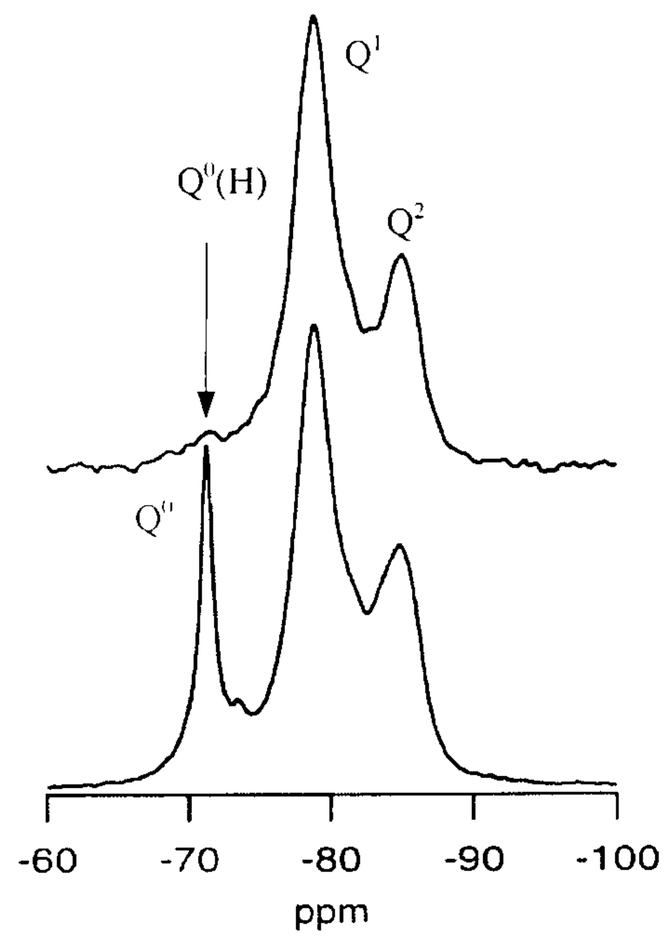


**Figure 2.26** – $^{29}Si$ single-pulse (bottom) and $^{1}H$-$^{29}Si$ CP (top) MAS NMR spectra of WPC 5 months old[13].

From the interpretation and fitting of these spectra, it was possible to observe that in the CP MAS NMR spectrum (top spectrum), there was an amount of hydrated monomer, $Q^0(H)$, and $Q^1$ and $Q^2$, the corresponding peaks to the different silicate species present in the hydration products. In the single-pulse spectrum, the first peak at around -71.3 ppm corresponded to unreacted belite ($Q^0$), the second peak around -73.5 ppm probably corresponded to anhydrous $\gamma$-$C_2S$, the third and fourth peaks at -79 and -85 ppm were

due to the end-chain ($Q^1$) and the middle-chain ($Q^2$) groups, respectively. The $Q^2$(1Al) peak is comprised between the $Q^1$ and $Q^2$. Using high-field $^{27}$Al MAS NMR[39,80], it was possible to distinguish the different octahedral and tetrahedral coordination of aluminium in a WPC paste, as the next figure demonstrates.

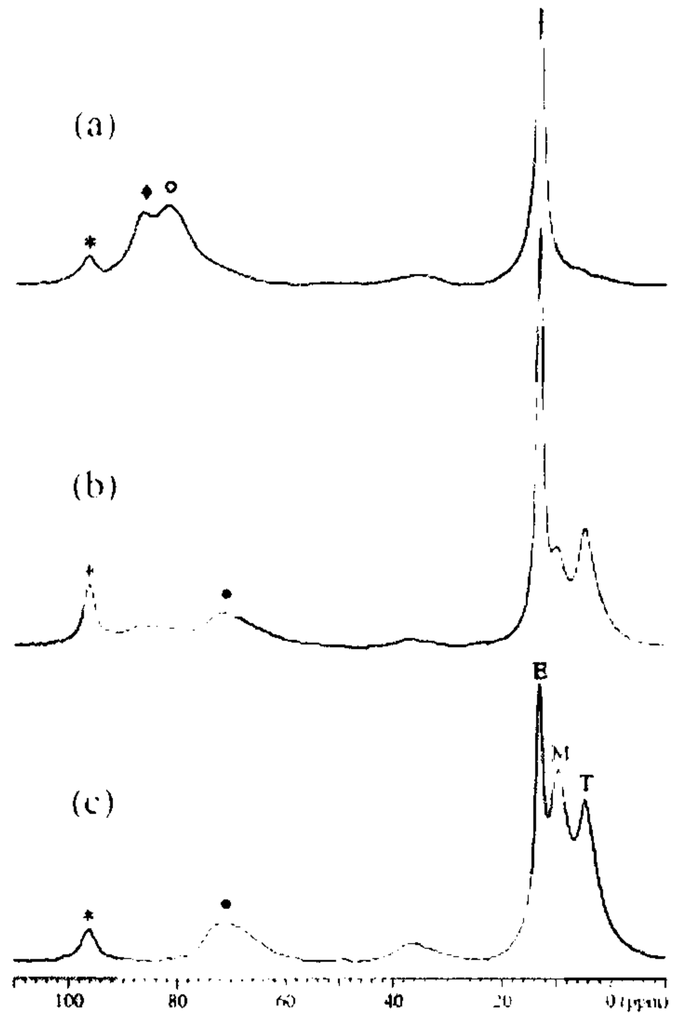


**Figure 2.27** – High- field $^{27}$Al MAS NMR spectra of WPC hydrated for (a) 6h, (b) 1 week and (c) 1 year. (* indicate spinning sidebands from ettringite, ♦ indicates Al incorporated in alite/belite, o Al in the calcium aluminate phase, • the Al incorporated in the C-S-H phase)[39].

After six hours of hydration, the tetrahedral resonances were assigned to aluminium incorporated in the calcium silicates alite and belite, as well as aluminium present in an impure form of calcium aluminate. In the one week spectrum, three different peaks were observed for the octahedral coordination, corresponding to ettringite, monosulfate and a third aluminate hydrate phase. Aluminium was also incorporated in the C-S-H phase, in a tetrahedral environment. After one year of hydration, the intensity of the peak corresponding to aluminium tetrahedrally coordinated in the C-S-H phase increased, and a peak corresponding to penta-coordinated aluminium was also clearly observed.

## 2.4 – PULVERISED FLY ASH

Pulverised fly ash (PFA) is a waste product recovered from the process of burning pulverised coal and, as a pozzolanic material, is widely used as a replacement for Portland cement. Fly ashes are very heterogeneous fine powders consisting mostly of rounded or spherical glassy particles of variable silica, alumina, and iron oxide contents; there are also some irregular or angular particles. According to the ASTM C618, fly ashes can be classified in three different classes, depending on the coal burnt process that originates it[81]:

- **Class C** is pozzolanic and cementitious fly ash usually produced from burning lignite or subbituminous coal; it has self-cementing properties leading to early strength development.
- **Class F** is also pozzolanic, usually derived from burning anthracite or bituminous coal; it has little or no cementing value alone, high silica content and slower early strength development.
- **Class N** is raw or calcinated natural pozzolan such as some diatomaceous earths, opaline cherts, and shales.

Variations in the coal composition, combustion conditions, ash collection systems, and other variables can affect largely the composition and fineness of fly ash. The fly ash composition originated by a single source may vary greatly over a relatively short daily time intervals[82-85]. Fly ash is also used as a fill material, soil stabilization and waste remediation. In blended cements, the use of fly ash can fulfil two main roles: participation in the cementitious hydration products and modification of the characteristics of the hydrated cement. As a binder in Portland cement blends, it presents several benefits such as enhanced workability and less water demand due to the spherical shape of the particles; reduced bleeding; increased ultimate strength; reduced permeability and chloride ion penetration; lower heat of hydration; greater resistance to sulfate attack; greater resistance to alkali-aggregate reactivity, i.e., resistance to the alkali-silica reaction, ASR; reduced drying shrinkage: etc... The alkali-silica reaction, ASR, has been effectively inhibited by class C fly ash. It suppresses or reduces the expansive reactions resulting from the ASR[81-84]. A "pozzolan" material is a siliceous or

a siliceous aluminous material which in itself possesses little or no cementitious value. However, when finely divided and in the presence of a moisture, it can react with calcium hydroxide giving products with cementitious properties. In the case of PFA, pozzolanic activity refers to the ability of the silica and alumina components to react with available alkali (calcium and or magnesium) from the hydration products present in the cement pastes. The pozzolanic reaction between the reactive silica and CH, producing C-S-H gels can be expressed according to the chemical reaction for pure materials:

$$xCH + yS + zH \Rightarrow C_xS_yH_{x+z} \qquad (Eqn.\ 2.16)$$

The alumina present in the pozzolan may lead to the formation of several hydrates including calcium aluminate hydrate ($C_4AH_{19}$), strätlingite ($C_2ASH_8$), ettringite ($C_3A{\cdot}C\bar{S}{\cdot}H_{32}$) and monosulfate ($C_4A\bar{S}H_{12}$). Nevertheless, aluminium can also be incorporated in the C-S-H phase, as seen before. After AFt-type phases are formed, if some carbonation occurs, calcium carboaluminate hydrates are formed and will tend to stabilize ettringite with respect to its transformation into monosulfate[81]. Kovacs[85] found that in fly ash blended cement pastes from Hungary, the hydration products were very similar to the ones found in the neat pastes. Using XRD and thermal analysis, it was also concluded that increasing the fly ash content, the CH phase decreased as it was consumed in the pozzolanic reaction. Besides the additional formation of C-S-H gels, the concentration of the calcium aluminate hydrates also increased, being poorly crystalline, and leading to additional problems in the XRD and TG interpretation. Kovacs also established a relationship between the fly ash content and the developed strength. Mohan and Taylor[86] studied pastes of $C_3S$ with a fly ash with high glass content. They confirmed the results from Kovacs' work and also found that about 15% of the fly ash reacted in twenty eight days and 45% in one year. It was also observed that the mean Ca/Si ratio decreased slightly and the degree of polymerization of C-S-H was significantly higher than the degree of polymerization observed in pure $C_3S$ pastes, after several weeks of hydration. The microstructure and composition of the hydrated products of similar pastes were studied by Rodger and Groves[87]. In general, the microstructure of the $C_3S$ paste was not very much affected by the presence of the PFA

particles, apart from a reduction in the quantity of CH crystals. On the other hand, the Ip and Op C-S-H compositions were affected, presenting a reduced Ca/Si ratio. It was also observed that Ip C-S-H was free of other elements but Op retained many trace elements, particularly large quantities of potassium. Considering the PFA reactivity, crystalline phases like mullite and iron oxide were unreactive, except quartz, alumino-silicate and silicate glass, which had a similar reactivity. When reacting, they formed a rim of dense C-S-H and, within this rim, there were also areas of low density radially fibrillar C-S-H. Partial shells of hydrogarnet were also present in the C-S-H phase. As with $C_3S$/PFA pastes, Rodger and Groves[88] reached similar conclusions in the study of OPC/PFA pastes. Once again, the microstructure of OPC/PFA was not greatly affected by the PFA presence and the Ca/Si ratio was reduced. Besides the natural hydrate phases present in OPC pastes like CH, C-S-H, and AFt/AFm-type phases intermixed with C-S-H, there were also regions of small particles of poorly crystalline iron-containing material and needles of hydrotalcite-type phases. Those regions probably were originated from $C_4AF$ interstitial phases in the cement clinker and these observations were made for both OPC and PFA blended OPC pastes. Some TEM micrographs illustrate these features:

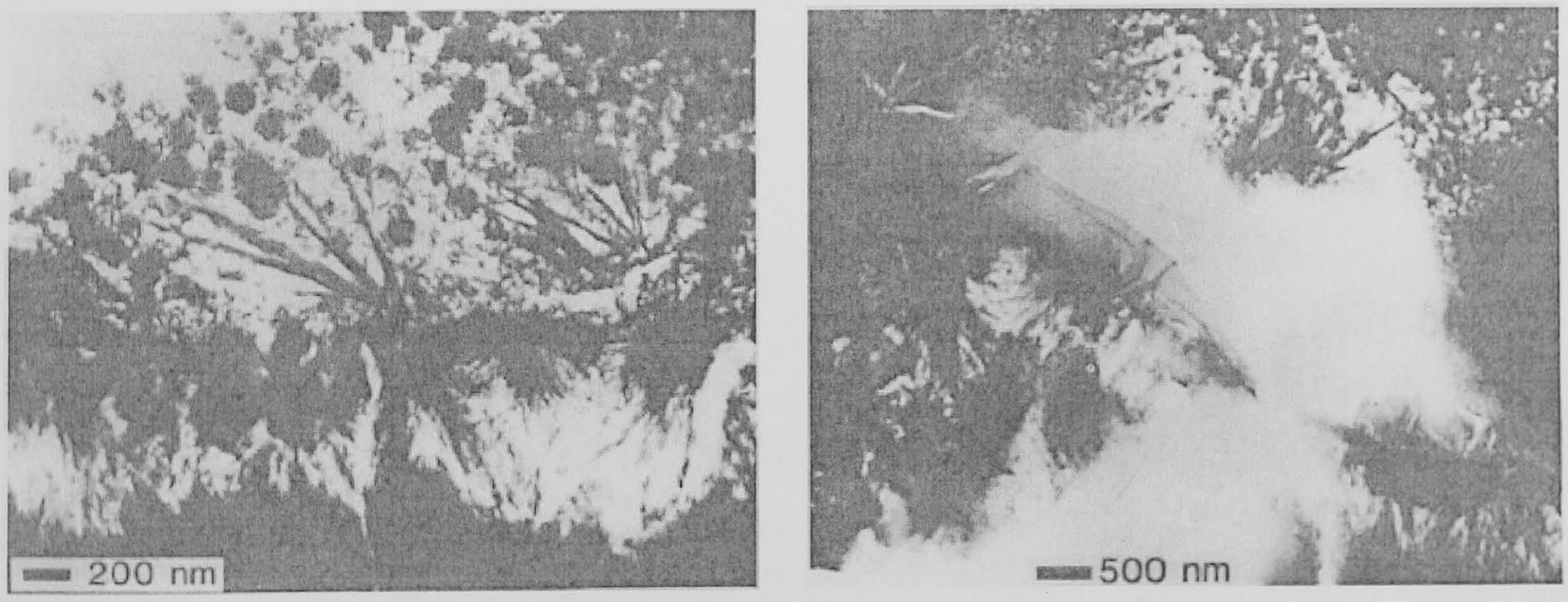


**Figure 2.28** – On the left side, a TEM photograph showing poorly crystalline iron-containing material intermixed with magnesium-rich crystalline needles and C-S-H, in a 30-month-old cement paste. On the right side, the same is observed with the magnesium-rich crystalline needles lying beside a region of Ip C-S-H and showing both phases within a fibrillar rim of C-S-H[88].

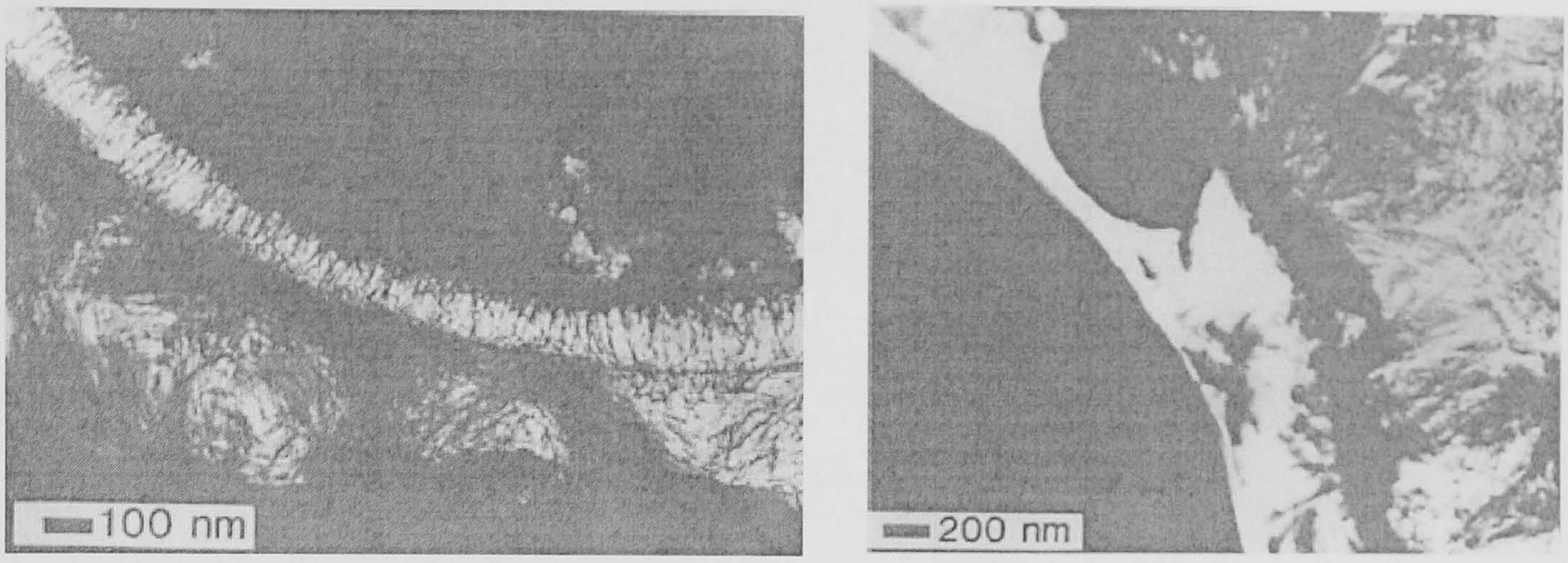


**Figure 2.29** – TEM photographs showing some reactive PFA particles and the fibrillar Op C-S-H gel at different ages less than one year. On the right side, it is possible to also observe an area of crystalline hydrogarnet within the original outer boundary of the particle[88].

Pietersen *et al.*[89] studied the OPC/PFA (class F) system by $^{29}Si$ MAS NMR. They found that an increase in the amount of silica middle groups ($Q^2$) at -84 ppm occurred when compared with the amount of silica end groups ($Q^1$), at -79 ppm. These results were in very good agreement with previous TMS studies on the same system, supporting the tendency to form longer C-S-H chains, at later ages. Figures 2.30 and 2.31, show the spectra of anhydrous fly ash and the time-evolution stack plot of the studied OPC/fly ash blend.

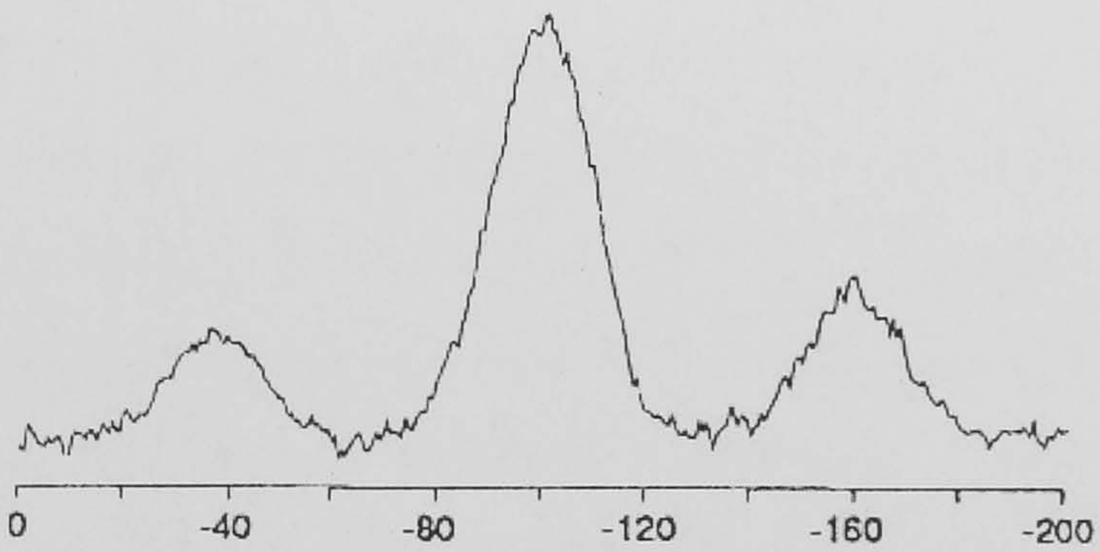


**Figure 2.30** – $^{29}Si$ NMR spectrum of class F fly ash after removal of magnetic material[89].

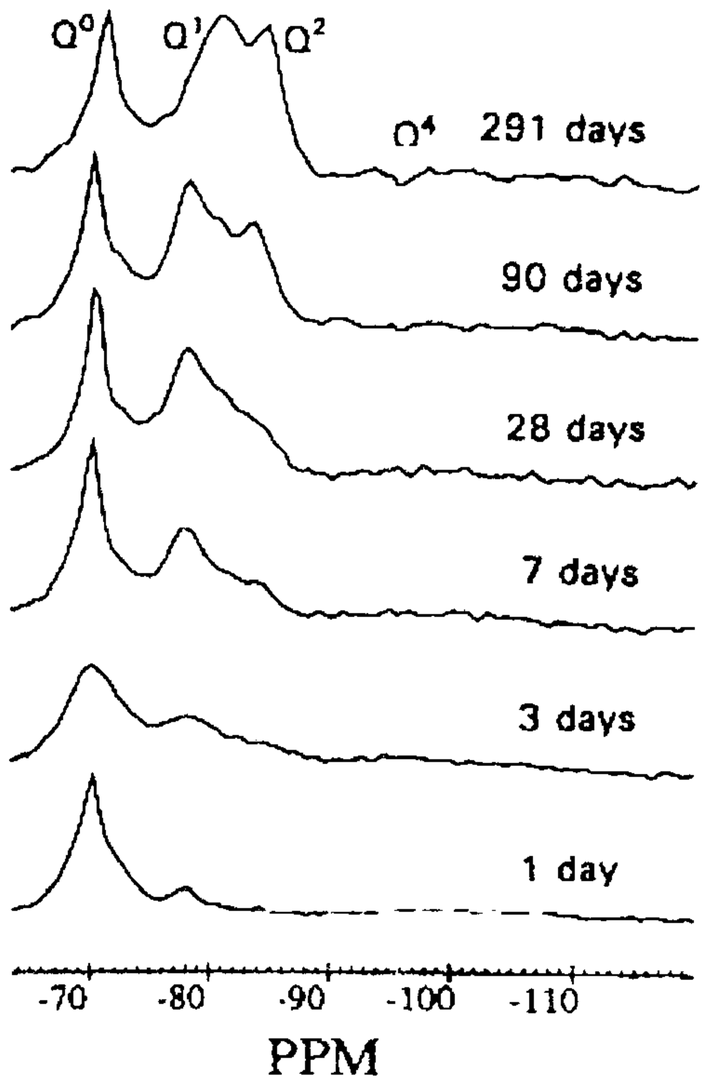


**Figure 2.31** – Evolution of the $Q^n$ distribution in a OPC/20% (m/m) class F fly ash blend[89].

The hydration reaction appeared to be affected by the size-distribution and glass-content of the fly ash used, reflecting a higher $Q^2/Q^1$ ratio and an increased initial hydration. It should be pointed out that a general problem in the deconvolution of the $Q^4$ chemical shift occurred because of the high paramagnetic iron content which made the peak broader. It was also observed that even when the Si signal was split up in several spinning bands it did not seemed to affect the distribution of the $Q^n$ species. Pietersen[90] also used TEM in order to characterize Portland fly ash cement pastes, accomplishing similar conclusions to the same that Rodger and Groves established before. Pietersen TEM studies were in good agreement with Rodger and Groves' proposed mechanism for the formation of concentric C-S-H rings, surrounding the fly ash spheres: the Liesegang-type ring mechanism. Love and Richardson[91] studied the composition and structure of C-S-H in the KOH-activated WPC/PFA system, by $^{29}Si$ MAS NMR and $^{1}H$-$^{29}Si$ CP MAS NMR, TEM, Energy-Loss Near Edge Spectroscopy (ELNES) and TMS-GPC. The following figures illustrate some of the observed results:

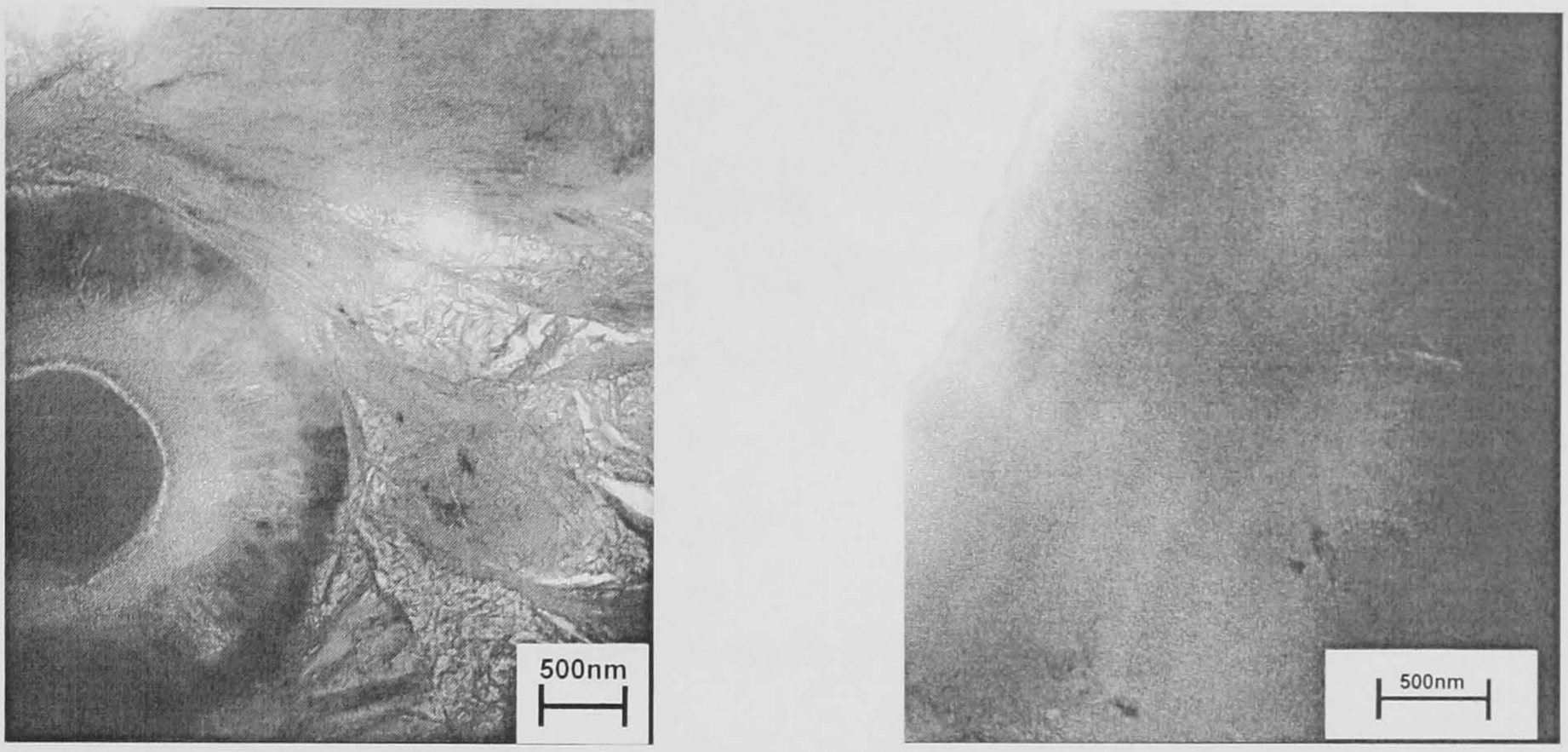


**Figure 2.32** – TEM micrographs showing, on the left side, Op C-S-H (foil-like morphology) and a partially hydrated fly ash grain. On the right side, typical Ip C-S-H (fine-scale and homogeneous morphology)[91].

Once more, Op C-S-H has a foil-like morphology, Ip C-S-H formed from alite is homogeneous and with a fine-scale and alkali activation led to microcrystalline CH and semicrystalline C-S-H.

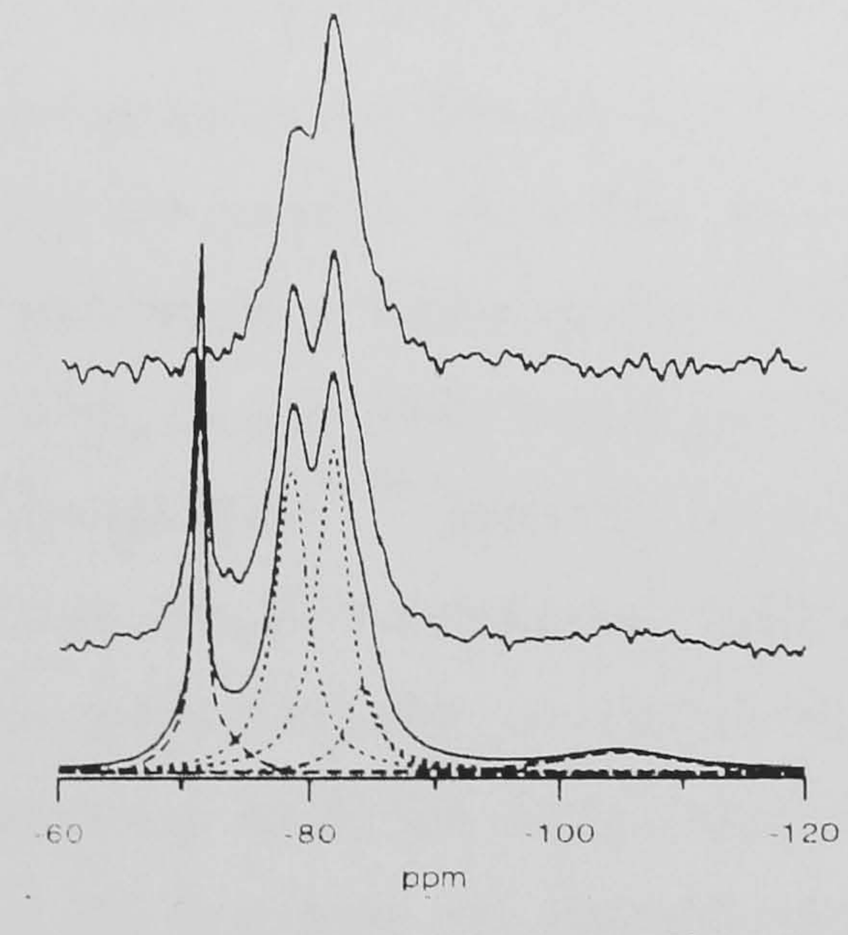


**Figure 2.33** – Single pulse $^{29}Si$ MAS NMR and $^{1}H$-$^{29}Si$ CP MAS NMR spectra of the WPC/30%PFA paste hydrated for 4 months. On the right side, TMS-GPC chromatogram of the same blend KOH activated, but hydrated for 7 months[91].

Regarding the silicate anion structure, the assignment of the NMR peaks in both spectra is presented in the next table:

**Table 2.7** - Single pulse $^{29}Si$ MAS NMR peak assignment in spectra corresponding to WPC/PFA blended pastes[91].

| Assignment | δ/ppm |
|---|---|
| **Unreacted belite ($Q^0$)** | -71.3 |
| **Unreacted PFA ($Q^4$)** | -105.0 |
| **$Q^1$** | -79.0 |
| **$Q^2$(1Al)** | -82.0 |
| **$Q^2$** | -85.0 |

In the $^1H$-$^{29}Si$ CP MAS NMR spectrum, there was no peak assigned as corresponding to $Q^1$(1Al) at around -75 ppm, meaning that aluminium only substituted for silicon in the bridging tetrahedra of the dreierkette chains, which was also confirmed by the TMS-GPC study. Finally, the Al/Si ratio found was 0.22 and the MCL 5.82, being in good agreement with previous studies on other systems with the same age.

Concerning class F fly ashes, LaRosa *et al.*[92,93] observed zeolite formation in OPC/PFA systems when alkali-activated with concentrated NaOH, cured for two days at room temperature, followed by six days at 90°C. Those samples presented higher compressive and flexural strengths than the equivalent ones that were water activated, and the presence of zeolite did not degrade the mechanical properties. One of the applications of cement pastes is for potential immobilization of low-level nuclear waste solutions and other hazardous wastes. In order to study this potential application, Brough *et al.*[94,95] found that waste forms made by reaction of a cementitious blend high in fly ash, with a simulated highly alkaline waste stream under adiabatic conditions led to zeolite formation, in addition with other amorphous and crystalline calcium silicate hydrates. As fly ash reacted, more zeolites were formed liberating additional heat which in the long-term can damage significantly the material. Although the strength was increased by the formation of zeolite, it also suffered a major decrease after fourteen days of hydration, possibly due to recrystallisation of C-S-H or its conversion to zeolite. Therefore, those rearrangements and the fact that zeolites were capable of going under pozzolanic reaction can also cause damage in the structure of the containers. Some other authors studied different systems using blends of fly ash[96,99], concluding that the type and composition of the zeolite formed depended strongly on many factors, including the

initial solution composition and the experimental conditions. Further studies should be performed in order to characterize fully the processes involved before predicting the long-term properties of these materials.

## 2.5 – CURING AT HIGH TEMPERATURE

In this section, a different hydration process is considered. Curing cement pastes at higher temperature than room temperature will affect the development of the physical properties of a cement paste because it affects the kinetics of hydration and the distribution/nature of the hydration products. Therefore, it will influence the composition, morphology and micro/nanostructure of C-S-H. Some of the previous works dealing with this atypical process of curing cement-based systems are reported.

Using SEM, Kjelssen *et al.*[100,101] found that the effect of high curing temperature led to an increase of the reaction rate and since it was faster than the rate of diffusion, most of the hydration product remaining near the cement grains, left the interstitial space relatively open: high concentrations of hydration products in the surrounding zones of the hydrating cement grains, and large pores in the interstitial space. This effect also led to a coarsening of the hydration products and they were less homogeneously distributed in the hydrated specimen. The C-S-H formed was denser and, apparently, stronger but it was also important to account with the porosity of the microstructure which will also have implications in the durability of the concrete. The CH crystals morphology was kept lamellar and elongated but the crystals were more compact. Similar conclusions were also drawn by Cao and Detwiler[102] regarding the coarsening of the hydration products, increasing of porosity and decreasing of the general uniformity of the microstructure. It was also demonstrated that the morphology reflected the curing temperature and degree of hydration. Paying more attention to the hydration products nature, namely their morphology/chemical composition, Scrivener[103] observed that, immediately after heat curing, the Ip C-S-H formed was brighter than the Ip that would have been observed at room temperature. After 35 days of subsequent curing at room temperature, a darker rim of Ip C-S-H formed inside the brighter rim and as hydration

continued the same darker rim had grown thicker. The chemical composition of both rims was the same and the difference of contrast was attributed to a greater degree of fine porosity in the material, which could be wholly or partly due to more water originally present in the C-S-H. Kjelssen[104] also found that, in heat curing and post-heat curing regimes, for a cement paste cured at 50°C, at later ages, the Ip C-S-H revealed a lower fine porosity than that of the corresponding Op or Ip C-S-H present in a cement paste cured at 5°C. Apparently, the Ca/Si ratios were not affected by the effect of temperature and the distribution of the reaction products were less uniformly distributed than the ones present in the cement paste cured at lower temperature. It also appeared that the (Al/Fe)/Ca ratio of the Ip C-S-H increased with decreasing temperature, which may have influenced the distribution and formation of the AFt and AFm-type phases in the matrix. AFm-type phases formed as small crystals in the capillary pores or were intermixed with C-S-H at later ages. Finally, Escalante-Garcia[105] observed that for different blended cement pastes (OPC-PFA) cured at 10, 20, 30, 40 and 60°C, increasing hydration temperature increased the porosity, the degree of hydration and the rate of the pozzolanic reaction between volcanic fly ash and CH.

Hime and Marusin[106] explained that the curing temperature is not the main cause for the delayed ettringite formation (DEF) that was previously observed in some steam-cured precast concrete products. Other factors were involved and related to the sulfate content and chemistry of the cement paste. In a review paper, Taylor *et al.*[7] concluded that temperature was a critical factor in relation to DEF. Expansion from this cause did not occur if the temperature within a mortar or concrete would not exceeded ~ 70°C. Using $^{29}$Si MAS NMR, Masse and Zanni[107] studied $C_3S$ and cement pastes cured for six hours or four days at 60, 80, 100 and 120°C. It was concluded that the C-S-H structure was only based on $Q^1$ and $Q^2$ entities. The anhydrous particles disappeared completely after 14 hours at 120°C and the chains became longer with temperature, with a $Q^2/Q^1$ ratio exceeding 1 after fourteen days cured above 80°C. The temperature rise accelerated the hydration reaction kinetics and the structural changes observed between 60°C and 120°C were probably linked to a change of the Ca/Si ratio. In a study by Cong and Kirkpactrick[108], synthetic samples of C-S-H were analysed by $^{29}$Si MAS NMR, XRD and thermal analysis. It was showed that heating removed interlayer water molecules and $OH^-$ groups from C-S-H, resulting in a more polymerized and disordered

structure. It was also observed that heating affected the $Q^1$ and $Q^2$ intensities: as temperature increased, the relative intensity of $Q^1$ decreased and $Q^2$ increased, and there may have been present some $Q^3$ Si-sites.

## 2.6 – DEGRADATION OF CEMENT PASTES

Degradation of cement pastes can also be considered as another atypical hydration process, and many factors can contribute to the degradation. The following table classifies several degradation processes as chemical or physical attack[1,109]:

**Table 2.8** - Classification of several degradation processes in cement pastes[109].

| Chemical Process | Physical Process |
|---|---|
| Carbonation | |
| Chloride Ion Penetration | Freeze/Thaw |
| Magnesium Sulfate (Seawater) | Erosion |
| Sulfate Attack | Early-age thermal cracking |
| ASR | Inadequate Abrasion Resistance |
| Leaching | High Curing Temperature |
| Acid Attack | |
| DEF | |

### 2.6.1 - Carbonation

Carbonation begins at exposed surfaces and then spreads inside the material. When atmospheric carbon dioxide dissolves in the pore solution of the cement paste, $CO_3^{2-}$ ions are produced and react with the $Ca^{2+}$ ions, giving $CaCO_3$. In order to charge-balance this reaction, $OH^-$ and $Ca^{2+}$ are required and obtained by dissolution of CH and decomposition of the hydrated silicate and aluminate phases. This reaction leads to many others including carbonation of $C_4AH_x$ which is converted into $C_4A\bar{C}H_{11}$ and in the end, into $CaCO_3$ and hydrous alumina; monosulfate and ettringite give $CaCO_3$,

hydrous alumina and gypsum; C-S-H is decalcified lowering its Ca/Si ratio and ultimately, converting itself to a highly porous hydrous form of silica. Like any other kind of physical and/or chemical attack, the degree of degradation will depend on the cement paste type and age. In the case of carbonation, it also depends on the diffusion rate into the paste and that is dependent on its permeability, chemical binding of carbon dioxide and degree of hydration of the paste. Carbonation is considered to have both good and bad effects on a cement paste. It decreases the strength (pore size dependent), increases porosity and also causes irreversible shrinkage[1,109]. Groves *et al.*[110] studied the progressive changes in the microstructure in a $C_3S$ paste due to carbonation, using $^{29}Si$ MAS NMR and TEM. It was found that the reaction of CH is initially more rapid than that of C-S-H but the core of a large CH particle is protected by the layer of calcium carbonate formed in the surface, which acts as a "shield" to further carbonation of CH. It was also found that there are significant differences in the various degradation products when carbonation occurs as a natural degradation with low atmospheric level of $CO_2$, or when it is induced by a concentrated $CO_2$ gas flow.

### 2.6.2 – Sulfate Attack

This kind of attack is made by exposure to some natural or polluted ground water as well to sulfate solutions in the soil. This form of degradation can easily lead to strength loss, expansion, cracking and, in the end, to disintegration. Once again, the extent of this kind of degradation will depend on the mobility of the sulfate ions. Sulfate reacts with calcium aluminate phases and CH leading to the formation of ettringite and often, some gypsum. CH is consumed and the Ca/Si ratio in the Ip C-S-H phase decreases and it might be converted into hydrous silica. The main source of $Al(OH)_4^-$ and $OH^-$, and some of the $Ca^{2+}$ to form ettringite is, at later age, AFm-type phase monosulfate, although they can also be supplied by unreacted aluminate or ferrite phases. Nevertheless, additional calcium is needed and this means that CH is dissolved and C-S-H decalcified. The sources of dissolved sulfates are usually calcium and magnesium sulfate. The latter is the more aggressive one. In this case, besides decalcification of C-S-H and CH dissolution, the $Mg^{2+}$ ions react with $OH^-$ from the pore solution to form brucite. Brucite can cause direct damage but also forms a hard and

dense skin on the material which can inhibit further degradation. A combination of carbonation and sulfate attack leads to the formation of thaumasite, $[Ca_3Si(OH)_6 \cdot 12H_2O](SO_4)(CO_3)$ or $C_3S\bar{S}\bar{C}H_{15}$, easily misidentified as ettringite due to their structural similarities. Ettringite probably functions as a nucleating agent but its formation is limited by the source of $Al_2O_3$. Assuming that there is a continuous supply of $SO_4^{2-}$, thaumasite formation will only be limited by the available amounts of CaO and $SiO_2$. Thus, it can be formed in large quantities and ultimately, since it is a poor binder, reduce the material to a paste[1,109].

### 2.6.3 – Chloride Ion Penetration

As with sulfate ions, the depth of penetration of the chloride ions depends on its mobility. If the chlorides present in the pore solution are at a concentration above a critical level, they are partly bonded to the calcium aluminate phases ($C_3A \cdot CaCl_2 \cdot 10H_2O$) but some are "free". The latter will tend to bond to hydroxyl ions and, once more, CH is dissolved. Carbonation may also lead to an increase in the chloride ion concentration in the cement pore solution. There is a substantial amount of evidence that blended cements containing fly ash or slag present a higher resistance to chloride ion penetration than neat OPC pastes. The most significant form of degradation by this process is the corrosion of embedded steel in reinforced concrete[1,109,110].

### 2.6.4 – Alkali-Silica Reaction

As explained before, alkali-silica reaction (ASR) produces an arbitrary network of fine and large cracks in the material, and potentially may occur in blended cement pastes that involve pozzolanic reactions. As in the pozzolanic reaction, ASR will depend on the particle size and distribution of the siliceous material. Hydroxyl ions attack the silica forming silicates that substitute the Si-O-Si bridges, deforming and breaking the framework. This leads to the formation of an alkali silicate gel very different from C-S-H, occurring as a massive and persistent phase that causes the expansion in the paste. The details of the mechanism are still poorly understood[1,109]. The reaction between silica and, for example, KOH leads to the formation of alkali silicate solutions

and gels[75]. A way of inhibiting or preventing, ASR is the use of alkali activated pastes in pozzolanic systems, because C-S-H becomes more dense and higher polymerised with little available amount of CH to react in the pozzolanic reaction[110].

### 2.6.5 – Leaching

Leaching is the process by which a soluble portion of a solid mixture is dissolved by some solvent. An example is the dissolving of inorganic/organic contaminants from rejects in a landfill, by infiltrating rain water. This kind of degradation is particularly important for the long-term storage of nuclear and other forms of wastes such as concrete dams. For research purposes, there are two usual methods of leaching cement pastes, ammonium nitrate and water leaching. In both cases, the final residue consists of hydrous forms of silica, alumina and iron oxide with all the CaO being lost, and leading to a disintegrated paste. CH is most likely to be the first to be removed from the material, followed by the remainder phases, including decalcification of the C-S-H phase. The leaching rate will depend on many factors namely the nature of the paste, the solution flow rate, its concentration or nature, temperature and concentrations of solutes. In general, water leaching is moderately slow and many studies have been performed with the objective of accelerating the leaching. Accelerated leaching techniques are unlikely to correspond to the natural leaching of a cement paste. Many authors used excessively concentrated ammonium nitrate solutions and some with the addition of other accelerating methods to carry out the leaching process[111-115]. Using highly concentrated ammonium nitrate corresponds to a reaction rate increased by a factor of three hundred, when compared with natural water leaching. CH reacts with the nitrate ions giving soluble calcium nitrate. This process induces mainly a total leaching of the CH and consequent rapid decalcification of C-S-H. Water leaching is another way of predicting the long-term properties of a cement container for wastes. It is expected that CH will be the first phase to be leached, followed by C-S-H. Porteneuve *et al.*[116,117] found that as the CH was leached, the C-S-H rearranged itself into a highly polymerized phase containing $Q^3$ (chain branching sites, probably pentameric units) peaks in the $^{29}Si$ MAS NMR spectra. This polymerization is a consequence of the C-S-H response to the leaching, in order to compensate the concentration gradient. In theory, it is expected that

the leaching will be easier in C-S-H that fits the T/CH viewpoint than the T/J one due to the nature of the structures. In both cases, the CaO layers will be leached from the layered structure but, in the T/CH point of view, there is some CH that will be first leached than the layers of CaO, meaning an easier CH leaching in the T/CH viewpoint. More recently, Harris *et al.*[118] concluded that the leaching behaviour of synthetic C-S-H gels was very similar to the leaching of cement pastes although it can not be said that this is validation for the use of synthetic C-S-H gels as a suitable analogue of the C-S-H phases formed in the hydration of Portland cement.

# III - EXPERIMENTAL

## 3.1 – MATERIALS

The used materials were a white Portland cement (WPC), *Ribble white PC 8108*, from Castle Cement Limited (Clitheroe, U.K.) and a class F pulverised fly ash (PFA), *PFA 8109*, from Drax power station (Selby, U.K.). The anhydrous WPC and PFA oxide composition obtained by X-Ray fluorescence spectroscopy (XRF) are shown in Table 3.1, as well as the mineral distribution as obtained from the Bogue-Taylor calculation[119] for the white cement. In Figure 3.1, the correspondent X-ray diffraction patterns (XRD) are also shown. XRD principles and experimental conditions are described in section 3.5.

**Table 3.1** – Anhydrous WPC and PFA oxide composition from XRF and Bogue-Taylor calculation for the WPC.

| **Oxides (%)** | **WPC** | **PFA** |
|---|---|---|
| $SiO_2$ | 24.81 | 52.92 |
| $Al_2O_3$ | 2.35 | 26.85 |
| $Fe_2O_3$ | 0.49 | 8.64 |
| MgO | 0.80 | 1.65 |
| CaO | 68.61 | 4.49 |
| $Na_2O$ | 0.15 | 1.20 |
| $SO_3$ | 2.03 | 0.44 |
| $K_2O$ | 0.06 | 3.26 |
| Cl | n.a. | 0.005 |
| **Total** | 99.30 | 99.46 |
| **Free CaO** | 2.03 | n.a. |
| **LOI* (at 1025°C)** | <0.01 | 4.36 |
| **Bogue-Taylor calculation:** | | |
| **% Alite** | 67.9 | |
| **% Belite** | 22.1 | |
| **% Aluminate** | 2.7 | |
| **% Ferrite** | 0.8 | |

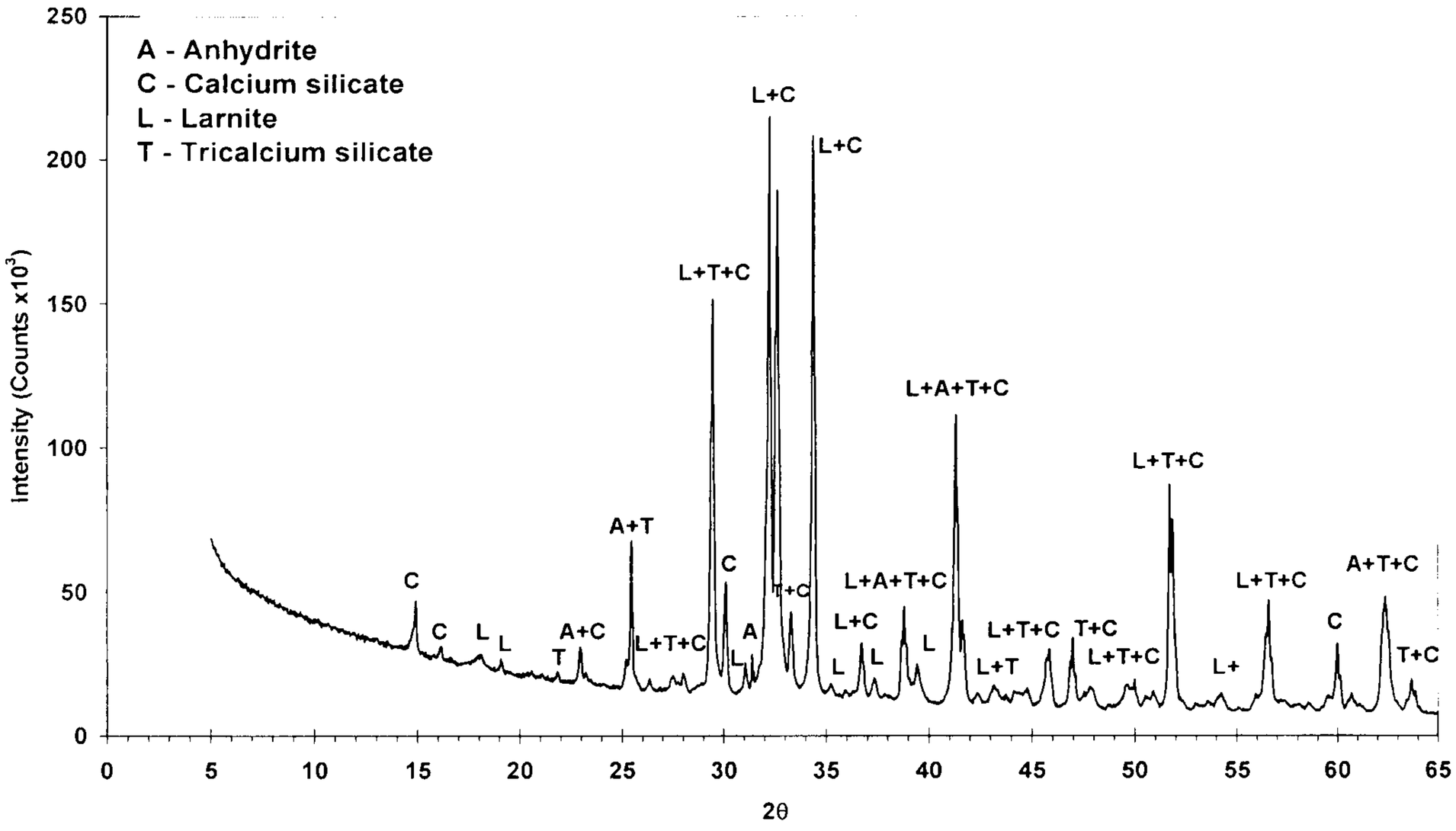


**Figure 3.1** – XRD pattern for the anhydrous WPC.

The above pattern shows that the anhydrous WPC was mainly composed of the following crystalline phases: anhydrite ($CaSO_4$), calcium silicate ($CaSiO_3$), larnite ($Ca_2SiO_4$) and tricalcium aluminate ($Ca_3Al_2O_6$).

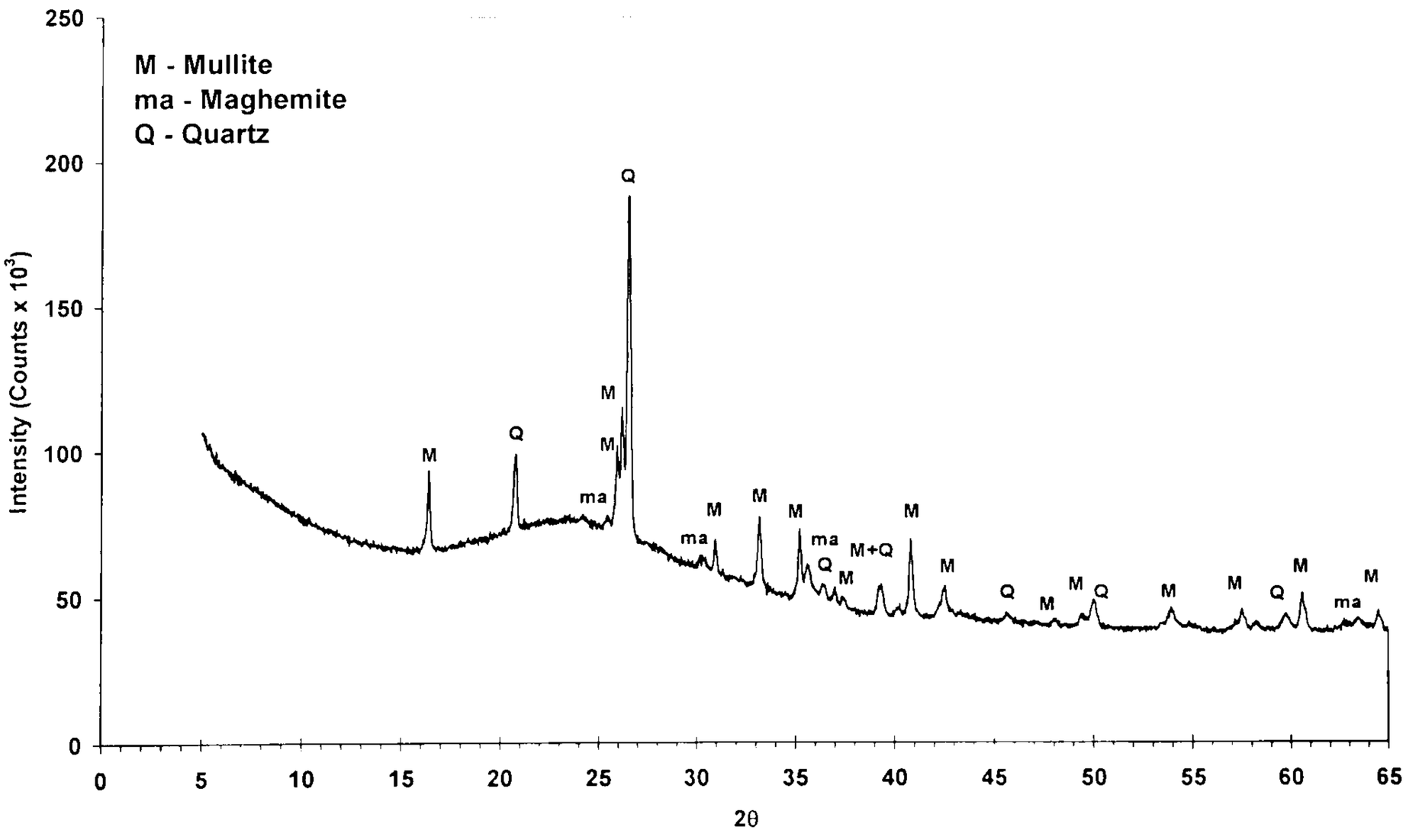


**Figure 3.2** – XRD pattern for the anhydrous PFA.

The latter XRD pattern illustrates that the anhydrous PFA was composed of an amorphous phase, as shown by the broadness of the baseline which is typical of a glassy phase, and also of crystalline phases such as mullite ($Al_{4.5}Si_{1.5}O_{9.75}$), quartz ($SiO_2$) and maghemite ($\gamma$-$Fe_2O_3$).

## 3.2 – SAMPLE PREPARATION

The neat pastes were hand mixed to a water/cement ratio of 0.5 (mL/g), with distilled water or 5*M* KOH solution. The blended WPC containing 30% or 60% class F PFA were also hand mixed to a water/binder ratio of 0.5 and were activated with distilled water or a 5*M* KOH solution. The mixes were cast in 7 ml polystyrene tubes, sealed in plastic bags and cured in a continuously stirred water bath at 25°C (±1°C). The pastes were analysed at different stages of hydration: one day, one month and one year of hydration. For the higher temperature studies, the samples were prepared in the same way as mentioned above, double sealed in plastic bags and placed in a continuously stirred distilled water bath at 55°C (±1°C), or 85°C (±1°C). The samples were analysed with one day and one month of hydration. It is possible that premature drying of the cement pastes might have occurred. However, when retrieving the samples there was no moisture evidence around the plastic tubes or in the plastic bags. In order to perform the degradation study, the blended cement paste with 30% of PFA replacement, water activated and cured in a continuously stirred distilled water bath at 25°C (±1°C) for one year, was used. For the water leaching experiment, the samples were demoulded and cut into 200 μm thick slices, using a *Buehler* cut off saw with a diamond blade slow saw speed. The slices were placed in a stainless steel apparatus, designed by Dr. Adrian Brough and as seen in Figure 3.3. They were then immersed in a closed and continuously stirred distilled water bath (2.6L), at room temperature. The samples were analysed with one to twelve weeks of leaching and the leachate was replaced by fresh distilled water each time the samples were collected for analysis, i.e. every week.

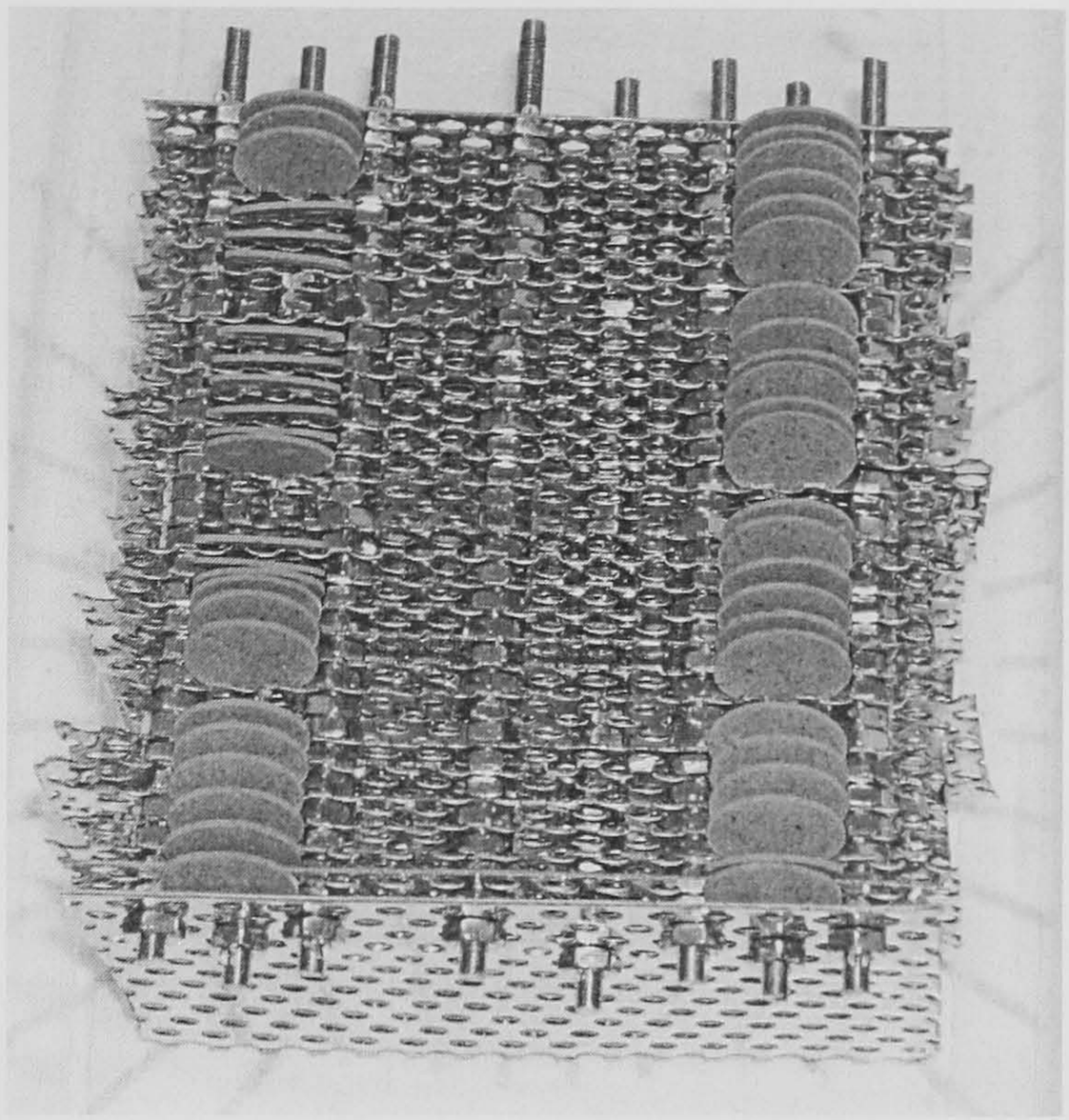

**Figure 3.3** - Stainless apparatus for the water leaching experiment.

## 3.3 – ISOTHERMAL CONDUCTION CALORIMETRY

### 3.3.1 – General Introduction to Conduction Calorimetry

Isothermal conduction calorimetry is an experimental technique used to follow the hydration behaviour of neat and blended cement pastes. Cement hydration reactions are mostly exothermal reactions where heat is released. The evolved heat of hydration can be measured as a function of time using isothermal conduction calorimetry. In reality, this technique gives information on the chemical reactions occurring during cement hydration, examines the hydration behaviour of different type of cements, estimates the heat evolved and provides the instantaneous rate of heat liberation at any time of the process[120]. It is a simple, direct and continuous method, independent of the type of cement and rapid with precise measurements. This technique is also used to study the rate of hydration at different temperatures, the role of admixtures like accelerators and retarders, and determine kinetics of hydration[120,121]. An example of a typical isothermal conduction calorimetry curve is presented in Figure 3.4:

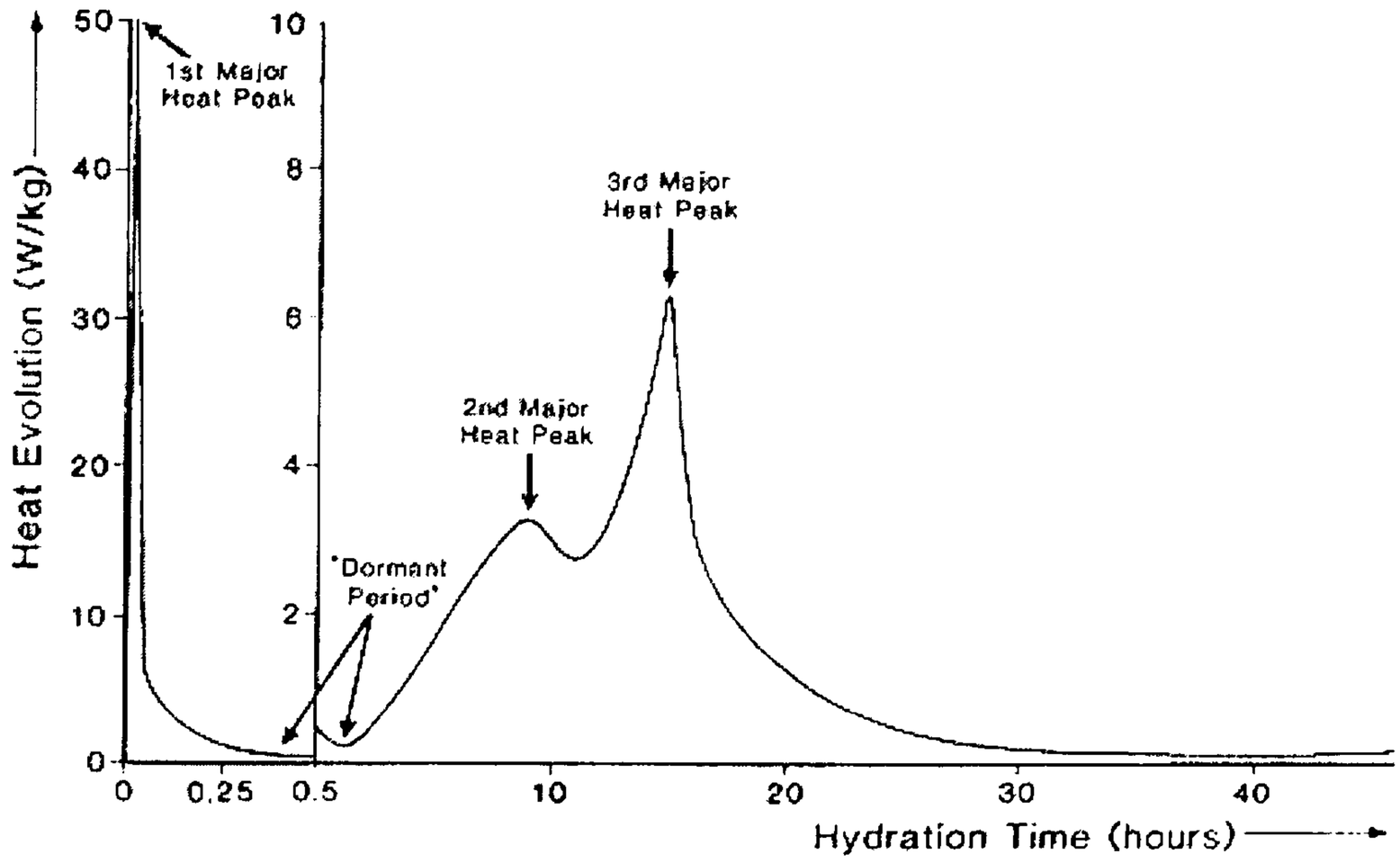


**Figure 3.4** – Example of a typical isothermal conduction curve for an OPC paste[121].

Usually, a first major peak is observed in only a few minutes of hydration which corresponds to the early-age reactions and AFt-type phases formation. This peak is then followed by a severe decrease of heat evolution, the dormant or induction period that lasts between 0.5-2 hours of hydration. After the induction period, the heat evolution accelerates giving a second heat peak where C-S-H is formed from mainly the hydration of alite. A third peak is observed after 12-15 hours of hydration time where the reactions involving the aluminate and/or ferrite phases occur and ettringite is also formed.

### 3.3.2 – Experimental Procedure

The samples were prepared by mixing 30 g of WPC or blended WPC containing 30% or 60% class F PFA to a distilled water/binder ratio of 0.5. After being hand mixed, the pastes were placed inside a polythene bag and heat sealed. The bag was formed around the aluminium heater disc connected to the lid of the sample holder. Around 20 mL of oil was placed in the can to act as a heat conductor from the sample bag and the sample holder. The lid with the sample bag formed around the heater was fitted to the sample holder and an anodised aluminium compensating ring was placed in the centre of the

*JAF* conduction calorimeter (*Wexham Developments*, U.K.). The sample holder was placed in the centre of the calorimeter and it was properly connected to an interface monitor and sealed before being immersed in the water bath at 25 °C (±1°C). The isothermal heat of hydration of the samples was constantly measured for seventy two hours and the data was processed and analysed using the software provided with the calorimeter system computer.

## 3.4 – STA-EGA

### 3.4.1 – General Introduction to Thermal Analysis

Thermal analysis is a general term which covers a variety of techniques that record the physical/chemical changes occurring in a substance as a function of temperature. It comprises techniques like thermogravimetry (TG), evolved gas analysis (EGA), differential thermal analysis (DTA) and differential scanning calorimetry (DSC). In thermogravimetry, the mass of a substance is measured as a function of temperature, i.e. the weight loss of a sample is monitored in a chosen atmosphere and under a controlled program of temperature. TG determines the weight changes occurring as temperature increases, but it is also often used simultaneously with differential thermal analysis. This combined technique is usually referred as STA. Differential thermal analysis is very useful and fulfils some of the TG handicaps such as detecting crystalline transitions that do not involve weight losses. In DTA, the difference in temperature between the sample and a reference material, under the same temperature program, is followed. DTA shows the exo/endothermal effects occurring in the sample and by determining the nature of the peak, the temperature of the characteristic peak and other features, it is possible to obtain qualitative and quantitative analysis[120]. The information provided by DTA can be enhanced when other techniques such as a mass spectrometer are combined. This type of hyphenated technique becomes very useful in the identification and quantification of the gases evolved in the process. Therefore, evolved gas analysis (EGA) provides chemical information of the gases generated as a function of time and temperature. Usually, a simple mass spectrometer is used: the ion

source is the DTA connected to the EGA by a heated capillary that prevents condensation of the gases until they reach the EGA. A turbo pump forces the gases to reach the mass analyser, usually a quadrupole ion trap that uses static radio frequency/electric fields to trap and analyse the ions. Finally, an electron multiplier is used to amplify the signal and provides the final mass spectrum where the measure of mass/charge (m/z) of the ions is plotted as a function of time or temperature[12].

### 3.4.2 – Experimental Procedure

The samples were demoulded and cut into 200 μm thick slices. Hydration was stopped through solvent exchange with propan-2-ol (Fischer Scientific) and the slices were dried in a vacuum desiccator. Stopping hydration with methanol, acetone and other organic solvents leads to alteration in the paste composition and the solvents are not completely removed by vacuum drying. Heating the sample to evaporate the solvent is not an option due to verified alteration in the composition of the samples. Therefore, any alteration to the composition will lead to incorrect interpretation of the results [10,122,123].

All dried samples were stored in glass tubes and placed in a desiccator containing silica gel, which was changed when required. Thermal analysis data was acquired using a *Stanton Redcroft STA1000* (U.K.) with simultaneous thermogravimetric and differential thermal analysis (STA). The samples were crushed and ground to finer powders in an agate mortar/pestle. Approximately 18 mg of sample was placed in a platinum crucible and heated up to 1000ºC with a rate of 20ºC/min, under a constant flow of nitrogen (BOC, U.K) at the rate of 58 ml/min. Regarding the STA apparatus, it was slightly unstable from run to run and, therefore, the obtained values were not absolute. An evolved gas analysis (EGA) interface (Cirrus mass spectrometer, *MKS Spectra Products Ltd.*, U.K.), provided with a mass spectrometer and a quadrupole residual gas analyser, was combined with the STA equipment in order to help the identification of the different gases involved in the thermal process. The thermogravimetric curve (TG), where the % weight loss is plotted as a function of temperature or time, was used to calculate the estimated amount of CH present in each sample. The following chemical reactions were considered[124]:

$$Ca(OH)_2 \Rightarrow CaCO_3 + H_2O \text{ (Dehydration)} \qquad \text{(Eqn. 3.1)}$$

$74\ gmol^{-1}$ $18\ gmol^{-1}$

$$Ca(OH)_2 + CO_2 \Rightarrow CaCO_3 + H_2O \text{ (Carbonation)} \qquad \text{(Eqn. 3.2)}$$

$74\ gmol^{-1}$ $100\ gmol^{-1}$

$$CaCO_3 \Rightarrow CaO + CO_2 \text{ (Decarbonation)} \qquad \text{(Eqn. 3.3)}$$

$100\ gmol^{-1}$ $44\ gmol^{-1}$

In the region of 420-550°C, dehydration of CH occurs, according to equation 3.1, where one mole of water ($18\ gmol^{-1}$) results from one mole of CH ($74\ gmol^{-1}$). Most care was taken when handling the samples, always in order to expose them to air as less as possible but carbonation of the CH might have occurred. Thus, the estimation of the amount of CH was also corrected considering equations 3.2 and 3.3 which illustrate the carbonation and decarbonation reactions. Decarbonation occurs in the region of 600-780°C and one mole of carbon dioxide results from one mole of calcium carbonate previously formed from carbonation of the CH. The total amount of CH was calculated according to the following equation:

$$\text{Estimated amount of CH} = (74/18)*(A) + (74/44)*(B) \qquad \text{(Eqn. 3.4)}$$

A is the weight loss in the TG curve corresponding to the dehydration of CH, and B the weight loss in the TG curve corresponding to the decarbonation reaction. The calculation of A and B was carried out as illustrated in the following example:

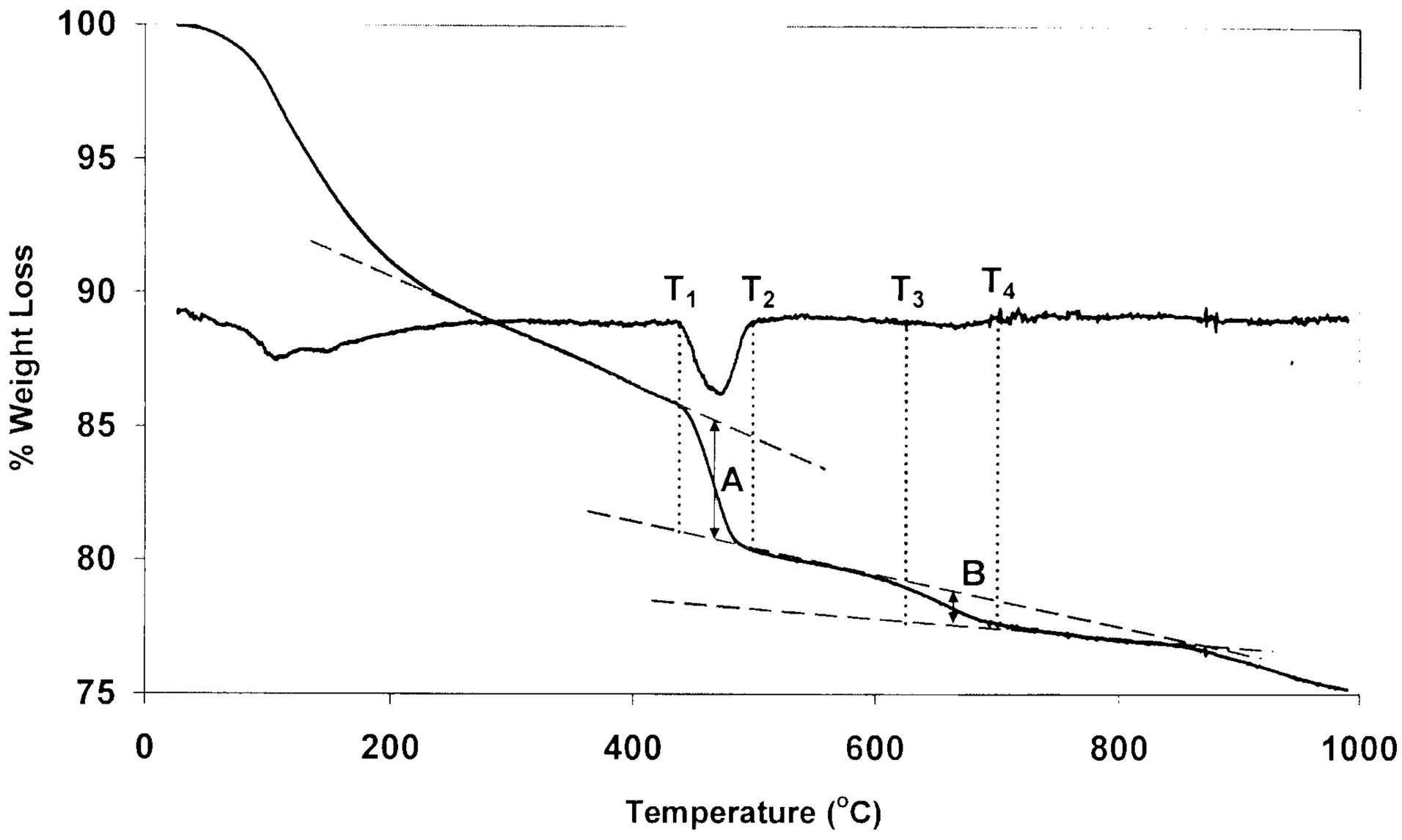


**Figure 3.5** – Example illustrating the calculation of A and B in the TG curve.

A corresponding derivative curve to the weight loss curve (blue) was plotted and two tangent lines (red) to the inflection points of the derivative curve were drawn as in Figure 3.5. Between the two tangent lines, a middle point was considered in the weight loss curve. The vertical length of the line (arrow) that unified the two tangent lines and passed through the previously found middle point was drawn and measured in terms of percentage of weight loss. This measurement corresponds to A in Equation 3.4. In this example, there was a small weight loss associated with carbonation, given by B and the estimated amount of CH was obtained after using Equation 3.4. Finally, the calculated amount of CH was divided by the percentage of residue left in the crucible, giving an estimated amount of CH as % of ignited weight (CH as % ig. wg.).

## 3.5 – XRD

### 3.5.1 – General Introduction to XRD

Electromagnetic radiation is the transmitted wave in space with two different electrical and magnetic components, and it also is associated to electromagnetic waves. These waves are associated to the movement of electrons and are usually represented in terms of their energy and wavelength in the electromagnetic spectrum, as showed in Figure 3.6.

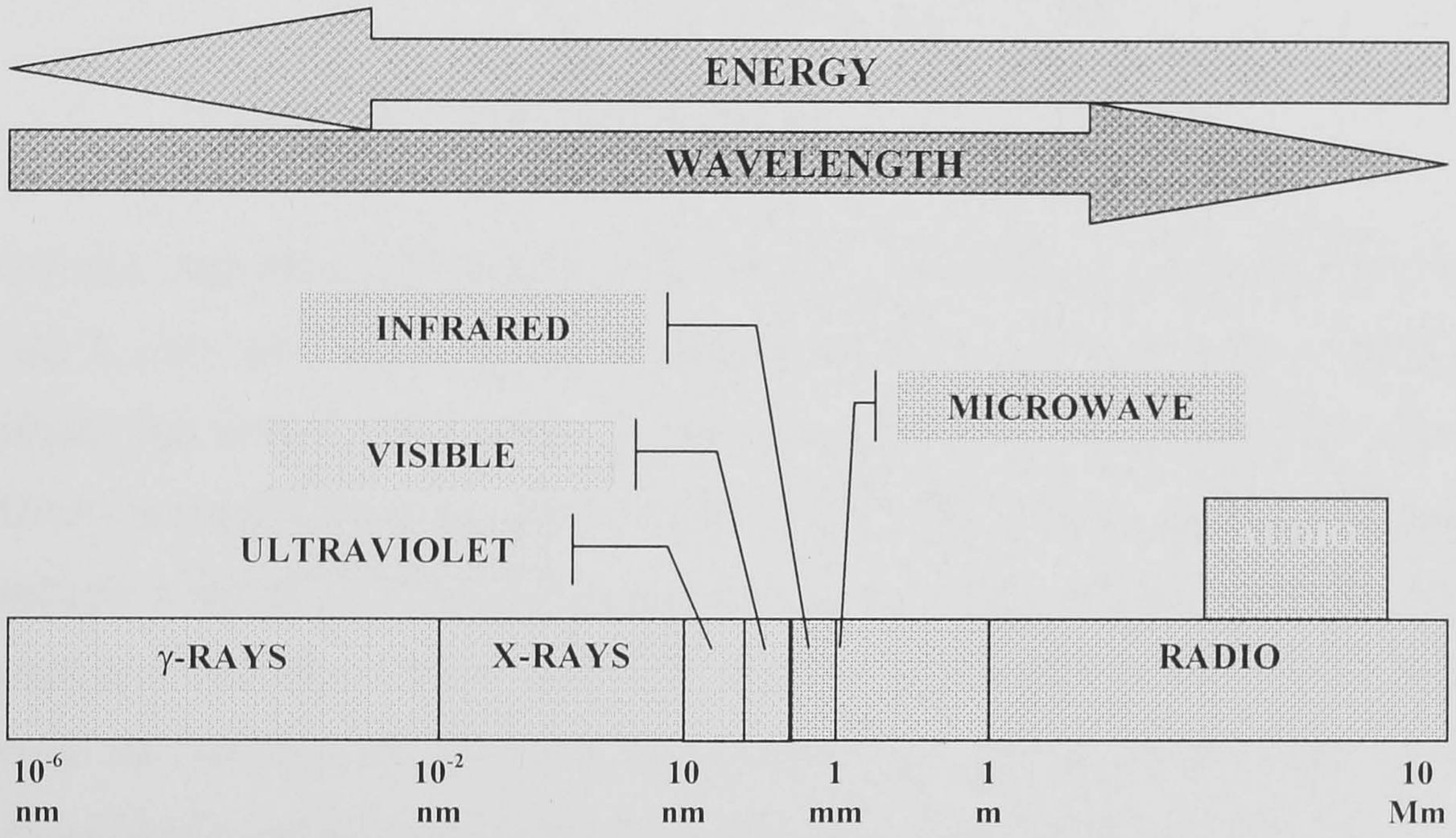


**Figure 3.6** – The electromagnetic spectrum.

X-rays are highly energetic photons resulting from electronic transitions in the atoms of a targeted metal by an incident of accelerated electron beam. An incident accelerated electron hits the metal atom and knocks out an electron from the K-shell (n = 1 shell) of the metal, and a vacancy or hole is left in that shell. If an electron from another shell fills in the vacancy (electron transitions), X-rays are emitted[125]. Figure 3.7 is a scheme of this event:

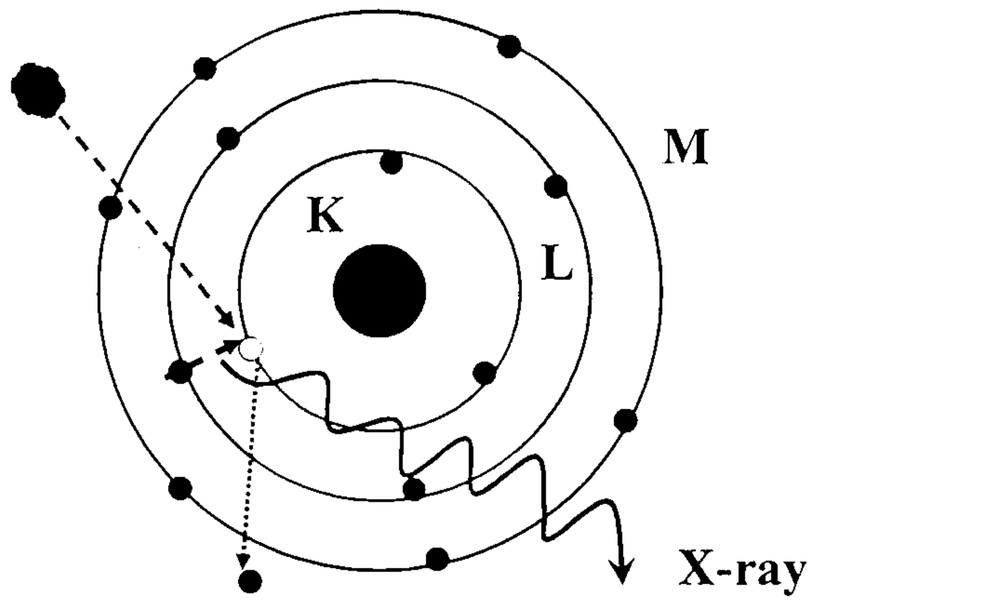


**Figure 3.7** – Schematic illustration X-rays emission.

Electronic transitions to the K-shell (n =1) are named $K_{X\text{-}rays}$ and electronic transitions to the L-shell (n = 2) are $L_{X\text{-}rays}$. These transitions are characteristic of each chemical element but only a small range is used as source of X-rays, typically copper. X-ray diffraction results from the diffraction of X-rays when they interact with a crystalline structure. Crystalline structures have regularly repeating atomic structures with typical interatomic distances in the same order as the wavelength of the X-rays. Bragg's law shows the relationship between the interatomic spacing (d-spacing), the angle of diffraction ($\theta$) and the wavelength of the incident X-ray radiation ($\lambda$)[125]:

$$2\ d\ \sin\theta = n\ \lambda \qquad \text{(Eqn. 3.5)}$$

The d-spacing and $\lambda$ are measured in angstroms, $\theta$ in degrees and n is an integer. The interaction between X-rays and a crystalline structure are presented in Figure 3.8.

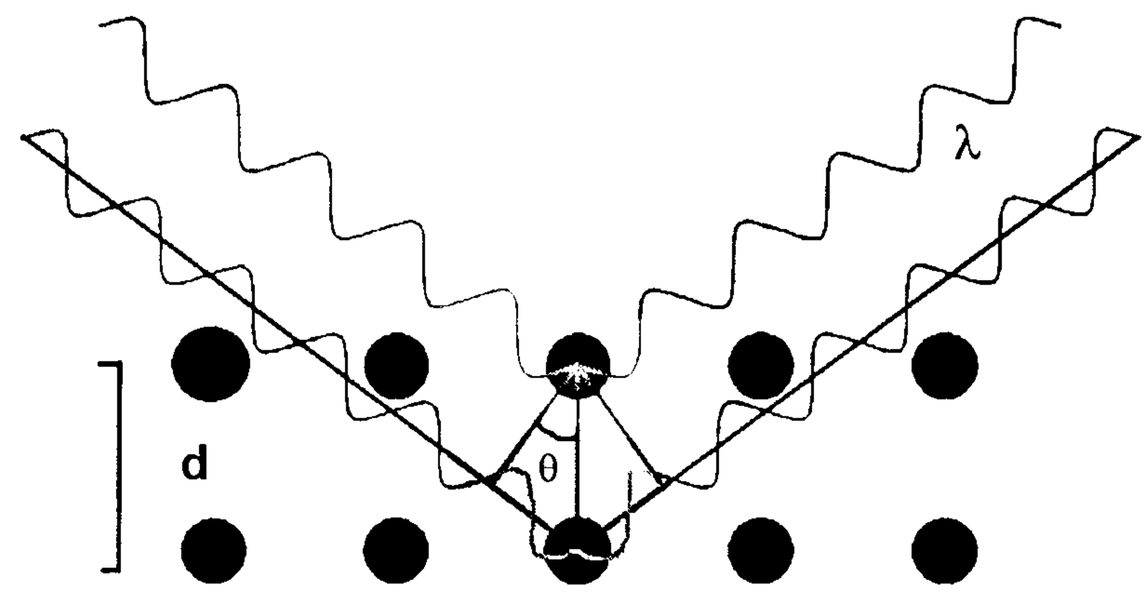


**Figure 3.8** – Bragg's law.

The diffracted beam is detected and recorded in a diffraction pattern. In a crystalline structure, the unit cell is the smallest possible volume that when repeated, is representative of the entire crystal and has an exclusive symmetry. By measuring the angle and d-spacing where a characteristic reflection line is observed, the crystalline(s) structure(s) can be determined and the different compound(s) present in a powder identified[125].

### 3.5.2 – Experimental Procedure

The XRD measurements were performed using a *Panalytical* diffractometer system X'PERT-PRO (with X'Celerator real time multiple strip detector), operated with Cu Kα radiation at 40mA and 45 kV (W. R. Grace & Co. (Boston, U.S.A.)). The samples were demoulded, freshly crushed and ground to finer powders in an agate mortar/pestle. Rutile was added as an internal standard (10% of the total weight of the sample), and the samples were mounted on a sample holder that was spun at 2 revolutions per second. XRD acquisition was carried out using a spinner sample stage running in a continuous scan mode over the range 6.03 to 54.95 °2θ with a step size of 0.01675° (i.e. 2921 steps) and a counting time of 34.29 seconds, corresponding to a total acquisition time of nearly 14 minutes. The patterns were analysed and the different phases were identified by *Panalytical* X'Pert HighScore software. The addition of an internal standard would give way to Rietveld refinement and consequent quantitative determination of the different phases formed in each sample. Regrettably, that was not possible due to contrasting peak intensities concerning rutile. The latter will be discussed in more detail in the next chapter.

## 3.6 – COMPRESSIVE STRENGTH

Mortar cubes were used in the compressive tests (carried out in W. R. Grace & Co. (Boston, U.S.A.). The mortar samples had a water/cement ratio of 0.5 (mL/g), with distilled water or 5*M* KOH solution. The blended WPC mortars containing 30% class F PFA had a water/binder ratio of 0.5 and were also activated with distilled water or a 5*M*

KOH solution. The mortar cubes were prepared with EN-196 sand, following the standard mortar protocol, and placed in environmental rooms at 25. 55 and 85°C, at high humidity. The compressive tests were performed after 1 day and 1 month of hydration.

## 3.7 – SOLID STATE MAS NMR

### 3.7.1 – General Introduction to Solid State MAS NMR

Solid state nuclear magnetic resonance spectroscopy is a very powerful technique that provides information about the structure and atomic environments of many materials. An extensive database of NMR spectra is established for well known materials and the structural characteristics of unknown materials can be obtained by comparison. The general principles of NMR are based in the physical spinning of the nucleus of a certain chemical element. Nuclei with a spin (quantum parameter) different from zero are used in NMR. When such nuclei are under the influence of a strong magnetic field, a split of the energy levels between the various spin states occurs, which is usually known as the Zeeman interaction[126]. Electronic transitions take place between adjacent energy levels, with the absorption or emission of a photon in the radiofrequency range (Figure 3.6). In a NMR experiment, the frequency of this radiofrequency is measured, giving information about the position of the resonance peak, the isotropic chemical shift (δ). In a solution or in a solid, the nuclei will experience the magnetic field in different ways and with different intensity due to their structural environment and electron neighbours. Thus, the nuclei will absorb or emit a photon of different frequency which is reflected on the value of its chemical shift. It is not possible to measure absolute frequencies and the frequencies are usually expressed as chemical shifts and relative to an external compound[126]. In summary, the nucleus is placed under an external strong nuclear field and the consequent split of the energy levels of the nucleus depends on their different structural environments. The nucleus is then perturbed by an applied pulse of radiofrequency radiation, which induces electronic transitions. The perturbation is removed and the returning of the nucleus to its fundamental or initial state will absorb a photon, whose frequency is measured as a chemical shift[126]. NMR was firstly used in

experiments involving liquids or solutions but NMR spectra of solids had very broad peaks caused by a variety of interactions, such as the dipolar broadening, chemical shift anisotropy and spin-spin/spin lattice relaxation. This problem was overcome by spinning the sample very rapidly, typically 10-15 kHz at an angle of 54.74° to the axis of the applied magnetic field, the magic angle spinning (MAS). Therefore, MAS reduces or cancels the line broadening in solid samples caused by a number of important nuclear interactions. $^{29}Si$ is a nucleus with odd mass number and half-integer spin and one of the most studied nuclei in solid state single pulse (SP) MAS NMR. The line broadening of the peaks also depend on the characteristic spin of the nuclei. Silicon is a nucleus with spin I = ½. $^{29}Si$ NMR chemical shifts for all silicates become more negative with increasing polymerisation due to the fact that they become more shielded and that affects their chemical shift[126]. In systems containing two nuclei, in which one has more abundant spins (frequently $^{1}H$) than the other, magnetisation can be transferred from the protons to the less abundant nuclei. The signal from the less abundant nuclei located in structural sites nearer to the protons, is improved. Cross polarization (CP) NMR is based on experimental measures where the less abundant nuclei signal is enhanced. Thus, additional information is obtained by comparing CP and SP spectra of the same sample[126].

### 3.7.2 – Experimental Procedure

The pastes were demoulded, freshly crushed and ground to finer powders in an agate mortar/pestle. The powders were packed in a 6 mm diameter zirconia rotor sealed with teflon end caps. The $^{29}Si$ single pulse proton decoupled and the $^{1}H$-$^{29}Si$ cross-polarization magic (CP) angle spinning solid-state nuclear magnetic resonance (MAS NMR) measurements were performed in a *Varian InfinityPlus* 300 MHz, equipped with *Chemagnetics* style MAS probes (U.S.A.), and operated at a magnetic field of 7.0 T. The $^{29}Si$ chemical shifts were given in ppm from tetramethylsilane (TMS). The spectra were acquired using a magic angle spinning speed of 6 kHz, pulse delay of 2 or 5 s, pulse width of 2 or 4 μs and acquisition time of 20.48 ms, with over 10000 scans. The single-pulse $^{29}Si$ MAS NMR spectra were iteratively fitted using software *Wavemetrics*

Igor Pro 5.0 (U.S.A.), with additional macros written particularly for the fitting of the spectra[127,128]. A 10kHz exponential line broadening was applied and zero filling to 8k; first and second order phasing of the spectra were done visually. Figure 3.9 shows the spectra corresponding to the anhydrous WPC and PFA and Figure 3.10 shows the spectra obtained for the anhydrous blended WPC with 30 and 60% PFA.

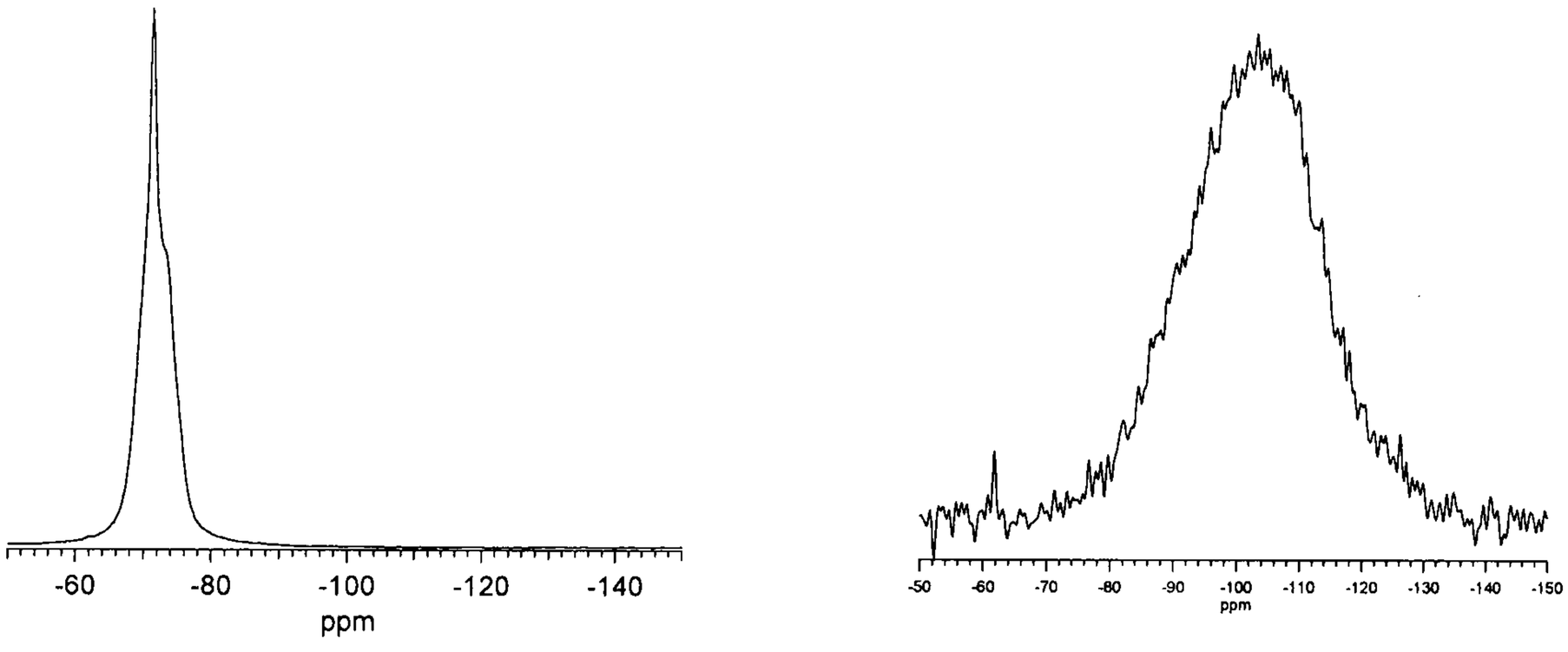


**Figure 3.9** – $^{29}$Si MAS NMR spectra for the anhydrous WPC (left) and PFA (right).

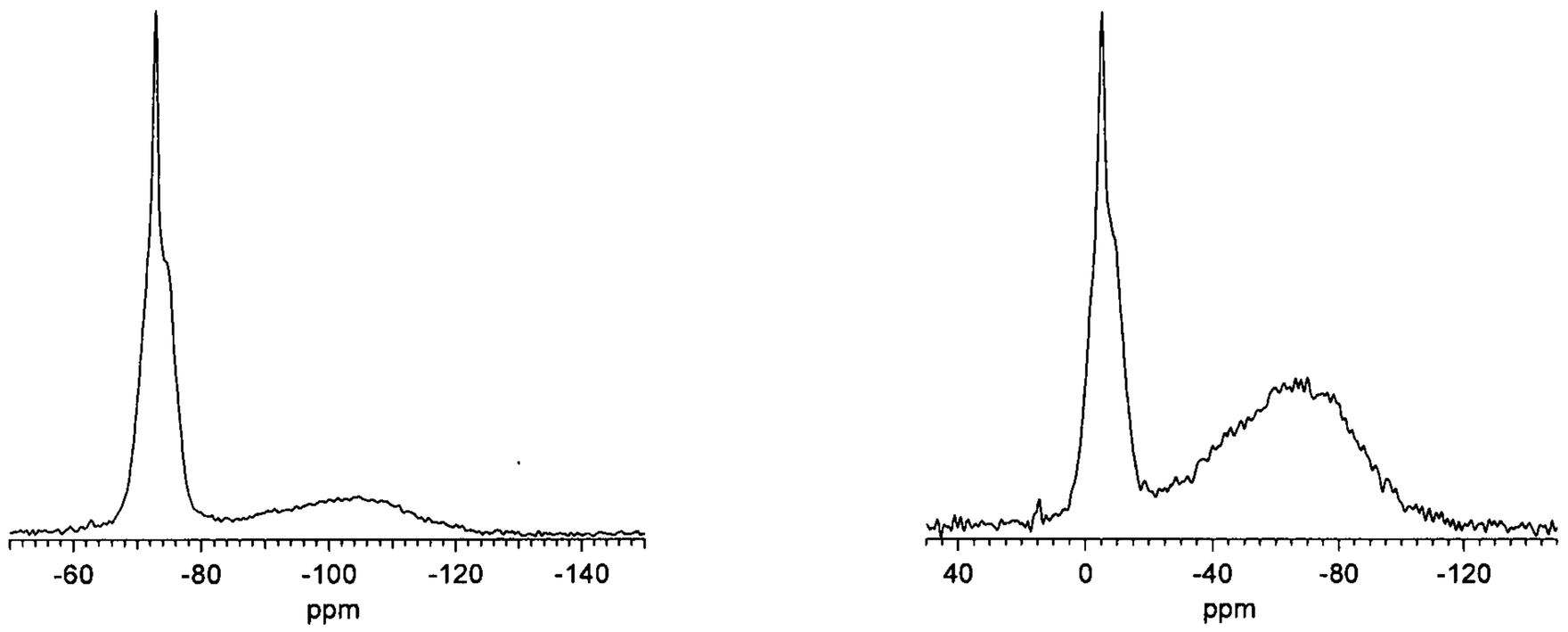


**Figure 3.10** – $^{29}$Si MAS NMR spectra for the anhydrous blends WPC with 30% PFA (left) and 60% PFA (right).

The acquired data was directly used as input data in Igor Pro software. Unless there was experimental evidence given by the other used experimental techniques, the fitting procedure was used assuming that the observed resonances corresponded to those of C-S-H, i.e. it was more sensible to fit the $^{29}$Si MAS NMR spectra on the basis of the

phases known to be present in the samples. Fitting of the spectra was started by subtracting, from the initial spectrum, the residual anhydrous WPC spectrum previously acquired in the same experimental conditions, i. e. subtraction of a contribution from a spectrum taken from anhydrous cement, which thus accounted for the unreacted alite and some of the belite. The distinct chemical shifts corresponding to alite are not yet reported, thus this subtraction avoids problems related with peaks due to alite leaving a residual peak corresponding to most of the belite present in the sample, which can be more easily fitted. The resulting spectrum was used for fitting and an example of this subtraction is shown in Figure 3.11.

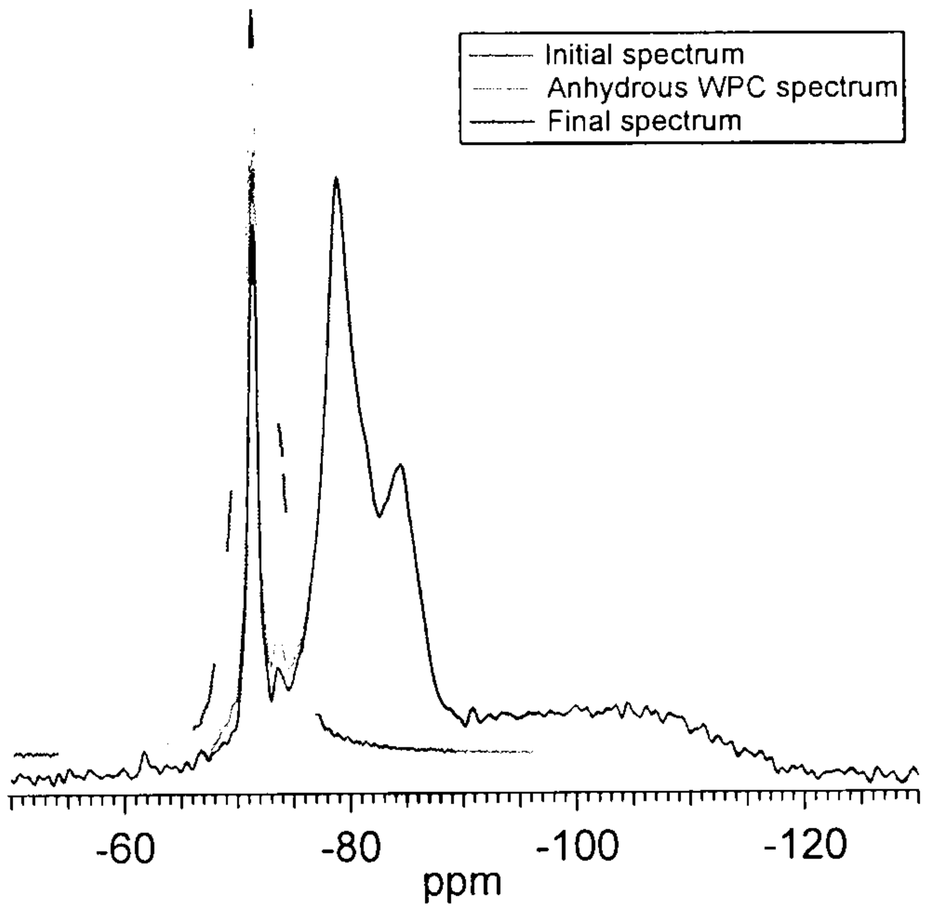


**Figure 3.11** – Example of $^{29}$Si MAS NMR single pulse spectrum for a WPC blend with 30% PFA, before and after the anhydrous WPC subtraction.

The baseline of the spectrum was iteratively fitted to a cubic polynomial function and the peaks to Voight line shapes where each peak had a shift, intensity, shape and width parameters. After the parameters for each present peak in the spectrum were fitted, the integrated areas of the fitted peaks were used to calculate the mean aluminosilicate chain length, the Al/Si ratio and the percentage of each present peak in the spectrum. The latter was always expressed as a percentage of the total silicon present in each studied system. In the case of the blended WPC pastes with 30% PFA, a few correction factors were tested because part of the signal was "lost" in the sidebands due to the paramagnetic interactions caused by the iron present in the PFA. Ideally, by iterative

fitting of the side bands. it would be possible to estimate the signal lost into the sidebands but it was not possible especially for the 60% PFA blended pastes due to very low signal/noise ratio. Figure 3.12 shows an example of a fitted and deconvoluted spectrum.

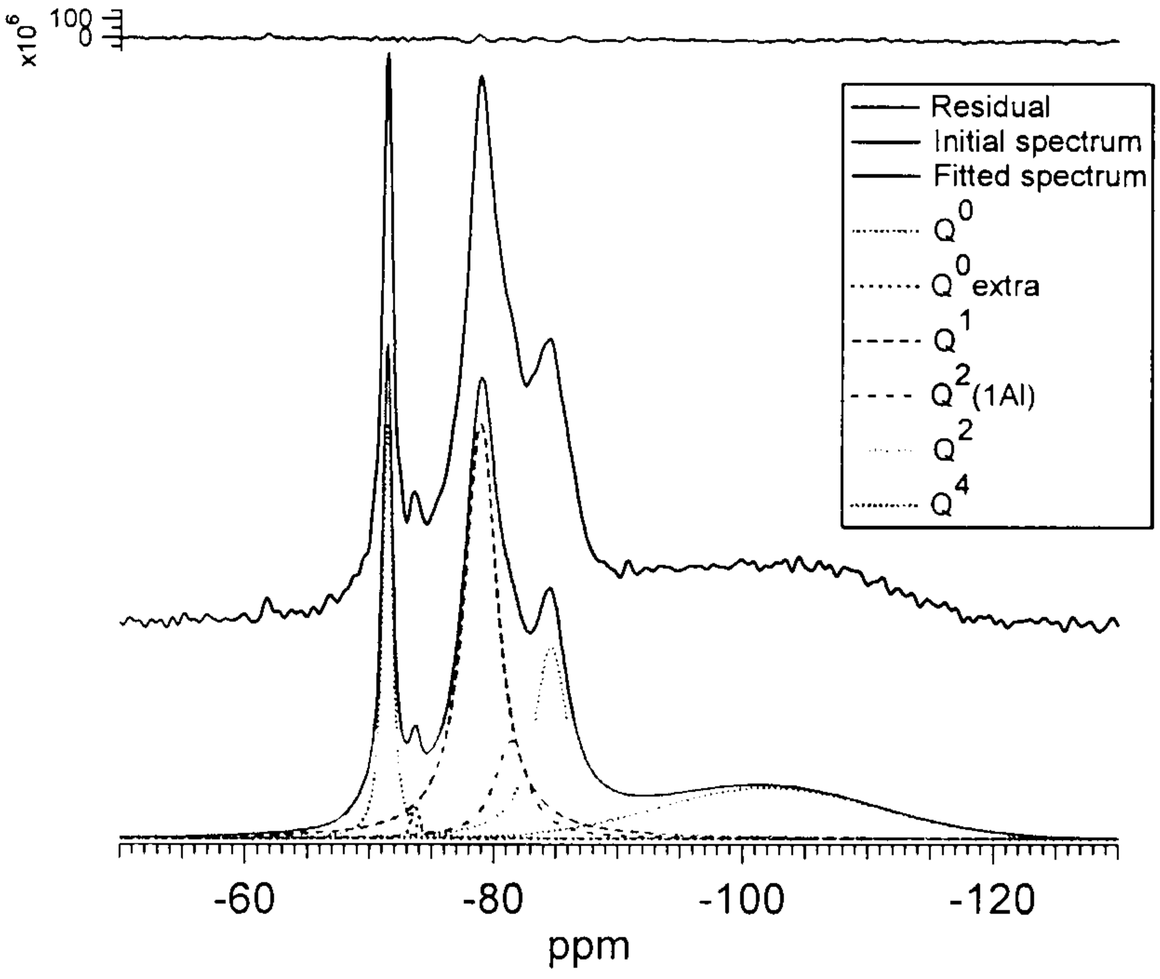


**Figure 3.12** – $^{29}$Si MAS NMR spectra deconvoluted fit for a WPC blend with 30% PFA.

The $^{1}$H-$^{29}$Si CP MAS NMR spectra were acquired using a magic angle spinning speed of 6 kHz, with a total of 10000 scans or, when the signal/noise ratio was not acceptable, a total of 80000 scans were acquired. All spectra were obtained with a pulse delay of 2 ms, $^{1}$H-90° pulse of 5 ms and a contact time of 1 ms.

## 3.8 – SCANNING ELECTRON MICROSCOPY

### 3.8.1 – General Introduction to SEM

In electron microscopy (EM), a beam of electrons of controlled energy, usually generated by thermionic emission, is directed at the specimen. The electron beam interacts with the sample and many events usually take place and some of the resulting signals are used in electron microscopy[129,130].

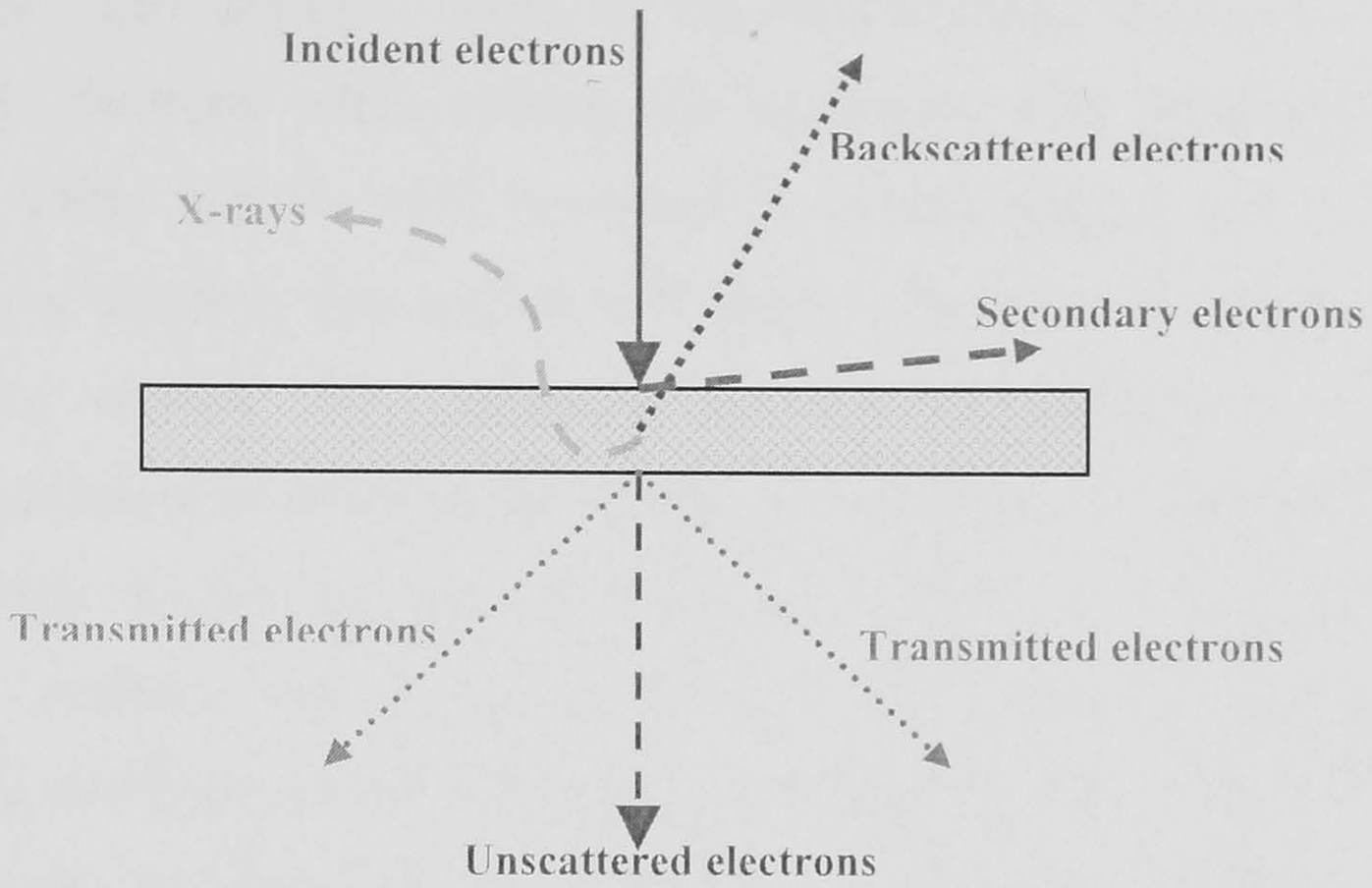


**Figure 3.13** – Schematic representation of the signals resulting from the electron beam interaction with a specimen.

As shown in Figure 3.13, different effects can result from the interaction between the electron beam and the electrons in the sample. Part of the electron beam will be unscattered but most of the electron beam interacts with the specimen and undergo inelastic and elastic scattering. In the first case, the direction of the primary electrons is changed but their overall energy is kept. Elastic scattering is very important in electron microscopy because most of the electrons are deflected and these are also the electrons that generate diffraction patterns. Inelastic scattered electrons change their direction and lose part of their energy[129,130]. Transmission electron microscopy is based in the scattering processes which will be discussed with more detail in the next section. Most of the electron beam energy will end up in the specimen as heat but it can also cause other events that are detected outside the specimen: secondary effects. Secondary effects include emitted secondary electrons, backscattered electrons and characteristic X-rays. The secondary electrons are generated when an incident electron changes its path and loses part of its energy which is transferred to an atom in the specimen (inelastic event), and leaves the sample with a very small energy. Each primary or incident electron can produce several secondary electrons, thus secondary electrons are abundant and the most used imaging signal (topography) in scanning electron microscopy (SEM). Backscattered electrons result from the collision between an incident electron with an

atom in the specimen and the incident electron loses part of its energy and is scattered "backward" 180 degrees. Some of the backscattered electrons can generate more secondary electrons when exiting the specimen. The production of backscattered electrons varies directly with the sample's atomic number and the higher the atomic number, the brighter that region will appear. X-rays production has been explained before in section 3.5, although in electron microscopy results from the de-energisation of an atom in the sample after a secondary electron is produced. These characteristic X-rays are an analytical signal and used in electron microscopy for chemical analysis. An X-ray spectrum emitted by the specimen provides both qualitative and quantitative information, allowing identification of which elements are present in the sample and how much of each element is detected. In addition to the emitted X-ray, a small amount of secondary X-ray can also be induced when the primary X-ray pass through the specimen and interacts with the sample's atoms. A key factor in SEM is the interaction volume. By definition, the interaction volume is the region into which the electron beam penetrates the specimen, i.e., the correspondent three-dimensional volume between the electron beam and the specimen atoms[129,130].

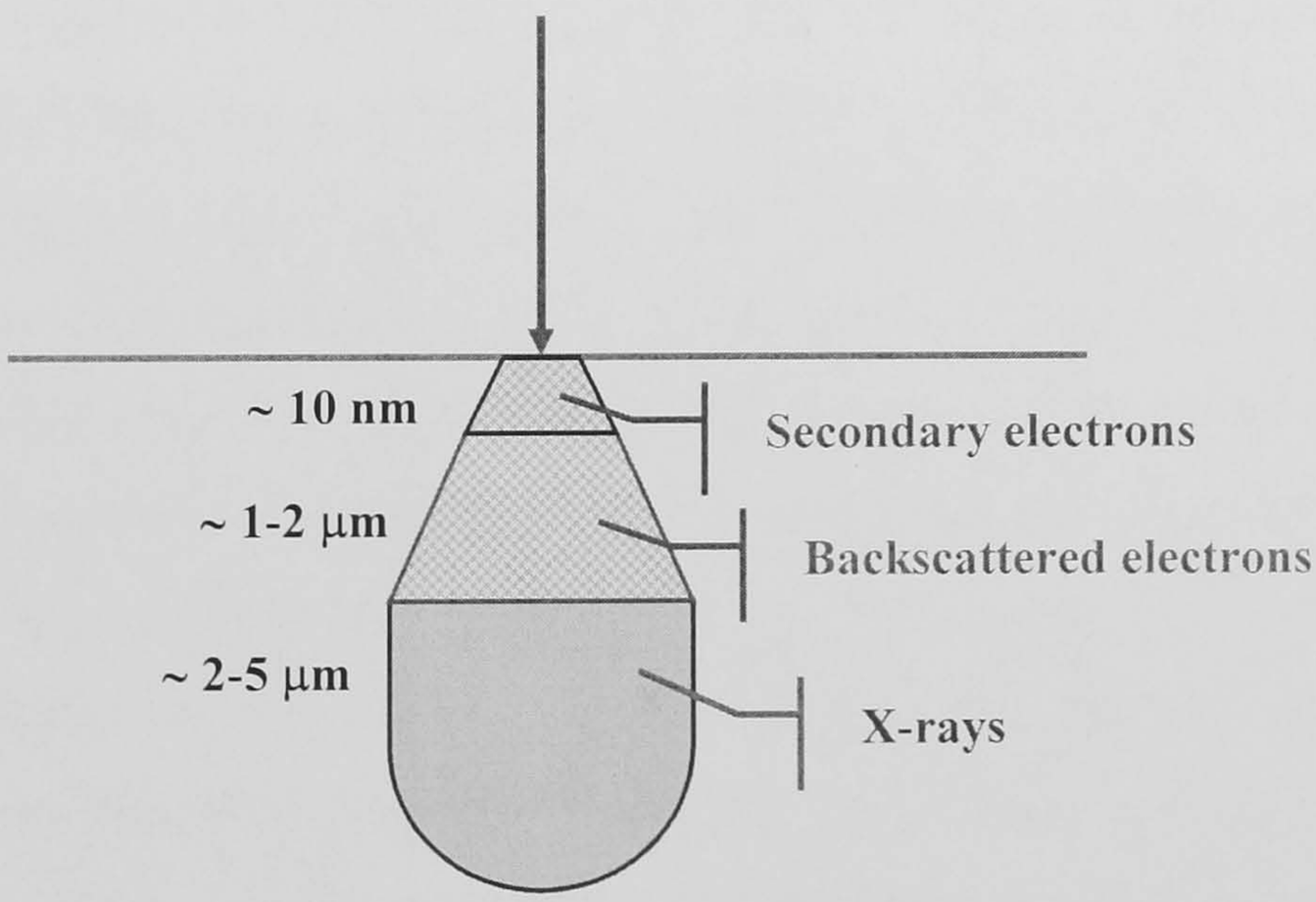


**Figure 3.14** – Schematic representation of the volume interaction in SEM.

The emission depth of the different signals used in SEM is influenced by the electron beam energy, the specimen nature and composition, and the sample preparation. The higher the accelerating voltage on the electron beam is, the larger the interaction volume

is. Specimen preparation is a critical factor because it will determine the depth of the X-ray generation and range. For a correct quantitative X-ray analysis, the sample needs to be polished into a flat surface, minimizing height differences at interfaces and eliminating the geometric effects that arise from the specimen surface[129,130]. In SEM, imaging is carried out by using the emission of secondary electrons (topography) and backscattered electrons (atomic number). Analytical X-rays provides qualitative and quantitative analysis of the studied samples.

### 3.8.2 – Experimental Procedure

The pastes were demoulded and cut into 400 μm thick slices, using a *Buehler* cut off saw with a diamond blade slow saw speed. Hydration was stopped through solvent exchange with propan-2-ol (Fischer Scientific) and the slices were dried in a vacuum desiccator. All dried samples were stored in glass tubes and placed in a desiccator containing silica gel. The latter was changed when required. The slices were impregnated with *Struers* epoxy-resin under vacuum and, after hardening, demoulded and polished to a flat surface in a *Struers* mechanical grinding (PdM-Force20 mounted on Rotopol-35) using *Struers* silicon carbide paper of different grades: 600, 1200 and 2400 μm grit. Subsequently, the samples were polished with diamond paste cloth of 3, 1 and ¼ μm (*Struers*, Glasgow, U.K.). The surface of the polished samples was carbon coated in a vacuum coating unit *EMSCOPE TB500* (U.K.), and analysed in a *CamScan Series 4* scanning electron microscope (SEM), equipped with an *Oxford Instruments UTW* energy dispersive X-ray (EDX) detector provided with the *Oxford Instruments* ISIS software for imaging/X-ray analysis (U.K.). The microscope was operated at an accelerating voltage of 20 kV and, when it was possible, the same magnification of 1000, 28 mm working distance and spot size of two or three, were used. For the C-S-H phase, between eighty and ninety points of EDX analysis were collected randomly in different areas of the sample. The EDX results were processed with the *ISIS* software, the matrix corrections were carried out with oxygen calculated by stoichiometry and the appropriate *ZAF* (the atomic number, absorption and fluorescence correction) procedure was applied to the data. Imaging of the microstructure was carried out in a *Philips XL30*

(U.K.) environmental scanning electron microscope (ESEM), which provided images with better definition and resolution.

## 3.9 – TRANSMISSION ELECTRON MICROSCOPY

### 3.9.1 – General Introduction to TEM

In transmission electron microscopy (TEM), the optical system is to some extent more complex than the one in SEM. All electron microscopes have an electron gun (either thermionic or field emission), a system of condenser lenses and signal detectors. However, the transmission electron microscope needs an objective lens and another set of lenses in order for an image to be projected onto a viewing screen. The objective lens forms a first intermediate image and a diffraction pattern. These image and pattern are consequently enlarged onto the viewing screen by the projector lenses[129,131]. An extremely important aspect in electron microscopy is the alignment of the electron beam. A correct alignment guarantees that the electrons can follow a straight line through the different lenses/apertures until they reach the specimen. The alignment also assures that optical aberrations, such as spherical aberration or astigmatism, are minimised and corrected, improving the image quality/resolution. The objective lens plays a very important role in TEM because it creates a diffraction pattern in the back focal plane, and also forms a static-beam image in the image plane. Diffraction patterns are very useful, in particular for identification of the different phases present in the sample and their crystallographic structures. When a selected-area diffraction (SAD) pattern is projected onto the viewing screen, the pattern can be used to perform two of the basic imaging operations in TEM. In a SAD pattern, a bright central spot containing the direct electrons is formed as well as some spots of the scattered electrons. If the central spot is used to form images, this is called bright-field imaging (BFI); if some or the totality of the scattered electrons are used to form images, it is named dark-field imaging (DFI). Both images are complementary and very useful to identify the specimen features and different morphologies[129,131]. Specimen preparation is another important aspect in TEM. The sample should be thin enough and beam transparent.

Thus, less scattered electrons will be produced. Very thin, almost transparent, specimens for TEM can be prepared using ion milling. The process involves bombarding the sample with energetic ions or neutral atoms that sputter material from the specimen until it is thin enough to be analysed. Argon is one of the most common ion sources and, controlling other parameters like the ion energy (current/voltage applied), angle of incidence, rotation and temperature of the sample, ion milling is the most versatile thinning process[129,131]. For thin specimens, the interaction volume is much smaller than the interaction volume in SEM, as seen in Figure 3.15.

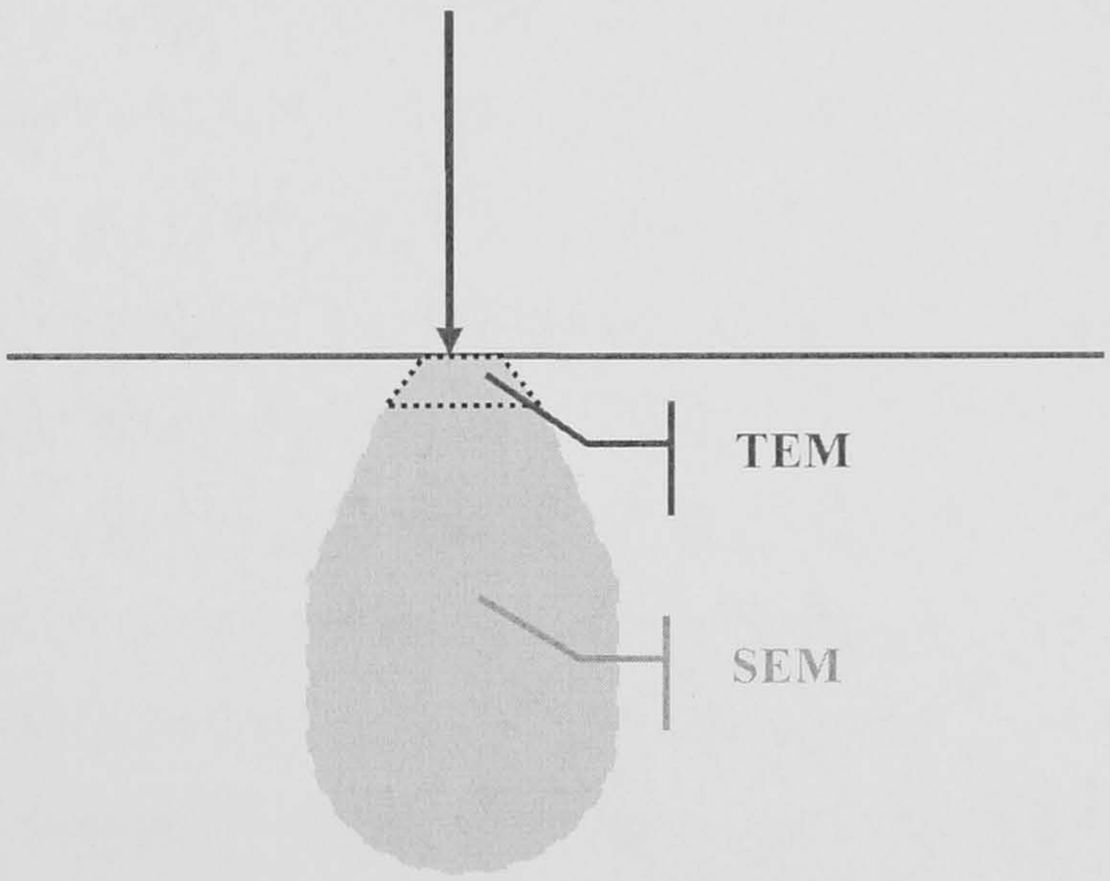


**Figure 3.15** – Schematic representation of the volume interaction in SEM and TEM.

In TEM, the total volume of material analysed is determined by the probe diameter and the sample thickness, in the nanometre scale. Therefore, X-ray generation will be much lower than for thick samples. As seen and explained for SEM, quantitative X-ray analysis in TEM can also be performed by relating the intensity of the different peaks present in the spectrum and their concentration in the specimen. In the analysis of very thin films, the ZAF correction or matrix correction are not needed because self absorption is negligible in thin films. Thus, absorption and X-ray fluorescence are ignored and this assumption is called the thin-foil criterion. Cliff and Lorimer related the intensity ratio to the concentration ratio and, usually, this is the correction applied when quantitative microanalysis is carried out in a TEM sample[129,131].

### 3.9.2 – Experimental Procedure

The samples were demoulded and cut into 200 μm thick slices. using a *Buehler* cut off saw with a diamond blade slow saw speed. Solvent exchange with propan-2-ol (Fischer Scientific) was used to stop hydration because freeze drying might induce cracking in the slices. After hydration was stopped, the slices were dried in a vacuum desiccator. All the dried samples were stored in glass tubes and placed in a desiccator containing silica gel, which was changed when required. The samples that were more fragile in handling were resin impregnated with *Struers* epoxy-resin, under vacuum. A slice was glued to a glass slide, using cyanoacrylate glue and then hand thinned using silicon carbide papers of different grades (600, 1200 and 2400 μm grit, *Struers*, Glasgow, U.K.), until they were approximately 30 μm thick and, at this stage, it was possible to read print through the specimen. The glass slide with the glued cement slice was placed face up in a glass Petri dish, and filled with acetone (*Fischer Scientific*) to dissolve the cyanoacrylate glue. The thinned slice floated from the glass slide and was removed and stored flat in a Petri dish on filter paper, in a desiccator as the slice was very fragile and easily to be carbonated in contact with air. Using araldite glue, 3 mm diameter Ni grids (with a 2x1 mm slot in them) were glued on one of the sides of the specimen. The grids were allowed to glue dry inside a covered Petri dish. The slice was turned over and more Ni grids were glued on the reverse, making a kind of "sandwich" with the cement paste between two grids, aligning the slots in the grids. The latter grids were allowed to dry and the sample was kept in a desiccator. Using the points of a pair of fine stainless tweezers, the "sandwiched" samples were trimmed to remove excess sample around the edges of the grided "sandwich". The samples were handled with extra care in order to avoid carbonation, which would be more rapid due to the thickness of the samples. Thus, when being handled, the samples were always on top of a Petri dish and covered by the corresponding lid. A mask was also used to avoid breathing into the sample and to protect from the dust produced in the hand thinning. Finally, using a *Fischione Instruments* Low Angle Ion Mill and Polishing System Model 1010 PA (U.S.A), the samples were argon ion-beam milled using a liquid nitrogen cooled stage in order to avoid excessive specimen heating, and consequent sample damage/alteration. The angle used was 15°, with a voltage of 4kV and a current of 3mA per ion gun. The ion-milling

was stopped when a hole was visible in the centre of the "sandwich", under an optical microscope incorporated in the equipment. After being milled, the specimens were carbon coated in an *Agar* turbo carbon coater provided with an *Agar* thickness monitor (U.K.). A *Philips CM20* (Netherlands) transmission electron microscope with energy dispersive X-ray analysis (TEM-EDX) was used to examine and obtain micrographs (bright field imaging) of the typical morphology of each studied system. The TEM was equipped with an *Oxford* UTW EDX detector (U.K.) and *Oxford* ISIS software for imaging/X-ray analysis in order to determine the chemical composition of each phase present in the pastes. For the most part of the samples, a total of thirty analysis points were taken for inner product C-S-H and fifty analysis points for outer-product C-S-H, and a fewer analysis points were also taken for other phases present in the samples. The EDX points were taken randomly around the thinner areas of the sample, using a magnification of 17500 and spot size four, with a corresponding analysis diameter of 150 nm. Before acquiring each EDX point of analysis, the inner (Ip) and outer-product (Op) C-S-H areas, the selected-area diffraction pattern was checked for intermixing with other crystalline phases. Thus, when it was possible, free intermixed areas were analysed by EDX. As seen in Figure 3.16, areas where the selected-area diffraction pattern showed spots (left image), were avoided and EDX analysis were taken in areas where the selected-area diffraction pattern did not show the presence of crystalline phases intermixed with C-S-H.

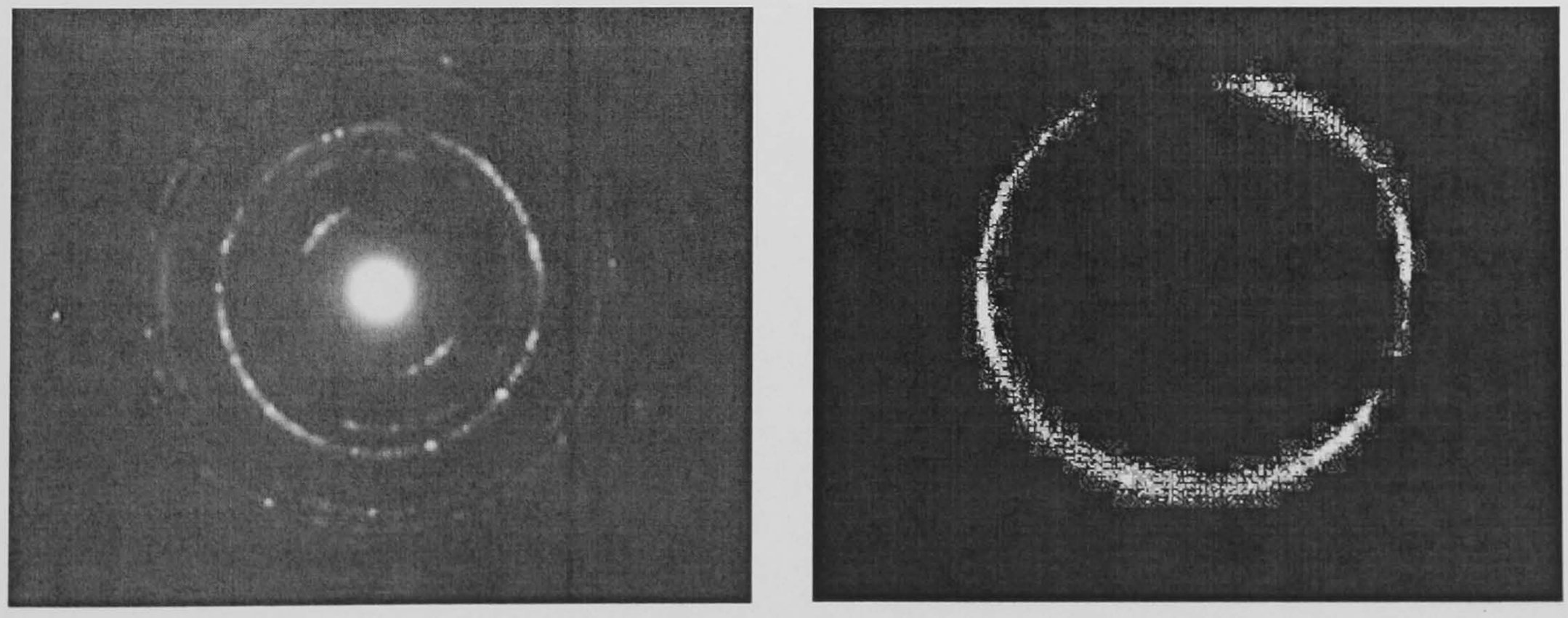

**Figure 3.16** – SAED patterns showing C-S-H intermixed with crystalline phases (left)[3] and amorphous C-S-H (right)[73].

The EDX results were processed with the *ISIS* software, with oxygen calculated by stoichiometry and the appropriate *Cliff Lorimer* correction was applied to the data.

# IV – RESULTS AND DISCUSSION: CURING AT 25°C

The experimental results related to the systems cured at 25°C are presented and discussed in this chapter. Different sections were created according to the techniques used to characterise the neat WPC and 30-60% PFA blended cement pastes. In the next chapters, the studied systems are referred to as:

- wpc and kwpc (neat WPC paste water and KOH activated, respectively);
- pfa30 (30% PFA blended WPC paste water activated);
- kpfa30 (30% PFA blended WPC paste KOH activated);
- pfa60 (60% PFA blended WPC paste water activated);
- kpfa60 (60% PFA blended WPC paste KOH activated).

## 4.1 – ISOTHERMAL CONDUCTION CALORIMETRY

Figure 4.1 shows the isothermal conduction curves measured for the water activated neat WPC paste as well as the corresponding curves for the 30 and 60% PFA blended cement pastes.

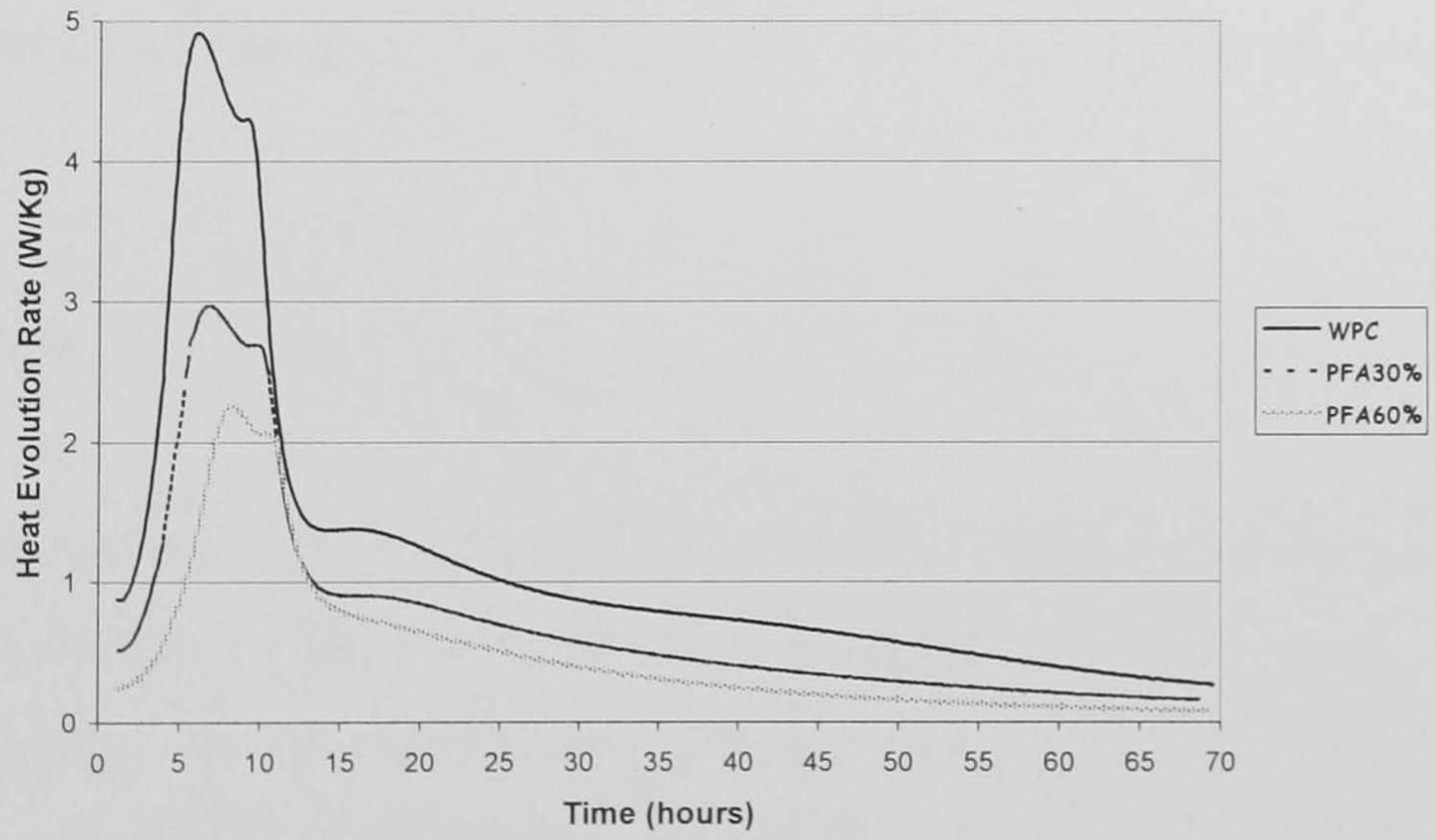


**Figure 4.1** – Isothermal conduction curves at 25°C for the water activated neat WPC and 30-60% PFA blended cement pastes.

Considering the isothermal conduction curve for the neat WPC paste, it was observed that after the induction period, the heat evolution accelerated and gave a heat peak after six hours of hydration. This peak corresponded to the formation of C-S-H gel resulting from alite hydration. A second peak was observed after nine hours of hydration time, where the reactions involving the aluminate and/or ferrite phases occurred and ettringite was also formed. The total heat evolved in the process was found to be 282.9 KJ/Kg, with a maximum rate of 4.916 W/Kg, after six hours of hydration, which was in good agreement with reported data[121]. The following table summarises the obtained data from the isothermal conduction calorimetric study.

**Table 4.1** – Evolved heat obtained by isothermal conduction calorimetry for the neat and blended systems cured at 25°C.

| | **WPC** | **PFA30** | **PFA60** |
|---|---|---|---|
| **Maximum rate (W/Kg)** | 4.92 (6.08 hours) | 2.97 (6.92 hours) | 2.26 (8.25 hours) |
| **Total heat (KJ/Kg)** | 282.9 | 175.5 | 118.9 |

The blended systems curves were comparable to the curve found for the neat paste, but presented lower heat evolution and later C-S-H formation, as seen in the previous table. Apparently, the addition of fly ash could accelerate hydration after the first day, acting as a nucleation site for C-S-H formation[1]. This was not verified in both blended cement pastes resultant calorimetric curves after seventy hours of continuous measuring.

## 4.2 – STA-EGA

STA-EGA was used in order to estimate the amount of calcium hydroxide (CH) present in the studied systems. Figure 4.2 shows an example of a STA curve, where it was possible to identify the exotherms that corresponded to C-S-H and CH dehydration around 120°C and 475°C, in that order, and estimate the amount of CH present in each sample. EGA helped to identify the evolved gases whilst the heating process took place.

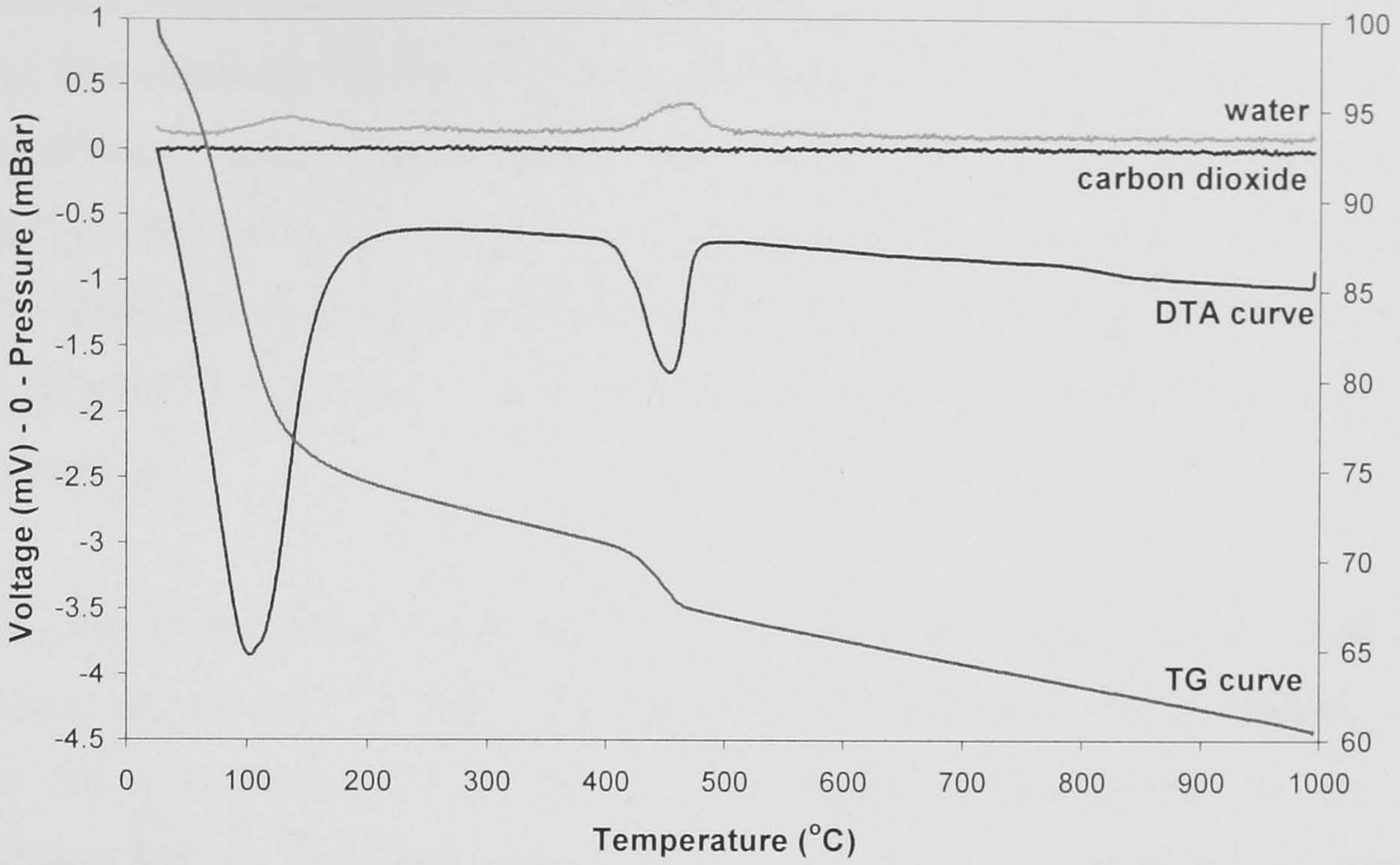


**Figure 4.2** – STA curve for the water activated neat WPC paste at 1 day, cured at 25°C.

As shown in Figure 4.2, in the TG curve two main weight losses occurred around 100°C and 450°C corresponding to the dehydration of C-S-H and CH, respectively. In the DTA curve, dehydration is recognised as exotherm peaks. From this example, it was also possible to identify the higher losses of water around those temperatures. Carbonation of the studied samples could also be easily detected by EGA if evolved carbon monoxide was detected around 600-780°C. Table 4.2 summarises the estimated CH as percentage of ignited weight obtained for all the studied systems at one day, one month and one year of hydration.

**Table 4.2** – Estimated amount of CH, as percentage of ignited weight, present in the water and KOH neat and blended cement pastes cured 1 day, 1 month and 1 year at 25°C.

| | **1 day** | **1 month** | **1 year** |
|---|---|---|---|
| **WPC** | 13 | 26 | 27 |
| **KWPC** | 18 | 31 | 37 |
| **PFA30** | 9 | 20 | 18 |
| **KPFA30** | 9 | 17 | 15 |
| **PFA60** | 7 | 11 | 5 |
| **KPFA60** | 8 | 5 | 3 |

Before any consideration, it should be kept in mind that the results are not absolute values. The results in Table 4.2 are only estimation of the amount of CH formed in each cementitious system. Considering the neat cement pastes, the amount of CH increased gradually with age. In the case of the kwpc sample, the amount of CH estimated was higher which indicated that the cement hydration rate and consequent production of CH were increased by the alkaline activation. In both neat systems at all ages, carbonation did not occur.

In the case of the blended systems, more attention was required when analysing the estimated amount of CH because besides cement hydration, the pozzolanic reaction where CH is consumed by the fly ash, also occurs simultaneously. In the systems containing 30% of PFA replacement, the amount of CH increased after one month of hydration but, after one year, part of it was consumed in the pozzolanic reaction. Apparently, the alkaline activation did not have the same effect on the blended cement paste as verified in the neat paste. Comparing the 60% PFA blends with the 30% PFA blends, a smaller amount of CH was present after one month. After one year of hydration, small quantities of CH were estimated. This could be due either to a higher extent of the pozzolanic reaction because more fly ash was present, or to the cement hydration rate was somehow slowed down by the greater amount of PFA. Again, EGA showed that none of the blended pastes was carbonated.

STA experimental results are not conclusive by themselves. If related with experimental data obtained from MAS NMR and electron microscopy, discussions considering the extension of the cement hydration and pozzolanic reactions can become clearer.

## 4.3 – XRD

XRD patterns were obtained by running the specimens with added rutile as internal standard (10% of the total mass of each sample). The following table summarises the different phases identified in the powder diffractograms obtained for the neat and 30%

PFA blended WPC pastes, either water or KOH activated, one day and one month, cured at 25°C. The corresponding XRD patterns are shown in Appendix A.

**Table 4.3** – Identified phases in the XRD patterns for the water and KOH neat and blended cement pastes cured 1 day and 1 month at 25°C.

| | **wpc** | **kwpc** | **pfa30** | **kpfa30** |
|---|---|---|---|---|
| **$C_3S$** | √ | √ | √ | √ |
| **β-$C_2S$** | √ | √ | √ | √ |
| **CH** | √ | √ | √ | √ |
| **Ettringite** | √ | X | √ | X |
| **Arcanite** | X | √ | X | √ |
| **Quartz** | X | X | √ | √ |

After one day of hydration portlandite and ettringite (AFt-type phase) were present and identified. This was in very good agreement with what usually happens in a Portland cement paste, where portlandite and ettringite are formed after one day of hydration and most of the alite reacts after twenty eight days. Belite has a smaller rate of hydration, therefore reacts slower than alite[1]. After one month, most of alite reacted but belite was still present. AFm-type phases were not present in sufficiently large quantity or with sufficiently large or ordered crystals to be detected by this technique. There was a discrepancy in the relative intensities obtained for rutile at both ages because the same rutile amount was always added to the samples. Considering the reflection around 28° of 2θ for rutile, at both ages it should be very similar. Although more ettringite could have been formed, it should not be more crystalline and lead to a higher relative intensity. Therefore, it appears that the amount of rutile added to both samples was not the same, i.e. 10% of the total mass of each sample. Consequently, Rietveld refinement was not carried out as well as quantification of the crystalline phases present in the sample. It was also confirmed that carbonation of the samples did not take place because there were no traces of peaks for any of the polymorphs of calcium carbonate.

In the alkaline systems, the peaks for CH were broader than those in the previous system due to small average crystal size[132]. Arcanite, $K_2SO_4$, was a crystalline phase

that was also formed due to the KOH activation. Alkaline activation reduces the activity of water in solution and destabilises AFt-type phases due to the number of water molecules needed in the formation of those phases[7]. Consequently, ettringite was not formed after one day or one month of hydration.

Considering the 30% fly ash blended systems, originally present in the anhydrous fly ash, unreacted quartz was also detected at both ages. As hydration took place, part of CH was consumed in the pozzolanic reaction, which was in good agreement with STA-EGA estimation.

## 4.4 – COMPRESSIVE STRENGTH

Compressive tests were carried out on mortars with the same chemical composition as the studied systems, cured at 25°C in an environmental chamber. The following table summarises the data obtained for the neat and 30% PFA blended WPC pastes, either water or KOH activated, one day and one month cured at 25°C.

**Table 4.4** – Compressive strength data obtained for the neat and 30% PFA blended cement pastes 1 day and 1 month, cured at 25°C.

| | | **Compressive Strength (MPa)** | ***s*** |
|---|---|---|---|
| **WPC** | **1 day** | 20.1 | 0.4 |
| | **1 month** | 72.4 | 5.0 |
| **KWPC** | **1 day** | 7.4 | 0.9 |
| | **1 month** | 15.3 | 0.7 |
| **PFA30** | **1 day** | 10.9 | 0.1 |
| | **1 month** | 49.2 | 0.7 |
| **KPFA30** | **1 day** | 2.9 | 0.6 |
| | **1 month** | 7.5 | 1.2 |

Generally, compressive strength increased after one month of hydration, indicating that the samples became more dense and compact. This was already expected because as hydration took place, the interstitial space originally filled with water, is replaced by the

resulting hydration products, such as C-S-H and CH[1]. However, in order to interpret correctly the above presented results, porosity of the samples should have been evaluated. Porosity, pore size and other microstructural features define the strength, elasticity and microhardness of cement pastes[1,120]. Several techniques are used in porosity structure determination and characterisation. The most commonly used are the helium inflow technique and mercury-intrusion porosimetry. An estimation of the level of porosity can also be obtained from backscattered electron microscopy (BSE), where resin impregnated samples reveal their porosity.

## 4.5 – SOLID STATE $^{29}$Si MAS NMR

$^{29}$Si MAS NMR was used to determine the silicate anion structure present in the C-S-H phase. The different used techniques (including TEM-EDX, Section 4.7) did not give evidence for the presence of any other polymerised aluminosilicate phase. Therefore, the fitting procedure was used assuming that the observed resonances corresponded to those of C-S-H. As explained in section 3.7.2.2, the acquired spectra were iteratively fitted and the integrated areas of the fitted peaks were used to calculate the mean aluminosilicate chain length and the Al/Si ratio. For the neat WPC pastes, it was possible to calculate the percentage of cement reacted, assuming that the total silicon present in the system and detected by MAS NMR was 100%. For the blended cement pastes, the same quantification was attempted by using the total percentage of silicon present in each system, calculated from the XRF results. Unfortunately, it was not possible to obtain an accurate and correct quantification as well as calculated percentages of cement and fly ash reacted. Two main reasons contributed to the lack of fully quantified MAS NMR data for the blended systems: not all the silicon present in those systems was detected by MAS NMR and part of the signal was "lost" in the sidebands, due to the paramagnetic interactions caused by the iron present in the fly ash. The use of several correction factors in order to relate the data with XRF results and balance the losses of signal proved to be inefficient. Iterative fitting of the sidebands was not possible. Therefore, data related to the 30% PFA blended systems should be considered semi-quantitative.

Preceding the analysis of the experimental spectra obtained for the different systems, a consideration/observation was attained. It was noticed that all MAS NMR spectra obtained for the hydrated systems showed a very small and sharp peak around -73.5 ppm. The latter was initially assigned to hydrated monomeric silicate species formed during the induction period, $Q^0(H)$, with a broad resonance in the region between -70 and -75 ppm[20,23]. The corresponding chemical shift for hydrated monomeric silicate species is not easy to be determined due to significant overlapping with the more intense $Q^1$ resonance. Cross-polarisation (CP) $^1H$-$^{29}Si$ MAS NMR spectra was acquired and, although $Q^0(H)$ resonance is very broad and much less intense than $Q^1$, evidence for the existence of $Q^0(H)$ species was not found, as shown in Figure 4.11. Therefore, the sharp peak enduringly found around -73.5 ppm should not correspond to hydrated $Q^n$ species and could only be assigned to species initially present in the anhydrous WPC. The main belite polymorph present in Portland cement is $\beta$-$C_2S$ and rarely, or in minor quantities, other polymorphs can be present[1]. Although belite contains enough stabilising ions to prevent the formation of $\gamma$-$C_2S$, another polymorph for belite, a small amount of $\gamma$-$C_2S$ can be formed depending on the clinker production [1]. $\gamma$-$C_2S$ is inert at ordinary temperatures and has no cementing ability. In order to investigate the possibility of $\gamma$-$C_2S$ being present in the white cement, a $^{29}Si$ MAS NMR spectrum for a synthetic $\gamma$-$C_2S$ was acquired[133]. As seen in Figure 4.3, $\gamma$-$C_2S$ has a sharp resonance around -73.5 ppm which was precisely the resonance found for the unknown resonance found in the spectra for the hydrated samples[30-36]. Other possibilities were considered but it was concluded that resonance at -73.5 ppm should be assigned to $\gamma$-$C_2S$.

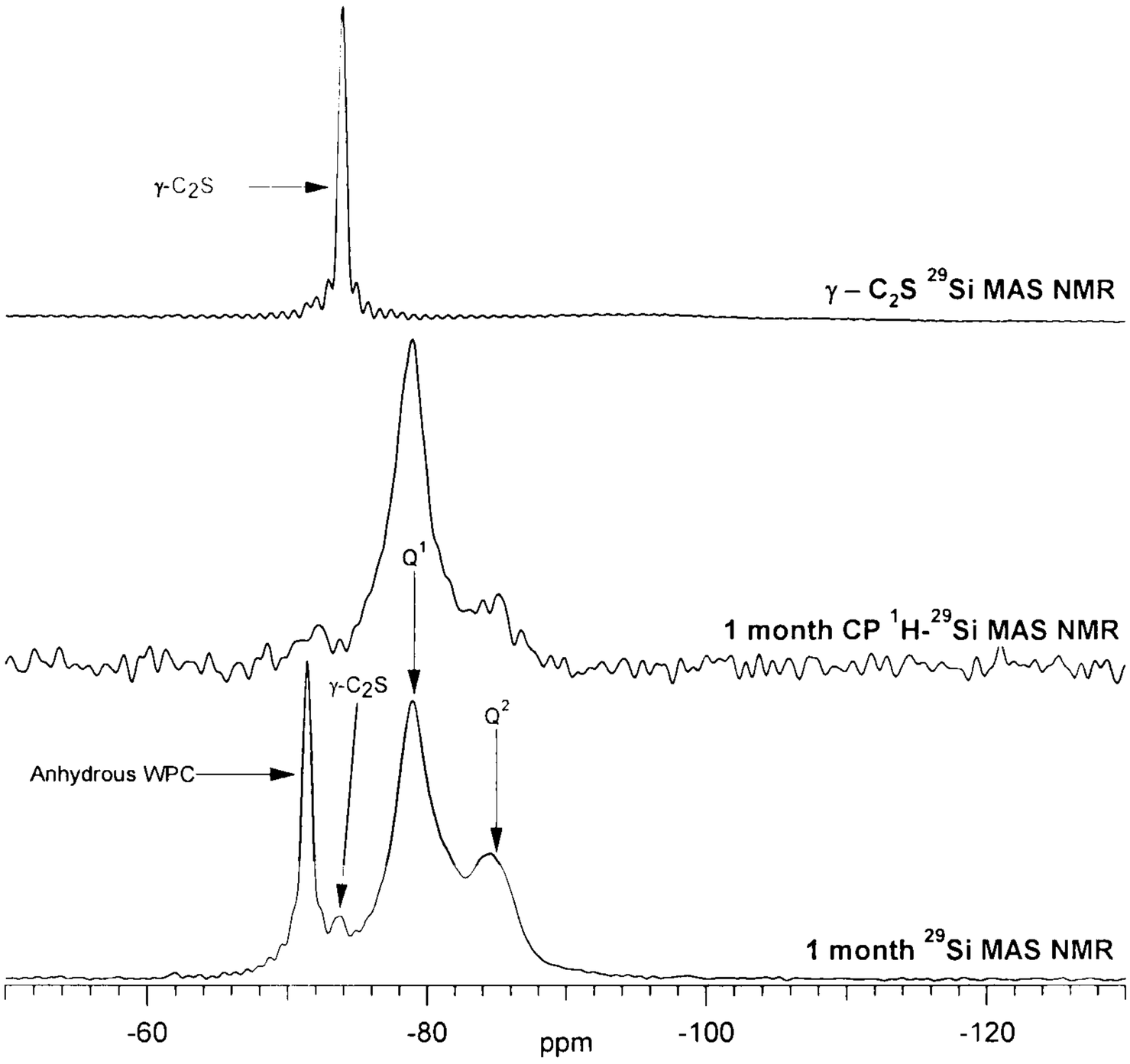


**Figure 4.3** – $^{29}$Si MAS NMR spectrum for synthetic anhydrous γ-$C_2S$ (upper), $^{1}$H-$^{29}$Si CP MAS NMR spectrum (middle) and single-pulse $^{29}$Si MAS NMR (bottom) for 1 month water activated WPC paste, cured at 25°C.

From the previously presented considerations and from the above spectra, it was possible to clearly assign the resonance at -73.5 ppm to γ-$C_2S$. The latter resonance was present in the single-pulse spectrum (bottom) but absent in the CP spectrum (middle).

The following figure illustrates the single pulse $^{29}$Si MAS NMR spectra obtained for the neat WPC water and KOH activated, cured at 25°C for one year.

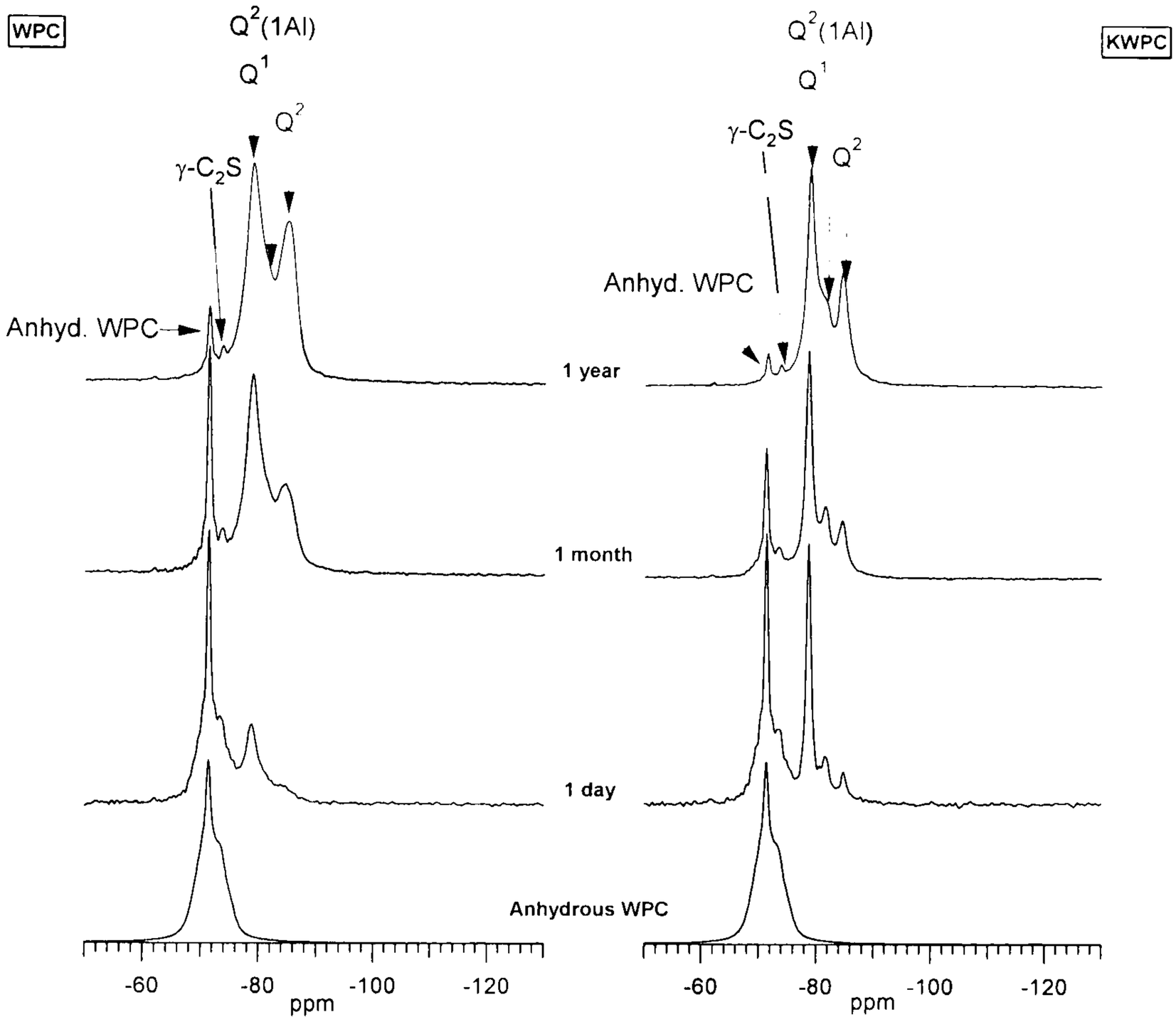


**Figure 4.4** – $^{29}$Si MAS NMR spectra for 1 day, 1 month and 1 year neat WPC pastes, cured at 25°C, water (left) and KOH (right) activated.

In view of the hydration evolution of the water activated neat WPC paste, after one day of curing at 25°C, three main peaks were observed: a first peak corresponding to anhydrous cement containing belite and alite ($Q^0$) at -71.3 ppm, a smaller peak at -79 ppm assigned to the resonance $Q^1$ (end chain groups), and a very small peak for $Q^2$ (chain middle groups) species at -84.9 ppm. It was possible to conclude that part of the cement reacted to give $Q^1$ species as dimers were formed and also polymerised to give $Q^2$ species. $Q^2$(1Al) species were also formed and accounted in the quantification proceedings described in Section 3.7.2.2. As hydration proceeded, the relative intensity of $Q^0$ decreased because most of the alite reacted to give C-S-H and part of belite remained unreacted. $Q^1$ increased, indicating that more cement reacted with more dimers and end chain groups being created. $Q^2$ relative intensity also increased because more chain middle groups were formed and consequent longer chain lengths. γ-$C_2S$ corresponding resonance was also present. After one year of hydration, most of the belite reacted seeing that the relative intensity of $Q^0$ decreased. The percentage of $Q^1$

decreased slightly, indicating that further polymerisation of C-S-H occurred with the consequent increase of $Q^2$ relative intensity. $\gamma$-$C_2S$ relative intensity remained the same after one year of hydration which was expected due to its inability to react at room temperature[1]. Considering that the total silicon present in the system was 100% and that the same percentage was detected by MAS NMR, the peaks were quantified as percentage of intensity. Table 4.5 presents the quantified data obtained from iterative deconvoluted fitting of the peaks, including the mean aluminosilicate chain length (MCL) found for C-S-H and corresponding Al/Si ratio. Other very useful parameters were determined like %B and $B_{water}/B_{KOH}$. The proportion of bridging tetrahedra that are occupied by aluminium is given by %B, according to the following equation[3]:

$$\%B = \frac{Q^2(1Al)}{\frac{2}{3}Q^2 + Q^2(1Al)} \qquad (Eqn.\ 4.1)$$

**Table 4.5** – $^{29}$Si MAS NMR quantitative data obtained for the neat cement pastes 1 day, 1 month and 1 year, cured at 25°C.

| | Water activated | | | KOH activated | | |
|---|---|---|---|---|---|---|
| | **1 day** | **1 month** | **1 year** | **1 day** | **1 month** | **1 year** |
| **MCL** | 2.7 | 3.3 | 4.3 | 2.8 | 3.4 | 4.0 |
| **Al/Si** | 0.050 | 0.056 | 0.066 | 0.069 | 0.093 | 0.083 |
| **% Anhydrous cement** | 63.4 | 19.8 | 5.4 | 52.6 | 22.6 | 3.4 |
| **% Cement reacted** | 36.6 | 80.2 | 94.6 | 47.4 | 77.4 | 96.6 |
| **% $\gamma$-$C_2S$** | - | 1.8 | 1.8 | 1.3 | 1.4 | 1.4 |
| **% $Q^1$** | 28.4 | 49.7 | 45.7 | 35.5 | 49.2 | 51.9 |
| **% $Q^2$(1Al)** | 3.7 | 8.8 | 12.2 | 6.3 | 14.2 | 15.9 |
| **% $Q^2$** | 4.6 | 19.9 | 34.9 | 4.3 | 12.7 | 27.5 |
| **% B** | 55 | 40 | 34 | 69 | 63 | 46 |
| **$B_{water}/B_{KOH}$** | 80 | 64 | 74 | - | - | - |
| **CH as % of ig. wt. (STA)** | 13 | 26 | 27 | 18 | 31 | 37 |

From the above experimental results, the amount of reacted cement increased as hydration took place. As expected, some polymerisation of C-S-H occurred but dimeric species were predominant at all ages in both neat pastes. Aluminium substitution in tetrahedral places in C-S-H occurred and increased a very small amount with time of hydration, because $Q^2$(1Al) relative intensity increased as well as the Al/Si ratio. In good agreement with all of these observations, the amount of CH resulting from the

cement reaction also increased, indicating that most of the cement reacted after one month of hydration. Similar results were found for the alkaline system. Better resolved spectra were obtained because KOH leads to greater degree of structural order, also observed in other KOH activated systems.[13,57,132] Therefore, the spectra obtained for the alkaline samples were used in order to help deconvolution of the corresponding spectra for the water activated samples. At one day, almost half of the cement reacted giving mainly $Q^1$ species. $Q^2(1Al)$ and $Q^2$ were perfectly distinguished in the spectrum. As hydration continued, most of the alite and part of the belite reacted and polymerisation of C-S-H also occurred, as the consequent increase of the relative intensity of $Q^2$ and $Q^2(1Al)$ demonstrated. After one year, around 97% of the cement was hydrated. The MCL found for C-S-H was 4 and the Al/Si ratio around 0.083. $\gamma$-$C_2S$ corresponding resonance was also present and had a constant relative intensity. After comparing the water and KOH activated neat WPC pastes, it was possible to conclude that the activation method did not influence the kinetics of cement hydration. Dimeric species were predominant at all ages in both systems. The Al/Si ratio in the alkaline neat cement paste was higher than that found for the water activated sample. The proportion of occupied bridging sites in the dreierkette chains that are occupied by $Al^{3+}$ and not $Si^{4+}$ (%B) slightly decreased with hydration time in both neat pastes. Consequently, the $B_{water}/B_{KOH}$ ratio was affected: around four fifths at one day, three fifths at one month and four fifths after one year of hydration. At one month and one year, the proportion of aluminium substituted bridging sites was mainly the same in the water activated cement paste. In the alkaline system and at all ages, more than half of the bridging sites in the C-S-H chain were aluminium substituted. Although the studied systems have very different Al/Si ratios and MCL values, the $B_{water}/B_{KOH}$ ratios were similar to those found for a 20% metakaolin blended white Portland cement (61% at one day and 82% at one month).[132]

The following figure and table illustrate the MAS NMR experimental results obtained for the 30% PFA blended white cement pastes. It should be kept in mind that these experimental results are semi-quantitative. The latter were expressed as percentages of intensity obtained from the iterative fitting of the spectra. The reasons for absent full quantitative data have been explained before. However, the information obtained for the

MCL and Al/Si ratio was considered to be accurate and acceptable. If a correction factor was found and used, it would affect all the obtained intensities by the same amount. Thus, by applying Equations 2.14 and 2.15, the ratio between the different intensities was invariable and not affected by the loss of signal that unable full quantification.

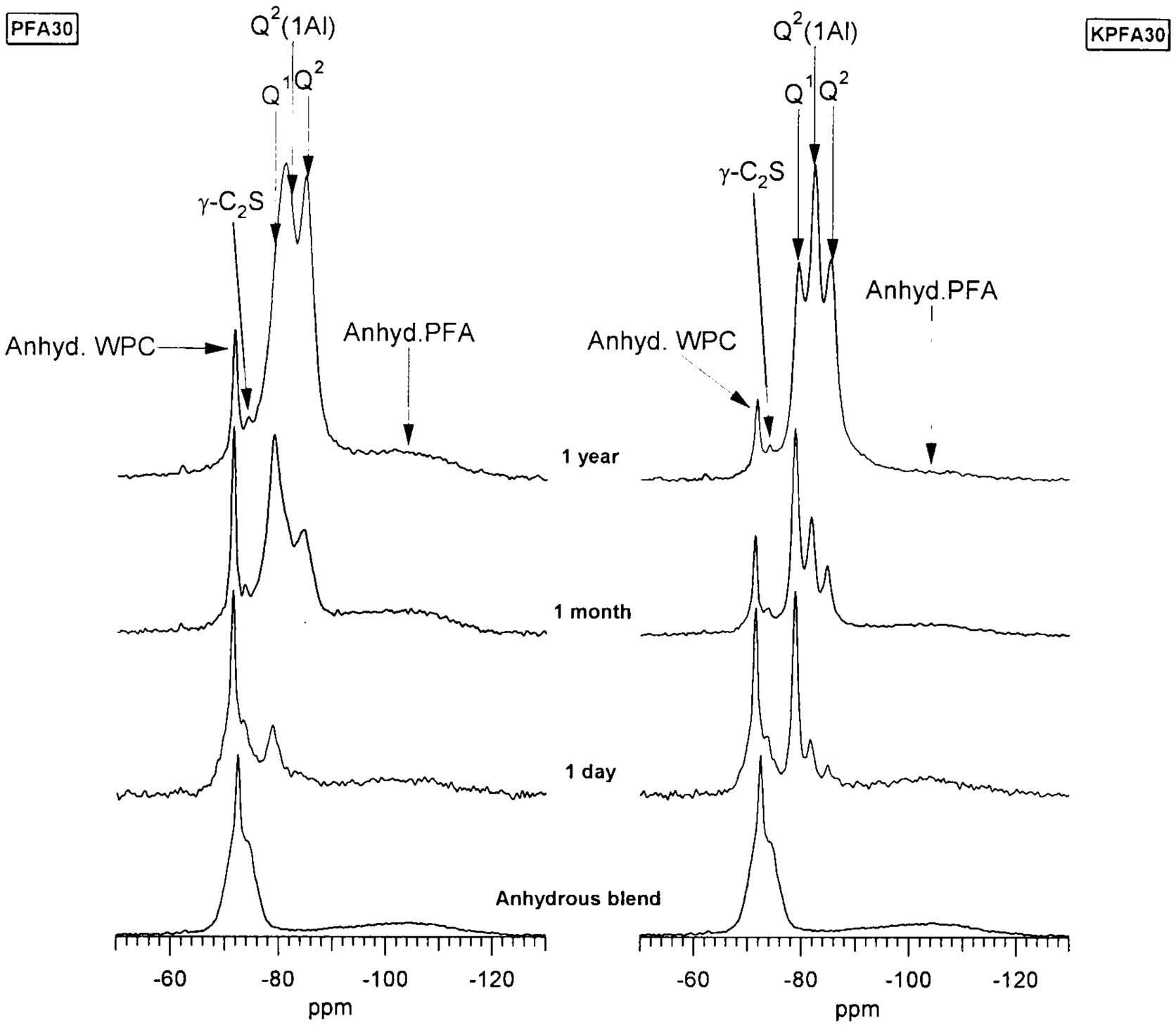


**Figure 4.5** – $^{29}$Si MAS NMR spectra for 1 day, 1 month and 1 year 30% PFA blended WPC pastes, cured at 25°C, water (left) and KOH (right) activated.

Considering the water activated blend, after one day of curing at 25°C, a peak corresponding to anhydrous cement containing belite and alite ($Q^0$) at -71.3 ppm, was observed, as well as a smaller peak at -79 ppm assigned to the resonance $Q^1$ (end chain groups). By this time of hydration, it was not possible to clearly distinguish the resonance assigned to γ-$C_2S$. The resonance $Q^4$ at -103 ppm corresponded to silicon present in the anhydrous PFA. With further hydration occurring, the relative intensity of $Q^0$ decreased due to the reaction of alite and some belite to give C-S-H. $Q^1$ relative intensity increased because more dimers and end chain groups were formed, as polymerisation of C-S-H also took place. A peak assigned to $Q^2$ resonance at -84.9 ppm

(chain middle groups were formed and consequent longer chain lengths) was identified, along with $\gamma$-$C_2S$ corresponding resonance. From deconvolution of the spectrum, a very small resonance for $Q^2$(1Al) was observed at -82 ppm. After one year of hydration, part of the belite reacted with corresponding decrease of the relative intensity of $Q^0$, as seen in Table 4.6. Further polymerisation of C-S-H occurred with the consequent decrease of $Q^1$ and increase of $Q^2$ relative intensity. $\gamma$-$C_2S$ relative intensity did not change significantly after one year of hydration, as expected. The relative intensity of $Q^4$ decreased with time indicating that PFA was consumed in the pozzolanic reaction. In Table 4.6, the spectra deconvolution results found for the water and KOH activated 30% PFA blends are presented.

**Table 4.6** – $^{29}$Si MAS NMR semi-quantitative data obtained for the 30% PFA blended cement pastes 1 day, 1 month and 1 year, cured at 25°C.

| | **Water activated** | | | **KOH activated** | | |
|---|---|---|---|---|---|---|
| | **1 day** | **1 month** | **1 year** | **1 day** | **1 month** | **1 year** |
| **MCL** | 2.5 | 3.6 | 11.5 | 2.9 | 4.2 | 8.8 |
| **Al/Si** | 0.020 | 0.070 | 0.189 | 0.09 | 0.145 | 0.214 |
| **% Anhydrous cement** | 39.3 | 14.3 | 6.1 | 32.3 | 12.0 | 4.4 |
| **% $\gamma$-$C_2S$** | - | 0.6 | 1.4 | - | 0.5 | 0.8 |
| **% $Q^1$** | 20.3 | 37.8 | 16.2 | 26.4 | 31.3 | 22.5 |
| **% $Q^2$(1Al)** | 1.0 | 9.0 | 29.7 | 6.0 | 16.6 | 35.0 |
| **% $Q^2$** | 3.4 | 17.6 | 32.5 | 2.9 | 9.3 | 24.1 |
| **% Anhydrous PFA** | 36.0 | 20.7 | 14.1 | 32.5 | 30.3 | 13.2 |
| **% B** | 31 | 43 | 58 | 12 | 32 | 73 |
| **$B_{water}/B_{KOH}$** | 259 | 138 | 79 | - | - | - |
| **CH as % of ig. wt. (STA)** | 9 | 20 | 18 | 9 | 17 | 15 |

From the above results, it was possible to conclude that polymerisation of C-S-H occurred with time because MCL and the relative intensity of $Q^2$ increased. The bridging silicon in C-S-H was substituted, to a certain extent, by aluminium because $Q^2$(1Al) relative intensity increased with time as well as the Al/Si ratio. Considering the pozzolanic reaction between PFA and CH, the decrease of the relative intensity of $Q^4$ indicated that as CH was formed from cement hydration, it was consumed by PFA to give additional C-S-H gel. However, after one year of hydration, some anhydrous PFA was still present in the sample as well as a considerable amount of CH. Regarding the alkaline 30% PFA blend sample, generally, similar results but better resolved spectra

were obtained. For example, the spectrum at one day of hydration showed that a resonance assigned to $Q^2(1Al)$ was present, although that was not visible in the corresponding water activated sample spectrum, and it was only identified after comparison with the spectrum for the alkaline blend and consequent iterative fitting. KOH activation led to shorter MCL, but to high aluminium substitution in C-S-H as continuing increase of Al/Si ratio and $Q^2(1Al)$ confirmed. Comparing the water and KOH activated 30% PFA blended WPC pastes, the alkaline activation did not influence the kinetics of cement hydration. Although KOH activation increased slightly the relative intensity of $Q^1$, $Q^2(1Al)$ and the Al/Si ratio, it did not accelerate or decelerate the reaction rate. However, this kind of activation influenced to a larger extent the silicon substitution in C-S-H, as proved by higher relative intensity of $Q^2(1Al)$ and Al/Si ratio. In both systems, most of the cement reacted at 1 month and further polymerisation of C-S-H took place till 1 year. Considering the proportion of bridging tetrahedra occupied by aluminium, it was higher in the water activated blend but it gradually decreased as hydration progressed. The $B_{water}/B_{KOH}$ ratio was around thirteen fifths at one day, seven fifths at one month and four fifths at one year. It was clear that as hydration advanced, the amount of bridging tetrahedra that were occupied by aluminium increased considerably (nine fifths) in the alkaline blended cement paste.

Finally, the MAS NMR results were compared between the neat and 30% PFA blended WPC pastes. Table 4.7 summarises the comparable parameters found for the water activated neat and blended (30% PFA) WPC pastes, after one month of hydration.

**Table 4.7** – $^{29}Si$ MAS NMR data comparison between water activated neat and 30% PFA blended cement pastes 1 month, cured at 25°C.

| | **Neat WPC** | **30% PFA blended WPC** |
|---|---|---|

| | | |
|---|---|---|
| **MCL** | 3.3 | 3.6 |
| **% Anhydrous cement** | 19.8 | 14.3 |
| **Al/Si** | 0.056 | 0.070 |
| **% $Q^2$(1Al)** | 8.8 | 9.0 |
| **CH as % of ig. wt. (STA)** | 26 | 20 |

As shown in the previous table, substituting WPC with class F PFA affected slightly the amount of reacted cement, because it was higher in the blend. On the other hand, it also led to higher polymerisation of C-S-H with a mean aluminosilicate chain length of four instead of three for the neat paste. Due to its higher aluminium content, fly ash acted as a source of aluminium free to substitute the central silicon in the C-S-H dreierkette chain. Therefore, the Al/Si ratio was slightly higher in the blend than in the neat white cement. It was expected that the relative intensity of $Q^2$(1Al) would also be higher. However, the discussed effects of PFA substitution were more obvious after one year. The blended sample presented a mean chain length of 12 and Al/Si ratio of 0.189 whereas the neat cement paste had a MCL of 4 and Al/Si ratio of 0.066. In addition, STA results showed that pozzolanic reaction between PFA and CH occurred. For example, after one year, both samples had the same degree of hydration/percentage of anhydrous cement, but less CH was present in the blended cement paste. Table 4.8 shows the same comparable parameters calculated for the KOH neat and 30% PFA blended WPC pastes, after one month of hydration.

**Table 4.8** – $^{29}$Si MAS NMR data comparison between KOH activated neat and 30% PFA blended cement pastes 1 month, cured at 25°C.

| | **Neat WPC** | **30% PFA blended WPC** |
|---|---|---|
| **MCL** | 3.4 | 4.2 |
| **% Anhydrous cement** | 22.6 | 12.0 |
| **Al/Si** | 0.093 | 0.145 |
| **% $Q^2$(1Al)** | 14.2 | 16.6 |
| **CH as % of ig. wt. (STA)** | 31 | 17 |

In the alkaline pastes, the effects of PFA substitution were not as clear as previously observed in the water activated cement pastes. The MCL was similar in both systems as well as the relative intensity of $Q^2$(1Al). The major differences were in the amount of

cement reacted and Al/Si ratio. After one month of hydration, there was only around 10% of anhydrous cement in the blend, but the double of the amount was present in the neat paste. It appears that alkaline activation promoted the cement hydration when the latter was competing with the pozzolanic reaction, but not when it was the main reaction taking place in the neat paste. Thus, comparing the amount of CH present in both samples, PFA consumed CH to give C-S-H. Ultimately, after one year, the KOH activated blended cement paste had a higher MCL and Al/Si ratio than the alkaline neat WPC paste.

The $^{29}Si$ MAS NMR spectra acquired for the water and KOH activated 60% PFA blended WPC cement pastes are shown in Appendix B. As said before, it was not possible to deconvolute and iterative fit these spectra due to a very low signal/noise ratio caused by the higher iron content of the fly ash. From the spectra, it was possible to verify that polymerisation of C-S-H occurred to a certain extent as hydration took place. Pozzolanic reaction between fly ash and calcium hydroxide also happened.

## 4.6 – SEM-EDX

SEM-EDX analysis was used in order to determine the chemical composition of different phases present in the neat and blended cement pastes. The samples were resin impregnated and flat polished, revealing porosity. Using this kind of sample preparation, the contrast due to topography is reduced but that due to different chemical compositions is enhanced. Considering the microstructure itself, it is possible to observe that CH grows in the water-filled space, forming isolated masses. C-S-H gel forms in situ from the anhydrous cement grains described as inner product C-S-H, Ip C-S-H. Outer product C-S-H, Op C-S-H, forms in the water-filled space. In the backscattered imaging mode, different phases with different chemical compositions show different greyscales. Usually, in a cement paste, the brightest phases are CH and anhydrous cement grains. C-S-H gel has a transitional greyscale and darkest regions usually correspond to pores filled with epoxy resin. In SEM-EDX, the interaction volume between the electron beam and the sample is quite large and signal interference from

intermixing with other phases present in the microstructure can not be avoided. Therefore, careful must be taken when analysing EDX data. In order to identify intermixing between phases and determine the Ca/Si and Al/Si ratios for C-S-H, EDX data is plotted in terms of atomic ratios. Plotting atomic ratios like Al/Ca against Si/Ca atomic ratio and S/Ca against Al/Ca, usually helps visualising if there are any trend lines. If a trend is found from the bulk of C-S-H chemical composition in the direction of other phase`s composition, then it is possible to say that C-S-H gel is intermixed with that phase, bearing in mind the total interaction volume between the electron beam and the sample. Figure 4.6 shows backscattered electron images illustrating the microstructure found in the neat WPC paste water activated one day, one month and one year, cured at 25°C. Low magnification images are shown on the left-hand side and higher magnification on the right-hand side.

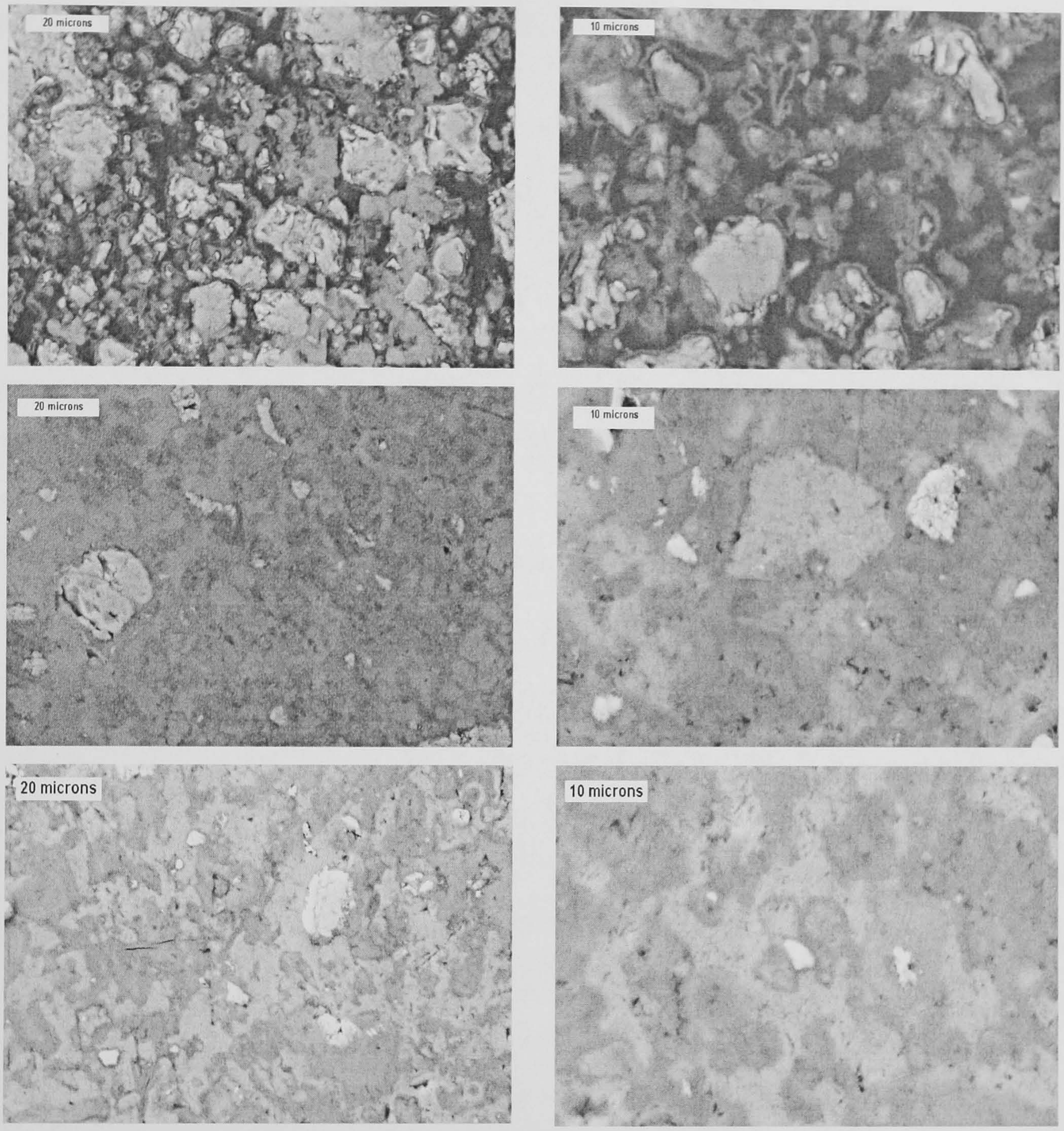


**Figure 4.6** – Backscattered electron images showing typical regions in the water activated WPC paste after 1 day (upper images), 1 month (middle) and 1 year (lower images) of hydration at 25°C.

From visual observation, it was possible to observe that, after 1-day hydration, the microstructure was very porous and some large areas of CH were formed. SEM backscattered electron images need to be cautiously analysed because removed material from the samples whilst polishing, can be easily mistaken for porosity. Anhydrous cement grains were also visible and the darker lines/spots inside the particles corresponded to traces of ferrite. Ip C-S-H rims were very well defined but generally not large enough to perform EDX analysis avoiding major intermixing with other

phases. The latter can be concealed underneath C-S-H but not easily noticed due to the interaction volume and consequent resolution of this technique. As hydration took place, at one year around 95% of the cement reacted and the microstructure became denser and better defined due to the formation of more Op C-S-H in the water-filled space. Areas of CH were detectable as well as some anhydrous cement grains. It was not possible to perfectly distinguish the chemical composition of Ip C-S-H from that of Op C-S-H. Partially reacted cement particles appeared to be hollow but, in fact, were filled with a low-density product, as images acquired using a field emission-SEM (FEG-SEM) demonstrated[136]. It has also been previously observed in other systems that these particles are not hollow[13]. Figure 4.7 shows plots for the EDX analysis. Ip and Op C-S-H were analysed and the corresponding points of analysis were referenced as *C-S-H*. Other interesting points of analysis were also plotted, such as *CH+*, *Pfa+* and *Anhyd*. *CH+* denominates CH in a non pure form, i.e., not free of intermixing; *Pfa+* for fly ash in an impure form and *Anhyd* corresponds to analysis of anhydrous cement particles. If trend lines were identified, they are represented by arrows pointing in the direction of the chemical composition of other phases intermixed with C-S-H, like CH or AFt-type phases or AFm-type phases. The Al/Ca atomic ratio for the pure phases of CH, AFt and AFm-type phases is 0, 0.33 and 0.5, respectively.

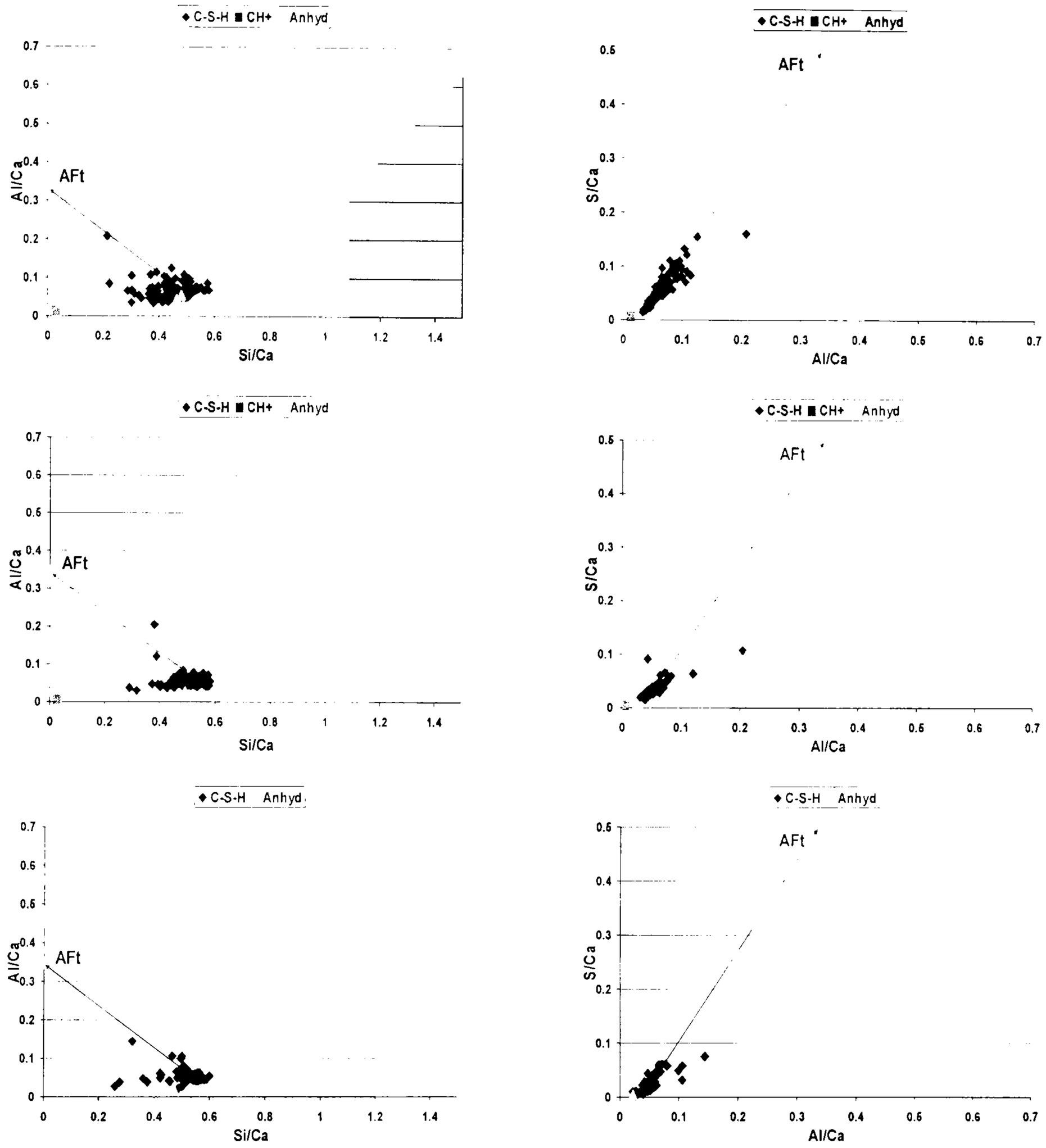


**Figure 4.7** – Al/Ca against Si/Ca (left) and S/Ca against Al/Ca (right) atomic ratio plots for the SEM-EDX phase analysis of the water activated WPC paste after 1 day (upper plots), 1 month (middle) and 1 year (lower plots) of hydration at 25°C.

The above figure clearly shows that plotting the EDX data in terms of the atomic ratio, a trendline going from the bulk of the C-S-H chemical composition towards the chemical composition of AFt-type phases was identified. Comparing the chemical composition of C-S-H with that of anhydrous cement, the mean Ca/Si ratio was slightly lower but the mean Al/Si ratio was generally higher. This could be understood as the fact that aluminium substitutes bridging silicon in the C-S-H chain but, as pointed out before, due to larger volume interaction inherent to this analytical technique, caution must be

taken when interpreting SEM-EDX experimental results. As hydration proceeded, after one month, the mean Ca/Si ratio decreased to 2.01 (s = 0.28) and to 2.02 (s = 0.38) after one year. The mean Al/Si ratio also decreased to 0.11 (s = 0.05) after one month and one year. This was due to a better organisation and distribution of the microstructure as well as maturing of the C-S-H gel. The mean atomic ratios obtained at one year are in very good agreement with those from a similar SEM-EDX prior study by Escalante-Garcia and Sharp.[135] Although experimental conditions of initial curing were quite different, the mean Ca/Si and Al/Si atomic ratios found for an OPC paste cured at 30°C for one year were 2.08 and 0.096, respectively. According to the authors, EDX analysis was individual for Ip C-S-H. However, considering prior TEM-EDX data and the chemical composition limits for C-S-H (discussed according to Richardson and Grove's structural models), it is clearly demonstrated that SEM-EDX analysis was not free of intermixing with other phases.[3,72]

Generally, similar findings were obtained for the other studied systems (kwpc, pfa30, kpfa30, pfa60 and kpfa60). The corresponding backscattered images can be found in Appendix C. The microstructure was usually porous after one day of hydration, becoming denser as hydration took place. Regions of CH, anhydrous and partially/fully hydrated particles of cement and fly ash (blended systems) were identified. Ip C-S-H rims, although well defined, were not EDX analysed. Again, partially reacted cement grains were not hollow but were filled with a less dense product.[13,136] Considering EDX analysis, intermixing between C-S-H and other phases like CH, AFm and AFt-type phases was clearly observed from the trend lines identified in the atomic ratio plots. Therefore, the chemical composition of C-S-H could not be determined by SEM-EDX. The atomic ratio plots for the other studied systems (kwpc, pfa30, kpfa30, pfa60 and kpfa60) are also presented in Appendix C. In the alkaline neat and blended pastes, a trend line was visible from bulk C-S-H composition towards CH composition. According to Groves[78], alkaline activation of a cement paste induces the formation of microcrystalline CH which is finely intermixed with C-S-H gel. Therefore, the trend line in the direction of CH confirms that microcrystalline CH was formed and was finely intermixed with C-S-H. As expected, and explained before, a trend line in the

direction of the AFt-type phases was not detected because those phases are not thermodynamically stable enough to be formed[7] in alkaline activated cement pastes.

The EDX data analysis relative to the neat and fly ash blended cement pastes, either water or KOH activated and cured at 25°C for one day, one month and one year, are presented in Table C1 (Appendix C). In order to estimate the precision of the EDX results, standard deviation, *s*, was also calculated. From the statistical point of view, the standard deviation values showed that precision of the measurements was higher in the estimation of the mean Al/Si atomic ratio than in the estimation of the mean Ca/Si atomic ratio. The calculated atomic ratios for C-S-H were influenced by the large interaction volume between the electron beam and the sample. In the next section, SEM-EDX results will be compared with those obtained using TEM-EDX, and it will be clearly showed that the chemical composition of C-S-H could only be determined by TEM-EDX.

## 4.7 – TEM-EDX

As explained in Chapter III, TEM-EDX provides information concerning the morphology of the different phases present in a system, as well as local chemical analysis for each of those phases. Due to a smaller interaction volume between the sample and the electron beam, intermixing with other phases is reduced to a larger extent than in SEM-EDX. For example, Op C-S-H might be intermixed with AFm-type phases according to SEM but TEM-EDX might show that AFm-type phases were not finely intermixed with the gel, because observation and analysis are done in a smaller scale. Besides this reason, in TEM-EDX, the samples are very thin, almost transparent, allowing observation and local analysis of phases nearly free of admixture with others.

### 4.7.1 – Morphology and Chemical Analysis

The studied systems using TEM-EDX were the water activated neat WPC and 30% PFA blended pastes, cured for one month, and the KOH activated neat WPC paste, also cured for one month. The reason for this choice was that by one month, the

microstructure of the system is better defined and more easily recognisable. The following micrographs show the morphology found for the water activated neat WPC paste.


**Figure 4.8** – TEM micrograph showing very fine and dense Ip C-S-H formed in the water activated neat WPC paste, 1 month cured at 25°C.

The above figure shows a fine and very dense Ip C-S-H formed in the water activated neat paste after one month of hydration at 25°C. This kind of morphology is typical for Ip C-S-H in most of Portland cement-based systems[3,8,42]. At room temperature, Ip C-S-H is formed of aggregates of small globular particles with 6-8 nm in diameter homogeneously distributed[3]. The microstructure of this sample was mainly composed of anhydrous particles of cement, large pieces of CH, fine and dense Ip C-S-H, fibrillar Op C-S-H and other phases intermixed with C-S-H such as AFt-type phases. AFm-type phases were also distinguished. The next figure also shows a fine and dense Ip C-S-H finely intermixed with relicts of AFt-type phases. The latter present a hexagonal form, as well as large fibres which, under the electron beam dehydrate and shrink to form relicts.


**Figure 4.9** – TEM micrograph showing fine and very dense Ip C-S-H finely intermixed with AFt-type phases, formed in the water activated neat WPC paste and cured at 25°C for 1 month.

Figure 4.10 shows the fine fibrillar Op C-S-H morphology, also typical in water activated neat Portland cements[3,8,42]. Op C-S-H morphology depends on the space that is available for it to be formed. If formed in large pore spaces, then it is considered to have coarse and fibrillar morphology; if formed in smaller spaces, it has fine fibrillar morphology. The space between the fibrils of Op C-S-H is the three-dimensional interconnected network, i.e., capillary porosity[3]. Figures 4.10 and 4.11 show Op C-S-H with fibrillar morphology. Although Op C-S-H appears to be coarse fibrillar, as seen in Portland-cement based systems cured at high temperature[42], it was probably beam damaged.

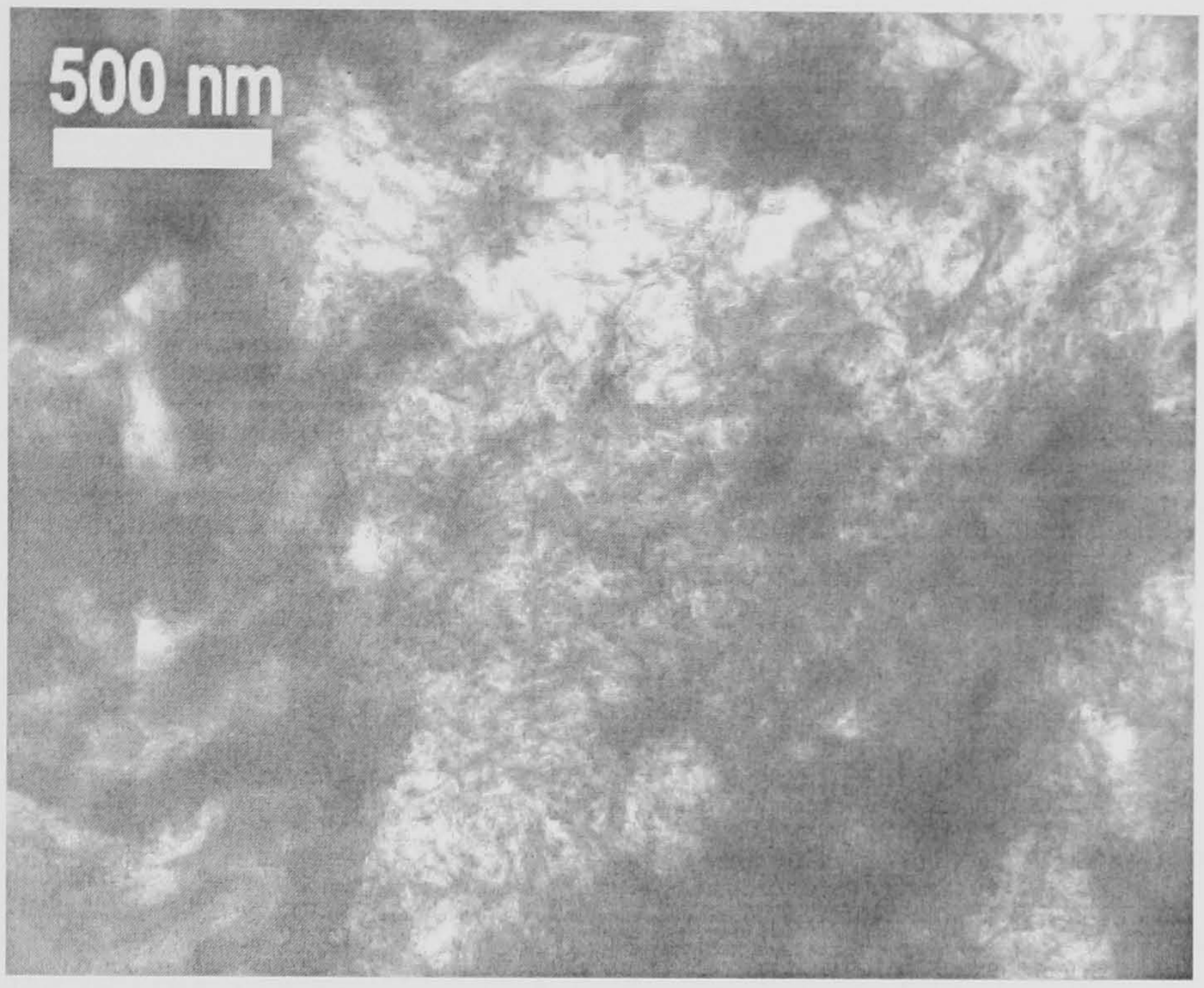


**Figure 4.10** – TEM micrograph showing fine fibrillar Op C-S-H formed in the water activated neat WPC paste, 1 month cured at 25°C.

The following figure shows a micrograph with more details of the fibrillar Op C-S-H morphology.

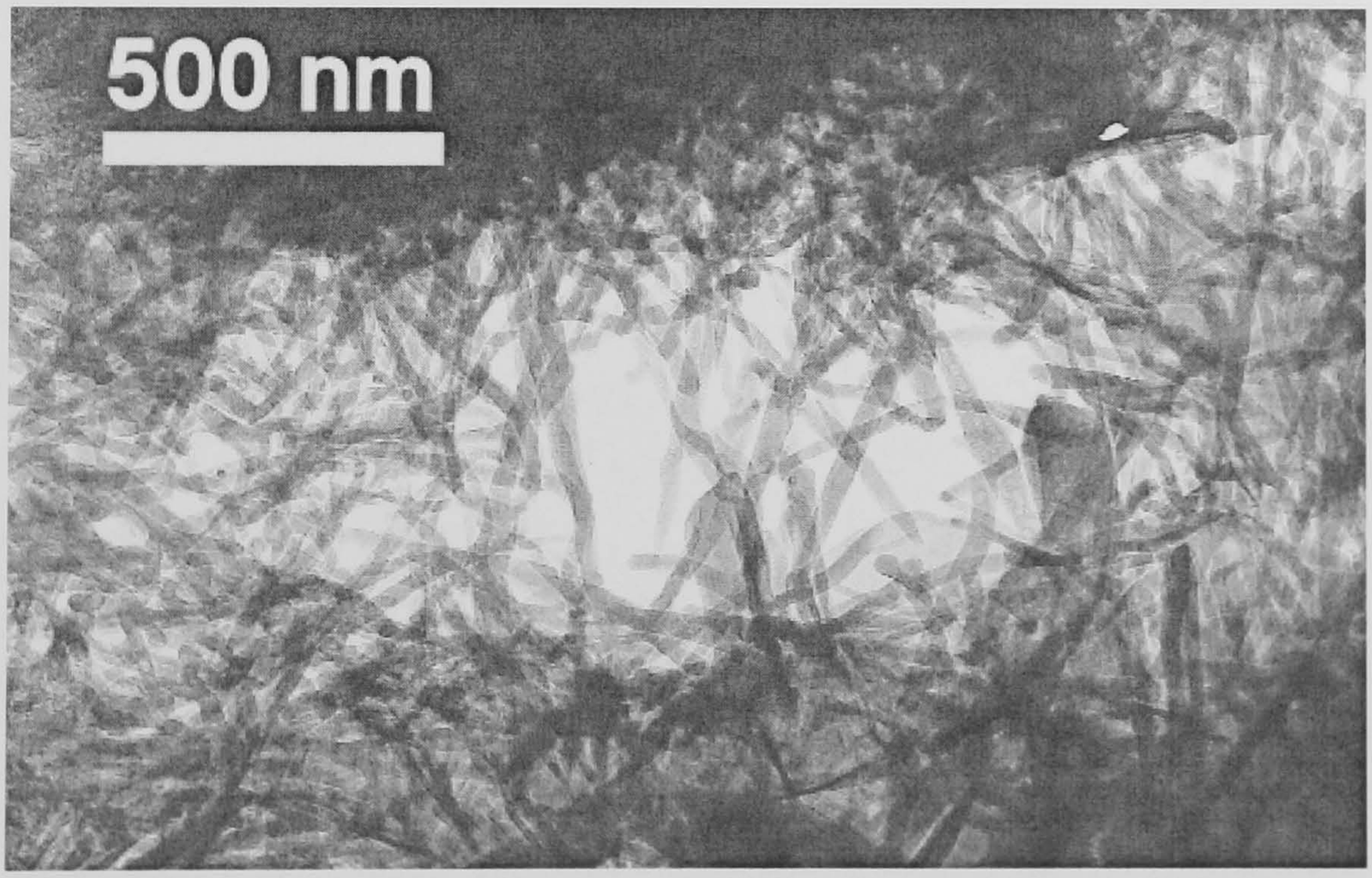


**Figure 4.11** – TEM micrograph showing fine fibrillar Op C-S-H formed in the water activated neat WPC paste and cured at 25°C for 1 month.

Figure 4.12 shows the atomic ratio plots obtained using EDX analysis. Ip and Op C-S-H gel were analysed as well as other interesting points of analysis such as AFt-type phases. If trend lines were identified, they are represented by arrows pointing in the direction of the chemical composition of other phases intermixed with C-S-H.

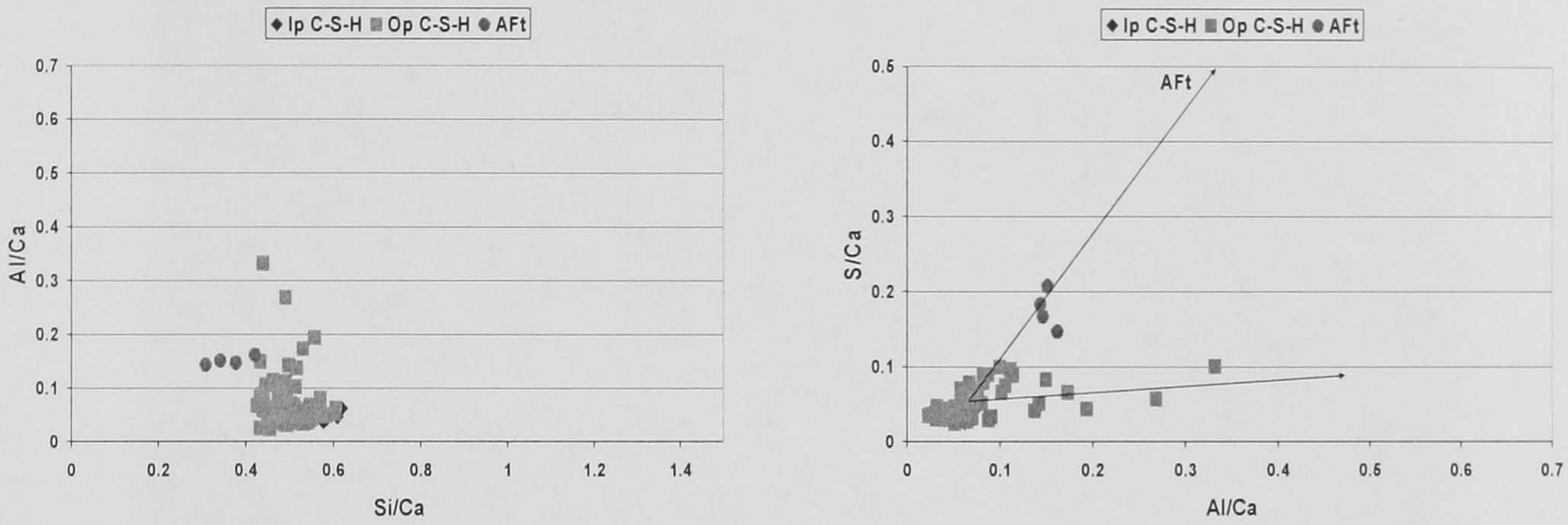


**Figure 4.12** – Al/Ca against Si/Ca (left) and S/Ca against Al/Ca (right) atomic ratio plots for the TEM-EDX phase analysis of the water activated neat WPC paste after 1 month of hydration at 25°C.

The atomic ratio plots show that Op C-S-H was finely intermixed with AFt-type phases and also with a calcium aluminoferrite hydrate phase with low sulfate content[135]. Ip C-S-H had a mean Ca/Si ratio of 1.75 (s = 0.09) and Al/Si ratio of 0.075 (s = 0.011). The mean Ca/Si ratio calculated for Op C-S-H was 2.00 (s = 0.17) and Al/Si ratio 0.114 (s = 0.048). Both atomic ratios were higher than those of Ip C-S-H. This is due to the higher degree of intermixing between Op C-S-H and other phases, while Ip C-S-H is formed locally in place of the anhydrous particles of cement.

The following figure illustrates a fully hydrated cement particle surrounded by Op C-S-H in the KOH activated neat WPC paste.

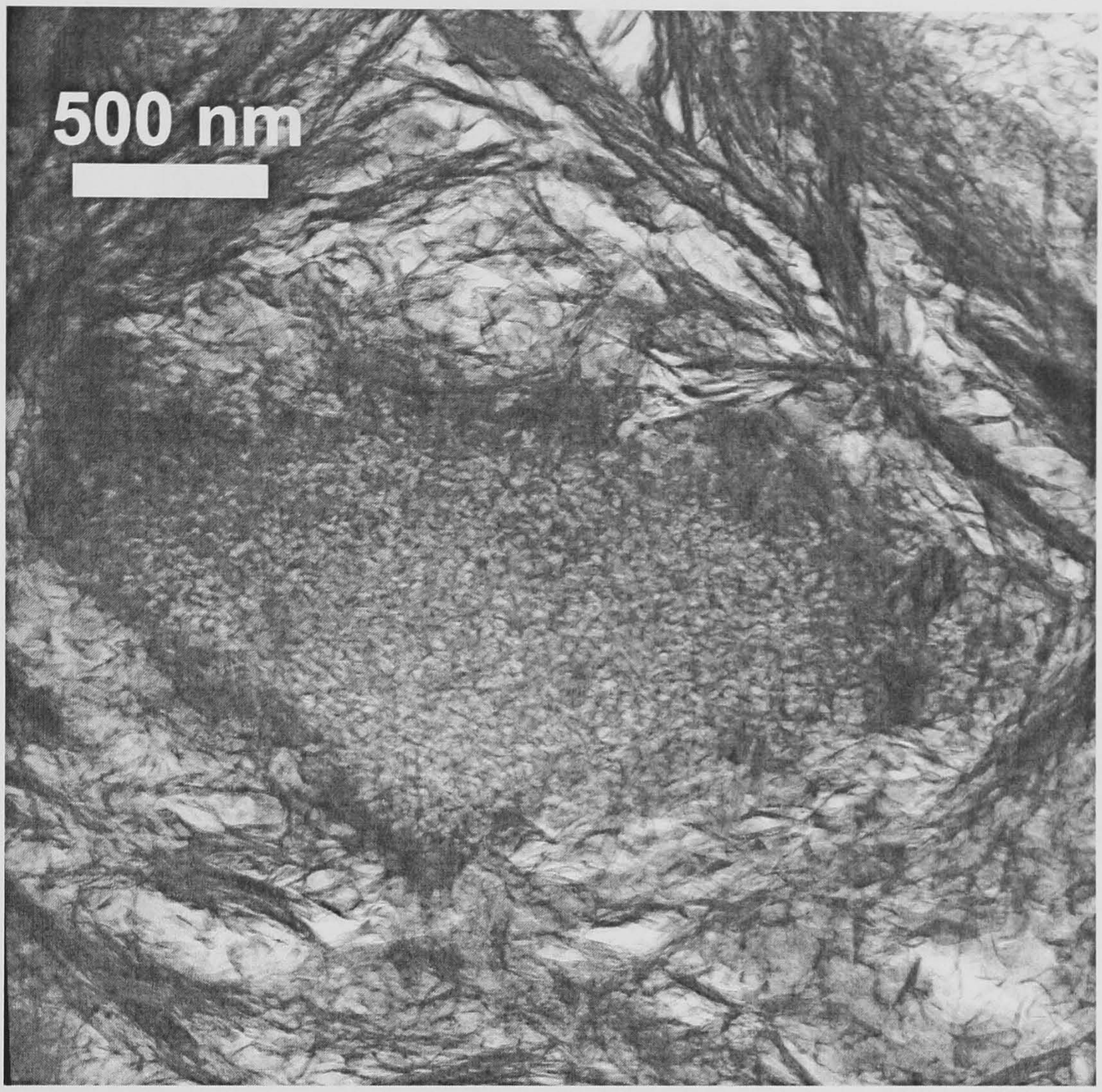


**Figure 4.13** – TEM micrograph showing a fully hydrated cement grain surrounded by foil-like Op C-S-H, in the KOH activated neat WPC paste 1 month, cured at 25°C.

As expected, activating a cement paste with alkalis decreased the Ca/Si ratio and, consequently, induced the foil-like morphology of Op C-S-H.[13] The previous micrograph shows a clear fully hydrated cement particle, where a dense Ip C-S-H was formed. Surrounding the grain, Op C-S-H with foil-like morphology was formed. Generally, Ip C-S-H had a fine and dense morphology, Op C-S-H a foil-like morphology, large pieces of CH were also observed as well as CH finely intermixed with C-S-H. AFm-type phases were also distinguished. The next figure illustrates Op C-S-H foil-like morphology.

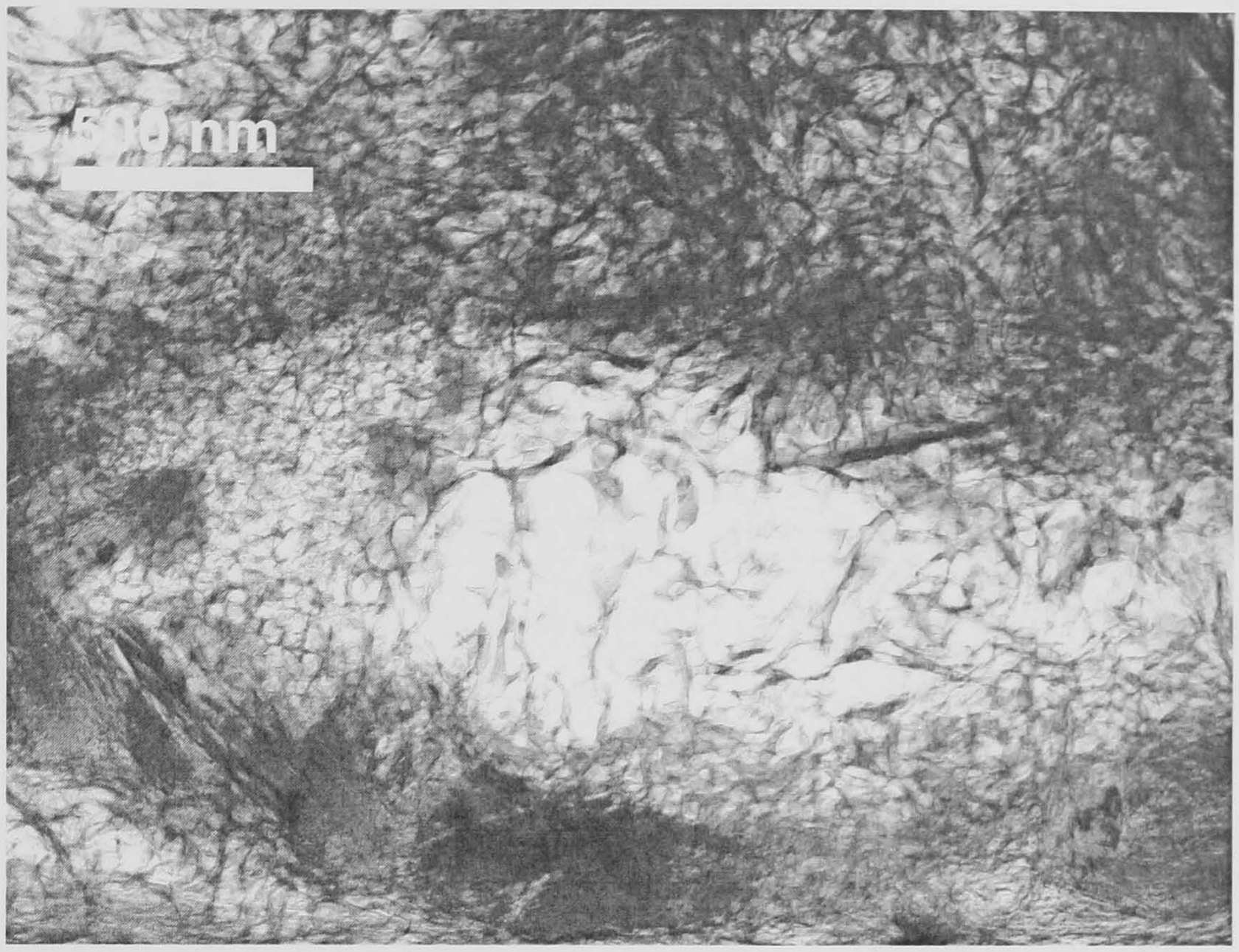


**Figure 4.14** – TEM micrograph showing foil-like Op C-S-H with different densities intermixed with CH, in the KOH activated neat WPC paste, cured at 25°C for 1 month.

Op C-S-H foil-like morphology presented different densities. In the above figure, it was possible to observe CH layers finely intermixed with Op C-S-H.

Figure 4.15 shows the EDX atomic ratio plots for the KOH activated neat WPC paste one month cured at 25°C.

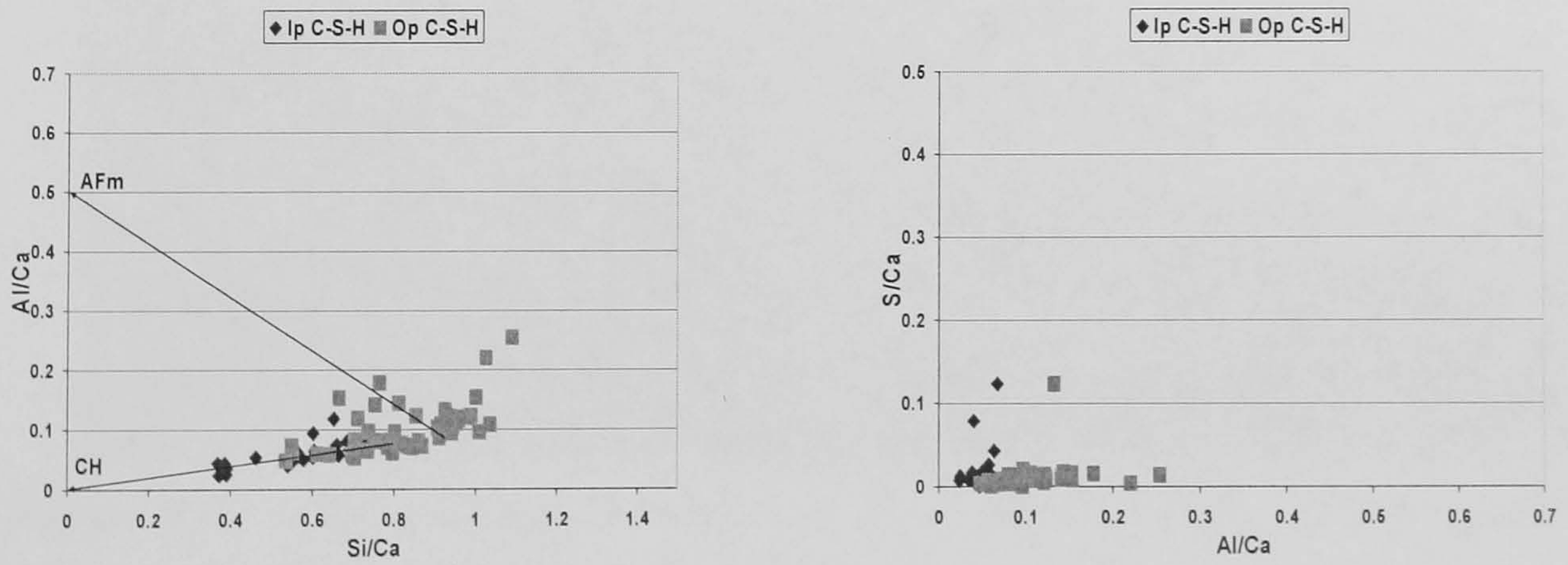


**Figure 4.15** – Al/Ca against Si/Ca (left) and S/Ca against Al/Ca (right) atomic ratio plots for the TEM-EDX phase analysis of the KOH activated neat WPC paste after 1 month of hydration at 25°C.

The previous plots show that Ip C-S-H was finely intermixed with CH as well as Op C-S-H, because alkaline activation besides inducing Op C-S-H foil-like morphology, it also induces microcrystalline CH formation. The latter was found finely intermixed with C-S-H[13]. Ip C-S-H had a mean Ca/Si ratio of 1.76 (s = 0.46) and Al/Si ratio of 0.101 (s = 0.008). The mean Ca/Si ratio calculated for Op C-S-H was 1.24 (s = 0.22) and Al/Si ratio 0.120 (s = 0.04). Comparing this sample with the corresponding water activated neat WPC paste, the expected alkaline effect on the C-S-H morphology and composition was verified. Op C-S-H had a lower mean Ca/Si ratio than that in the water activated neat WPC paste, the morphology changed from fibrillar to foil-like and the mean Al/Si ratio was slightly increased.

Figure 4.16 illustrates Op C-S-H formed in the water activated 30% PFA blended WPC paste.

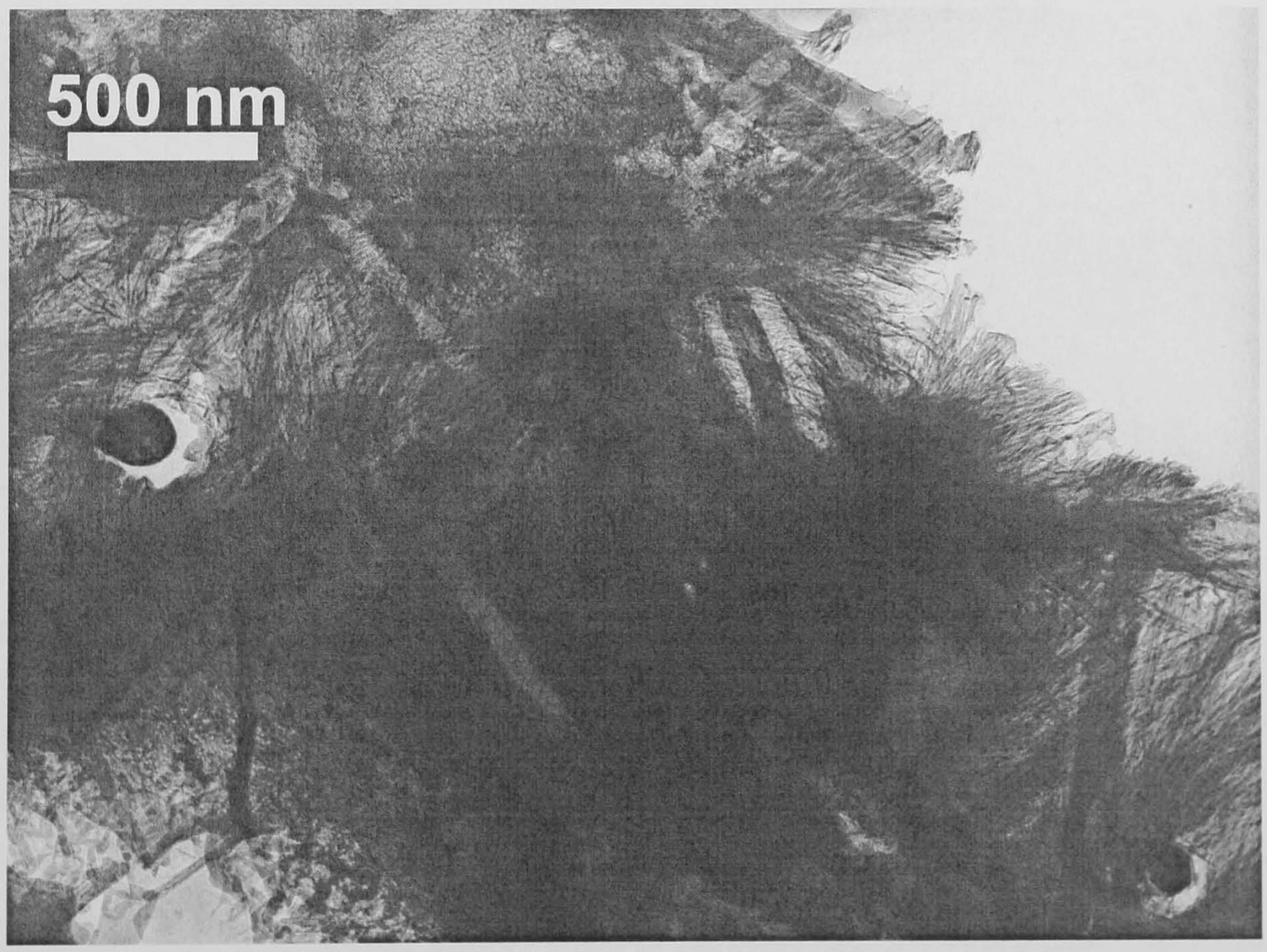


**Figure 4.16** – TEM micrograph showing fibrillar Op C-S-H, in the water activated 30% PFA blended WPC paste 1 month, cured at 25°C.

The previous micrograph shows fine fibrillar Op C-S-H finely intermixed with AFt-type phases relicts. In this sample, Ip C-S-H presented a fine and dense morphology, chunks

of CH were also detected and Op C-S-H was fine and fibrillar. AFm-type phases were also distinguished. Intermixing between C-S-H and other phases was also observed. The following figure also shows fine fibrillar Op C-S-H.

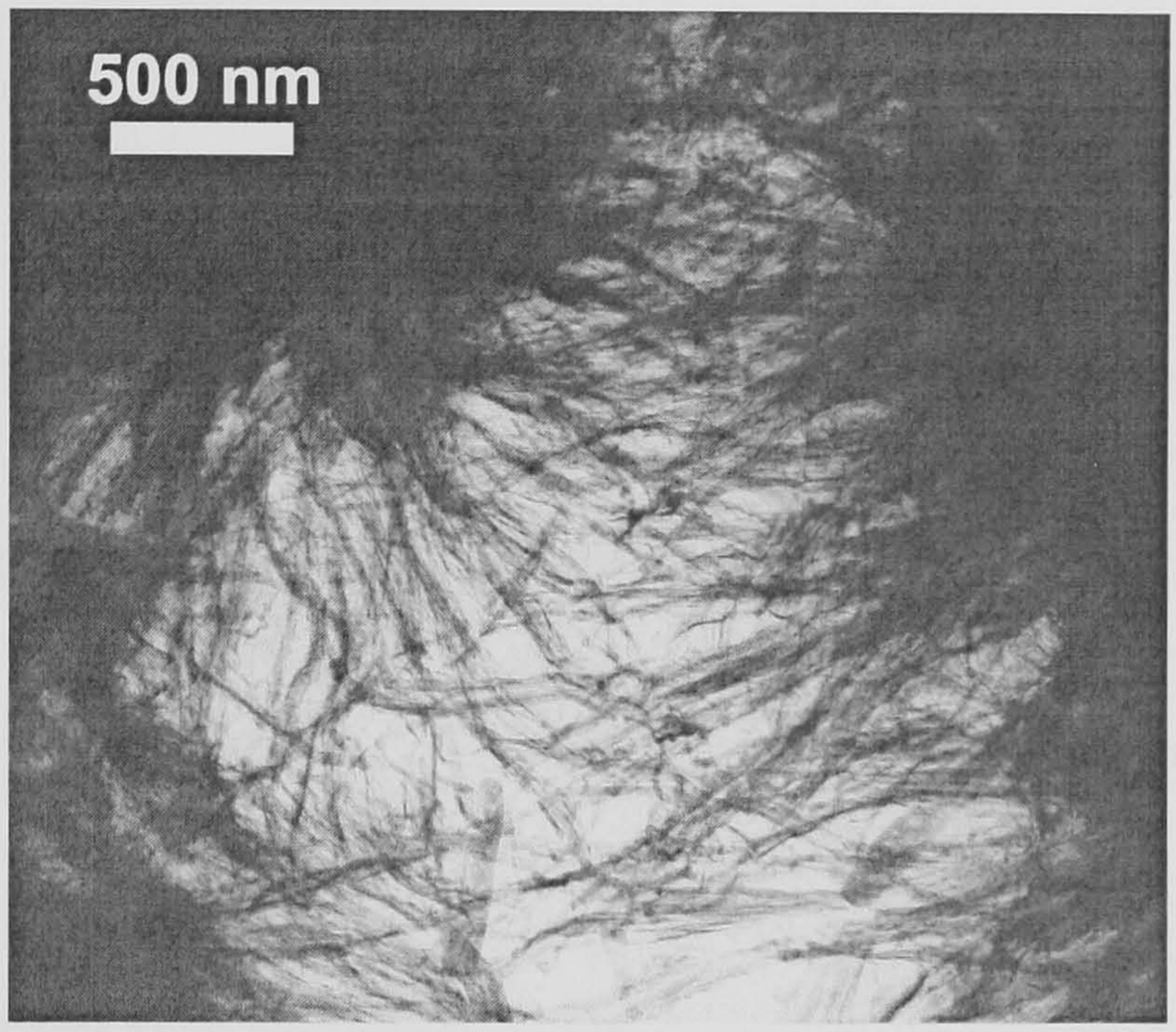


**Figure 4.17** – TEM micrograph showing fibrillar Op C-S-H, in the water activated 30% PFA blended WPC paste, cured at 25°C for 1 month.

EDX atomic ratio plots obtained for the water activated 30% PFA blended WPC paste are displayed in the following figure.

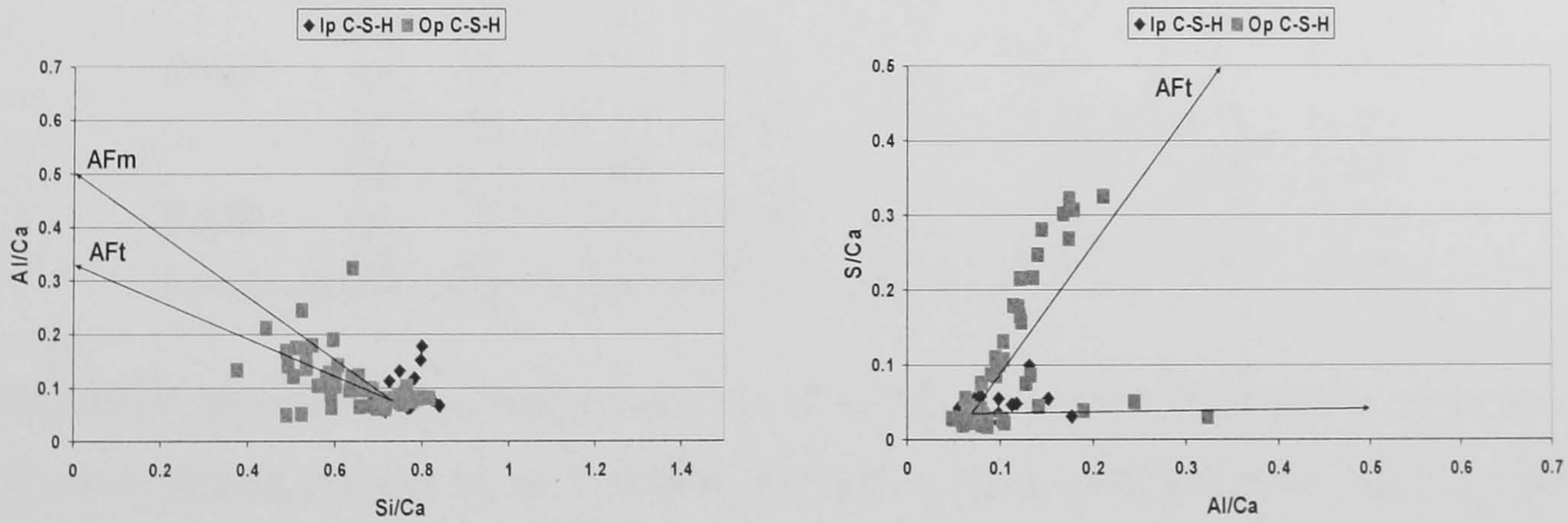


**Figure 4.18** – Al/Ca against Si/Ca (left) and S/Ca against Al/Ca (right) atomic ratio plots for the TEM-EDX phase analysis of the water activated 30% PFA blended cement paste after 1 month of hydration at 25°C.

The atomic ratio plot on the right side shows two trendline in the direction of the Aft and AFm-type phases but the S/Ca against Al/Ca atomic ratio plot confirmed that

clearly Op C-S-H was finely intermixed with AFt-type phases and with a calcium aluminoferrite hydrate phase with low sulphate content[135]. Ip C-S-H had a mean Ca/Si ratio of 1.34 (s = 0.08) and Al/Si ratio of 0.113 (s = 0.055). The mean Ca/Si ratio calculated for Op C-S-H was 1.62 (s = 0.29) and Al/Si ratio 0.186 (s = 0.109). Comparing this sample with the corresponding water activated neat WPC paste, PFA replacement lowered the mean Ca/Si ratio increased the mean Al/Si ratio because the aluminium content in the blended system was higher than in the neat system. Although the pozzolanic replacement changed the mean atomic ratios, it did not change Ip or OP C-S-H morphologies. Table 4.9 resumes the EDX results obtained for the analysed samples. EDX data was carefully examined and the mean atomic ratios were calculated for Ip and Op C-S-H on a significant basis, i.e. data that clearly showed intermixing with other phases was not accounted for the Ip and Op C-S-H mean atomic ratios calculations.

**Table 4.9** – Mean Ca/Si and Al/Si atomic ratios obtained for C-S-H using TEM-EDX, for the water or KOH activated neat WPC pastes and for the water activated 30% PFA blended cement paste, 1 month cured at 25°C.

| | | | Ca/Si | | Ca/(Al+Si) | | Al/Si | |
|---|---|---|---|---|---|---|---|---|
| | | *N* | *mean* | *s* | *mean* | *s* | *mean* | *s* |
| **Wpc** | **Op** | 39 | 2.00 | 0.17 | 1.95 | 0.93 | 0.114 | 0.048 |
| | **Ip** | 8 | 1.75 | 0.09 | 1.75 | 0.30 | 0.075 | 0.011 |
| | **All** | 67 | 2.00 | 0.18 | 1.91 | 0.93 | 0.106 | 0.050 |
| **Kwpc** | **Op** | 50 | 1.24 | 0.22 | 1.11 | 0.20 | 0.120 | 0.040 |
| | **Ip** | 30 | 1.76 | 0.46 | 1.60 | 0.43 | 0.101 | 0.008 |
| | **All** | 80 | 1.44 | 0.42 | 1.29 | 0.39 | 0.113 | 0.036 |
| **Pfa30** | **Op** | 51 | 1.62 | 0.29 | 1.35 | 0.20 | 0.186 | 0.109 |
| | **Ip** | 30 | 1.34 | 0.08 | 1.21 | 0.08 | 0.113 | 0.035 |
| | **All** | 81 | 1.52 | 0.27 | 1.30 | 0.18 | 0.159 | 0.096 |

TEM-EDX proved to be a very powerful technique. It allowed differentiation between the many phases present in each system, as well as their morphologies. EDX analysis gave more accurate mean atomic ratios for Ip and Op C-S-H, as well as clear trendlines indicating fine intermixing between C-S-H and other calcium aluminoferrite hydrate phases.

Finally, it is very useful to compare the different chemical compositions obtained for C-S-H using different techniques. Table 4.10 summarises the mean Ca/Si and Al/Si atomic ratios obtained using TEM-EDX, SEM-EDX and MAS NMR.

**Table 4.10** – Mean Ca/Si and Al/Si atomic ratios obtained for C-S-H using TEM-EDX, SEM-EDX and MAS NMR, for the water or KOH activated neat WPC pastes and for the water activated 30% PFA blended cement paste, 1 month cured at 25°C.

| | All Ca/Si | Ca/Si (SEM) | All Al/Si | Al/Si (SEM) | Al/Si (NMR) |
|---|---|---|---|---|---|
| **Wpc** | 2.00 | 2.01 | 0.106 | 0.110 | 0.056 |
| **Kwpc** | 1.44 | 3.46 | 0.113 | 0.100 | 0.093 |
| **Pfa30** | 1.52 | 1.74 | 0.159 | 0.150 | 0.070 |

Comparing SEM-EDX with TEM-EDX, it was concluded that due to greater interaction volume in SEM, intermixing with other phases was not avoided. Therefore, the mean Ca/Si ratio was generally higher than that found for C-S-H using TEM-EDX. A better agreement was found between the mean Al/Si ratios obtained by these electron microscopy techniques. No reasonable agreement was obtained between TEM-EDX and MAS NMR. Although MAS NMR is a bulk technique, it should give very similar results to those from TEM-EDX[3,8,42]. Regrettably, that was not verified and a cause for this discrepancy was not found.

### 4.7.2 – T/J and T/CH-based models for the structure of C-S-H

In this section, the applicability of the structural models tobermorite-jennite (T/J) and tobermorite-"solid-solution" calcium hydroxide (T/CH) for the nanostructure of C-S-H to the studied cement-based systems was discussed. According to Richardson and Groves[3,49-51], in some systems data could only be consistent with T/CH viewpoint but many others could also be consistent with T/CH and T/J structural models. A few considerations were arranged in order to plot correctly both models. Firstly, respecting the polymerisation sequence, dimmers, pentamers, octamers, (3n-1) structural units for tobermorite and jennite were considered. For these structural units, Si/Ca and Al/Ca ratios were calculated and accounted for fully protonated, half protonated and unprotonated tobermorite and jennite structural units. It should be pointed out that the

degree of protonation is only estimated because it is not possible to know exactly $mH_2O$ in Equation 2.9. The degree of protonation was assessed accounting with atomic ratios calculated from TEM-EDX. The latter are intimately related to the mean aluminosilicate chain length given by $^{29}$Si MAS NMR. Finally, aluminium substitution for silicon was also considered in the structural units. For the latter concern, the proportion of bridging tetrahedra occupied by aluminium was calculated, according to the following equation[3]:

$$\%B = \frac{bridging\ tetrahedra\ occupied\ by\ Al}{bridging\ tetrahedra\ occupied\ by\ Al\ and\ Si} = \frac{Q^2(1Al)}{2_3 Q^2 + Q^2(1Al)} \qquad \text{(Eqn. 4.1)}$$

The following plot shows structural units for tobermorite (T) and jennite (J) with different degrees of protonation and different percentage of aluminium substitution in tobermorite-based units:

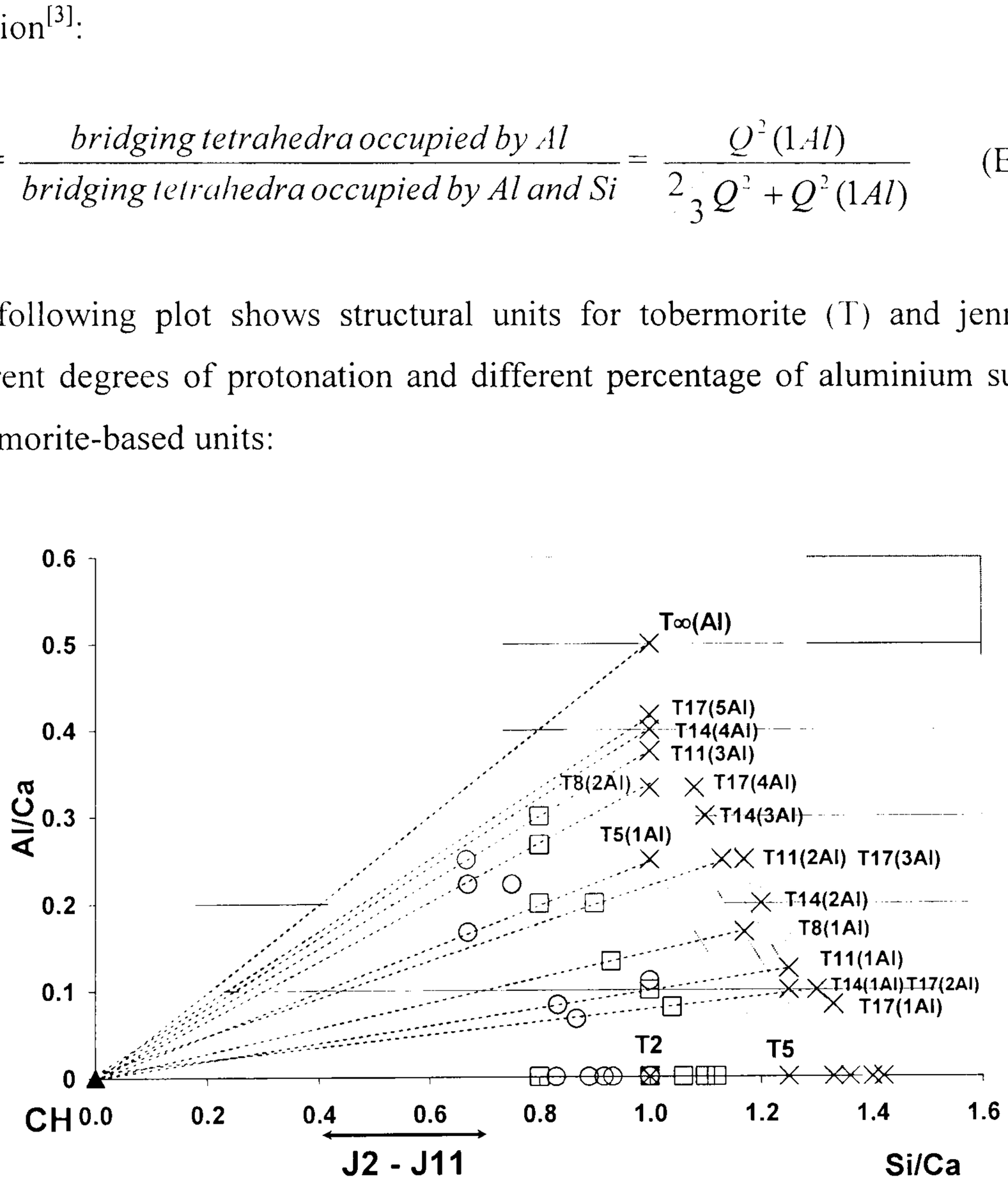


**Figure 4.19** – Al/Ca against Si/Ca atomic plot for tobermorite and jennite structural units with different degrees of protonation and proportion of bridging tetrahedra occupied by aluminium (X fully protonated; □ half protonated; O unprotonated).

Figure 4.19 shows representing points for tobermorite-based units with chain lengths of 2, 5, 8, 11, 14, 17 and ∞. The same was prepared for the jennite-based units with chain

lengths between 2 and 11. Different degrees of protonation were also shown: x symbol for fully protonated units, □ symbol for half protonated units and O symbol for unprotonated units. Aluminium substitution in bridging tetrahedra in tobermorite-based units was also considered and, for example, indicated by T5(1Al) or T17(4Al). The dashed lines between CH and tobermorite-based units with the minimum (O) and maximum (X) degree of protonation represent the T/CH viewpoint where tobermorite-based units are intermixed with layers of calcium hydroxide.

The next table summarises the experimental data that was accounted for application of the different structural models for the TEM-EDX analysed systems.

**Table 4.11** – Experimental data used in Al/Ca against Si/Ca atomic plots discussing the applicability of the T/CH and T/J structural models for C-S-H, in the systems cured at 25°C.

| | Ip Ca/Si | Op Ca/Si | Ip Al/Si | Op Al/Si | Al/Si (NMR) | MCL | %B |
|---|---|---|---|---|---|---|---|
| **Wpc** | 1.75 | 2.00 | 0.075 | 0.114 | 0.056 | 3.3 | 40 |
| **Kwpc** | 1.76 | 1.24 | 0.101 | 0.120 | 0.093 | 3.4 | 63 |
| **Pfa30** | 1.34 | 1.62 | 0.113 | 0.186 | 0.070 | 3.6 | 43 |

Regarding the water activated neat WPC paste, MCL was around 3.3 which means that dimeric and pentameric units should be considered. In terms of aluminium substitution, tobermorite and jennite dimer-based units (T2 and J2, in that order) do not hold aluminium substitution. Aluminium substitution was only considered in tobermorite-based units[3]. Pentamers tobermorite-based (T5) have one bridging tetrahedra that can be aluminium substituted, T5(1Al). The %B calculated was around 40% which indicates that less than half of the bridging sites were occupied by aluminium. Therefore, T2/J2/T5 and T5(1Al) must be considered because MCL was around 3 and %B indicated that aluminium substitution took place in less than half of the bridging sites of T5 units. If data was comprised between the atomic ratios for T5(1Al) and those for T2/J2, then it would be possible to say that experimental data was consistent with T/J point of view. If data was comprised between the atomic ratios for T5(1Al) and those for T2/J2, but clear trendline(s) from T5(1Al) and/or T2/J2 were found in the direction of CH, then it would be possible to say that experimental data was consistent with T/CH point of view. Figure 4.20 illustrates Ip and Op C-S-H TEM-EDX data in the Al/Ca

against Si/Ca atomic ratio plot considering the T/J and T/CH structural models. For testing the models, TEM-EDX raw data points were plotted. Only data points that clearly showed that C-S-H was intermixed with other phases or those points that clearly followed a trend line were excluded.

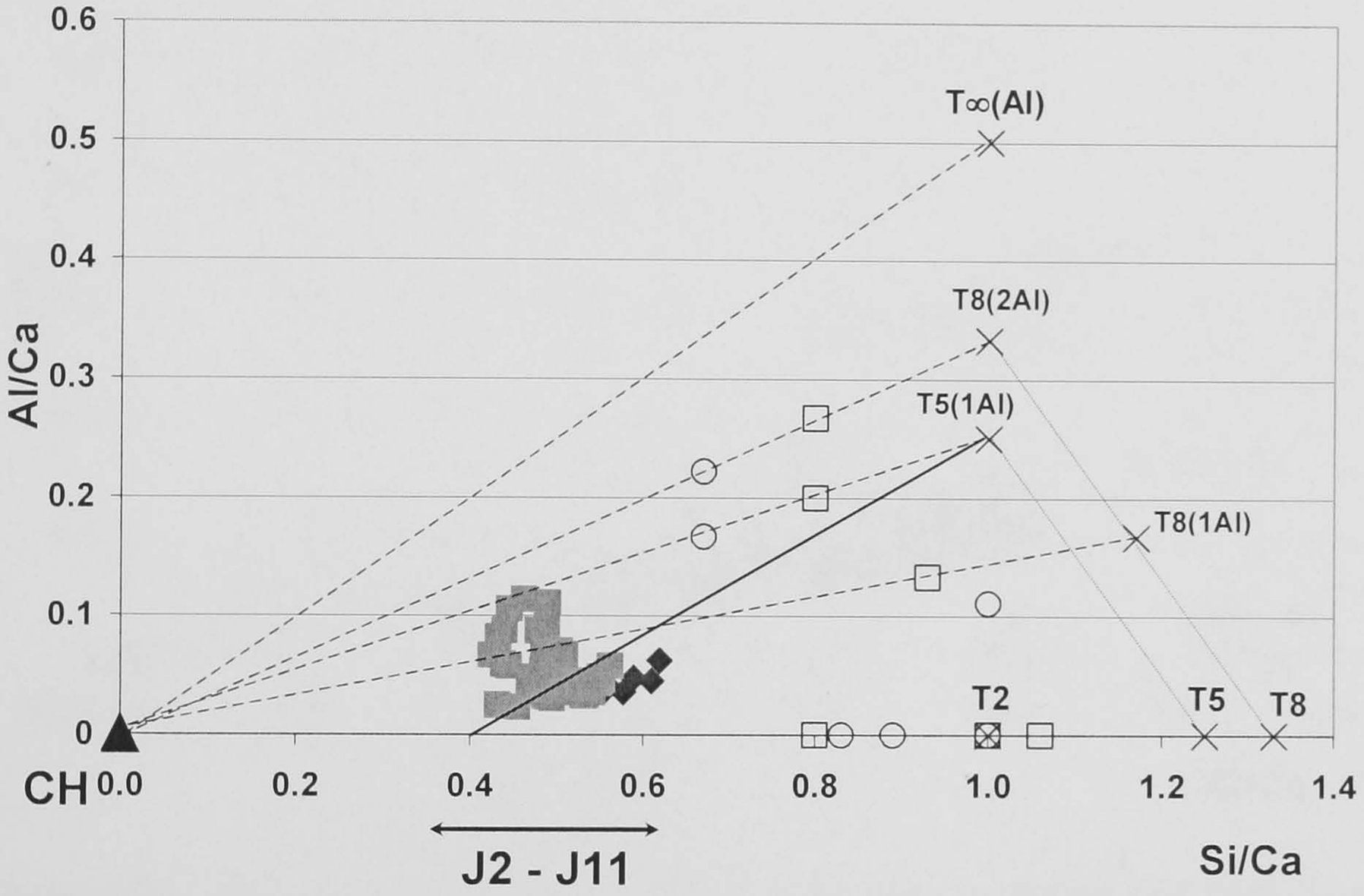


**Figure 4.20** – Al/Ca against Si/Ca atomic plot for the water activated neat WPC paste cured for 1 month at 25°C, accounting with T/J and T/CH viewpoints (♦ Ip C-S-H, ■ Op C-S-H, O unprotonated units, □ half protonated, X fully protonated, T∞ tobermorite, --- T/CH, — T/J).

From the above figure, it was possible to verify that C-S-H experimental data for the water activated neat WPC paste cured at 25°C, was consistent with the T/J structural model. The dashed lines represent T/CH viewpoint and it was observed that both Ip and Op C-S-H corresponding points were not distributed along the trendline between CH and T5(1Al). Ip and Op C-S-H data was compactly distributed around the mean Si/Ca for jennite-based units and most of them distributed between the trendline from T5(1Al) and J2. It was considered that jennite-based structural units do not include aluminium substitution but aluminium substitution in C-S-H occurred. As seen in the previous figure, experimental data distribution revealed that C-S-H was mainly composed of dimers of tobermorite and jennite, and some pentamers with and without aluminium

substitution. The following figure shows the Al/Ca against Si/Ca atomic ratio plot considering the T/CH and T/J models for the KOH activated neat WPC paste, one month cured at 25°C.

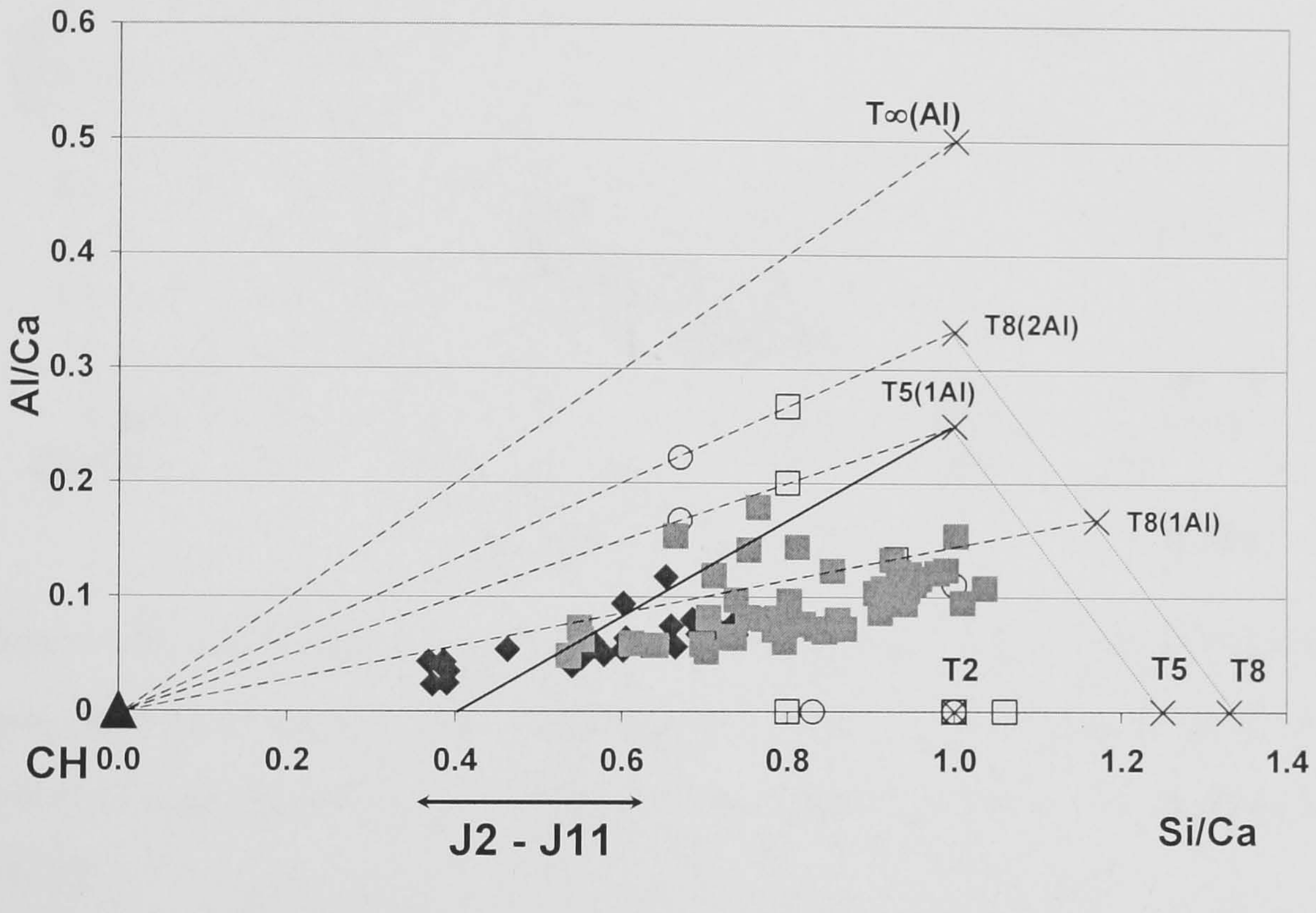


**Figure 4.21** – Al/Ca against Si/Ca atomic plot for the KOH activated neat WPC paste cured for 1 month at 25°C, accounting with T/J and T/CH viewpoints (♦ Ip C-S-H, ■ Op C-S-H, O unprotonated units, □ half protonated, X fully protonated, T∞ tobermorite, --- T/CH, — T/J).

As shown in Figure 4.21, C-S-H data was consistent with the T/CH viewpoint because most of the data "fell" into trendlines in the direction of CH, and not on the trendline from T5(1Al) to J2.

Figure 4.22 shows the application of the two models to experimental data obtained for the water activated 30% PFA blended system. This system had a MCL of 3.6 and aluminium occupying 43% of the bridging tetrahedra.

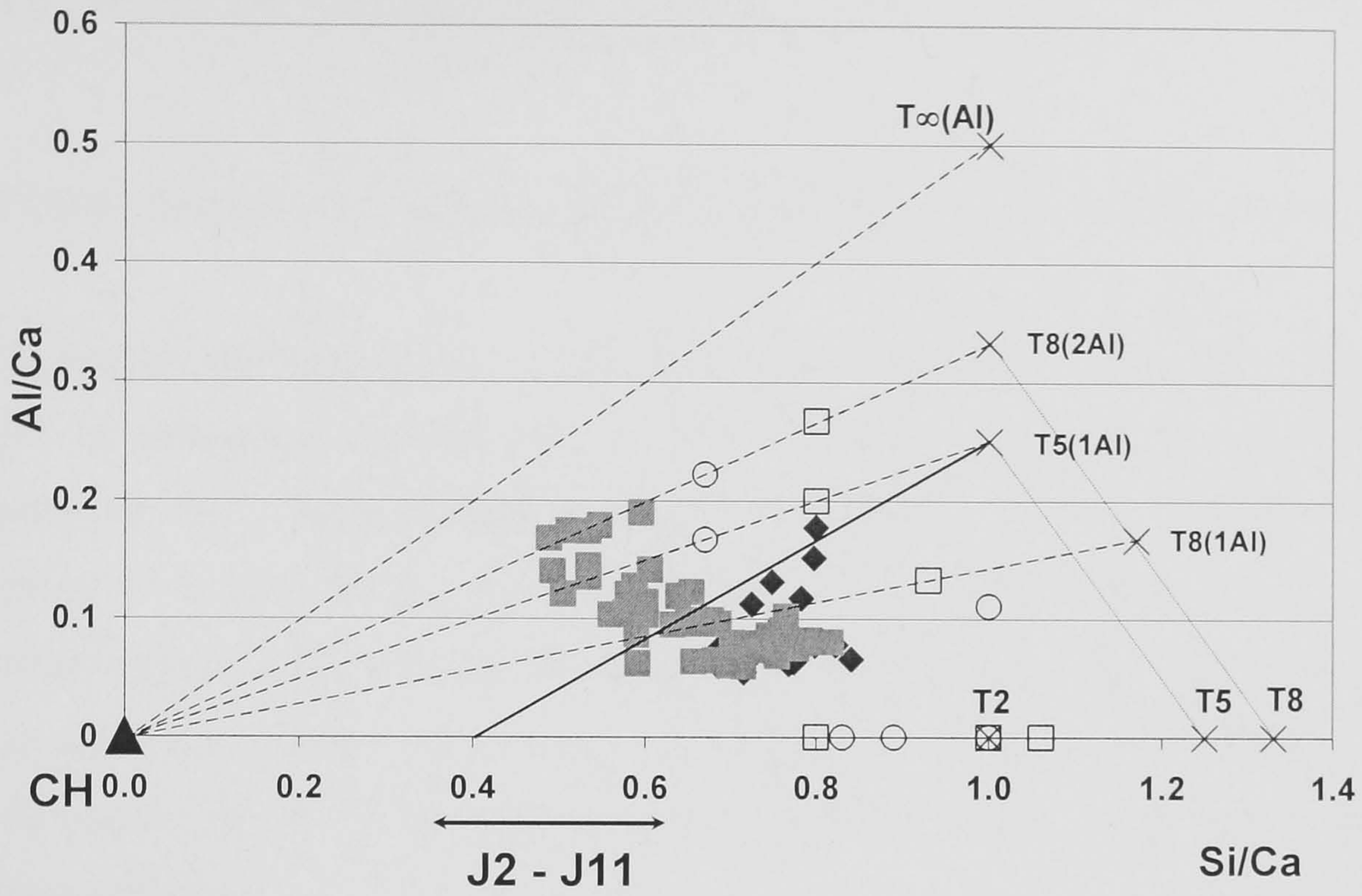


**Figure 4.22** – Al/Ca against Si/Ca atomic plot for the water activated 30% PFA blended WPC paste cured for 1 month at 25°C, accounting with T/J and T/CH viewpoints (◆ Ip C-S-H, ■ Op C-S-H, O unprotonated units, □ half protonated, X fully protonated, T∞ tobermorite, --- T/CH, — T/J).

The above figure shows that data was more scattered than in neat systems and it was consistent with both T/J and T/CH viewpoints, as shown by the distribution of the data around trendlines in the direction of CH but some as well in the direction of jennite-based units.

## 4.8 - C-S-H STRUCTURAL-CHEMICAL COMPOSITION

C-S-H chemical composition can be easily determined according to both T/J and T/CH viewpoints and using TEM-EDX and MAS NMR data.

From the T/J point of view, C-S-H structural-chemical composition can be determined according to the following expression[3]:

$$\{Ca_{2n}H_w(Si_{1-a}R_a^{[4]})_{(3n-1)}O_{9n-2}\}I^{c+}_{\frac{a}{c}(3n-1)}\cdot(OH)_{w+n(y-2)}\cdot Ca_{\frac{ny}{2}}\cdot mH_2O \qquad \text{(Eqn. 2.11)}$$

If $0\leq y\leq 2$ then $n(2-y)\leq w\leq 2n$; if $2\leq y\leq 4$ then $0\leq w\leq 2n$; and if $4\leq y\leq 6$ then $0\leq w\leq n(6-y)$.

The number of silanol groups (SiOH) is given by $w$ and $R^{[4]}$ is a trivalent cation, mainly $Al^{3+}$ in tetrahedral coordination. $I^{c+}$ is an interlayer ion, either a monovalent alkali cation or $Ca^{2+}$ charge-balancing the $R^{3+}$ substituting for $Si^{4+}$. In alkaline activated pastes, $I^{c+}$ is considered to be $K^+$. The latter can not be considered in water activated simple systems. The number of water molecules bound to C-S-H is given by $m$ but it can not be accurately determined. Assuming that charge compensation of the $R^{3+}$ substitution for $Si^{4+}$ is entirely by alkali cations, the mean *Ca/Si* atomic ratio can be expressed as:

$$Ca/Si = \frac{n(4+y)}{2(1-a)(3n-1)} \qquad \text{(Eqn. 4.2)}$$

Finally, the mean *Al/Si* ratio can be determined by:

$$Al/Si = \frac{a}{1-a} \qquad \text{(Eqn. 4.3)}$$

The mean *Ca/Si* and *Al/Si* atomic ratios are given by TEM-EDX that consequently gives $a$. MAS NMR results give the mean chain length, *(3n-1)* and also the mean *Al/Si* atomic ratio that should be very similar to that obtained using TEM-EDX. After substitution into Equations (4.2) and (4.3), $y$ is obtained as well as a possible range of values for the degree of protonation of the silicate chains, *w/n*.

From the T/CH point of view, C-S-H chemical composition can be determined by:

$$(Ca_xH_{(6n-2x)}(Si_{1-a}R_a^{[4]})_{(3n-1)}O_{9n-2}\cdot I^{c+}_{\frac{a}{c}(3n-1)}\cdot zCa(OH)_2\cdot mH_2O \qquad \text{(Eqn. 2.12)}$$

$X$ is the number of $Ca^{2+}$ ions necessary to charge-balance ($X = 0.5(6n\text{-}w)$) and $z$ is the number of $Ca(OH)_2$ units in "solid-solution" ($z = 0.5(w + n(y\text{-}2)$). Equation 2.12 can be rearranged assuming that some of the charge is compensated by $Ca^{2+}$:

$$\{Ca_{2n}H_w(Si_{1-a}R_a^{[4]})_{(3n-1)}O_{9n-2}\}I^{c+}_{\frac{a}{c}(3n-1)} \cdot (OH)_{w+n(y-2)} \cdot Ca_{\frac{ny}{2}} \cdot Ca_{ny} \cdot mH_2O \quad \text{(Eqn. 4.4)}$$

The mean $Al/Si$ atomic ratio is also given by Equation 4.3 and the mean $Ca/Si$ ratio is determined by:

$$Ca/Si = \frac{n(4+y') + a(3n-1)}{2(1-a)(3n-1)} \quad \text{(Eqn. 4.5)}$$

Table 4.12 resumes the data used in the determination of C-S-H chemical composition from the T/J and T/CH viewpoints. Minimum of protonation was considered, i.e. the minimum limit value for $w$ was used in the calculations.

**Table 4.12** – TEM-EDX and MAS NMR data used in the determination of C-S-H chemical composition according to the T/J and T/CH structural viewpoints for the systems cured at 25°C.

| | **Ca/Si (TEM)** | ***y*** | ***w*** | ***y'*** | **w'** | **Al/Si (TEM)** | **Al/Si (NMR)** | ***a*** | **MCL (3n-1)** | ***n*** |
|---|---|---|---|---|---|---|---|---|---|---|
| **Wpc** | 2.00 | 4.74 | 0 | 4.62 | 0 | 0.106 | 0.056 | 0.05 | 3.3 | 1.43 |
| **Kwpc** | 1.44 | 2.11 | 0 | 1.92 | 0.12 | 0.113 | 0.093 | 0.09 | 3.4 | 1.47 |
| **Pfa30** | 1.52 | 2.15 | 0 | 1.82 | 0.26 | 0.159 | 0.070 | 0.14 | 3.6 | 1.53 |

C-S-H chemical composition determined according to the T/J structural point of view is given in Table 4.13.

**Table 4.13** – C-S-H chemical composition determined according to the T/J structural viewpoint for the systems cured at 25°C.

| | **T/J (minimum degree of protonation)** |
|---|---|
| **Wpc** | $\{Ca_{2.86}(Si_{0.95}Al_{0.05})_{3.3}O_{12.9}\}\cdot(OH)_{3.92}\cdot Ca_{3.39}\cdot mH_2O$ |
| **Kwpc** | $\{Ca_{2.94}(Si_{0.91}Al_{0.09})_{3.4}O_{11.2}\}\cdot K_{0.29}\cdot(OH)_{0.16}\cdot Ca_{1.55}\cdot mH_2O$ |
| **Pfa30** | $\{Ca_{3.06}(Si_{0.86}Al_{0.14})_{3.6}O_{11.8}\}\cdot(OH)_{0.23}\cdot Ca_{1.64}\cdot mH_2O$ |

Chemical composition inside the brackets indicates the tobermorite-based skeleton of C-S-H. The presence of hydroxyl groups outside the brackets indicates that there must be some jennite-like structure besides tobermorite-like units. In the alkaline neat paste, it was assumed that substitution of $Si^{4+}$ by $Al^{3+}$ is charge balanced entirely by $K^+$ ions. The structure of C-S-H can also be reorganised according to the T/CH viewpoint, resumed in Table 4.14:

**Table 4.14** – C-S-H chemical composition determined according to the T/CH structural viewpoint for the systems cured at 25°C.

| | **T/CH (minimum degree of protonation)** |
|---|---|
| **Wpc** | $Ca_{4.29}(Si_{0.95}Al_{0.05})_{3.3}O_{12.9}\cdot Ca_{0.09}\cdot 1.87Ca(OH)_2\cdot mH_2O$ |
| **Kwpc** | $Ca_{4.35}H_{0.12}(Si_{0.91}Al_{0.09})_{3.4}O_{11.2}\cdot K_{0.29}\cdot 4.35Ca(OH)_2\cdot mH_2O$ |
| **Pfa30** | $Ca_{4.45}H_{0.28}(Si_{0.86}Al_{0.14})_{3.6}O_{11.8}\cdot Ca_{0.25}\cdot 0.002Ca(OH)_2\cdot mH_2O$ |

Finally, it should be kept in mind that according to the plots for the structural models (Figures 4.14 to 4.16) C-S-H formed in wpc was consistent with the T/J point of view, that in kwpc with T/CH viewpoint and that in pfa30 with both structural models.

# V – RESULTS AND DISCUSSION: CURING AT 55°C

The experimental results related to the systems cured at 55°C are presented and discussed in this chapter. The studied systems will be designated by the previously used notation.

## 5.1 – STA-EGA

The amount of calcium hydroxide (CH) present in the different systems cured at 55°C was estimated by STA-EGA. Figures 5.1 shows the STA-EGA curve obtained for the 30% PFA blended WPC paste. EGA gave identification of the evolved gases during the heating process and carbonation of the samples did not take place.

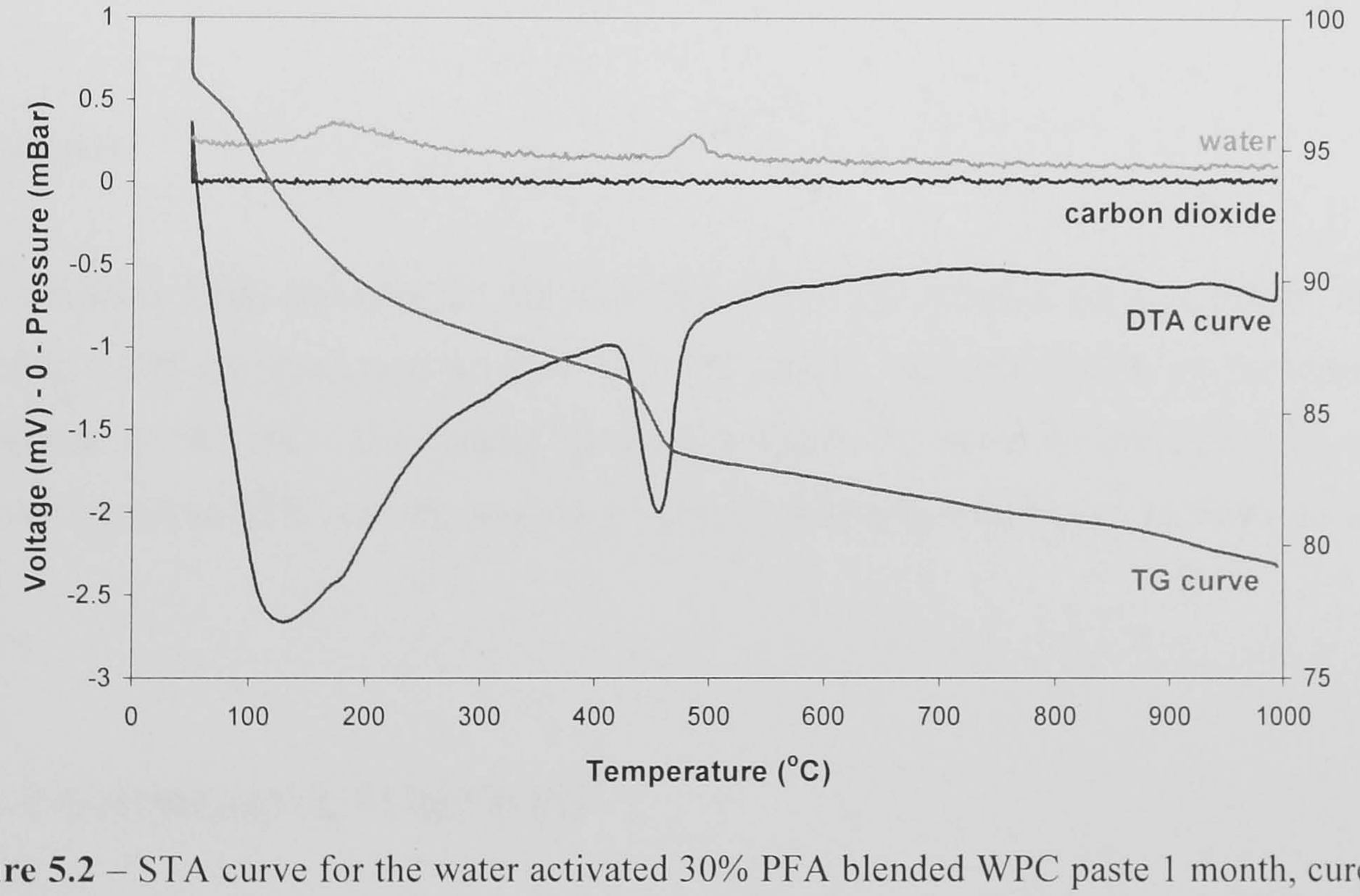


**Figure 5.2** – STA curve for the water activated 30% PFA blended WPC paste 1 month, cured at 55°C.

Table 5.1 summarises the estimated CH as percentage of ignited weight obtained for all the systems cured at 55°C after one day and one month of hydration. It should be kept in mind that the obtained results are only estimated and that they are not absolute values.

**Table 5.1** – Estimated amount of CH, as percentage of ignited weight, present in the water and KOH activated neat and blended cement pastes cured at 55°C at 1 day and 1 month.

| | 1 day | 1 month |
|---|---|---|
| **WPC** | 21 | 27 |
| **KWPC** | 25 | 35 |
| **PFA30** | 15 | 13 |
| **KPFA30** | 13 | 11 |
| **PFA60** | 7 | 6 |
| **KPFA60** | 5 | 3 |

Comparing these results with those obtained at 25°C (Table 4.1), apparently higher curing temperature increased slightly the kinetics of the cement hydration as higher amounts of CH were estimated. As mentioned in the previous chapter, STA results give a good indication of the amount of CH that was formed in each system. However, the results are not conclusive by themselves and are not very accurate in quantitative terms.

## 5.2 – XRD

The obtained XRD patterns for the neat and 30% PFA blended cement pastes, either water or KOH activated, and cured at 55°C for one day and one month are presented in Appendix A (A5-A8). The results were very similar to those obtained for the same systems cured at 25°C, i.e. the same type and number of phases were identified (Table 4.2).

## 5.3 – COMPRESSIVE STRENGTH

Compressive tests were carried out on mortars with the same chemical composition as the studied systems, cured at 55°C in an environmental chamber. The following table summarises the data obtained for the water and KOH activated neat and 30% PFA blended WPC pastes at one day and one month, cured at 55°C.

**Table 5.2** – Compressive strength data obtained for the neat and 30% PFA blended cement pastes after 1 day and 1 month, cured at 55°C.

| | | Compressive Strength (MPa) | *s* |
|---|---|---|---|
| **WPC** | **1 day** | 27.6 | 1.2 |
| | **1 month** | 66.0 | 1.9 |
| **KWPC** | **1 day** | 10.0 | 1.0 |
| | **1 month** | 18.1 | 0.9 |
| **PFA30** | **1 day** | 14.7 | 0.2 |
| | **1 month** | 43.2 | 0.3 |
| **KPFA30** | **1 day** | 13.0 | 0.8 |
| | **1 month** | 30.4 | 6.7 |

Compressive strength increased after one month of hydration, indicating that the microstructure of the samples became more dense and packed. As hydration took place, the resulting hydration products, especially Op C-S-H filled in the interstitial space originally filled with water. As mentioned in the previous chapter, compressive strength results should be analysed along with data indicating the type and degree of porosity present in the microstructure. Porosity, pore size and other microstructural features define the strength, elasticity and microhardness of cement pastes[1,120]. Backscattered electron microscopy can also give some information regarding porosity.

Comparing these results with those from the previous chapter, it was verified that the water activated neat and blended cement pastes acquired higher strength after one day of hydration but lower strength after one month of curing at 55°C. The alkaline neat and blended cement pastes presented higher strength after one day and one month. It was concluded that, although it appears that higher curing temperature increased cement hydration, it does not mean that the final physical properties are improved. Accurate evaluation of the porosity should be conducted.

## 5.4 – SOLID STATE $^{29}$Si MAS NMR

Single pulse $^{29}$Si MAS NMR provides quantitative information on the silicate anion structure of the C-S-H gel, namely the fractions of silicon present in different tetrahedral environments, $Q^n$, where n denotes the connectivity of the silicate tetrahedron, in dreierkette chains. Quantification was achieved in the case of the neat WPC pastes but only semi-quantitative data was obtained for the 30% PFA blended systems. For the 60% PFA blended pastes, only qualitative analysis was conducted. The spectra are included in Appendix B (B2-B4). The interpretation of the spectra was very similar to that done for the same cementitious systems cured at 25°C (Chapter IV, Section 4.5). The following table summarises the quantitative MAS NMR data found for the neat WPC pastes.

**Table 5.3** – $^{29}$Si MAS NMR quantitative data obtained for the neat cement pastes 1 day and 1 month, cured at 55°C.

| | **Water activated** | | **KOH activated** | |
|---|---|---|---|---|
| | **1 day** | **1 month** | **1 day** | **1 month** |
| **MCL** | 3.5 | 6.5 | 3.5 | 5.2 |
| **Al/Si** | 0.058 | 0.095 | 0.098 | 0.103 |
| **% Anhydrous cement** | 41.9 | 9.6 | 41.8 | 6.9 |
| **% Cement reacted** | 58.1 | 90.4 | 58.2 | 93.1 |
| **% $\gamma$-$C_2S$** | 4.0 | 2.6 | 5.9 | 3.7 |
| **% $Q^1$** | 32.6 | 29.5 | 32.5 | 38.2 |
| **% $Q^2$(1Al)** | 6.3 | 16.8 | 10.3 | 18.4 |
| **% $Q^2$** | 15.2 | 41.5 | 9.5 | 32.9 |
| **% $Q^3$** | - | - | - | - |
| **%B** | 38 | 62 | 38 | 46 |
| **$B_{water}/B_{KOH}$** | 62 | 83 | - | - |
| **CH as % of ig. wt. (STA)** | 21 | 27 | 25 | 35 |

The above data shows that the amount of reacted cement increased with time of hydration. Polymerisation of C-S-H also occurred because MCL increased as well as the relative intensity of $Q^2$. After one month - when most of the cement reacted - the MCL indicated that the aluminosilicate chains were either mainly pentameric, or mixtures of dimers with longer chains. Aluminium substitution in tetrahedral places in C-S-H occurred and also increased as hydration took place, as the relative intensity of $Q^2$(1Al) increased along with the Al/Si ratio. STA estimation of the amount of CH present in

each system (Table 5.1) was in good agreement with all of these observations. The amount of CH resulting from cement hydration increased with time. As expected in the case of alkaline activation[78], the spectra were better deconvoluted indicating greater degree of structural order. $\gamma$-$C_2S$ corresponding resonance was also present and had a more or less constant relative intensity[1]. Comparing the water and KOH activated neat WPC pastes, alkaline activation appeared not to have any effect on the kinetics of the cement reaction. Shorter mean aluminosilicate chain lengths were formed. This is intimately related with $Q^2$ resonance because the latter indicates the extent of C-S-H polymerisation. The proportion of occupied bridging sites in the dreierkette chains that are occupied by $Al^{3+}$ and not $Si^{4+}$ remained unchanged between one day and one month with water activation (at 38%) but reduced with KOH activation (from 62% to 46%). As a consequence the ratio of $B_{water}/B_{KOH}$ was affected. At one day, KOH activation produced five thirds as much aluminium substitution as did water, and at one month it produced six fifths (the mean Al/Si atomic ratios were the same but MCL was shorter with KOH). Interestingly, these values fall either side of the value observed previously for ground granulated blast-furnace slag/WPC blends with 50 and 90% slag - which had four thirds as much aluminium substitution with KOH[57] - and were the same as those for a metakaolin (MK)/WPC blend containing 20% MK[132], despite having very different mean Al/Si atomic ratios and mean aluminosilicate chain lengths. STA data also supports the idea that the percentage of reacted cement increased slightly with the alkaline activation because the amount of estimated CH was higher than the amount of estimated CH present in the water activated neat paste.

Comparing with the same systems cured at 25°C, the effect of temperature affected to some extent the cement hydration. In both systems, curing at 55°C led to slightly higher MCL indicating that further polymerisation of C-S-H occurred with decreasing of the relative intensity of $Q^1$ and increasing of the relative intensity of $Q^2$. It also increased the percentage of cement reacted as well as the Al/Si ratio and the relative intensity of $Q^2(1Al)$.

The semi-quantitative MAS NMR data obtained for the 30% fly ash blends cured at 55°C for one day and one month are presented in the next table.

**Table 5.4** – $^{29}Si$ MAS NMR semi-quantitative data obtained for the 30% PFA blended cement pastes 1 day and 1 month, cured at 55°C.

| | **Water activated** | | **KOH activated** | |
|---|---|---|---|---|
| | **1 day** | **1 month** | **1 day** | **1 month** |
| **MCL** | 4.0 | 12.4 | 4.2 | 10.7 |
| **Al/Si** | 0.099 | 0.181 | 0.147 | 0.247 |
| **% Anhydrous cement** | 20.9 | 12.5 | 20.2 | 19.3 |
| **% $\gamma$-$C_2S$** | 7.2 | 7.8 | 7.7 | 1.8 |
| **% $Q^1$** | 18.7 | 12.6 | 19.0 | 16.6 |
| **% $Q^2$(1Al)** | 6.7 | 24.0 | 10.1 | 35.0 |
| **% $Q^2$** | 8.5 | 29.6 | 5.3 | 19.3 |
| **% $Q^3$** | - | - | - | - |
| **% Anhydrous PFA** | 38.0 | 13.5 | 37.7 | 16.3 |
| **%B** | 54 | 74 | 55 | 73 |
| **$B_{water}/B_{KOH}$** | 73 | 75 | - | - |
| **CH as % of ig. wt. (STA)** | 15 | 13 | 13 | 11 |

In the blended system, the relative intensity of the $Q^2$(1Al) peak, the Al/Si atomic ratio and the MCL were higher and PFA replacement provided more available aluminium to be incorporated in the C-S-H structure. Regarding the KOH activated blend, the percentage of cement and PFA reacted increased after one month and, as expected, the alkaline activation caused a decrease of the MCL but an increase of the relative intensity of $Q^2$(1Al) and Al/Si atomic ratio. Comparing the water and KOH activated 30% PFA blended WPC pastes, alkaline activation did not affect significantly the kinetics of the cement reaction or that of the pozzolanic reaction. Considering aluminium substitution, %B was higher in the alkaline pastes indicating higher number of aluminium substituted sites. The %B increased the same amount in both systems. Consequently $B_{water}/B_{KOH}$ was also the same at both ages although the mean Al/Si increased as well as MCL. From STA data (Table 5.1) it appears that pozzolanic reaction took place.

Finally, the MAS NMR results were compared between the neat and 30% PFA blended WPC pastes. Table 5.5 resumes the comparable parameters found for the water activated neat and blended (30% PFA) WPC pastes, after one month of hydration at 55°C.

**Table 5.5** – $^{29}$Si MAS NMR data comparison between water activated neat and 30% PFA blended cement pastes 1 month, cured at 55°C.

| | Neat WPC | 30% PFA blended WPC |
|---|---|---|
| **MCL** | 6.5 | 12.4 |
| **% Anhydrous cement** | 9.6 | 12.5 |
| **Al/Si** | 0.095 | 0.181 |
| **% $Q^2$(1Al)** | 16.8 | 24.0 |
| **CH as % of ig. wt. (STA)** | 27 | 13 |

As observed in the previous chapter, PFA replacement slightly affected the amount of reacted cement and increased polymerisation of C-S-H, with a mean aluminosilicate chain length of 12.4. PFA substitution was a source of aluminium for C-S-H and, as a result, the Al/Si ratio and the relative intensity of $Q^2$(1Al) were also higher in the blended cement paste. Pozzolanic reaction occurred as STA results confirmed. Table 5.6 shows the same comparable parameters calculated for the KOH neat and 30% PFA blended WPC pastes, after one month of hydration.

**Table 5.6** – $^{29}$Si MAS NMR data comparison between KOH activated neat and 30% PFA blended cement pastes 1 month, cured at 55°C.

| | Neat WPC | 30% PFA blended WPC |
|---|---|---|
| **MCL** | 5.2 | 10.7 |
| **% Anhydrous cement** | 6.9 | 19.3 |
| **Al/Si** | 0.103 | 0.247 |
| **% $Q^2$(1Al)** | 18.4 | 35.0 |
| **CH as % of ig. wt. (STA)** | 35 | 11 |

Table 5.6 clearly shows the effect of PFA replacement when comparing the neat and blended alkaline systems. The MCL doubled its value in the blend as well as the mean Al/Si ratio and relative intensity of $Q^2$(1Al).

Ultimately, it was necessary to compare the MAS NMR obtained at 55°C with those at 25°C presented in the previous chapter. In order to simplify the comparison, the results were compared after one month of hydration because by then most of the cement

reacted and the microstructure formed is better defined and distributed, i.e. the cement paste reaches higher maturity. Starting with the water activated neat and blended systems, Table 5.7 summarises the key data obtained using MAS NMR.

**Table 5.7** – $^{29}Si$ MAS NMR data comparison between water activated neat and 30% PFA blended cement pastes 1 month, cured at 25°C and 55°C.

| | **Neat WPC (25°C)** | **Neat WPC (55°C)** | **30% PFA Blended (25°C)** | **30% PFA Blended (55°C)** |
|---|---|---|---|---|
| **MCL** | 3.3 | 6.5 | 3.6 | 12.4 |
| **% Anhydrous cement** | 19.8 | 9.6 | 14.3 | 12.5 |
| **Al/Si** | 0.056 | 0.095 | 0.070 | 0.181 |
| **% $Q^2$(1Al)** | 8.8 | 16.8 | 9.0 | 24.0 |
| **CH (STA)** | 26 | 27 | 20 | 13 |

From the above results, it was concluded that, generally, higher curing temperature increased slightly the rate of the cement hydration. Further polymerisation also occurred because, at 55°C, in both neat and blended systems, the MCL was much higher. High curing temperature increased the mean Al/Si ratio as well as the amount of central silicon substituted by aluminium in the C-S-H dreierkette chain. Table 5.8 summarises the MAS NMR results obtained for the alkaline neat and blended cement pastes cured for one month, at 25°C and 55°C.

**Table 5.8** – $^{29}Si$ MAS NMR data comparison between KOH activated neat and 30% PFA blended cement pastes 1 month, cured at 25°C and 55°C.

| | **Neat WPC (25°C)** | **Neat WPC (55°C)** | **30% PFA Blended (25°C)** | **30% PFA Blended (55°C)** |
|---|---|---|---|---|
| **MCL** | 3.4 | 5.2 | 4.2 | 10.7 |
| **% Anhydrous cement** | 22.6 | 6.9 | 12.0 | 19.3 |
| **Al/Si** | 0.093 | 0.103 | 0.145 | 0.247 |
| **% $Q^2$(1Al)** | 14.2 | 18.4 | 16.6 | 35.0 |
| **CH (STA)** | 31 | 35 | 17 | 11 |

Similarly to the comparison between the water activated samples cured at both temperatures, higher temperature increased MCL, the rate of cement hydration and the amount of aluminium present in the C-S-H aluminosilicate chain. In general, MAS NMR experimental results showed that PFA replacement in a WPC system and higher curing temperature enhanced incorporation of aluminium in the C-S-H phase in the bridging tetrahedra of dreierkette chains. C-S-H polymerised as hydration took place and the cement hydration and pozzolanic reaction rates were generally increased by higher curing temperature.

## 5.5 – SEM-EDX

The backscattered electron images illustrating the microstructure found in the neat and 30% or 60% fly ash blended cement pastes (water or KOH activated) one day and one month, cured at 55°C are presented in Appendix C. Low magnification images are shown on the left-hand side and higher magnification on the right-hand side. The features identified in the microstructure of the different systems were very identical to those observed in the same systems cured at 25°C. Nevertheless, another very interesting feature in the microstructure of the water activated systems was noticed. The grey level of C-S-H was in places quite similar to the CH: that is, it was brighter than in pastes cured at lower temperature (Chapter IV, Section 4.6), an observation that is in good agreement with previous studies[103,138-140]. Figure 5.2 shows the similarity between the grey scale found for C-S-H and that of CH.

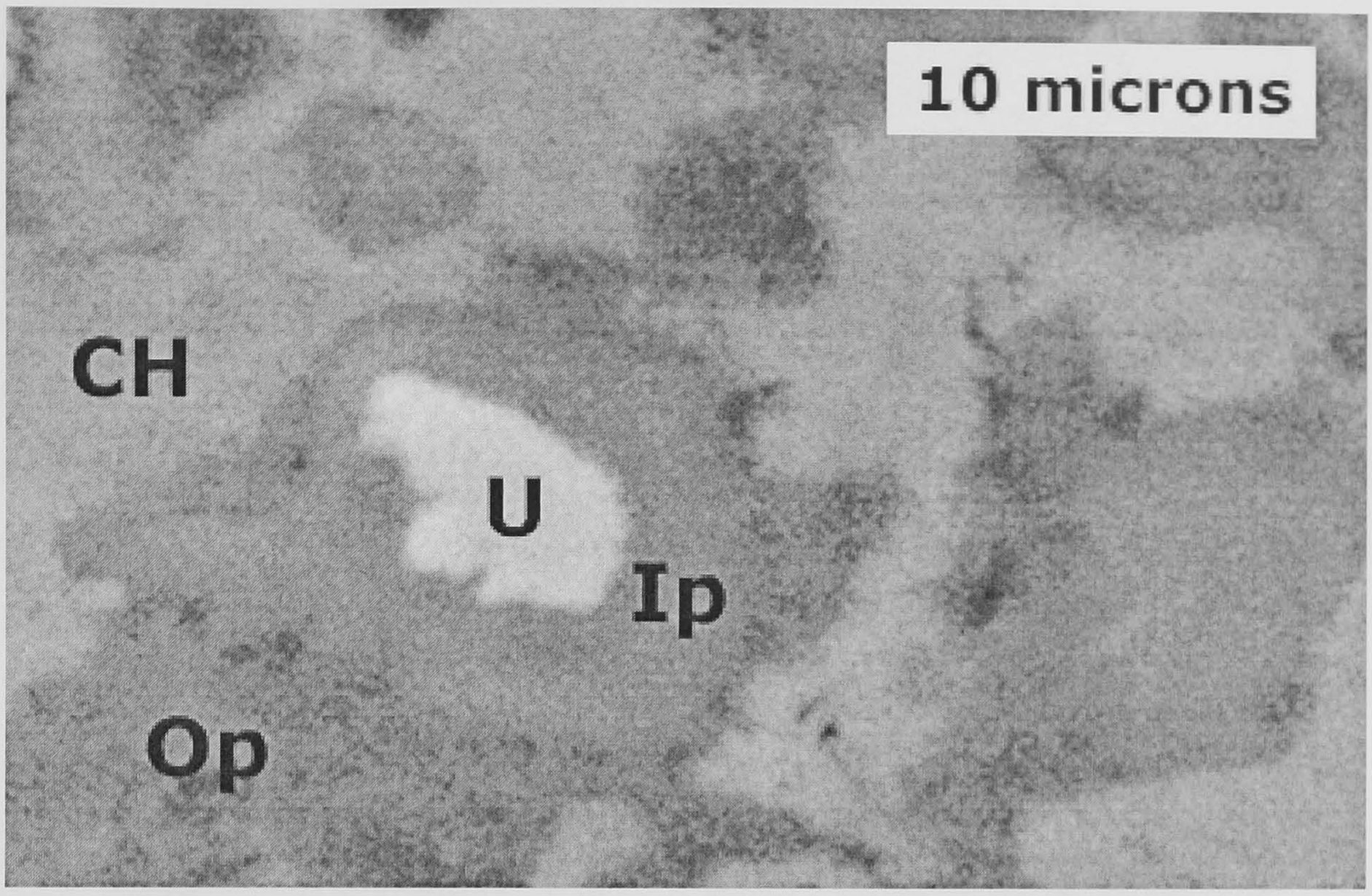


**Figure 5.2** – Backscattered image that illustrates an area of dense microstructure of the water activated 30% PFA blended WPC paste 1 month, cured at 55°C. Regions of calcium hydroxide (CH), unreacted cement (U), inner product C-S-H (Ip) and outer product C-S-H (Op) are labelled.

Regarding EDX analysis, as seen in the previous chapter, C-S-H chemical composition could not be accurately obtained for the same reasons presented before. The corresponding EDX plots are illustrated in Appendix C as well as EDX calculated data (Table C2). The mean Ca/Si atomic ratios for the water activated neat cement paste (one day: 2.12, s = 0.51; one month: 1.93, s = 0.20; Appendix C, Table C2), were very similar to values found previously using the same technique by Escalante-Garcia and Sharp[134] for Ip C-S-H present in two ordinary Portland cements with w/c of 0.5 hydrated at 60°C and by Kjellsen[137] for both Ip and Op C-S-H in an OPC-based high performance concrete (containing 5% silica fume) with water/binder ratio of 0.31 hydrated at 50°C; the distribution of the data is similar to those in the work of Escalante-Garcia and Sharp. The data is, however, at the high end of values measured previously by TEM-EDX for C-S-H in Portland cement pastes hydrated at lower temperature (20°C)[72] and those for the KOH activated system were much higher than is possible to achieve for C-S-H in models for the structure of C-S-H[3].

## 5.6 – TEM-EDX

### 5.6.1 – Morphology and Chemical Analysis

The systems cured at 55°C and studied using TEM-EDX were the water and KOH activated neat WPC and 30% PFA blended pastes, cured for one month. As stated before, the reason for this choice was that by one month, the microstructure is better defined and its features and phase are more easily recognisable. The following micrographs show the morphology found for the water activated neat WPC paste cured at 55°C for one month.

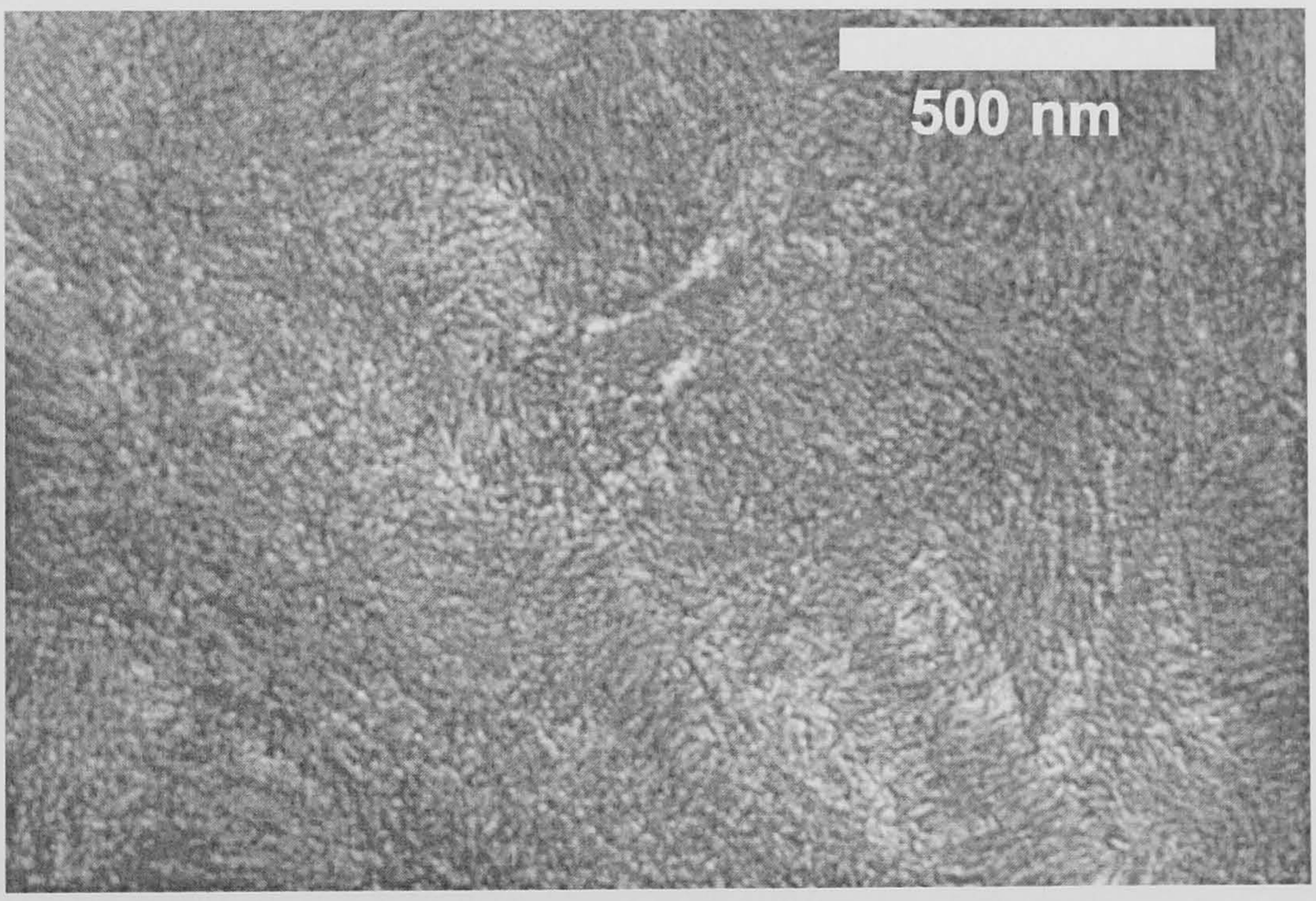


**Figure 5.3** – TEM micrograph showing fine and dense Ip C-S-H formed in the water activated neat WPC paste, 1 month cured at 55°C.

The above micrograph shows Ip C-S-H had a very fine homogeneous morphology formed in the water activated WPC paste that has been observed previously in cements hydrated at 20°C[13,72], also in the previous chapter at 25°C. The Op C-S-H was also similar to that formed at lower temperatures in being essentially fibrillar, although often somewhat coarser fibrillar, which is consistent with previous observations at high temperature[42]. Anhydrous particles of cement, large crystals of CH and relicts of AFt-

type phases were also observed in the microstructure. The following figure shows the EDX data plots found for the water activated WPC paste cured at 55°C, for one month.

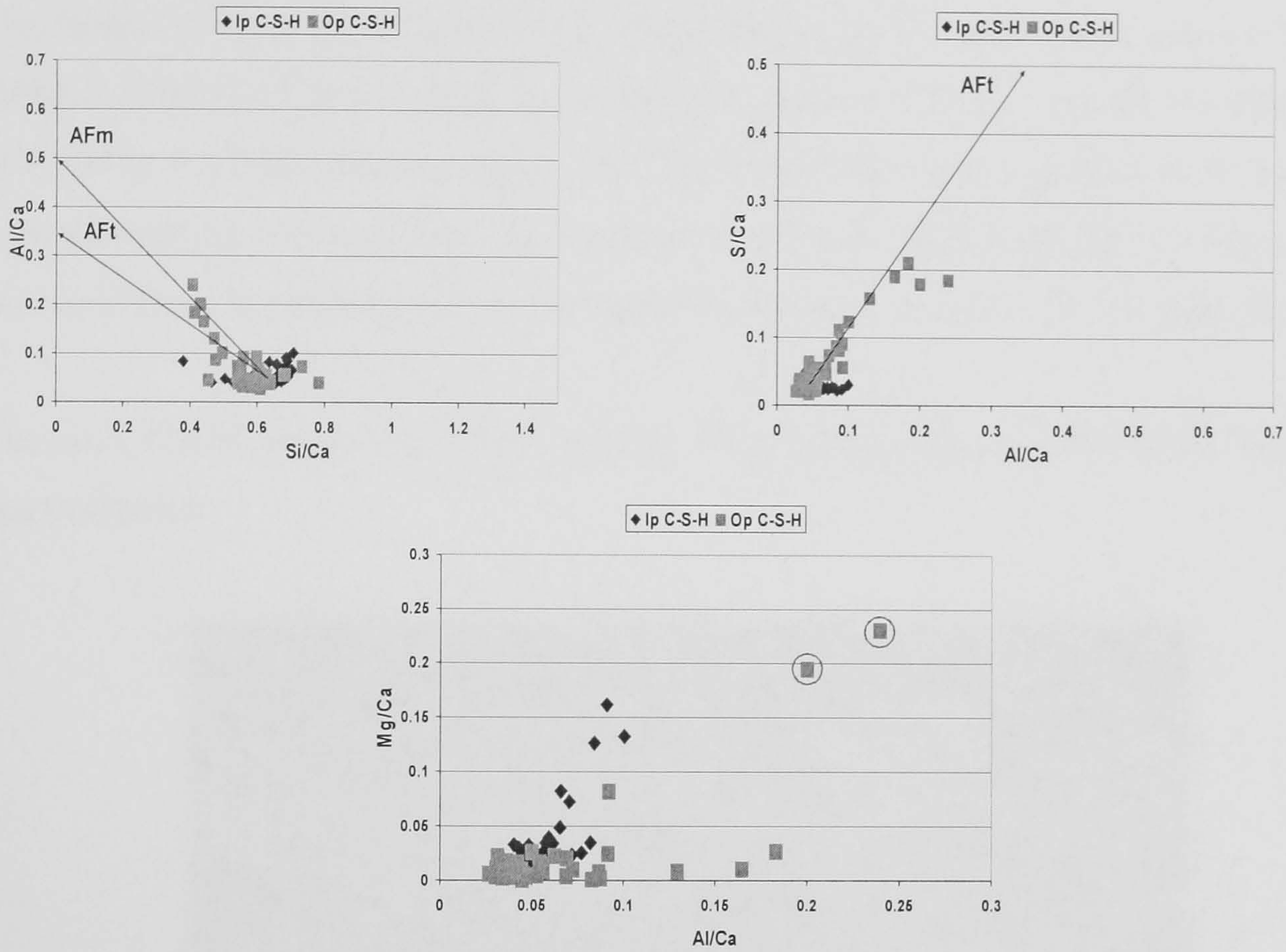


**Figure 5.4** – Al/Ca against Si/Ca (top left), S/Ca against Al/Ca (top right) and Mg/Ca against Al/Ca (bottom) atomic ratio plots for the TEM-EDX phase analysis of the water activated neat WPC paste after 1 month of hydration at 55°C.

It was sometimes difficult to select areas totally free of relicts of AFt-type phases which, because they were partially decomposed, could not be discarded on the basis of the presence of crystalline reflections on the SAED pattern. The following micrographs will illustrate that fine intermixing between C-S-H and relicts of AFt-type phases. Analyses of such mixtures contained enhanced amounts of Ca, Al and S, as seen in the above figure. Such analyses were excluded when calculating the mean atomic compositions for the C-S-H. The two analyses of Op C-S-H that have the highest Al/Ca atomic ratio, together with a number of analyses of Ip C-S-H, also appear to include a contribution from microcrystals of a hydrotalcite-like phase (i.e. a Mg, Al double hydroxide phase, which can contain various interlayer anions), as indicated in the bottom plot from Figure 5.4. The Al/Ca against Si/Ca atomic ratio plot showed two

trendlines in the direction of the calcium aluminoferrite hydrate phases but the S/Ca against Al/Ca showed only a clear trendline in the direction of the AFt-type phases. Therefore, it was concluded that Op C-S-H was finely intermixed with AFt-type phases. The mean Ca/Si ratio calculated for Ip C-S-H was 1.56 (s = 0.16) and mean Al/Si ratio 0.084 (s = 0.021). Op C-S-H had a mean Ca/Si ratio of 1.78 (s = 0.028) and Al/Si ratio of 0.107 (s = 0.083). The corresponding $^{27}$Al MAS NMR spectrum (Figure 5.7) showed a broad resonance assigned to AFm-type phases. From TEM-EDX observations, it was concluded that the broad peak also included a resonance assigned to AFt-type phases.

The next figure shows Op C-S-H typical morphology found in the KOH neat WPC microstructure.

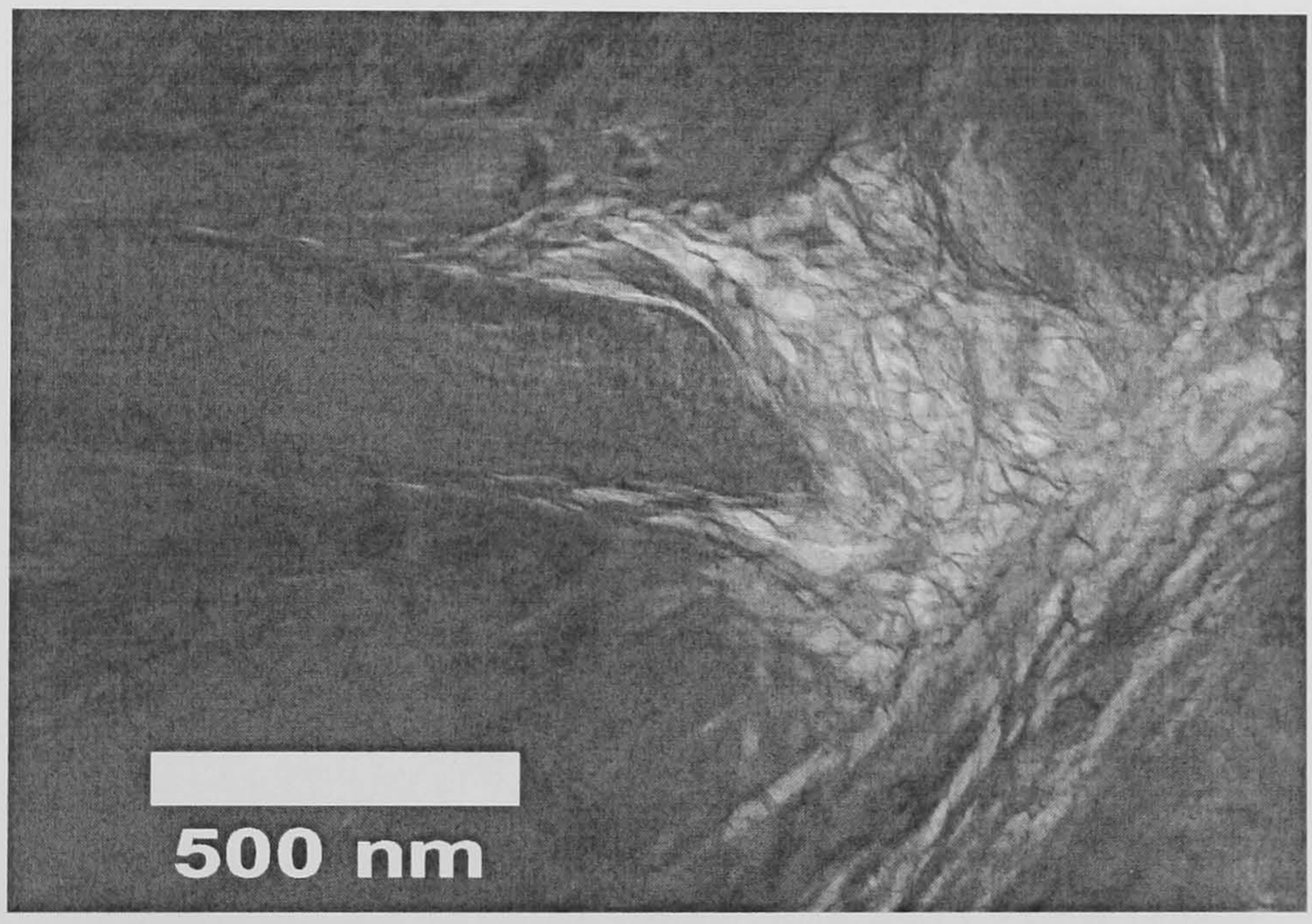


**Figure 5.5** – TEM micrograph showing large CH crystals and foil-like Op C-S-H formed in the KOH activated neat WPC paste, 1 month cured at 55°C.

The micrograph in Figure 5.5 illustrates large crystals of CH surrounding foil-like Op C-S-H. The morphology of Op C-S-H formed with KOH activation was foil- and lath-like rather than fibrillar. The laths appeared to consist of stacks of very poorly ordered layers, which merge with crumpled foils. This observed morphology is in good agreement with that found in other systems[57] cured at 25°C. The foil-like morphology of Op C-S-H was also consistent with that characterised in the same system cured at 25°C, previously seen in Chapter IV. Due to the alkaline activation, Op C-S-H

morphology changed from coarse fibrillar to foil-like. The microcrystalline nature of CH in the KOH activated neat paste indicated by XRD (Appendix A, Figure A6) was confirmed by TEM. In the next figure (bottom right), the CH microcrystals appeared darker where they are oriented such that they Bragg-reflect electrons strongly. This is a typical feature of KOH activated systems, as previously reported for pastes of neat WPC and slag-WPC blends[57] and a metakaolin-WPC blend[132] hydrated at 25°C. Microcrystalline CH intermixed with C-S-H has not been observed in water activated Portland cement pastes of normal w/c ratio hydrated at 20-25°C. Whilst such fine intermixing has been observed in pastes hydrated at 80°C[3] it was not observed in this study. The following micrograph shows an interface between fine and dense Ip C-S-H and foil-like Op C-S-H.

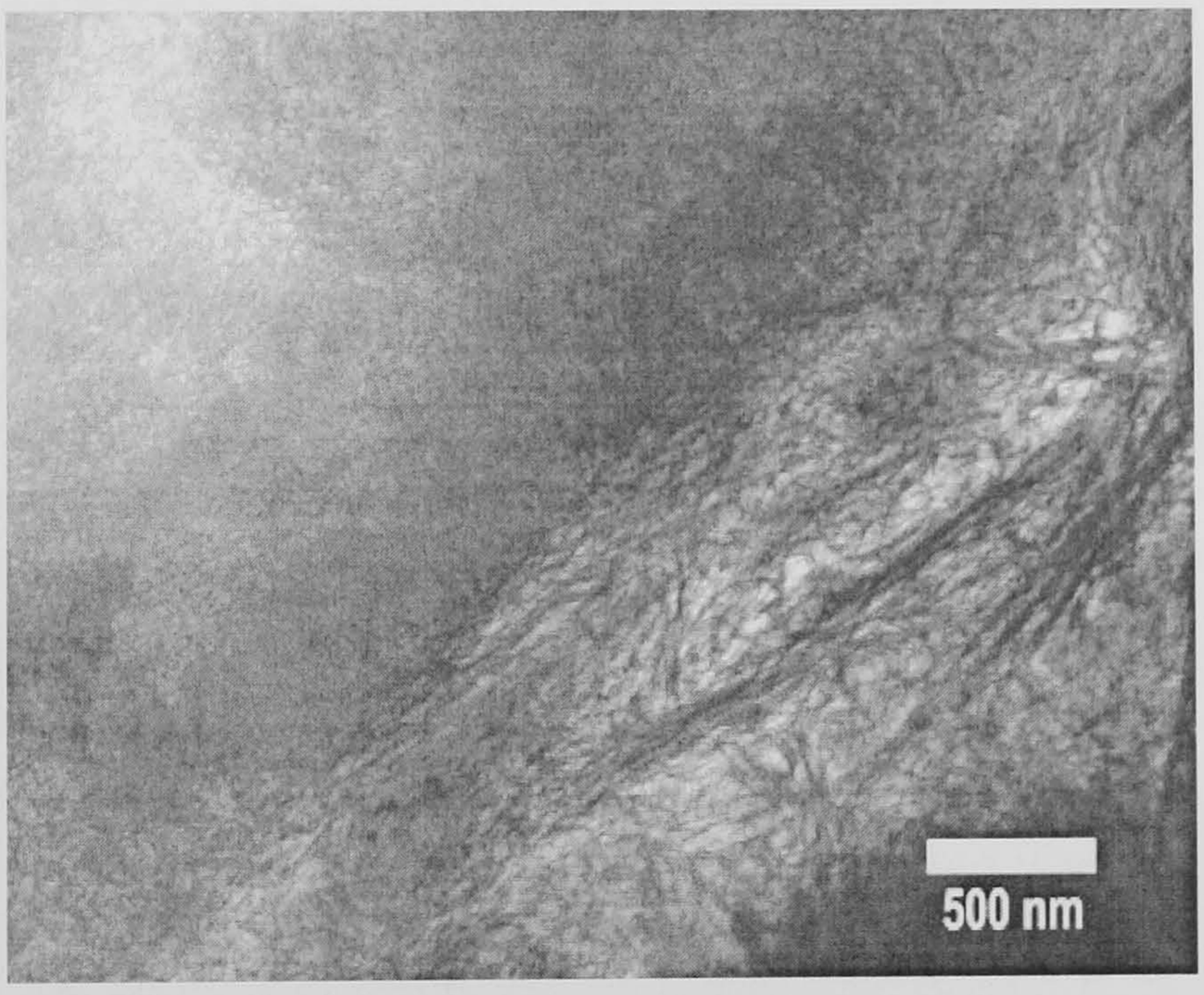


**Figure 5.6** – TEM micrograph showing the interface between fine and dense Ip and foil-like Op C-S-H formed in the KOH activated neat WPC paste, 1 month cured at 55°C.

The subsequent figure shows the foil-like Op C-S-H morphology in more detail. The microstructure of this system was mainly formed of some AFm-type phases crystals, foil-like Op C-S-H, fine and dense Ip C-S-H, large crystals of CH as well as microcrystalline CH finely intermixed with C-S-H.

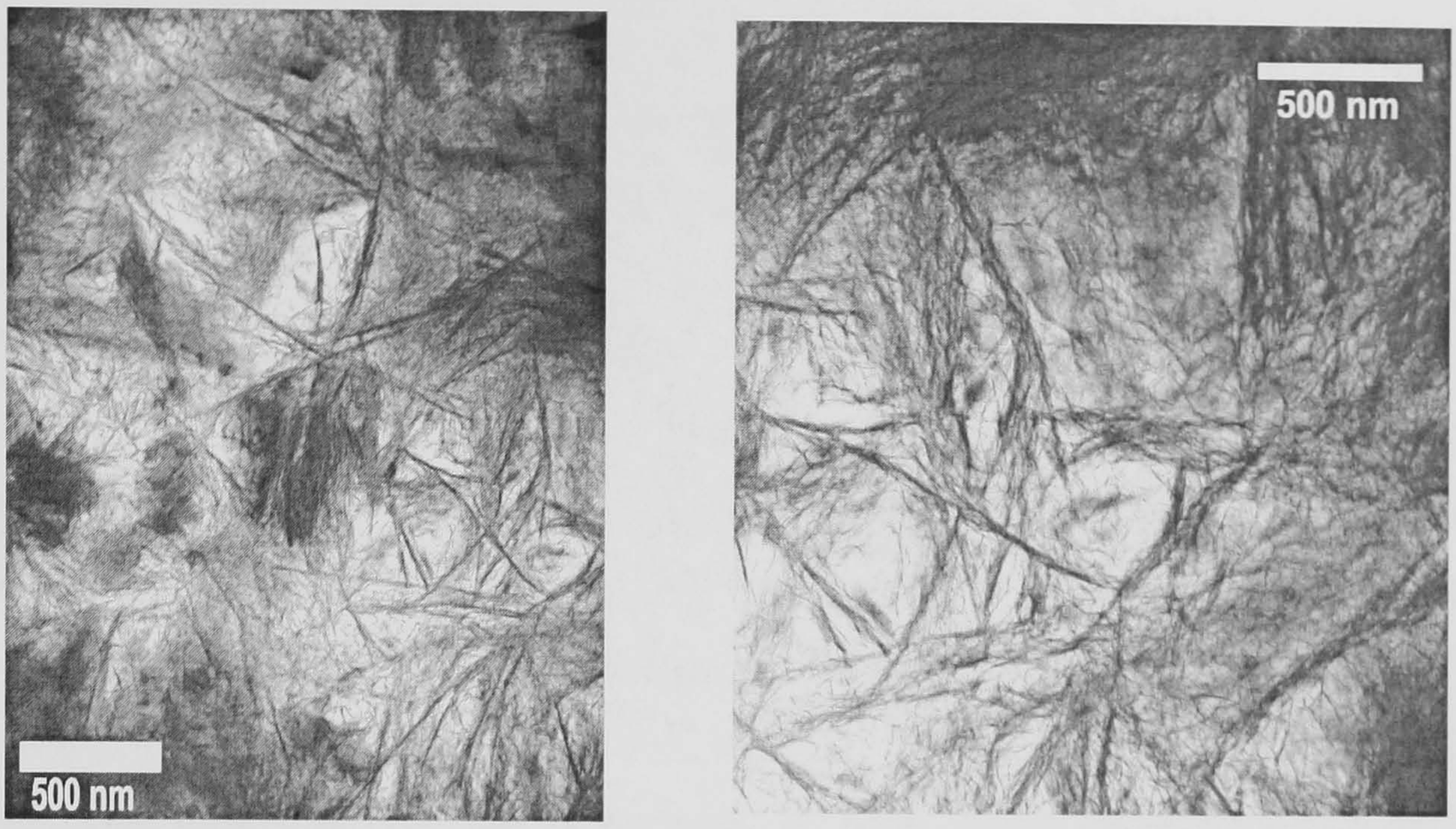


**Figure 5.7** – TEM micrographs showing details of the foil-like Op C-S-H formed in the KOH activated neat WPC paste, 1 month cured at 55°C.

EDX data plots corresponding to this sample are illustrated in the next figure.

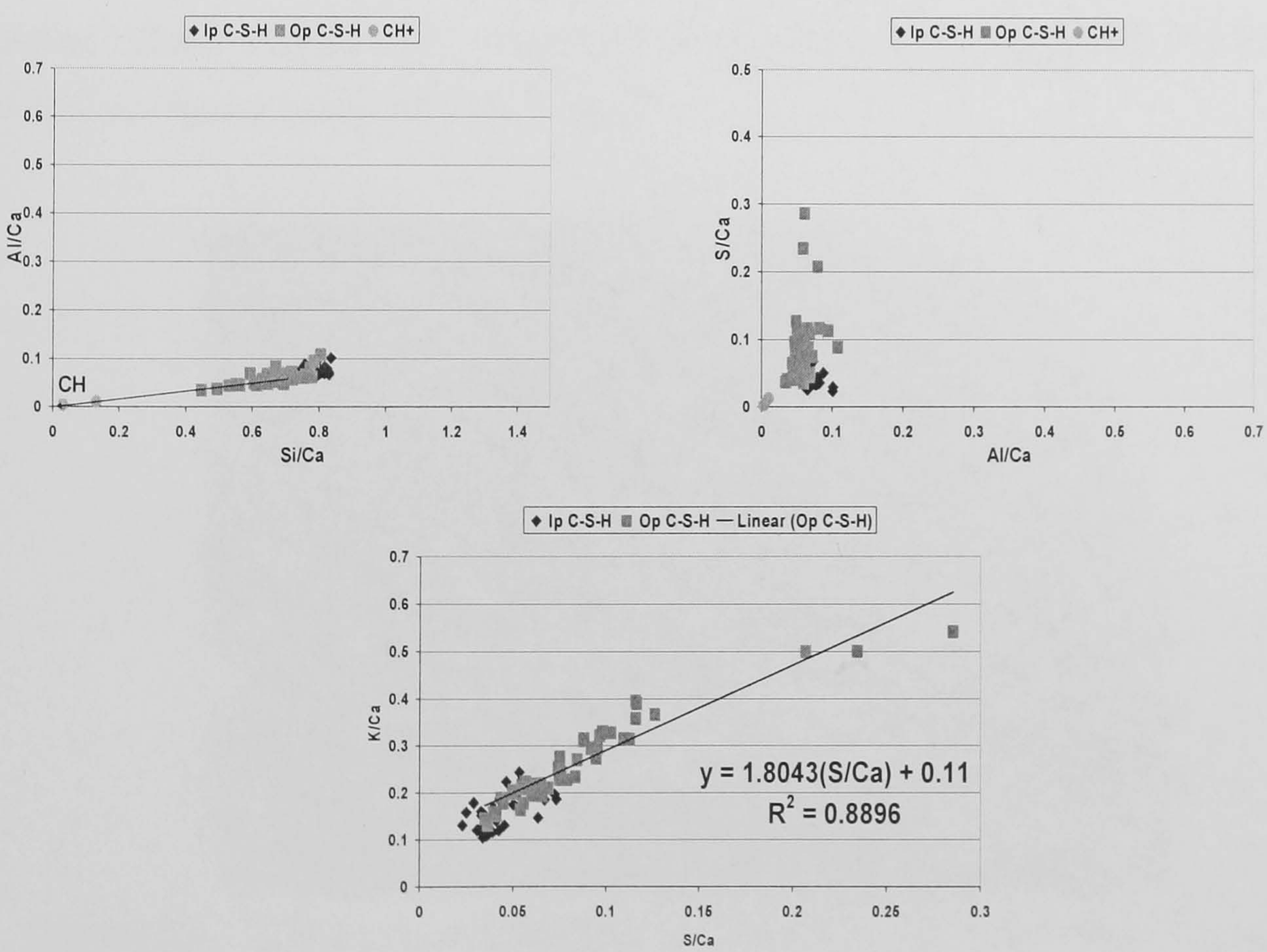


**Figure 5.8** – Al/Ca against Si/Ca (top left), S/Ca against Al/Ca (top right) and K/Ca against S/Ca (bottom) atomic ratio plots for the TEM-EDX phase analysis of the KOH activated neat WPC paste after 1 month of hydration at 55°C.

The previous atomic ratio plots clearly showed that Op C-S-H was finely intermixed with microcrystalline CH. As previously observed in the last chapter for the alkaline neat paste, relicts of AFt-type crystals were not observed in the KOH activated specimen. This is also in very good agreement with recent work on a metakaolin-WPC blend activated with KOH[132]. As a consequence, the mean Al/Ca atomic ratio against the mean Si/Ca atomic ratio and the S/Ca against Al/Ca plots show that none of the analyses contain contribution from AFt-type phases. Whilst AFm-type phases can occur in KOH activated cements[73], there was no contribution from such phase in these data. Ip C-S-H had a mean Ca/Si ratio of 1.28 (s = 0.05) and Al/Si ratio 0.093 (s = 0.012). The mean Ca/Si ratio for Op C-S-H was 1.50 (s = 0.28) and mean Al/Si ratio of 0.096 (s = 0.019). The higher S/Ca values were clearly associated with enhanced K/Ca, i.e. the K/Ca and S/Ca values increased in an approximate 2:1 ratio suggesting strongly that $SO_4^{2-}$ ions were adsorbed on the C-S-H balanced by potassium ions. The regression line indicated that the C-S-H itself had a K/Ca ratio of 0.09.

Regions of the microstructure of the 30% PFA blended WPC paste cured for one month at 55°C are shown in the following figures.

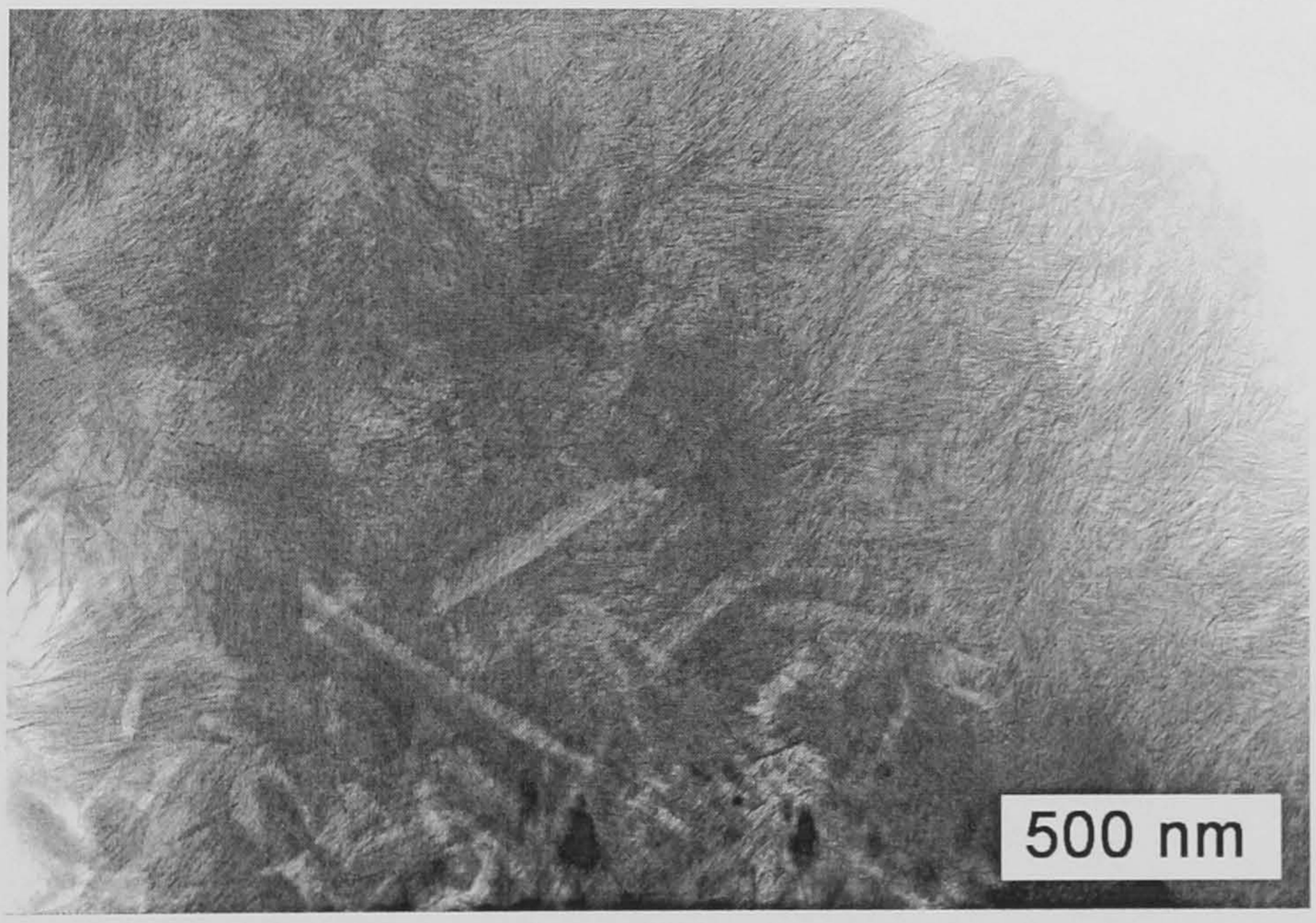


**Figure 5.9** – TEM micrograph showing coarse fibrillar Op C-S-H formed in the water activated 30% PFA blended WPC paste, 1 month cured at 55°C.

Figure 5.9 illustrates coarse fibrillar Op C-S-H intermixed with AFt-type phase relicts. The microstructure observed in this sample was mainly fine and dense Ip C-S-H, coarse

fibrillar Op C-S-H, AFt-type relicts intermixed with Ip and Op C-S-H, and large crystals of CH and AFm-type phases. The next figure shows a small fully hydrated cement particle, surrounded by dense and coarse fibrillar Op C-S-H. The latter was finely intermixed with AFt and AFm-type phases.

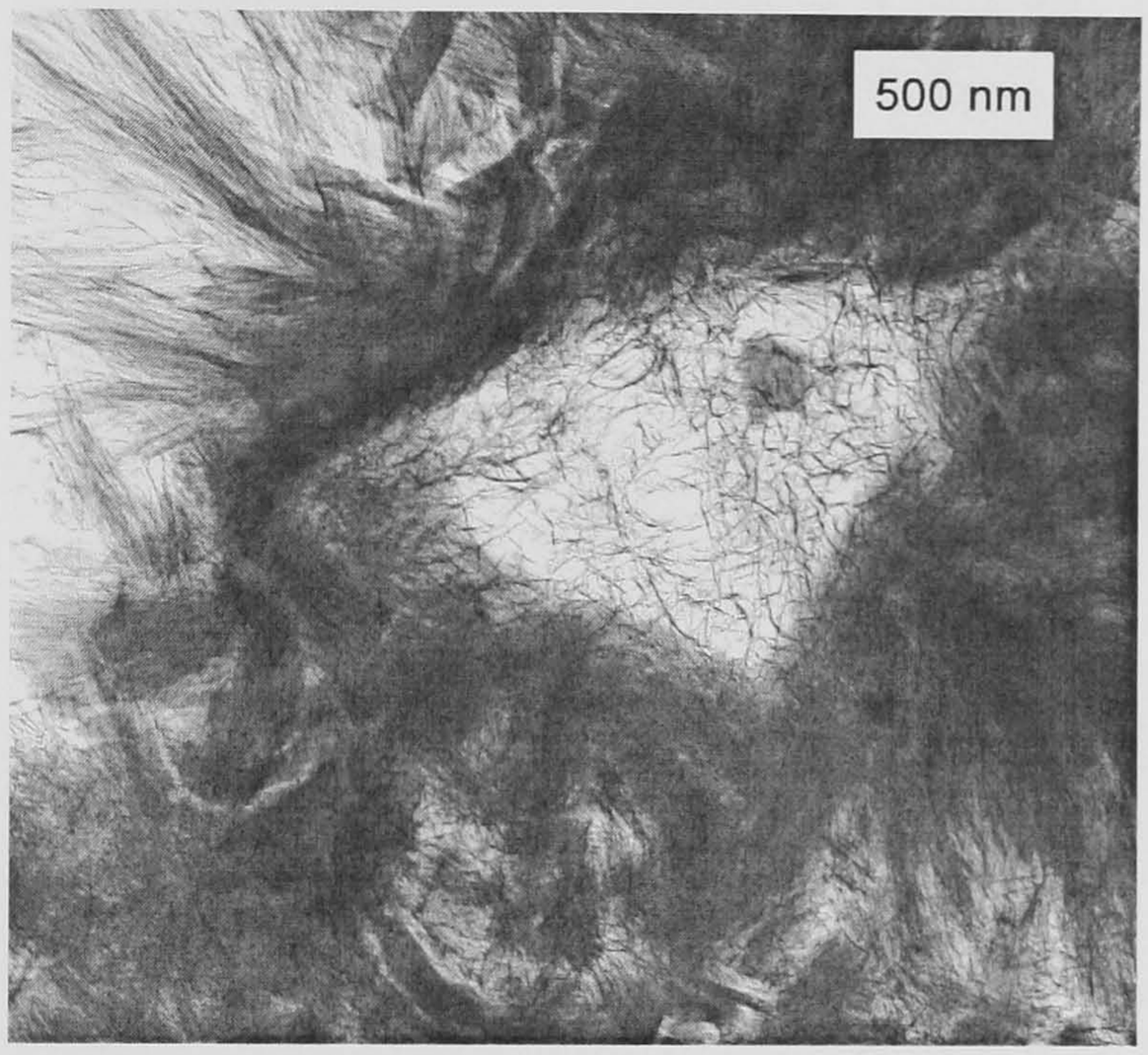


**Figure 5.10** – TEM micrograph showing a small fully hydrated cement grain in the water activated 30% PFA blended WPC paste, 1 month cured at 55°C.

It was observed that in fully reacted cement grains, the interior is not hollow, but filled with a less dense and porous product, Ip C-S-H with a foil-like morphology. Contrary to fine and dense Ip C-S-H formed in large grains, small fully hydrated particles are filled with an almost transparent product, with similar morphology to the fine foil-like Op C-S-H observed in water activated slag pastes or alkaline Portland cement pastes[3]. This microstructure of this system presented mainly fine and dense Ip C-S-H, coarse fibrillar Op C-S-H, AFt and AFm-type phases intermixed with Op C-S-H and large crystals of AFm-type phases or CH. The following figures illustrate the difference in morphology in a partially and fully reacted PFA particle.

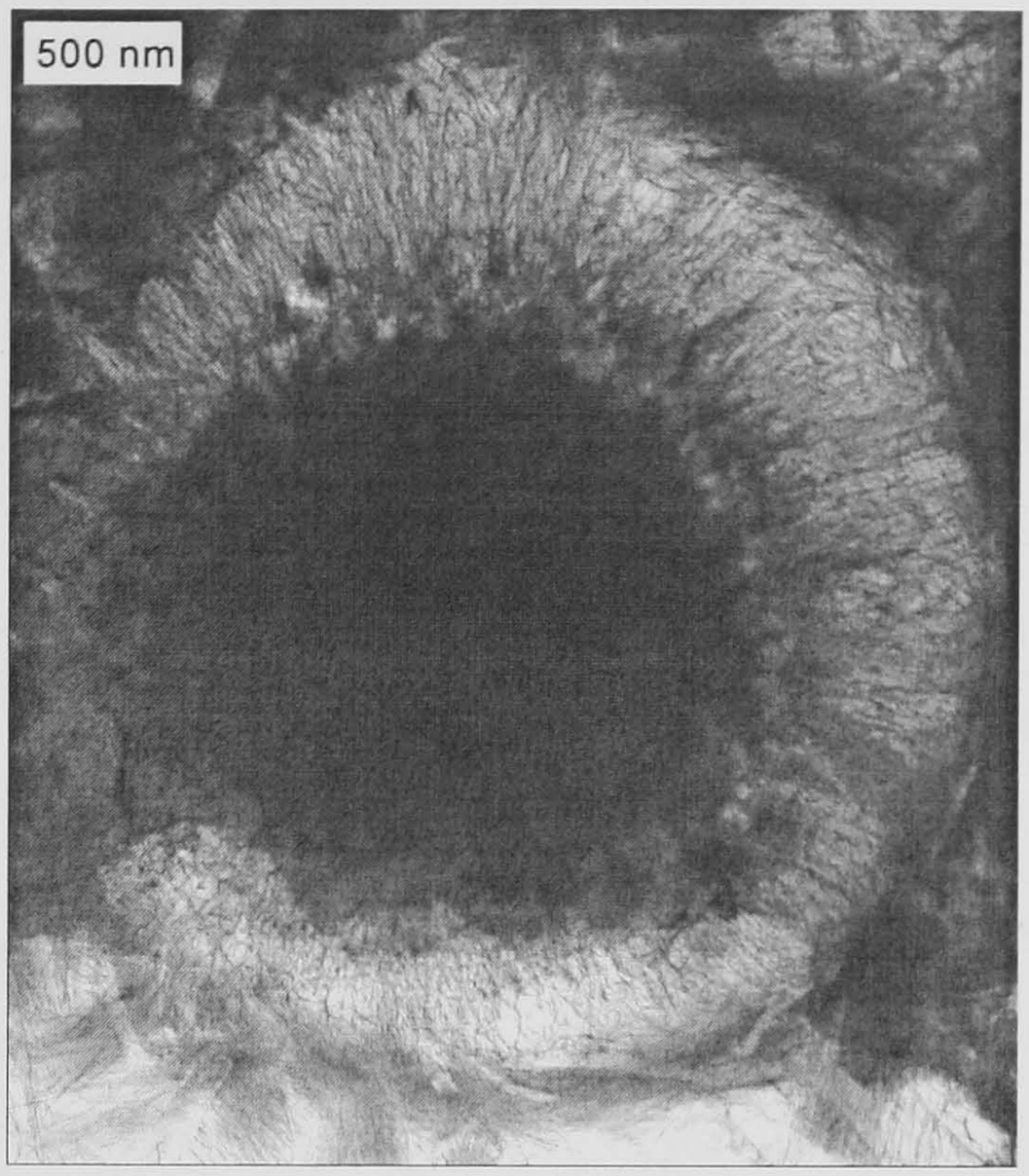


**Figure 5.11** – TEM micrograph showing a partially hydrated PFA particle in the water activated 30% PFA blended WPC paste, 1 month cured at 55°C.

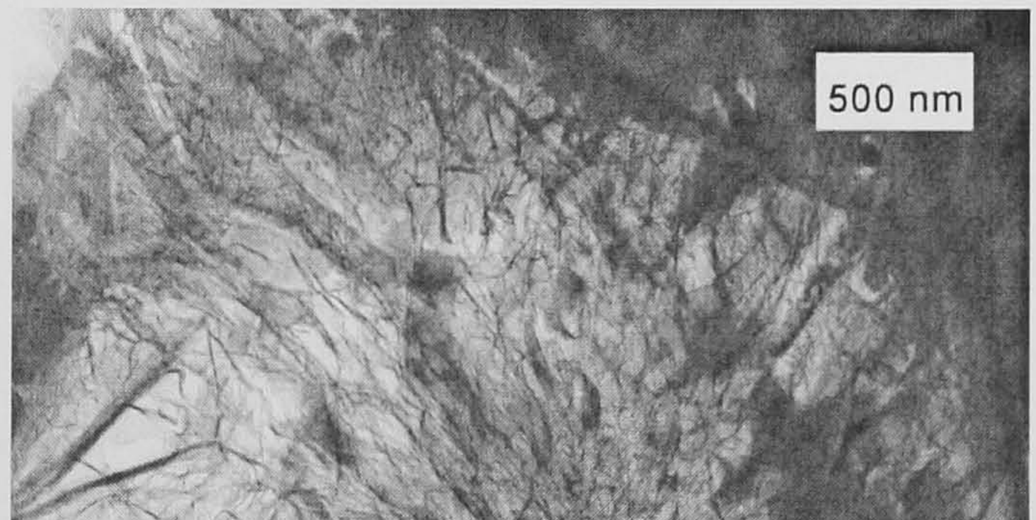


**Figure 5.12** – TEM micrograph showing a fully hydrated PFA particle in the water activated 30% PFA blended WPC paste, 1 month cured at 55°C.

The above figures show that PFA reacts from the outside to the inside of their particles. Small fully hydrated PFA particles have morphology very similar to the foil-like morphology small fully hydrated cement grains. EDX data plots are in the next figure.

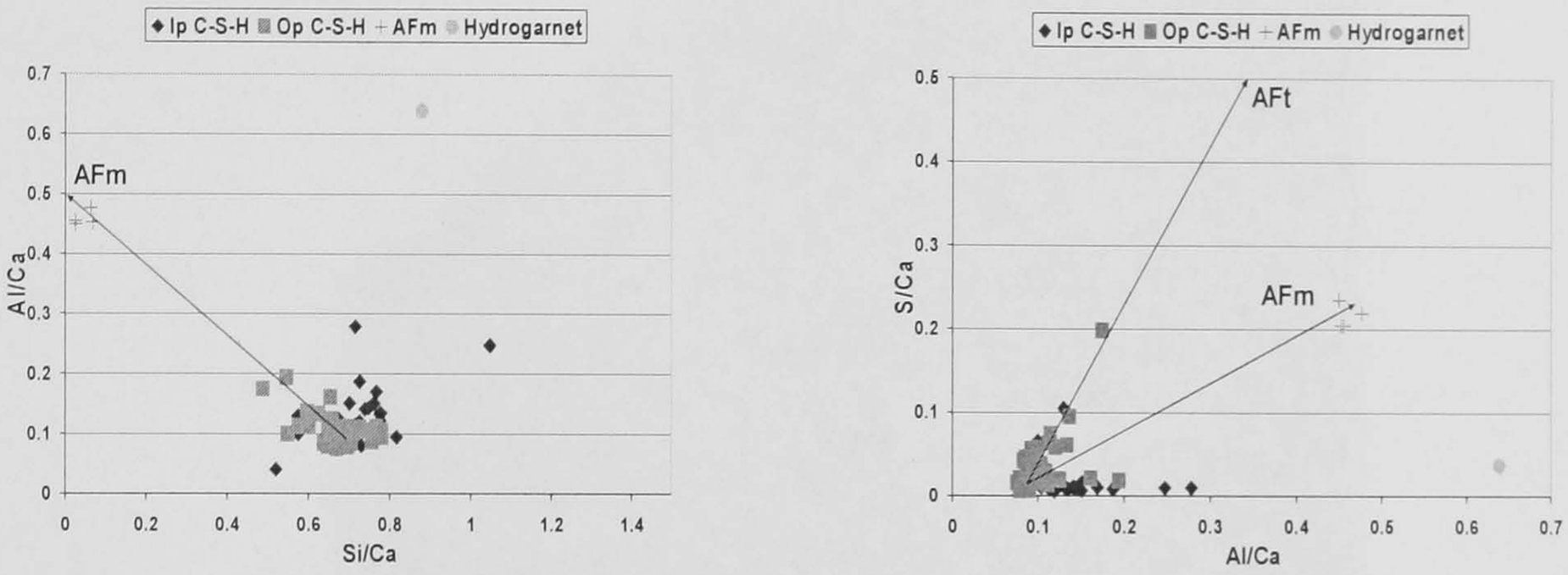


**Figure 5.13** – Al/Ca against Si/Ca (left) and S/Ca against Al/Ca (right) atomic ratio plots for the TEM-EDX phase analysis of the water activated 30% PFA blended cement paste after 1 month of hydration at 55°C.

The first plot indicated that Ip and Op C-S-H were finely intermixed with AFm-type phases but the second plot showed that Ip C-S-H was finely intermixed with AFm-type phases and Op C-S-H with AFt-type phases. Hydrogarnet-type phases were also intermixed with C-S-H. Usually, hydrogarnet-type phases are formed in ordinary Portland cement paste, but not typically in WPC pastes[1]. The mean Ca/Si and Al/Si ratios for Ip C-S-H were 1.42 (s = 0.18) and 0.178 (s = 0.059), respectively. Op C-S-H had a mean Ca/Si ratio of 1.52 (s = 0.16) and Al/Si ratio 0.165 (s =0.058).

The next figures show in detail fine and dense Ip C-S-H as well as foil-like Op C-S-H formed in the KOH activated 30% PFA blended WPC paste.

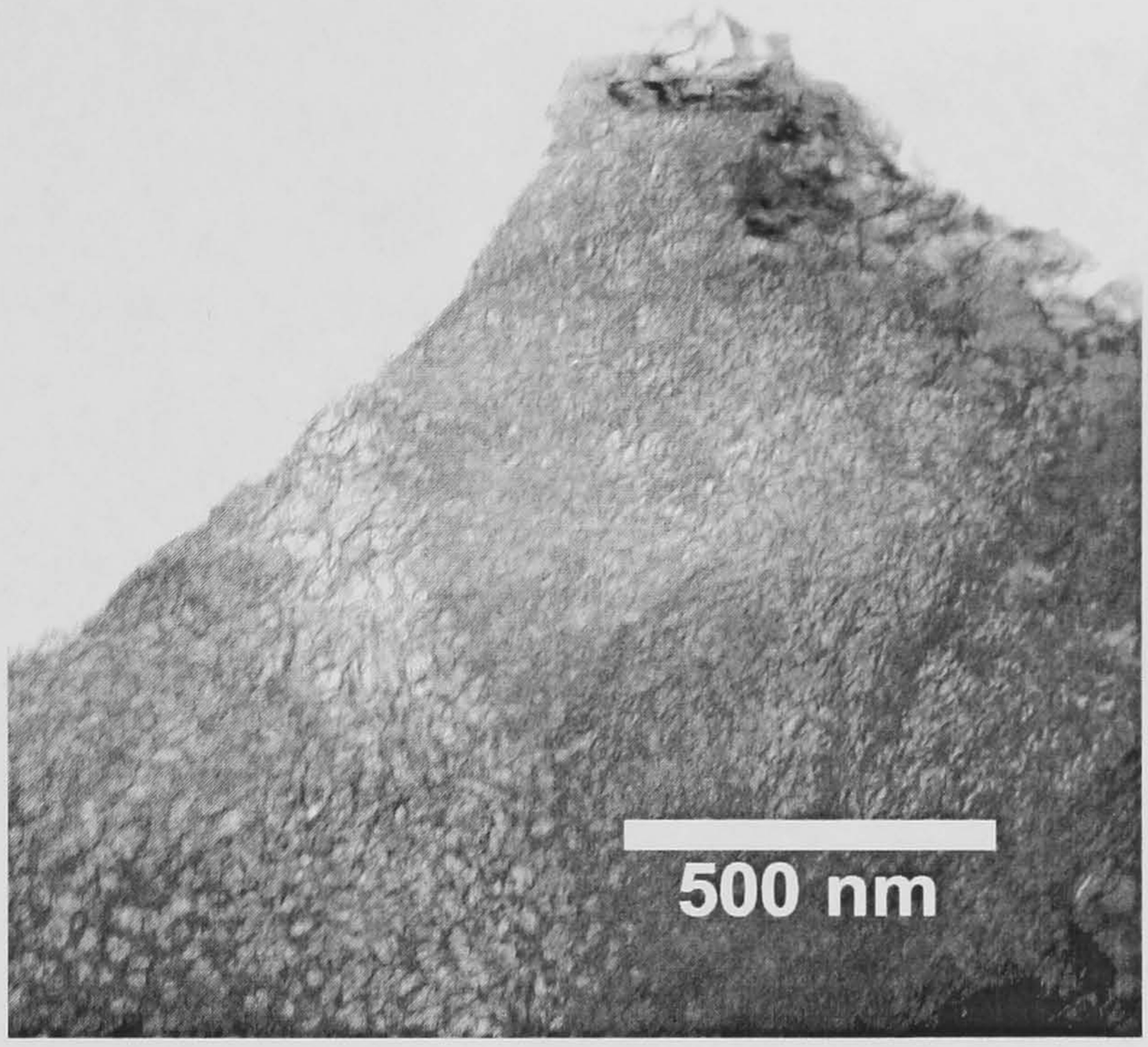


**Figure 5.14** – TEM micrograph showing details of the foil-like Op C-S-H formed in the KOH activated neat WPC paste, 1 month cured at 55°C.

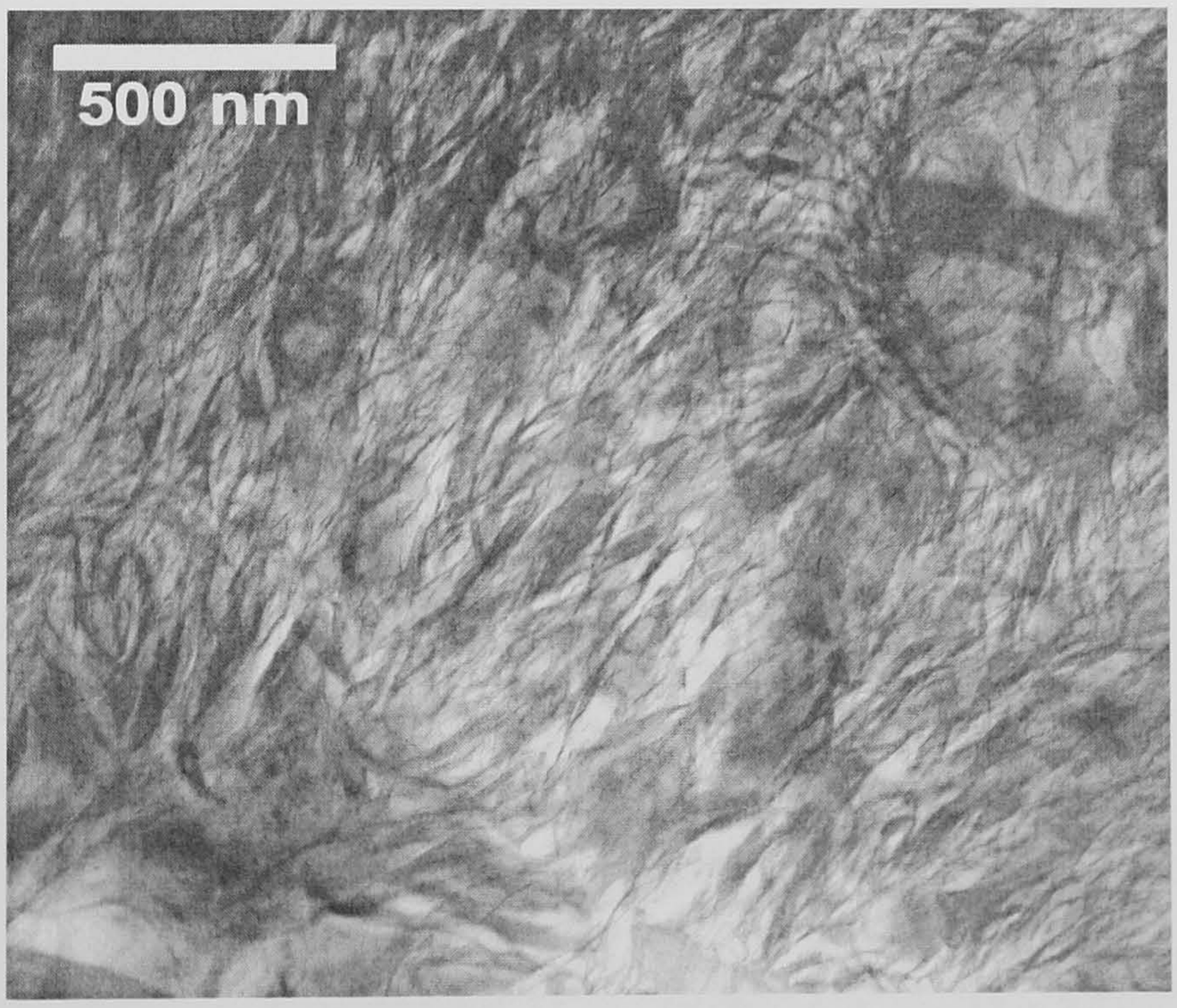


**Figure 5.15** – TEM micrograph showing details of the foil-like Op C-S-H formed in the KOH activated neat WPC paste, 1 month cured at 55°C.

The following micrographs illustrate CH finely intermixed with foil-like Op C-S-H and a partially reacted PFA particle.

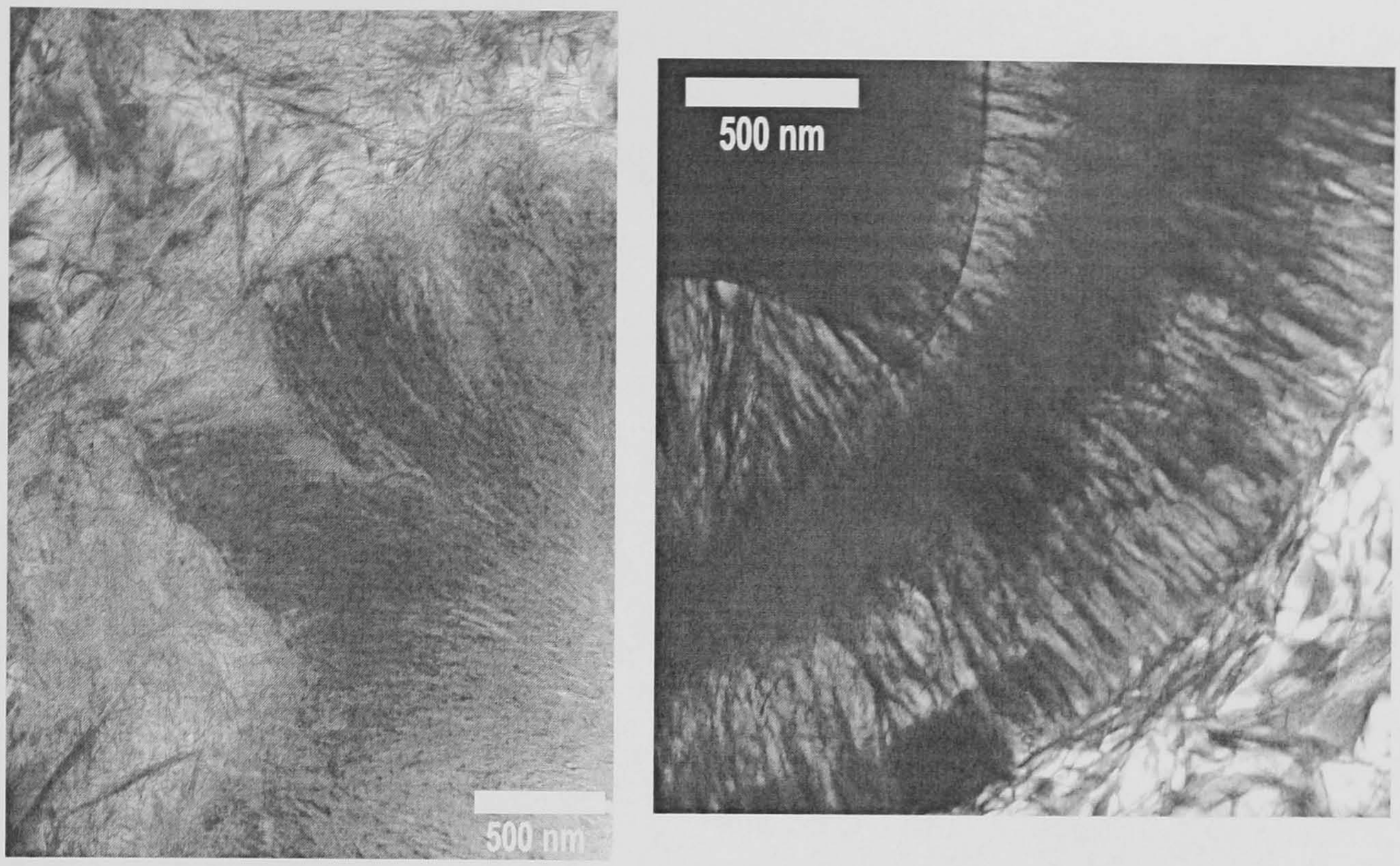


**Figure 5.16** – TEM micrographs showing details of the foil-like Op C-S-H intermixed with CH and a partially hydrated PFA particle in the KOH activated neat WPC paste, 1 month cured at 55°C.

EDX data atomic ratio plots for the KOH activated 30% PFA blended WPC paste, hydrated for one month at 55°C, are presented in Figure 5.17.

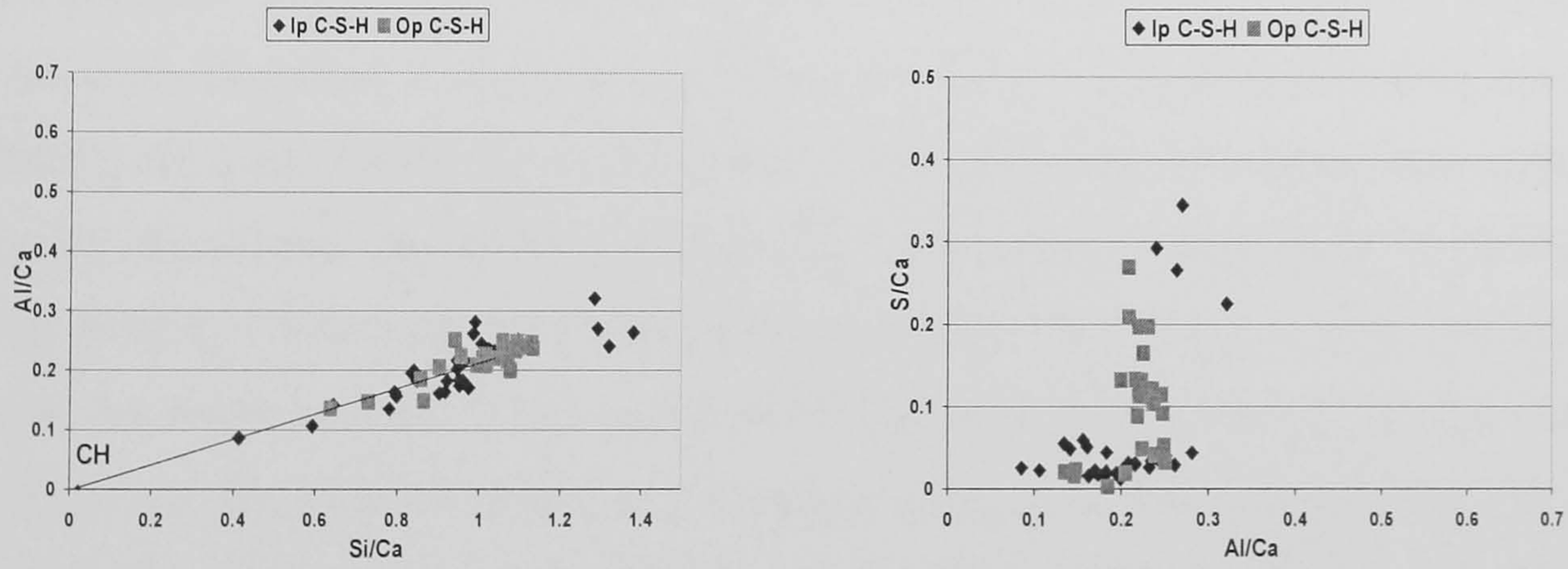


**Figure 5.17** – Al/Ca against Si/Ca (left) and S/Ca against Al/Ca (right) atomic ratio plots for the TEM-EDX phase analysis of the KOH activated 30% PFA blended cement paste after 1 month of hydration at 55°C.

The atomic ratio plots demonstrated that Ip and Op C-S-H were both finely intermixed with microcrystalline CH. Ip C-S-H presented a mean Ca/Si ratio of 1.12 (s = 0.32) and

Al/Si ratio of 0.211 (s = 0.028). The mean Ca/Si and Al/Si ratios for Op C-S-H were 1.02 (s =0.16) and 0.215 (s = 0.017), in that order. Table 5.9 resumes the mean Ca/Si and Al/Si ratios obtained for the systems studied using TEM-EDX.

**Table 5.9** – Mean Ca/Si and Al/Si atomic ratios obtained for C-S-H using TEM-EDX, for the water or KOH activated, neat WPC pastes and 30% PFA blended cement paste, 1 month cured at 55°C.

| | | Ca/Si | | | Ca/(Al+Si) | | Al/Si | |
|---|---|---|---|---|---|---|---|---|
| | | *N* | *mean* | *s* | *mean* | *s* | *mean* | *s* |
| **Wpc** | **Op** | 35 | 1.78 | 0.28 | 1.60 | 0.16 | 0.107 | 0.083 |
| | **Ip** | 40 | 1.56 | 0.16 | 1.44 | 0.15 | 0.084 | 0.021 |
| | **All** | 75 | 1.64 | 0.21 | 1.51 | 0.18 | 0.087 | 0.032 |
| **Kwpc** | **Op** | 44 | 1.50 | 0.28 | 1.37 | 0.11 | 0.096 | 0.019 |
| | **Ip** | 30 | 1.28 | 0.05 | 1.17 | 0.05 | 0.093 | 0.012 |
| | **All** | 74 | 1.40 | 0.14 | 1.29 | 0.13 | 0.090 | 0.013 |
| **Pfa30** | **Op** | 34 | 1.52 | 0.16 | 1.29 | 0.09 | 0.165 | 0.058 |
| | **Ip** | 26 | 1.42 | 0.18 | 1.21 | 0.18 | 0.178 | 0.059 |
| | **All** | 60 | 1.46 | 0.16 | 1.25 | 0.14 | 0.164 | 0.048 |
| **Kpfa30** | **Op** | 24 | 1.02 | 0.16 | 0.84 | 0.13 | 0.215 | 0.017 |
| | **Ip** | 30 | 1.12 | 0.32 | 0.92 | 0.27 | 0.211 | 0.028 |
| | **All** | 54 | 1.07 | 0.26 | 0.89 | 0.22 | 0.213 | 0.023 |

Generally, as shown in the above table, the mean Ca/Si ratio found for Op C-S-H was higher than that for Ip C-S-H. Op C-S-H morphology changed according to its Ca/Si: the decrease of the Ca/Si changed the fibrillar morphology to a foil-like morphology. The mean Ca/Si and Ca/(Al+Si) atomic ratios of the Ip C-S-H were in both neat pastes statistically significantly lower than those of the Op C-S-H. The mean value of the mean Ca/(Al+Si) atomic ratio of the C-S-H present in the alkaline paste (1.29, s = 0.13) is also significantly lower than with water activation (1.51, s = 0.18), which was consistent with the lower amount of CH in the water activated paste (Table 5.3). The same was verified in the blended systems. Regarding KOH activation, intuitively, one would expect the smaller average crystal size of the CH to lead to a smaller cluster in the SEM-EDX data than that with water activation (Appendix C). However, in contrast to the water activated neat and blended cement pastes, almost all the CH in the alkaline pastes was in fact intimately mixed with C-S-H, ranging from small microcrystals embedded in C-S-H to large CH-rich regions that had small amounts of C-S-H interstratified between layers of CH; such intermixing resulted in the wide range of Si/Ca atomic ratio observed in both the SEM-EDX and TEM-EDX data. Comparing the

mean Ca/Si atomic ratio found for Ip and Op C-S-H in the neat and blended pastes, PFA replacement decreased the mean Ca/Si ratio. There was no difference between the mean Al/Si atomic ratios of the Ip and Op C-S-H in the neat pastes and as well as in the blended cement pastes. Due to more available aluminium provided by the PFA replacement and consequently, Ip and Op C-S-H had higher mean Al/Si atomic ratios.

Table 5.10 resumes TEM-EDX, SEM-EDX and MAS NMR experimental results found for the water and KOH activated neat and 30% PFA blended WPC pastes cured for one month at 55°C.

**Table 5.10** – Mean Ca/Si and Al/Si atomic ratios obtained for C-S-H using TEM-EDX, SEM-EDX and MAS NMR, for the water or KOH activated, neat WPC pastes and 30% PFA blended cement paste, 1 month cured at 55°C.

| | All Ca/Si | Ca/Si (SEM) | All Al/Si | Al/Si (SEM) | Al/Si (NMR) |
|---|---|---|---|---|---|
| **Wpc** | 1.64 | 1.93 | 0.087 | 0.106 | 0.095 |
| **Kwpc** | 1.40 | 2.66 | 0.090 | 0.098 | 0.103 |
| **Pfa30** | 1.46 | 1.73 | 0.164 | 0.325 | 0.181 |
| **Kpfa30** | 1.07 | 1.62 | 0.213 | 0.272 | 0.247 |

Comparing the mean Ca/Si and Al/Si ratios using TEM-EDX and SEM-EDX, it was concluded that due to the different volume interaction verified in both techniques, SEM-EDX analysis always led to higher values. It was noted in Section 5.5 that the mean Al/Ca atomic ratio against the mean Si/Ca atomic ratio plot for the water activated neat paste (Appendix C) was very similar to data reported by Escalante-Garcia and Sharp[134] for Ip C-S-H. Those authors considered that such clusters of analyses corresponded to essentially pure C-S-H. However, comparison of the SEM-EDX data with the TEM-EDX showed that in this case it was unlikely that the considered cluster was due solely to C-S-H; the difference between the mean values for the Ca/Si atomic ratios determined by SEM-EDX and TEM-EDX is statistically extremely significant, so the SEM-EDX data would appear to be due to C-S-H intermixed with other phases, in particular CH: that is, that many crystals of CH and other hydration products were sufficiently small compared with the size of the X-ray generation volume - and evenly distributed - that the intermixture of phases in the cluster of analyses observed by SEM-EDX, which understandably could be interpreted as being due to "pure" C-S-H. A good

agreement was found between the mean Al/Si atomic ratios obtained using TEM-EDX and $^{29}$Si MAS NMR, bearing in mind that in the first technique, chemical composition analysis is not free of phase intermixing and that MAS NMR is a bulk technique.

Finally, it was also necessary to compare the TEM-EDX data obtained for these systems cured at 55°C, with that found for these pastes cured at 25°C. Table 5.11 resumes those experimental results.

**Table 5.11** – Comparison between the mean Ca/Si and Al/Si atomic ratios obtained for the cement-based studied systems after 1 month cured at 25°C and 55°C.

| | **Ip Ca/Si (25°)** | **Ip Ca/Si (55°)** | **Op Ca/Si (25°)** | **Op Ca/Si (55°)** | **Ip Al/Si (25°)** | **Ip Al/Si (55°)** | **Op Al/Si (25°)** | **Op Al/Si (55°)** |
|---|---|---|---|---|---|---|---|---|
| **Wpc** | 1.75 | 1.56 | 2.00 | 1.78 | 0.075 | 0.084 | 0.114 | 0.107 |
| **Kwpc** | 1.76 | 1.28 | 1.24 | 1.50 | 0.101 | 0.093 | 0.120 | 0.096 |
| **Pfa30** | 1.34 | 1.12 | 1.62 | 1.02 | 0.113 | 0.211 | 0.186 | 0.215 |

From the presented data, it was concluded that, in all the systems, the Ip C-S-H mean Ca/Si ratio decreased with higher curing temperature. Op C-S-H mean Ca/Si ratio and Ip C-S-H mean Al/Si ratio decreased in the water activated systems, after curing at 55°C. Finally, Op C-S-H mean Al/Si ratio decreased in the neat cement pastes with higher curing temperature but increased in the water activated blend.

In summary, TEM-EDX allowed characterisation of Ip and Op C-S-H morphology and it was concluded that with higher curing temperature, they became coarser. It also demonstrated that CH and AFt-type phases were finely intermixed with Ip C-S-H and AFm-type phases with Op C-S-H. In the 30% PFA blended cement paste, hydrogarnet-type phases were formed and intermixed with C-S-H, which is not often observed in WPC pastes. Some agreement was found between the mean Ca/Si ratios obtained using SEM-EDX and TEM-EDX. Good agreement was found between the mean values for the Al/Si atomic ratios, when using TEM-EDX and MAS NMR.

### 5.6.2 – T/J and T/CH-based models for the structure of C-S-H

The next table summarises data that was used for application of the different structural models for the TEM-EDX analysed systems.

**Table 5.12** – Experimental data used in Al/Ca against Si/Ca atomic plots discussing the applicability of the T/CH and T/J structural models for C-S-H, in the systems cured at 55°C.

| | Ip Ca/Si | Op Ca/Si | Ip Al/Si | Op Al/Si | Al/Si (NMR) | MCL | %B |
|---|---|---|---|---|---|---|---|
| **Wpc** | 1.56 | 1.78 | 0.084 | 0.107 | 0.095 | 6.5 | 38 |
| **Kwpc** | 1.28 | 1.50 | 0.093 | 0.096 | 0.103 | 5.2 | 46 |
| **Pfa30** | 1.42 | 1.52 | 0.178 | 0.165 | 0.181 | 12.4 | 55 |
| **Kpfa30** | 1.12 | 1.02 | 0.211 | 0.215 | 0.247 | 10.7 | 73 |

Figure 5.18 shows Ip and Op C-S-H raw data in Al/Ca against Si/Ca atomic ratio plot considering the T/J and T/CH structural models.

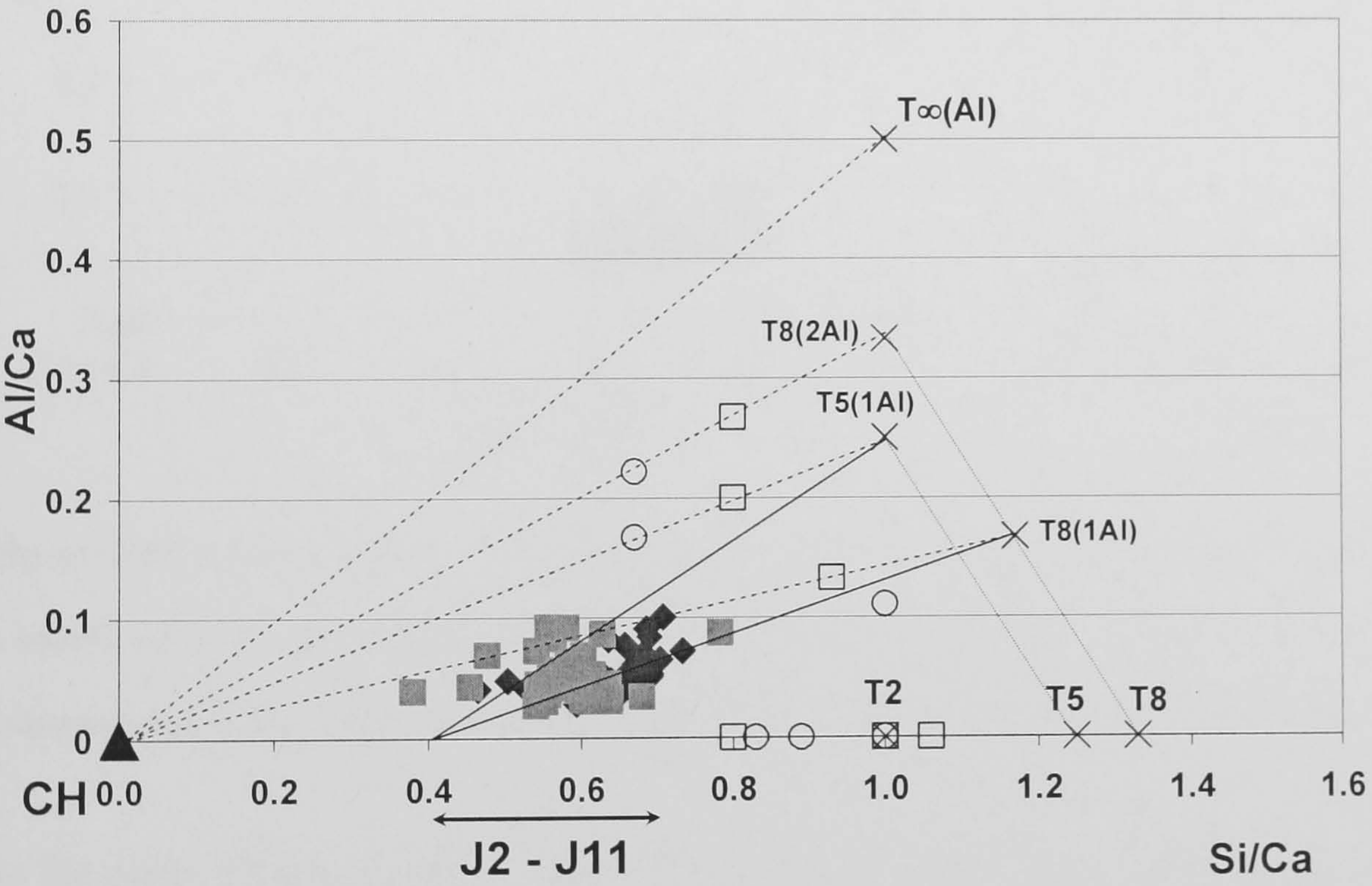


**Figure 5.18** – Al/Ca against Si/Ca atomic plot for the water activated neat WPC paste cured for 1 month at 55°C, accounting with T/J and T/CH viewpoints (◆ Ip C-S-H, ■ Op C-S-H, O unprotonated units, □ half protonated, X fully protonated, T∞ tobermorite, --- T/CH, — T/J).

From evaluation of the above plot, it was concluded that the T/J point of view was consistent with experimental data. The dashed lines represent T/CH viewpoint and it was observed that both Ip and Op C-S-H corresponding points were not distributed

along the trendline between CH and T8(1Al), and CH and T5(1Al). Ip and Op C-S-H data was mainly distributed around the mean Si/Ca for jennite-based units and most of them distributed between the trendline from T5(1Al) and T8(1Al) to J2.

The following figure shows the Al/Ca against Si/Ca atomic ratio plot considering the T/CH and T/J models for the KOH activated neat WPC paste, one month cured at 55°C.

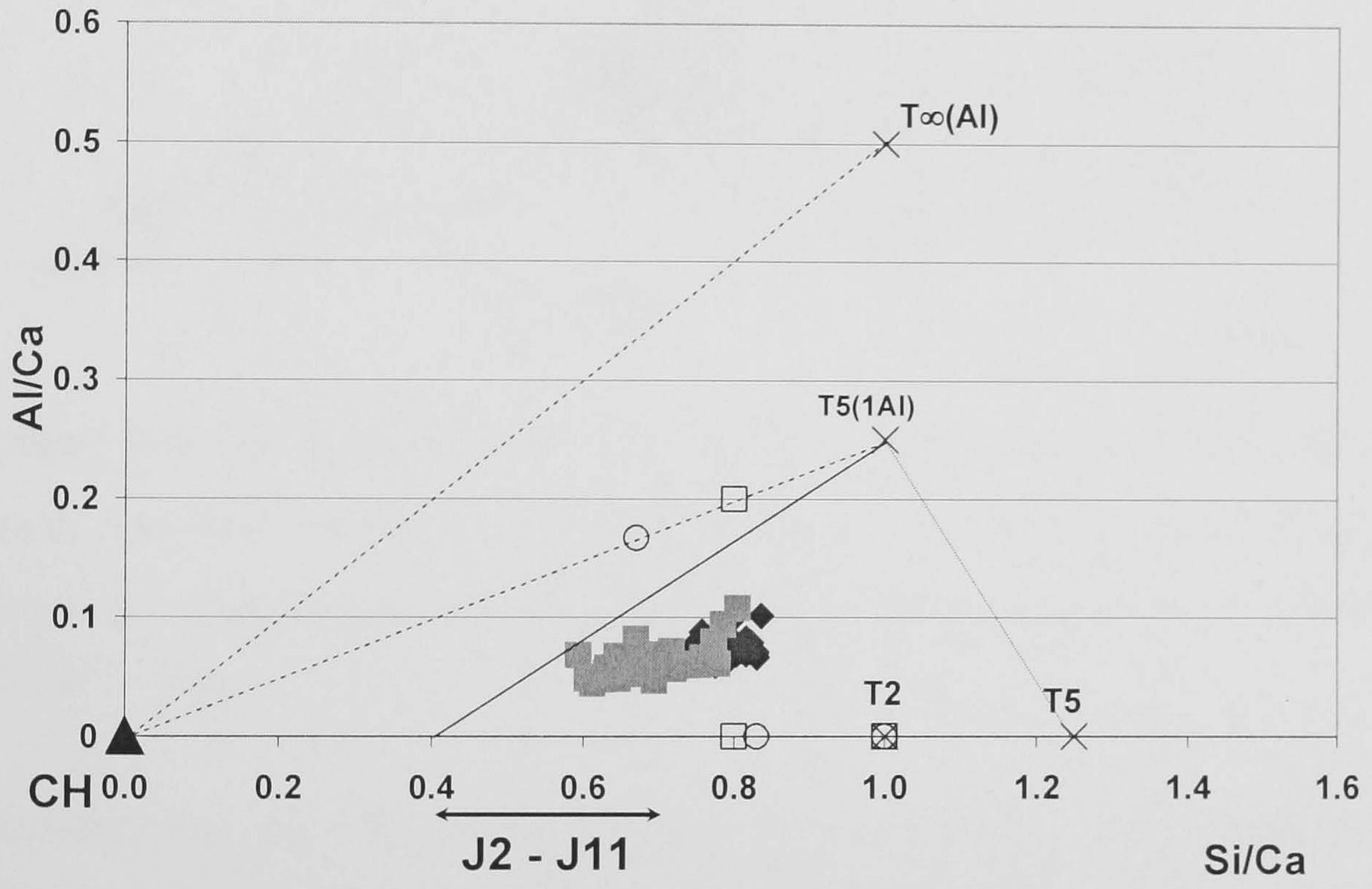


**Figure 5.19** – Al/Ca against Si/Ca atomic plot for the KOH activated neat WPC paste cured for 1 month at 55°C, accounting with T/J and T/CH viewpoints (♦ Ip C-S-H, ■ Op C-S-H, O unprotonated units, □ half protonated, X fully protonated, T∞ tobermorite, --- T/CH, — T/J).

As the above figure illustrates, C-S-H data was consistent with T/CH viewpoint because most of the data was consistent with trendlines in the direction of CH, and not on the trendline from T5(1Al) to J2.

Figure 5.20 shows the application of the two models to experimental data obtained for the water activated 30% PFA blended system, one month cured at 55°C.

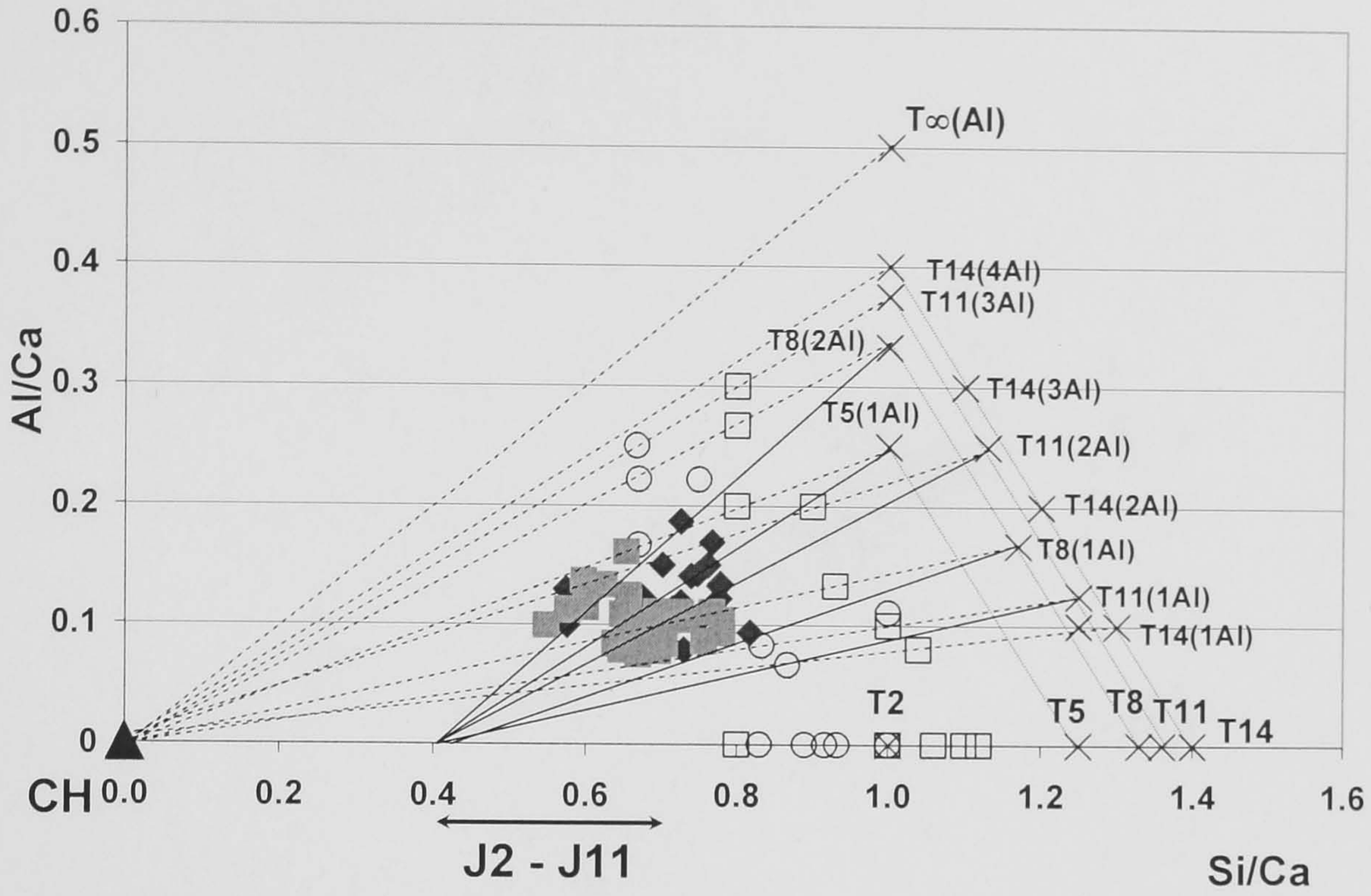


**Figure 5.20** – Al/Ca against Si/Ca atomic plot for the water activated 30% PFA blended WPC paste cured for 1 month at 55°C, accounting with T/J and T/CH viewpoints (◆ Ip C-S-H, ■ Op C-S-H, O unprotonated units, □ half protonated, X fully protonated, T∞ tobermorite, --- T/CH, — T/J).

Although data was more scattered than in neat systems and it was consistent with both T/J and T/CH viewpoints, as shown by the distribution of the data around trendlines in the direction of J2 from T11(1Al), T11(2Al), T8(1Al), T8(2Al) and T5(1Al). It could also be considered that some of the data was consistent with trendlines going from tobermorite-based units to CH.

Finally, the next figure shows the atomic ratio plot for the KOH activated 30% PFA blended WPC, cured for one month at 55°C.

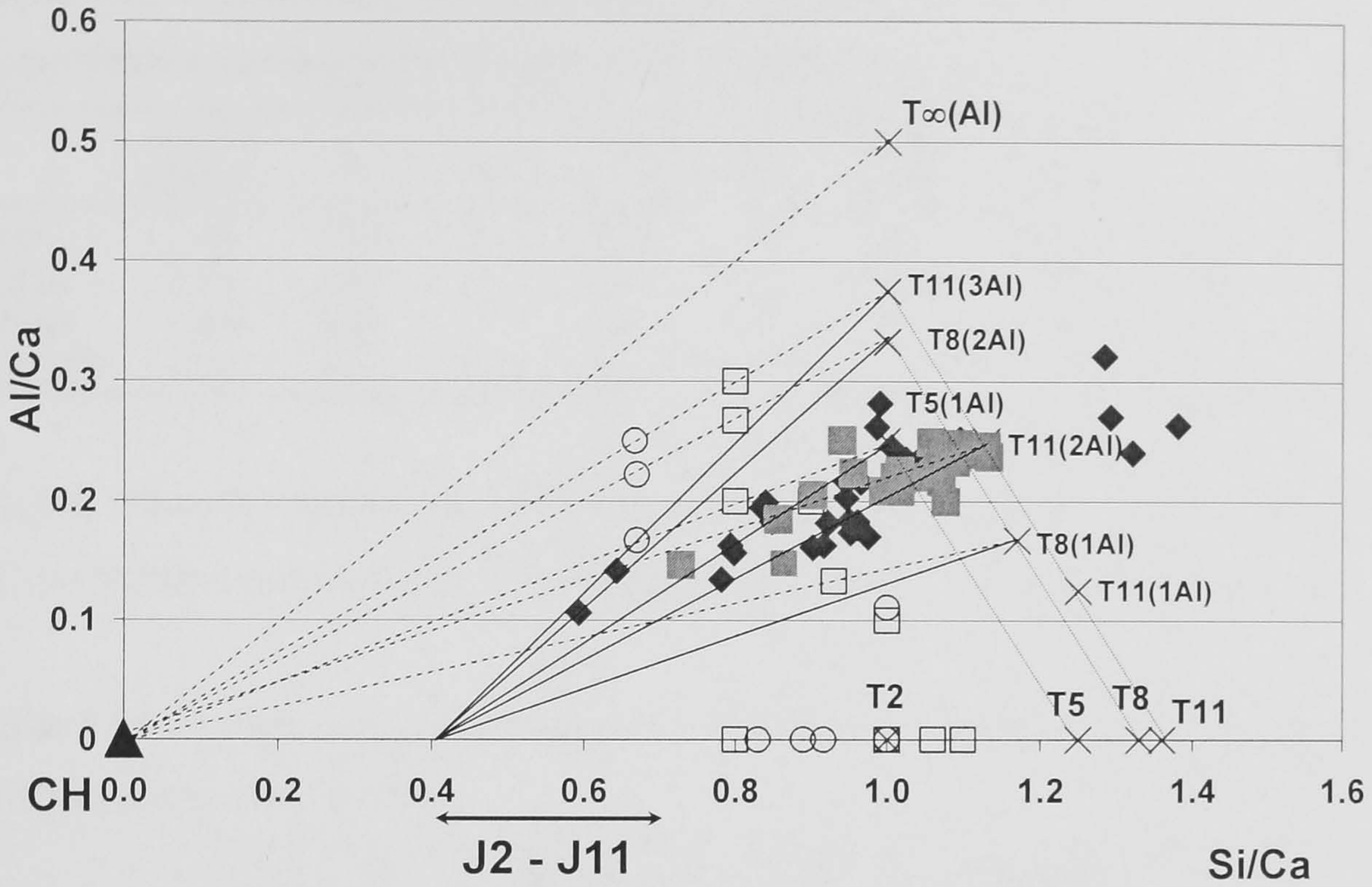


**Figure 5.21** – Al/Ca against Si/Ca atomic plot for the KOH activated 30% PFA blended WPC paste cured for 1 month at 55°C, accounting with T/J and T/CH viewpoints (♦ Ip C-S-H, ■ Op C-S-H, O unprotonated units, □ half protonated, X fully protonated, T∞ tobermorite, --- T/CH, — T/J).

It was concluded that most of the data, especially Op C-S-H, was consistent with the trendline from T11(2Al) in the direction of J2 but also in the direction of CH. The same was verified for the tie line from T5(1Al) to J2 or CH. Therefore, experimental data for this system was consistent with both T/J and T/CH viewpoints.

## 5.7 - C-S-H STRUCTURAL-CHEMICAL COMPOSITION

C-S-H chemical composition can be easily determined according to both T/J and T/CH viewpoints and using TEM-EDX and MAS NMR data. Using the equations 4.2 to 4.7 (Chapter IV), the structural-chemical composition of C-S-H was determined and Table 5.13 resumes the data used in the calculations:

**Table 5.13** – TEM-EDX and MAS NMR data used in the determination of C-S-H chemical composition according to the T/J and T/CH structural viewpoints for the systems cured at 55°C.

| | Ca/Si (TEM) | *y* | *w* | *y'* | w' | Al/Si (TEM) | Al/Si (NMR) | *a* | MCL (3n-1) | *n* |
|---|---|---|---|---|---|---|---|---|---|---|
| **Wpc** | 1.64 | 3.80 | 0 | 3.59 | 0 | 0.087 | 0.095 | 0.08 | 6.5 | 1.4 |
| **Kwpc** | 1.40 | 2.67 | 0 | 2.47 | 0 | 0.090 | 0.103 | 0.08 | 5.2 | 2.1 |
| **Pfa30** | 1.46 | 2.92 | 0 | 2.5 | 0 | 0.164 | 0.181 | 0.14 | 12.4 | 4.5 |
| **Kpfa30** | 1.07 | 0.9 | 4.18 | 0.43 | 5.97 | 0.213 | 0.247 | 0.18 | 10.7 | 3.8 |

Again, minimum degree of protonation was considered. C-S-H chemical composition determined according to the T/J structural point of view is given in Table 5.14.

**Table 5.14** – C-S-H chemical composition determined according to the T/J structural viewpoint for the systems cured at 55°C.

| | T/J (minimum degree of protonation) |
|---|---|
| **Wpc** | $\{Ca_5(Si_{0.91}Al_{0.09})_{6.5}O_{20.5}\}\cdot(OH)_{3.7}\cdot Ca_{4.6}\cdot mH_2O$ |
| **Kwpc** | $\{Ca_{4.13}(Si_{0.91}Al_{0.09})_{5.2}O_{16.6}\}\cdot K_{0.47}\cdot(OH)_{1.21}\cdot Ca_{2.67}\cdot mH_2O$ |
| **Pfa30** | $\{Ca_9(Si_{0.86}Al_{0.14})_{13.4}O_{38.5}\}\cdot(OH)_{4.14}\cdot Ca_{13.1}\cdot mH_2O$ |
| **Kpfa30** | $\{Ca_{7.6}H_{4.2}(Si_{0.86}Al_{0.14})_{10.7}O_{34.2}\}\cdot K_{1.9}\cdot Ca_{3.4}\cdot mH_2O$ |

As seen in the previous chapter, the chemical composition inside the brackets indicates the tobermorite-based skeleton of C-S-H. The presence of hydroxyl groups outside the brackets indicates that there must be some jennite-like structure besides tobermorite-like units. In the alkaline neat paste, it was assumed that substitution of $Si^{4+}$ by $Al^{3+}$ is charge balanced entirely by $K^+$ ions. The structure of C-S-H can also be reorganised according to the T/CH viewpoint, resumed in Table 5.15.

**Table 5.15** – C-S-H chemical composition determined according to the T/CH structural viewpoint for the systems cured at 55°C.

| | T/CH (minimum degree of protonation) |
|---|---|
| **Wpc** | $Ca_{7.5}(Si_{0.91}Al_{0.09})_{6.5}O_{20.5}\cdot Ca_{0.3}\cdot 1.84Ca(OH)_2\cdot mH_2O$ |
| **Kwpc** | $Ca_{6.2}(Si_{0.91}Al_{0.09})_{5.2}O_{16.6}\cdot K_{0.47}\cdot 0.61Ca(OH)_2\cdot mH_2O$ |
| **Pfa30** | $Ca_{13.5}(Si_{0.86}Al_{0.14})_{13.4}O_{38.5}\cdot Ca_{0.94}\cdot 1.1Ca(OH)_2\cdot mH_2O$ |
| **Kpfa30** | $Ca_{8.4}H_6(Si_{0.86}Al_{0.14})_{10.7}O_{34.2}\cdot K_{1.9}\cdot mH_2O$ |

In the alkaline neat paste, the presence of hydroxyl groups outside the brackets again indicates that on the T/J viewpoint for the nanostructure of C-S-H, there must be some J-like structure. However, in this case, the distribution of TEM-EDX (Figure 5.19)

indicated clearly that the T/CH viewpoint was more adequate than the T/J, so the formula for an average structural unit more appropriate should be the one in Table 5.8. Interestingly, the K/Ca atomic ratio on that formula (K/Ca=0.07) is very similar to the atomic ratio given by the regression equation in Figure 5.8 for C-S-H. (i.e., the value at S/Ca=0, on the assumption that all sulfur was adsorbed on the C-S-H as sulfate ions balanced by potassium ions). Regarding the pfa30 paste, the structural formulas show that on the T/J point of view, there was some J-like contribution and on the T/CH point of view, there were also some CH units in "solid-solution". This is in very good agreement with both models as previously seen in Figure 5.20 where both models were consistent with the TEM-EDX data. Finally, considering the alkaline blended paste, the structural formulas showed that there were no jennite units present (T/J viewpoint) as well as CH "solid solution" units (T/CH viewpoint). However, Figure 5.21 shows that TEM-EDX data for this system was consistent with both models.

# VI – RESULTS AND DISCUSSION: CURING AT 85°C

The experimental results related to the systems cured at 85°C are presented and discussed in this chapter. The studied systems will be designated by the previously used notation.

## 6.1 – STA-EGA

The amount of CH present in the different systems cured at 85°C was estimated by STA-EGA. Figures 6.1 shows STA-EGA curve obtained for the water activated neat, after one month of hydration. EGA indicated that carbonation of the analysed samples did not occur and the main exotherms corresponding to C-S-H and CH around 120°C and 475°C, in that order.

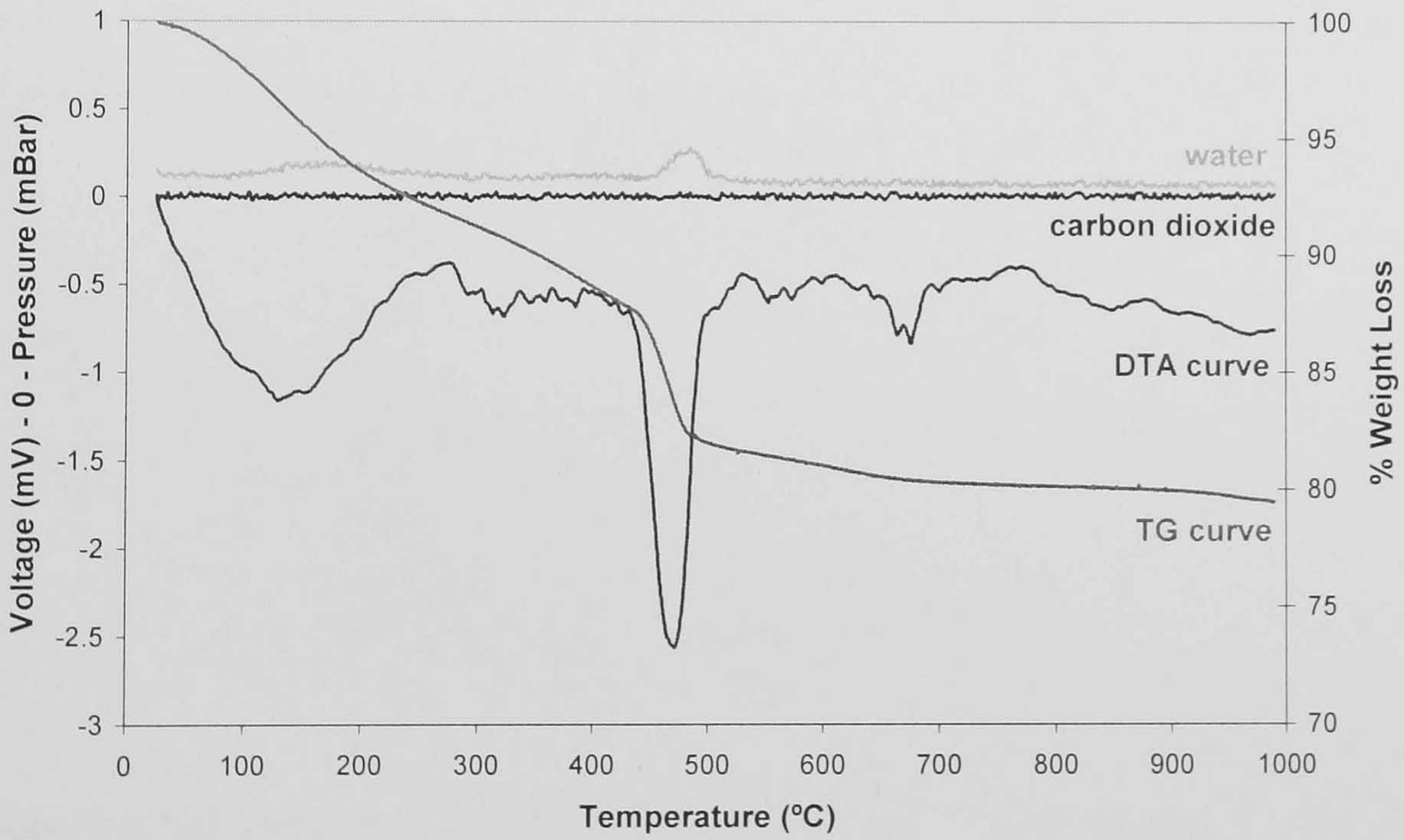


**Figure 6.1** – STA curve for the water activated neat WPC paste 1 month, cured at 85°C.

Estimated CH as percentage of ignited weight obtained for all the systems cured at 85°C, after one day and one month of hydration, is presented in Table 6.1.

**Table 6.1** – Estimated amount of CH, as percentage of ignited weight, present in the water and KOH activated neat and blended cement pastes cured at 85°C at 1 day and 1 month.

| | **1 day** | **1 month** |
|---|---|---|
| **WPC** | 25 | 25 |
| **KWPC** | 25 | 30 |
| **PFA30** | 11 | 8 |
| **KPFA30** | 2 | 6 |
| **PFA60** | 4 | 0 |
| **KPFA60** | 2 | 0 |

As mentioned in the previous chapters, the estimated amount of CH gives a good indication of the reaction extension but STA results are not conclusive by themselves or very accurate in quantitative terms.

The next table resumes the estimated amount of CH obtained at 25°C, 55°C and 85°C.

**Table 6.2** – Estimated amount of CH, as percentage of ignited weight, present in the water and KOH activated neat and blended cement pastes one month cured at 25°C, 55°C and 85°C.

| | **25°C** | **55°C** | **85°C** |
|---|---|---|---|
| **WPC** | 26 | 27 | 25 |
| **KWPC** | 31 | 35 | 30 |
| **PFA30** | 20 | 13 | 8 |
| **KPFA30** | 17 | 11 | 6 |
| **PFA60** | 11 | 6 | 0 |
| **KPFA60** | 5 | 3 | 0 |

Comparison between the STA results obtained at different temperatures clearly indicates that higher curing temperature increased the pozzolanic reaction rate and could also have affected the cement hydration rate.

## 6.2 – XRD

Appendix A includes the obtained XRD patterns for the neat and 30% PFA blended cement pastes, either water or KOH activated, and cured at 85°C for one day and one month. The results were very similar to those obtained for the same systems cured at 25°C and 55°C, i.e. the same type and number of phases were identified. However, additional phases were also identified in the diffractograms.

**Table 6.3** – Identified phases in the XRD patterns for the water and KOH neat and blended cement pastes cured 1 day and 1 month at 85°C.

| | **wpc** | **kwpc** | **pfa30** | **kpfa30** |
|---|---|---|---|---|
| **$C_3S$** | √ | √ | √ | √ |
| **β-$C_2S$** | √ | √ | √ | √ |
| **CH** | √ | X | √ | X |
| **Microcrystalline CH** | X | √ | X | √ |
| **Ettringite** | √ | X | X | X |
| **C-S-H (I)** | X | √ | X | √ |
| **Microcrystalline Hydrogarnet** | √ | X | √ | √ |
| **Arcanite** | X | √ | X | √ |
| **Quartz** | X | X | √ | √ |

By twenty eight days, in the water activated neat pastes, AFt and AFm-type phases were not present in sufficiently large quantities or with sufficiently large or ordered crystals to be detected by the technique. In the alkaline paste, the peaks for CH were broad indicating a small average crystal size, as observed previously for the alkaline samples in Chapters IV and V, as well as in other KOH activated systems[132]. However, the peaks were not all broadened to the same extent, indicating that the crystals were anisotropic. The crystalline phases present in the water activated pastes and in the alkaline blend included a significant quantity of a microcrystalline hydrogarnet phase.

## 6.3 – COMPRESSIVE STRENGTH

Compressive tests were carried out on mortars with the same chemical composition as the studied systems, cured at 85°C in an environmental chamber. The following table summarises the data obtained for the water and KOH activated neat and 30% PFA blended WPC pastes at one day and one month, cured at 85°C.

**Table 6.4** – Compressive strength data obtained for the neat and 30% PFA blended cement pastes after 1 day and 1 month, cured at 85°C.

| | | Compressive Strength (MPa) | *s* |
|---|---|---|---|
| **WPC** | **1 day** | 45.3 | 3.8 |
| | **1 month** | 54.0 | 7.7 |
| **KWPC** | **1 day** | 14.6 | 1.7 |
| | **1 month** | 23.9 | 11.4 |
| **PFA30** | **1 day** | 42.7 | 2.9 |
| | **1 month** | 43.4 | 14.5 |
| **KPFA30** | **1 day** | 27.6 | 1.3 |
| | **1 month** | 45.0 | 3.9 |

From the above table, it was concluded that compressive strength increased after one month of hydration. This was due to further developing of the microstructure that became more dense and packed. As hydration took place, the resulting hydration products, especially Op C-S-H filled in the interstitial space originally filled with water. Backscattered electron microscopy should provide some information regarding porosity of the different systems cured at 85°C.

The following table resumes the compressive strength experimental results obtained for all the studied systems, cured for one day and one month at 25°C, 55°C and 85°C.

**Table 6.5** – Compressive strength data obtained for all the studied systems cured for 1 day and 1 month, at 25°C, 55°C and 85°C.

| | | Compressive Strength (MPa) 1 day | Compressive Strength (MPa) 1 month |
|---|---|---|---|
| **WPC** | **25°C** | 20.1 | 72.4 |
| | **55°C** | 27.6 | 66.0 |
| | **85°C** | 45.3 | 54.0 |
| **KWPC** | **25°C** | 7.4 | 15.3 |
| | **55°C** | 10.0 | 18.1 |
| | **85°C** | 14.6 | 23.9 |
| **PFA30** | **25°C** | 10.9 | 49.2 |
| | **55°C** | 14.7 | 43.2 |
| | **85°C** | 42.7 | 43.4 |
| **KPFA30** | **25°C** | 2.9 | 7.5 |
| | **55°C** | 13.0 | 30.4 |
| | **85°C** | 27.6 | 45.0 |

Comparing these results, it was verified that increasing the curing temperature increased the compressive strength. However, by one month, that was not verified because there was no linear relationship between increasing hydration temperature and this physical property of the cement mortars. Therefore, although higher curing temperature probably accelerated cement hydration, it did not bring further enhanced strength to the tested mortar cubes. Again, it is necessary to bear in mind that accurate evaluation of the porosity should be conducted.

## 6.4 – SOLID STATE $^{29}$Si MAS NMR

Single pulse $^{29}$Si MAS NMR provides quantitative information on the silicate anion structure of the C-S-H gel. Quantification was achieved in the case of the neat WPC pastes but only semi-quantitative data was obtained for the 30% PFA blended systems. For the 60% PFA blended pastes, only qualitative analysis was conducted. The spectra are included in Appendix B. As seen in the neat systems cured at 25°C and 55°C the

deconvolution/fitting of the spectra for the same pastes cured at 85°C were very similar. $Q^0$ for the anhydrous WPC at -71 ppm (mainly the sharp peak component from belite), $Q^1$ for the chain-end group tetrahedra at -79 ppm, $Q^2$ for the middle-chain groups at -85 ppm and $Q^2(1Al)$ for the middle-chain groups where one of the adjacent tetrahedra is occupied by Al at -82 ppm (this substitution results in a down-field shift of around 3 ppm). Following previous studies and what was shown in Chapter IV, the chemical shift around -73.5 ppm was assigned to anhydrous $\gamma$-$C_2S$[133]. Table 6.6 summarises the data obtained from fitting of the spectra.

**Table 6.6** – $^{29}$Si MAS NMR quantitative data obtained for the neat cement pastes 1 day and 1 month, cured at 85°C.

| | **Water activated** | | **KOH activated** | |
|---|---|---|---|---|
| | **1 day** | **1 month** | **1 day** | **1 month** |
| **MCL** | 8.2 | 9.9 | 5.5 | 7.4 |
| **Al/Si** | 0.108 | 0.099 | 0.120 | 0.118 |
| **% Anhydrous cement** | 20.4 | 5.0 | 39.6 | 3.2 |
| **% Cement reacted** | 79.6 | 95.0 | 60.4 | 96.8 |
| **% $\gamma$-$C_2S$** | - | 1.8 | - | 2.1 |
| **% $Q^1$** | 21.6 | 20.7 | 24.7 | 28.6 |
| **% $Q^2(1Al)$** | 17.2 | 18.5 | 14.4 | 22.4 |
| **% $Q^2$** | 40.8 | 54.1 | 21.3 | 43.7 |
| **% $Q^3$** | - | - | - | - |
| **% B** | 39 | 34 | 50 | 43 |
| **% $B_{water}/B_{KOH}$** | 77 | 78 | - | - |
| **CH as % of ig. wt. (STA)** | 25 | 25 | 25 | 30 |

After one day of hydration, part of the cement reacted and the silicate anion of the C-S-H gel was polymerised. Following one month, most of the anhydrous cement reacted and further polymerisation of C-S-H occurred. MCL increased slightly as well as the relative intensity of $Q^2$. Octamers, pentamers, dimers and mixtures of those structural units were present in both pastes at one day and one month of hydration. Aluminium substitution in tetrahedral places in C-S-H occurred but the relative intensity of $Q^2(1Al)$ and the Al/Si ratio were more or less the same at one day and one month. %B and % $B_{water}/B_{KOH}$ also confirm that the amount of tetrahedra aluminium substituted was mainly the same for both systems at both ages. It should be pointed out that the degree of hydration after one month in the water activated sample was the same as that found in the same system cured at 25°C, after one year of hydration (Table 4.5). STA

estimation of the amount of CH present in each system was in poor agreement with MAS NMR observations because more cement reacted with time and the estimated amount of CH was constant at one day and one month. As expected in the case of alkaline activation[78], the spectra were better deconvoluted due to higher degree of structural order induced by KOH activation. $\gamma$-$C_2S$ corresponding resonance was also present and had the same relative intensity in both systems[133]. Comparing the water and KOH activated neat WPC pastes, it was concluded that alkaline activation led shorter mean aluminosilicate chain lengths, and that the relative intensity of $Q^2$ was slightly lower than that in the water activated WPC paste. However, alkaline activation did not affect the kinetics of cement reaction. $Q^2$(1Al) and the Al/Si ratio were higher in the alkaline paste. STA data showed that more CH was produced after one month, when more cement reacted.

Before analysing the spectra and corresponding data for the 30% PFA blended cement pastes, a few considerations were taken in account. Alkaline cements can be considered as an alternative to Portland cements. Two types of cementitious materials are produced by alkaline activation: a first type based on Si and Al composition; a second type based on Si and Ca, that includes alkali activation of fly ashes[141]. Some previous studies showed that zeolites were formed but the nature of the aluminosilicate obtained from the alkali activation depends on many parameters like alkalinity, temperature, particle size and silicon source[141]. Therefore, curing at 85°C the KOH activated fly ash blends could easily lead to zeolites (or zeolites precursors) formation. However, other experimental data for those samples indicated that no such type of phases was obtained. The XRD patterns for the one day and one month KOH activated 30% PFA blend gave evidence for microcrystalline phases like CH, hydrogarnet and C-S-H (I). The latter is a semi-crystalline C-S-H phase with a layered structure related to tobermorite with linear silicate chains ($Q^1$ and $Q^2$). TEM-EDX data also did not give evidence for the presence of zeolites or zeolites precursors. Consequently, it seemed most sensible to fit the NMR spectra on the basis of the phases known to present (i.e. fit with $Q^1$, $Q^2$, $Q^2$(1Al)), rather than to speculate the presence of an amorphous zeolite precursor.

In the spectra (Appendix B), $Q^3$ represents branching sites and $Q^4$ cross-linking sites (anhydrous fly ash) in a three dimensional framework were identified. There was an additional peak at around -89 ppm in the spectrum for the KOH activated 30% PFA blend after one month of hydration. This peak could have indicated the presence of an amorphous zeolite precursor[141]. Nevertheless, the peak was assigned to silicon present in a hydrogarnet phase: hydrogarnet was detected by XRD (Appendix A) and a peak at this chemical shift has been reported recently for hydrogarnet[142]. The following table presents the semi-quantitative NMR data obtained for the water and KOH activated 30% PFA blended pastes.

**Table 6.7** – $^{29}$Si MAS NMR semi-quantitative data obtained for the 30% PFA blended cement pastes 1 day and 1 month, cured at 85°C.

| | **Water activated** | | **KOH activated** | |
|---|---|---|---|---|
| | **1 day** | **1 month** | **1 day** | **1 month** |
| **MCL** | 19.7 | 16.6 | 12.6 | 11.7 |
| **Al/Si** | 0.187 | 0.139 | 0.274 | 0.226 |
| **% Anhydrous cement** | 19.6 | 7.9 | 52.4 | 21.1 |
| **% $\gamma$-$C_2S$** | - | 1.0 | - | 4.1 |
| **% $Q^1$** | 8.5 | 11.1 | 7.6 | 14.9 |
| **% $Q^2$(1Al)** | 26.3 | 22.5 | 20.7 | 32.3 |
| **% $Q^2$** | 35.5 | 47.2 | 9.5 | 24.2 |
| **% $Q^3$** | - | - | - | 0.9 |
| **% Anhydrous PFA** | 10.1 | 13.4 | 9.7 | 2.4 |
| **% B** | 53 | 42 | 77 | 67 |
| **% $B_{water}/B_{KOH}$** | 69 | 63 | - | - |
| **CH as % of ig. wt. (STA)** | 11 | 8 | 2 | 6 |

Generally, both systems had higher MCL and Al/Si ratios because PFA replacement provided more available aluminium to be incorporated in the C-S-H structure. After one month of hydration, more cement appears to have reacted in the water activated sample than in the alkaline blend. On the other hand, more PFA reacted in the KOH system, well supported by STA-EGA evidence. It appeared that alkaline reaction inhibited the cement hydration. In the water activated blend, $Q^2$ was the most intense peak indicating that C-S-H had a longer chain, whereas the most intense peak in the kpfa30 was $Q^2$(1Al) indicating that although MCL was shorter, the chains were more aluminium substituted as the calculated Al/Si ratio and the %B confirm. Considering aluminium substitution, %B decreased very slightly after one month but $\%B_{water}/B_{KOH}$ was mainly

the same at both ages. The same ratio $\%B_{water}/B_{KOH}$ showed that alkaline activation produced more Al substitution in the blended system than in the neat system. Tables 6.8 and 6.9 show data comparison between the water activated samples and that between the alkaline pastes.

**Table 6.8** – $^{29}Si$ MAS NMR data comparison between water activated neat and 30% PFA blended cement pastes 1 month, cured at 85°C.

| | **Neat WPC** | **30% PFA blended WPC** |
|---|---|---|
| **MCL** | 9.9 | 16.6 |
| **% Anhydrous cement** | 5.0 | 7.9 |
| **Al/Si** | 0.099 | 0.139 |
| **% $Q^2$(1Al)** | 18.5 | 22.5 |
| **CH as % of ig. wt. (STA)** | 25 | 8 |

As observed in the previous chapter, PFA substitution affected the amount of reacted cement and increased polymerisation of C-S-H because the mean aluminosilicate chain length was higher. PFA substitution also resulted in the increase of the Al/Si ratio and relative intensity of $Q^2$(1Al). STA results showed that pozzolanic reaction between PFA and CH took place. Table 6.9 shows the same comparable parameters calculated for the KOH neat and 30% PFA blended WPC pastes, after one month of hydration at 85°C.

**Table 6.9** – $^{29}Si$ MAS NMR data comparison between KOH activated neat and 30% PFA blended cement pastes 1 month, cured at 85°C.

| | **Neat WPC** | **30% PFA blended WPC** |
|---|---|---|
| **MCL** | 7.4 | 11.7 |
| **% Anhydrous cement** | 3.2 | 21.1 |
| **Al/Si** | 0.118 | 0.226 |
| **% $Q^2$(1Al)** | 22.4 | 32.3 |
| **CH as % of ig. wt. (STA)** | 30 | 6 |

The effect of PFA replacement is clearly shown in the above table. The MCL was higher in the blend as well as the mean Al/Si ratio and relative intensity of $Q^2$(1Al). After one month of hydration, more anhydrous cement was left in the blended sample

which perhaps indicates that KOH activation did not increase the rate of the cement hydration. Alkaline activation appears to have favoured the pozzolanic reaction because the estimated amount of CH present after one month was a lot less in the blended system than in the neat sample.

Ultimately, the MAS NMR results obtained at 85°C were compared with those at 25°C and 55°C. The results were compared at one month of hydration. Starting with the water activated neat and blended systems, Table 6.10 resumes the key data obtained using MAS NMR.

**Table 6.10** – $^{29}$Si MAS NMR data comparison between water activated neat and 30% PFA blended cement pastes 1 month, cured at 25°C, 55°C and 85°C.

| | **WPC (25°C)** | **WPC (55°C)** | **WPC (85°C)** | **PFA30 (25°C)** | **PFA30 (55°C)** | **PFA30 (85°C)** |
|---|---|---|---|---|---|---|
| **MCL** | 3.3 | 6.5 | 9.9 | 3.6 | 12.4 | 16.6 |
| **% Anhydrous cement** | 19.8 | 9.6 | 5.0 | 14.3 | 12.5 | 7.9 |
| **Al/Si** | 0.056 | 0.095 | 0.099 | 0.070 | 0.181 | 0.139 |
| **% $Q^2$(1Al)** | 8.8 | 16.8 | 18.5 | 9.0 | 24.0 | 22.5 |
| **% B** | 40 | 62 | 34 | 43 | 74 | 42 |
| **CH (STA)** | 26 | 27 | 25 | 20 | 13 | 8 |

The above results show that the higher curing temperature, the more accelerated was the rate of cement hydration, as well as the rate of the pozzolanic reaction. Further polymerisation was also enhanced by higher curing temperature as the increase of MCL showed. The %B indicated that at 55°C the proportion of bridging tetrahedra occupied by aluminium was higher than that at the other curing temperatures. Table 6.11 summarises the MAS NMR results obtained for the alkaline neat and blended cement pastes cured for one month, at 25°C, 55°C and 85°C.

**Table 6.11** – $^{29}Si$ MAS NMR data comparison between KOH activated neat and 30% PFA blended cement pastes 1 month, cured at 25°C, 55°C and 85°C.

| | KWPC (25°C) | KWPC (55°C) | KWPC (85°C) | KPFA30 (25°C) | KPFA30 (55°C) | KPFA30 (85°C) |
|---|---|---|---|---|---|---|
| **MCL** | 3.4 | 5.2 | 7.4 | 4.2 | 10.7 | 11.7 |
| **% Anhydrous cement** | 22.6 | 6.9 | 3.2 | 12.0 | 19.3 | 21.1 |
| **Al/Si** | 0.093 | 0.103 | 0.118 | 0.145 | 0.247 | 0.226 |
| **% $Q^2$(1Al)** | 14.2 | 18.4 | 22.4 | 16.6 | 35.0 | 32.3 |
| **% B** | 63 | 46 | 43 | 32 | 73 | 67 |
| **CH (STA)** | 31 | 35 | 30 | 17 | 11 | 6 |

In a similar way to what was concluded before for Table 6.10, higher temperature increased MCL, the rate of cement hydration and the amount of aluminium present in the C-S-H aluminosilicate chain. The %B decreased with higher curing temperature in the neat paste but increased in the blended paste. At 55°C and 85°C, the %B was mainly the same for both systems. Generally, MAS NMR experimental results showed that the PFA replacement in a WPC system and higher curing temperature enhanced incorporation of aluminium substituting for central silicon in the C-S-H phase. In all systems, C-S-H polymerised as hydration took place and the cement hydration and pozzolanic reaction rates were generally increased by higher curing temperature.

## 6.5 – SEM-EDX

Backscattered electron images for the microstructure of the neat WPC paste water activated one day and one month, cured at 85°C, are presented in Appendix C. Low magnification images are shown on the left-hand side and higher magnification on the right-hand side. As observed in all systems cured at 55°C, the grey level of C-S-H was similar to that of CH and brighter than that formed in pastes cured at 25°C (Chapter IV) and at lower temperature, an observation consistent with other studies[103,138-140]. The microstructure was generally porous at one day but it also presented areas of quite higher density. This indicated that the distribution of the hydration products was less

homogeneous due to high curing temperature, which is in very good agreement with previous studies[100-102,105], where the effect of curing temperature on the microstructure in several cement-based systems were analysed using scanning electron microscopy. The authors concluded that increasing curing temperature led, generally, to coarsening of the hydration products, increased porosity and decreasing of the general uniformity of the microstructure. In fact, some of the studied systems in this chapter exhibited many areas with low and high porosity, i.e., porosity was not uniform in the whole microstructure. Higher curing temperature also increased the degree of hydration, as MAS NMR results demonstrated (Table 6.10), and increased the rate of the pozzolanic reaction. Finally, evaluating the effect of curing temperature on the microstructure of cement-based systems should be carried out using more than one experimental technique like scanning electron microscopy because extrapolated observations and/or conclusions can become misleading.

## 6.6 – TEM-EDX

### 6.6.1 – Morphology and Chemical Analysis

The systems cured at 85°C and studied using TEM-EDX were the water activated neat WPC and 30% PFA blended pastes, cured for one month. The following micrographs show the morphology found for the water activated neat WPC paste cured at 85°C for one month.

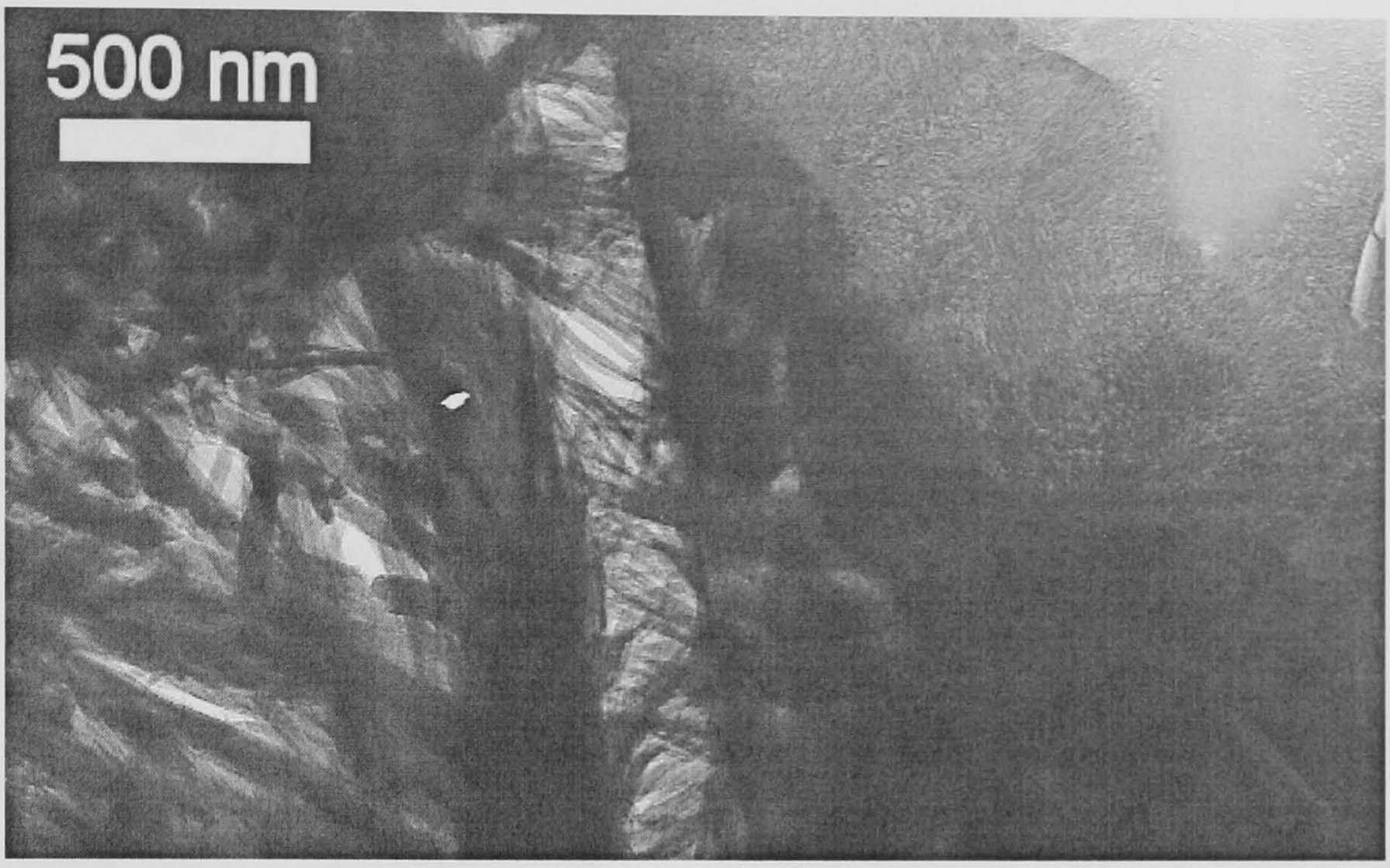


**Figure 6.2** – TEM micrograph showing the interface between fine and dense Ip C-S-H and coarse fibrillar Op C-S-H formed in the water activated neat WPC paste, 1 month cured at 85°C.

The previous micrograph shows the interface between Ip C-S-H Op C-S-H. Ip C-S-H had a fine scale homogeneous morphology already previously observed at 25°C in Chapter IV, and also in other Portland cement-based systems hydrated at 20°C.[72] Op C-S-H was similar to that formed at lower temperatures but it was coarser than at 55°C (Chapter V), which is in good agreement with earlier observations at higher curing temperature.[42] In this microstructure, large crystals of CH and AFm-type phases were identified. Small fully hydrated cement grains contained a less dense Ip C-S-H with a foil-like morphology typically observed for Op C-S-H in other cement based systems.[57]. The following figures show the coarse morphology of Op C-S-H.

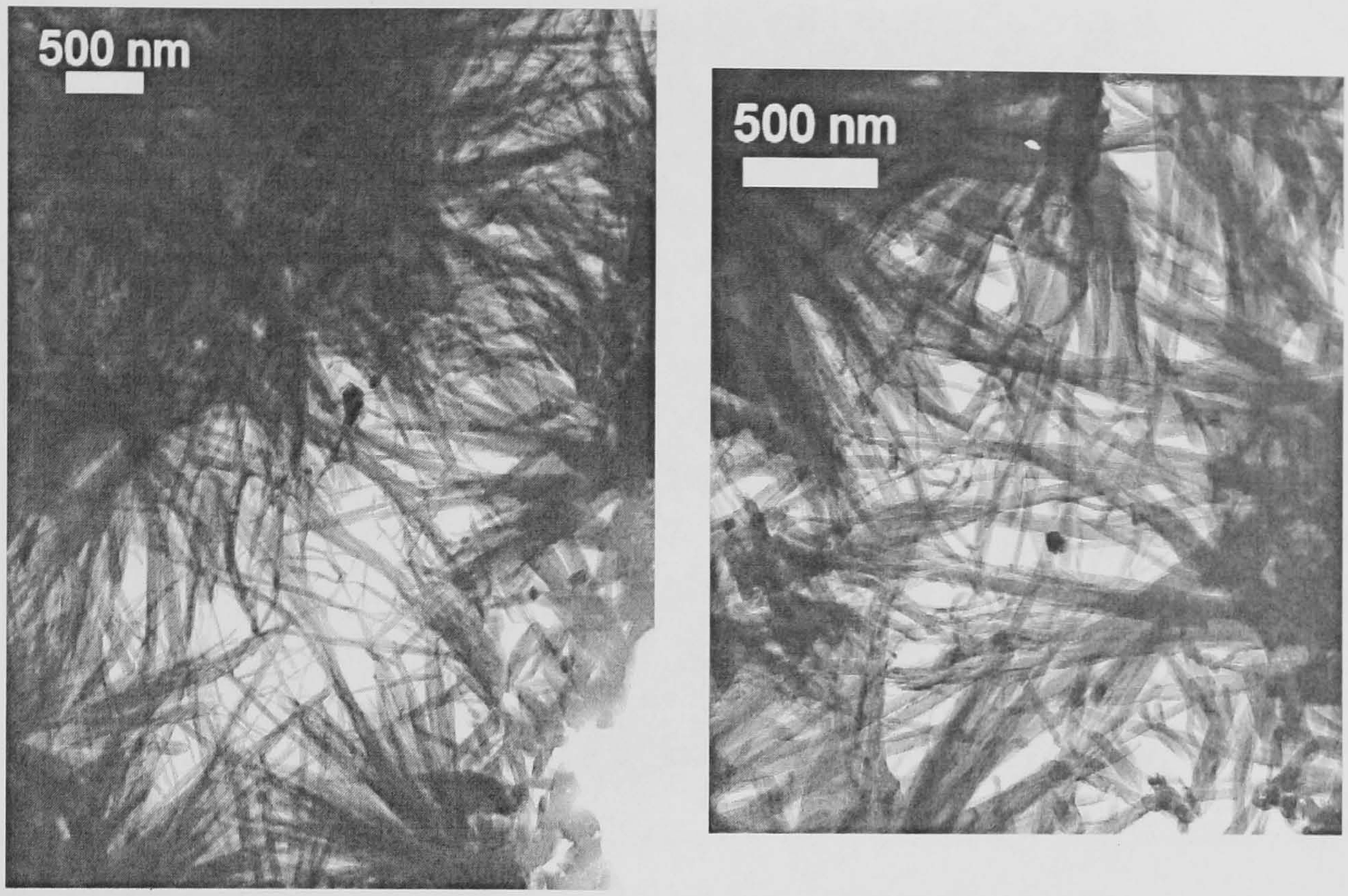


**Figure 6.3** – TEM micrographs showing coarse fibrillar Op C-S-H formed in the water activated neat WPC paste, 1 month cured at 85°C.

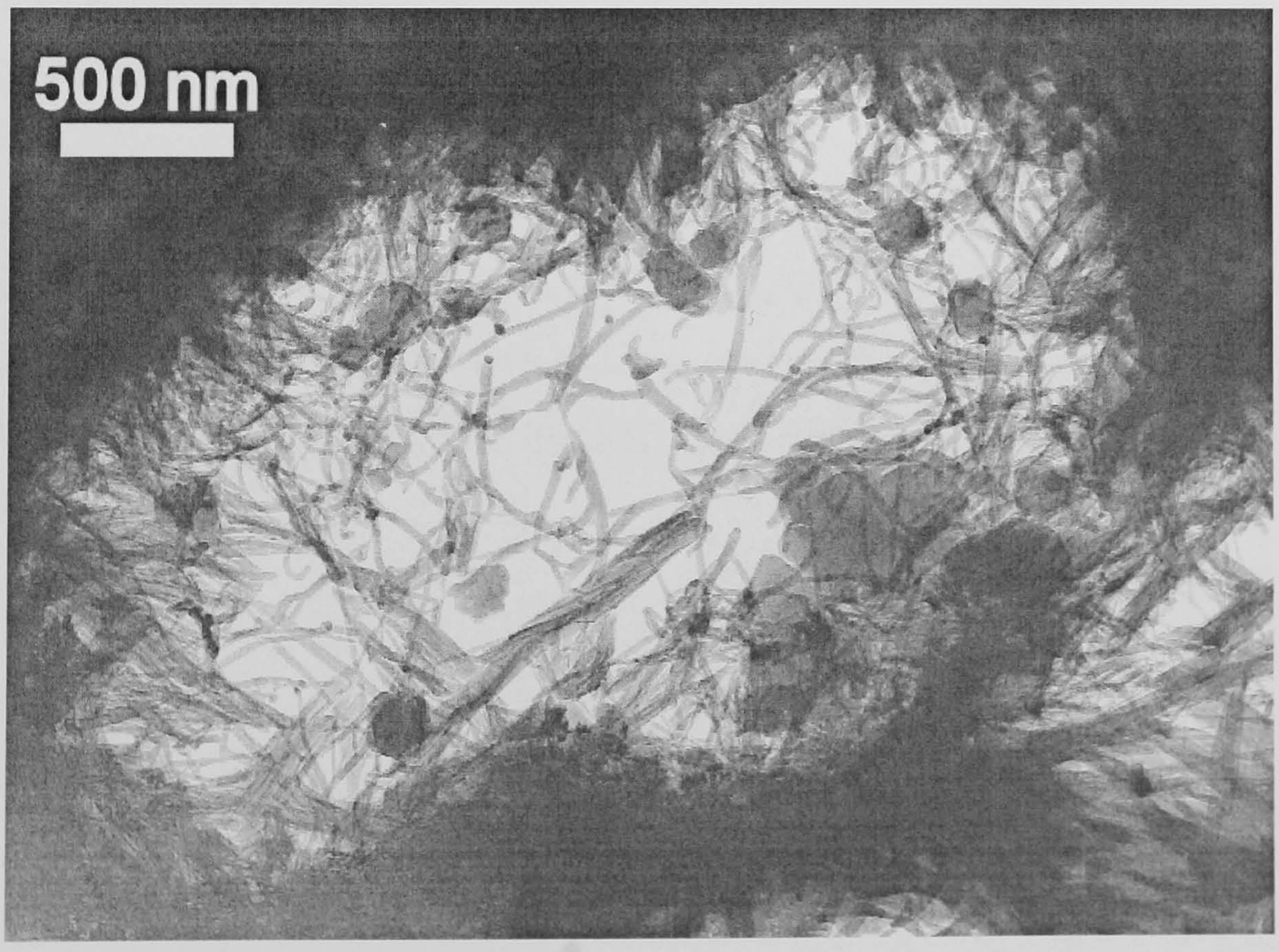


**Figure 6.4** – TEM micrograph showing coarse fibrillar Op C-S-H and some globules formed in the water activated neat WPC paste, 1 month cured at 85°C.


**Figure 6.5** – TEM micrograph showing CH surrounding coarse fibrillar Op C-S-H and small globules formed in the water activated neat WPC paste, 1 month cured at 85°C.

Figure 6.5 shows a different and curious feature also observed in the microstructure: some globules were formed and dispersedly embedded in Op C-S-H coarse fibrils. In this neat cement paste most of the globules were too small or thick for EDX to be used. CH closely surrounding Op C-S-H is illustrated in Figure 6.6. The next micrographs show the difference between bright and dark field TEM imaging for a partially hydrated cement grain. In Figure 6.7, the dark field image shows a different contrast from the one observed in bright field. The brighter area corresponds to crystalline material and the light-grey corresponds to amorphous Ip and Op C-S-H. Complementing these two imaging modes is very helpful in distinguishing crystalline areas from less crystalline or amorphous products.

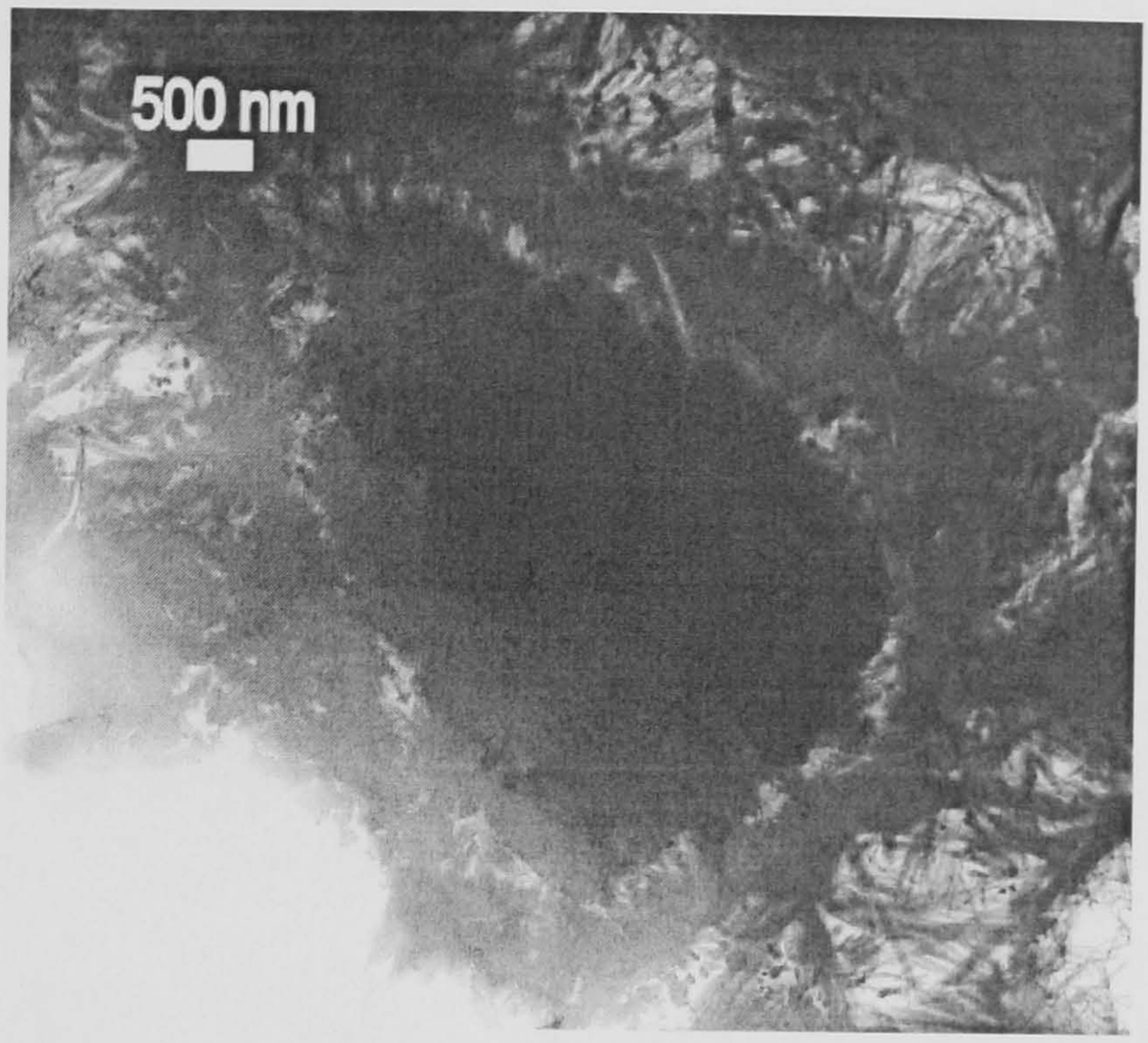


**Figure 6.6** – Bright field TEM micrograph showing a partially hydrated cement grain in the water activated neat WPC paste, 1 month cured at 85°C.

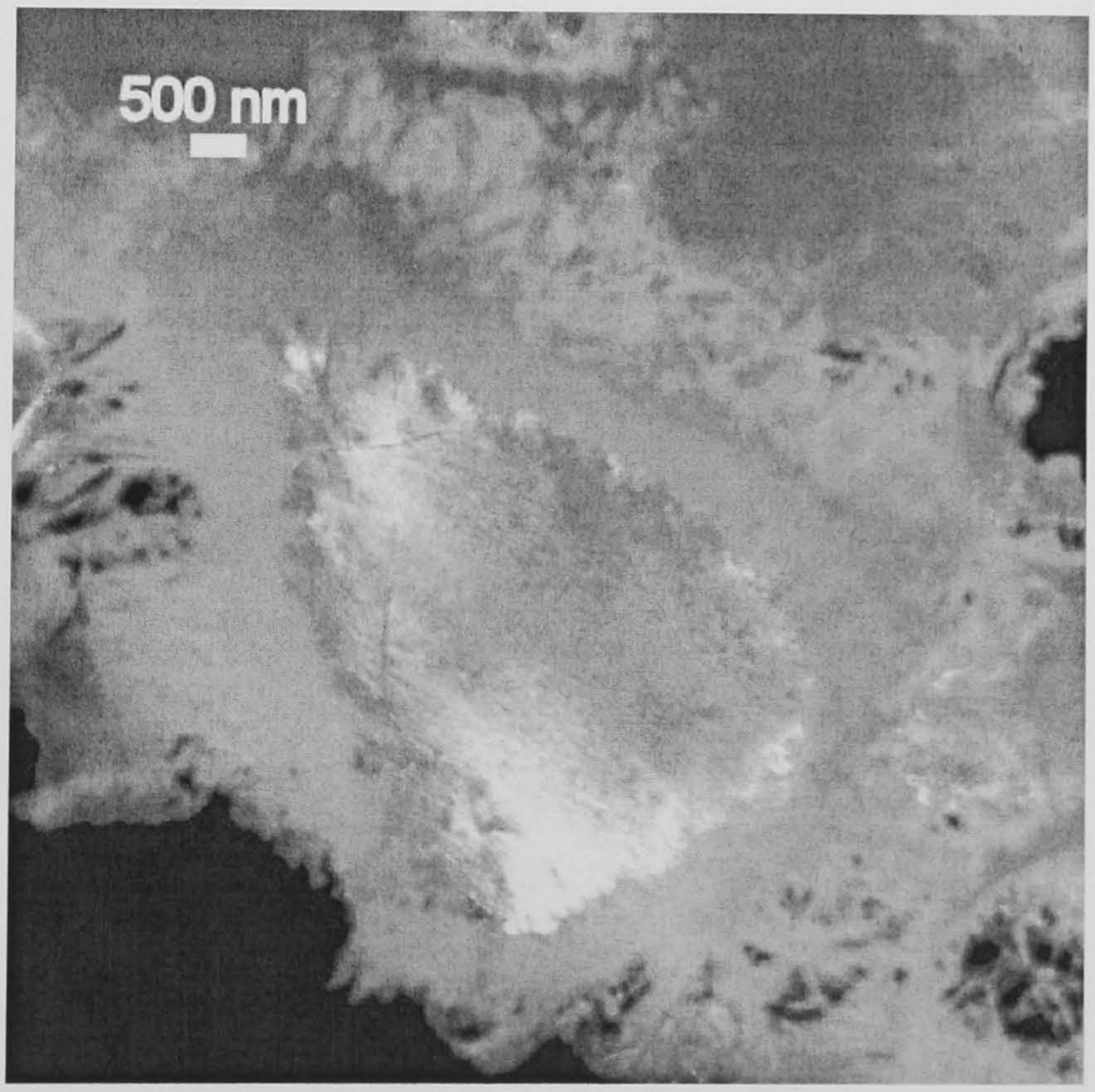


**Figure 6.7** – Dark field TEM micrograph corresponding to Figure 6.30 for a partially hydrated cement grain in showing in the water activated neat WPC paste, 1 month cured at 85°C.

The following figure shows the EDX data plots found for the water activated WPC paste cured at 85°C, for one month.

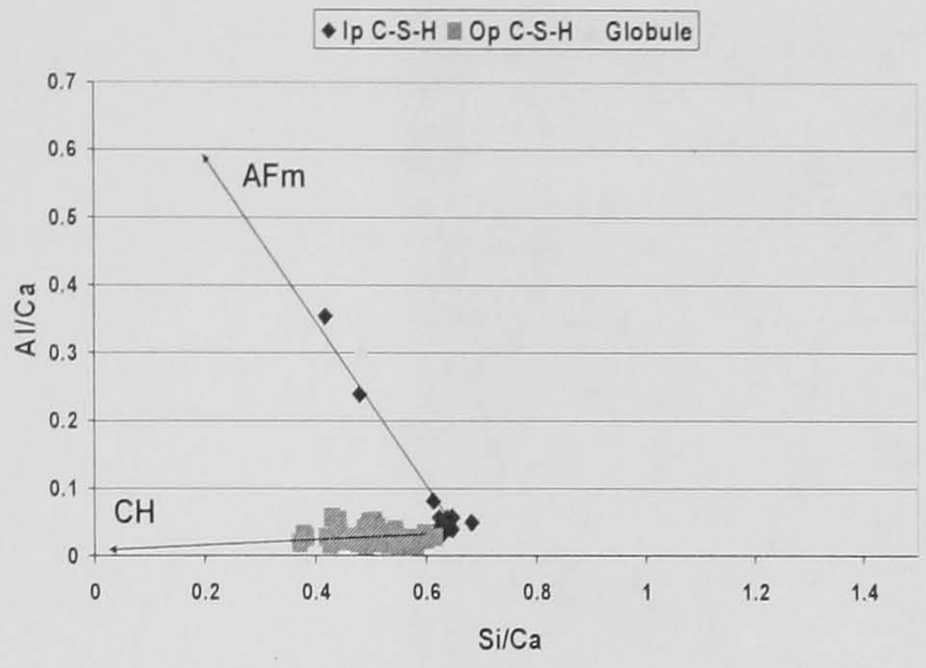


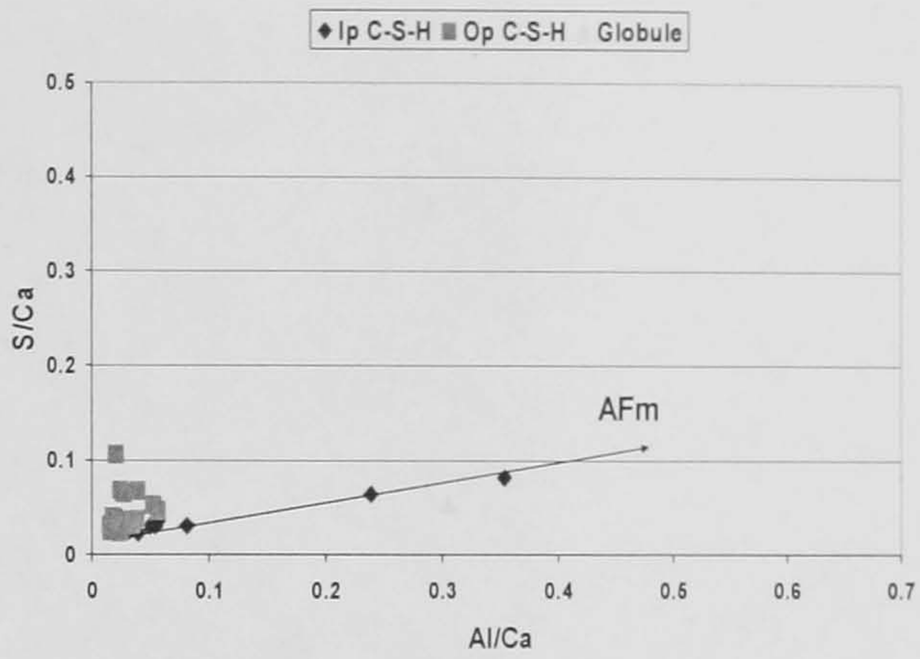


**Figure 6.8** – Al/Ca against Si/Ca (right) and S/Ca against Al/Ca (left) atomic ratio plots for the TEM-EDX phase analysis of the water activated neat WPC paste after 1 month of hydration at 85°C.

The Al/Ca against Si/Ca atomic ratio plot showed two trendlines: one in the direction of high aluminium AFm-type phases and another less clear in the direction of CH. The S/Ca against Al/Ca plot showed only one trendline in the direction of the AFm-type phases. Therefore, Ip C-S-H was finely intermixed with AFm-type phases rich in aluminium but with low sulfate content. Op C-S-H appears to be finely intermixed with microcrystalline CH, although the micrographs and XRD did not give any evidence of that because the extension of this intermixing was probably very small. The mean Ca/Si ratio calculated for Ip C-S-H was 1.61 (s = 0.08) and mean Al/Si ratio 0.066 (s = 0.023). Op C-S-H had a mean Ca/Si ratio of 1.91 (s = 0.29) and Al/Si ratio of 0.052 (s = 0.026).

The other analysed sample using TEM-EDX was the water activated 30% PFA blend. The following figure shows CH and fine dense Ip C-S-H interfacing with coarse fibrillar Op C-S-H.

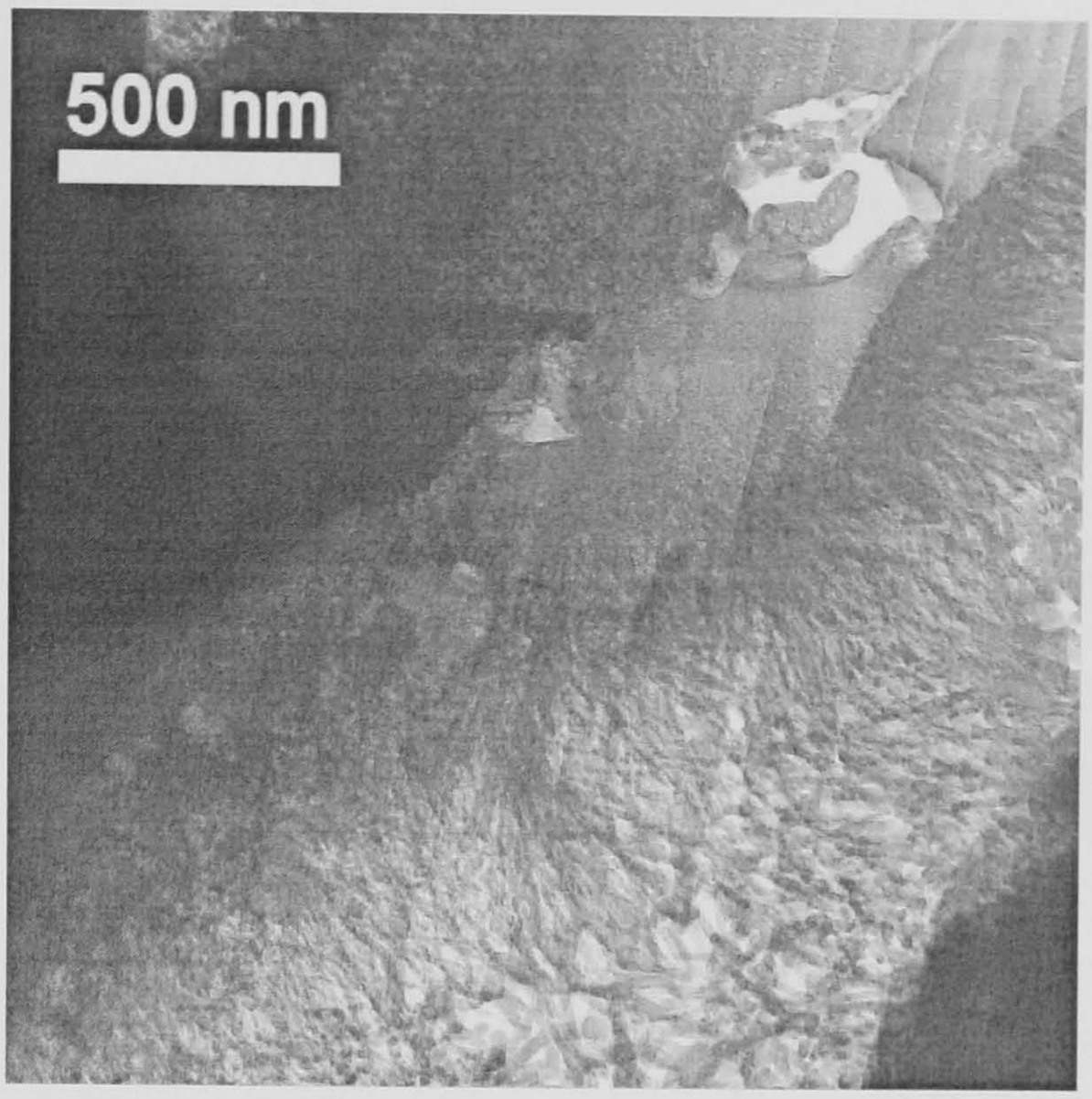


**Figure 6.9** – TEM micrograph showing CH, dense Ip C-S-H and coarse fibrillar Op C-S-H formed in the water activated 30% PFA blended WPC paste, 1 month cured at 85°C.

Again, the effect of high curing temperature changed Op C-S-H morphology into a coarse fibrillar one. Ip C-S-H was dense and fine, large crystals of CH and AFm-type phases were observed. As in the previous system, blobs dispersed in Op C-S-H were observed. Most of those globules were large enough to be analysed but some of them were still too thick to be identified by EDX analysis. The majority had a chemical composition very similar to that of Op C-S-H although a few were higher in aluminium content. The next micrograph shows some globules surrounded by coarse fibrillar Op C-S-H.

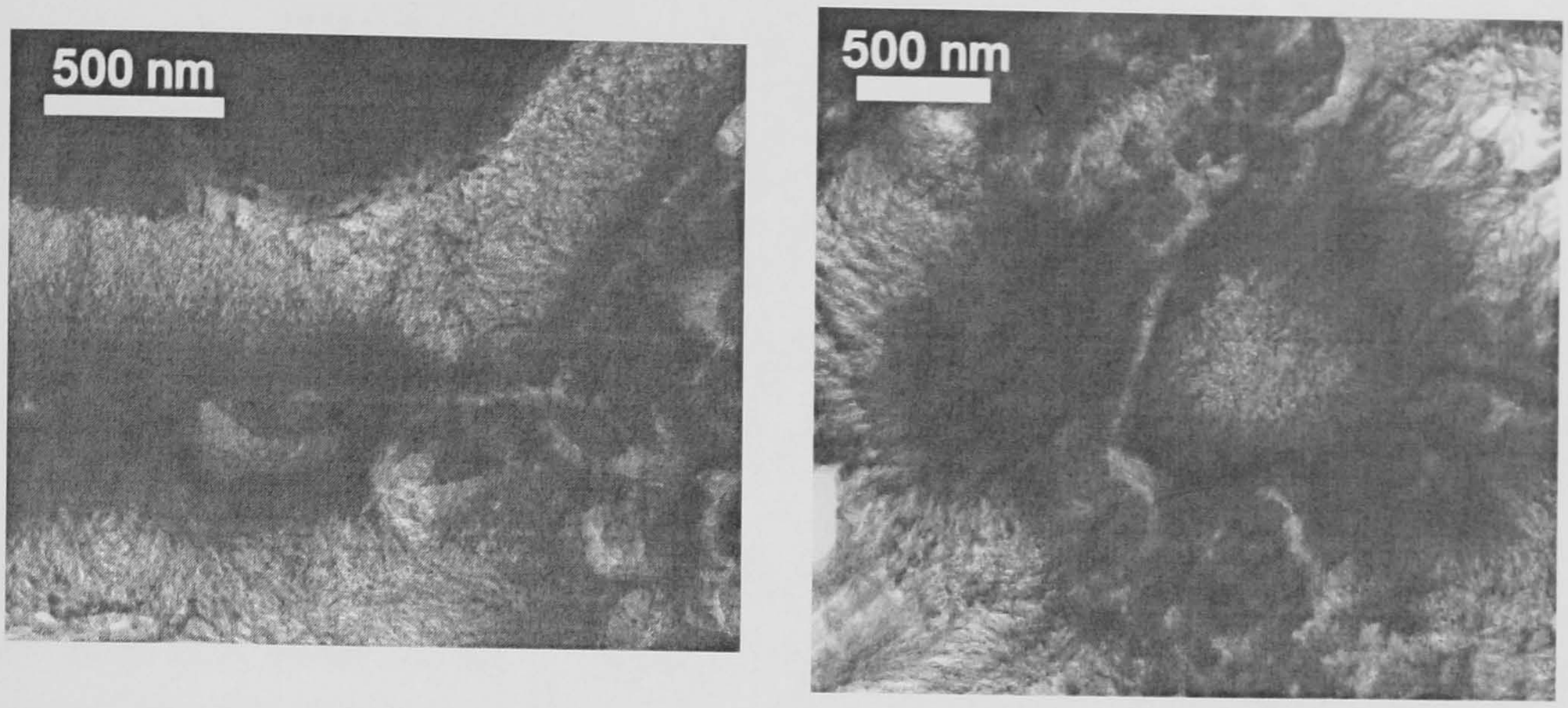


**Figure 6.10** – TEM micrographs showing coarse fibrillar Op C-S-H and some large globules formed in the water activated 30% PFA blended WPC paste, 1 month cured at 85°C.

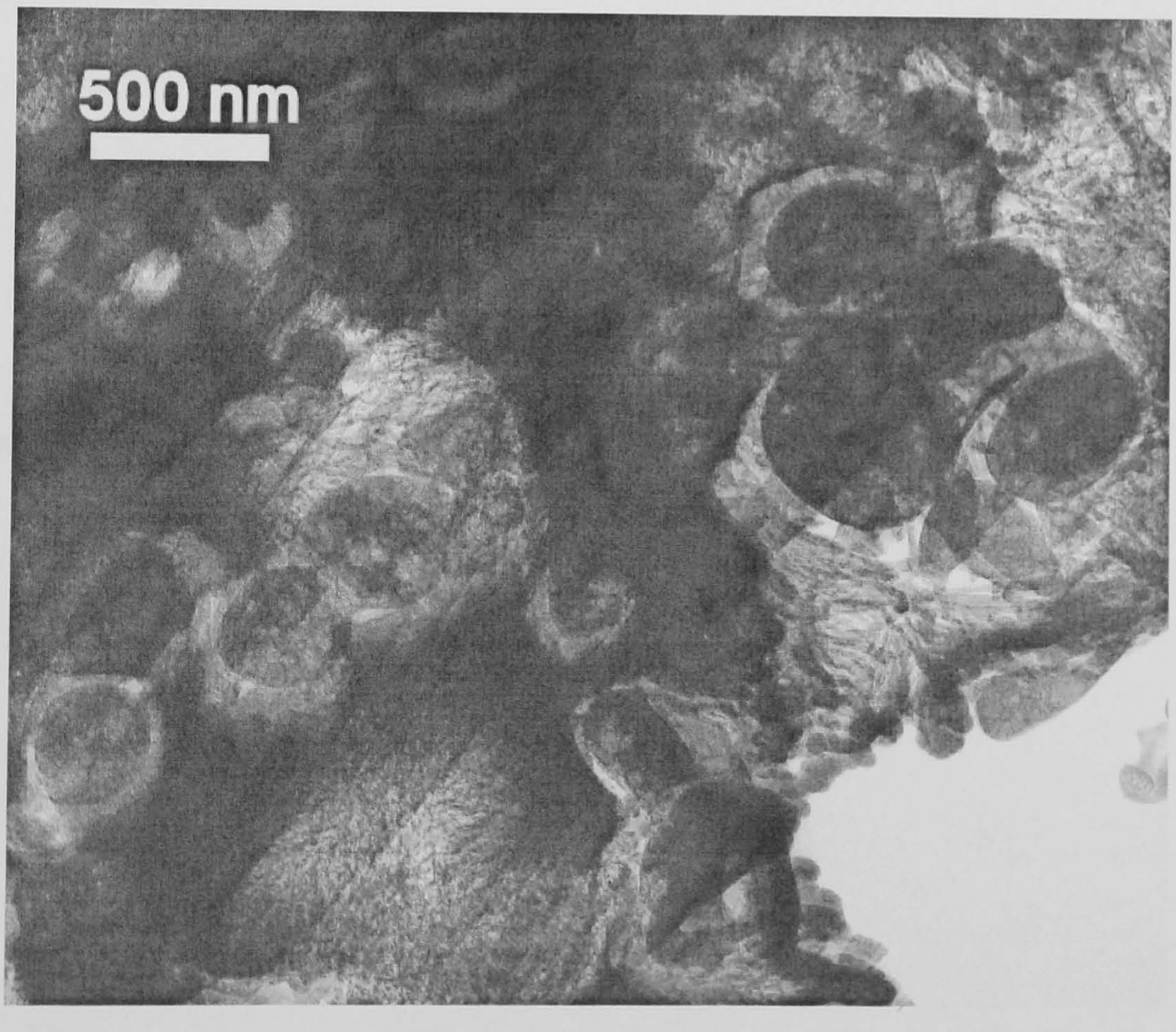


**Figure 6.11** – TEM micrograph showing details of globules embedded in coarse fibrillar Op C-S-H formed in the water activated 30% PFA blended WPC paste, 1 month cured at 85°C.

Figure 6.12 shows EDX atomic ratio plots for the water activated 30% PFA blended WPC paste.

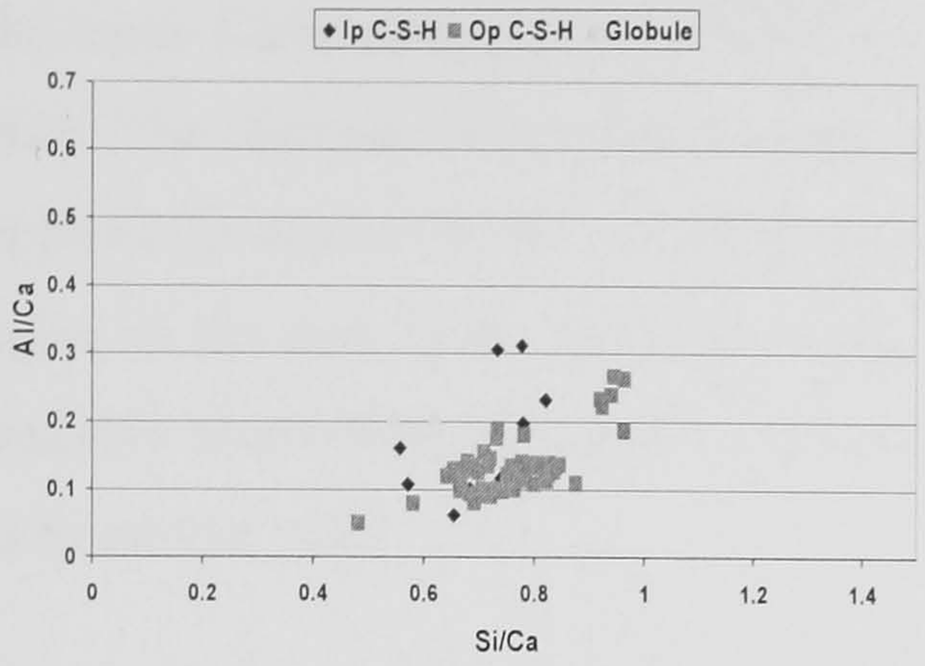


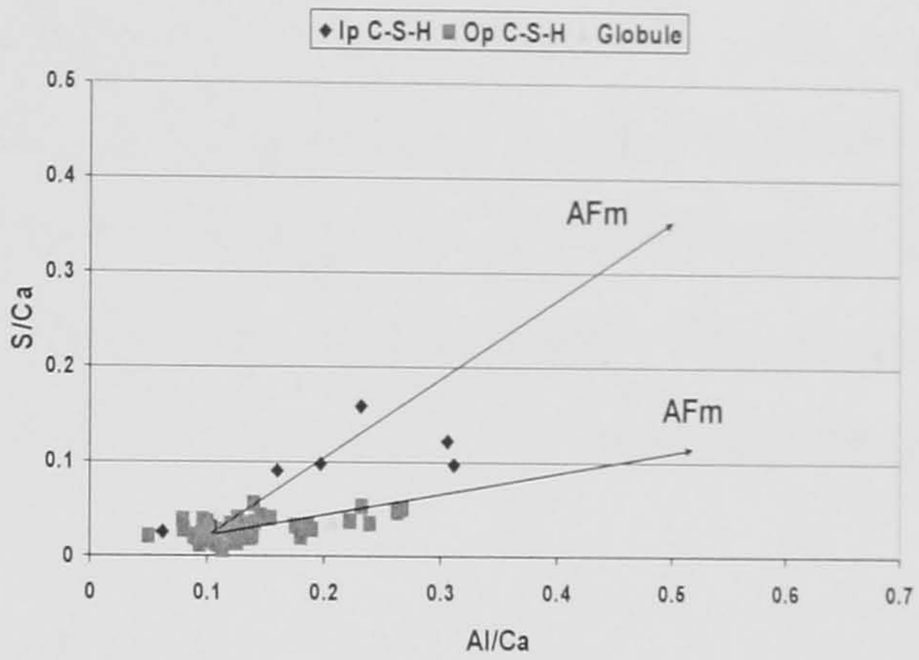


**Figure 6.12** – Al/Ca against Si/Ca (right) and S/Ca against Al/Ca (left) atomic ratio plots for the TEM-EDX phase analysis of the water activated 30% PFA blended WPC paste after 1 month of hydration at 85°C.

The first plot showed Op C-S-H data slightly scattered and did not indicate any trendline in the direction of the calcium aluminoferrite hydrate phases. It was not clear enough if Op C-S-H was intermixed with microcrystalline CH. The S/Ca against Al/Ca atomic ratio plot showed a clear trendline from Op C-S-H and AFm-type phases with low sulfur. A less clear trendline was identified in the direction of AFm-type phases with usual chemical composition. It was concluded that Ip C-S-H was finely intermixed with AFm-type phases as well as Op C-S-H. The mean Ca/Si and Al/Si ratios for Ip C-S-H were 1.48 (s = 0.21) and 0.201 (s = 0.069), respectively. Op C-S-H had a mean Ca/Si ratio of 1.34 (s = 0.11) and Al/Si ratio 0.165 (s = 0.032).

Table 6.12 resumes the mean Ca/Si and Al/Si ratios obtained for the systems studied using TEM-EDX.

**Table 6.12** – Mean Ca/Si and Al/Si atomic ratios obtained for C-S-H using TEM-EDX, for the water activated neat WPC and 30% PFA blended cement pastes, 1 month cured at 85°C.

| | | Ca/Si | | Ca/(Al+Si) | | Al/Si | |
|---|---|---|---|---|---|---|---|
| | | *N* | *mean* | *s* | *mean* | *s* | *mean* | *s* |
| **Wpc** | **Op** | 26 | 1.91 | 0.29 | 1.81 | 0.03 | 0.052 | 0.026 |
| | **Ip** | 18 | 1.61 | 0.08 | 1.51 | 0.25 | 0.066 | 0.023 |
| | **All** | 44 | 1.79 | 0.27 | 1.69 | 0.25 | 0.058 | 0.026 |
| **Pfa30** | **Op** | 44 | 1.34 | 0.11 | 1.16 | 0.17 | 0.165 | 0.032 |
| | **Ip** | 7 | 1.48 | 0.21 | 1.12 | 0.19 | 0.201 | 0.069 |
| | **All** | 51 | 1.36 | 0.14 | 1.15 | 0.18 | 0.170 | 0.041 |

The mean Ca/Si ratio found for Op C-S-H was higher than that for C-S-H Ip in the neat paste. The opposite was verified in the blend but, as explained and verified before PFA replacement decreases the mean Ca/Si ratio of C-S-H. Thus, the mean Ca/Si ratio was higher in the neat paste and mean Al/Si ratio higher in the blended paste. Due to more available aluminium provided by PFA replacement, Ip and Op C-S-H had higher mean Al/Si atomic ratios.

Table 6.13 resumes TEM-EDX, SEM-EDX and MAS NMR experimental results found for the water and KOH activated neat and 30% PFA blended WPC pastes cured for one month at 85°C.

**Table 6.13** – Mean Ca/Si and Al/Si atomic ratios obtained for C-S-H using TEM-EDX, SEM-EDX and MAS NMR, for the water activated neat WPC and 30% PFA blended cement pastes, 1 month cured at 85°C.

| | **All Ca/Si** | **Ca/Si (SEM)** | **All Al/Si** | **Al/Si (SEM)** | **Al/Si (NMR)** |
|---|---|---|---|---|---|
| **Wpc** | 1.79 | 2.08 | 0.058 | 0.10 | 0.099 |
| **Pfa30** | 1.36 | 1.58 | 0.170 | 0.24 | 0.139 |

Comparing the mean Ca/Si and Al/Si ratios obtained by the two microscopy techniques, they were statistically significantly different as a consequence of the difference in the interaction volume between the electron beam and the sample, i.e. the higher interaction volume in SEM-EDX led to higher mean atomic ratios for C-S-H. The mean Al/Si atomic ratios obtained for both samples using TEM-EDX and $^{29}$Si MAS NMR were in some agreement.

Finally, it was also necessary to compare the TEM-EDX data obtained for these systems cured at 55°C, with that found for these pastes cured at 25°C. Table 6.14 summarises those experimental results.

**Table 6.14** – Comparison between the mean Ca/Si and Al/Si atomic ratios obtained for the cement-based studied systems after 1 month cured at 25°C, 55°C and 85°C.

| | | WPC | PFA30 |
|---|---|---|---|
| **All Ca/Si** | **25°** | 2.00 | 1.52 |
| | **55°** | 1.64 | 1.46 |
| | **85°** | 1.79 | 1.36 |
| **All Al/Si** | **25°** | 0.106 | 0.159 |
| | **55°** | 0.087 | 0.164 |
| | **85°** | 0.058 | 0.170 |

The previous data did not show clear relationships between increasing curing temperature and its effect on the mean atomic ratios for C-S-H. Before analysing the effect caused by curing at 85°C, it was concluded that higher temperature decreased the mean Ca/Si ratio for Ip and Op C-S-H in both systems; increased the mean Al/Si ratio of Ip C-S-H in both systems; and decreased Op C-S-H Al/Si ratio in the neat paste but increased in the blended pastes. Comparing these relationships with additional data at 85°C, the mean Ca/Si ratio for Ip and Op C-S-H in both systems increased. It was possible to conclude that the variation of the mean atomic ratios was not systematic with increased curing temperature. Escalante-Garcia and Sharp also found that for SEM-EDX studies, the atomic ratios for C-S-H did not vary consistently in a systematic way with increasing hydration temperature[134].

In summary, TEM-EDX allowed characterisation of Ip and Op C-S-H morphology in different systems cured at different temperatures. Op C-S-H changed its morphology from fine fibrils to coarse fibrils and Ip C-S-H was formed of slightly larger globular particles. It was also demonstrated that either CH, AFt/AFm/hydrogarnet-type phases were finely intermixed with Ip and/or Op C-S-H. Some agreement was found between the mean Ca/Si ratios obtained using SEM-EDX and TEM-EDX and, generally, good agreement was found between the mean values for the Al/Si atomic ratios, when using TEM-EDX and MAS NMR.

### 6.6.2 – T/J and T/CH-based models for the structure of C-S-H

Application of the different structural models to TEM-EDX data relative to the analysed systems is presented in this section.

**Table 6.15** – Experimental data used in Al/Ca against Si/Ca atomic plots discussing the applicability of the T/CH and T/J structural models for C-S-H, in the systems cured at 85°C.

| | Ip Ca/Si | Op Ca/Si | Ip Al/Si | Op Al/Si | Al/Si (NMR) | MCL | %B |
|---|---|---|---|---|---|---|---|
| **Wpc** | 1.67 | 1.91 | 0.126 | 0.052 | 0.099 | 9.9 | 34 |
| **Pfa30** | 1.48 | 1.34 | 0.201 | 0.165 | 0.139 | 16.6 | 42 |

Figure 6.13 shows Ip and Op C-S-H raw data in the Al/Ca against Si/Ca atomic ratio plot considering the T/J and T/CH structural models.

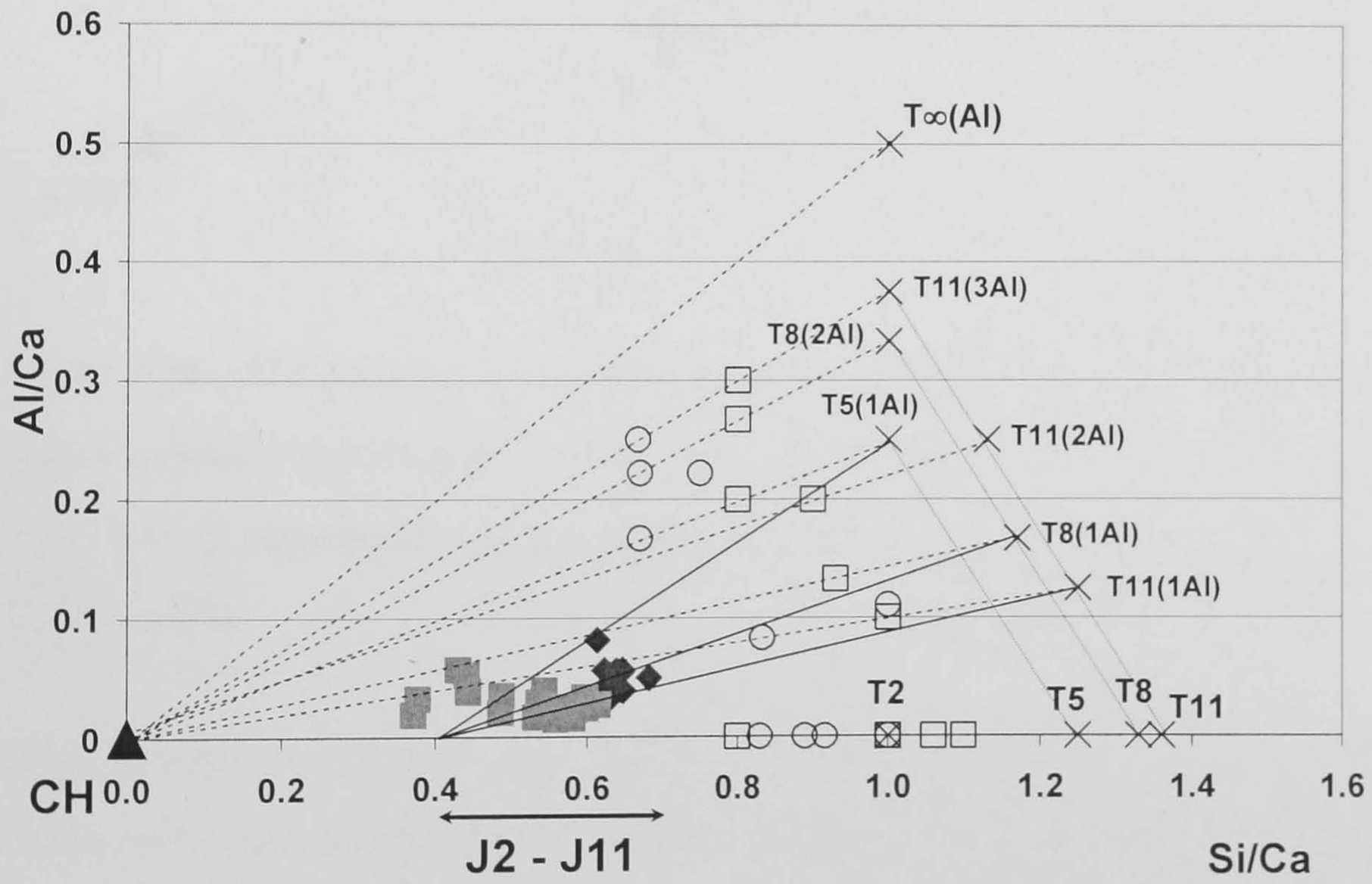


**Figure 6.13** – Al/Ca against Si/Ca atomic plot for the water activated neat WPC paste cured for 1 month at 85°C, accounting with T/J and T/CH viewpoints (♦ Ip C-S-H, ■ Op C-S-H, O unprotonated units, □ half protonated, X fully protonated, T∞ tobermorite, --- T/CH, — T/J).

The previous plot shows that data was consistent with both models: tie line from T11(1Al) or T11(2Al) in the direction of CH but also trendlines from T5(1Al), T8(1Al) and T11(1Al) in the direction of J2.

The following figure shows the Al/Ca against Si/Ca atomic ratio plot considering the T/CH and T/J models for the KOH activated neat WPC paste, one month cured at 55°C.

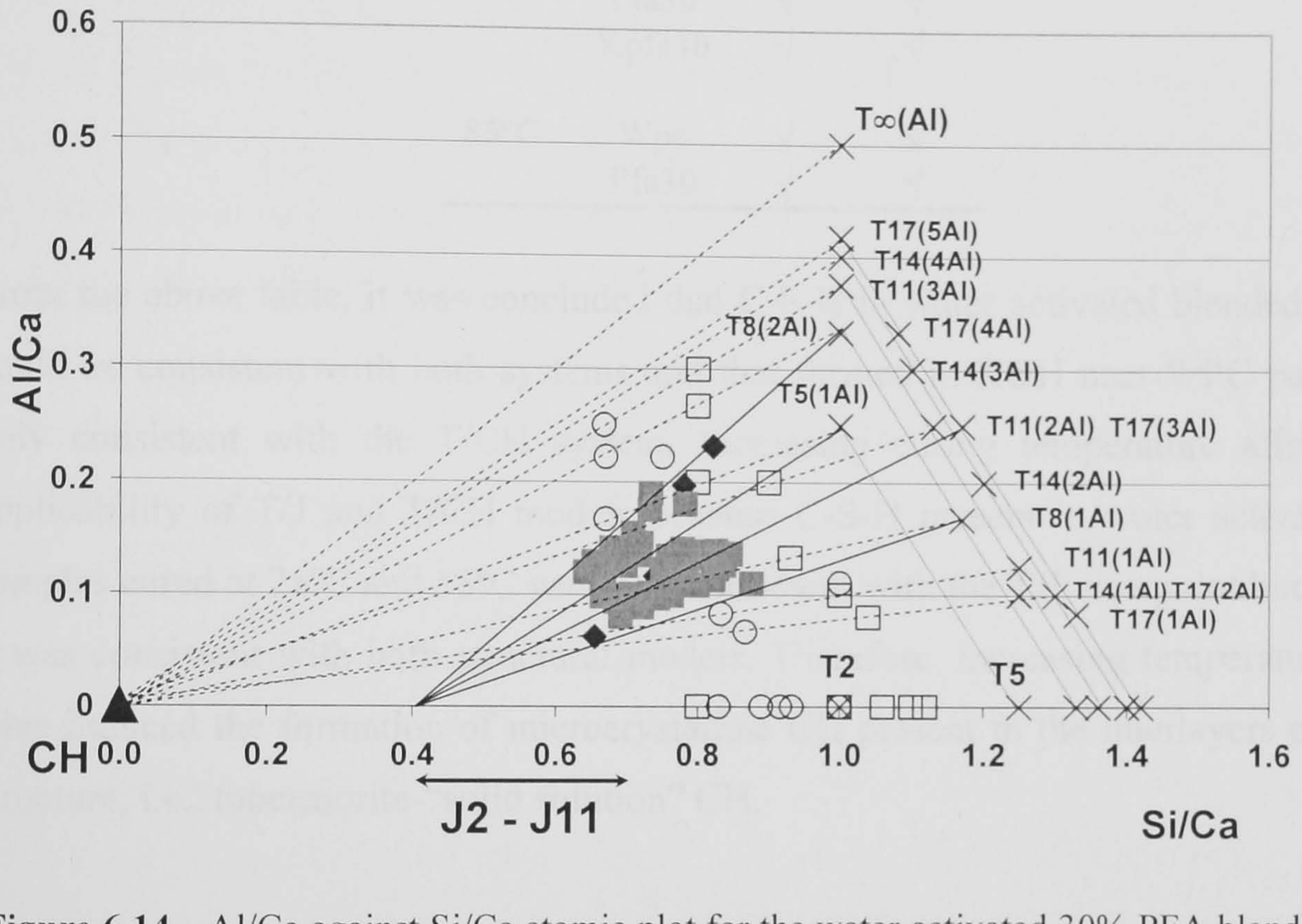


**Figure 6.14** – Al/Ca against Si/Ca atomic plot for the water activated 30% PFA blended WPC paste cured for 1 month at 85°C, accounting with T/J and T/CH viewpoints (◆ Ip C-S-H, ■ Op C-S-H, O unprotonated units, □ half protonated, X fully protonated, T∞ tobermorite, --- T/CH, — T/J).

Although data was slightly more scattered than in neat systems, it was considered to be consistent to both models: tie line from T17(3Al) in the direction of J2 for the T/J point of view, and T8(1Al) in the direction of CH for the T/CH viewpoint.

Comparing the applicability of T/J and T/CH structural models, the following table resumes it for the studied systems cured at different temperatures:

**Table 6.16** – Applicability of T/CH and T/J structural models for C-S-H formed in the studied systems cured at 25°C, 55°C and 85°C for one month.

| | T/J | T/CH |
|---|---|---|

| | | | |
|---|---|---|---|
| | Wpc | √ | X |
| **25°C** | Kwpc | X | √ |
| | Pfa30 | √ | √ |
| | Wpc | √ | X |
| **55°C** | Kwpc | X | √ |
| | Pfa30 | √ | √ |
| | Kpfa30 | √ | √ |
| **85°C** | Wpc | √ | √ |
| | Pfa30 | √ | √ |

From the above table, it was concluded that C-S-H in water activated blended systems could be consistent with both systems and that formed in KOH neat WPC pastes was only consistent with the T/CH system. Increasing curing temperature affected the applicability of T/J and T/CH models because C-S-H present in water activated neat samples cured at 25°C and 55°C was only consistent with the T/J viewpoint but at 85°C, it was consistent with both structural models. Therefore, increasing temperature could have induced the formation of microcrystalline CH present in the interlayers of C-S-H structure, i.e., tobermorite-"solid solution" CH.

## 6.7 - C-S-H STRUCTURAL-CHEMICAL COMPOSITION

C-S-H chemical composition can be easily determined according to both T/J and T/CH viewpoints and using TEM-EDX and MAS NMR data. Using the equations 4.2 to 4.7 (Chapter IV), the structural-chemical composition of C-S-H was determined and Table 6.17 resumes the data used in the calculations:

**Table 6.17** – TEM-EDX and MAS NMR data used in the determination of C-S-H chemical composition according to the T/J and T/CH structural viewpoints for the systems cured at 55°C.

| | **Ca/Si (TEM)** | ***y*** | ***w*** | ***y'*** | **w'** | **Al/Si (TEM)** | **Al/Si (NMR)** | ***a*** | **MCL (3n-1)** | ***n*** |
|---|---|---|---|---|---|---|---|---|---|---|
| **Wpc** | 1.79 | 5.10 | 0 | 4.99 | 0 | 0.06 | 0.099 | 0.06 | 9.9 | 3.6 |
| **Pfa30** | 1.36 | 2.50 | 0 | 2.10 | 0 | 0.17 | 0.139 | 0.15 | 16.6 | 5.9 |

Again, minimum degree of protonation was considered. C-S-H chemical composition determined according to the T/J structural point of view is given in Table 6.18.

**Table 6.18** – C-S-H chemical composition determined according to the T/J structural viewpoint for the systems cured at 55°C.

| | **T/J (minimum degree of protonation)** |
|---|---|
| **Wpc** | $\{Ca_{7.2}(Si_{0.94}Al_{0.06})_{9.9}O_{30.4}\}\cdot(OH)_{11.2}\cdot Ca_{9.2}\cdot mH_2O$ |
| **Pfa30** | $\{Ca_{11.8}(Si_{0.85}Al_{0.15})_{16.6}O_{51.1}\}\cdot(OH)_{2.95}\cdot Ca_{7.4}\cdot mH_2O$ |

Chemical composition inside the brackets indicates the tobermorite-based skeleton of C-S-H. The presence of hydroxyl groups outside the brackets indicates that there must be some jennite-like structure besides tobermorite-like units. The structure of C-S-H can also be reorganised according to the T/CH viewpoint, resumed in Table 6.19.

**Table 6.19** – C-S-H chemical composition determined according to the T/CH structural viewpoint for the systems cured at 55°C.

| | **T/CH (minimum degree of protonation)** |
|---|---|
| **Wpc** | $Ca_{10.5}(Si_{0.94}Al_{0.06})_{9.9}O_{0.4}\cdot Ca_{0.3}\cdot 5.4Ca(OH)_2\cdot mH_2O$ |
| **Pfa30** | $Ca_{17.7}(Si_{0.85}Al_{0.15})_{16.6}O_{51.1}\cdot Ca_{1.25}\cdot 0.3Ca(OH)_2\cdot mH_2O$ |

In the water neat paste, the presence of hydroxyl groups outside the braces indicates that on the T/J viewpoint for the nanostructure of C-S-H, there was some J-like structure. However, in this case, the distribution of TEM-EDX (Figure 6.13) indicated that the both points of view were applicable. Interestingly, Table 6.19 shows a high amount of calcium hydroxide present in the structural-chemical formula for C-S-H. Regarding the pfa30 paste, the structural formulas show that on the T/J point of view, there was some J-like contribution and on the T/CH point of view, there was only a small amount of CH units in "solid-solution". This is in good agreement with both models as previously seen in Figure 6.15 where both models were consistent with the TEM-EDX data.

# VII – RESULTS AND DISCUSSION: WATER LEACHING

In this chapter, experimental results related to the one year old water activated 30% PFA blended WPC paste water leached, are presented and discussed.

## 7.1 – STA-EGA

After one year of hydration, the water activated 30% PFA blended WPC paste was cut into 200 μm thick slices and immersed in a closed and continuously stirred distilled water bath, kept at room temperature. The samples were analysed after 1 to 12 weeks of leaching and the leachate was replaced by fresh distilled water each time the samples were collected for analysis. The samples did not carbonate verified by the EGA curves.

STA-EGA results are presented in the following figure.

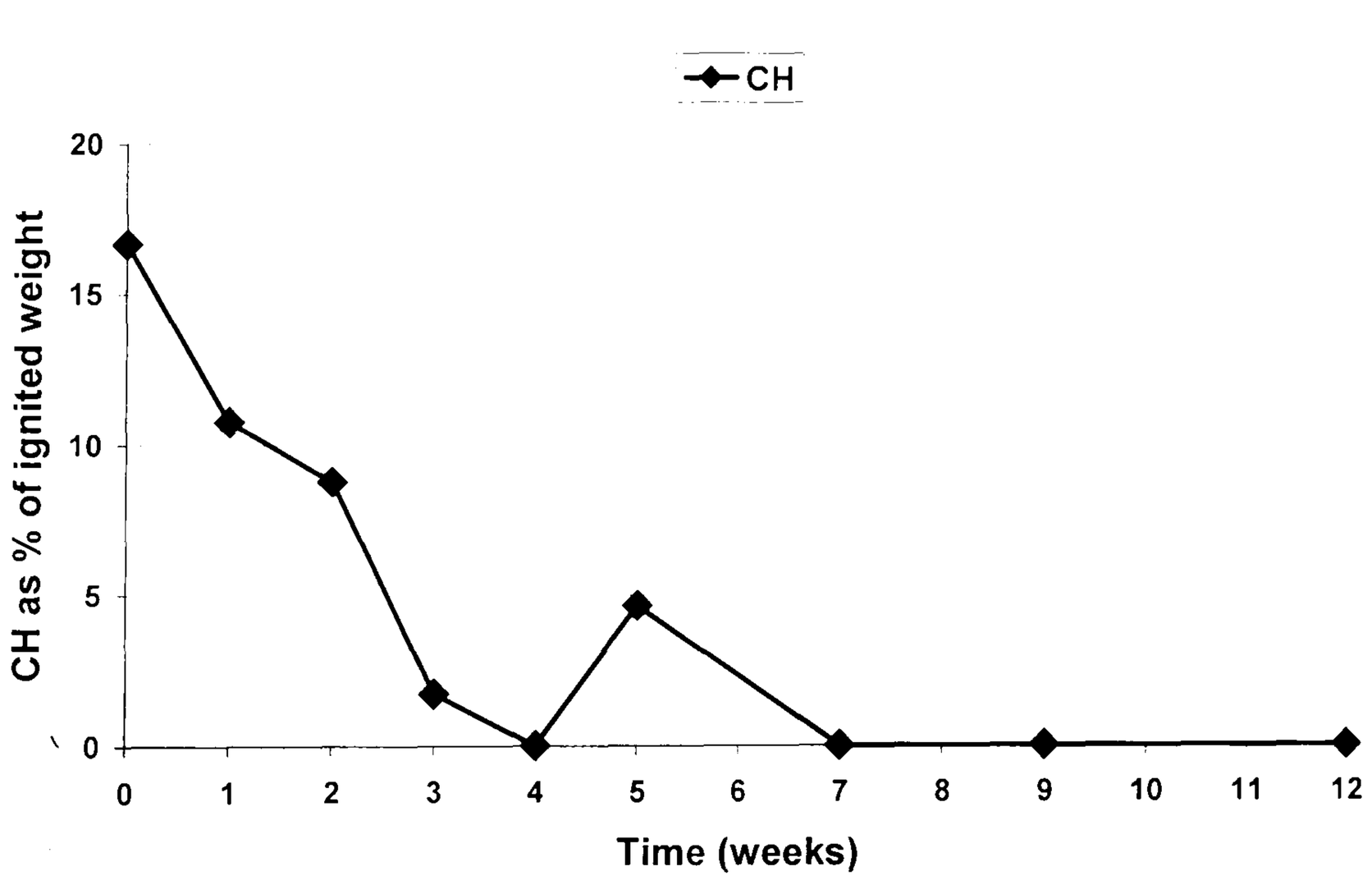


**Figure 7.1** – CH evolution during 12 weeks of water leaching the mature PFA blended paste.

STA-EGA demonstrated that as leaching progressed, the amount of CH decreased because it was removed from the paste into the leachate. Another possible explanation is that water leaching enhanced the pozzolanic reaction between CH and PFA to give

additional C-S-H. Both processes could have happened at the same time. The amount of CH decreased with time of leaching and by four weeks, no CH was detected. After five weeks, a very small amount of CH was present in the sample. Although CH was leached or consumed in the pozzolanic reaction, it was possible that the residual anhydrous cement reacted to give additional C-S-H as well as CH. From seven weeks till twelve weeks, CH was not detected by STA-EGA because it was either leached or consumed in the pozzolanic reaction. MAS NMR should give some evidence that might support one of these two justifications, or even both. As explained in the previous chapters, STA results might have been affected by a small error associated to the estimations.

## 7.2 – SOLID STATE $^{29}$Si MAS NMR

$^{29}$Si MAS NMR was used to determine the silicate anion structure present in the C-S-H phase. As previously explained, the leached sample was a 30% PFA blended cement paste and, therefore, only semi-quantitative data was obtained from iterative fitting of the spectra. The obtained spectra and corresponding figure showing the $Q^n$ relative intensity evolution during the twelve weeks of water leaching are presented in Appendix B (B8-B9).

After four weeks of leaching it was possible to observe small differences between the spectra, indicating that the silicate anion structure was altered and most probably the C-S-H chemical composition was also affected. However, the main change observed in the spectrum was the appearance of another resonance assigned to $Q^3$ crossed-linked entities. This has also been previously observed in high performance concrete samples leached for one year[116]. After twelve weeks of water leaching, most of the anhydrous cement reacted as well as $\gamma$-$C_2S$. Chain branching sites were formed to greater extent as $Q^3$ became the second most intense peak in the spectrum. Apparently, anhydrous fly ash ($Q^4$) was relatively in the same amount after seven weeks but decreased significantly after nine weeks of leaching. It should be pointed out that as the pozzolanic reaction occurs, the corresponding broad resonance might shift slightly and is mainly assigned to

the silicon present in the three dimensional framework of the non reactive fraction of fly ash, i.e. the peak assigned to $Q^4$ (anhydrous fly ash) becomes slightly deconvoluted and that causes a shift of the chemical shift. Nevertheless, it was also observed that all chemical shifts moved around 1 ppm in the direction to lower chemical shifts. This can be explained by a matrix effect[116], i.e. when a systems experiences a concentration gradient it reacts to re-establish equilibrium. In the MAS NMR spectra, all the peaks were shifted the same amount and the relative intensity of a certain resonance may be enhanced. In this particular case, the relative intensity of the anhydrous fly ash was enhanced (between three and seven weeks of leaching), as shown in Table 7.1 where the semi-quantitative data obtained from iterative spectra fitting is summarised.

**Table 7.1** – $^{29}$Si MAS NMR semi-quantitative data obtained for the 30% PFA blended cement paste 1 year, water leached for 12 weeks.

| | UNL | 1WK | 2WK | 3WK | 4WK | 5WK | 7WK | 9WK | 12WK |
|---|---|---|---|---|---|---|---|---|---|
| **MCL** | 11.6 | 10.5 | 9.0 | 8.2 | 9.2 | 9.2 | 11.1 | 14.5 | 14.7 |
| **Al/Si** | 0.184 | 0.175 | 0.143 | 0.131 | 0.132 | 0.131 | 0.133 | 0.133 | 0.133 |
| **% WPC** | 4.5 | 3.8 | 3.1 | 2.8 | 2.1 | 1.8 | 1.6 | 0.6 | 0.1 |
| **% $\gamma$-$C_2S$** | 1.5 | 1.4 | 0.7 | 0.8 | 0.6 | 0.4 | 0.6 | 0 | 0 |
| **% $Q^1$** | 14.7 | 16.5 | 17.8 | 18.5 | 16.3 | 16.3 | 12.9 | 9.6 | 8.7 |
| **% $Q^2$(1Al)** | 26.3 | 25.9 | 20.1 | 17.7 | 17.5 | 17.4 | 16.9 | 16.3 | 15.0 |
| **% $Q^2$** | 30.5 | 31.5 | 32.3 | 31.4 | 32.5 | 32.5 | 33.6 | 35.6 | 32.6 |
| **% $Q^3$** | - | - | - | - | 2.7 | 2.1 | 1.7 | 20.6 | 30.9 |
| **% PFA** | 22.6 | 21.0 | 26.1 | 28.9 | 28.2 | 29.2 | 32.7 | 17.2 | 12.7 |
| **% B** | 56 | 55 | 48 | 46 | 45 | 45 | 43 | 41 | 41 |
| **CH (STA)** | 16.7 | 10.8 | 8. 8 | 1.7 | 0 | 4.6 | 0 | 0 | 0 |

It was concluded that as the leaching process continued, MCL decreased for three weeks but increased till twelve weeks of leaching. The final MCL was 14.7, higher than that found for the unleached sample. The Al/Si atomic ratio decreased with increasing time of leaching but after three weeks, it remained relatively constant. The Al/Si atomic ratio was roughly the same during the twelve leaching weeks. Therefore, aluminium was not removed from the C-S-H structure. The proportion of aluminium substituted tetrahedra (%B) decreased slightly in the first four weeks, remaining constant for the remaining leaching time. Most of the anhydrous cement and $\gamma$-$C_2S$ reacted. The relative intensity of $Q^1$ increased as more cement reacted but after three weeks of leaching, it started to decrease. $Q^2$ was always the most intense peak and $Q^2$(1Al) relative intensity decreased

gradually. At four weeks of leaching, the bridging sites aluminium substituted became unstable and were probably destroyed when cross-linking occurred. Around this time, all the CH was leached and then the CaO layers in the dreierkette structure of C-S-H. In order to stabilise and react to the concentration gradient, C-S-H rearranged itself into a highly polymerised phase and as a result, $Q^3$ species were formed. The latter increased massively till twelve weeks of leaching indicating that the difference in the concentration gradient caused further cross-linking of the silicate anion structure. Finally, the decrease of the CH amount was attributed mainly to the leaching process because the intensity of the anhydrous fly ash resonance only decreased after seven weeks of leaching. In order to better visualise the data in Table 7.1, some plots are shown in the following figures.

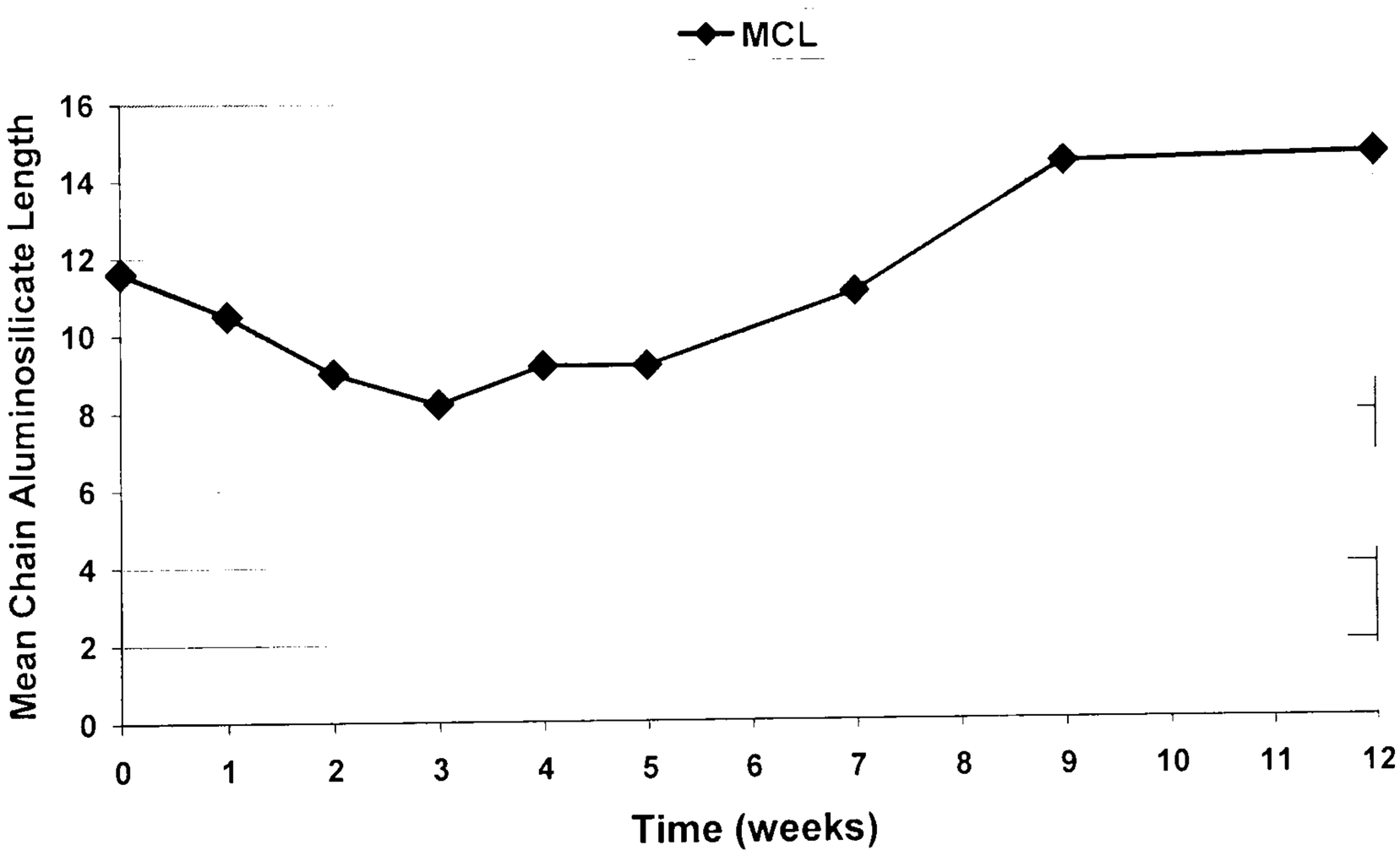


**Figure 7.2** – Mean chain aluminosilicate length evolution during 12 weeks of water leaching the mature PFA blended paste.

The above figure and the following one show the MCL and Al/Si ratio evolution during twelve weeks of water leaching.

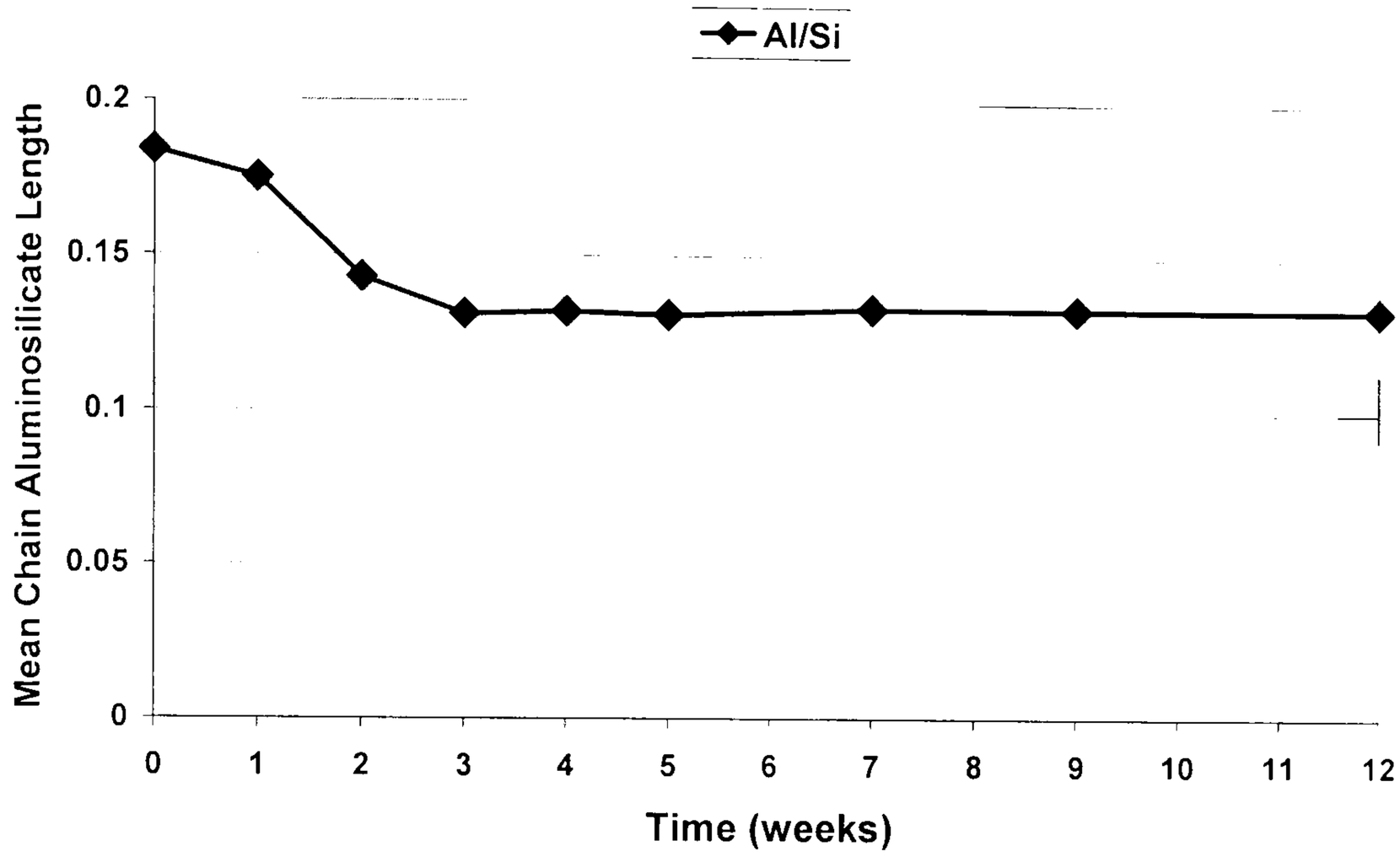


**Figure 7.3** – Al/Si ratio evolution during 12 weeks of water leaching the mature PFA blended paste.

## 7.3 – TEM-EDX

### 7.3.1 – Morphology and Chemical Analysis

The unleached sample and the same sample leached for four weeks were analysed using TEM-EDX. SEM-EDX was not used because porosity could be easily mistaken for material removed from the paste during water leaching[136]. Based on the STA-EGA and MAS NMR results and as previously observed, the C-S-H silicate anion changed after four weeks of leaching. By that time, all the CH was leached from the sample as well as CaO layers of the dreierkette structure with consequent cross-linking that should affect the chemical composition of C-S-H. The next figures show the microstructure of the unleached sample, the water activated 30% PFA blended WPC paste one year old cured at 25°C.

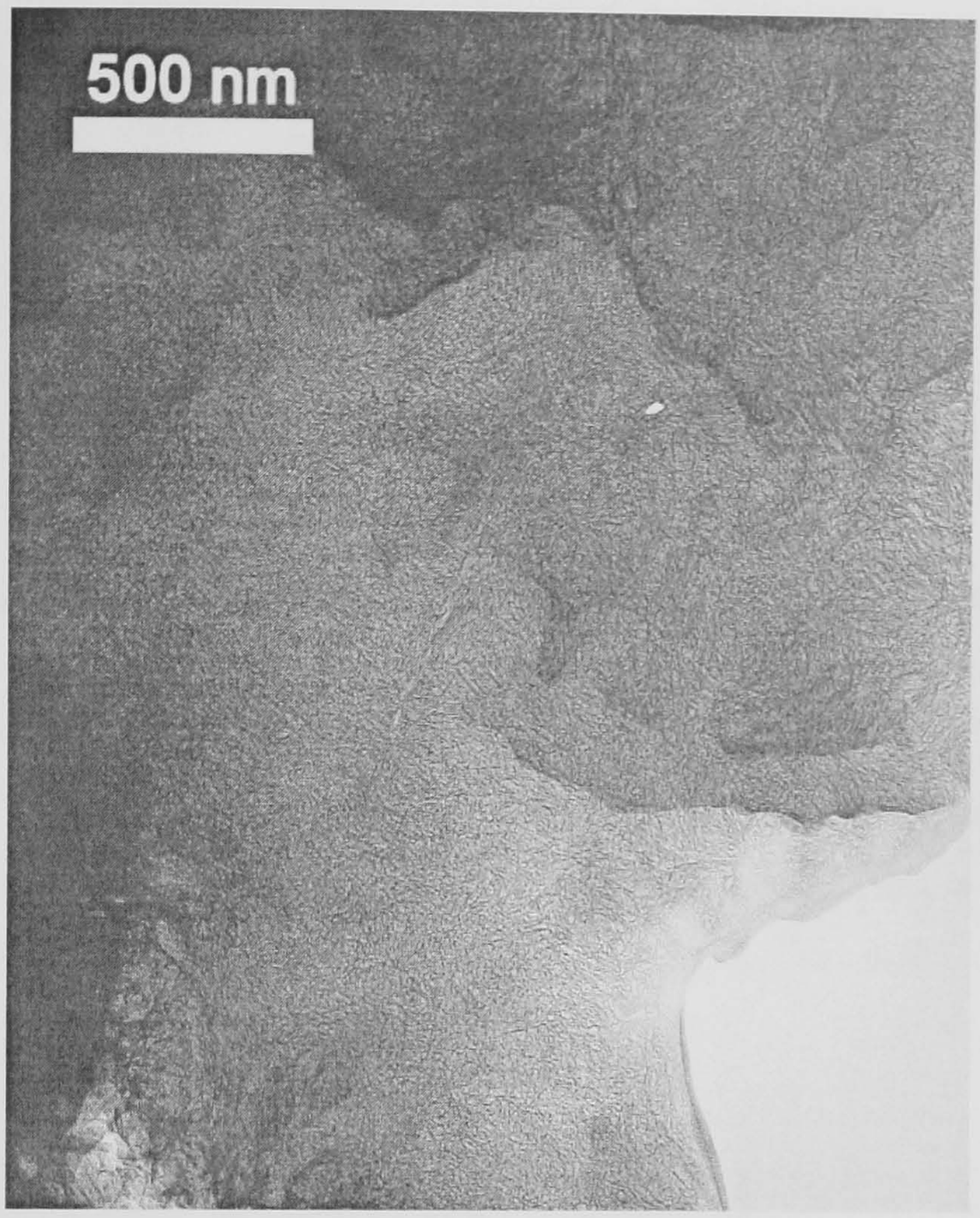


**Figure 7.4** – TEM micrograph showing fine and dense Ip C-S-H in the water activated 30% PFA blended paste one year.

It was observed that PFA blend had a typical microstructure where Ip C-S-H was very dense and fine, Op C-S-H fine and fibrillar, large crystals of CH and AFt-type relicts were also present. The microstructure was very similar to that of the same sample cured at 25°C for one month (Chapter IV, Section 4.7.1). The micrograph in Figure 7.5 shows the fine and fibrillar morphology of Op C-S-H.

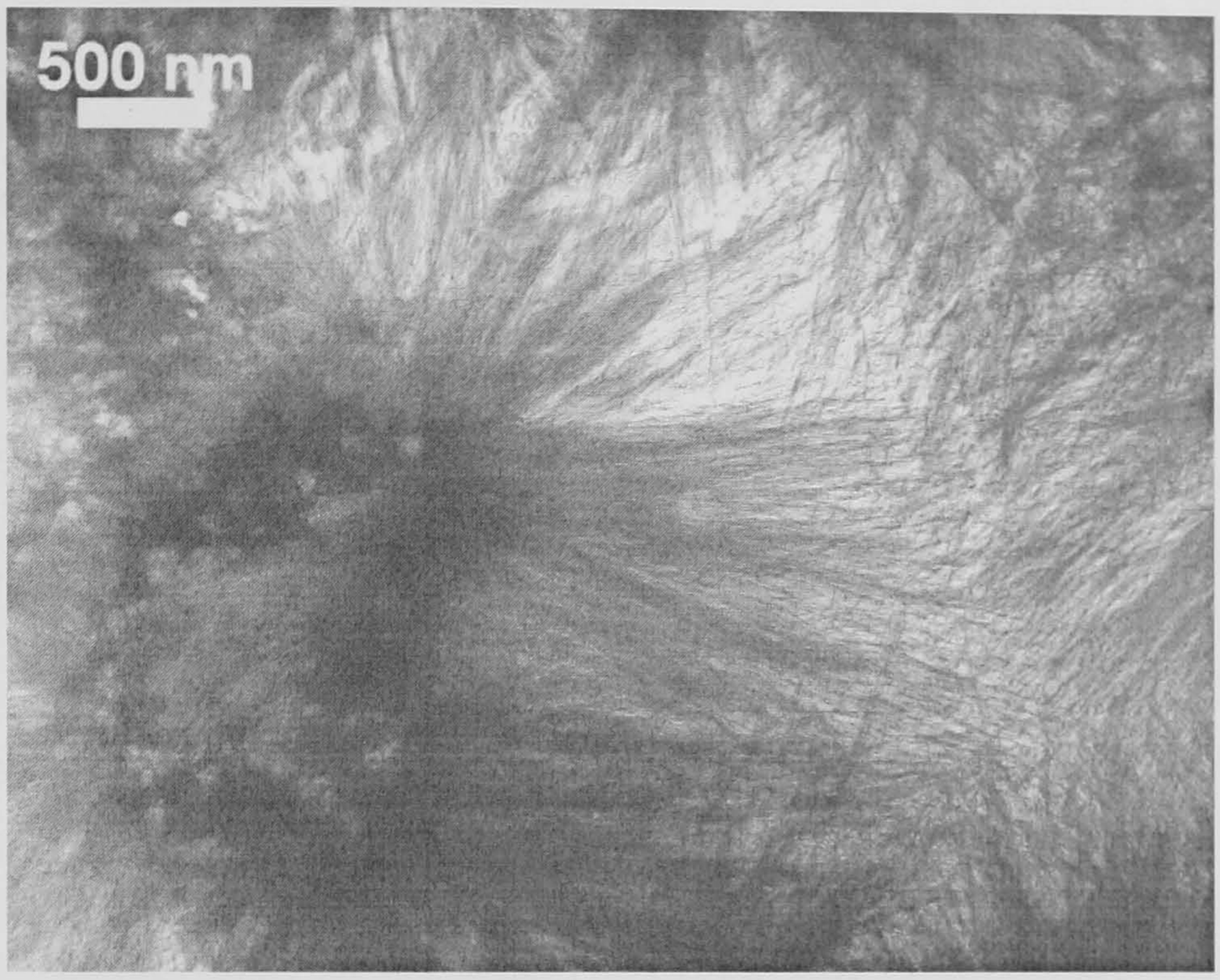


**Figure 7.5** – TEM micrograph showing fine and fibrillar Op C-S-H in the water activated 30% PFA blended paste one year.

The following micrograph shows a fully hydrated fly ash particle.

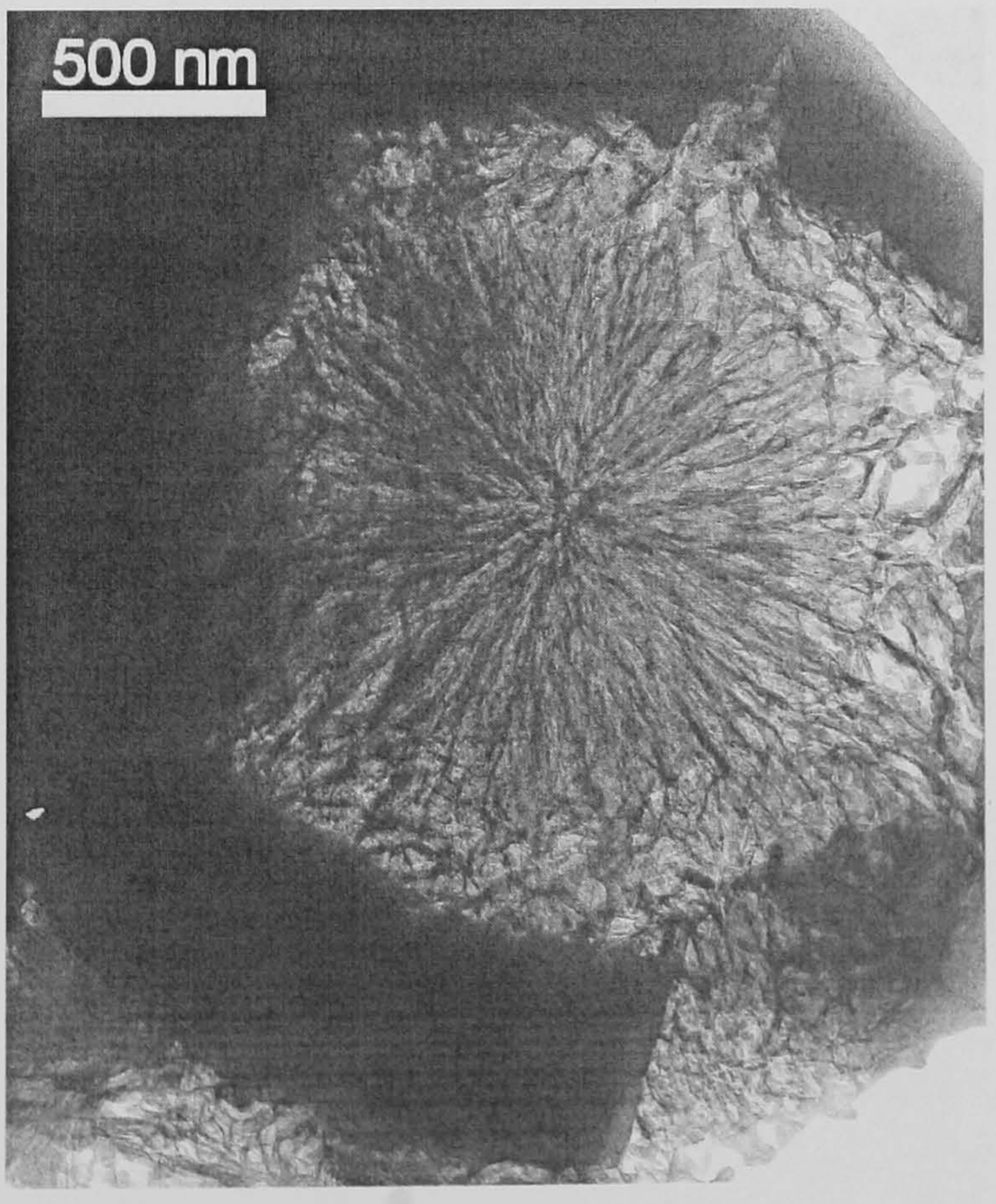


**Figure 7.6** – TEM micrograph showing a fully hydrated PFA particle in the water activated 30% PFA blended paste one year.

Figure 7.6 shows a fully hydrated PFA particle where it was possible to observe the difference in density between the centre of the particle and the outside crystalline rim. Fly ash particles react with CH from the outside rim towards the centre. The morphology of Ip C-S-H was the same as that observed in small fully hydrated cement grains containing a less dense Ip C-S-H with a foil-like morphology (Chapter V, Section 5.6), typically observed for Op C-S-H in other cement based systems.[13,57].

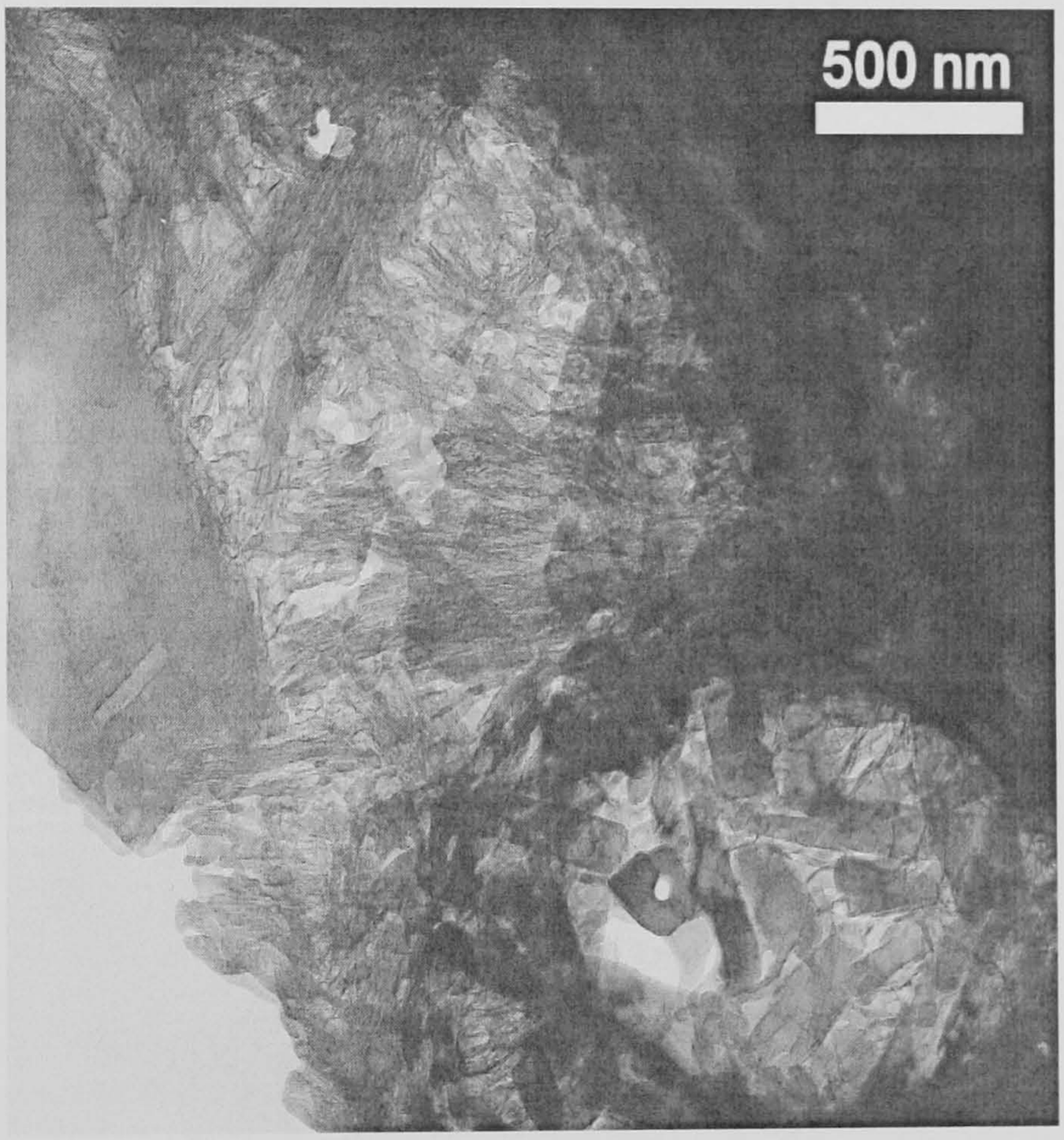


**Figure 7.7** – TEM micrograph showing CH, fine fibrillar Op C-S-H and AFt-type relicts in the water activated 30% PFA blended paste one year.

As the above micrograph clearly shows, relicts of AFt-type phases were identified and finely intermixed with fibrillar Op C-S-H.

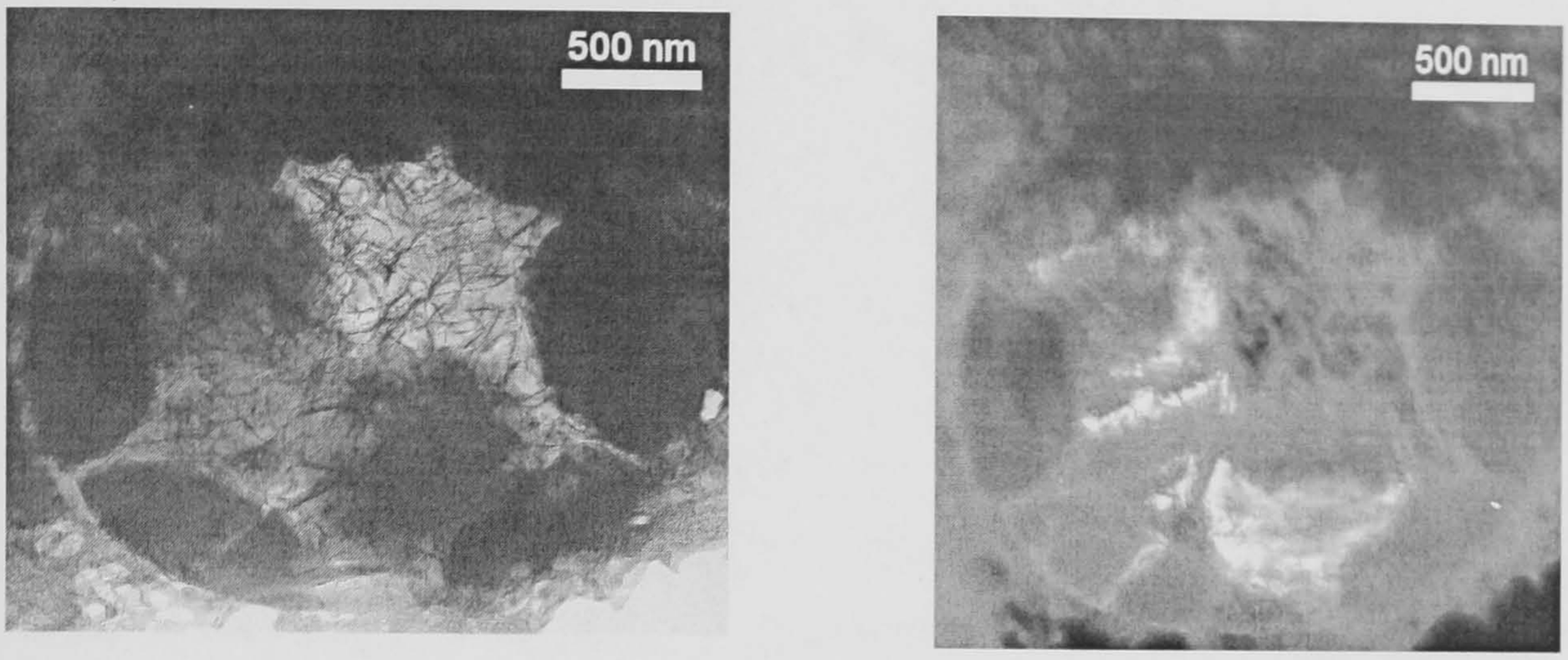


**Figure 7.8** – TEM micrograph showing bright field image (left) and dark field image (right) of a semi-reacted PFA particle in the water activated 30% PFA blended paste one year.

The above micrograph bright field (left) and dark field (right) images of a semi-reacted particle of PFA. It was possible to distinguish inside the particle the amorphous material from the crystalline one. The latter appears darker in the bright field image and brighter in the dark field image. EDX data analysis for the studied system is presented in the next figure.

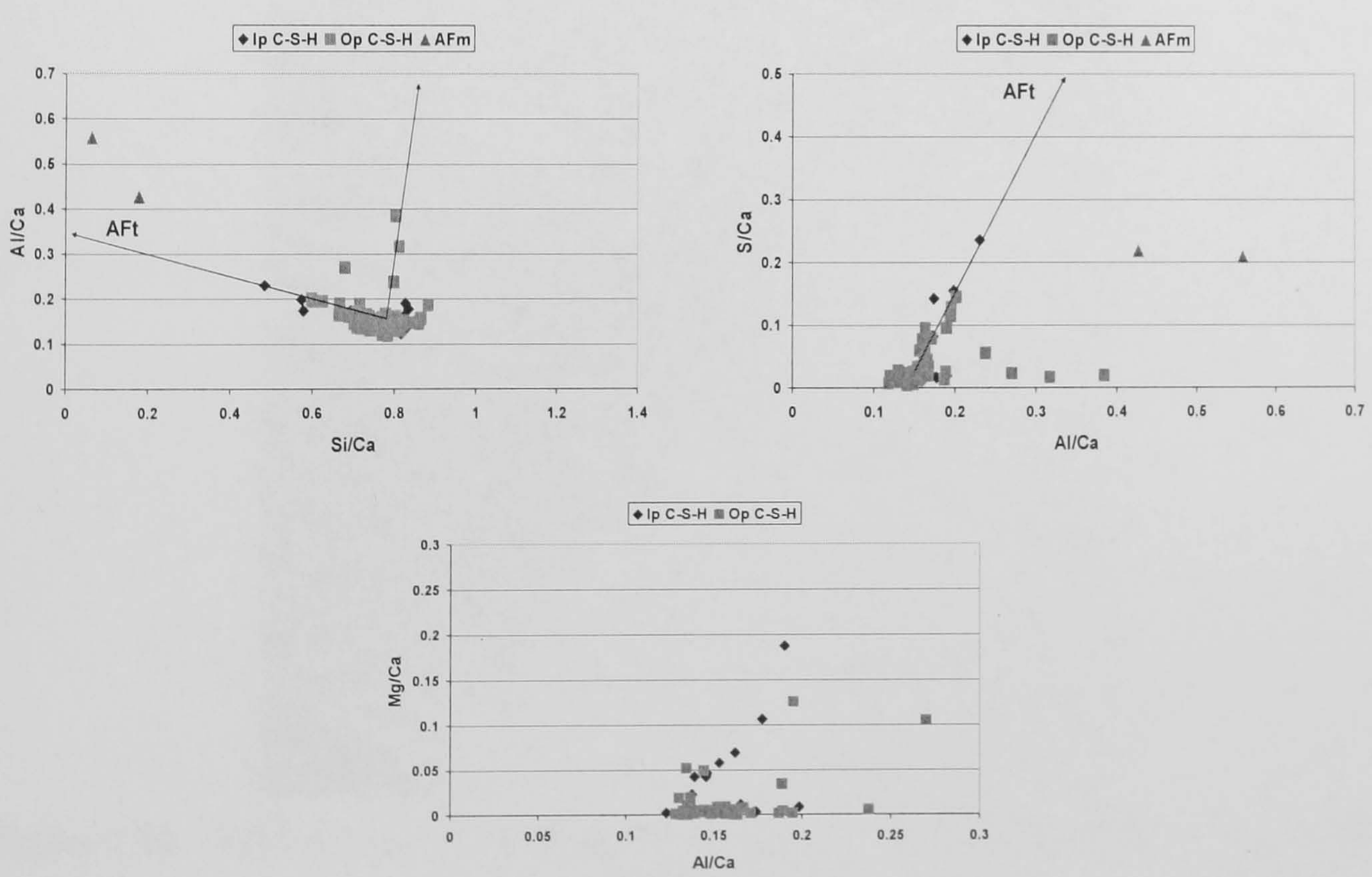


**Figure 7.9** – Al/Ca against Si/Ca (left top), S/Ca against Al/Ca (right top) and Mg/Ca against Al/Ca (bottom) atomic ratio plots for the TEM-EDX phase analysis of the water activated 30% PFA blended WPC paste, before water leaching.

The Al/Ca against Si/Ca atomic plot showed two distinct trendlines. A first trendline was identified in the direction of the AFt-type phases and another probably in the direction of hydrogarnet-type phases. As explained before, hydrogarnet-type phases are not usually formed in WPC pastes. The sulfur plot confirmed fine intermixing between Op C-S-H and AFt-type phases. Intermixing between Ip C-S-H and AFt-type phases could too be considered. The same plot also showed a less clear trendline in the direction of a sulfur free phase, probably hydrogarnet-type phases. The analyses of Ip and Op C-S-H that have the highest Al/Ca atomic ratio appear to include a contribution from microcrystals of a hydrotalcite-like phase. The latter was not observed at one month of hydration (Chapter IV, Section 4.7.1).

The following figures show micrographs for the microstructure of the four weeks water leached sample.

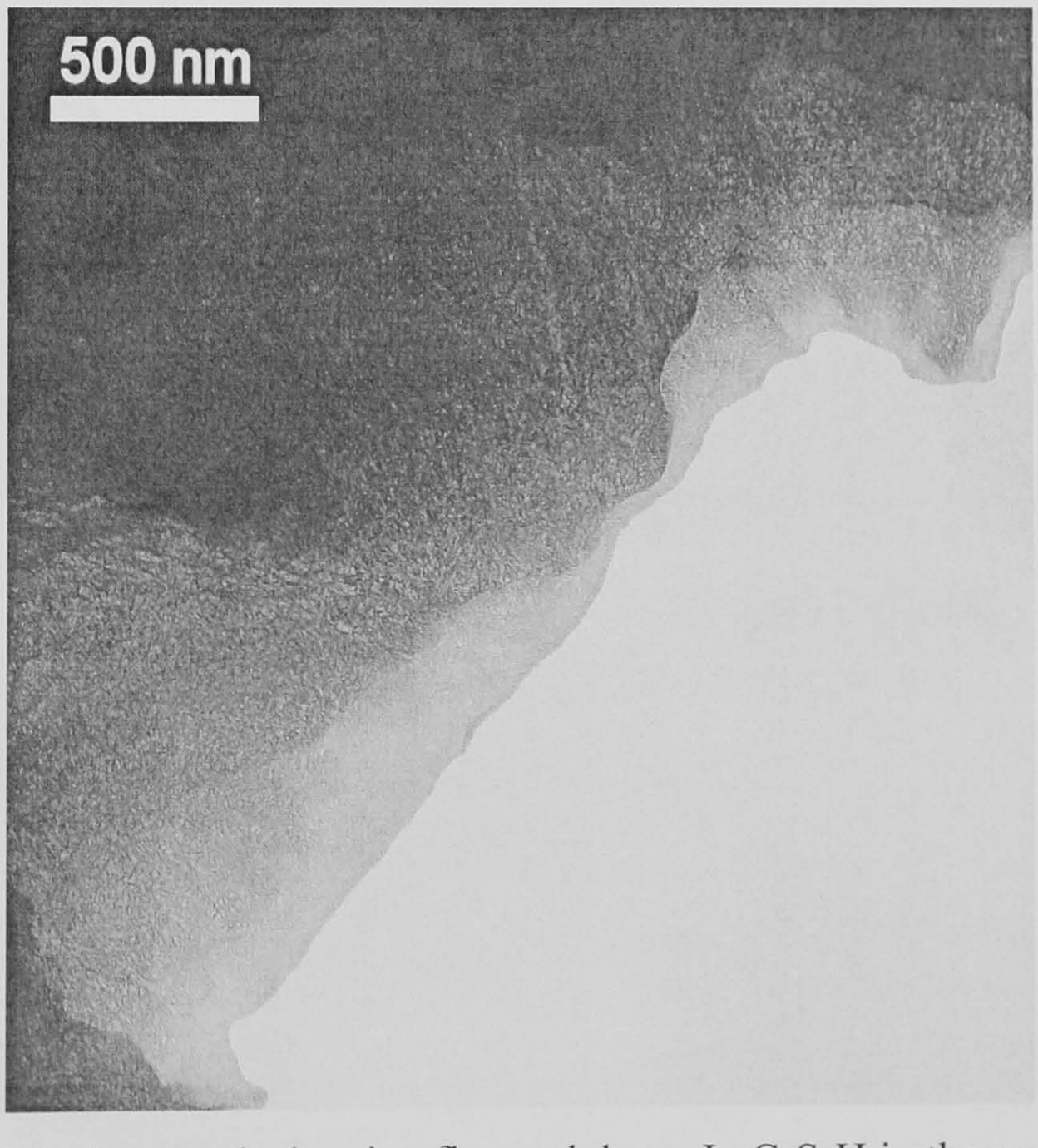


**Figure 7.10** – TEM micrograph showing fine and dense Ip C-S-H in the water activated 30% PFA blended paste one year after 4 weeks water leached.

The previous figure showed that, after four weeks of water leaching, Ip C-S-H had the same fine scale homogeneous morphology as that in the unleached sample. In the

microstructure of the leached system fine fibrillar Op C-S-H, crystals of CH and AFm-type phases and very small relicts of AFt-type phases were also observed. Although after four weeks of leaching STA showed that there was no CH in the sample, TEM-EDX showed that CH was still present in the microstructure. This discrepancy can be explained by limitations of STA and the error associated to the estimation of the amount of CH formed in the system.

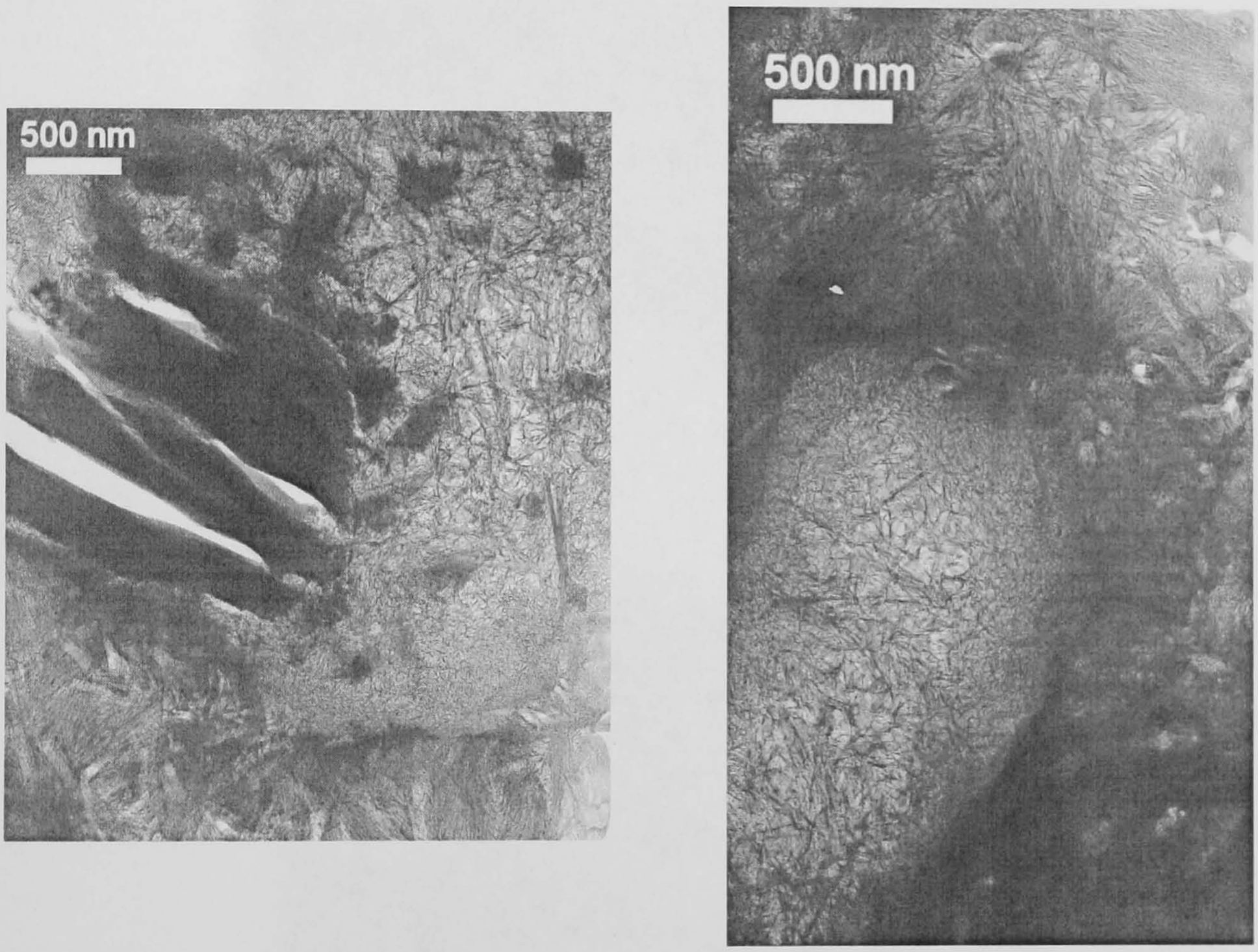


**Figure 7.11** – TEM micrograph showing fine fibrillar Op C-S-H and large crystals of AFm-type phases (left) and a fully hydrated cement grain surrounded by fine fibrillar Op C-S-H (right) present in the microstructure of the water activated 30% PFA blended paste one year, after 4 weeks water leached.

The previous micrographs showed the fine and fibrillar Op C-S-H, crystals of AFm-type phases and a fully hydrated cement grain. The latter contained Ip C-S-H with a foil-like morphology, surrounded by fibrillar Op C-S-H finely intermixed with very small AFt-type relicts. The foil-like morphology of Ip C-S-H formed in fully hydrated cement grains is demonstrated in the next figures.

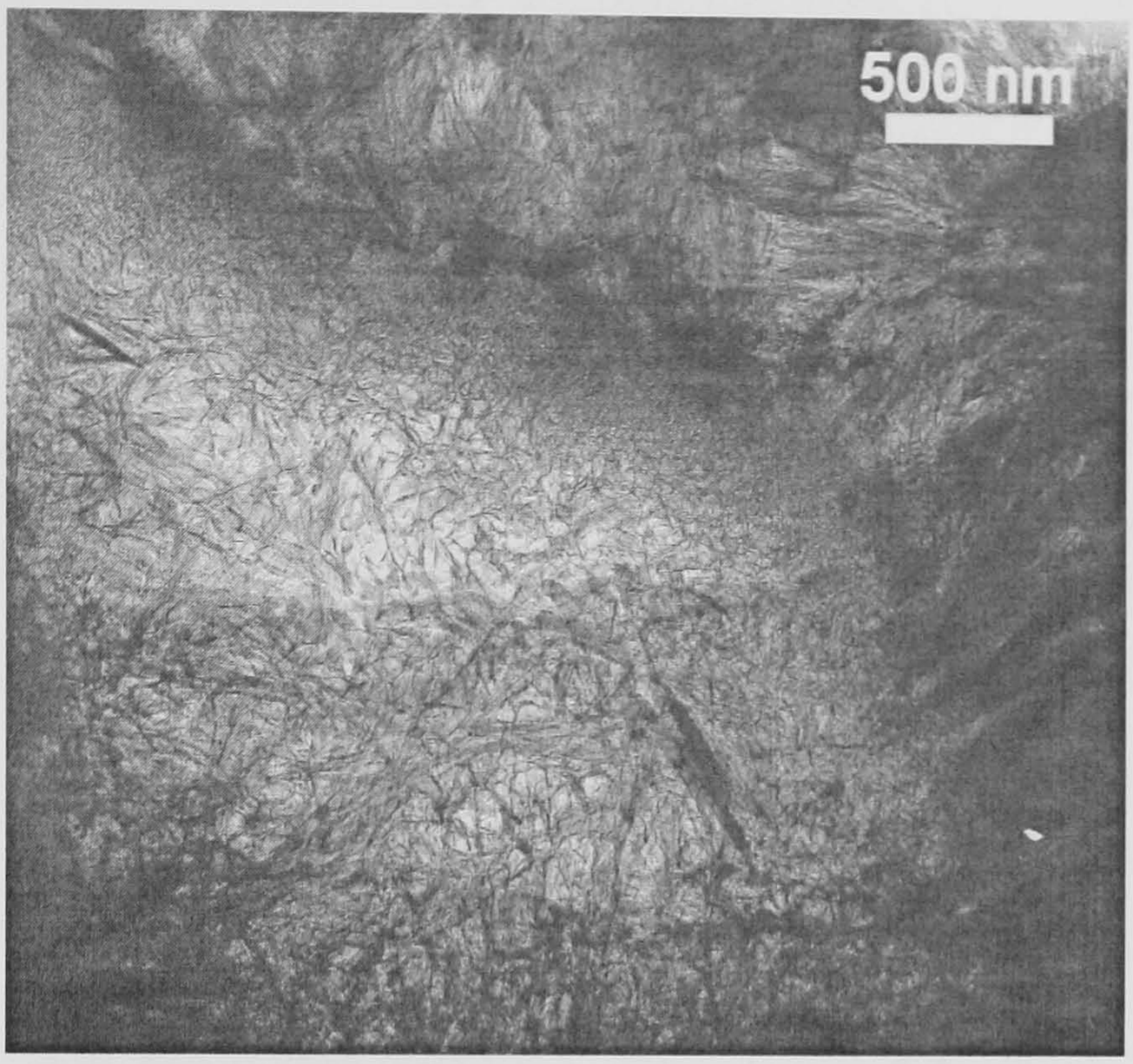


**Figure 7.12** – TEM micrograph showing a fully hydrated cement grain surrounded by Op C-S-H, in the water activated 30% PFA blended paste one year, after 4 weeks water leached.

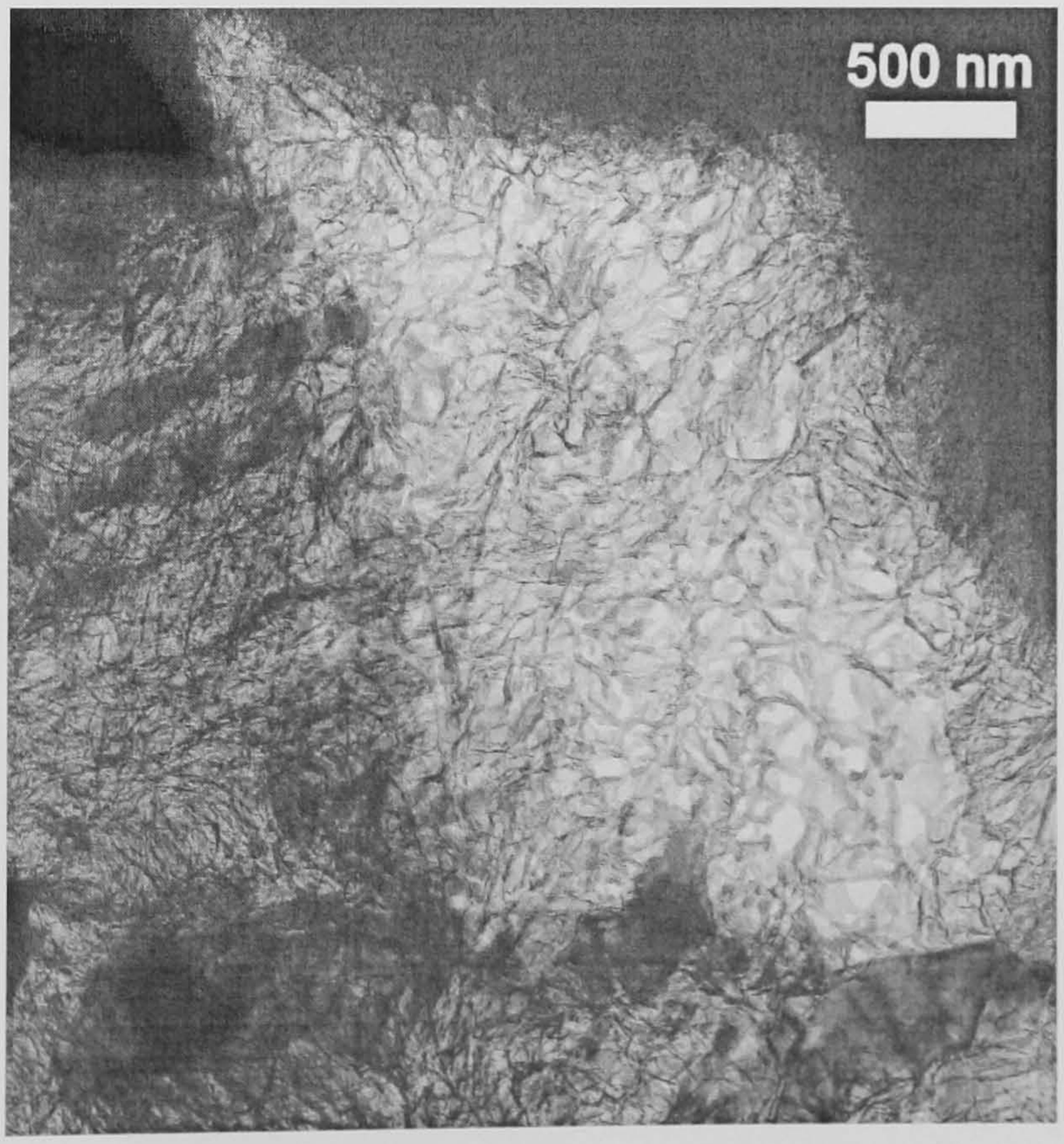


**Figure 7.13** – TEM micrograph showing fibrillar Op C-S-H surrounding a fully hydrated cement grain, in the water activated 30% PFA blended paste one year, 4 weeks water leached.

The following figure shows fibrillar Op C-S-H and some CH crystals present in the microstructure.

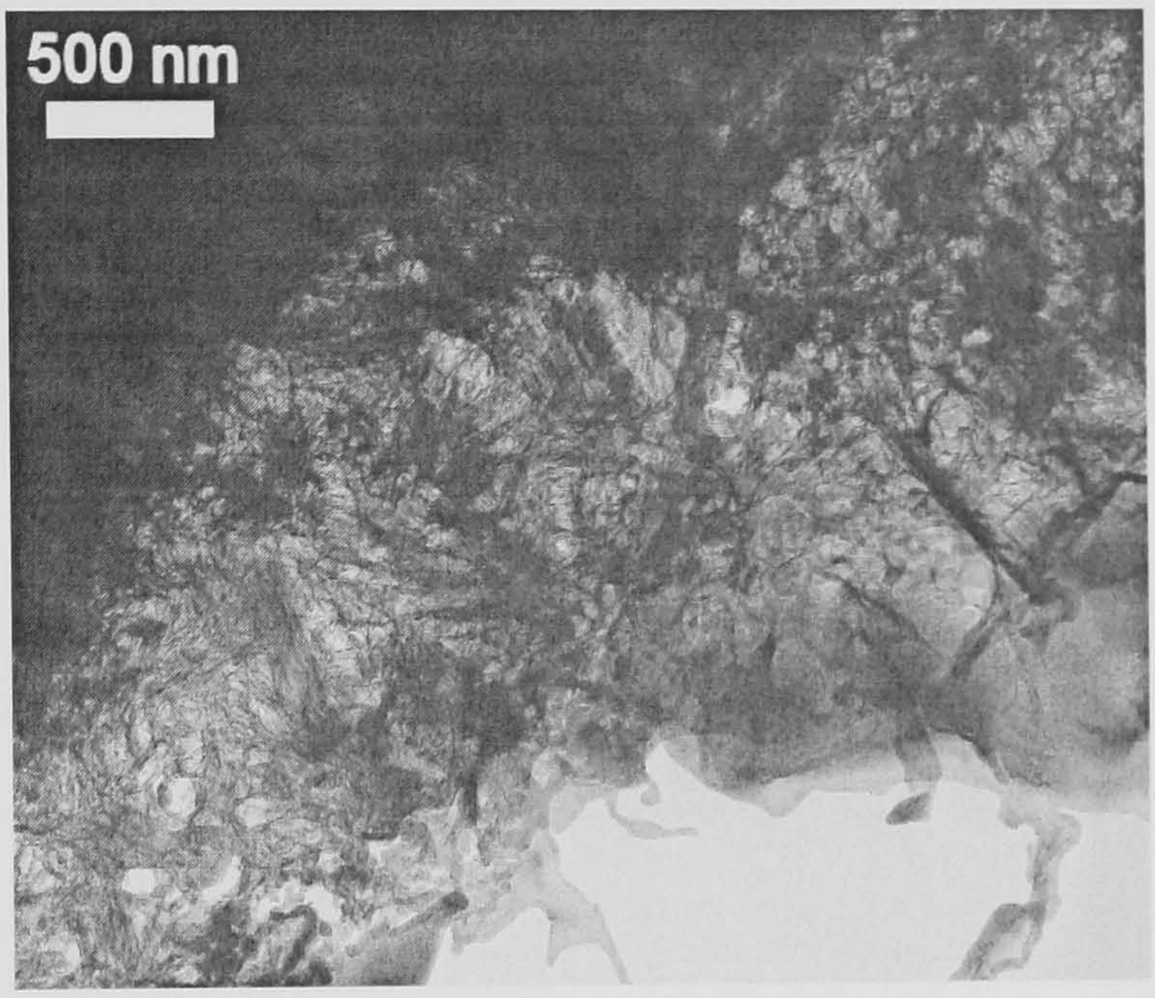


**Figure 7.14** – TEM micrograph showing fine fibrillar Op C-S-H and CH, in the water activated 30% PFA blended paste one year, after 4 weeks water leached.

Generally, Op C-S-H had a fine and fibrillar morphology. However, many areas of Op C-S-H with a foil-like morphology were also observed. Figure 7.15 shows an example of the different morphologies observed for Op C-S-H in the four weeks leached blend.

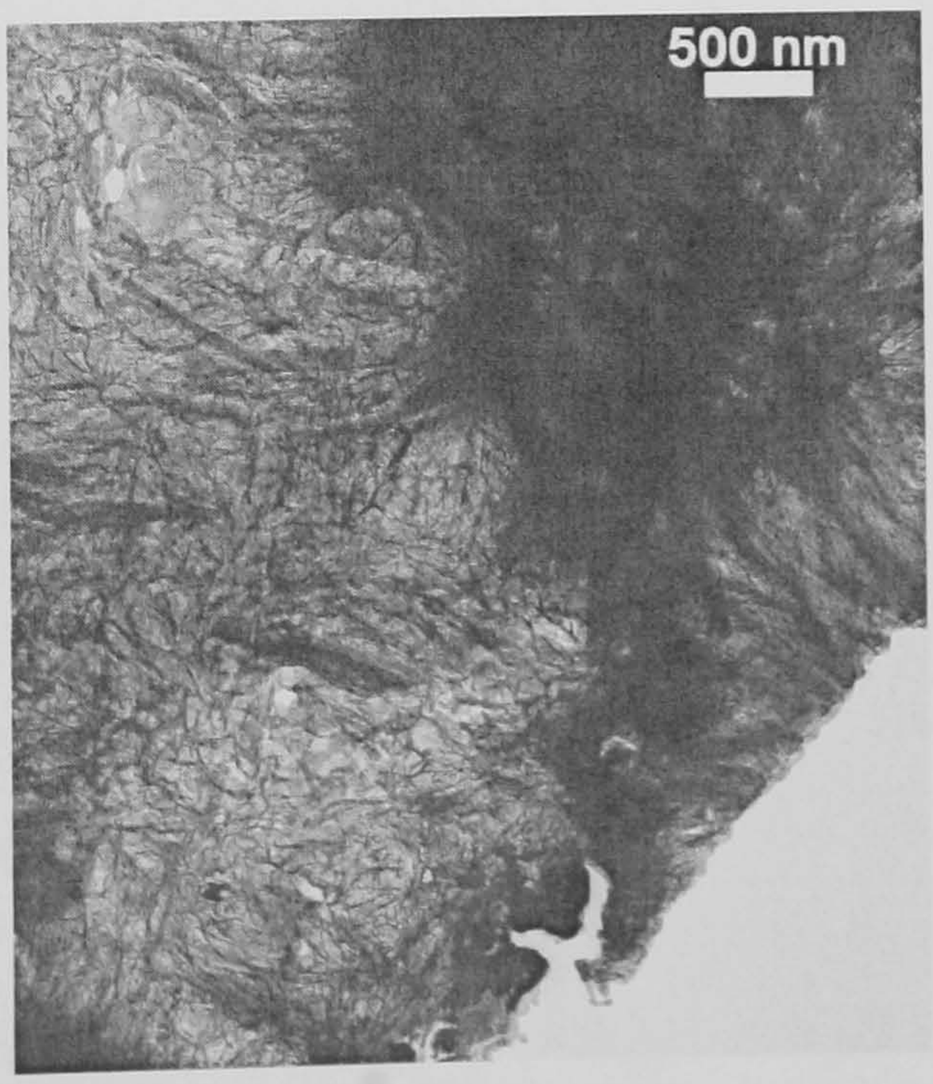


**Figure 7.15** – TEM micrograph showing both fine fibrillar (right) and foil-like (left) Op C-S-H in the water activated 30% PFA blended paste one year, after 4 weeks water leached.

The two different morphologies found for Op C-S-H were observed coexisting in the microstructure. In Figure 7.15, small relicts of AFt-type phases were identified in both fibrillar and foil-like morphologies. The next figure illustrates EDX data atomic ratio plots for the PFA blended cement paste water leached for four weeks.

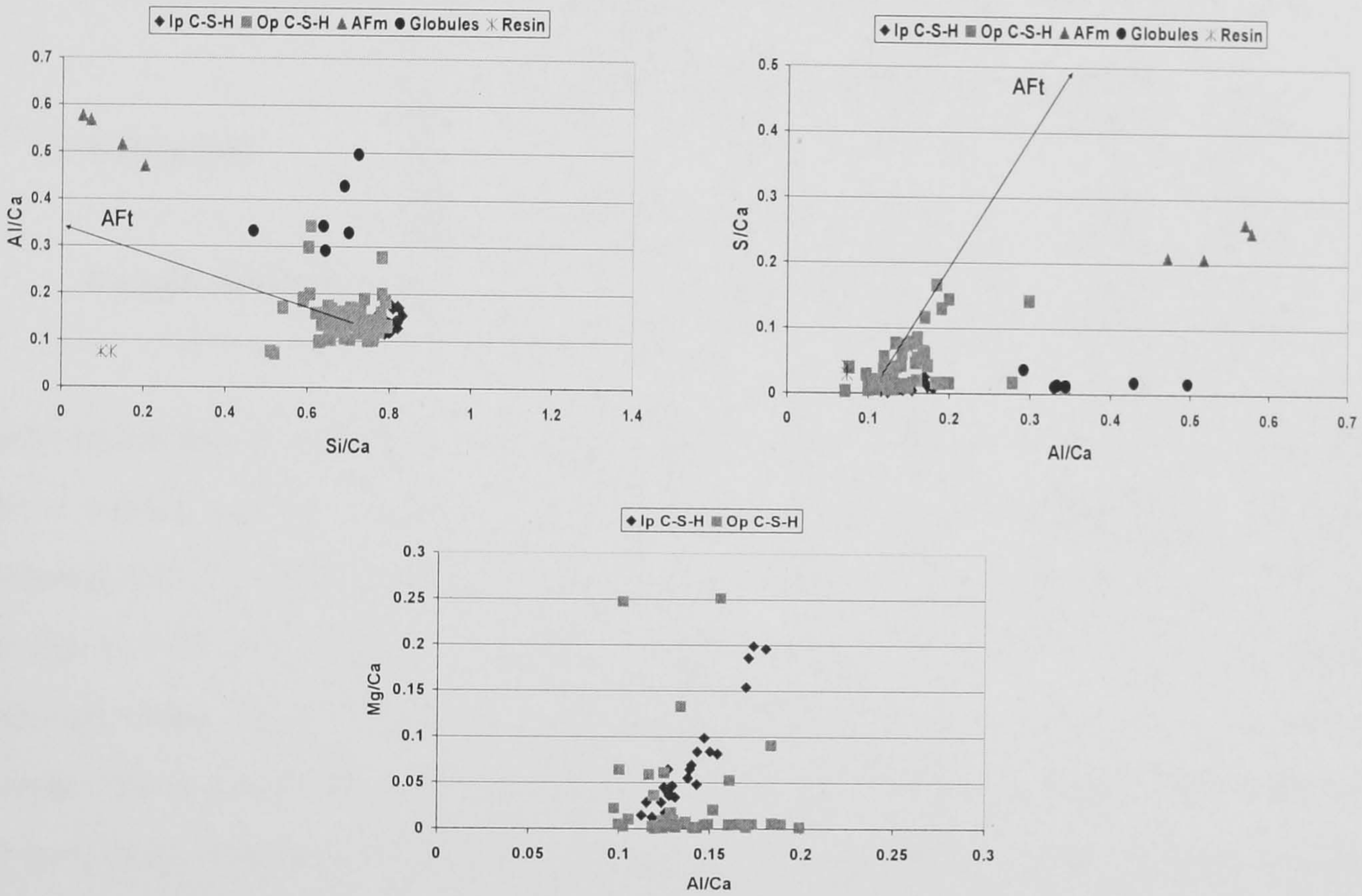


**Figure 7.16** – Al/Ca against Si/Ca (left top), S/Ca against Al/Ca (right top) and Mg/Ca against Al/Ca (bottom) atomic ratio plots for the TEM-EDX phase analysis of the water activated 30% PFA blended WPC paste, after 4 weeks water leached.

EDX analysis showed that there was no difference between the chemical composition of the foil-like Op C-S-H and that of fibrillar Op C-S-H. In the first plot, a clear trendline from bulk Op C-S-H in the direction of the AFt-type phases was identified. The analysis points for the globules appeared to go in the direction of hydrogarnet-type phases. S/Ca against Al/Ca atomic ratio plot confirmed fine intermixing between Op C-S-H and AFt-type phases. The same fine intermixing was observed in the unleached sample. A second trendline could also be considered in this second plot, going from Op C-S-H in the direction of a free sulfate phase that could be hydrogarnet-type phases. As previously observed for the unleached sample, there was a contribution from microcrystals of a hydrotalcite-like phase to the mean atomic ratios of Ip C-S-H. Table

7.2 summarises the EDX data obtained for the reference sample and for the sample leached four weeks.

**Table 7.2** – Mean Ca/Si and Al/Si atomic ratios obtained for C-S-H using TEM-EDX, for the water activated 30% PFA blended WPC paste, before water leaching and 4 weeks leached.

| | | Ca/Si | | | Ca/(Al+Si) | | Al/Si | |
|---|---|---|---|---|---|---|---|---|
| | | *N* | *mean* | *s* | *mean* | *s* | *mean* | *s* |
| **Unleached** | **Op** | 63 | 1.31 | 0.11 | 1.10 | 0.15 | 0.198 | 0.039 |
| | **Ip** | 14 | 1.33 | 0.19 | 1.09 | 0.11 | 0.212 | 0.055 |
| | **All** | 77 | 1.32 | 0.13 | 1.10 | 0.15 | 0.201 | 0.043 |
| **4 weeks leached** | **Op** | 53 | 1.42 | 0.11 | 1.19 | 0.11 | 0.195 | 0.043 |
| | **Ip** | 32 | 1.28 | 0.05 | 1.09 | 0.05 | 0.172 | 0.020 |
| | **All** | 85 | 1.37 | 0.15 | 1.15 | 0.11 | 0.186 | 0.038 |

In the unleached sample, the mean atomic ratios were very similar for Ip and Op C-S-H. These values can be compared with those obtained for an OPC-30% fly ash blend hydrated for 17 months, where the mean Ca/Si atomic ratio for Ip C-S-H was 1.50 and for Op C-S-H was 1.56[88]. It can be concluded that the obtained values are similar although those for the unleached sample were slightly lower. Considering the leached sample, the mean Ca/Si and Al/Si atomic ratios were higher for Op C-S-H than those for Ip C-S-H. The mean Ca/(Al+Si) atomic ratio was similar in both samples. As TEM micrographs showed, inner and outer product C-S-H morphologies were the same as those found for Ip and Op C-S-H formed in unleached PFA blended cement paste, except that foil-like Op C-S-H was also identified. As seen in the previous chapters for the alkaline pastes (and other cement-based systems[57]), the change of fibrillar Op C-S-H morphology into foil- or lath-like was associated with a decrease of the mean Ca/Si atomic ratio, when compared with the corresponding water activated systems. However, that was not verified for these two systems, i.e. a statistically significantly decrease of the mean Ca/Si atomic ratio was not observed for Op C-S-H in the two samples that would be associated to the change of Op C-S-H morphology. Therefore, it appears that Op C-S-H morphology might not be solely associated to its mean Ca/Si atomic ratio. In the following table, TEM-EDX results were compared with those from MAS NMR.

**Table 7.3** – Mean Ca/Si and Al/Si atomic ratios obtained for C-S-H using TEM-EDX and MAS NMR, for the 30% PFA blended WPC paste, before water leaching and 4 weeks leached.

| | All Al/Si | Al/Si (NMR) |
|---|---|---|
| **Unleached** | 0.201 | 0.184 |
| **4 Weeks leached** | 0.186 | 0.133 |

Some agreement was found between TEM-EDX data and MAS NMR for the unleached sample.

### 7.3.2 – T/J and T/CH-based models for the structure of C-S-H

Application of the different structural models to TEM-EDX data relative to the analysed systems is presented in this section.

**Table 7.4** – Experimental data used in Al/Ca against Si/Ca atomic plots discussing the applicability of the T/CH and T/J structural models for C-S-H, in the unleached and 4 weeks water leached systems.

| | Ip Ca/Si | Op Ca/Si | Ip Al/Si | Op Al/Si | Al/Si (NMR) | MCL | %B |
|---|---|---|---|---|---|---|---|
| **Unleached** | 1.33 | 1.31 | 0.212 | 0.198 | 0.184 | 11.6 | 56 |
| **4 weeks leached** | 1.28 | 1.42 | 0.172 | 0.195 | 0.132 | 9.2 | 45 |

Figure 7.17 shows Ip and Op C-S-H data in the Al/Ca against Si/Ca atomic ratio plot considering the T/J and T/CH structural models.

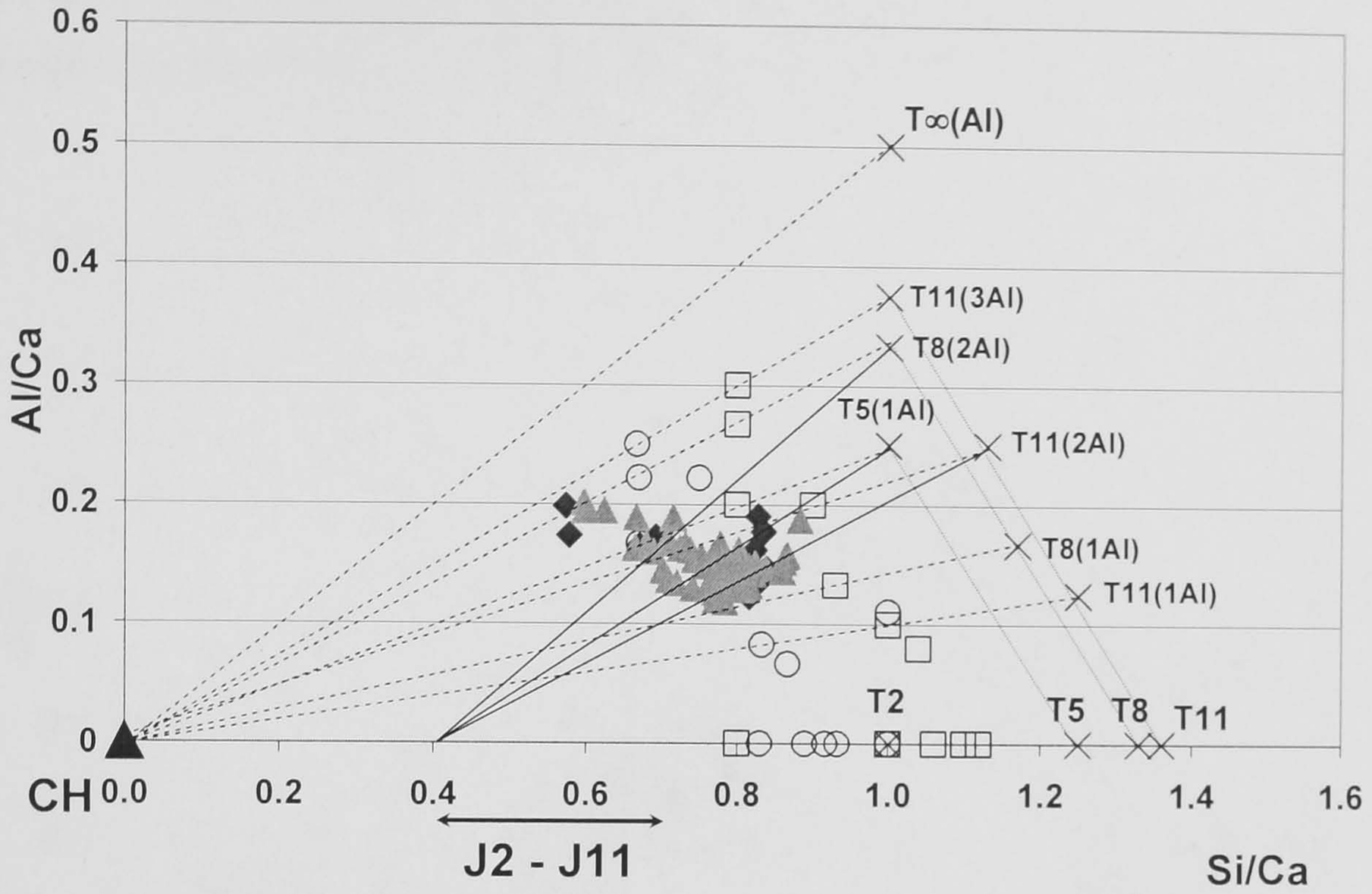


**Figure 7.17** – Al/Ca against Si/Ca atomic plot for the water activated 30% PFA blended WPC paste cured for 1 year at 25°C, accounting with T/J and T/CH viewpoints (♦ Ip C-S-H, ■ Op C-S-H, O unprotonated units, □ half protonated, X fully protonated, T∞ tobermorite, --- T/CH, — T/J).

The previous plot shows that data was consistent with the T/J structural model because most of the results fitted in the tie lines from T11(2Al) and T5(1Al) in the direction of J2 and some data also in the trendline from T8(2Al) to J2. It should be pointed out that this system after one month cured 25°C, C-S-H data was consistent with both structural models. Apparently, with increasing hydration time, C-S-H structure became more consistent with the T/J point of view.

From the viewpoint of the models, water leaching should firstly remove CH formed from cement hydration. After most of the CH is removed, than CH is removed from C-S-H. If C-S-H is consistent with the T/CH model, than CH present in the interlayers is removed and MCL should not be disturbed to a very large extent because C-S-H will preserve its T/J structure. In the case of C-S-H being consistent with the T/J model, CH is removed from C-S-H and the T/J structure is not maintained leading to the decrease

of MCL. The following figure shows the Al/Ca against Si/Ca atomic ratio plot considering the T/CH and T/J models for the four weeks water leached sample.

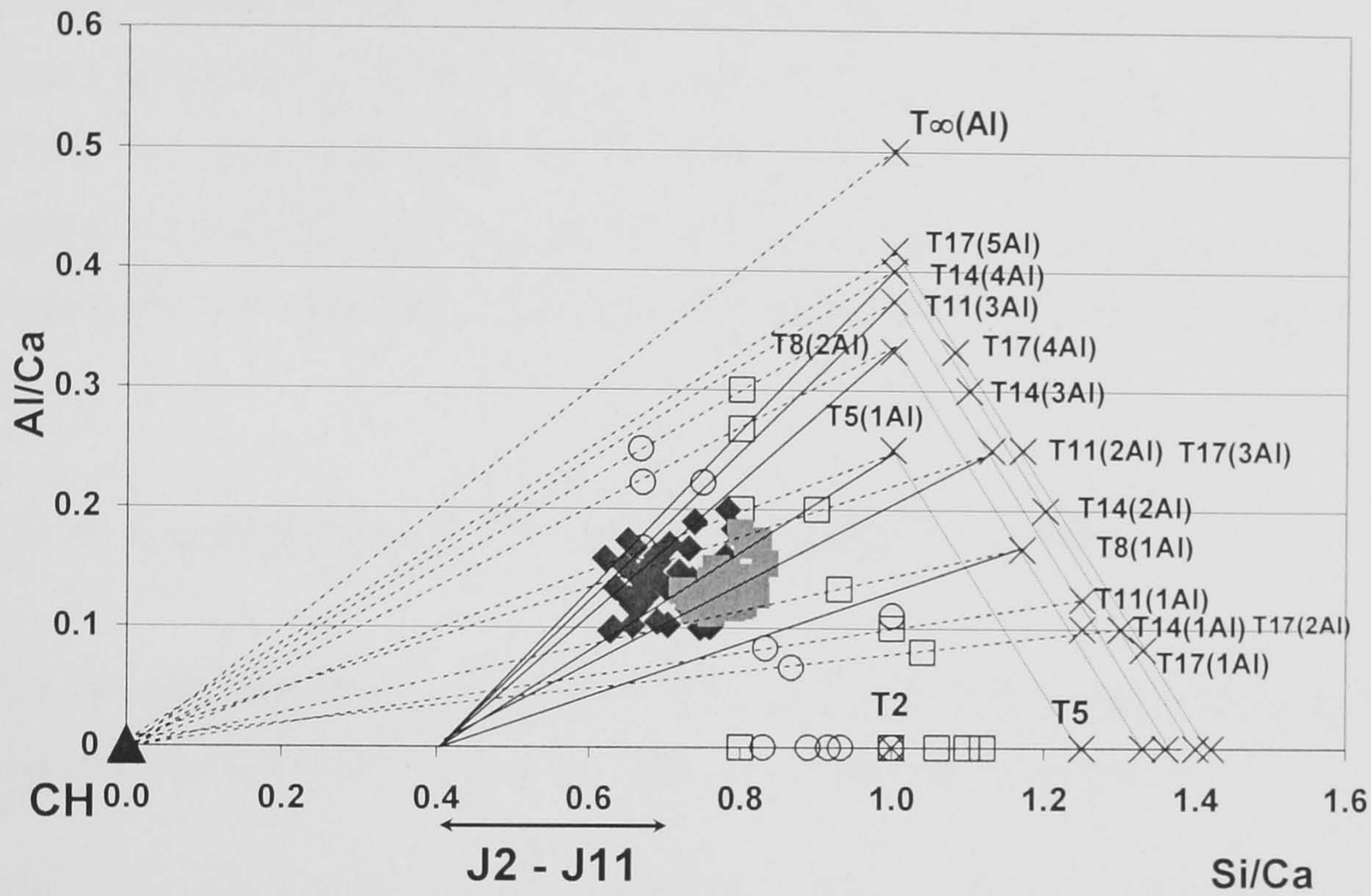


**Figure 6.18** – Al/Ca against Si/Ca atomic plot for the 4 weeks water leached sample, accounting with T/J and T/CH viewpoints (♦ Ip C-S-H, ■ Op C-S-H, O unprotonated units, □ half protonated, X fully protonated, T∞ tobermorite, --- T/CH, — T/J).

Although data was slightly less scattered than that in the unleached system, C-S-H was still consistent with the T/J viewpoint. This was indicated by the trendlines T11(2Al), T8(2Al) and T5(1Al) in the direction J2. It was concluded that even after four weeks of continuous water leaching of this system, C-S-H was consistent with the T/J structural model. Although MCL did not changed significantly (it would indicate that C-S-H data was consistent with the T/CH point of view for the reasons explained before), the plots indicate that after twelve weeks of water leaching, C-S-H nanostructure was still consistent with the tobermorite-jennite structural model.

As explained before, the water leaching process removes most of the CH formed in the cementitious paste and possibly part of the AFm/AFt-type phases. Then, the calcium oxide from C-S-H starts to be also leached. The leaching behaviour and consequent

changes in the system depend on the nanostructure of C-S-H and also on the T/J and T/CH viewpoints. If the nanostructure is consistent with the T/CH point of view, then calcium hydroxide layers from C-S-H are removed but the tobermorite-structure of C-S-H is preserved. On the other hand, if it is more consistent with the T/J viewpoint, then CaO layers from the tobermorite-structure will be leached and the skeleton of C-S-H is profoundly affected, responding by rearranging itself onto a higher polymerised structure ($Q^3$ species are formed). Ultimately, leaching can destabilise and destroy the C-S-H nanostructure reducing the gel into a soft mass of silica gel.

## 7.4 - C-S-H STRUCTURAL-CHEMICAL COMPOSITION

The structural-chemical composition of C-S-H was determined (equations 4.2 to 4.7, Chapter IV), and Table 7.5 resumes the data used in the calculations:

**Table 7.5** – TEM-EDX and MAS NMR data used in the determination of C-S-H chemical composition according to the T/J and T/CH structural viewpoints for the unleached and leached systems.

| | Ca/Si (TEM) | *y* | *w* | *y'* | w' | Al/Si (TEM) | Al/Si (NMR) | *a* | MCL (3n-1) | *n* |
|---|---|---|---|---|---|---|---|---|---|---|
| **Unl.** | 1.32 | 2.05 | 0 | 1.58 | 1.76 | 0.20 | 0.184 | 0.17 | 11.6 | 4.2 |
| **Leac.** | 1.37 | 2.47 | 0 | 2.02 | 0 | 0.19 | 0.133 | 0.16 | 14.7 | 5.2 |

Tables 7.6 and 7.7 resume the structural composition obtained for the unleached and leached samples according to the T/J and TCH viewpoints.

**Table 7.6** – C-S-H chemical composition determined according to the T/J structural viewpoint for the unleached and leached systems.

| | T/J (minimum degree of protonation) |
|---|---|
| **Unleached** | $\{Ca_{8.4}(Si_{0.83}Al_{0.17})_{11.6}O_{35.8}\}\cdot(OH)_{0.21}\cdot Ca_{4.31}\cdot mH_2O$ |
| **4 weeks Leached** | $\{Ca_{10.5}(Si_{0.84}Al_{0.16})_{14.7}O_{45.1}\}\cdot(OH)_{2.46}\cdot Ca_{0.46}\cdot mH_2O$ |

The structure of C-S-H can also be reorganised according to the T/CH viewpoint, resumed in Table 7.7.

**Table 7.7** – C-S-H chemical composition determined according to the T/CH structural viewpoint for the unleached and leached systems.

| | **T/CH (minimum degree of protonation)** |
|---|---|
| **Unleached** | $Ca_{11.7}(Si_{0.83}Al_{0.17})_{11.6}O_{35.8}\cdot Ca_{0.99}\cdot mH_2O$ |
| **4 weeks Leached** | $Ca_{15.7}(Si_{0.84}Al_{0.16})_{14.7}O_{45.1}\cdot Ca_{1.18}\cdot 0.05Ca(OH)_2\cdot mH_2O$ |

The presence of hydroxyl groups outside the brackets indicates that on the T/J viewpoint for the nanostructure of C-S-H, there was some J-like structure. As previously observed for the blend at one month (Chapter IV, Section 4.8), there was hardly any "solid-solution" CH units. Figures 7.17 and 7.18 also show that both samples were consistent with the T/J point of view.

# VIII – CONCLUSIONS

## 8.1 – GENERAL CONCLUSIONS

### 8.1.1 – STA-EGA and XRD

The amount of calcium hydroxide formed in the studied systems was simply estimated using STA. The analysed samples carbonate because EGA curves did not give evidence for the presence of any evolved $CO_2$ gas.

XRD patterns showed that the main crystalline phases present in the anhydrous white Portland cement were anhydrite ($CaSO_4$), alite ($CaSiO_3$), belite ($Ca_2SiO_4$) and tricalcium aluminate ($Ca_3Al_2O_6$). The fly ash was mainly composed of an amorphous phase as well as crystalline phases such as mullite ($Al_{4.5}Si_{1.5}O_{9.75}$), quartz ($SiO_2$) and maghemite ($\gamma$-$Fe_2O_3$). CH was formed in all hydrated systems but its nature depended on the type of activation and the curing temperature. AFm-type phases were not present in sufficiently large quantity or with sufficiently large or ordered crystals to be detected by this technique. Considering the water activated neat and blended pastes ettringite and portlandite were formed and remaining alite and belite were present after one month of hydration. In the KOH activated pastes, ettringite was not formed and additional arcanite, $K_2SO_4$, was identified. As hydration continued, residual quartz was also identified in the blended pastes corresponding powder diffractograms. In the alkaline systems, microcrystalline CH had a smaller average crystal size (causing broadening of the peaks), and ranged from microcrystalline particles intermixed with C-S-H and large regions with small amounts of it interstratified with C-S-H. XRD also confirmed that none of the samples was carbonated (STA-EGA) because there was no evidence for any of the calcium carbonate polymorphs.

### 8.1.2 – $^{29}$Si Solid State MAS NMR

$^{29}$Si MAS NMR was used to determine the silicate anion structure present in the C-S-H phase. This technique provided quantitative information on the silicate anion structure of the C-S-H gel, namely the fractions of silicon present in different tetrahedral environments, $Q^n$, where n denotes the connectivity of the silicate tetrahedron, in dreierkette chains. Quantification was achieved in the case of the neat WPC pastes but only semi-quantitative data was obtained for the 30% PFA blended systems. In the spectra obtained for all the hydrated systems, $Q^0$ resonance (around -71.3 ppm) was assigned to belite. This broad resonance is a convolution between a sharp peak component from belite (at -71 ppm) and a broader peak component from alite. A peak at -79 ppm was assigned to the resonance $Q^1$ (end chain groups), another peak for $Q^2$ (chain middle groups where both adjacent tetrahedra are occupied by silicon) species at -84.9 ppm, and a resonance for $Q^2$(1Al) at -82 ppm (chain middle groups where one of the adjacent tetrahedra is occupied by aluminium) which results in a down-field shift of around 3 ppm. In the blended pastes, an additional resonance at around -103 ppm was assigned to a broad peak $Q^4$ (cross-linking sites in a three dimensional framework) corresponding to silicon present in the anhydrous fly ash. It was observed that as hydration proceeded, dimers were formed ($Q^1$ species) that also polymerised to give $Q^2$ species and $Q^2$(1Al) species. The mean length of the aluminosilicate anions (MCL) in the C-S-H polymerised and it was higher in the fly ash blended pastes. Alkali activation resulted in C-S-H with slightly more structural order than with water. Formulae were presented for the average structural units in the C-S-H present in the systems analysed by TEM-EDX. At 25°C and 55°C, alkaline activation did not influence the kinetics of the cement reaction or that of the pozzolanic reaction. In the blended systems, more aluminium was available to substitute for silicon in the dreierkette chain of the silicate anion of C-S-H (PFA reaction), leading to higher mean Al/Si atomic ratio in C-S-H.

### 8.1.3 – SEM-EDX

SEM-EDX provided very useful information regarding the microstructure development as hydration took place. Generally, as hydration occurred, the microstructure became

more dense and better packed because more Op C-S-H was formed in the water filled spaces and additional C-S-H resulted from the pozzolanic reaction. The values for the mean atomic ratios were influenced by the large interaction volume between the electron beam and the sample, leading to higher Ca/Si and Al/Si atomic ratios for C-S-H due to the extension of intermixing with other phases. The data was at the high end of values measured previously by TEM-EDX for C-S-H in Portland cement pastes hydrated at lower temperature (20°C)[72] and those for the KOH activated system were much higher than is possible to achieve for C-S-H in models for the structure of C-S-H[3]. Therefore, it was not possible to determine the chemical composition of C-S-H free of intermixture with other phases by X-ray analysis in the SEM; the higher resolution of TEM-EDX was necessary.

### 8.1.4 – TEM-EDX

TEM-EDX is a very powerful technique since it provided information concerning the morphology of the different phases present in the systems and local chemical analysis (EDX). Generally, inner product and outer product C-S-H presented different morphologies. At 25°C, Ip C-S-H had a fine and dense morphology and Op C-S-H was fine and fibrillar. These morphologies were typical in room temperature cured pastes which was consistent with previous observations in other systems. Op C-S-H morphology changed from fine fibrillar to foil or lath-like with alkali, also consistent with previous observations. Fly ash replacement did not affect the morphology of Ip and Op C-S-H. Large crystals of CH and AFm-type phases were identified in the microstructure as well as smaller relicts of AFt-type phases that were usually finely intermixed with Ip and/or Op C-S-H. Small fully hydrated cement and PFA particles were filled with a less dense Ip C-S-H with morphology very similar to the foil-like one. EDX analysis gave accurate mean atomic ratios for Ip and Op C-S-H. Generally, the mean Ca/(Al+Si) atomic ratio was lower in the water activated blends than that in the neat cement pastes due to the fly ash reaction. Plots for the obtained mean atomic ratios showed clear trendlines indicating fine intermixing between C-S-H and other calcium aluminoferrite hydrate phases like AFt-type phases, AFm-type phases with low sulfate

content or sulfate free phases. In the alkaline pastes, a fine intermixing between Ip and Op C-S-H with microcrystalline CH was observed, confirming evidence given by XRD. Comparing TEM-EDX and $^{29}Si$ MAS NMR results for the mean Al/Si atomic ratio, generally some agreement was not found. Although MAS NMR is a bulk technique, it should have given very similar results to those using $^{29}Si$ TEM-EDX as previously reported works confirmed. A plausible explanation for the NMR giving a higher value than that measured in the TEM is that for C-S-H that has a high mean Ca/Si atomic ratio there is an additional peak at a similar chemical shift to $Q^2(1Al)$ that is not associated with aluminium; clearly the omission of such a peak from deconvolution procedure would result in an overestimation of the mean Al/Si atomic ratio. Based on TEM-EDX and MAS NMR results, the composition-structure data was discussed in terms of the structural models proposed for the nanostructure of C-S-H.

## 8.2 – GENERAL EFFECTS OF CURING AT HIGH TEMPERATURE

### 8.2.1 – STA-EGA and XRD

The main crystalline hydration products were CH and AFt-type phases with water activation, and microcrystalline CH with alkali. At 85°C, the calcium hydroxide and hydrogarnet phases present in the KOH activated systems were microcrystalline. The CH microcrystals were anisotropic because the peaks were not broadened to the same extent.

### 8.2.2 - Compressive Strength

There was no linear relationship between increasing hydration temperature and this physical property. Therefore, although higher curing temperature accelerated cement hydration, it did not enhance strength of the tested mortar cubes. Again, it is necessary to bear in mind that accurate evaluation of the porosity should have been conducted.

### 8.2.3 – $^{29}$Si Solid State MAS NMR

Higher curing temperature accelerated the rate of cement hydration. Polymerisation of C-S-H was also affected. MCL of the C-S-H anions was much higher than that of C-S-H formed at lower temperatures and was higher in the blended pastes than with neat cement. Generally, the method of activation had no effect on the kinetics of the cement and/or pozzolanic reaction.

### 8.2.4 – SEM-EDX

Increasing the curing temperature led, generally, to coarsening of the hydration products, increased porosity and decreasing of the general uniformity of the microstructure. Many of the studied systems exhibited non uniform porosity in their microstructure. With higher curing temperature, the grey level of C-S-H was in places very similar to that of the calcium hydroxide[138-140]. EDX data was again unrewarding and the chemical composition of C-S-H free of intermixture was not found using SEM-EDX.

### 8.2.5 – TEM-EDX

Inner product C-S-H with a fine scale, homogeneous morphology, was abundant in all systems cured at 55°C and 85°C. Op C-S-H was generally fibrillar with water, and foil-like with alkali. However, the higher temperature curing did result in coarser fibrillar morphology (water activated systems) than that formed at lower temperatures.

Considering EDX analysis, relationships between increasing curing temperature and its effect on the mean atomic ratios for C-S-H were not very clear. Little agreement was found between the mean Ca/Si ratios obtained using SEM-EDX and TEM-EDX but, generally, some agreement was found between the mean values for the mean Al/Si atomic ratios, when using TEM-EDX and MAS NMR.

## 8.3 – WATER LEACHING

### 8.3.1 – $^{29}$Si Solid State MAS NMR

After four weeks of water leaching, small differences were observed in the nanostructure of C-S-H, the appearance of an additional resonance assigned to $Q^3$ cross-linked entities[116]. As leaching proceeded, chain branching sites were formed to greater extent as $Q^3$ became the second most intense peak in the spectra. It was observed that all the chemical shifts moved around 1 ppm in the direction to lower chemical shifts, explained by the matrix effect[116]. The increase of the relative intensity of $Q^4$ resonance between three and seven weeks was another evidence for the matrix effect.

### 8.3.2 – TEM-EDX

Considering the unleached system, after one year, the observed microstructure was very similar to that after one month of hydration. Ip C-S-H was fine and dense and Op C-S-H was fine and fibrillar. The microstructure in the four weeks of leaching changed because it affected Op C-S-H morphology. Many areas where Op C-S-H had a foil-like morphology coexisting with Op C-S-H with fibrillar morphology were observed. A statistically significantly decrease of the mean Ca/Si atomic ratio was not observed for Op C-S-H in the two samples that would have been associated with the change of Op C-S-H morphology. Therefore, it appears that Op C-S-H change of morphology might not be solely associated to its mean Ca/Si atomic ratio. $^{29}$Si MAS NMR results were in some agreement with those from TEM-EDX.

## 8.4 – FUTURE WORK

In general, some gaps were left in this work and other ideas can outcome for future work. For example, isothermal calorimetry should be conducted on both neat and blended cement-based systems at 55°C and 85°C. This study would provide information regarding the induction period and the heat evolution in those systems cured at higher

temperature. Corresponding peaks to C-S-H resulting from alite hydration and reactions involving the aluminate and/or ferrite phases with ettringite formation would be identified. Evaluation of the microstructure porosity through SEM imaging analysis, or using other techniques like helium inflow technique or mercury-intrusion porosimetry, would give complementary information to compressive strength results. TEM-EDX should also be carried out on the KOH activated 30% PFA blended system after one month of hydration, as well as on the 60% PFA blended pastes. Mature pastes one year old like the water and KOH activated neat WPC and KOH 30%PFA blended pastes should also be analysed by TEM-EDX. With the purpose of balancing the TEM-EDX results obtained for the 85°C study, alkaline neat and blended pastes should be characterised. Finally, considering the water leaching study, $^{29}$Si MAS NMR showed that the silicate anion structure changed between four and twelve weeks of leaching. TEM-EDX characterisation of those samples leached between four and twelve weeks would give very helpful data regarding the nature of C-S-H formed in the same systems. After one month of being cured at 55°C and 85°C, the studied samples were placed in a water bath at room temperature. It would also be very interesting to observe their microstructure after a certain period of time cured at room temperature. Water leaching all the systems cured at higher temperature would also give very interesting information regarding their behaviour in those conditions and application of the structural models for C-S-H.

A sideline work was conducted regarding the study of the pozzolanic reaction between PFA and CH and the nature of C-S-H formed in that system. Mixes of fly ash and calcium hydroxide were prepared and cured at 55°C and 85°C. Curiously, at both temperatures and, at one day and one month, aluminium solid state MAS NMR ($^{27}$Al MAS NMR) presented two resonances assigned to tetrahedrally coordinated Al present in C-S-H and a third aluminate hydrated (TAH) for a slightly broad peak centred at 3 ppm[80]. TEM-EDX would allow characterisation of C-S-H morphology as well as that of TAH whose nature and chemical composition is still unknown.

## REFERENCES


**[1]** - Taylor H.F.W. *Cement Chemistry*. London: Academic Press, 1990.

**[2]** - Richardson I.G. and Groves G.W. Models for the composition and structure of calcium silicate hydrate (C-S-H) gel in hardened tricalcium silicate pastes. *Cement and Concrete Research* 1992; 22: 1001-1010.

**[3]** - Richardson I.G. Tobermorite/jennite- and tobermorite/calcium hydroxide-based models for the structure of C-S-H: applicability to hardened pastes of tricalcium silicate, β-dicalcium silicate, Portland cement, and blends of Portland cement with blast-furnace slag, metakaolin, or silica fume. *Cement and Concrete Research* 2005; 34: 1733-1777.

**[4]** - Hewlett P.C. *Lea's Chemistry of Cement and Concrete*. 4th Edition, London: Arnold, 1998.

**[5]** - Bye G.C. *Portland Cement: composition, production and properties*. 2nd Edition, London: Thomas Telford, 1999.

**[6]** - Skibsted J., Henderson E. and Jakobsen H.J. Characterization of calcium aluminate phases in cements by $^{27}Al$ MAS NMR spectroscopy. *Inorganic Chemistry* 1993; 32: 1013-1027.

**[7]** - Taylor H.F.W., Famy C. and Scrivener K.L. Delayed ettringite formation. *Cement and Concrete Research* 2001; 31: 683-693.

**[8]** - Richardson I.G. The nature of the hydration products in hardened cement pastes. *Cement & Concrete Composites* 2000; 22: 97-113.

**[9]** - Csizmadia J., Balazs G. and Tamas F.D. Chloride ion binding capacity of

aluminoferrites. *Cement and Concrete Research* 2001; 31: 577-588.

**[10]** - Taylor H.F.W. and Turner A.B. Reactions of tricalcium silicate paste with organic liquids. *Cement and Concrete Research* 1987; 17: 613-623.

**[11]** - V.S. Ramachandran, R.M. Paroli, J.J.Beaudoin and A. H. Delgado. *Handbook of thermal analysis of construction materials.* Norwich (USA): Noyes Publications/William Andrew Publishing, 2003.

**[12]** - D.A. Skoog, F.J. Holler and T.A. Nieman *Principles of instrumental analysis.* 5th Edition, Philadelphia: Saunders College Publishing, 1998.

**[13]** - Richardson I.G. The nature of C-S-H in hardened cements. *Cement and Concrete Research* 1999; 29: 1131-1147.

**[14]** - Tamas F. and Varady T. Role of poly-reactions in the hydration of cement. *Hungarian Journal of Industrial Chemistry* 1975; 3: 347-354.

**[15]** - Mohan K. and Taylor H.F.W. A trimethylsilylation study of tricalcium silicate pastes. *Cement and Concrete Research* 1982; 12: 25-31.

**[16]** - Engelhardt G. and Michel D. *High-Resolution Solid-State NMR of Silicates and Zeolites*; Berlin: John Wiley & Sons, 1987.

**[17]** - Bell G.M.M., Bensted J., Glasser F.P., Lachowski E.E., Roberts D.R. and Taylor M.J. Study of calcium silicate hydrates by solid state high resolution $^{29}Si$ nuclear magnetic resonance. *Advances in Cement Research* 1990; 9: 23-37.

**[18]** - Mägi M., Lippmaa E., Samoson A., Engelhardt G. and Grimmer A.R. Solid-

state high-resolution silicon-29 chemical shifts in silicates. *Journal of Physical Chemistry* 1984; 88: 1518-1522.

**[19]** - Rodger S.A, Groves G.W., Clayden N.J. and Dobson C.M. Hydration of tricalcium silicate followed by Si-29 NMR with cross-polarization. *Journal of the American Ceramic Society* 1988; 71: 91-96.

**[20]** - Brough A.R., Dobson C.M., Richardson I.G. and Groves G.W. In situ solid-state NMR studies of $Ca_3SiO_5$: hydration at room temperature and at elevated temperatures using $^{29}Si$ enrichment. *Journal of Materials Science* 1994; 29: 3926-3940.

**[21]** - Dent-Glasser L.S., Lachowski E.E. and Qureshi M.Y. Identification of some of the polysilicate components of trimethylsilylated cement paste. *Cement and Concrete Research* 1981; 11: 775-780.

**[22]** - Hirljac J., Wu Z.Q. and Young J.F. Silicate polymerization during the hydration of alite. *Cement and Concrete Research* 1983; 13: 877-886.

**[23]** - Brough A.R., Dobson C.M., Richardson I.G. and Groves G.W. A study of the pozzolanic reaction by solid-state $^{29}Si$ nuclear magnetic resonance using selective isotopic enrichment. *Journal of Materials Science* 1995; 30: 1671-1678.

**[24]** - Young J.F. Investigations of calcium silicate hydrate structure using silicon-29 nuclear magnetic resonance spectroscopy. *Journal of the American Ceramic Society* 1988; 71: C118-C120.

**[25]** - Rodger S.A., Groves G.W., Clayden N.J. and Dobson C.M. Hydration of tricalcium silicate followed by $^{29}Si$ NMR with cross-polarization. *Journal of the American Ceramic Society* 1988; 71: 91-96.

**[26]** - Richardson I.G. and Cabrera J.G. The nature of C-S-H in model slag-

cements. *Cement & Concrete Composites* 2000; 22: 259-266.

**[27]** - Clayden N.J., Dobson C.M., Hayes C.J. and Rodger S.A. Hydration of tricalcium silicate followed by solid-state $^{29}Si$ NMR spectroscopy. *Journal of the Chemical Society, Chemistry Communications* 1984; 1396-1397.

**[28]** - King T.C., Dobson C.M. and Rodger S.A. Hydration of tricalcium silicate with D2O. *Journal of Materials Science Letters* 1988; 7: 861-863.

**[29]** - Grimmer A.-R., Lampe F., Mägi M. And Lippmaa E. High-resolution solid-state $^{29}Si$ NMR of polymorphs of $Ca_2SiO_4$. *Cement and Concrete Research* 1985; 15: 467-473.

**[30]** - Hing S.-H. and Young J.F. Hydration kinetics and phase stability of dicalcium silicate synthesized by the Pechini process. *Journal of the American Ceramic Society* 1999; 82: 1681-1686.

**[31]** - Skibsted J., Jakobsen H.J. and Hall C. Direct observation of aluminium guest ions in the silicate phases of cement minerals by $^{27}Al$ MAS NMR spectroscopy. *Journal of the Chemical Society: Faraday Transactions* 1994; 90: 2095-2098.

**[32]** - Tong Y., Du H. and Fei L. Hydration process of beta-dicalcium silicate followed by MAS and CP/MAS nuclear magnetic resonance. *Cement and Concrete Research* 1991; 21: 355-358.

**[33]** - Tong Y., Du H. and Fei L. Comparison between the hydration processes of tricalcium silicate and beta-dicalcium silicate. *Cement and Concrete Research* 1991; 21: 509-514.

**[34]** - Skibsted J., Hjorth J. and Jakobsen J. Correlation between $^{29}Si$ NMR

chemical shifts and mean Si-O bond lengths for calcium silicates. *Chemical Physics Letters* 1990; 172: 279-283.

**[35]** - Sun G., Brough A.R. and Young J.F. $^{29}Si$ NMR study of the hydration of $Ca_3SiO_5$ and $\beta$-$Ca_2SiO_4$ in the presence of silica fume. *Journal of the American Ceramic Society* 1999; 82: 3225-3230.

**[36]** - Cong X. and Kirkpatrick R.J. $^{17}O$ and $^{29}Si$ MAS-NMR study of $\beta$-$C_2S$ hydration and the structure of calcium silicate hydrates. *Cement and Concrete Research* 1993; 23: 1065-1077.

**[37]** - Chudek J.A., Hunter G., Jones M.R., Scrimgeour S.N., Hewlett P.C. and Kudryavtsev A.B. Aluminium-27 solid state NMR spectroscopic studies of chloride binding in Portland cement and blends. *Journal of Materials Science* 2000; 35: 4275-4288.

**[38]** - Skibsted J., Jensen O.M. and Jakobsen H.J. Hydration kinetics for the alite, belite and calcium aluminate phase in Portland cements from $^{27}Al$ and $^{29}Si$ MAS NMR spectroscopy. *Proceedings on the 10th International Conference on Cement and Concrete* 1997; 2ii: 056.

**[39]** - Andersen M.D., Jakobsen H.J. and Skibsted J. Incorporation of aluminium in the calcium silicate hydrate (C-S-H) of hydrated Portland cements: a high-field Al-27 and Si-29 MAS NMR investigation. *Inorganic Chemistry* 2003; 42: 2280-2287.

**[40]** - Skibsted J., Jakobsen H.J. and Hall C. Quantitative aspects of $^{27}Al$ MAS NMR of calcium aluminoferrites. *Advances in Cement Based Materials* 1998; 7: 57-59.

**[41]** - Skibsted J., Rasmussen S., Herfort D. and Jakobsen H.J. $^{29}Si$ Cross-polarization magic-angle spinning NMR spectroscopy – an efficient tool for

quantification of thaumasite in cement-based materials. *Cement & Concrete Composites* 2003; 25: 823-829.

**[42]** - Richardson I.G. *Electron Microscopy of Cements*. in: Bensted J and Barnes P. (Eds). Chapter 22 in *Structure and performance of cements*. 2nd edition, London: Spon Press, 2002.

**[43]** - Groves G.W., Le Sueur P.J. and Sinclair W. Transmission electron microscopy and mycroanalytical studies of ion-beam-thinned sections of tricalcium silicate paste. *Journal of the American Ceramic Society* 1986; 69: 353-356.

**[44]** - Scrivener K.L. Backscattered electron imaging of cementitious microstructures: understanding and quantification. *Cement & Concrete Composites* 2004; 26: 935-945.

**[45]** - Taylor H.F.W. Proposed structure for calcium silicate hydrate gel. *Journal of the American Ceramic Society* 1986; 69: 464-467.

**[46]** - Taylor H.F.W. Tobermorite, jennite, and cement gel. *Zeitschrift fur Kristallographie* 1992; 202: 41-50.

**[47]** - Bonaccorsi E. and Merlino S. The crystal structure of tobermorite 14 A° (Plombierite), a C-S-H phase. *Journal of the American Ceramic Society* 2005: 88: 505-512.

**[48]** - Bonaccorsi E., Merlino S. And Taylor H.F.W. The crystal structure of jennite, $Ca_9Si_6O_{18}(OH)_6 \cdot 8H_2O$. *Cement and Concrete Research* 2004; 34: 1481-1488.

**[49]** - Richardson I.G. and Groves G.W. The incorporation of minor and trace elements into calcium silicate hydrate (C-S-H) gel in hardened cement pastes.

*Cement and Concrete Research* 1993; 23: 131-138.

**[50]** - Taylor H.F.W. A discussion of the papers "Models for the composition and structure of calcium silicate hydrate (C-S-H) gel in hardened tricalcium silicate pastes" and "The incorporation of minor and trace elements into calcium silicate hydrate (C-S-H) gel in hardened cement pastes". *Cement and Concrete Research* 1993; 23: 995-998.

**[51]** - Richardson I.G. and Groves G.W. A reply to discussions by HFW Taylor of the papers "Models for the composition and structure of calcium silicate hydrate (C-S-H) gel in hardened tricalcium silicate pastes" and "The incorporation of minor and trace elements into calcium silicate hydrate (C-S-H) gel in hardened cement pastes". *Cement and Concrete Research* 1993; 23: 999-1000.

**[52]** - Faucon P., Charpentier T., Bertrandie D., Donat A., Virlet J. and Petit J.C. Characterization of calcium aluminate hydrates and related hydrates of cement pastes by $^{27}$Al MQ-MAS NMR. *Journal of Inorganic Chemistry* 1998; 37: 3726-3733.

**[53]** - Faucon P., Charpentier T., Petit J.C., Richet C., Marchand J.M. and Zanni H. Aluminum incorporation in calcium silicate hydrates (C-S-H) depending on their Ca/Si ratio. *Journal of Physical Chemistry B* 1999; 103: 7796-7802.

**[54]** - Richardson I.G., Brough A.R., Brydson R., Groves G.W. and Dobson C.M. Location of aluminum in substituted calcium silicate hydrate (C-S-H) gels as determined by $^{29}$Si and $^{27}$Al NMR and EELS. *Journal of the American Ceramic Society* 1993; 76: 2285-2288.

**[55]** - Brydson R., Richardson I.G., McComb D.W. and Groves G.W. Parallel electron energy loss microscopy study of Al-substituted calcium silicate

hydrate (C-S-H) phases present in hardened cement pastes. *Solid State Communications* 1993; 88: 183-187.

**[56]** - Brydson R., Richardson I.G. and Groves G.W. Determining the local coordination of aluminum in cement using Electron Energy Loss Near-Edge Structure. *Mikrochimica Acta* 1994; 114: 221-229.

**[57]** - Richardson I.G. and Groves G.W. The structure of the calcium silicate hydrate phases present in hardened pastes of white Portland cement/blast-furnace slag blends. *Journal of Materials Science* 1997; 32: 4793-4802.

**[58]** - Cong X and Kirkpatrick R.J. $^{29}Si$ and $^{17}O$ NMR investigation of the structure of some crystalline calcium silicate hydrates. *Advanced Cement Based Materials* 1996; 3: 133-143.

**[59]** - Cong X and Kirkpatrick R.J. $^{29}Si$ MAS NMR study of the structure of calcium silicate hydrate. *Advanced Cement Based Materials* 1996; 3: 144-156.

**[60]** - Cong X. and Kirkpatrick R.J. $^{17}O$ MAS NMR investigation of the structure of calcium silicate hydrate gel. *Journal of the American Ceramic Society* 1996; 79: 1585-1592.

**[61]** - Kirkpatrick R.J, Yarger J.L., McMillan P.F., Yu P. and Cong X. Raman spectroscopy of C-S-H , tobermorite and jennite. *Advanced Cement Based Materials* 1997; 5: 93-99.

**[62]** - Yu P., Kirkpatrick R.J., Poe B., McMillan P.F. and Cong X. Structure of calcium silicate hydrate (C-S-H): Near-, Mid-, and Far-Infrared spectroscopy. *Journal of the American Ceramic Society* 1999; 82: 742-748.

**[63]** - Grutzeck M.W. A new model for the formation of calcium silicate hydrate (C-S-H). *Materials Research Innovations* 1999; 3: 160-170.

**[64]** - Grutzeck M.W., Kwan S., Thompson J.L. and Benes A. A sorosilicate model for calcium silicate hydrate (C-S-H) *Journal of Materials Science, Letters* 1999; 18: 217-220.

**[65]** - Jennings H.M. and Tennis P.D. Model for the developing microstructure in Portland cement pastes. *Journal of the American Ceramic Society* 1994; 77: 3161-3172.

**[66]** - Chen J.J., Thomas J.J., Taylor H.F.W. and Jennings H.M. Solubility and structure of calcium silicate hydrate. *Cement and Concrete Research* 2004; 34: 1499-1519.

**[67]** - Jennings H.M. A model for the microstructure of calcium silicate hydrate in cement paste. *Cement and Concrete Research* 2000; 30: 10-116.

**[68]** - Tennis P.D. and Jennings H.M. A model for two types of calcium silicate hydrate in the microstructure of Portland cement pastes. *Cement and Concrete Research* 2000; 30: 855-863.

**[69]** - Jennings H.M. Colloid model of C-S-H and implications to the problem of creep and shrinkage. *Materials and Structures/Concrete Science and Engineering* 2004; 37: 59-70.

**[70]** - Taylor H.F.W and Newbury D.E. An electron microprobe study of a mature cement paste. *Cement and Concrete Research* 1984; 14: 565-573.

**[71]** Richardson I.G and Groves G.W. Microstructure and microanalysis of hardened cement pastes involving ground granulated blast-furnace slag. *Journal of Materials Science* 1992; 27: 6204-6212.

**[72]** - Richardson I.G. and Groves G.W. Microstructure and microanalysis of hardened ordinary Portland cement pastes. *Journal of Materials Science*

1993; 28: 265-277.

[73] - Richardson I.G., Brough A.R., Groves G.W. and Dobson C.M. The characterization of hardened alkali-activated blast-furnace slag pastes and the nature of the calcium silicate hydrate (C-S-H) phase. *Cement and Concrete Research* 1994; 24: 813-829.

[74] - Richardson I.G. and Groves G.W. The structure of the calcium silicate hydrate phases present in hardened pastes of white cement/blast-furnace slag blends. *Journal of Materials Science* 1997; 32: 4793-4802.

[75] - Brough A.R., Dobson C.M., Richardson I.G. and Groves G.W. Alkali activation of reactive silicas in cements: *in situ* $^{29}$Si MAS NMR studies of the kinetics of silicate polymerization. *Journal of Materials Science* 1996; 31: 3365-3373.

[76] - Richardson I.G., Brough A.R., Brydson R., Groves G.W. and Dobson C.M. Location of aluminum in substituted calcium silicate hydrate (C-S-H) gels as determined by $^{29}$Si and $^{27}$Al NMR and EEELS. *Journal of the American Ceramic Society* 1993; 76: 2285-2288.

[77] - Hansen P.L., Brydson R., McComb D.W. and Richardson I.G. EELS fingerprint of Al-coordination in silicates. *Microscopy, Microanalysis and Microstructure* 1994; 5: 173-182.

[78] - Groves G.W. Microcrystalline calcium hydroxide in Portland cement pastes of low water/cement ratio. *Cement and Concrete Research* 1981; 11: 713-718.

[79] - Barnes J.R., Clague A.D.H., Clayden N.J., Dobson C.M., Hayes C.J., Groves G.W. and Rodger S.A. Hydration of Portland cement followed by $^{29}$Si solid-

state NMR spectroscopy. *Journal of Materials Science Letters* 1985; 4:1293-1295.

**[80]** - Andersen M.D., Jakobsen H.J. and Skibsted J. A new aluminium-hydrate species in hydrated Portland cements characterized by $^{27}Al$ and $^{29}Si$ MAS NMR spectroscopy. *Cement and Concrete Research* 2006; 36: 3-17.

**[81]** - Helmuth R. *Fly Ash in Cement and Concrete*. Portland Cement Association, Skokie, Ill: Portland Cement Association.USA:1987.

**[82]** - Watt J.D. and Thorne D.J. Composition and pozzolanic properties of pulverised fuel ashes. I. Composition of fly ashes from some british power stations and properties of their component particles. *Journal of Applied Chemistry* 1965; 15: 585-594.

**[83]** - Watt J.D. and Thorne D.J. Composition and pozzolanic properties of pulverised fuel ashes. II. Pozzolanic properties of fly ashes, as determined by crushing strength tests on lime mortar. *Journal of Applied Chemistry* 1965; 15: 595-604.

**[84]** - Watt J.D. and Thorne D.J. Composition and pozzolanic properties of pulverised fuel ashes. III. Pozzolanic properties of fly ashes, as determined by chemical methods. *Journal of Applied Chemistry* 1966; 16: 33-39.

**[85]** - Kovacs R. Effect of the hydration products on the properties of fly-ash cements. *Cement and Concrete Research* 1975; 5: 73-82.

**[86]** - Mohan K. and Taylor H.F.W. Pastes of tricalcium silicate with fly ash – analytical electron microscopy, trimethylsilylation and other studies. *In*

*Effects of Fly Ash Incorporation in Cement and Concrete*. Materials Research Society. USA:1981.

**[87]** - Rodger S.A. and Groves G.W. The microstructure of tricalcium silicate/pulverized-fuel ash blended cement pastes. *Advances in Cement Research* 1988; 1: 84-91.

**[88]** - Rodger S.A. and Groves G.W. Electron microscopy study of ordinary Portland cement and ordinary Portland-pulverized fuel ash blended cements. *Journal of the American Ceramic Society* 1989; 72: 1037-1039.

**[89]** - Pietersen H.S., Kentgens A.P.M., Nachtegaal G.H., Veeman W.S. and Bijen J.M.J.M. The reaction mechanisms of blended cements: a $^{29}Si$ NMR study. *4th International Conference on Fly Ash, Silica Fume, Slag and Natural Pozzolans in Concrete* 1993, American Concrete Institute Special Publication 132; Volume 1: 795-812.

**[90]** - Pietersen H.S. Application of TEM to characterize fly ash- and slag cements. *Heron* 1999; 44: 299-312.

**[91]** - Love C.A. and Richardson I.G. The composition and structure of C-S-H in blended cement pastes containing fly ash. *Electron Microscopy and Analysis Group Conference EMAG* 1999; 161: 393-396.

**[92]** - LaRosa J.L., Kwan S. and Grutzeck M.W. Zeolite formation in class F flay ash belended cement pastes. *Journal of the American Ceramic Society* 1992; 75: 1574-1580.

**[93]** - LaRosa J.L., Kwan S. and Grutzeck M.W. Self-generating zeolite-cement composites. *Symposium on Advanced Cementitious Systems : Mechanisms*

*and Properties, Materials Research Society Symposium Proceedings* 1992: 245: 211-216.

**[94]** - Brough A.R., Katz A., Bakharev T., Sun G.K., Kirkpatrick R.J., Struble L.J. and Young J.F. Microstructural aspects of zeolite formation in alkali activated cements containing high levels of fly ash. *Materials Research Society Symposium Proceedings* 1995; 370: 199-208.

**[95]** - Brough A.R., Katz A., Sun G.K., Struble L.J., Kirkpatrick R.J. and Young J.F. Adiabatically cured, alkali-activated cement-based wasteforms containing high levels of fly ash. Formation of zeolites and Al-substituted C-S-H. *Cement and Concrete Research* 2001; 31: 1437-1447.

**[96]** - Quillin K.C., Duerden S. and Majumbar A.J. Formation of zeolites in OPC-PFA mixes. *Cement and Concrete Research* 1993; 23: 991-992.

**[97]** - Grutzeck M.W. Zeolite synthesis from fly ash and cement kiln dust. *98th Annual Meeting of the American Ceramic Society, Environmental Issues and Waste Management Technologies II* 1996; 353-364.

**[98]** - Grutzeck M.W. Zeolites synthesized from class F fly ash and sodium aluminate slurry. *Journal of the American Ceramic Society* 1997; 80: 2449-2453.

**[99]** - Grutzeck M.W., Kwan S. and DiCola M. Zeolite formation in alkali-activated cementitious systems. *Cement and Concrete Research* 2004; 34: 949-955.

**[100]** - Kjelssen, K.O., Detwiler, R.J., Gjørv O.E. Backscattered electron imaging of cement pastes hydrated at different temperatures. *Cement and Concrete Research* 1990; 20: 308-311.

**[101]** - Kjelssen, K.O., Detwiler, R.J., Gjorv O.E. Development of microstructures in plain cement pastes hydrated at different temperatures. *Cement and Concrete*

*Research* 1991; 21: 179-189.

**[102]** - Cao Y. and Detwiler R. J. Backscattered electron imaging of cement pestas cured at elevated temperatures. *Cement and Concrete Research* 1995; 25: 627-638.

**[103]** - Scrivener K.L. The effect of heat treatment on inner product C-S-H. *Cement and Concrete Research* 1992; 22: 1224-1226.

**[104]** - Kjelssen K.O. Heat curing and post-heat curing regimes of high-performance concrete: influence on microstructure and CSH composition. *Cement and Concrete Research* 1996; 26:295-307.

**[105]** - Escalante-Garcia J.I. and Sharp J.H. The microstructure and mechanical properties of blended cements hydrated at various temperatures. *Cement and Concrete Research* 2001; 31: 695-702.

**[106]** - Hime W.G. and Marusin S.L. Letter to the editor. *Cement and Concrete Research* 1996; 26:1605.

**[107]** - Masse S. and Zanni H. 29Si Solid state NMR study of tricalcium silicate and cement hydration at high temperature. *Cement and Concrete Research* 1993; 23: 1169-1177.

**[108]** - Cong X. and Kirkpatrick R.J. Effects of the temperature and relative humidity on the structure of C-S-H gel. *Cement and Concrete Research* 1995; 25: 1237-1245.

**[109]** - Spooner D.C. A guide to the properties and selection of cements conforming to British and European standards. *British Cement Association* 1995; Interim

Technical Note 13.

**[110]** - Groves G.W., Brough A.R., Richardson I.G. and Dobson C.M. Progressive changes in the structure of hardened $C_3S$ cement pastes due to carbonation. *Journal of the American Ceramic Society* 1991; 74: 2891-2896.

**[111]** - Carde C., François R. and Torrenti J.M. Leaching of both calcium hydroxide and C-S-H from cement paste: modeling the mechanical behavior. *Cement and Concrete Research* 1996; 26: 1257-1268.

**[112]** - Carde C. and François R. Effect of the leaching of calcium hydroxide from cement paste on mechanical and physical properties. *Cement and Concrete Research* 1997; 27: 539-550.

**[113]** - Henkamp F.H., Ulm F.J. and Germaine J.T. Mechanical properties of calcium-leached cement pastes. Triaxial stress states and the influence of the pore structure. *Cement and Concrete Research* 2001; 31: 767-774.

**[114]** - Constantinides G. and Ulm F.J. The effect of two types of C-S-H on the elasticity of cement-based materials: results from nanoidentation and micromechanical modelling. *Cement and Concrete Research* 2004; 34: 67-80.

**[115]** - Thomas J.J., Chen J.J. and Jennings H.M. Effects of decalcification on the microstructure and surface area of cement and tricalcium silicate pastes. *Cement and Concrete Research* 2004; 12: 2297-2307.

**[116]** - Porteneuve C., Zanni H., Vernet C., Kjellsen K.O., Korb J.P. and Petit D. Nuclear magnetic resonance characterization of high- and ultrahigh-performance concrete. Application to the study of water leaching. *Cement and Concrete Research* 2001; 31: 1887-1893.

**[117]** - Porteneuve C., Zanni H., Korb J.P. and Petit D. Water leaching of high and ultra high performance concrete: a nuclear magnetic resonance study.

*Comptes Rendus de l'Academie des Sciences Serie II Fascicule C-Chimie* 2001; 4: 809-814.

**[118]** - Harris A.W., Manning M.C., Tearle W.M. and Tweed C.J. Testing of models of the dissolution of cements – leaching of synthetic CSH gels. *Cement and Concrete Research* 2002; 32: 731-746.

**[119]** - Taylor H.F.W. Modification of the Bogue calculation. Advances in Cement Research 1989; 2: 73-77.

**[120]** - *Handbook of Analytical Techniques in Concrete Science and Technology: Principles, Techniques and Applications*. Edited by V.S. Ramachandran and J. J. Beaudoin. Norwich (USA): Noyes Publications/William Andrew Publishing, 1999.

**[121]** - Bensted J. Some applications of conduction calorimetry to cement hydration. *Conduction Calorimetry Meeting*, King's College London, 1986.

**[122]** - Day R.L. Reactions between methanol and Portland cement paste. *Cement and Concrete Research* 1981; 11: 341-349.

**[123]** - Beaudoin J.J., Gu P., Marchand J., Tamtsia B., Myers R.E. and Liu Z. Solvent replacement studies of hydrated Portland cement systems: the role of calcium hydroxide. *Advances in Cement Research* 1998; 8: 56-65.

**[124]** - Cabrera J.G. and Lynsdale C.J. The effect of superplasticisers on the hydration of normal Portland cement. *Private Communication*.

**[125]** - A.R. West. *Basic Solid State Chemistry*. Chinchester: Wiley, 1988.

**[126]** - K.J.D. MacKenzie and M. E. Smith. *Multinuclear Solid-State NMR of Inorganic Materials*. Amsterdam, London: Pergamon, 2002.

**[127]** - Brough A.R. D. Phil. Thesis, *Solid state NMR studies of inorganic materials*, University of Oxford, 1993.

**[128]** - Love C.A. PhD Thesis, *Microstructure and silicate anion structure of hardened blended cement pastes*, University of Leeds, UK, 2002.

**[129]** - P.J. Goodhew, J. Humphreys, R. Beanland. *Electron Microscopy and Analysis*. 3rd Edition. London: Taylor & Francis, 2001.

**[130]** - J. Golstein, D.E. Newbury, D.C. Joy, C.E. Lyman, P. Echlin, E. Lifshin, L.C. Sawyer and J. R. Michael. Scanning Electron Microscopy and X-ray Microanalysis. New York, London: Kluwer Academic/Plenum Publishers, 2003.

**[131]** - D.B. Williams and C.B. Carter. *Transmission Electron Microscopy: a Textbook for Materials Science*. New York, London: Plenum Press, 1996.

**[132]** - Love C.A., Richardson I. G. and Brough A. R. Composition and structure of C–S–H in white Portland cement–20% metakaolin pastes hydrated at 25°C. *Cement and Concrete Research* 2007; 37: 109-117.

**[133]** - Rodger S. A. D. Phil. Thesis, *The Chemistry of Admixture Interaction during Cement Hydration*, University of Oxford, UK, 1986.

**[134]** - Escalante-Garcia J. I. and Sharp J. H. Variation in the composition of C-S-H gel in Portland cement pastes cured at various temperatures. *Journal of the American Ceramic Society* 1999; 82: 3237-3241.

**[135]** - Famy C. PhD Thesis, *Expansion of heat-cured mortars*, University of London, UK, 1999.

**[136]** - Unpublished work.

**[137]** - Kjellsen K. O. Heat curing and post-heat curing regimes of high-performance concrete: Influence in microstructure and C-S-H composition. *Cement and Concrete Research* 1996; 26: 295-307.

**[138]** - Kjellsen K. O., Detwiler O. E. and Gjørv O. E. Backscattered electron imaging of cement pastes hydrated at different temperatures. *Cement and Concrete Research* 1990; 20: 308.311.

**[139]** - Escalante-Garcia J. I. and Sharp J. H. Effect of temperature on the hydration of the main clinker phases in Portland cements: Part I, Neat cements. *Cement and Concrete Research* 1998; 28: 1245-1257.

**[140]** - Famy C., Scrivener K. L. and Crumbie A. K. What causes differences of C-S-H gel grey levels in backscattered electron images. *Cement and Concrete Research* 2002; 32: 1465-1471.

**[141]** - Palomo A., Alonso S., Fernandez-Jiménez A., Sobrados I. and Sanz J. Alkaline activation of fly ashes: NMR study of the reaction products. *Journal of the American Ceramic Society* 2004; 87: 1141-1145.

**[142]** - Mercury J. M. R., Pena P., De Aza A. H., Turrillas X., Sobrados I. and Sanz J. *Acta Materialia* 2007; 55: 1183-1191.

# APPENDICES

# APPENDIX A

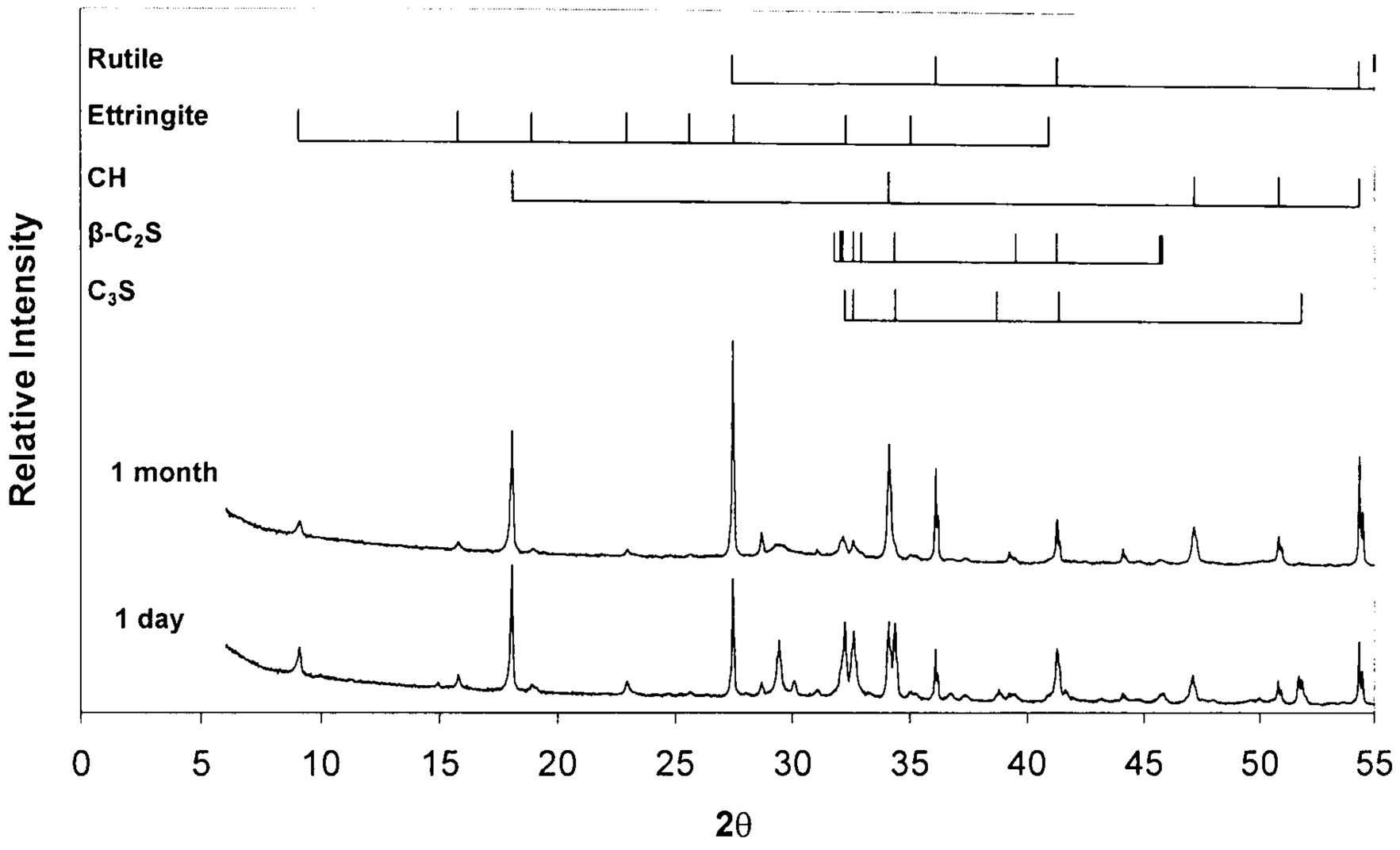


**Figure A1** – Powder diffractograms for the 1 day and 1 month neat WPC paste water activated cured at 25°C.

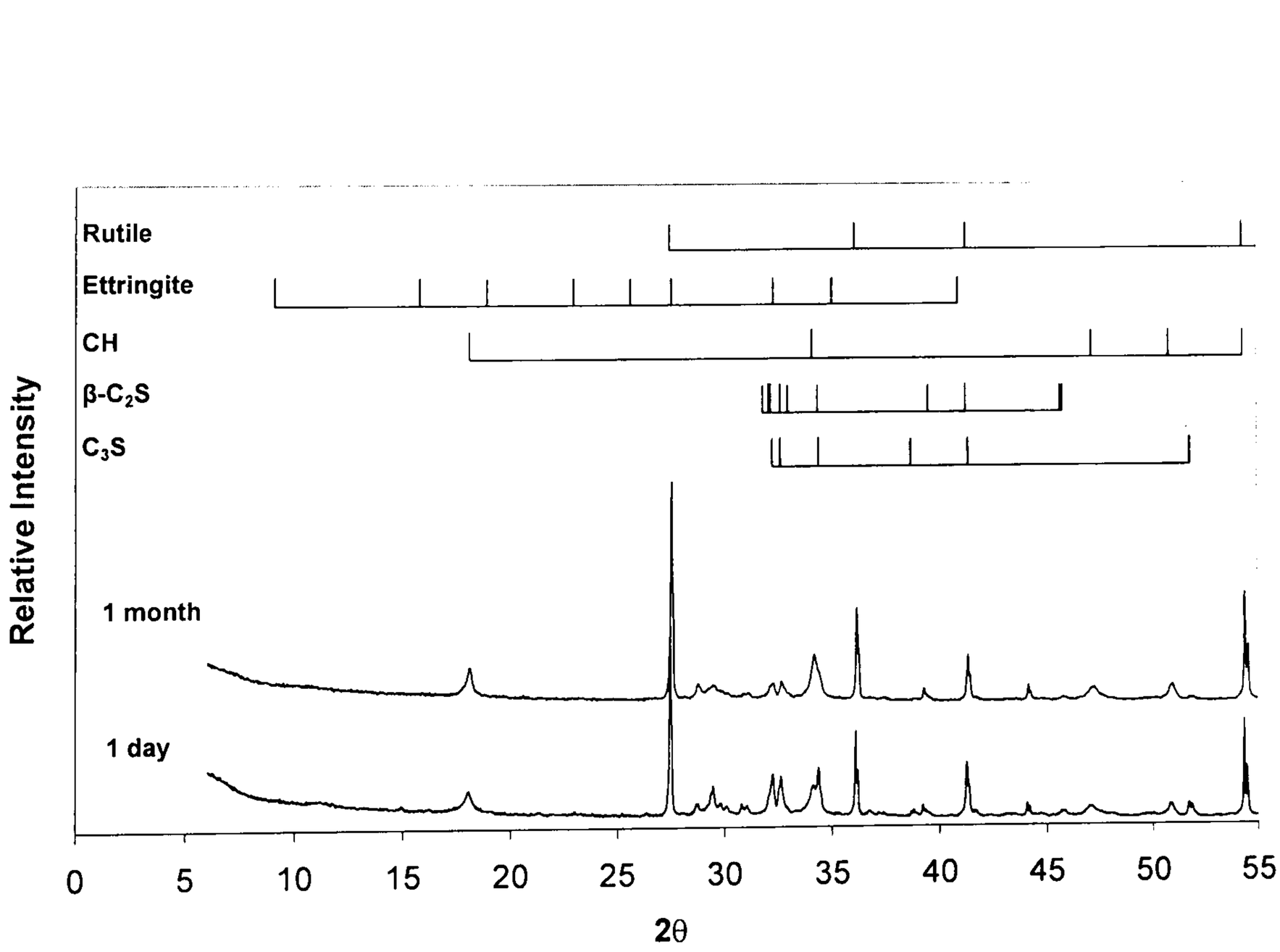


**Figure A2** – Powder diffractograms for the 1 day and 1 month neat WPC paste KOH activated cured at 25°C.

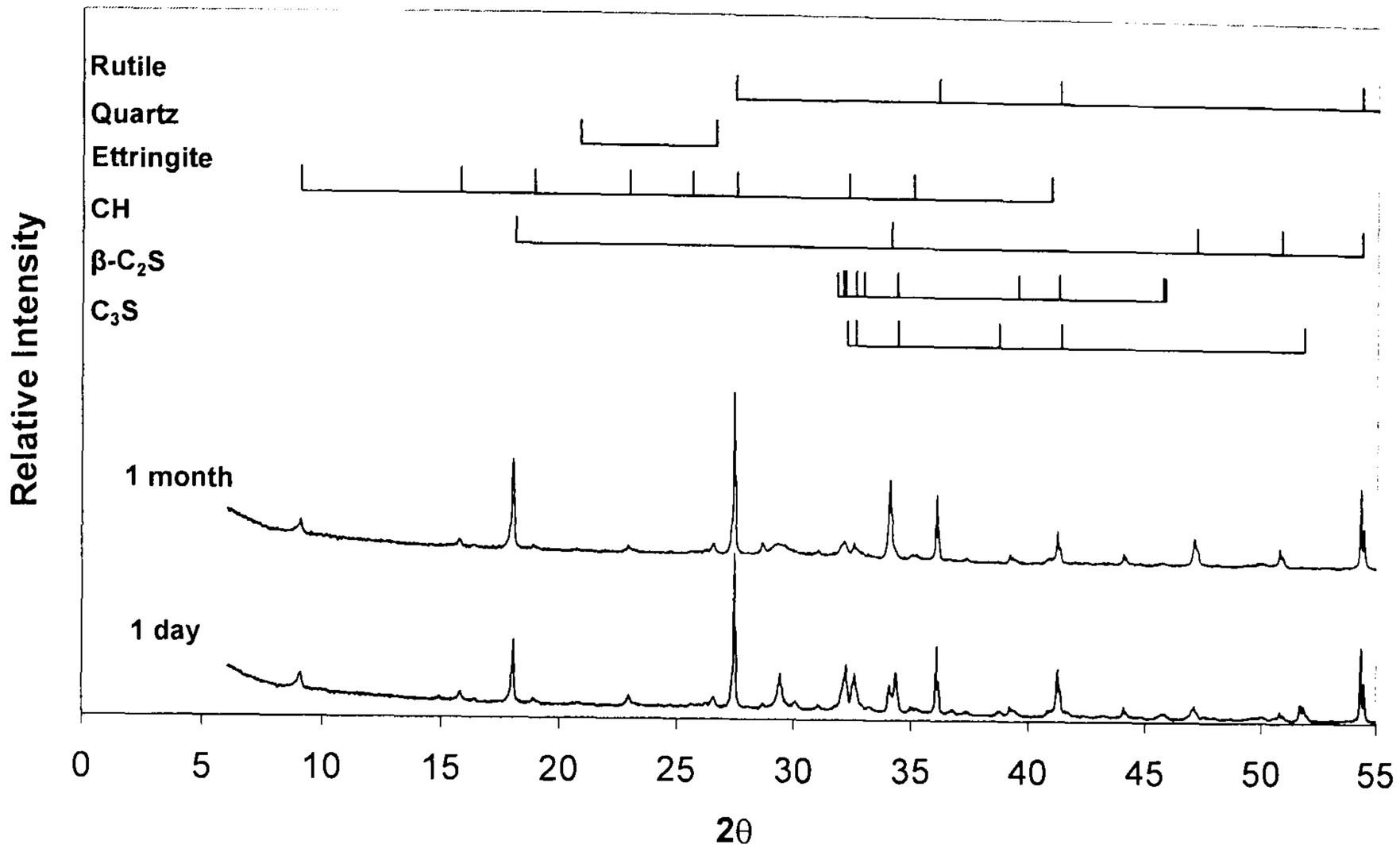


**Figure A3** – Powder diffractograms for the 1 day and 1 month 30% PFA blended WPC paste water activated cured at 25°C.

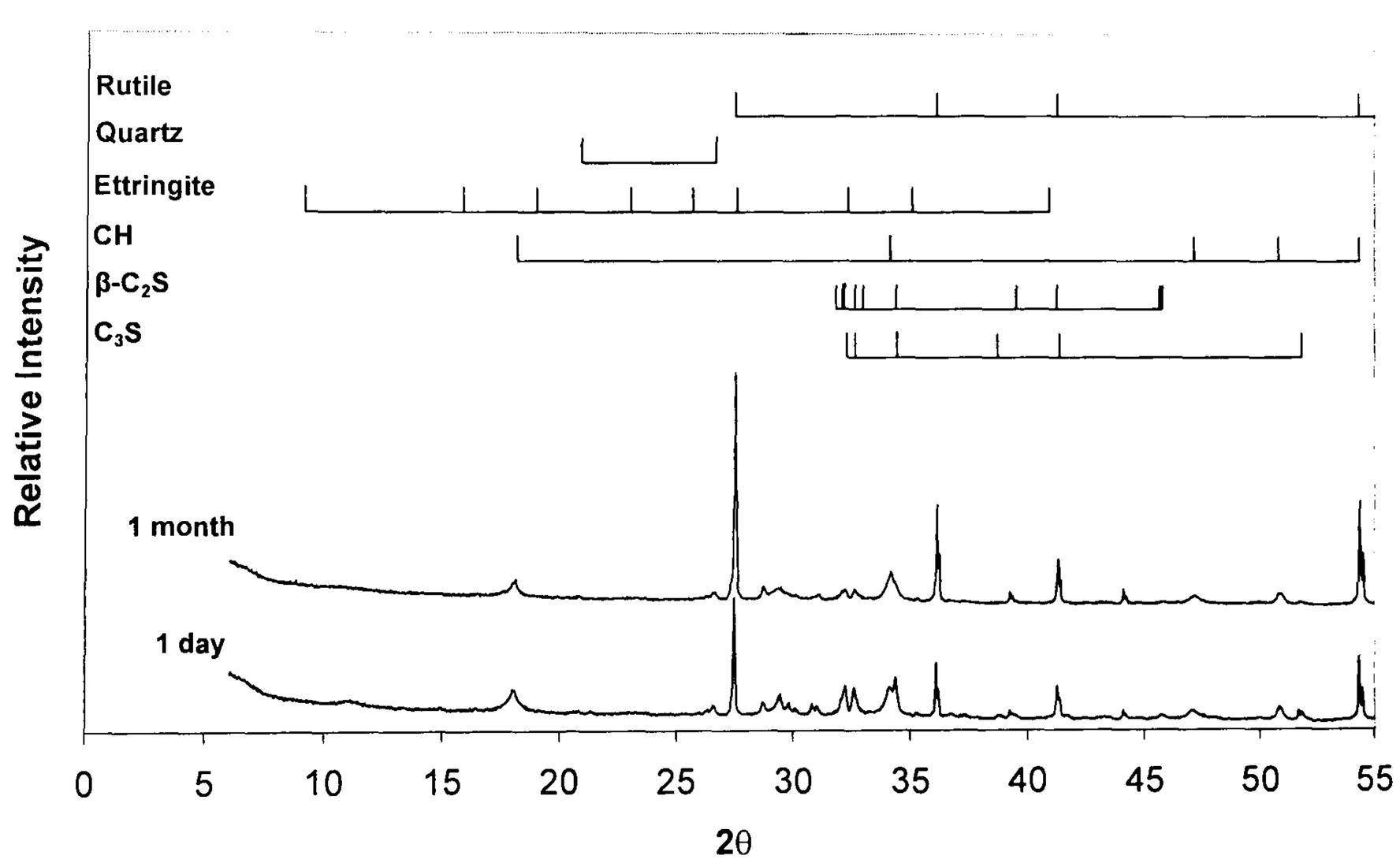


**Figure A4** – Powder diffractograms for the 1 day and 1 month 30% PFA blended WPC paste KOH activated cured at 25°C.

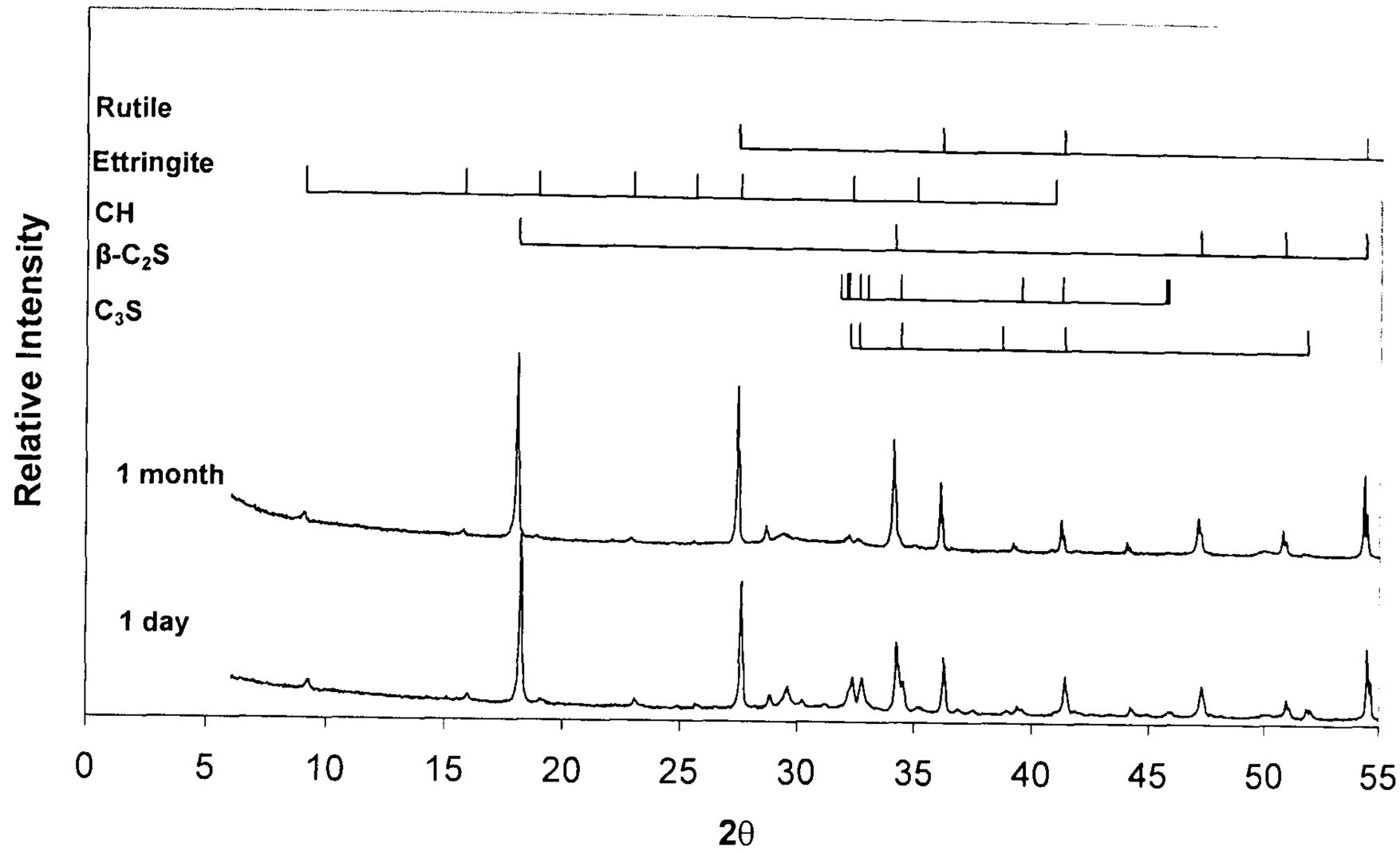


**Figure A5** – Powder diffractograms for the 1 day and 1 month neat WPC paste water activated cured at 55°C.

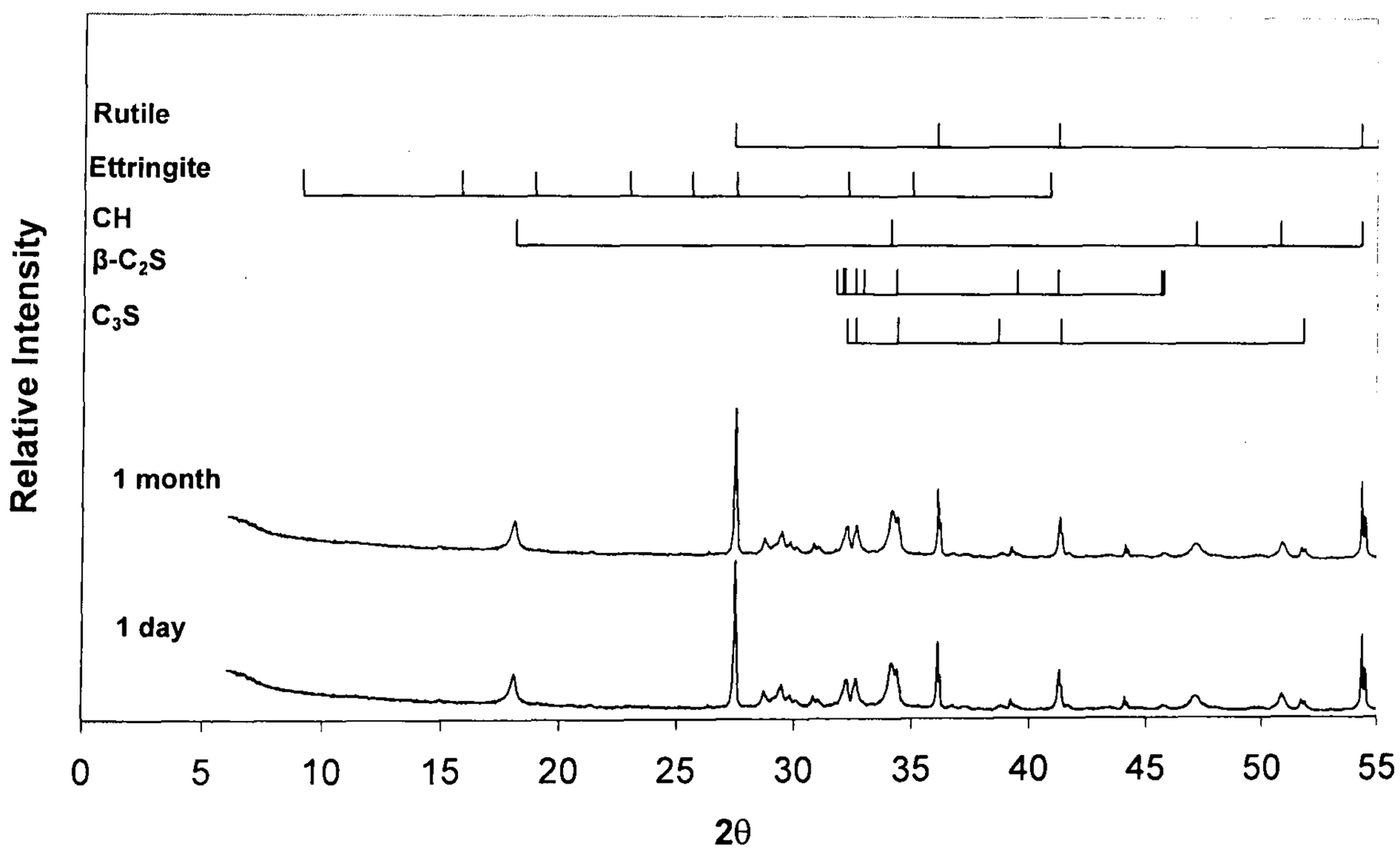


**Figure A6** – Powder diffractograms for the 1 day and 1 month neat WPC paste KOH activated cured at 55°C.

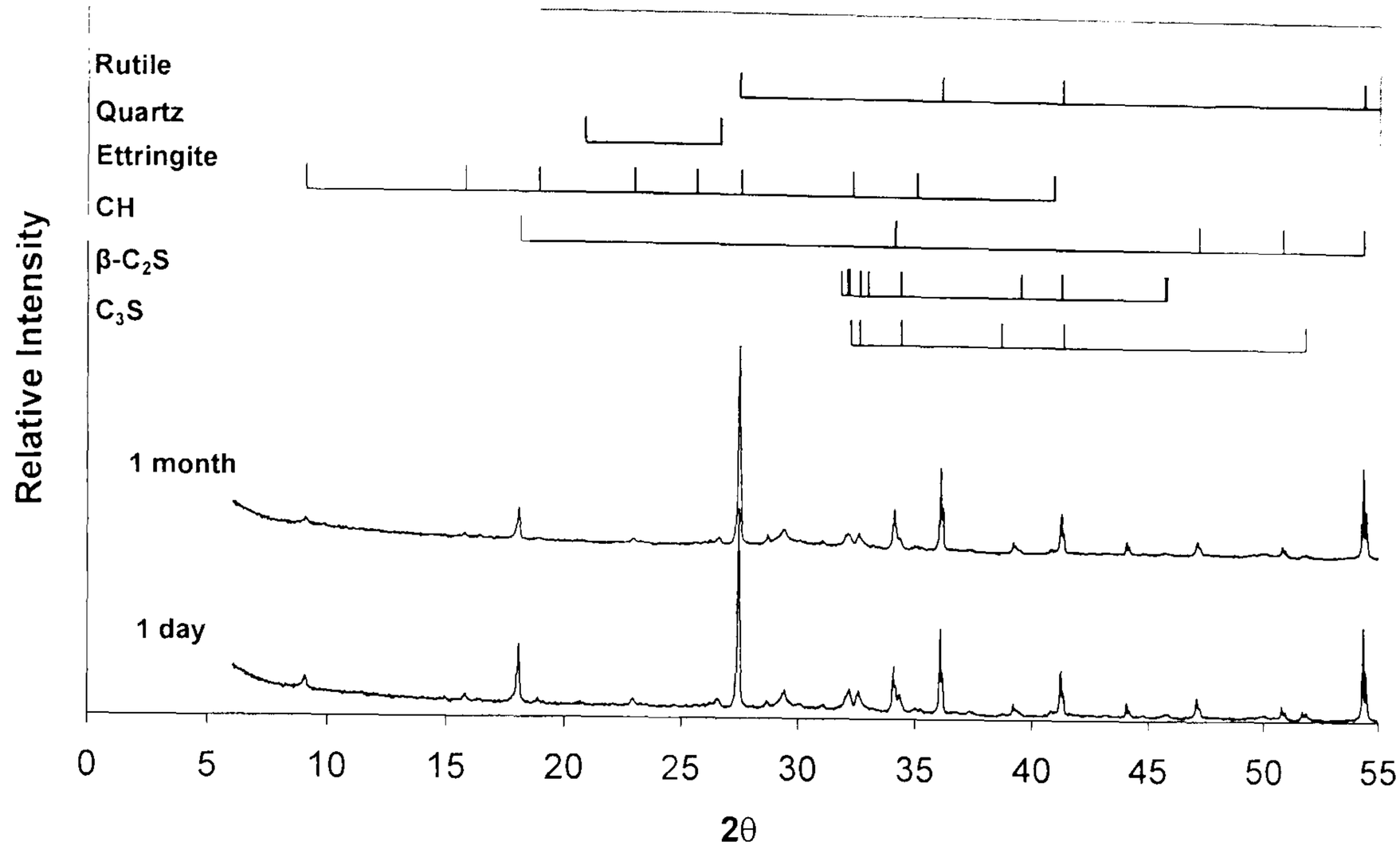


**Figure A7** – Powder diffractograms for the 1 day and 1 month 30% PFA blended WPC paste water activated cured at 55°C.

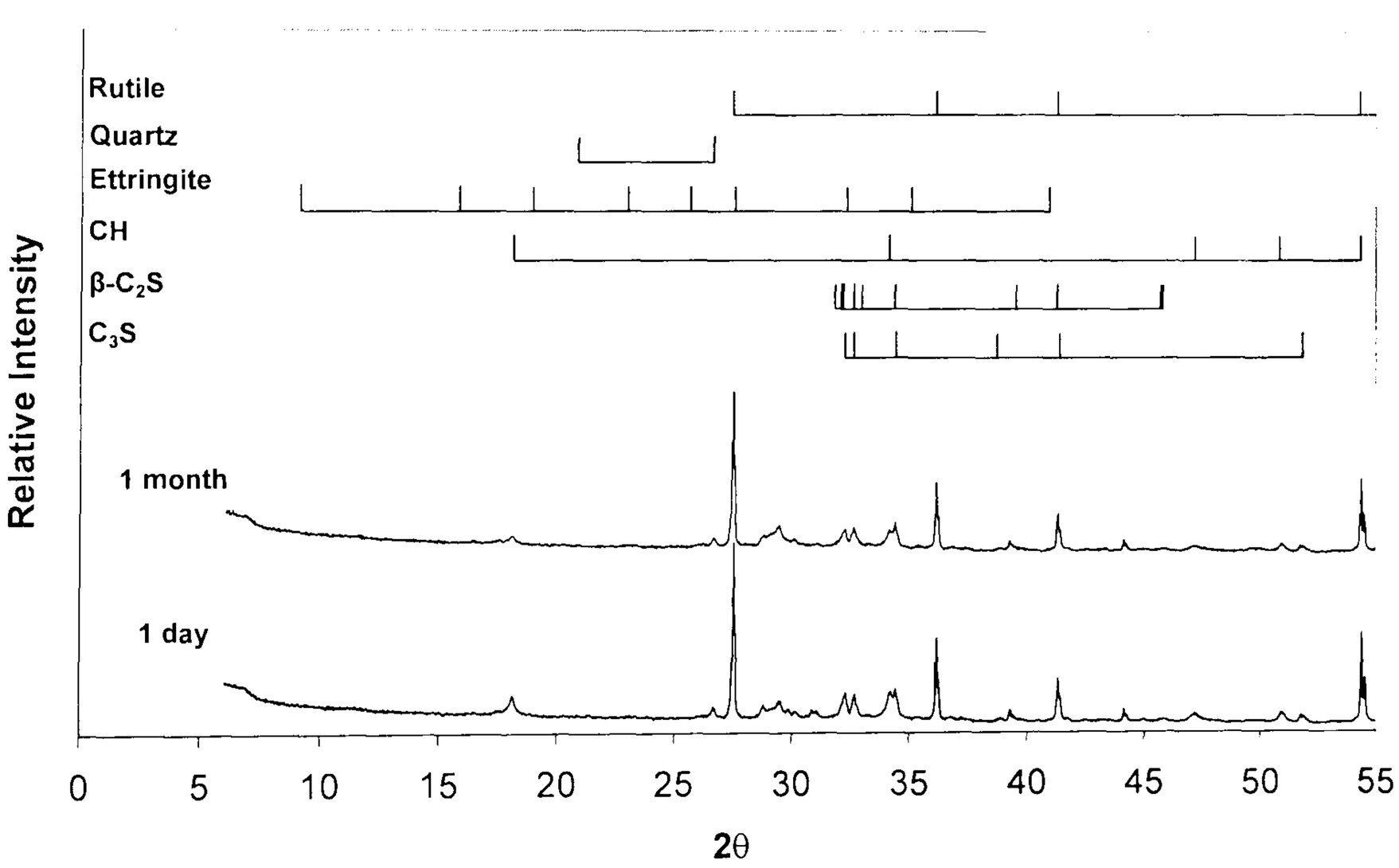


**Figure A8** – Powder diffractograms for the 1 day and 1 month 30% PFA blended WPC paste KOH activated cured at 55°C.

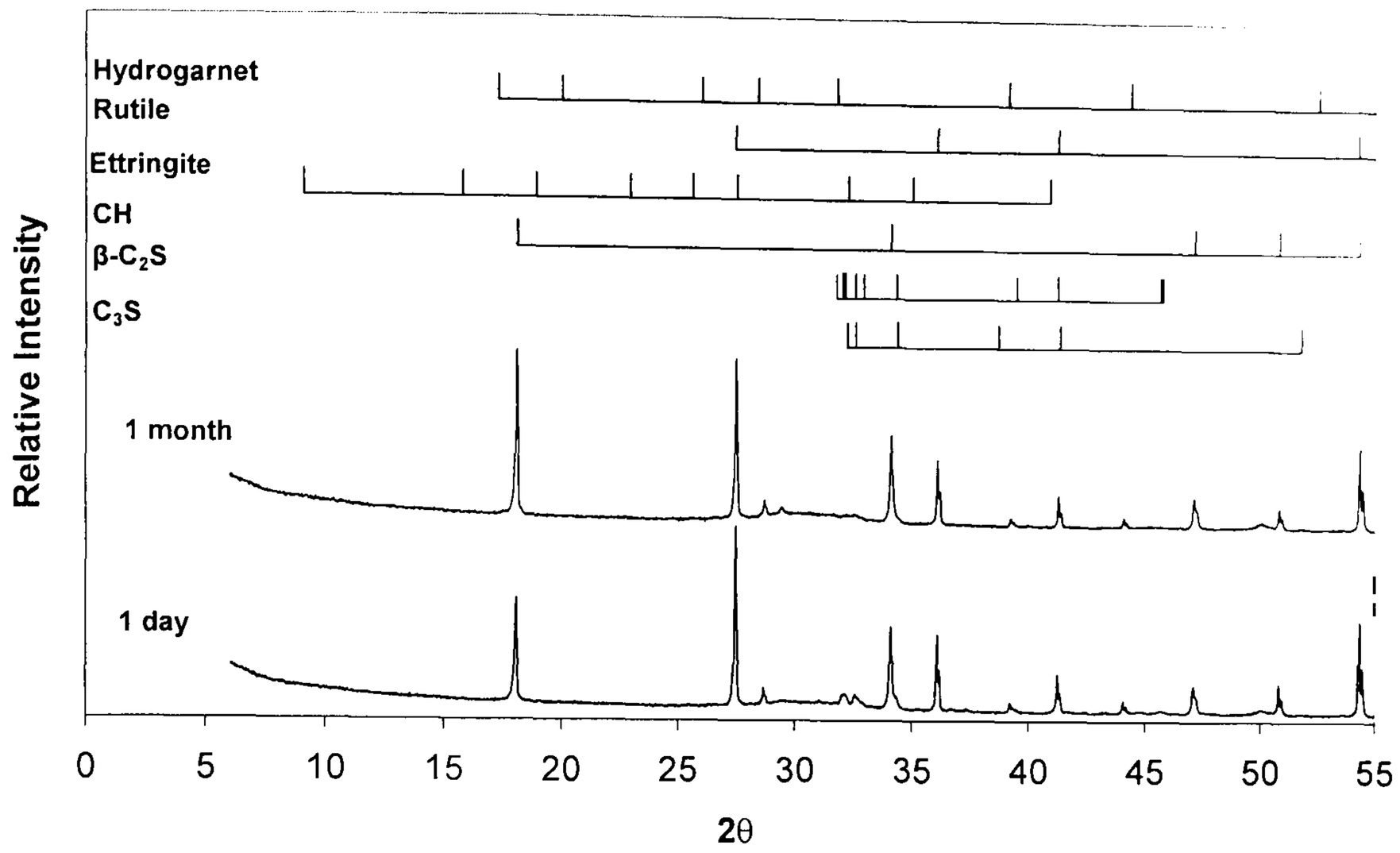


**Figure A9** – Powder diffractograms for the 1 day and 1 month neat WPC paste water activated cured at 85°C.

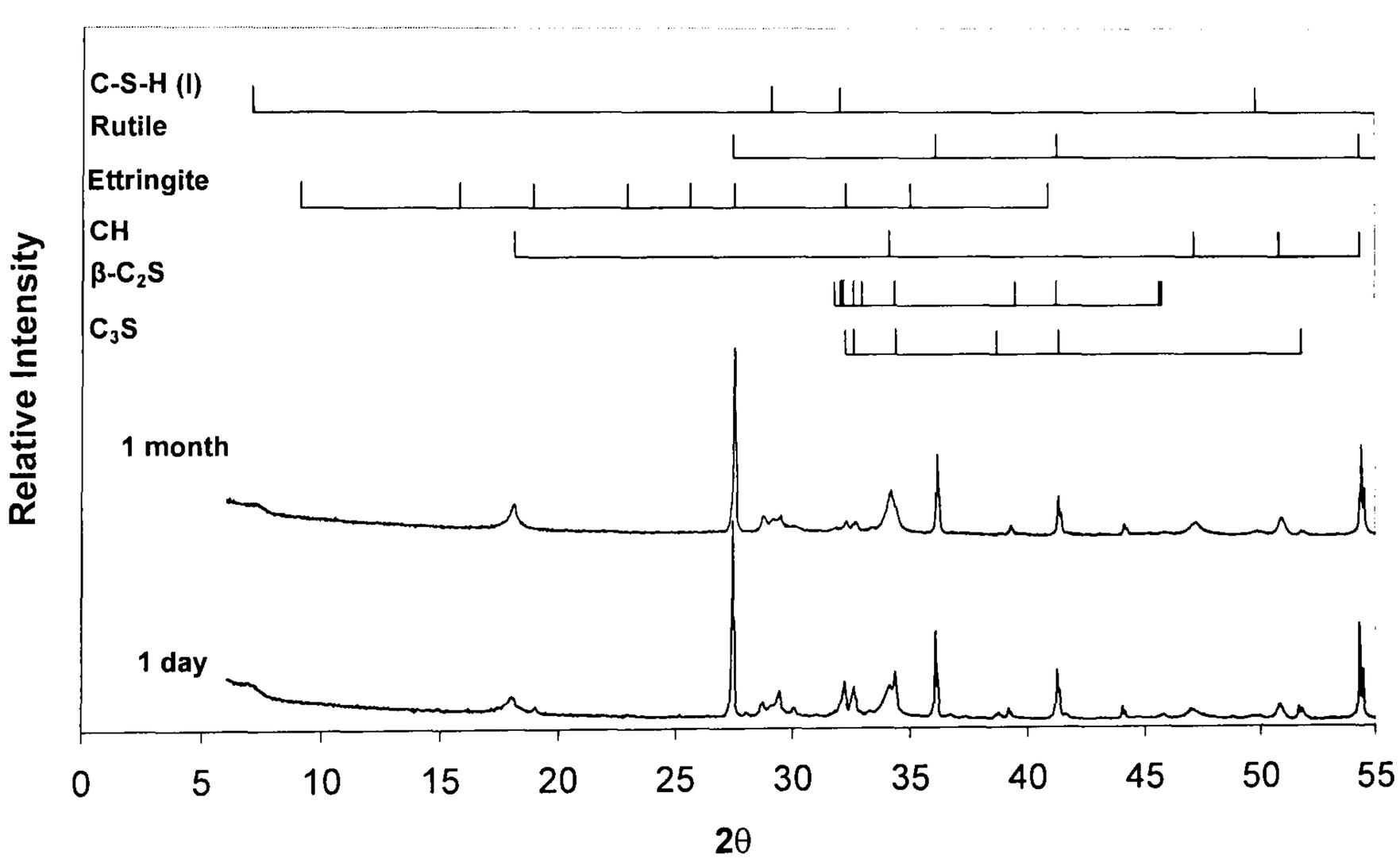


**Figure A10** – Powder diffractograms for the 1 day and 1 month neat WPC paste KOH activated cured at 85°C.

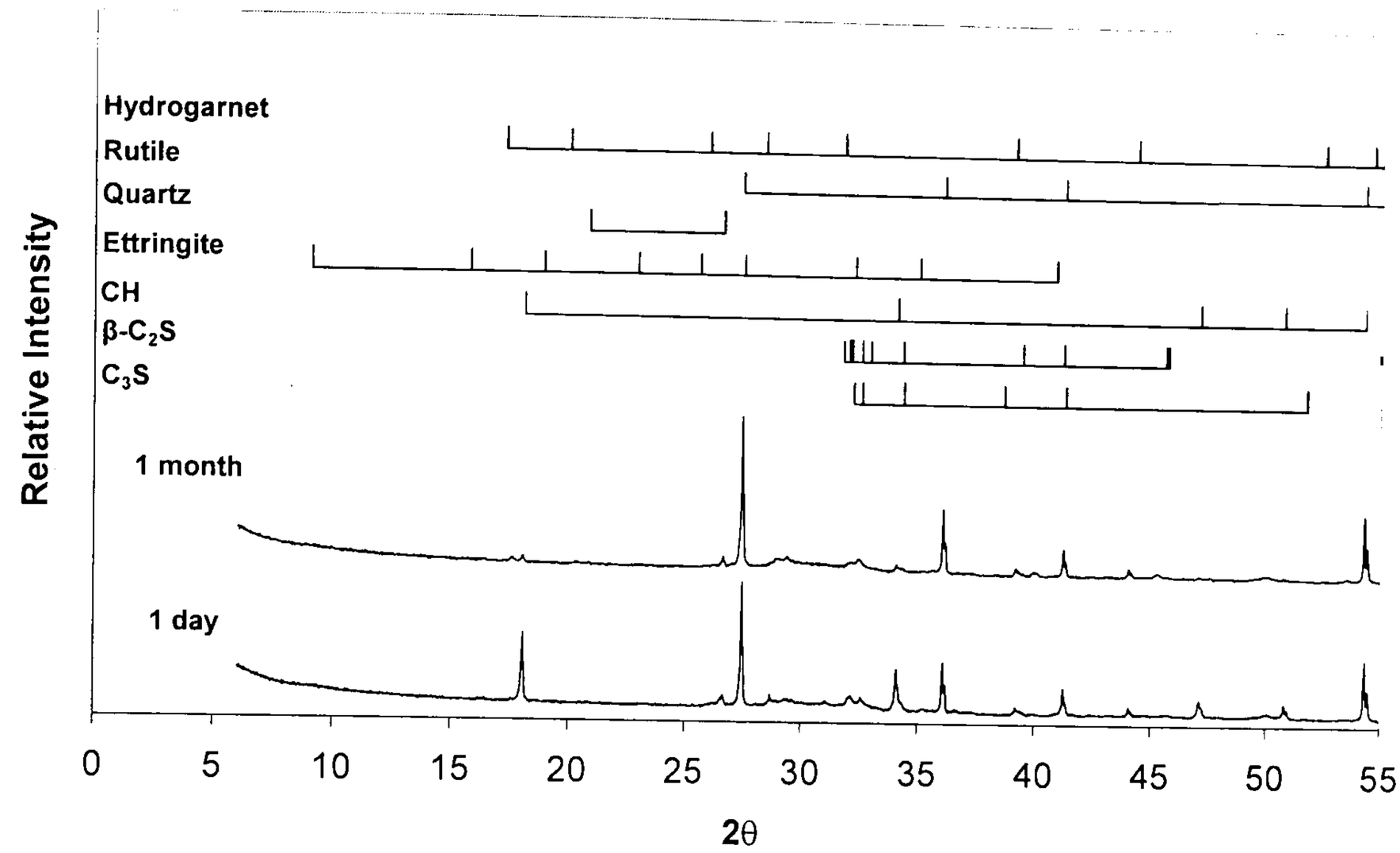


**Figure A11** – Powder diffractograms for the 1 day and 1 month 30% PFA blended WPC paste water activated cured at 85°C.

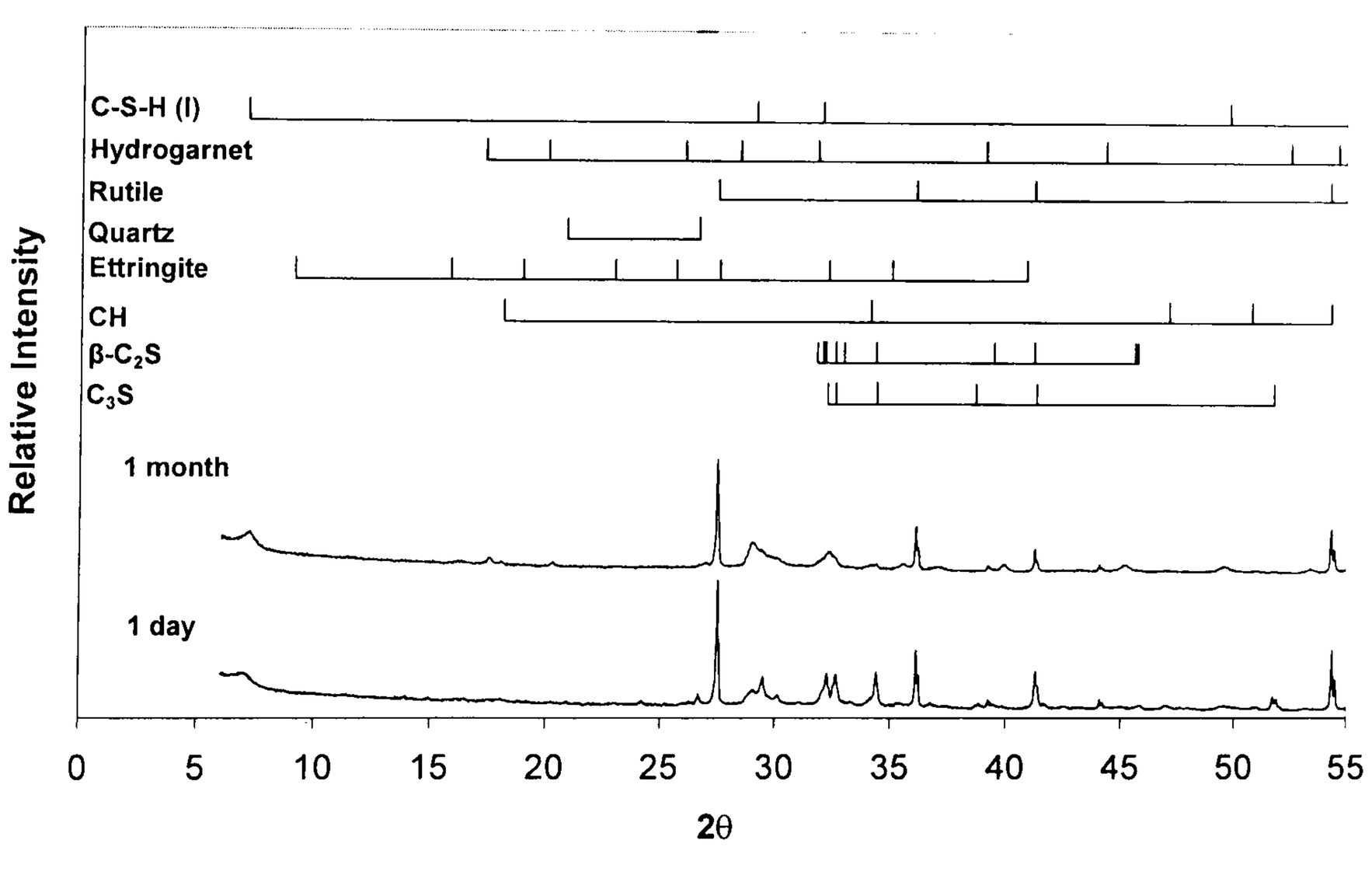


**Figure A12** – Powder diffractograms for the 1 day and 1 month 30% PFA blended WPC paste KOH activated cured at 85°C.

# APPENDIX B

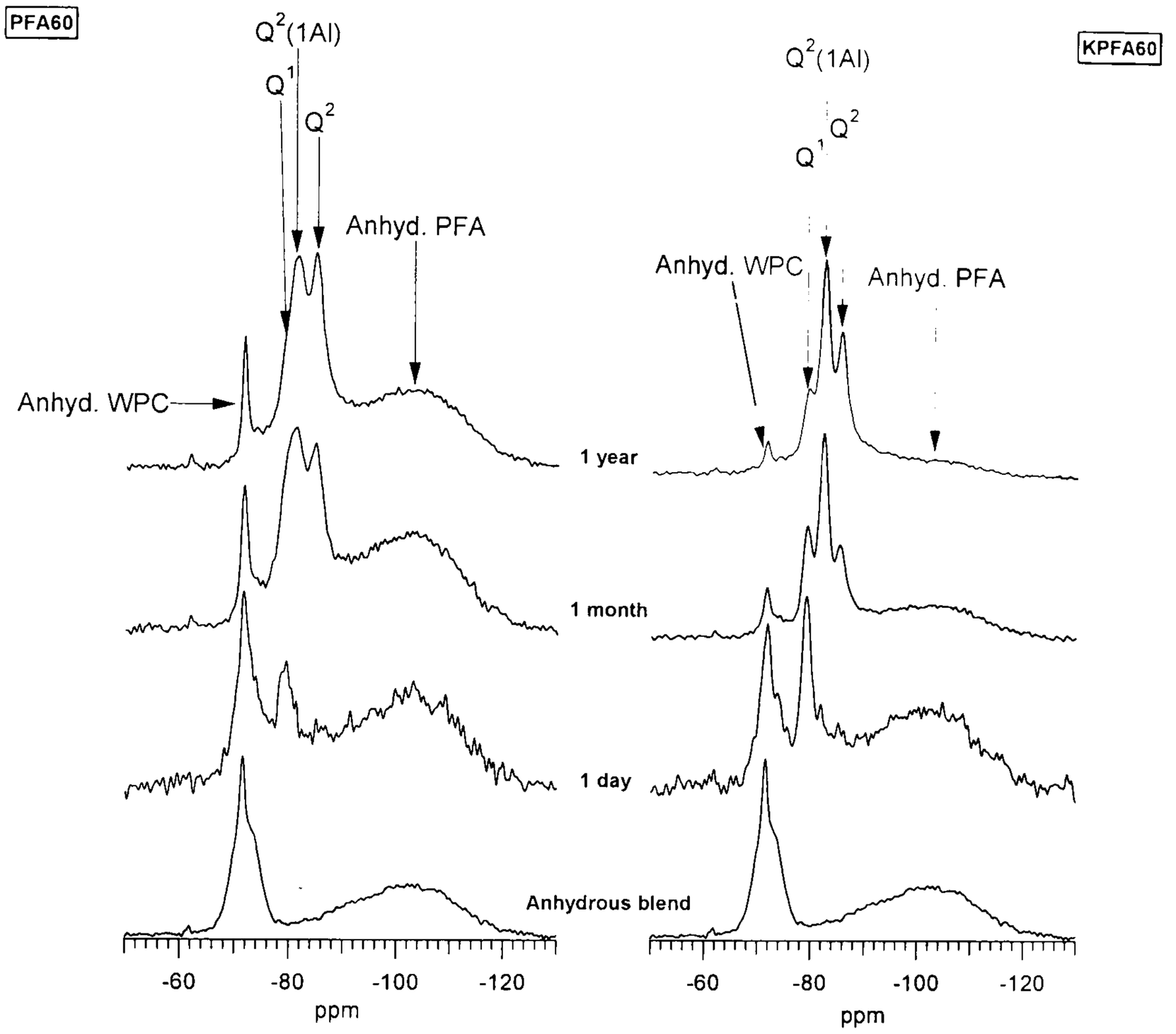


**Figure B1** – $^{29}$Si MAS NMR spectra for 1 day, 1 month and 1 year 60% PFA blended WPC pastes, cured at 25°C, water (left) and KOH (right) activated.

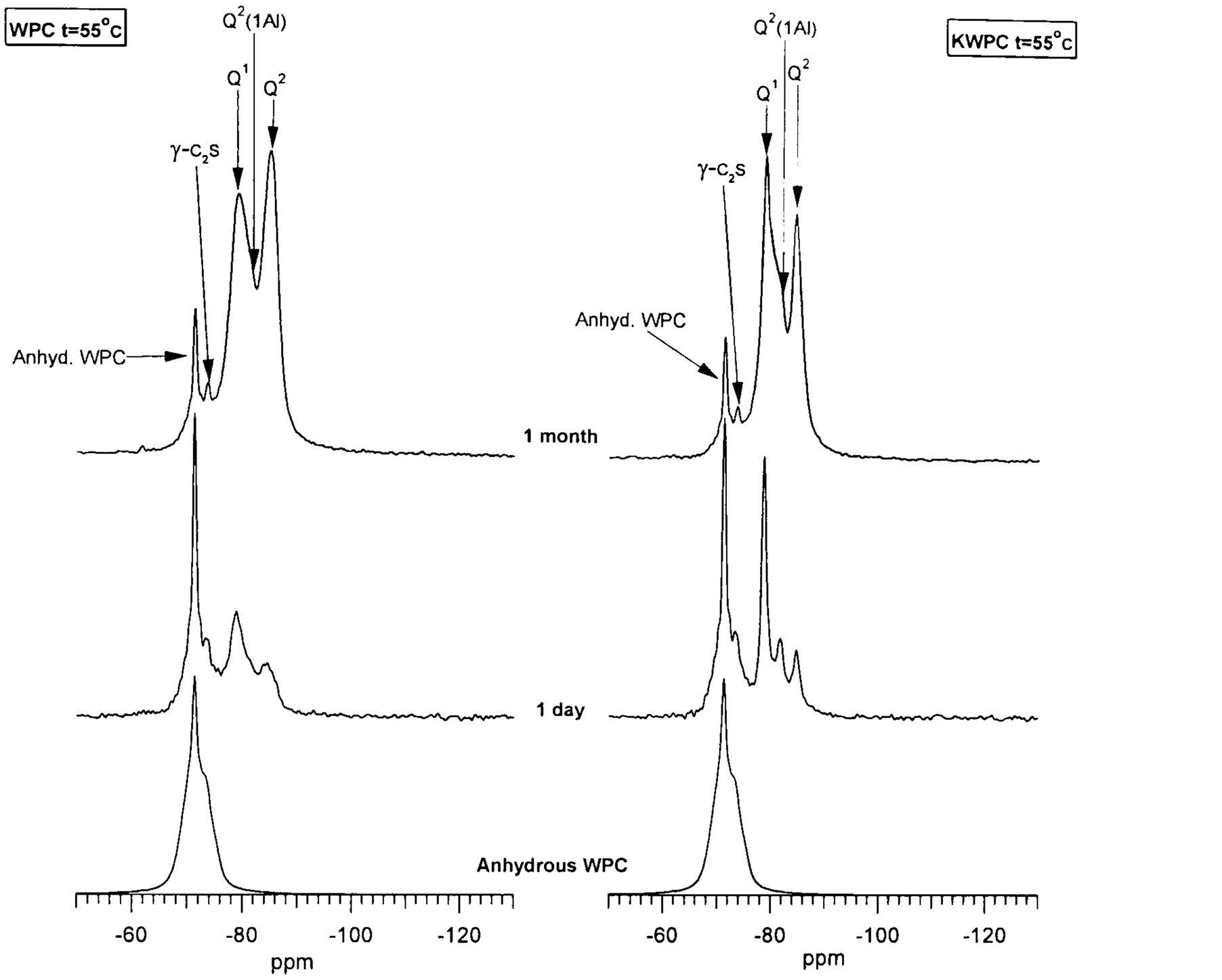


**Figure B2** – $^{29}$Si MAS NMR spectra for 1 day and 1 month neat WPC pastes, cured at 55°C, water (left) and KOH (right) activated.

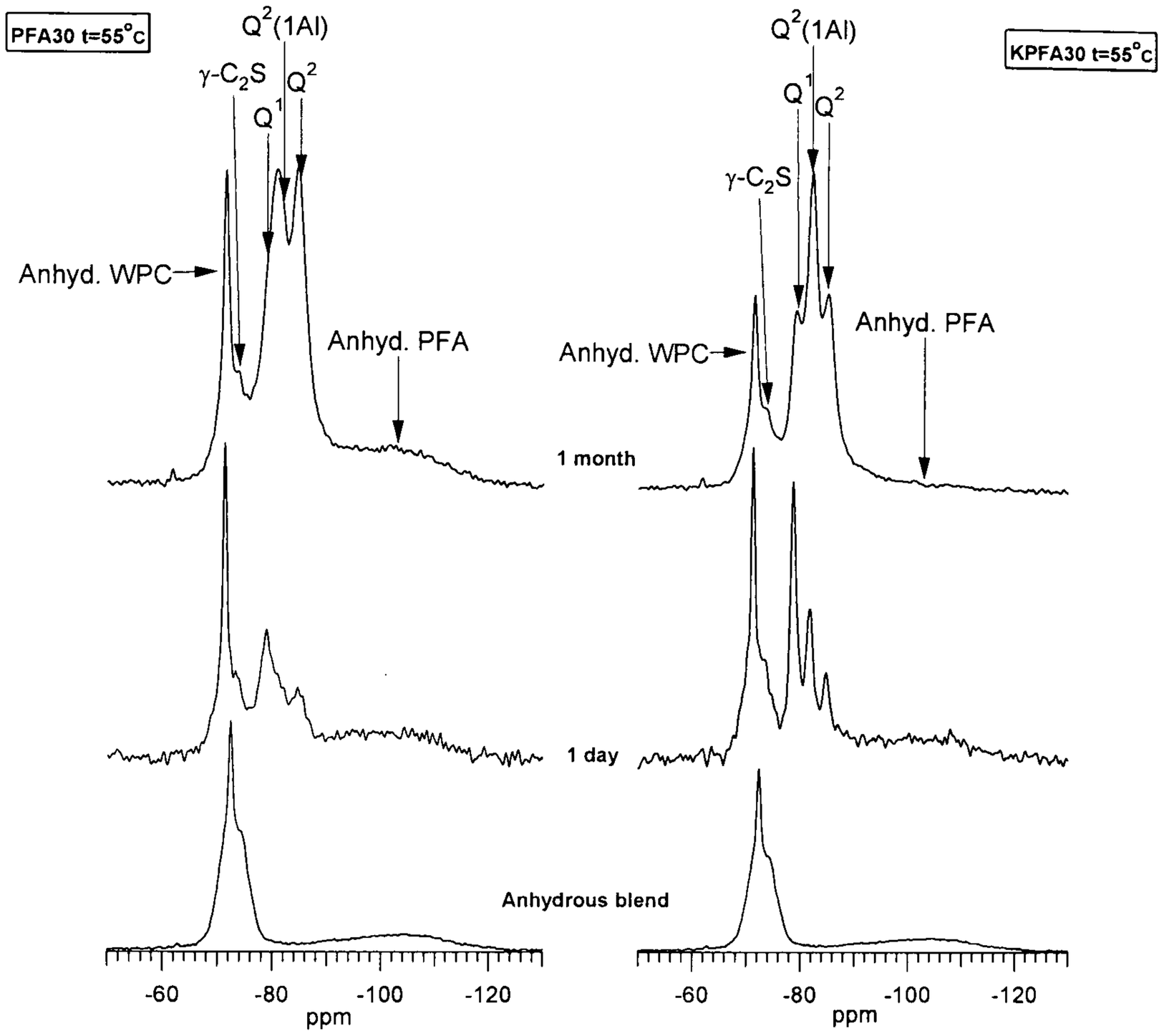


**Figure B3** – $^{29}$Si MAS NMR spectra for 1 day and 1 month 30% PFA blended WPC pastes, cured at 55°C, water (left) and KOH (right) activated.

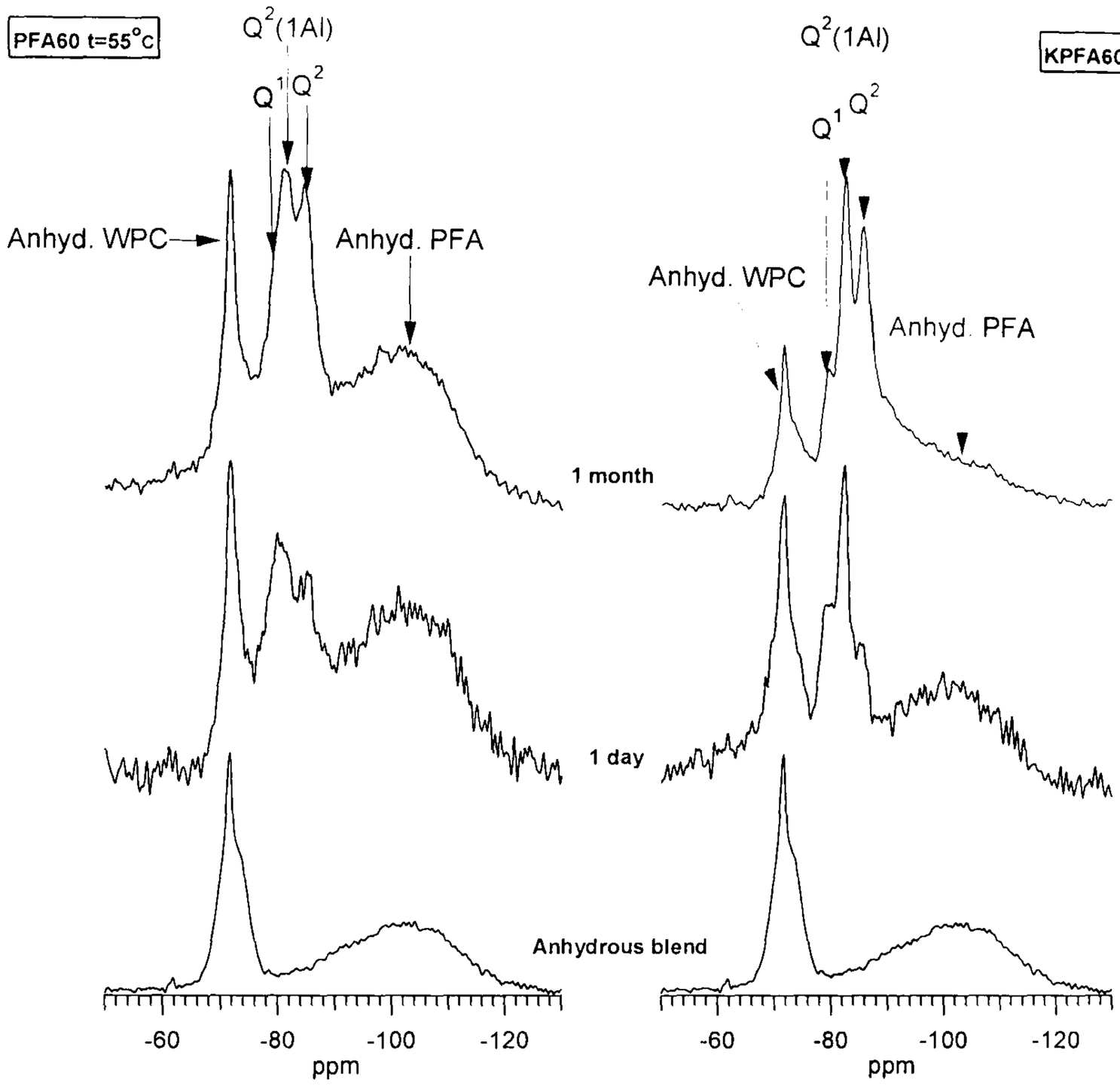


**Figure B4** – $^{29}$Si MAS NMR spectra for 1 day and 1 month 60% PFA blended WPC pastes, cured at 55°C, water (left) and KOH (right) activated.

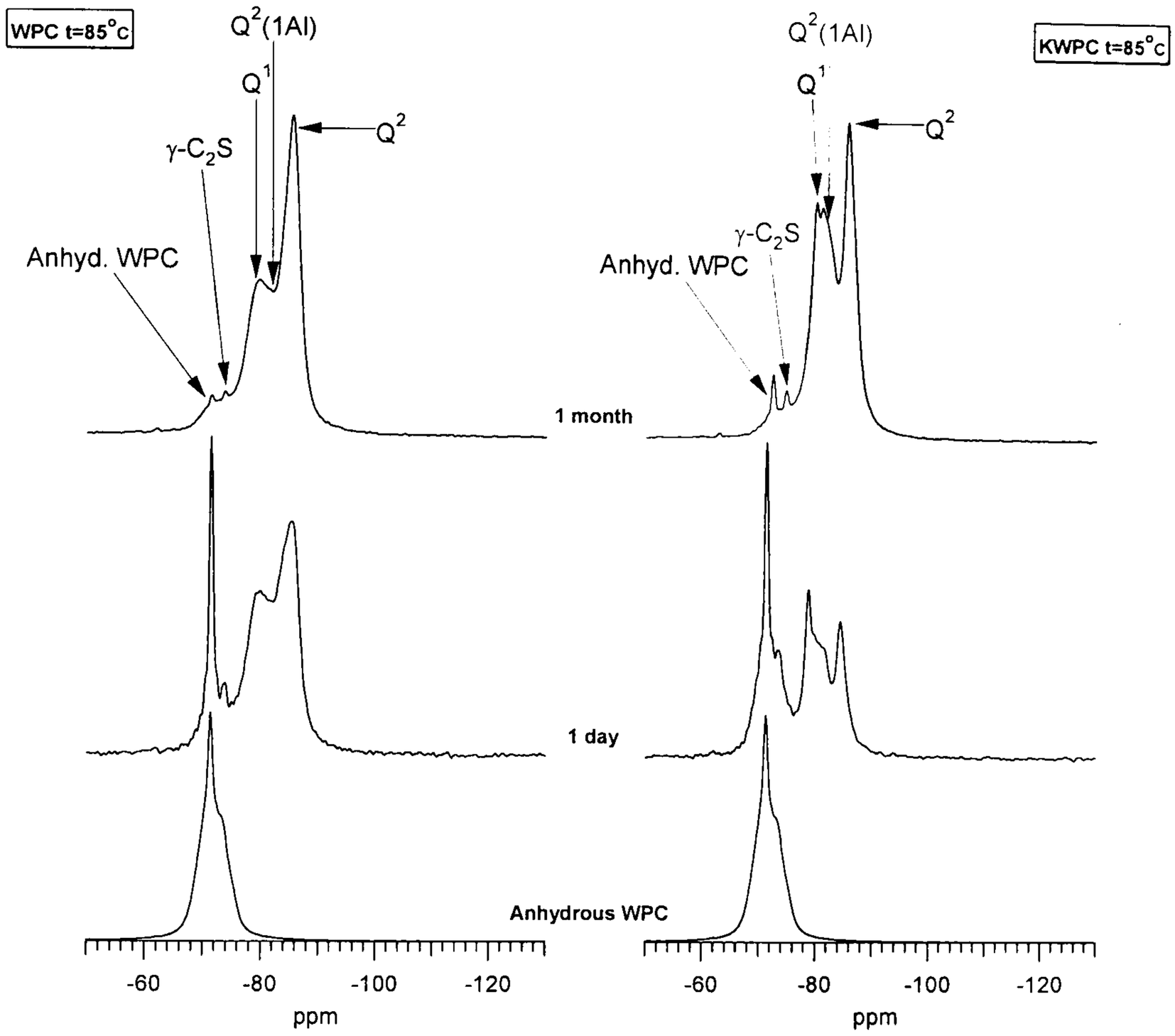


**Figure B5** – $^{29}$Si MAS NMR spectra for 1 day and 1 month neat WPC pastes, cured at 85°C, water (left) and KOH (right) activated.

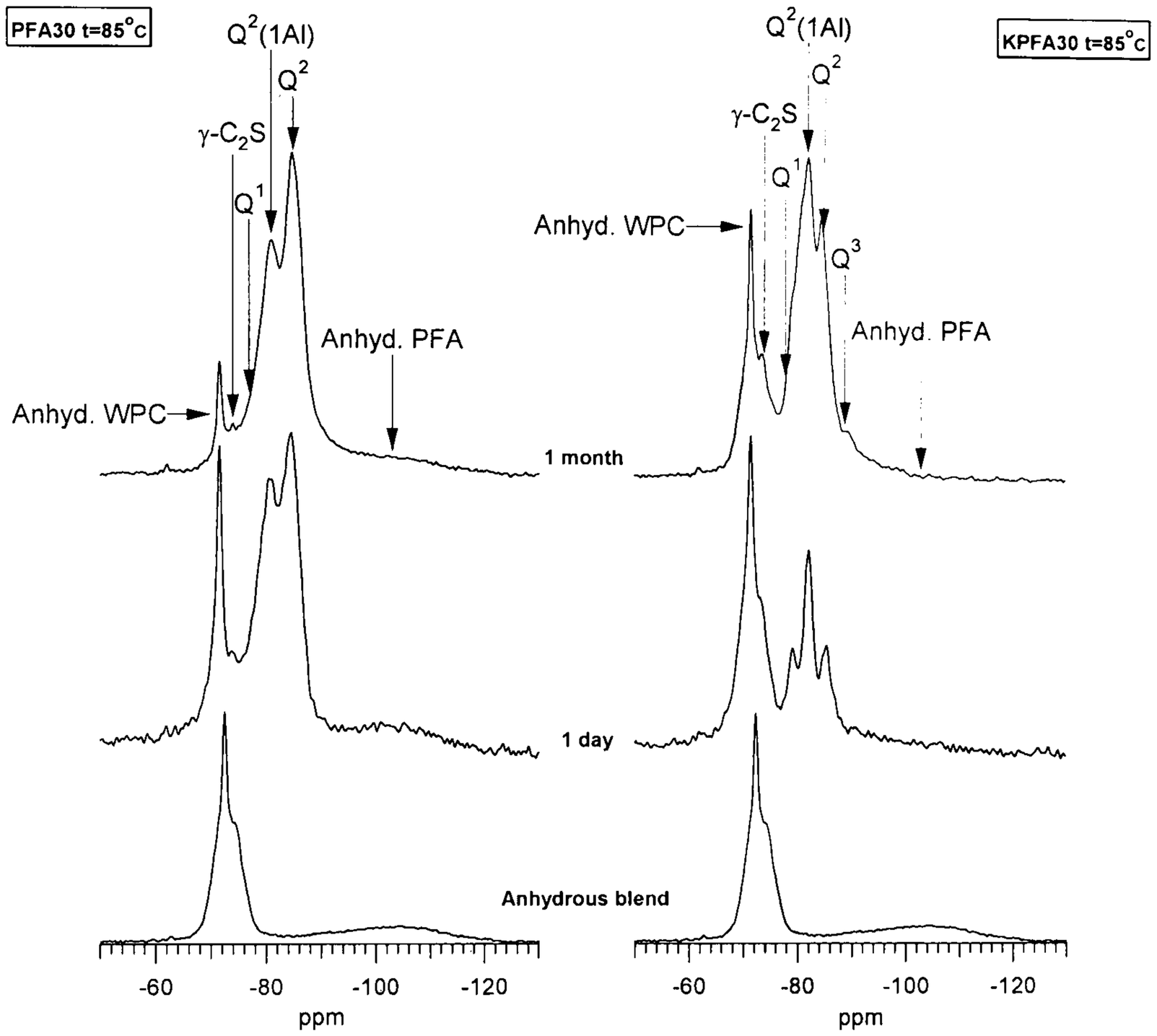


**Figure B6** – $^{29}$Si MAS NMR spectra for 1 day and 1 month 30% PFA blended WPC pastes, cured at 85°C, water (left) and KOH (right) activated.

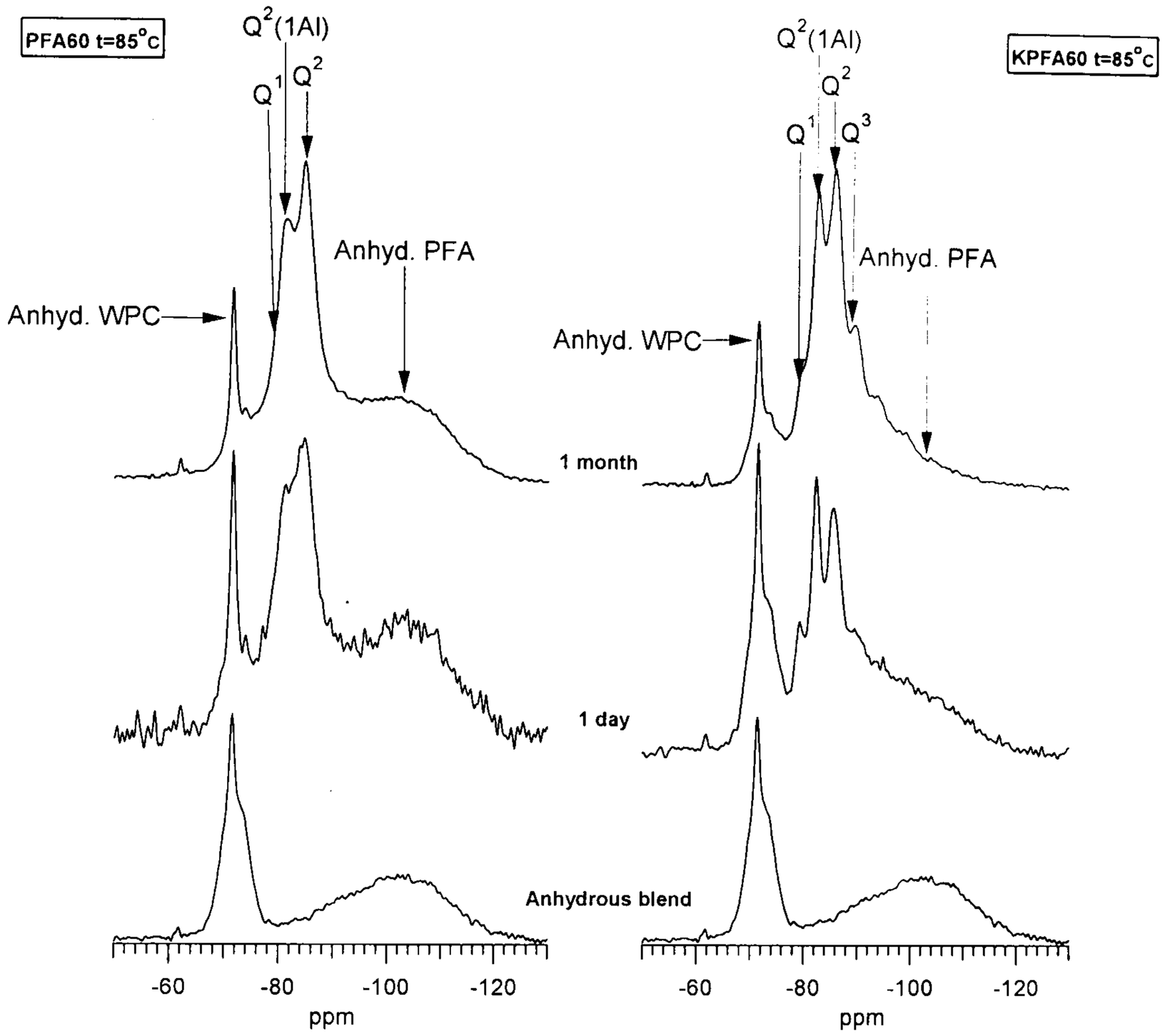


**Figure B7** – $^{29}$Si MAS NMR spectra for 1 day and 1 month 60% PFA blended WPC pastes, cured at 85°C, water (left) and KOH (right) activated.

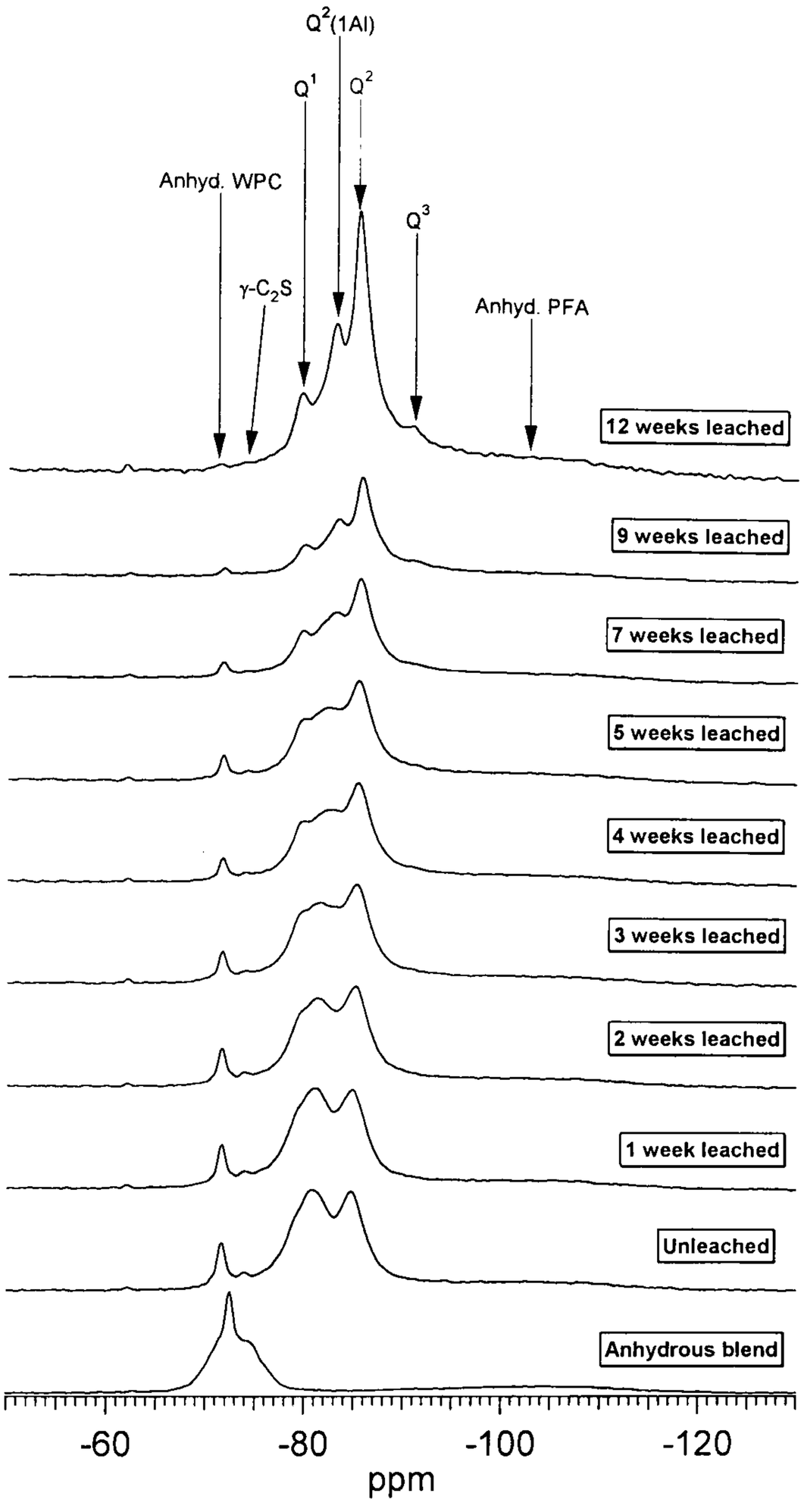


**Figure B8** – $^{29}$Si MAS NMR spectra for the PFA blended cement paste leached for 12 weeks.

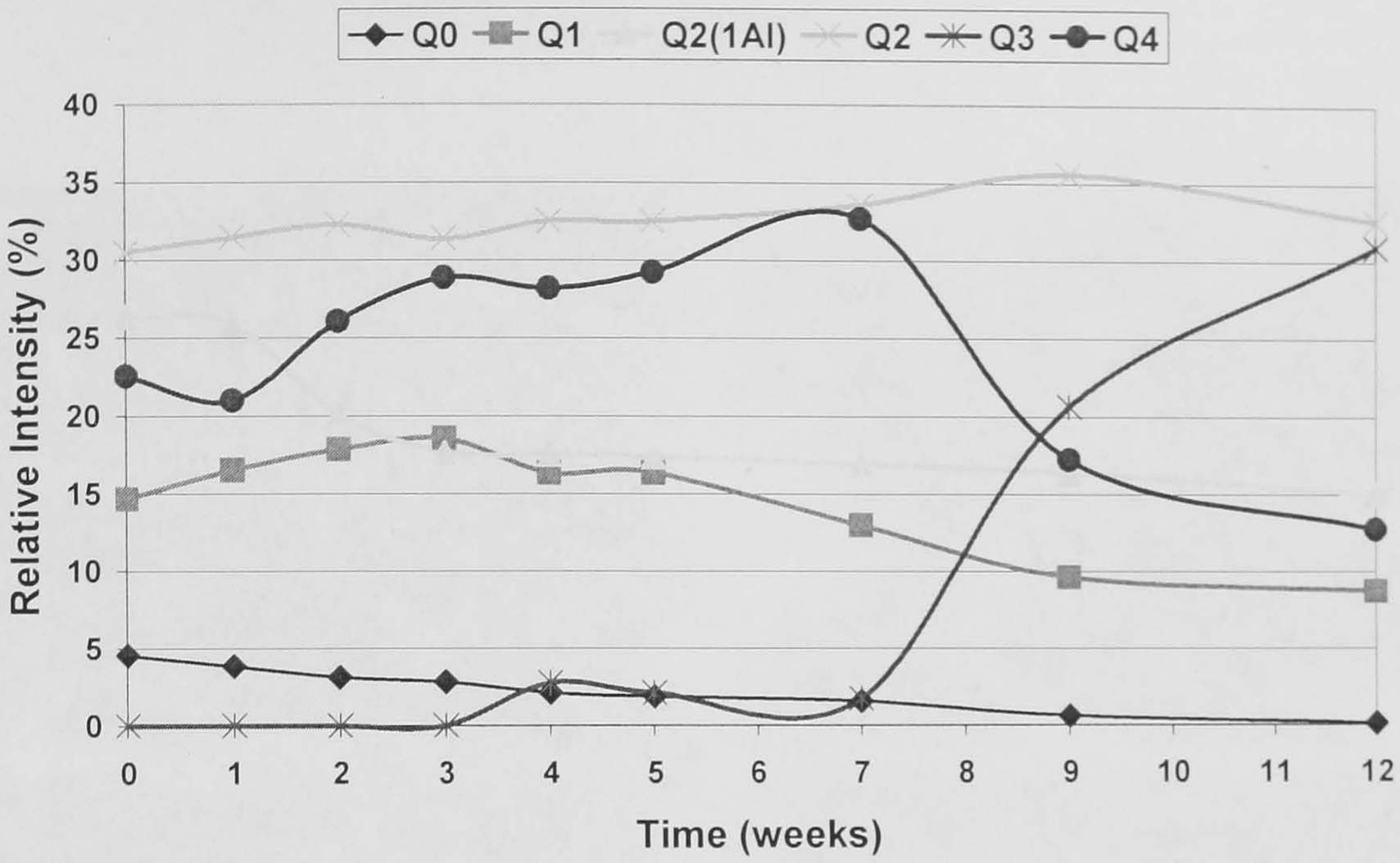


**Figure B9** – $Q^n$ relative intensity evolution during 12 weeks of water leaching the mature PFA blended paste.

# APPENDIX C

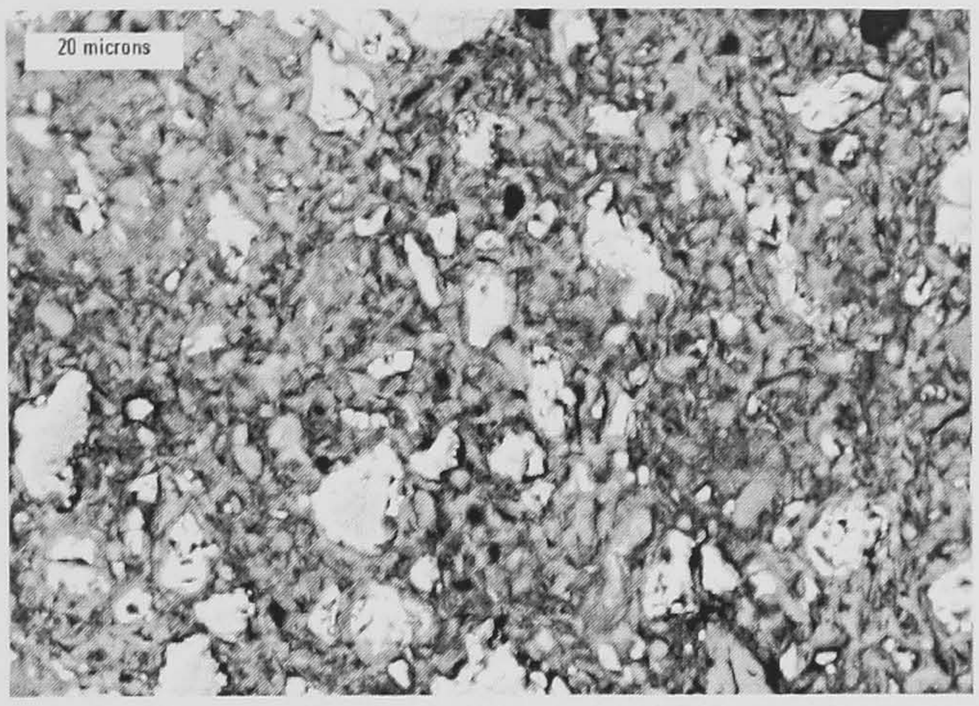


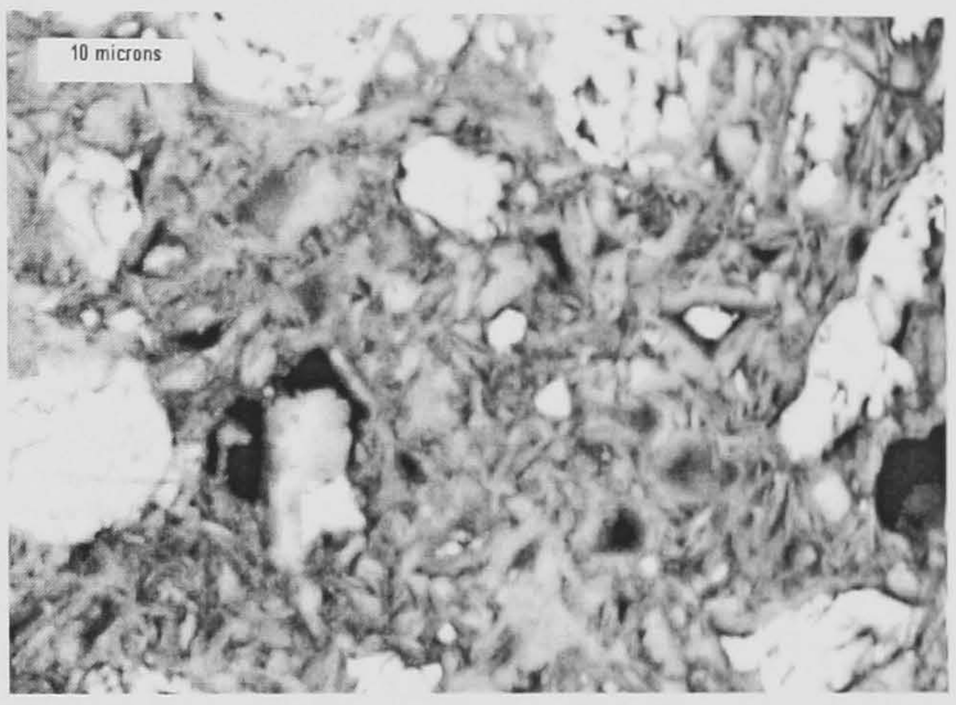


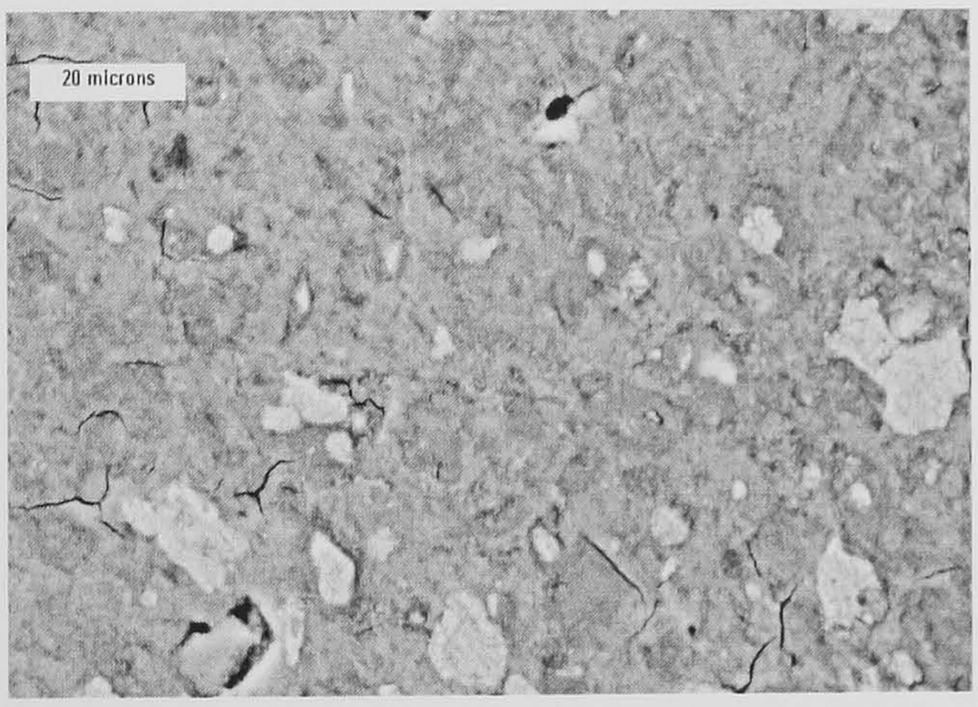


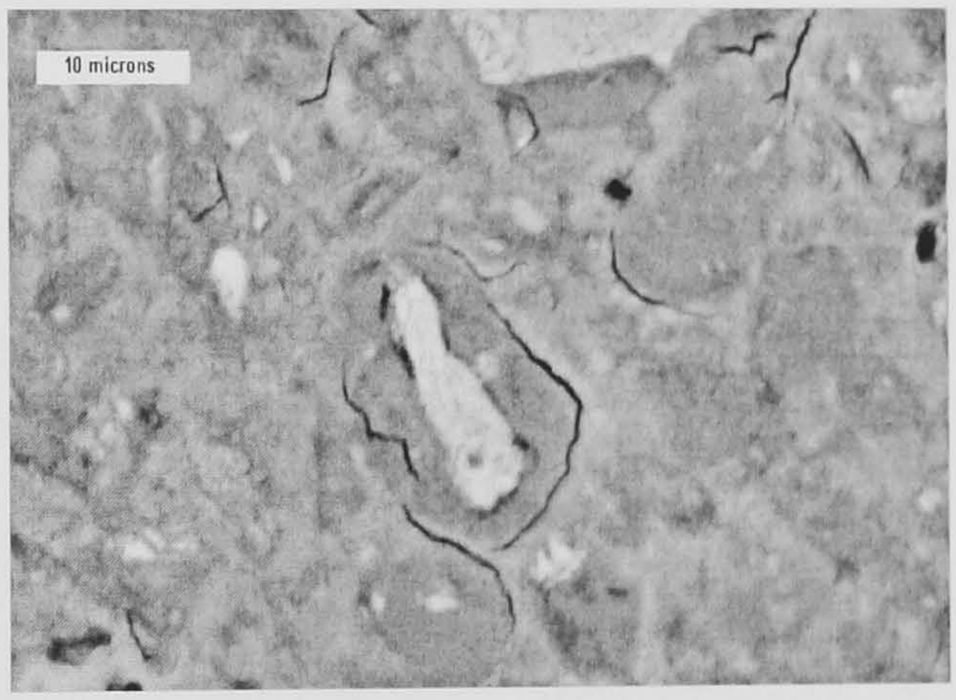


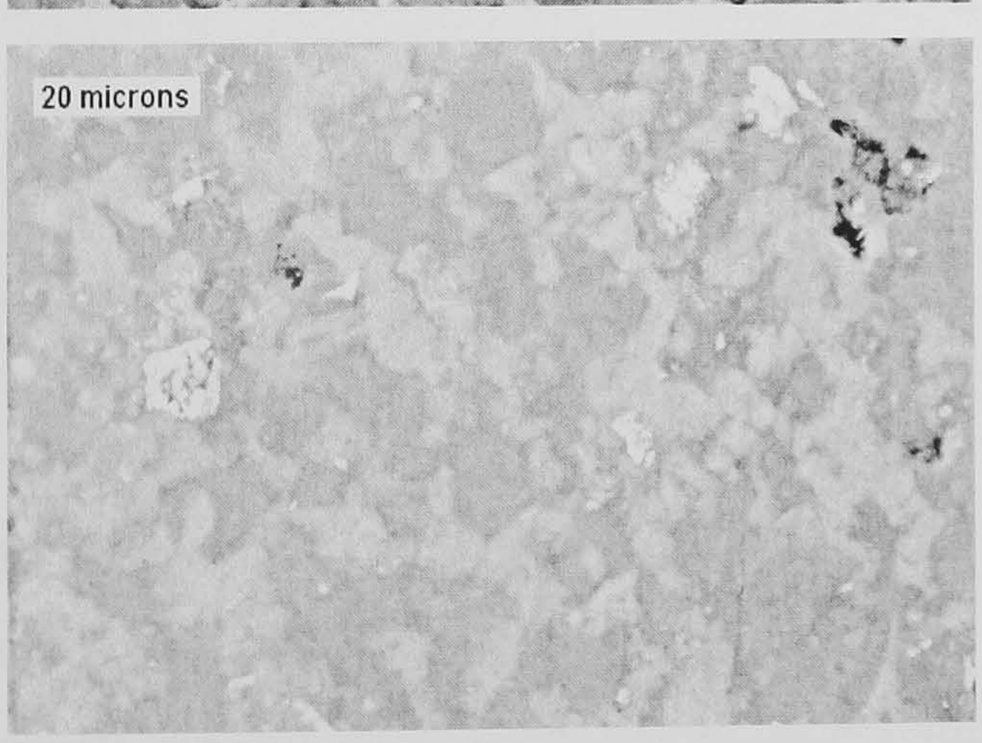


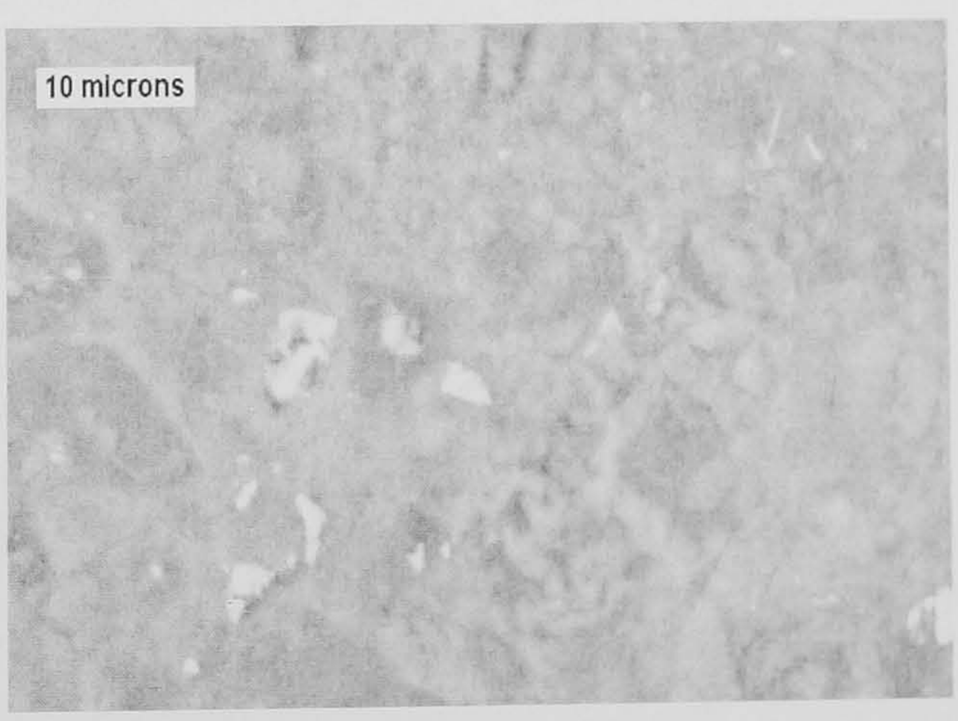


**Figure C1** – Backscattered electron images showing typical regions in the KOH activated WPC paste after 1 day (upper images), 1 month (middle) and 1 year (lower images) of hydration at 25°C.


**Figure C2** – Al/Ca against Si/Ca (left) and S/Ca against Al/Ca (right) atomic ratio plots for the SEM-EDX phase analysis of the KOH activated WPC paste after 1 day (upper plots), 1 month (middle) and 1 year (lower plots) of hydration at 25°C.

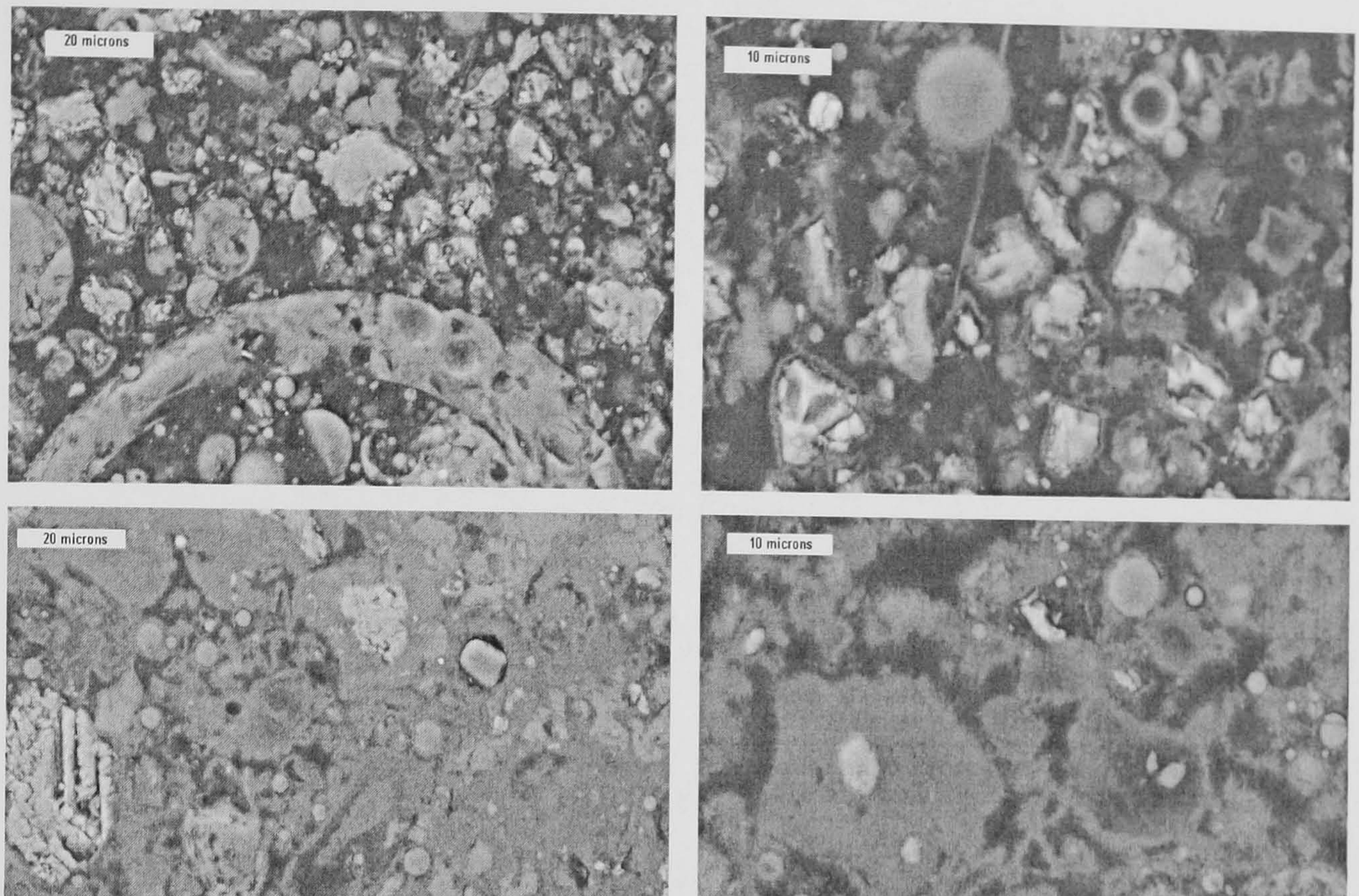


**Figure C3** – Backscattered electron images showing typical regions in the water activated 30% PFA blended paste after 1 day (upper images), 1 month (middle) and 1 year (lower images) of hydration at 25°C.

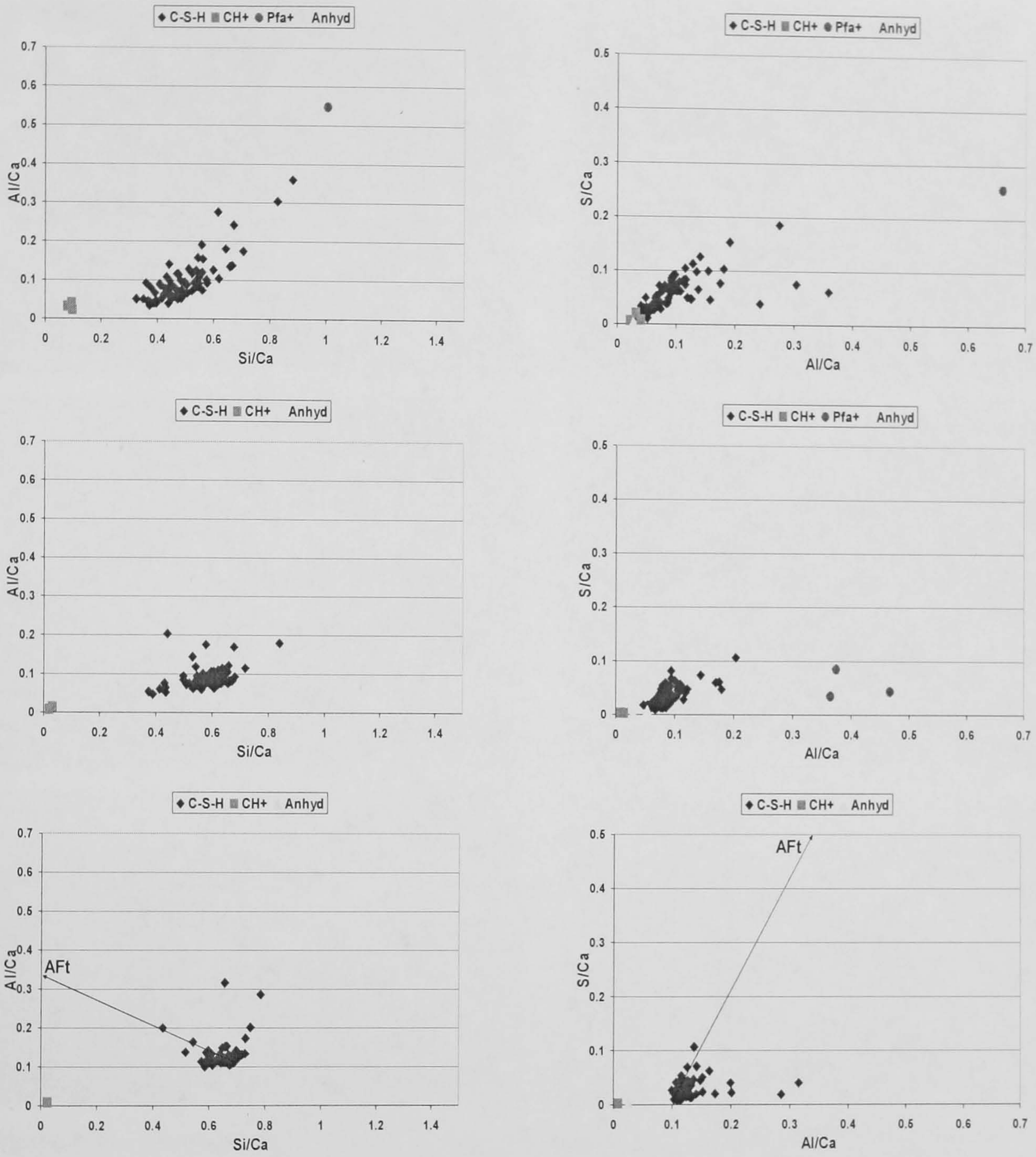


**Figure C4** – Al/Ca against Si/Ca (left) and S/Ca against Al/Ca (right) atomic ratio plots for the SEM-EDX phase analysis of the water activated 30% PFA blended paste after 1 day (upper plots), 1 month (middle) and 1 year (lower plots) of hydration at 25°C.

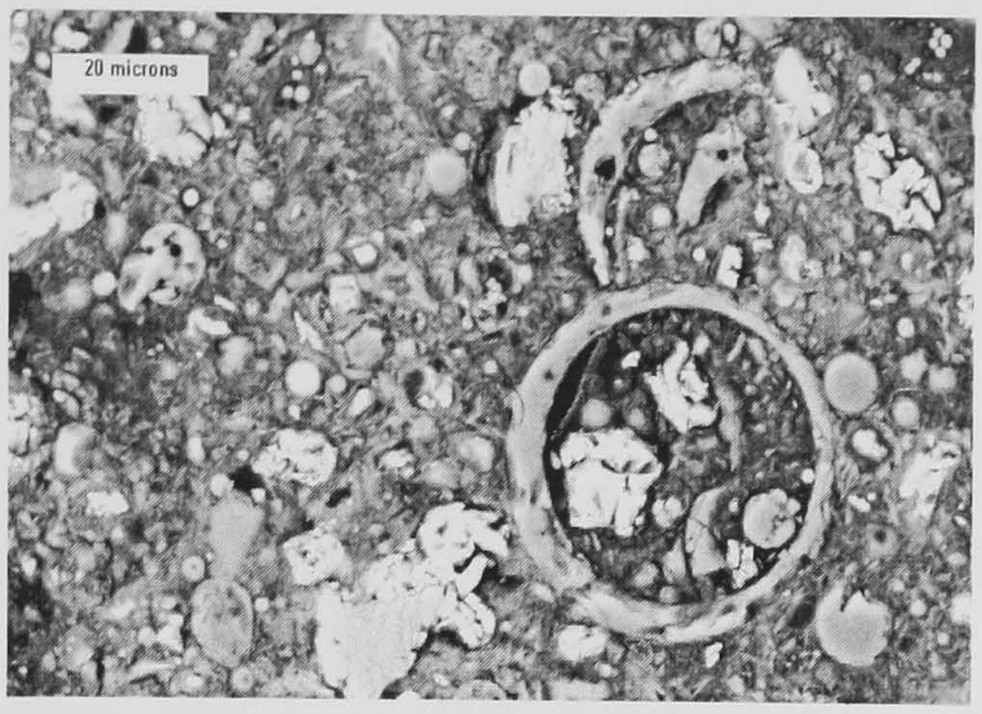


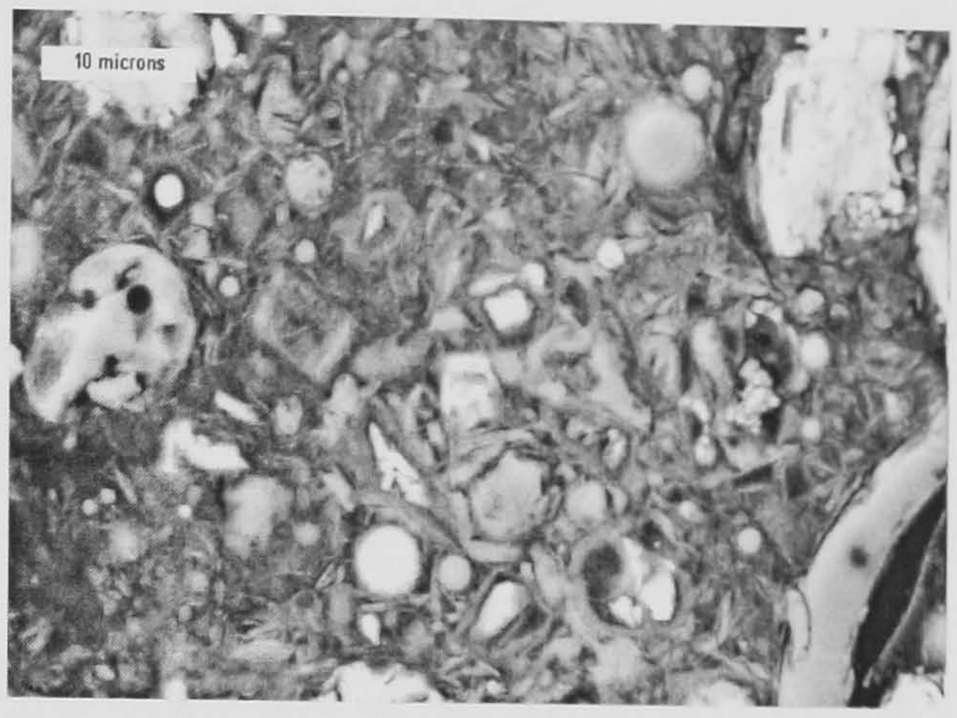


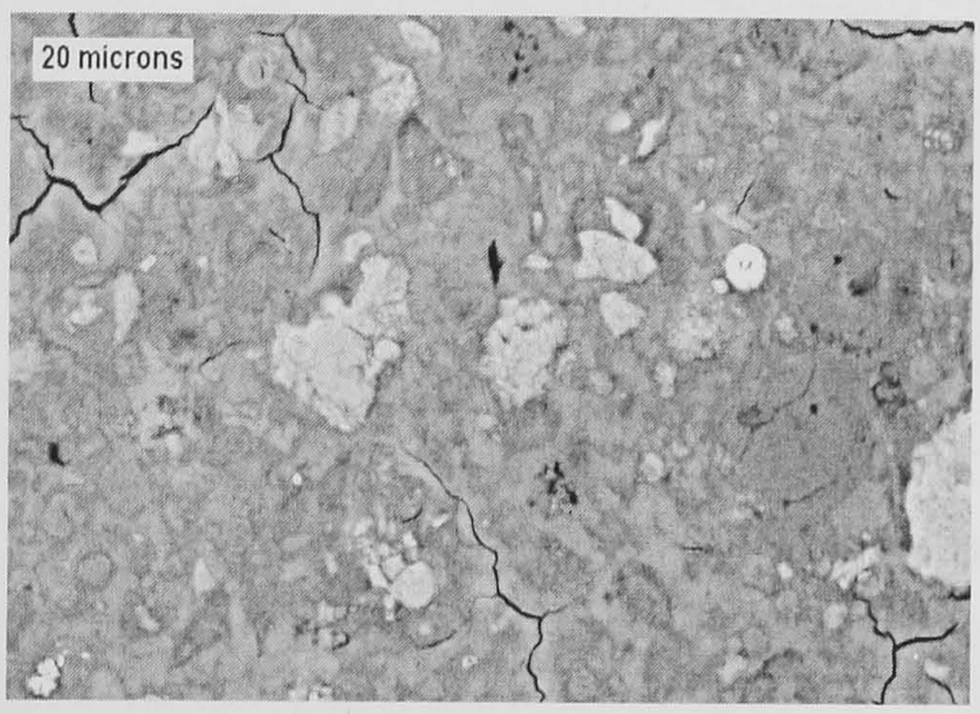


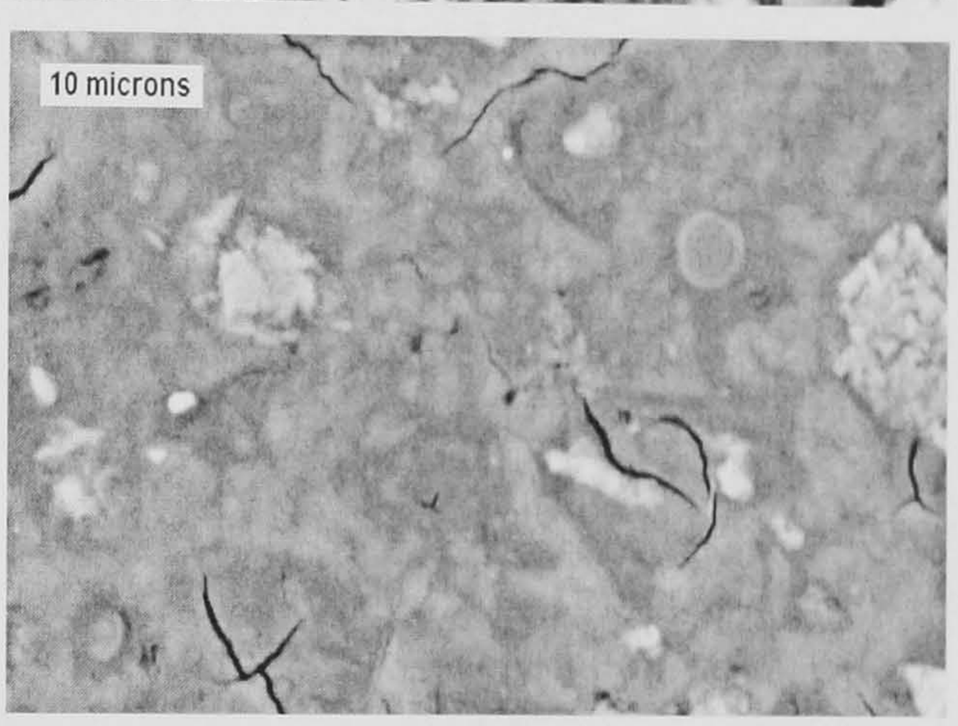




**Figure C5** – Backscattered electron images showing typical regions in the KOH activated 30% PFA blended paste after 1 day (upper images), 1 month (middle) and 1 year (lower images) of hydration at 25°C.

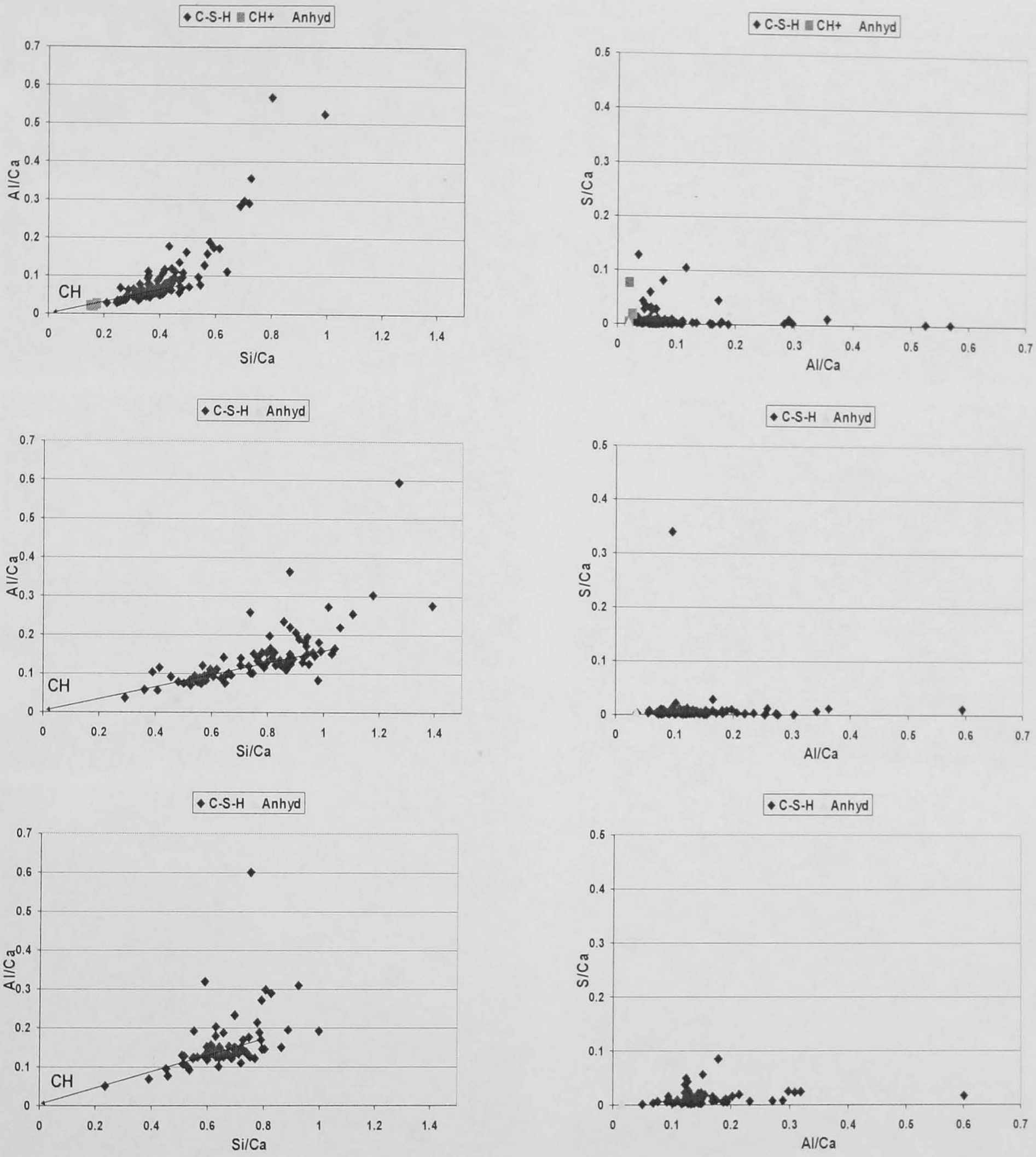


**Figure C6** – Al/Ca against Si/Ca (left) and S/Ca against Al/Ca (right) atomic ratio plots for the SEM-EDX phase analysis of the KOH activated 30% PFA blended paste after 1 day (upper plots), 1 month (middle) and 1 year (lower plots) of hydration at 25°C.

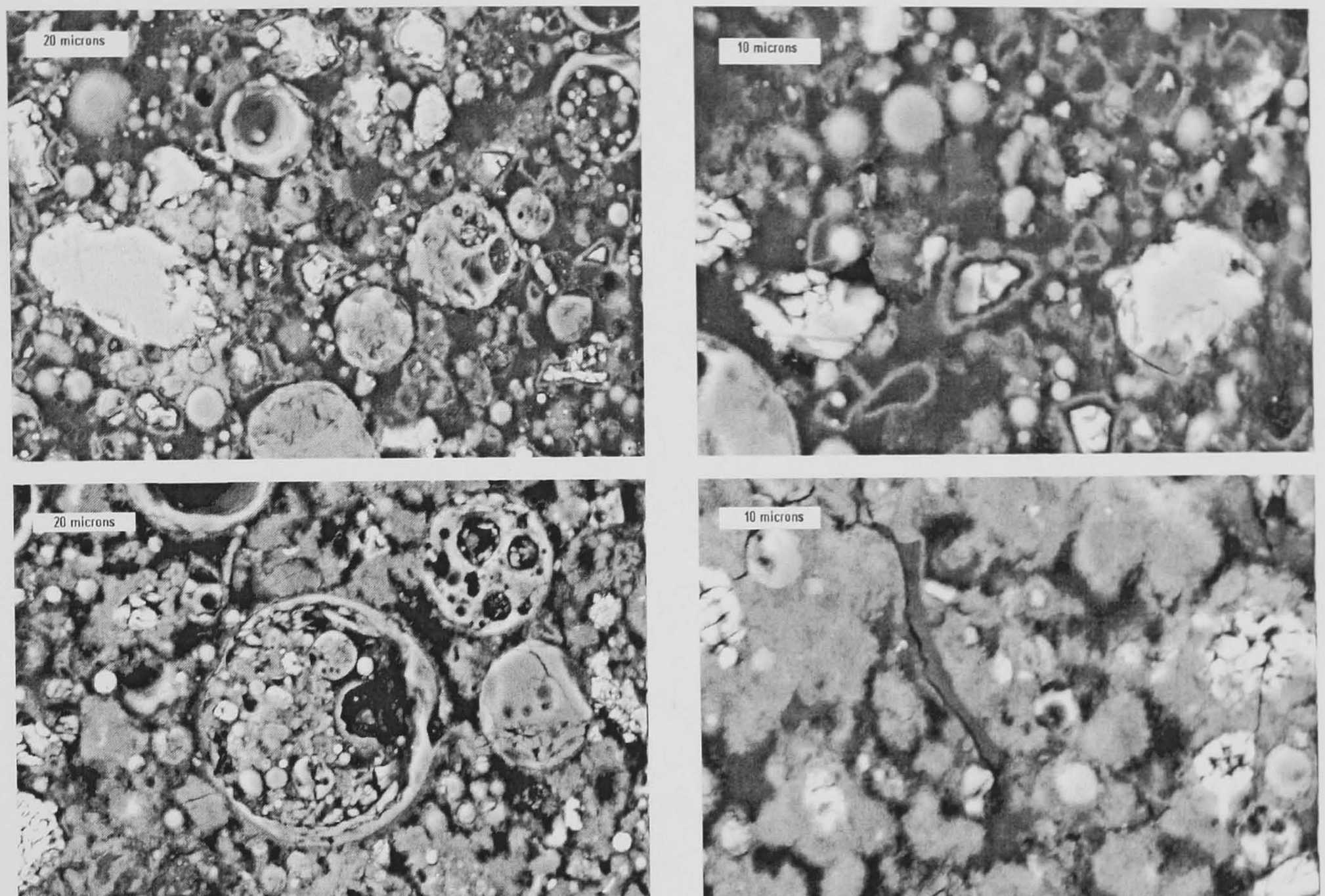


**Figure C7** – Backscattered electron images showing typical regions in the water activated 60% PFA blended paste after 1 day (upper images), 1 month (middle) and 1 year (lower images) of hydration at 25°C.

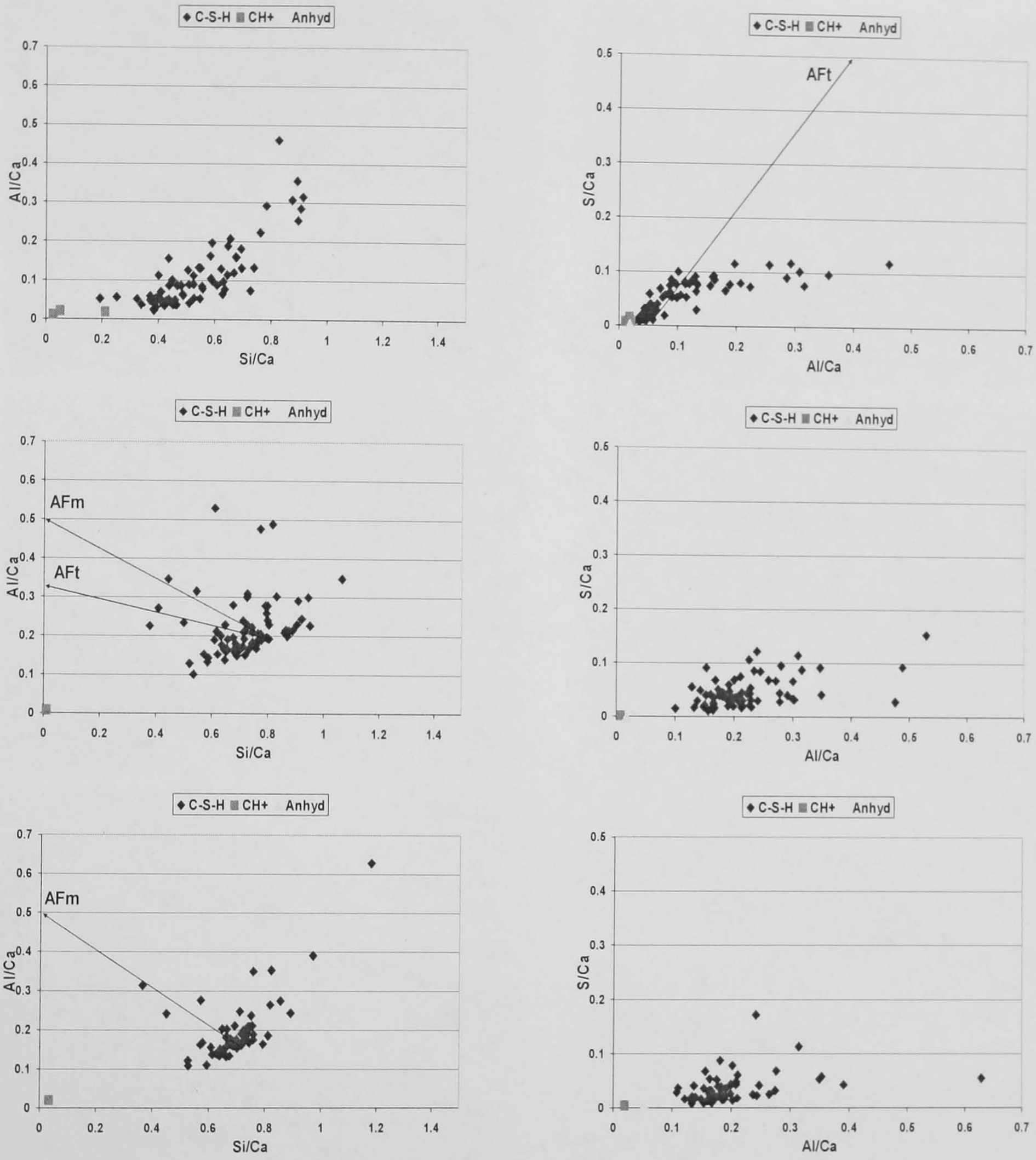


**Figure C8** – Al/Ca against Si/Ca (left) and S/Ca against Al/Ca (right) atomic ratio plots for the SEM-EDX phase analysis of the water activated 60% PFA blended paste after 1 day (upper plots), 1 month (middle) and 1 year (lower plots) of hydration at 25°C.

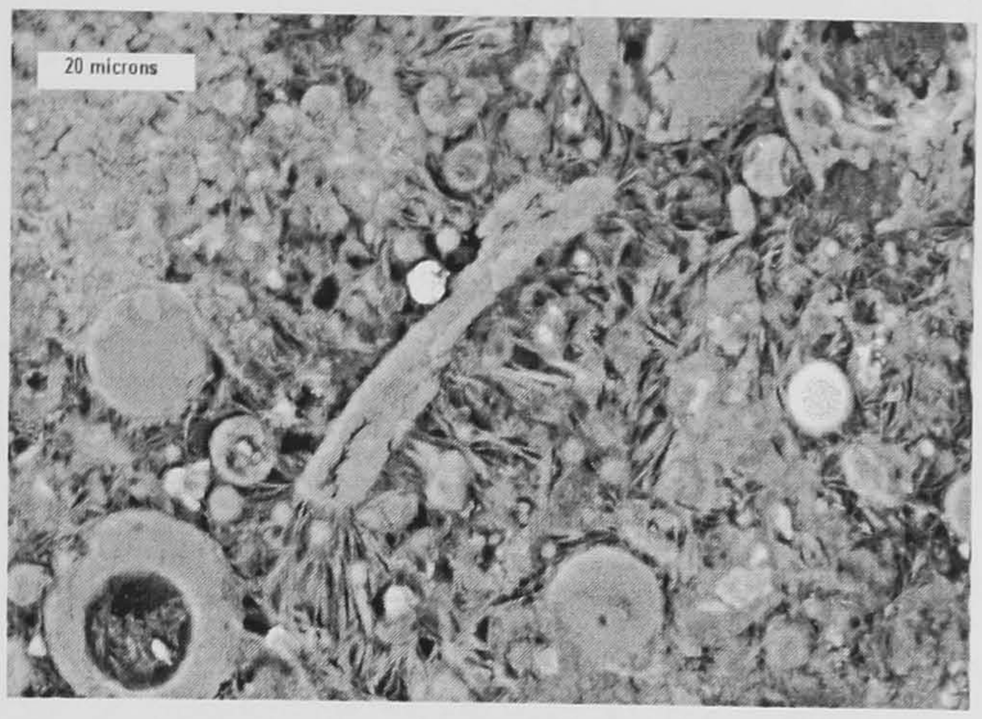



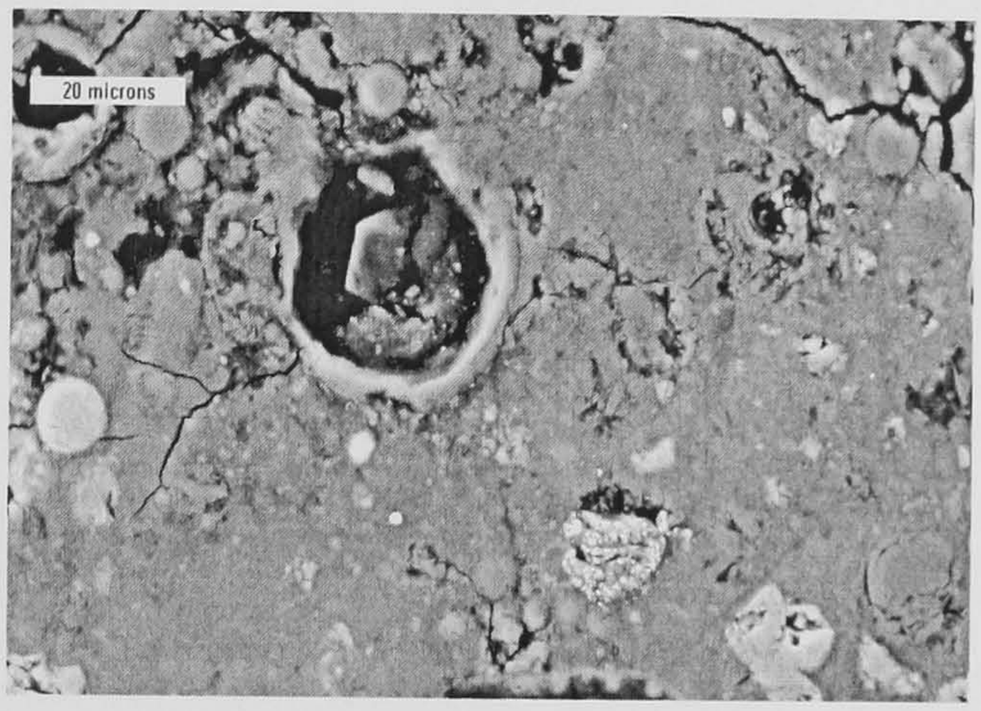


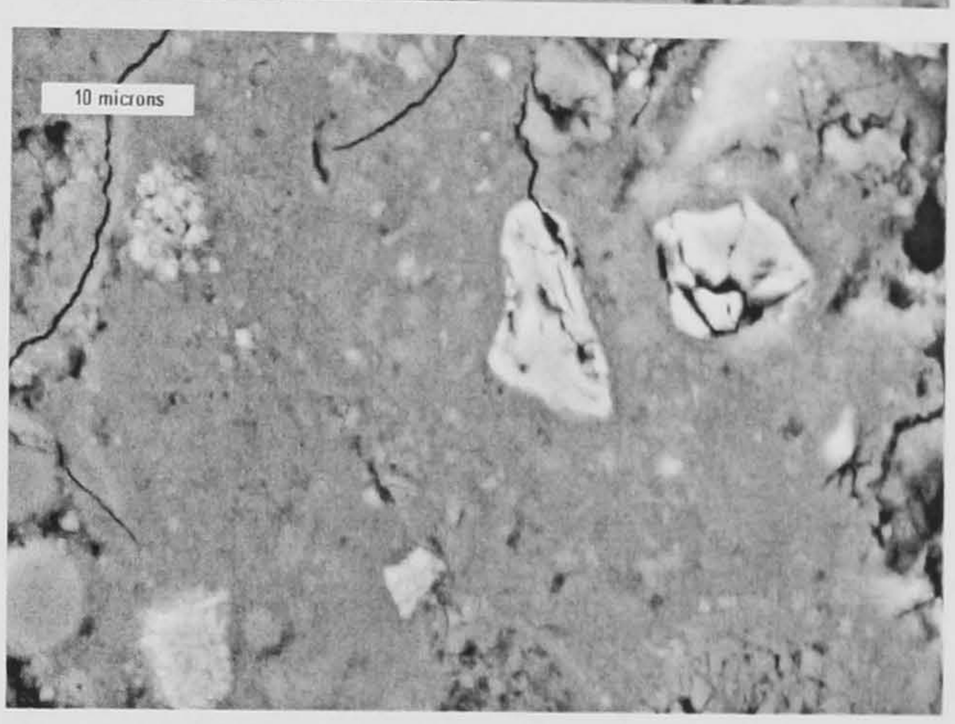


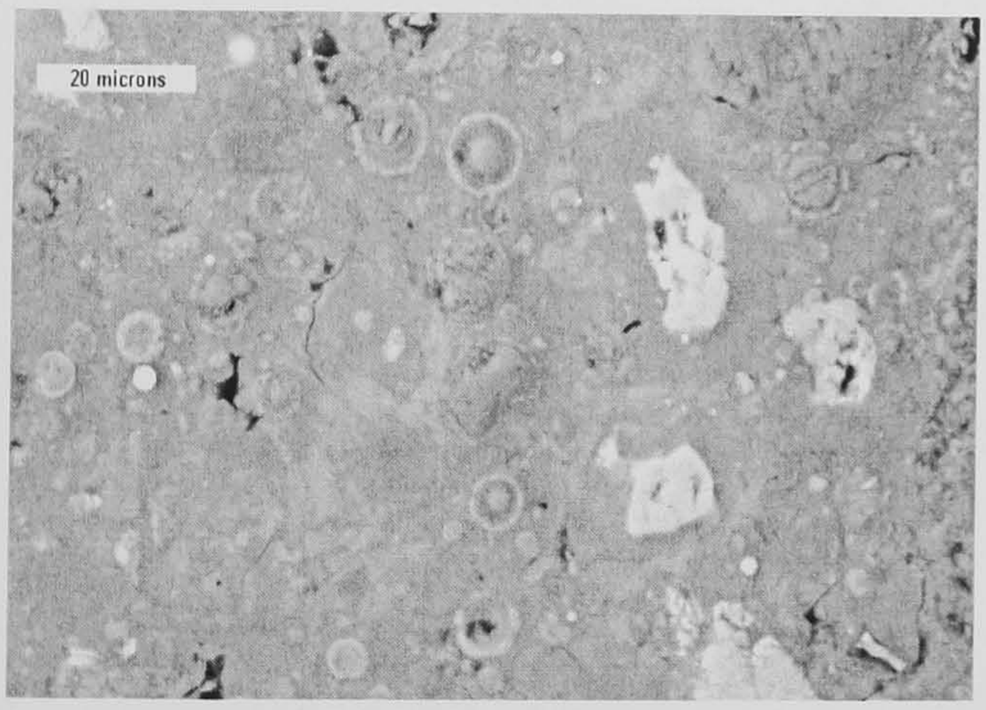


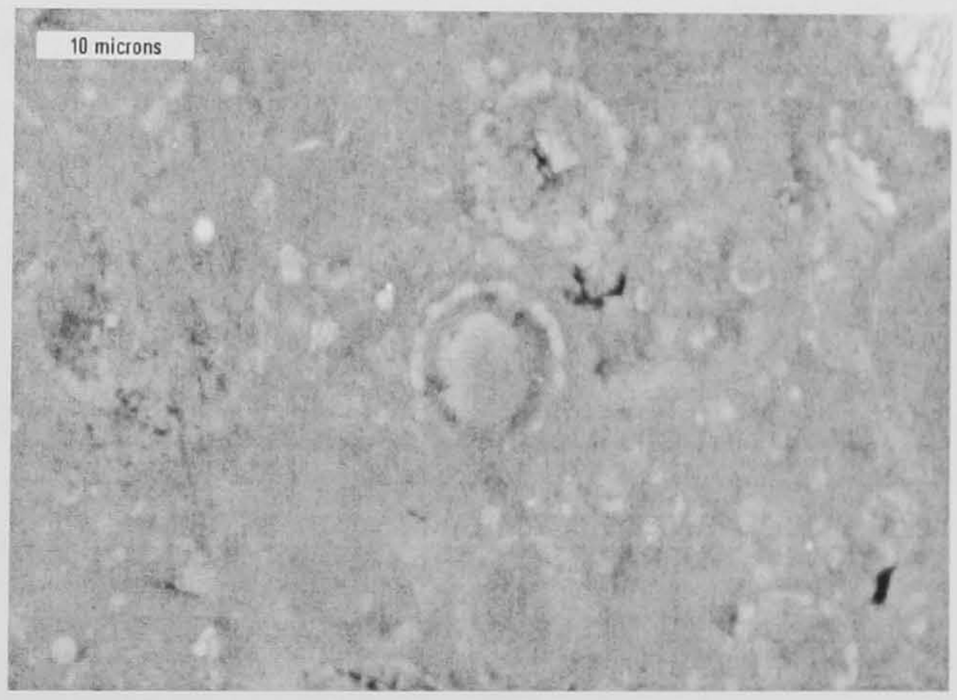


**Figure C9** – Backscattered electron images showing typical regions in the KOH activated 60% PFA blended paste after 1 day (upper images), 1 month (middle) and 1 year (lower images) of hydration at 25°C.

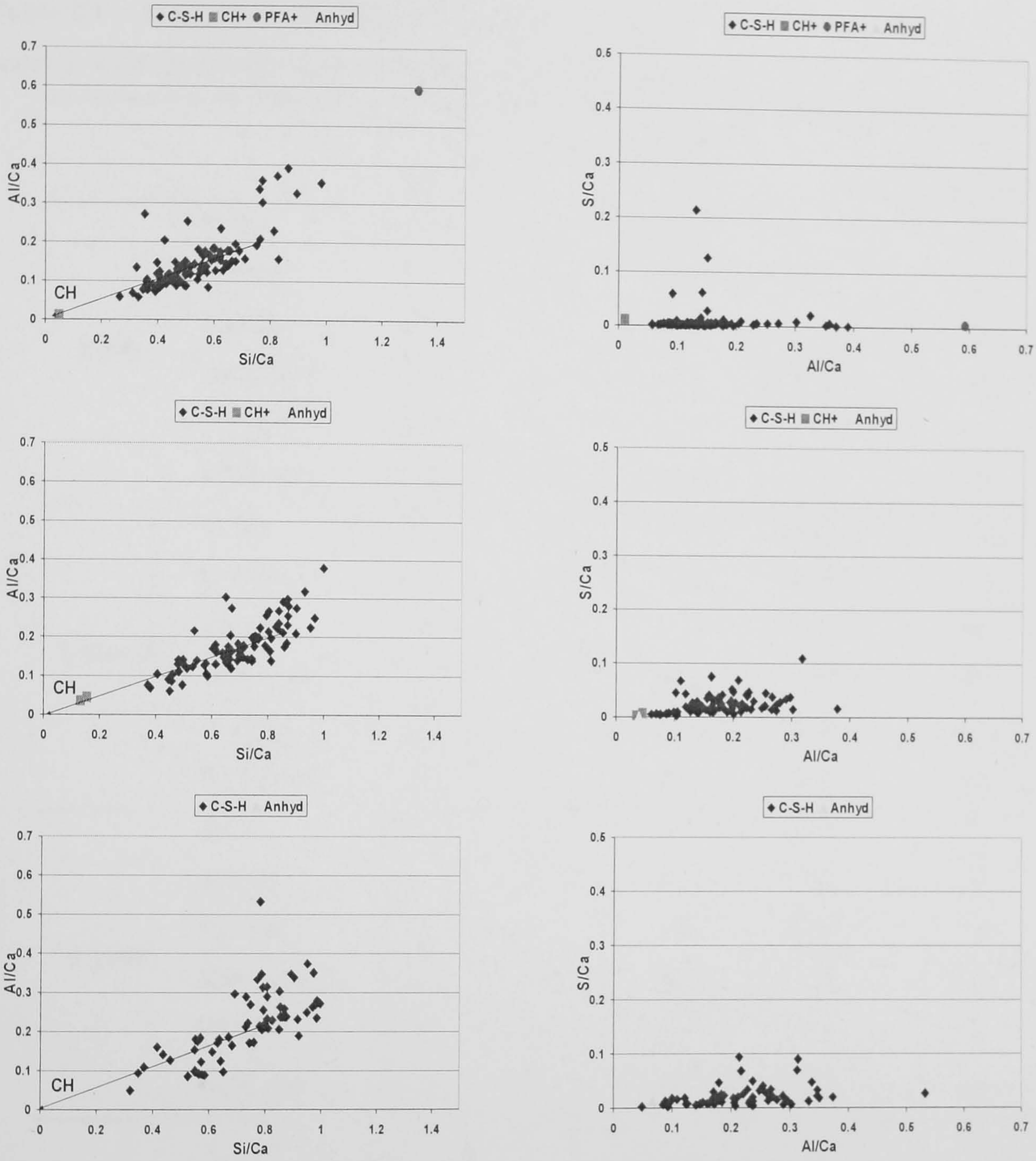


**Figure C10** – Al/Ca against Si/Ca (left) and S/Ca against Al/Ca (right) atomic ratio plots for the SEM-EDX phase analysis of the KOH activated 30% PFA blended paste after 1 day (upper plots), 1 month (middle) and 1 year (lower plots) of hydration at 25°C.

**Table C1** – Mean Ca/Si and Al/Si atomic ratios obtained for C-S-H using SEM-EDX, for the water or KOH activated neat and blended pastes, cured at 25°C for 1 day, 1 month and 1 year.

| | | Mean Ca/Si ratio | *s* | Mean Al/Si ratio | *s* | Number Analysis (N) |
|---|---|---|---|---|---|---|
| 1 day | **WPC** | 2.31 | 0.50 | 0.17 | 0.10 | 89 |
| | **KWPC** | 3.21 | 0.50 | 0.17 | 0.05 | 88 |
| | **PFA30** | 2.10 | 0.40 | 0.19 | 0.07 | 70 |
| | **KPFA30** | 2.56 | 0.71 | 0.21 | 0.12 | 96 |
| | **PFA60** | 2.04 | 0.65 | 0.18 | 0.09 | 75 |
| | **KPFA60** | 1.96 | 0.54 | 0.28 | 0.10 | 97 |
| 1 month | **WPC** | 2.01 | 0.28 | 0.11 | 0.05 | 102 |
| | **KWPC** | 3.46 | 1.10 | 0.10 | 0.02 | 101 |
| | **PFA30** | 1.74 | 0.25 | 0.15 | 0.05 | 92 |
| | **KPFA30** | 1.30 | 0.54 | 0.21 | 0.12 | 95 |
| | **PFA60** | 1.52 | 0.30 | 0.32 | 0.13 | 73 |
| | **KPFA60** | 1.52 | 0.38 | 0.25 | 0.06 | 82 |
| 1 year | **WPC** | 2.02 | 0.38 | 0.11 | 0.05 | 71 |
| | **KWPC** | 1.91 | 0.29 | 0.10 | 0.03 | 79 |
| | **PFA30** | 1.54 | 0.14 | 0.20 | 0.06 | 75 |
| | **KPFA30** | 1.58 | 0.42 | 0.24 | 0.09 | 71 |
| | **PFA60** | 1.47 | 0.28 | 0.29 | 0.11 | 54 |
| | **KPFA60** | 1.47 | 0.45 | 0.29 | 0.09 | 64 |

# APPENDIX C - SEM-EDX

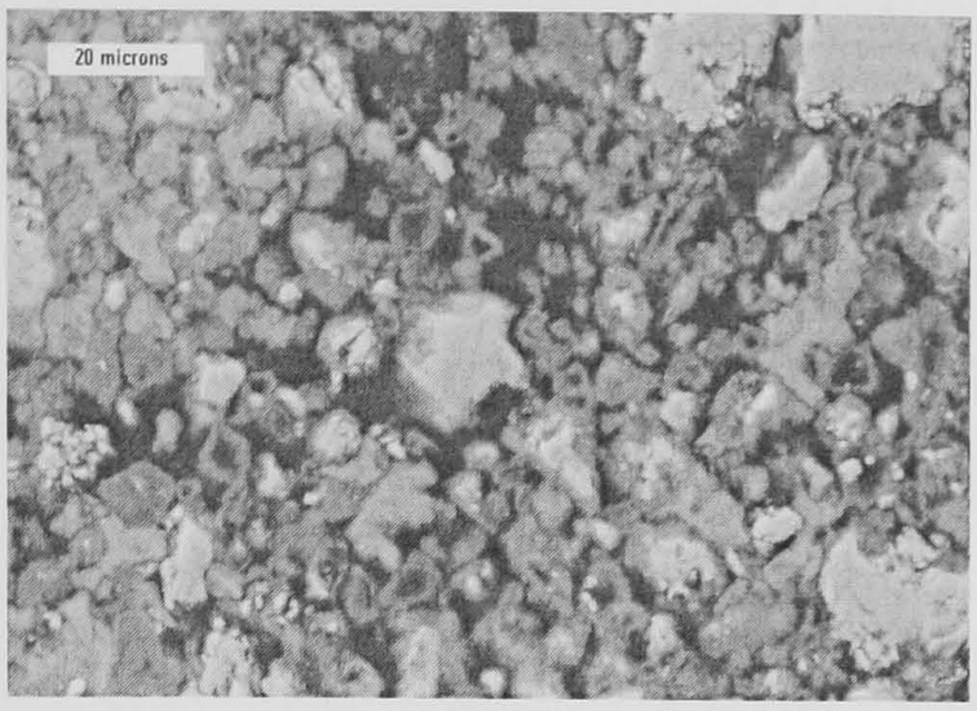


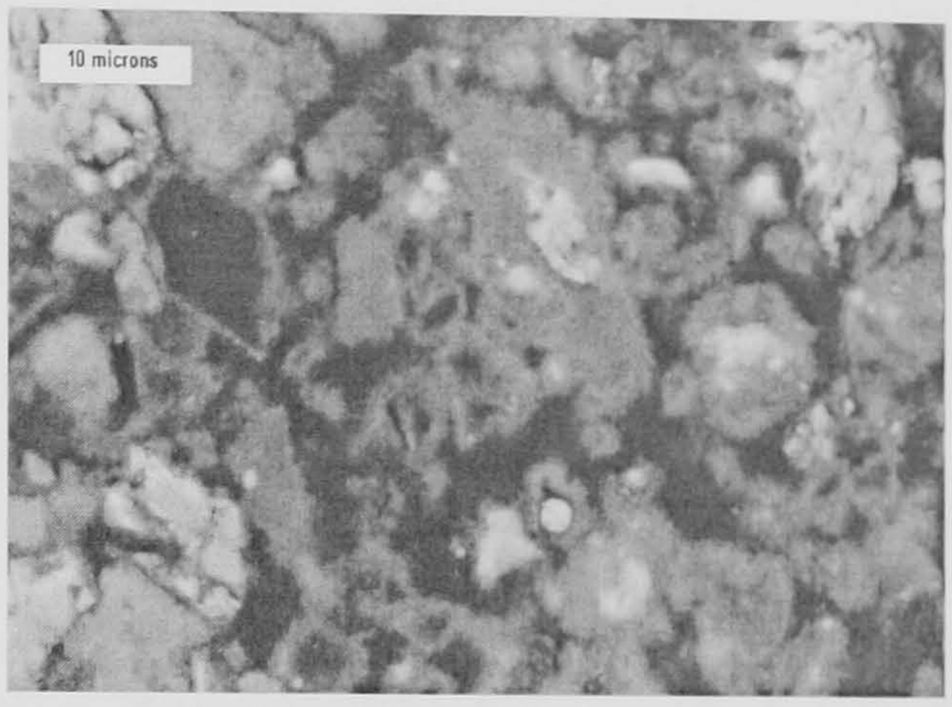


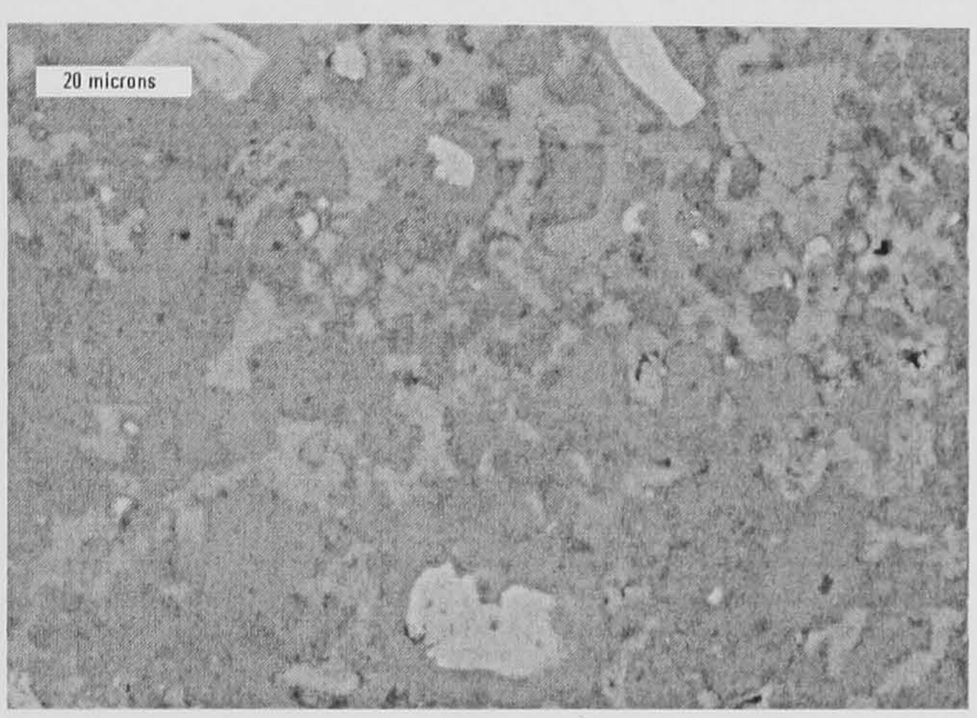


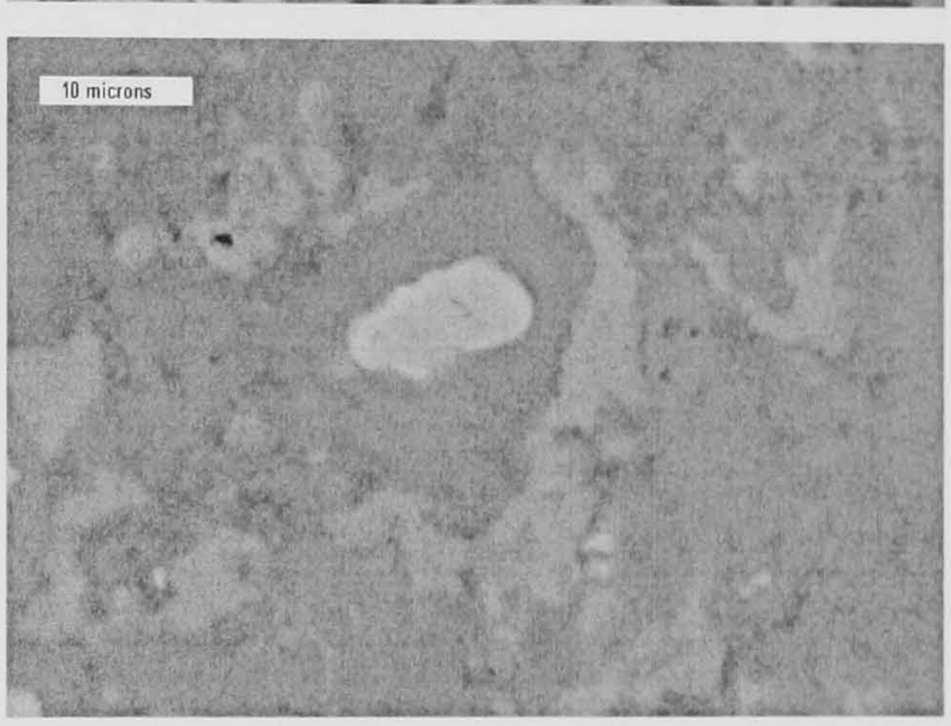


**Figure C11** – Backscattered electron images showing typical regions in the water activated WPC paste after 1 day (upper images) and 1 month (lower images) of hydration at 55°C.

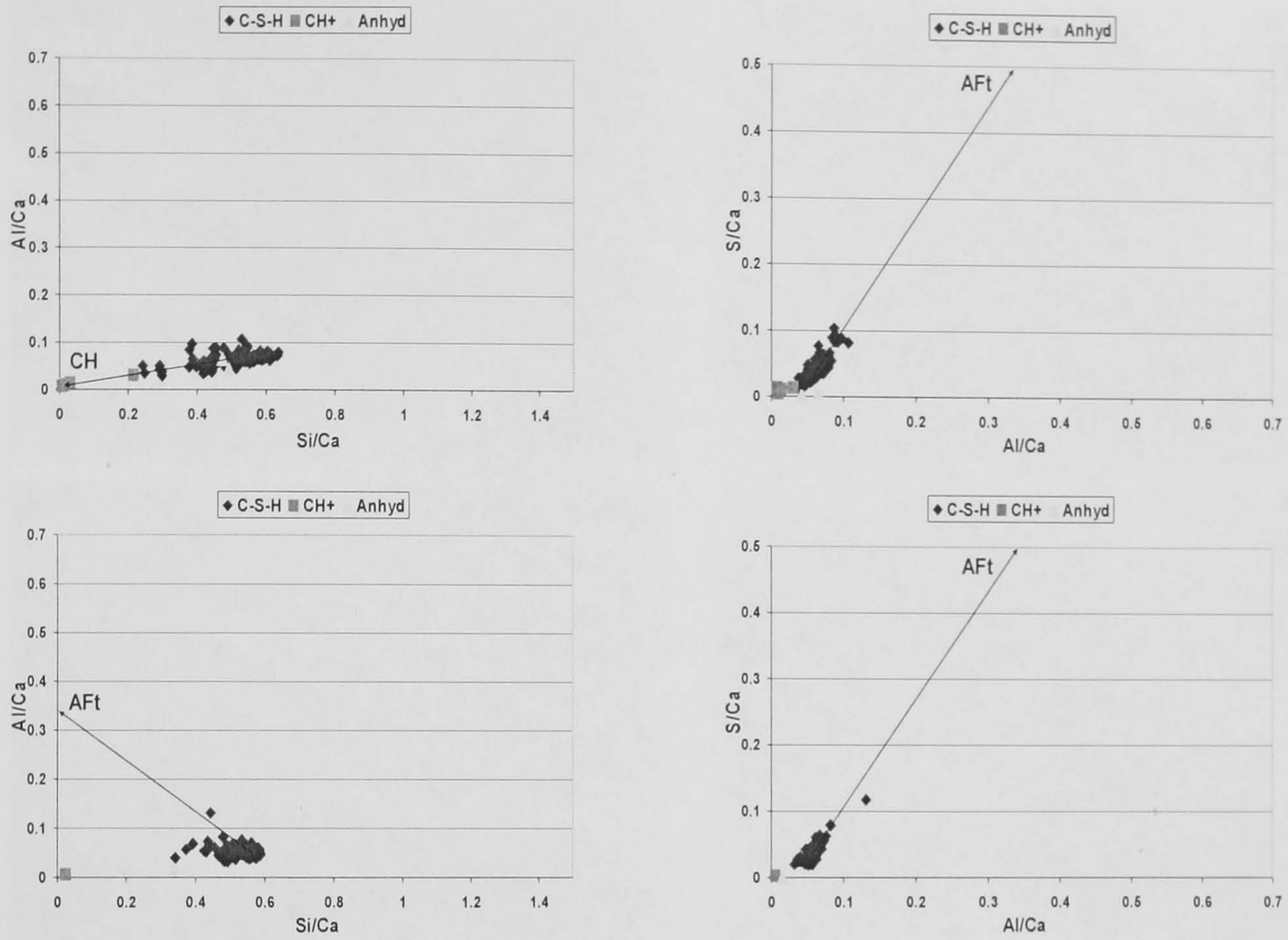


**Figure C12** – Al/Ca against Si/Ca (left) and S/Ca against Al/Ca (right) atomic ratio plots for the SEM-EDX phase analysis of the water activated WPC paste after 1 day (upper plots) and 1 month (lower plots) of hydration at 55°C.

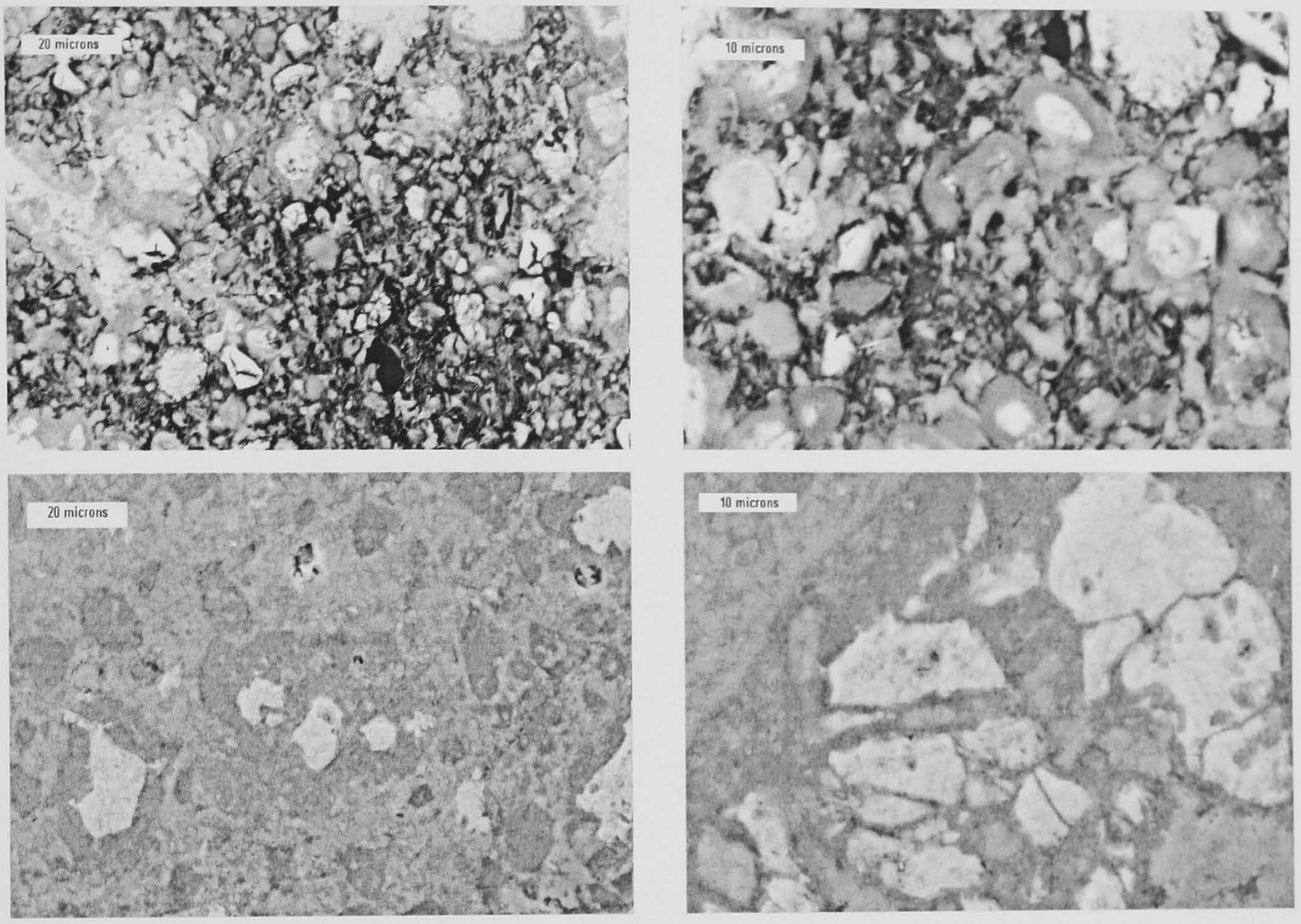


**Figure C13** – Backscattered electron images showing typical regions in the KOH activated WPC paste after 1 day (upper images) and 1 month (lower images) of hydration at 55°C.

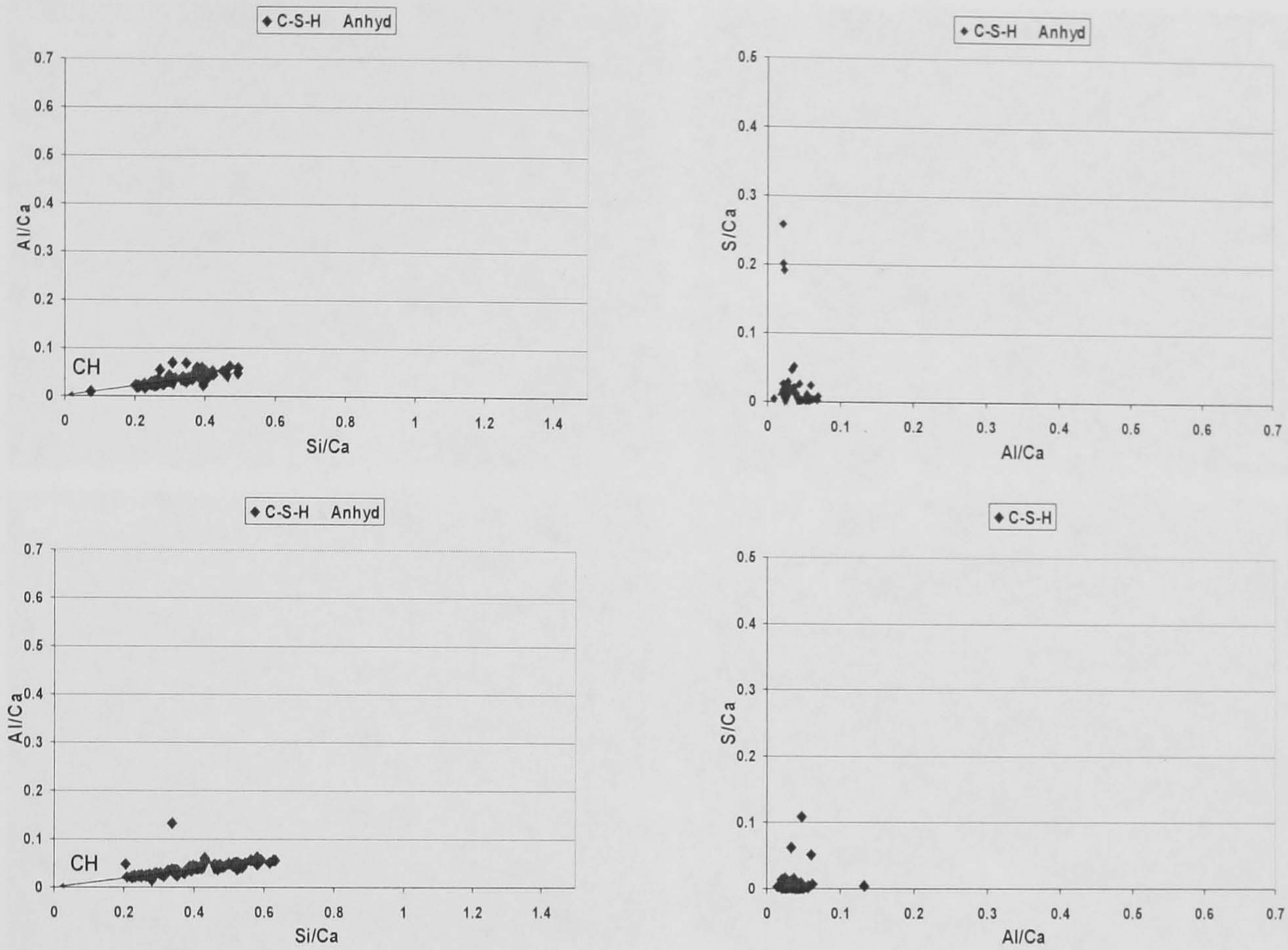


**Figure C14** – Al/Ca against Si/Ca (left) and S/Ca against Al/Ca (right) atomic ratio plots for the SEM-EDX phase analysis of the KOH activated WPC paste after 1 day (upper plots) and 1 month (lower plots) of hydration at 55°C.

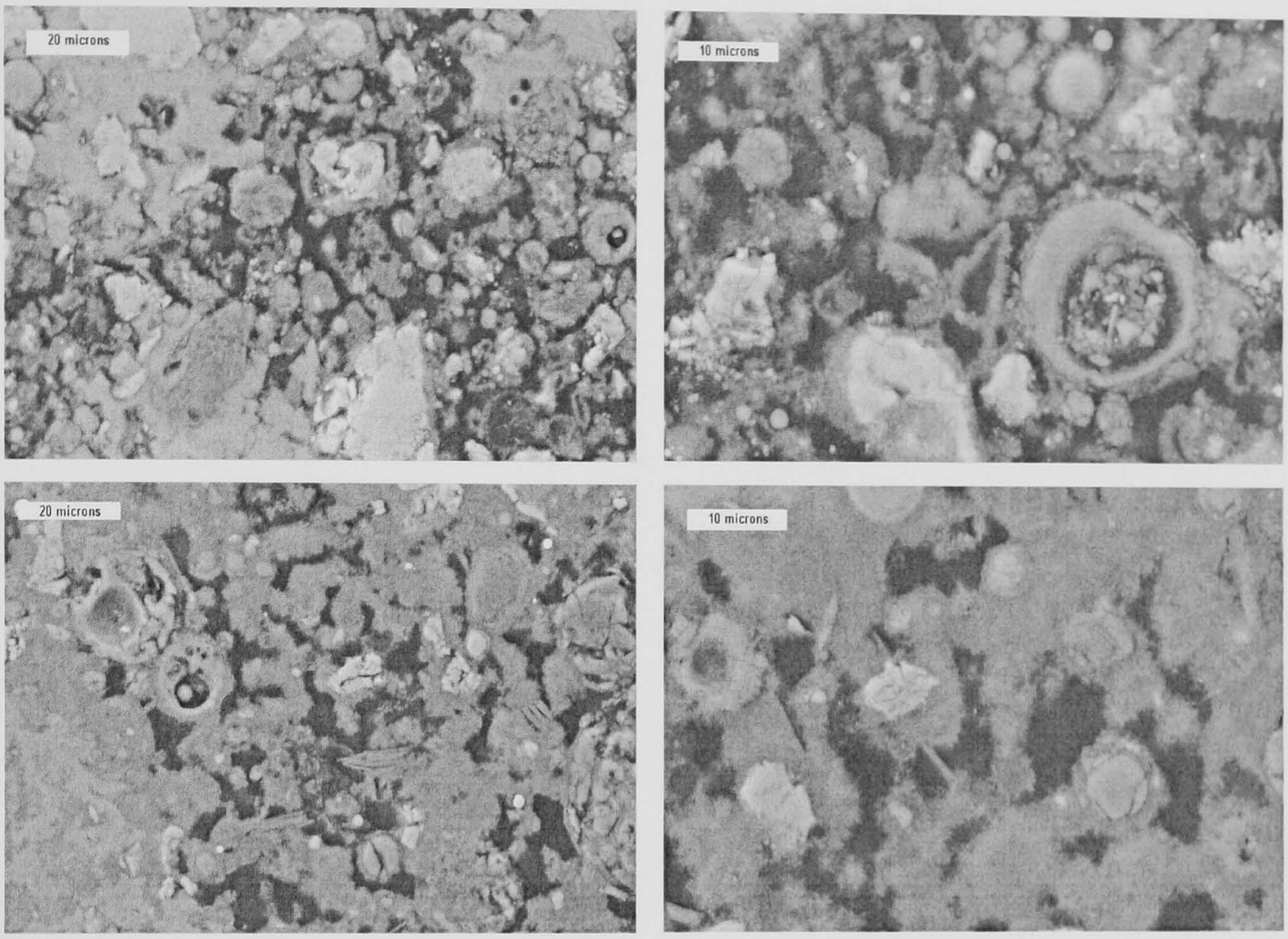


**Figure C15** – Backscattered electron images showing typical regions in the water activated 30% PFA blended paste after 1 day (upper images) and 1 month (lower images) of hydration at 55°C.

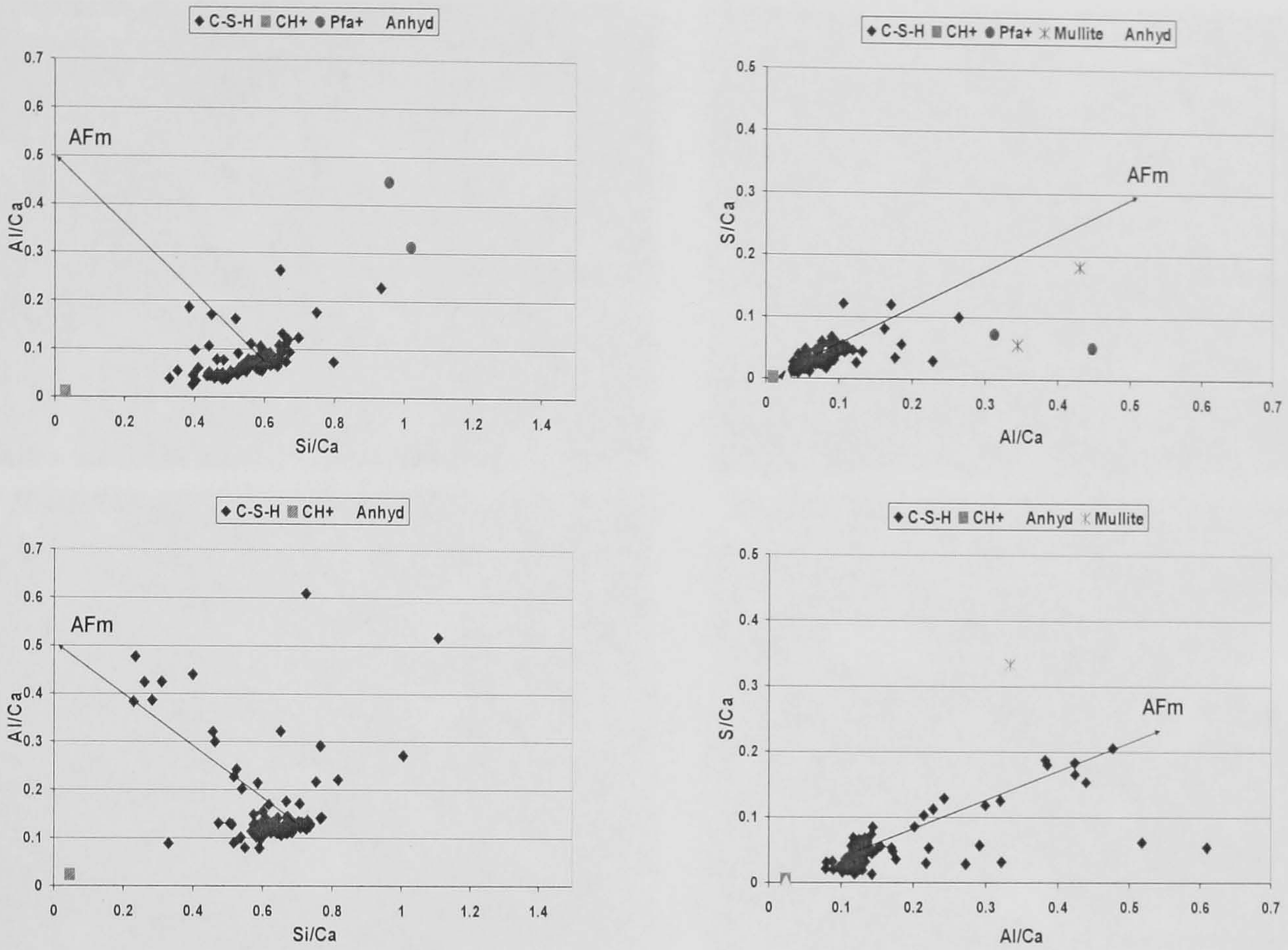


**Figure C16** – Al/Ca against Si/Ca (left) and S/Ca against Al/Ca (right) atomic ratio plots for the SEM-EDX phase analysis of the water activated 30% PFA blended paste after 1 day (upper plots) and 1 month (lower plots) of hydration at 55°C.

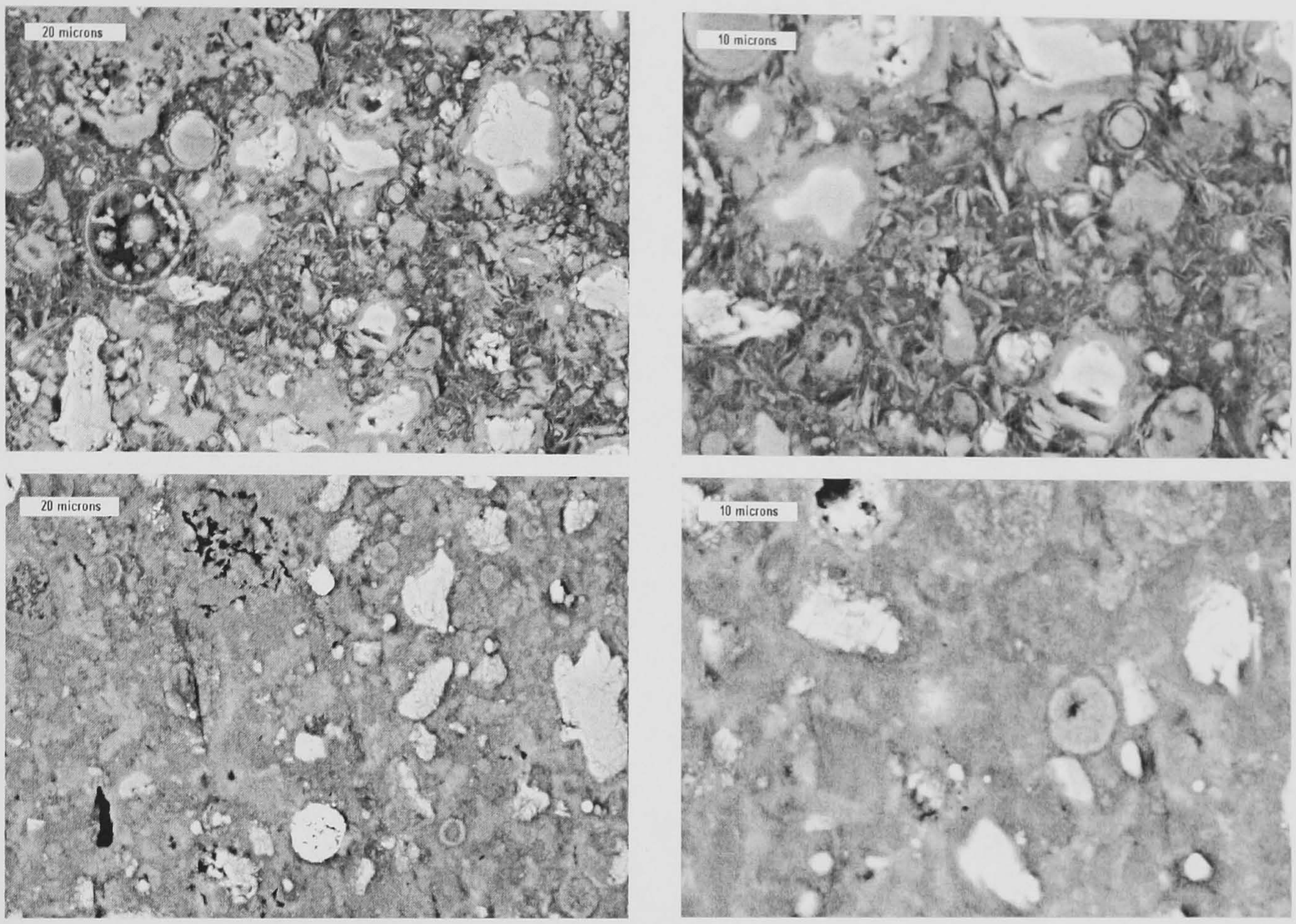


**Figure C17** – Backscattered electron images showing typical regions in the KOH activated 30% PFA blended paste after 1 day (upper images) and 1 month (lower images) of hydration at 55°C.

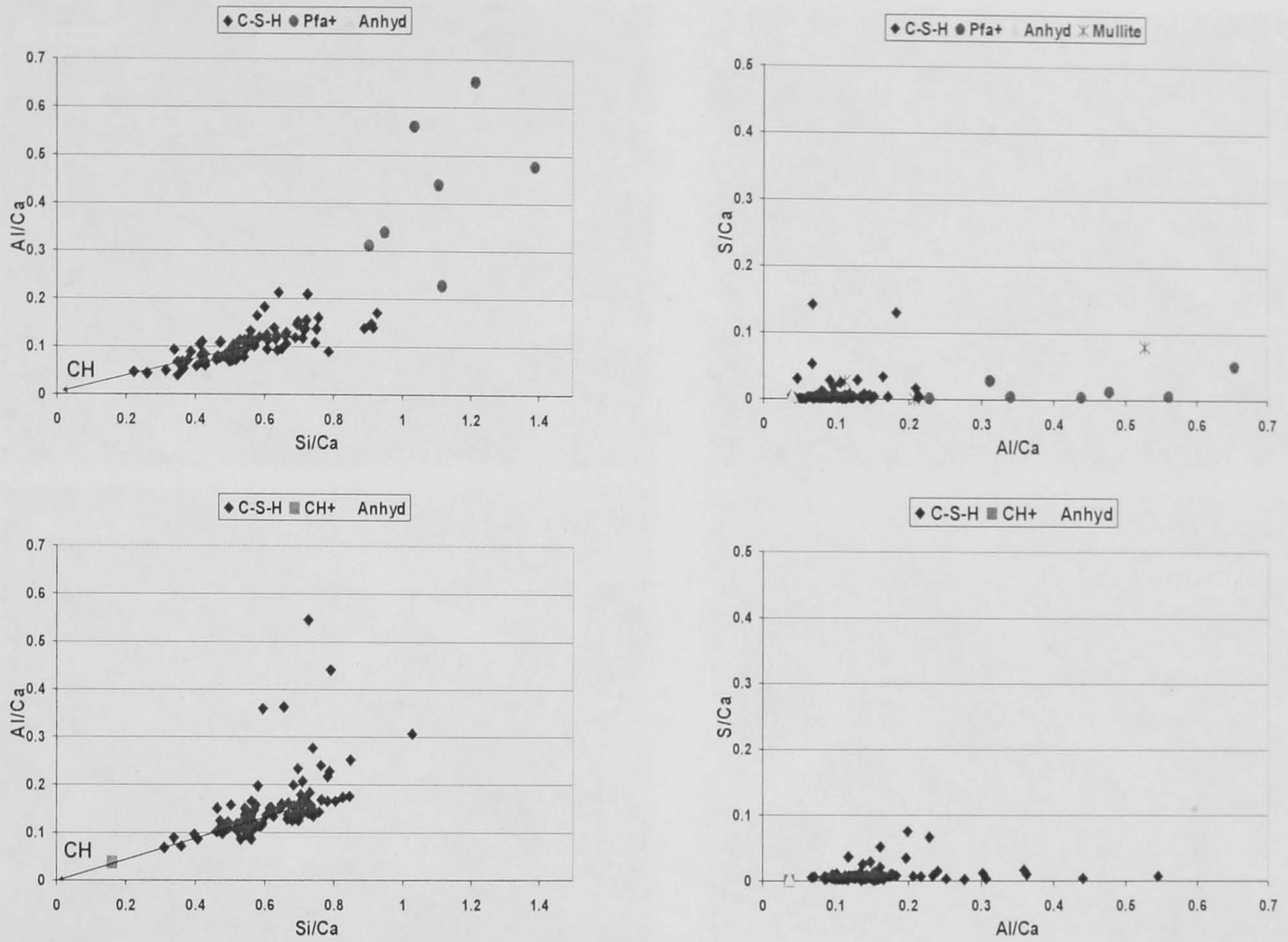


**Figure C18** – Al/Ca against Si/Ca (left) and S/Ca against Al/Ca (right) atomic ratio plots for the SEM-EDX phase analysis of the KOH activated 30% PFA blended paste after 1 day (upper plots) and 1 month (lower plots) of hydration at 55°C.

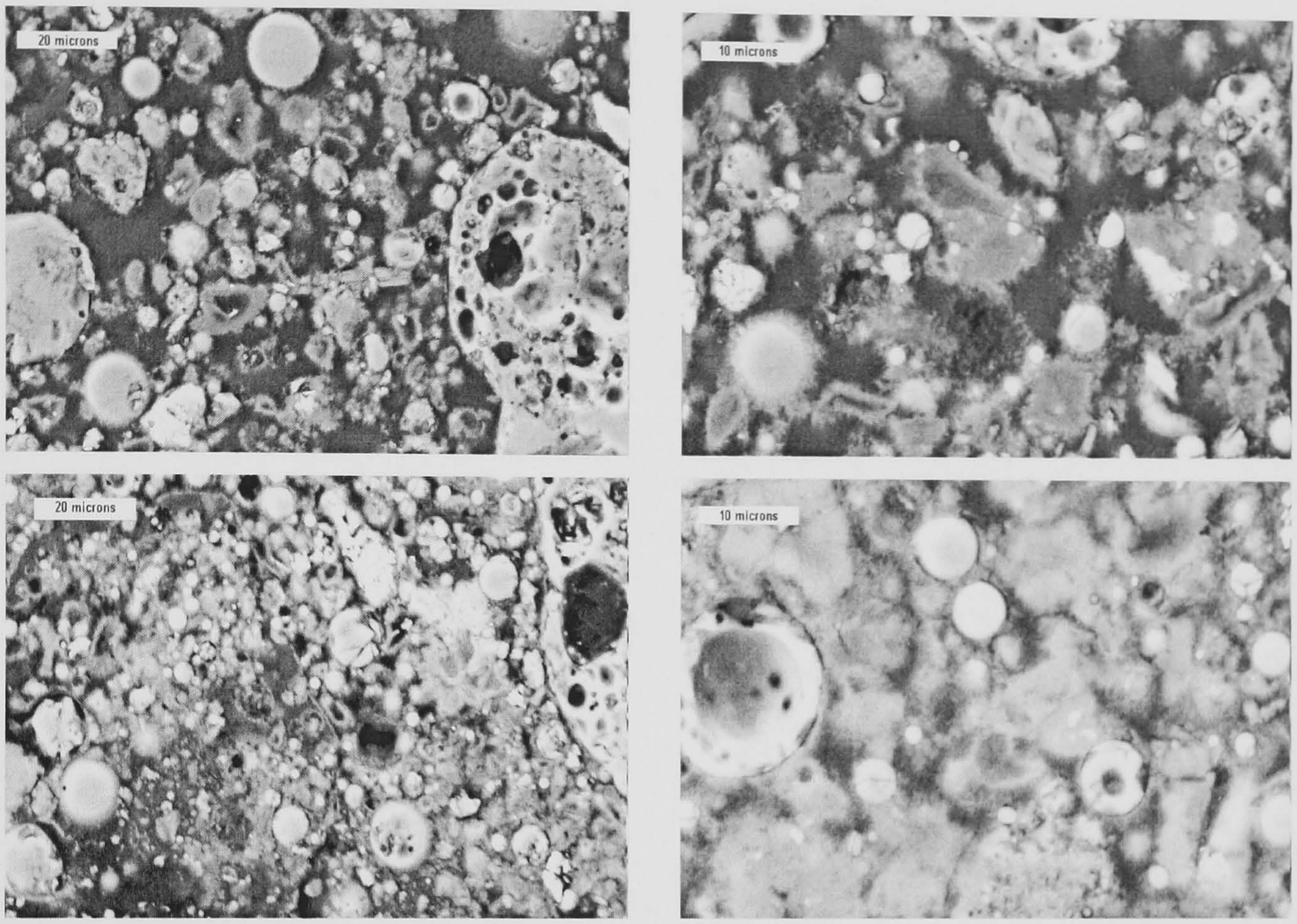


**Figure C19** – Backscattered electron images showing typical regions in the water activated 60% PFA blended paste after 1 day (upper images) and 1 month (lower images) of hydration at 55°C.

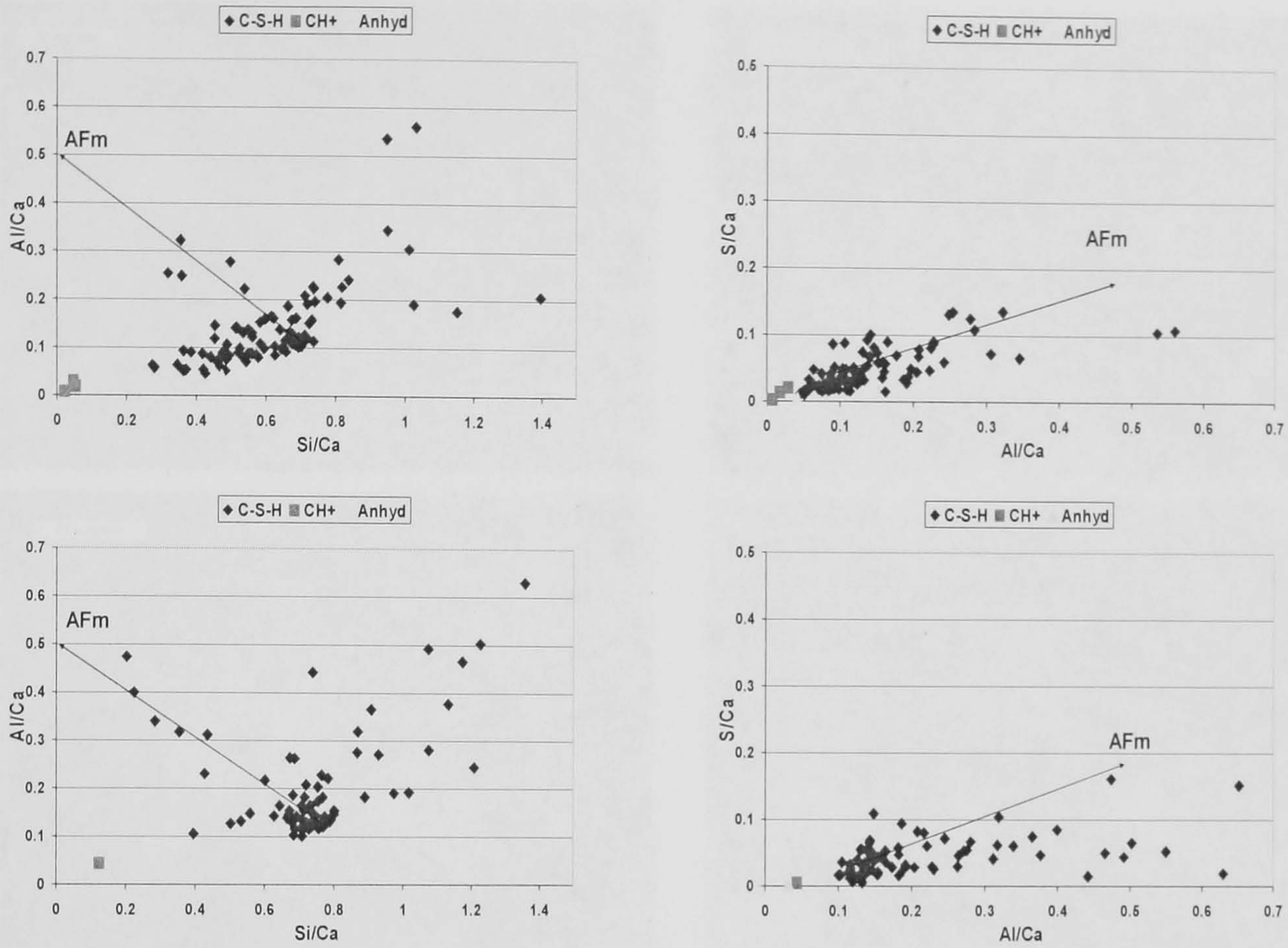


**Figure C20** – Al/Ca against Si/Ca (left) and S/Ca against Al/Ca (right) atomic ratio plots for the SEM-EDX phase analysis of the water activated 60% PFA blended paste after 1 day (upper plots) and 1 month (lower plots) of hydration at 55°C.

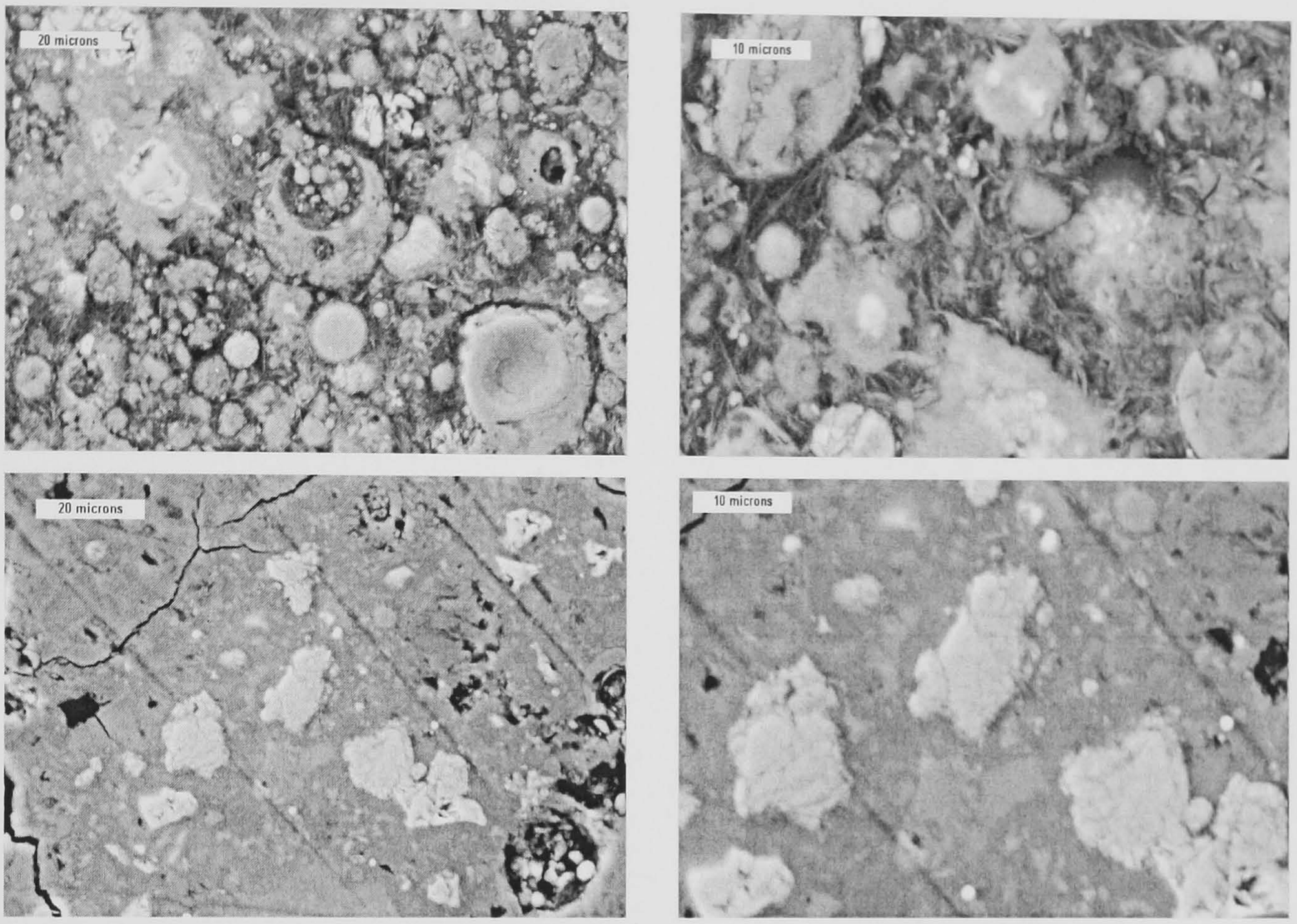


**Figure C21** – Backscattered electron images showing typical regions in the KOH activated 60% PFA blended paste after 1 day (upper images) and 1 month (lower images) of hydration at 55°C.

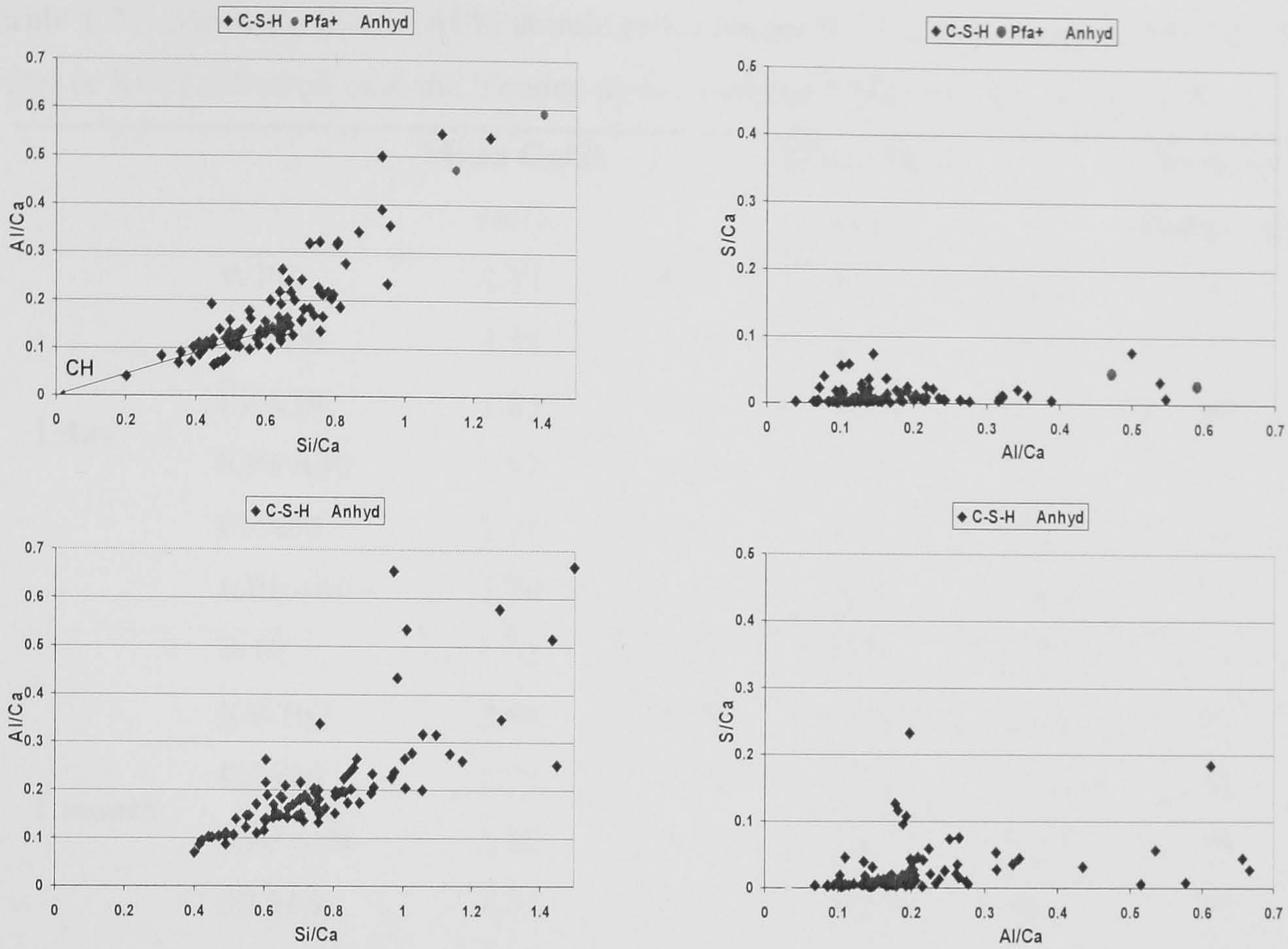


**Figure C22** – Al/Ca against Si/Ca (left) and S/Ca against Al/Ca (right) atomic ratio plots for the SEM-EDX phase analysis of the KOH activated 30% PFA blended paste after 1 day (upper plots) and 1 month (lower plots) of hydration at 55°C.

**Table C2** – Mean Ca/Si and Al/Si atomic ratios obtained for C-S-H using SEM-EDX, for the water or KOH activated neat and blended pastes, cured at 55°C for 1 day and 1 month.

| | | Mean Ca/Si ratio | *s* | Mean Al/Si ratio | *s* | Number Analysis (N) |
|---|---|---|---|---|---|---|
| **1 day** | **WPC** | 2.12 | 0.51 | 0.13 | 0.03 | 82 |
| | **KWPC** | 3.45 | 1.38 | 0.11 | 0.03 | 74 |
| | **PFA30** | 1.83 | 0.39 | 0.15 | 0.09 | 86 |
| | **KPFA30** | 1.92 | 0.63 | 0.19 | 0.04 | 84 |
| | **PFA60** | 1.71 | 0.65 | 0.26 | 0.17 | 98 |
| | **KPFA60** | 1.70 | 0.61 | 0.27 | 0.10 | 96 |
| **1 month** | **WPC** | 1.93 | 0.20 | 0.11 | 0.03 | 99 |
| | **KWPC** | 2.66 | 0.79 | 0.10 | 0.04 | 90 |
| | **PFA30** | 1.73 | 0.60 | 0.33 | 0.35 | 89 |
| | **KPFA30** | 1.62 | 0.42 | 0.27 | 0.17 | 96 |
| | **PFA60** | 1.31 | 0.77 | 0.36 | 0.33 | 87 |
| | **KPFA60** | 1.38 | 0.43 | 0.27 | 0.09 | 94 |

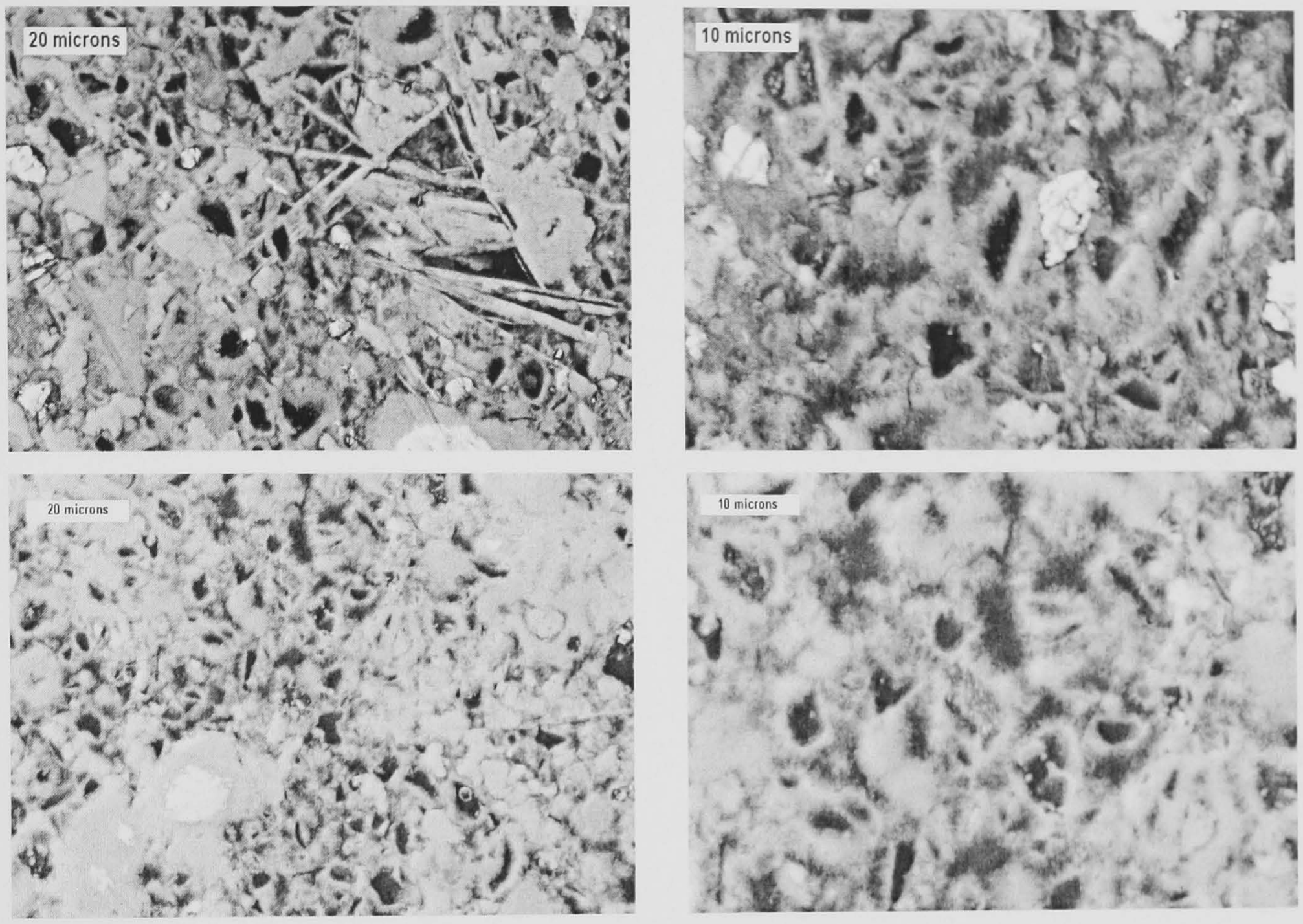


**Figure C24** – Backscattered electron images showing typical regions in the water activated WPC paste after 1 day (upper images) and 1 month (lower images) of hydration at 85°C.

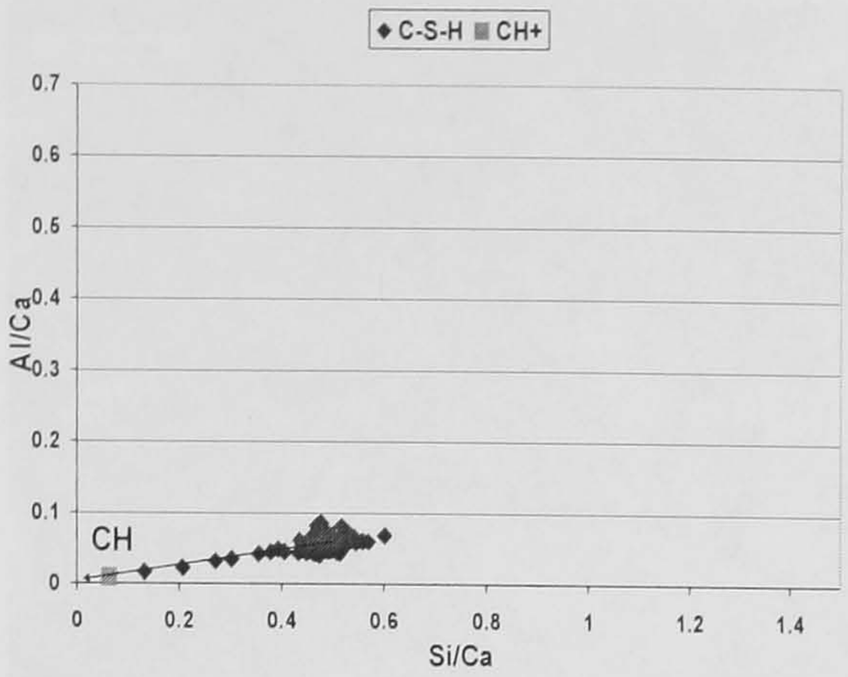


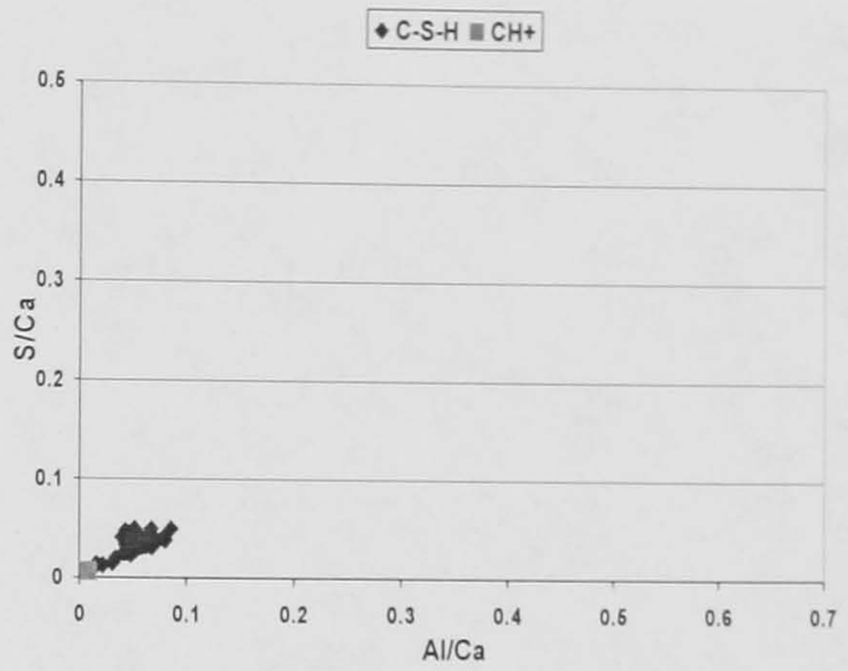


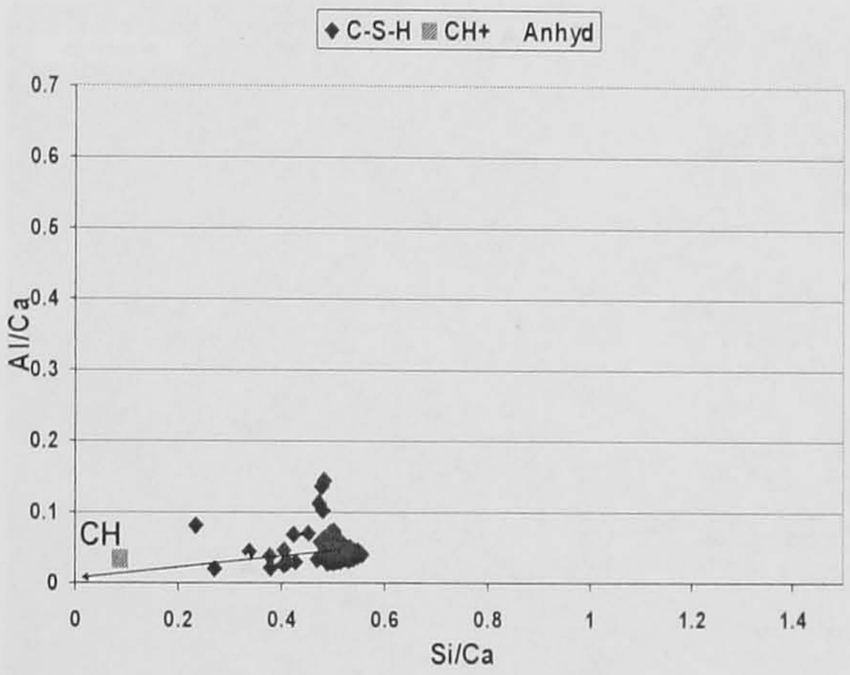


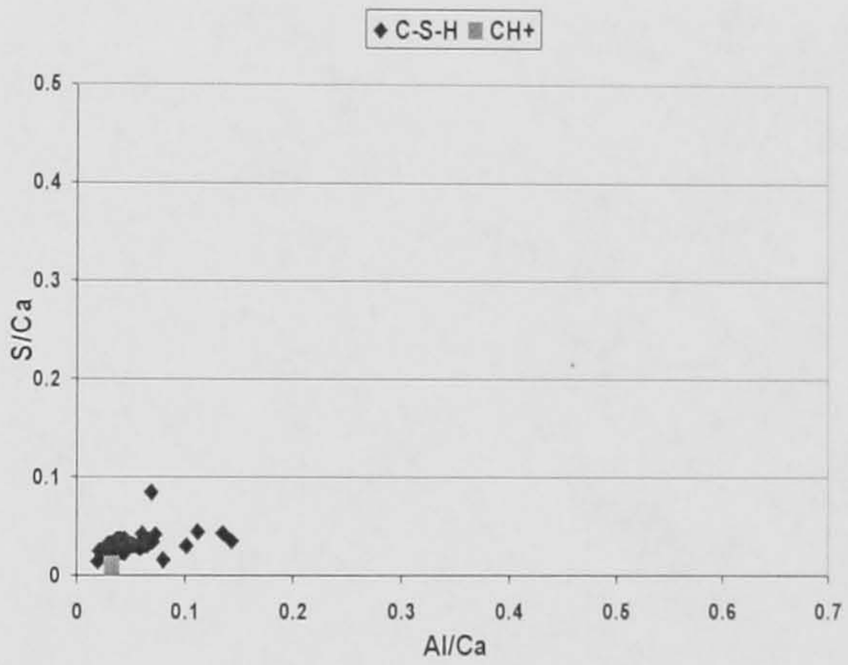


**Figure C25** – Al/Ca against Si/Ca (right) and S/Ca against Al/Ca (left) atomic ratio plots for the SEM-EDX phase analysis of the water activated WPC paste after 1 day (upper plots) and 1 month (lower plots) of hydration at 85°C.

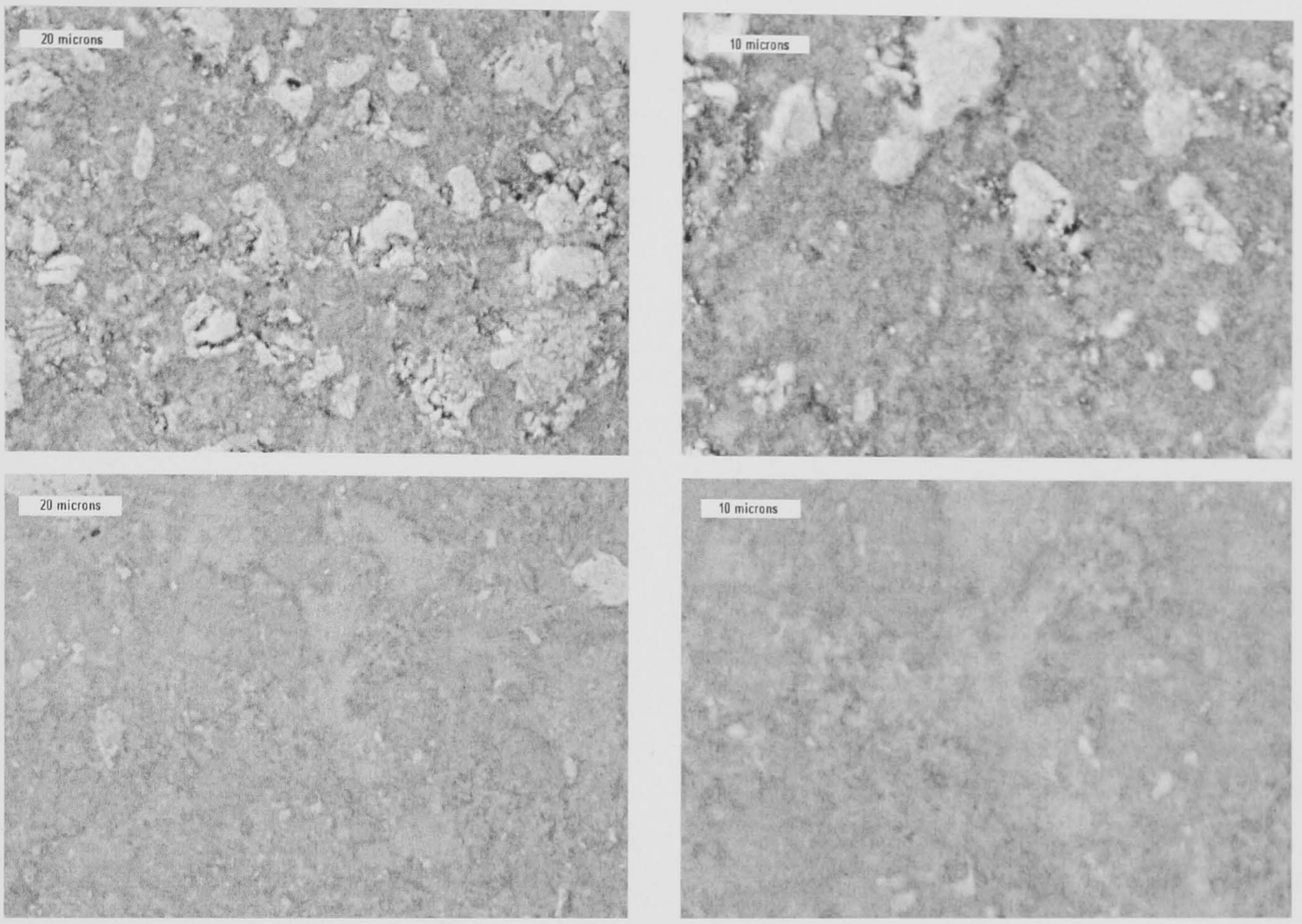


**Figure C26** – Backscattered electron images showing typical regions in the KOH activated WPC paste after 1 day (upper images) and 1 month (lower images) of hydration at 85°C.

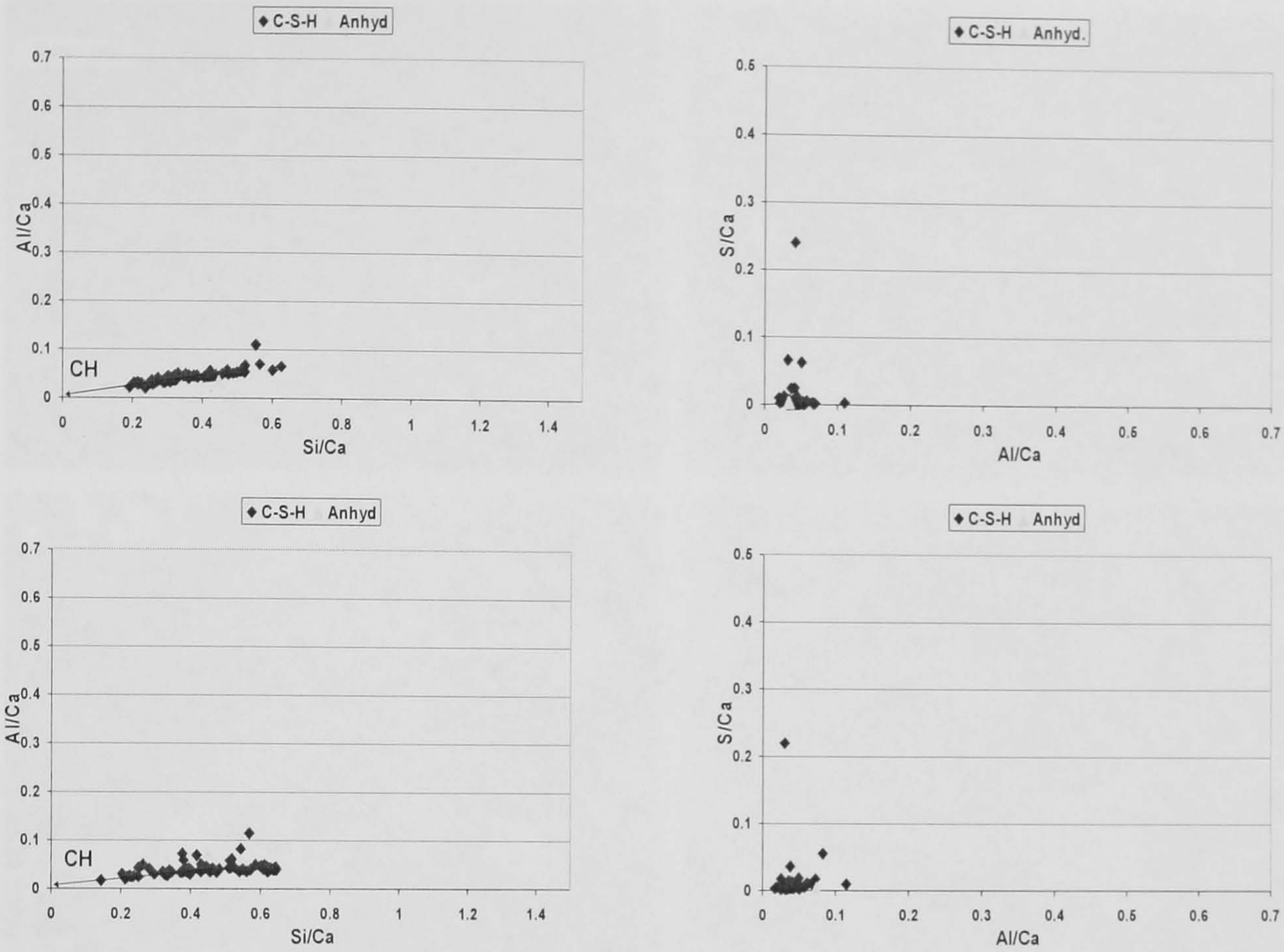


**Figure C27** – Al/Ca against Si/Ca (right) and S/Ca against Al/Ca (left) atomic ratio plots for the SEM-EDX phase analysis of the KOH activated WPC paste after 1 day (upper plots) and 1 month (lower plots) of hydration at 85°C.

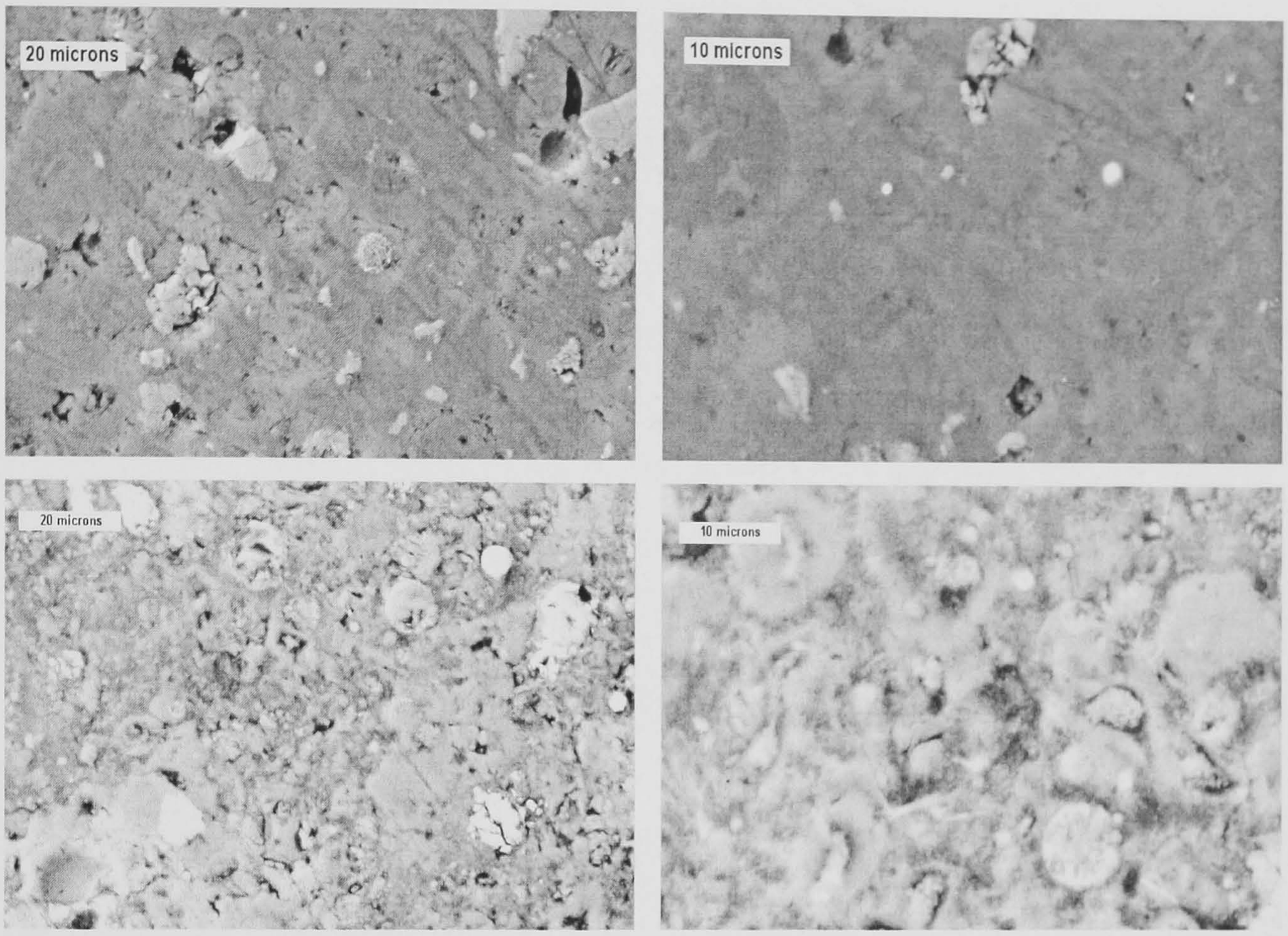


**Figure C28** – Backscattered electron images showing typical regions in the water activated 30% PFA blended paste after 1 day (upper images) and 1 month (lower images) of hydration at 85°C.

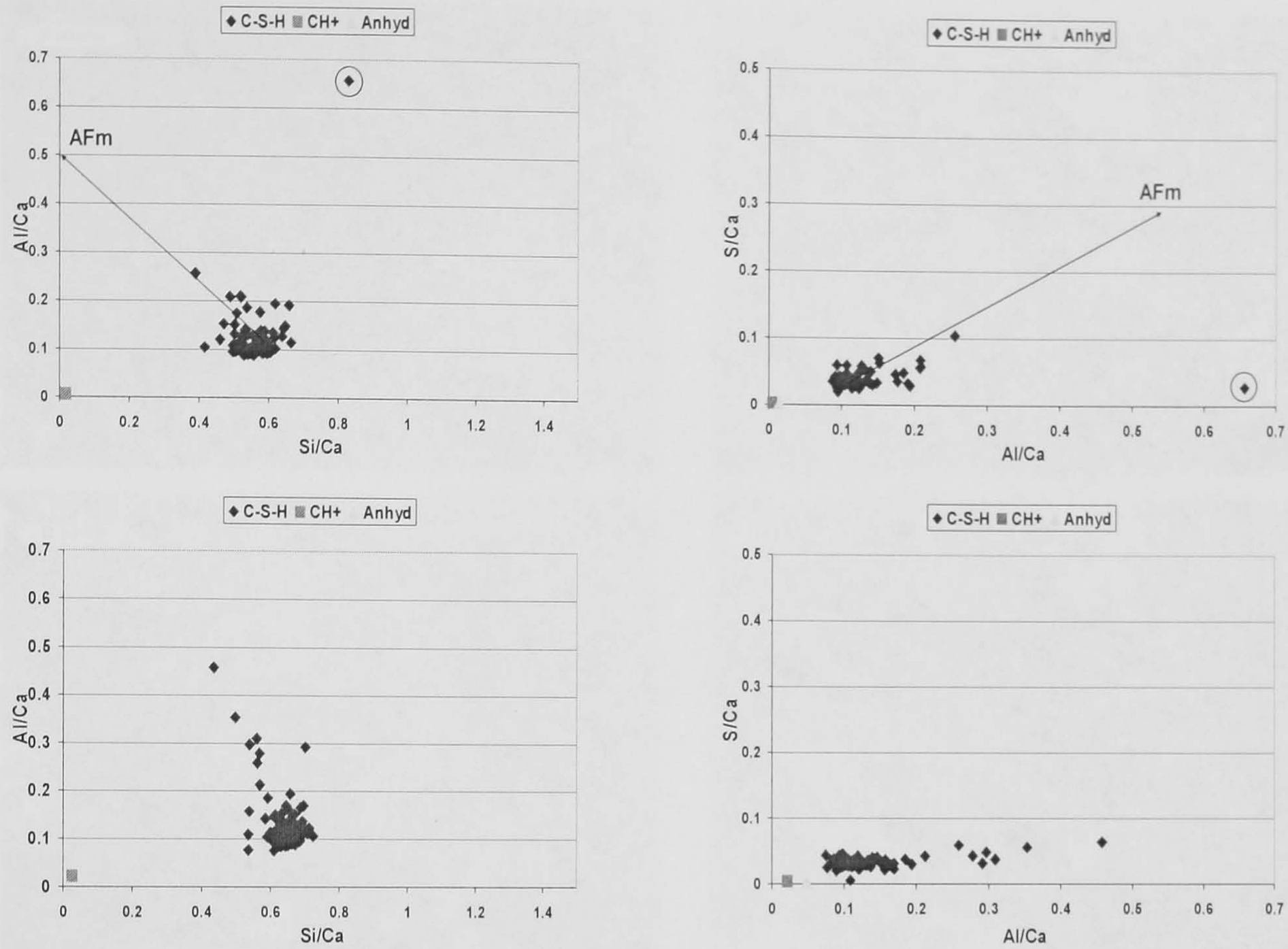


**Figure C29** – Al/Ca against Si/Ca (right) and S/Ca against Al/Ca (left) atomic ratio plots for the SEM-EDX phase analysis of the water activated 30% PFA blended paste after 1 day (upper plots) and 1 month (lower plots) of hydration at 85°C.

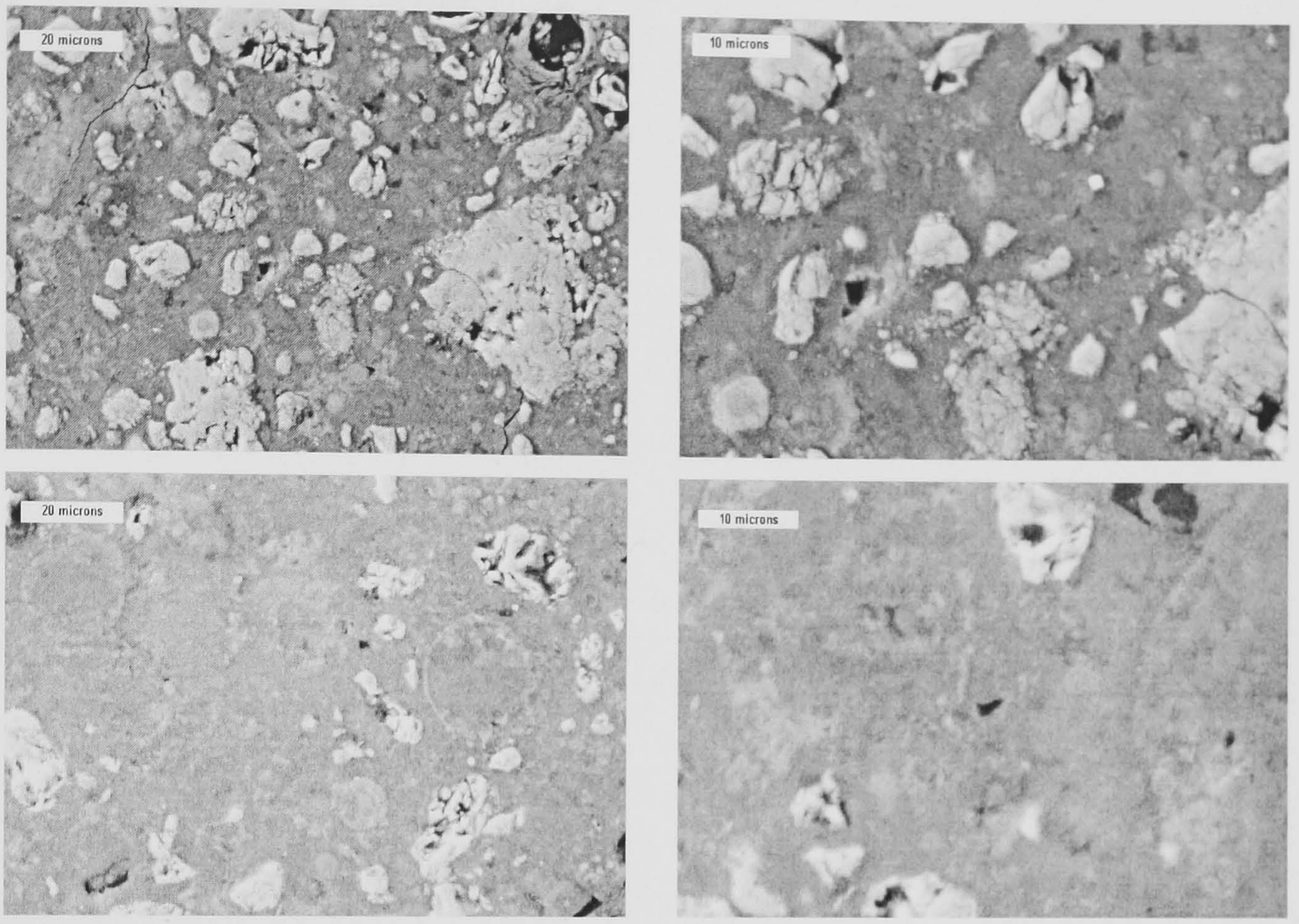


**Figure C30** – Backscattered electron images showing typical regions in the KOH activated 30% PFA blended paste after 1 day (upper images) and 1 month (lower images) of hydration at 85°C.

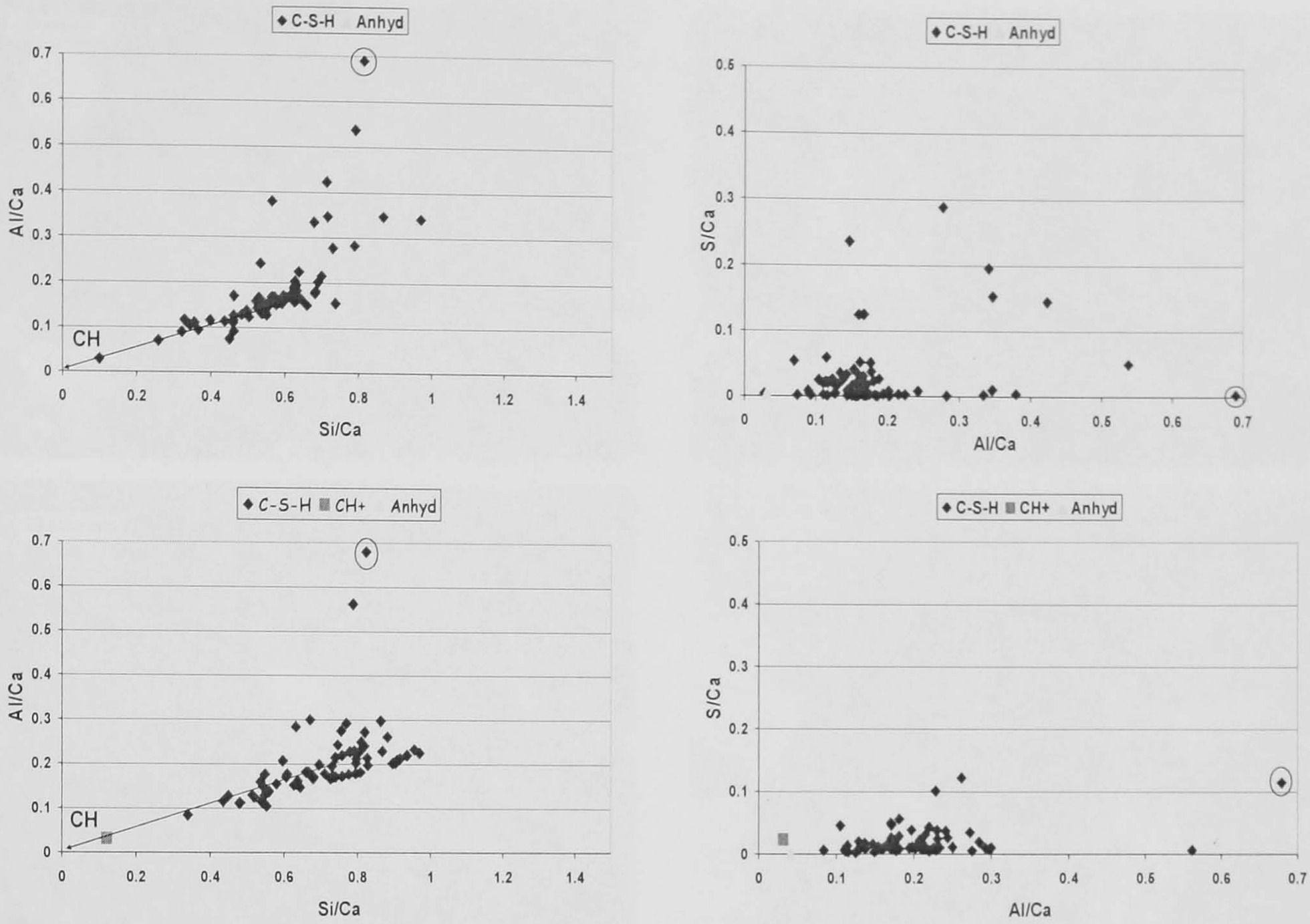


**Figure C31** – Al/Ca against Si/Ca (right) and S/Ca against Al/Ca (left) atomic ratio plots for the SEM-EDX phase analysis of the KOH activated 30% PFA blended paste after 1 day (upper plots) and 1 month (lower plots) of hydration at 85°C.

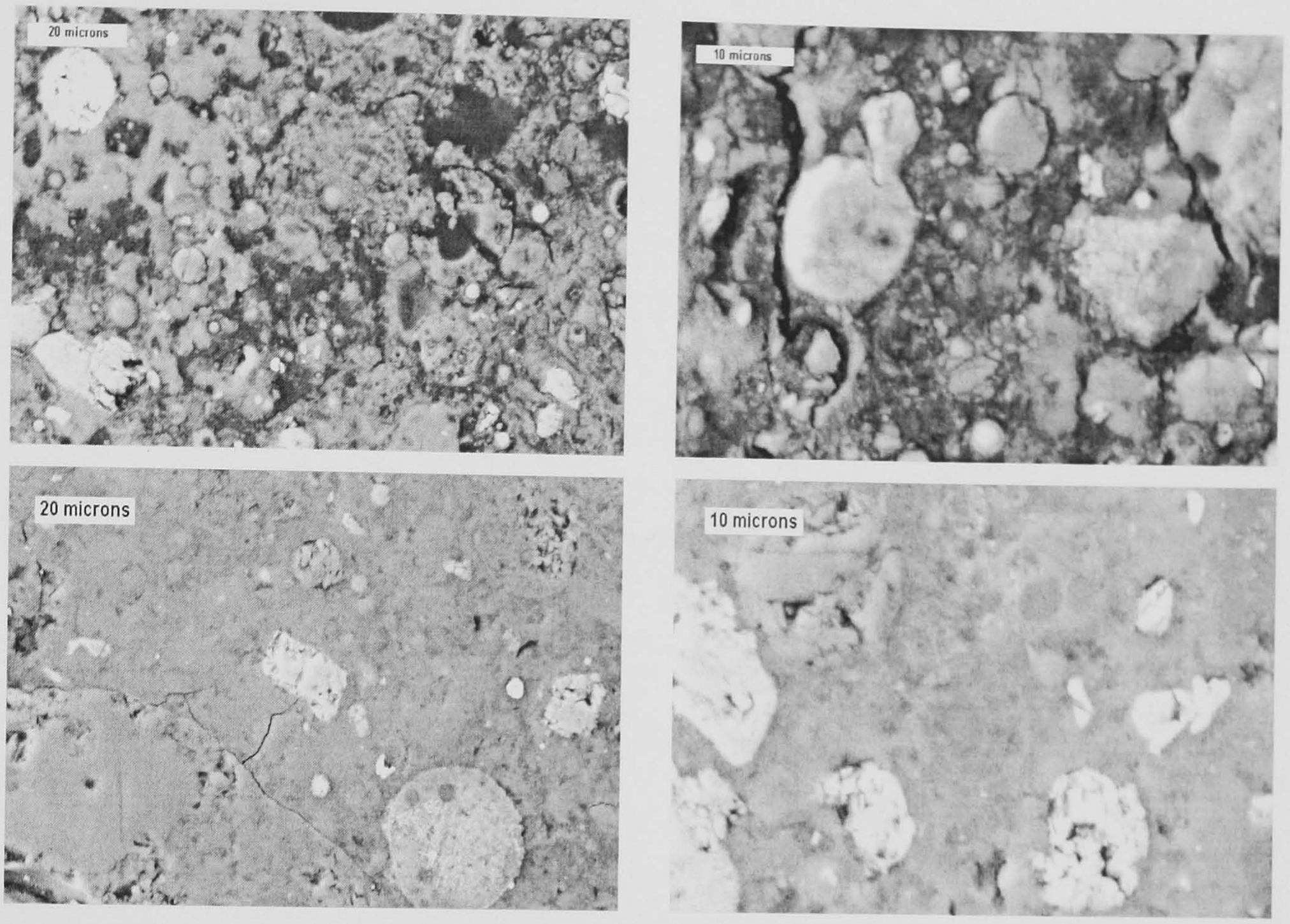


**Figure C32** – Backscattered electron images showing typical regions in the water activated 60% PFA blended paste after 1 day (upper images) and 1 month (lower images) of hydration at 85°C.

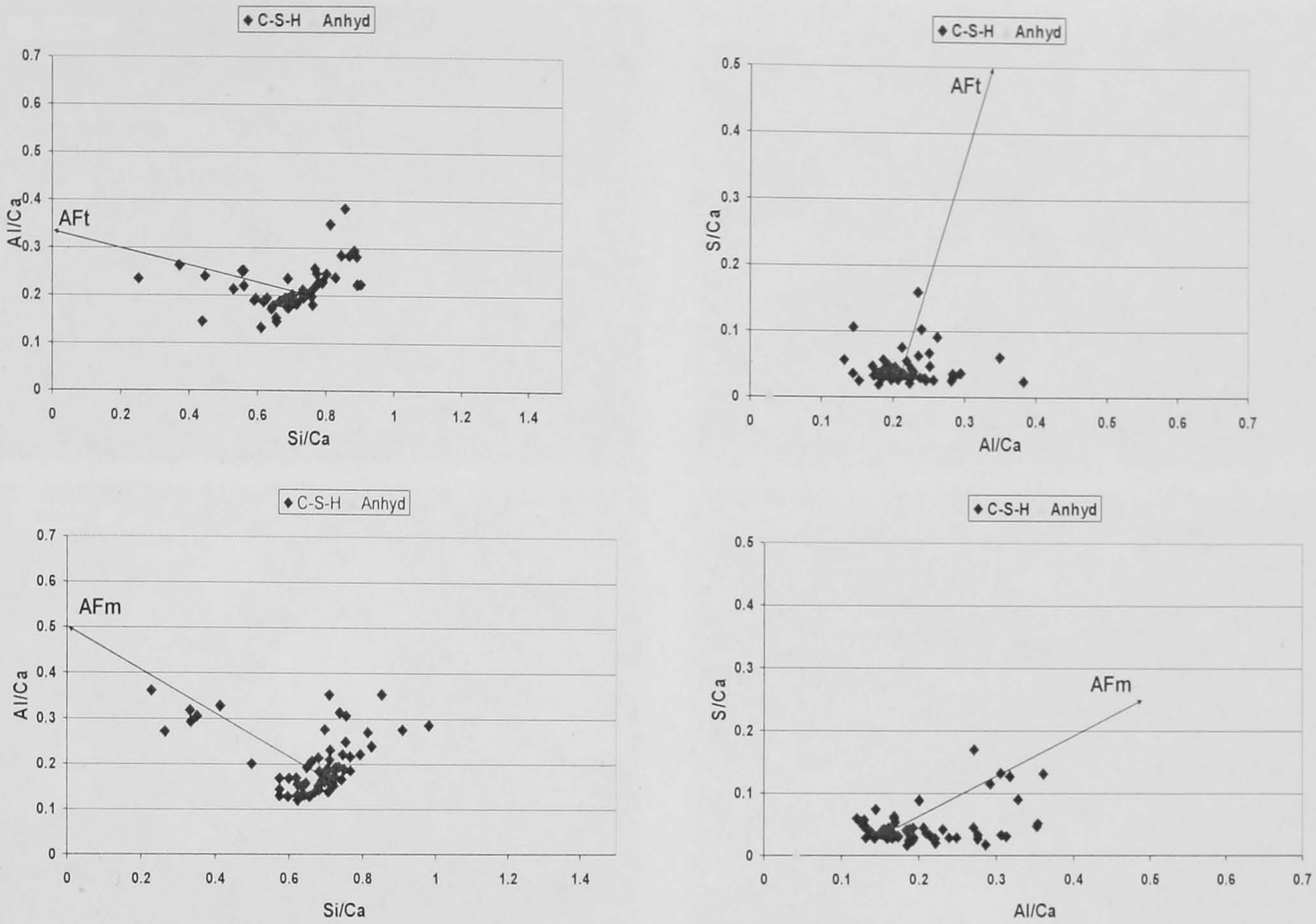


**Figure C33** – Al/Ca against Si/Ca (right) and S/Ca against Al/Ca (left) atomic ratio plots for the SEM-EDX phase analysis of the water activated 60% PFA blended paste after 1 day (upper plots) and 1 month (lower plots) of hydration at 85°C.

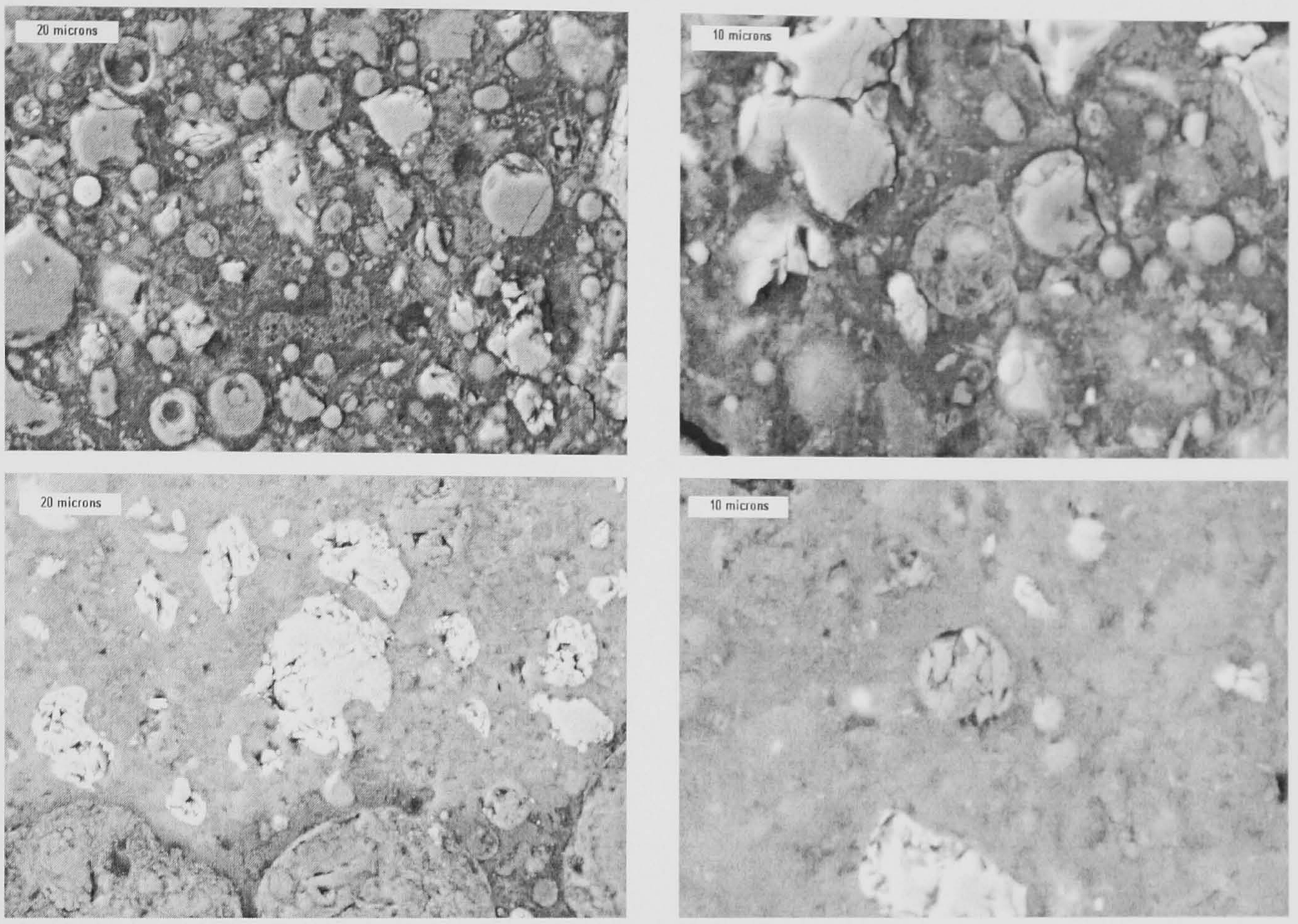


**Figure C34** – Backscattered electron images showing typical regions in the KOH activated 60% PFA blended paste after 1 day (upper images) and 1 month (lower images) of hydration at 85°C.

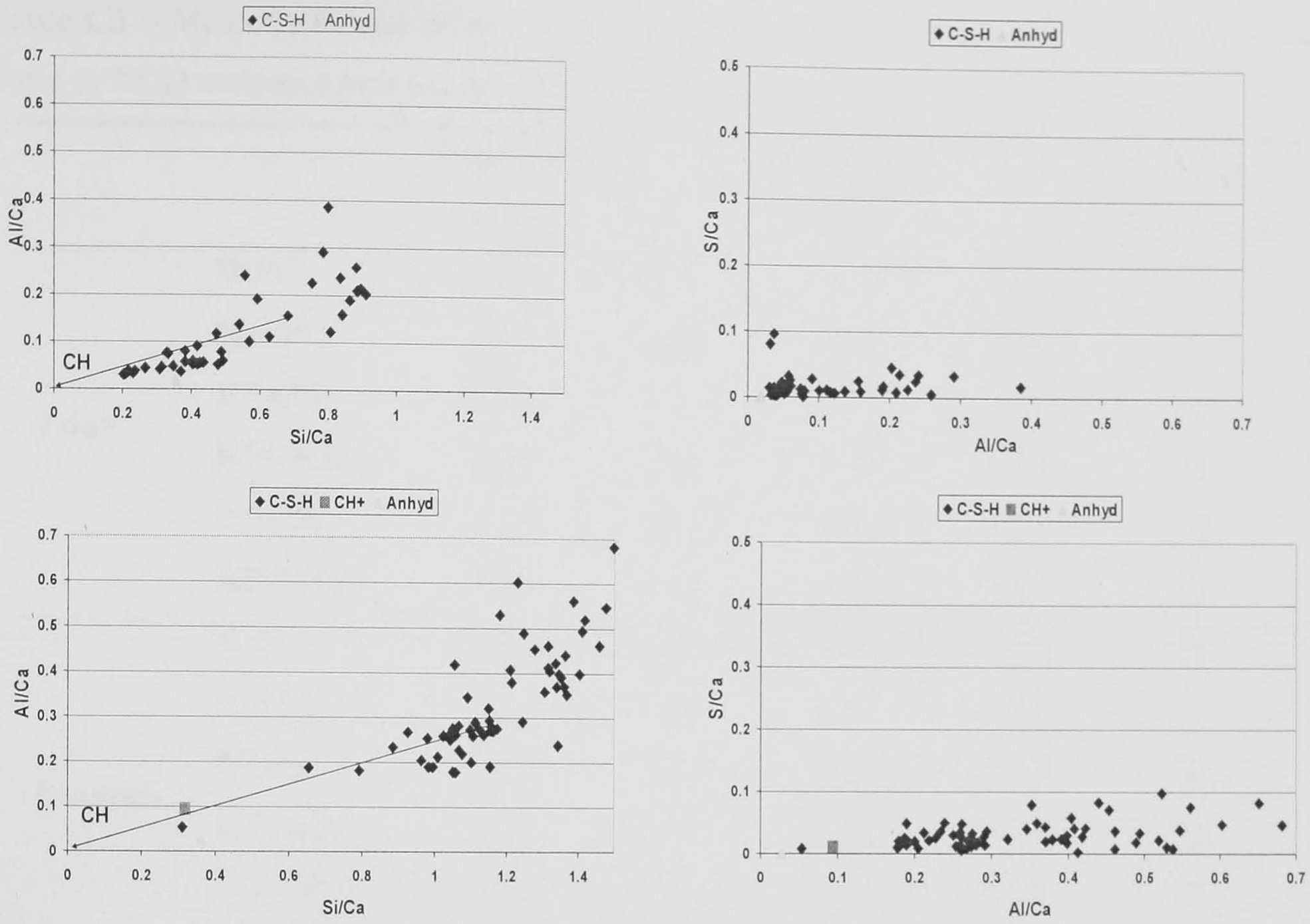


**Figure C35** – Al/Ca against Si/Ca (right) and S/Ca against Al/Ca (left) atomic ratio plots for the SEM-EDX phase analysis of the KOH activated 60% PFA blended paste after 1 day (upper plots) and 1 month (lower plots) of hydration at 85°C.

**Table C3** – Mean Ca/Si and Al/Si atomic ratios obtained for C-S-H using SEM-EDX, for the water or KOH activated neat and blended pastes, cured at 85°C for 1 day and 1 month.

| | | Mean Ca/Si ratio | *s* | Mean Al/Si ratio | *s* | Number Analysis (N) |
|---|---|---|---|---|---|---|
| **1 day** | **WPC** | 2.20 | 0.74 | 0.11 | 0.02 | 78 |
| | **KWPC** | 3.03 | 0.80 | 0.12 | 0.02 | 70 |
| | **PFA30** | 1.80 | 0.20 | 0.24 | 0.14 | 76 |
| | **KPFA30** | 1.93 | 1.09 | 0.34 | 0.17 | 72 |
| | **PFA60** | 1.52 | 0.46 | 0.33 | 0.12 | 50 |
| | **KPFA60** | 2.39 | 1.12 | 0.20 | 0.08 | 42 |
| **1 month** | **WPC** | 2.08 | 0.37 | 0.10 | 0.05 | 78 |
| | **KWPC** | 2.65 | 1.03 | 0.10 | 0.03 | 71 |
| | **PFA30** | 1.58 | 0.15 | 0.24 | 0.18 | 76 |
| | **KPFA30** | 1.48 | 0.35 | 0.28 | 0.10 | 66 |
| | **PFA60** | 1.63 | 0.60 | 0.35 | 0.25 | 60 |
| | **KPFA60** | 1.55 | 0.83 | 0.24 | 0.03 | 10 |